

**The Galaxy Environment of
Quasars in the Clowes-Campusano
Large Quasar Group**

Christopher Paul Haines

A thesis submitted in partial fulfilment
of the requirements for the degree of
Doctor of Philosophy.

Centre for Astrophysics
Department of Physics, Astronomy and Mathematics
University of Central Lancashire

June 2001

Declaration

The work presented in this thesis was carried out in the Department of Physics, Astronomy and Mathematics, University of Central Lancashire. Unless otherwise stated it is the original work of the author.

While registered for the degree of Doctor of Philosophy, the author has not been a registered candidate for another award of the University. This thesis has not been submitted in whole, or in part, for any other degree.

Christopher Haines

June 2001

Abstract

Quasars have been used as efficient probes of high-redshift galaxy clustering as they are known to favour overdense environments. Quasars may also trace the large-scale structure of the early universe ($0.4 \lesssim z \lesssim 2$) in the form of Large Quasar Groups (LQGs), which have comparable sizes ($\sim 100\text{--}200 h^{-1}\text{Mpc}$) to the largest structures seen at the present epoch.

This thesis describes an ultra-deep, wide-field optical study of a region containing three quasars from the largest known LQG, the Clowes-Campusano LQG of at least 18 quasars at $z \simeq 1.3$, to examine their galaxy environments and to find indications of any associated large-scale structure in the form of galaxies.

The optical data were obtained using the Big Throughput Camera (BTC) on the 4-m Blanco telescope at the Cerro Tololo Interamerican Observatory (CTIO) over two nights in April 1998, resulting in ultra-deep V , I imaging of a 40.6×34.9 arcmin² field centred at $10^{\text{h}}47^{\text{m}}30^{\text{s}}$, $+05^{\circ}30'00''$ containing three quasars from the LQG as well as four quasars at higher redshifts. The final catalogues contain $\approx 10^5$ sources and are 50% complete to $V \simeq 26.35$ and $I \simeq 25.85$ in the fully exposed areas.

The Cluster Red Sequence method of Gladders & Yee (2000) is used to identify and characterise galaxy clusters in the BTC field. The method is motivated by the observation that the bulk of early-type galaxies in all rich clusters lie along a tight, linear colour-magnitude relation — the cluster red sequence — which evolves with redshift, allowing the cluster redshift to be estimated from the colour of the red sequence. The method is applied to the detection of high-redshift clusters in the BTC field through the selection of galaxies redder than the expected colour of the $z = 0.5$ red sequence. A 2σ excess of these red galaxies is found in the BTC field in comparison to the 27 arcmin^2 EIS-DEEP HDF-South field. These galaxies are shown from the EIS-DEEP $UBVRIZJK$, photometry to be early-type galaxies at $0.7 \lesssim z \lesssim 1.5$. This excess, corresponding to ≈ 1000 extra red galaxies over the BTC field, along with the 3σ excess of MgII absorbers observed at $1.2 < z < 1.3$ (Williger et al., 2000), supports the hypothesis that the Clowes-Campusano LQG traces a large-scale structure in the form of galaxies at $z \simeq 1.3$.

Four high-redshift cluster candidates are found, one of which is confirmed by

additional K data to be at $z = 0.8 \pm 0.1$. Two of the high-redshift clusters are associated with quasars: the $z = 1.426$ quasar is located on the periphery of a cluster of $V - I \simeq 3$ galaxies; and the $z = 1.226$ LQG quasar is found within a large-scale structure of 100–150 red galaxies extending over $2\text{--}3h^{-1}\text{Mpc}$. Additional K imaging confirms their association with the quasar, with red sequences at $V - K \simeq 6.9$ and $I - K \simeq 4.3$ indicating a population of 15–18 massive ellipticals at $z = 1.2 \pm 0.1$ that are concentrated in two groups on either side of the quasar.

The four $z \simeq 1.3$ quasars in the BTC field are found in a wide variety of environments, from those indistinguishable from the field, to being associated with rich clusters, but are on average in overdense regions comparable to poor clusters. These results are similar to those of previous studies of quasars at these redshifts, and are consistent with the quasars being hosted by massive ellipticals which trace mass in the same biased manner. It is also notable how the quasars associated with clustering are located on the cluster peripheries rather than in the high-density cluster cores, a result which is initially surprising given that quasars are thought to be hosted by massive elliptical galaxies, but in retrospect can be understood in the framework of both galaxy interaction and galaxy formation quasar triggering mechanisms.

Contents

1	Introduction	1
1.1	Overview of the Thesis	1
1.2	The Standard Cosmological Model	2
1.3	Statistical Descriptors of Clustering	5
1.4	Structure Formation and Evolution	7
1.5	Large Scale Structure at Low Redshifts	11
1.6	Quasars — A Summary	14
1.7	The Galaxy Environments of Quasars	18
1.8	Quasar Clustering	21
1.9	Large Quasar Groups	25
1.9.1	The Webster LQG at $z \simeq 0.37$	25
1.9.2	The Crampton et al. LQG at $z \simeq 1.1$	26
1.9.3	The Clowes-Campusano LQG at $z \simeq 1.3$	31
1.9.4	Other Large Quasar Groups	32
2	Ultra-deep Imaging of the Clowes-Campusano Large Quasar Group	35
2.1	Introduction	35
2.2	BTC Observations	37
2.3	Reduction of the BTC Images	41
2.3.1	Summary	41
2.3.2	Initial Reduction Steps	42
2.3.3	Distortion modelling and removal	46
2.3.4	Photometric Calibration	54
2.3.5	Producing the Final Images	58
2.3.6	Astrometric Calibration	58

2.3.7	Production of a False Colour Image	63
2.4	Source Extraction — Producing the Final Catalogue	64
2.4.1	Extraction	64
2.4.2	Photometry	65
2.4.3	Background Modelling and Weight Maps	68
2.4.4	Star - Galaxy Separation	72
2.4.5	Source Parameters Output to the Final Catalogue	76
2.5	Sources in the BTC images	78
2.5.1	Magnitude Limits	78
2.5.2	Galaxy Counts	84
2.6	Summary	89
3	Analysis of Galaxy Clustering in the BTC Images	90
3.1	Introduction	90
3.2	The Cluster Red Sequence Method	91
3.2.1	The Red Sequence in Nearby Clusters	92
3.2.2	Evolution of the Cluster Red Sequence	97
3.2.3	Motivation for using the Cluster Red Sequence Method	100
3.2.4	Basic Implementation of the Cluster Red Sequence method to Identify Clusters	103
3.3	Cluster Analysis Methods	103
3.3.1	Parametric Methods	104
3.3.2	A non-parametric approach to cluster analysis	104
3.3.3	Estimating the probability density function	105
3.3.4	Cluster Identification and Analysis	108
3.3.5	Estimating the Significance of Substructure	113
3.4	Applying the CRS Method to the BTC Images	115
3.4.1	Definition of the Redshift Slices	115
3.4.2	Estimating the Galaxy Surface Density	116
3.5	Example Clusters from the Redshift Slices	124
3.6	Summary	128

4	The Identification of Galaxy Clustering Associated with the Clowes-Campusano Large Quasar Group.	129
4.1	Introduction	129
4.2	High Redshift Galaxies in the BTC images	130
4.3	Comparison with the EIS-DEEP HDF-South Field	135
4.4	Clustering of the Red Galaxies	148
4.5	Spatial Distribution of the Red Galaxies	152
4.6	Galaxy Clustering Around Density Maxima #70 and #71	158
4.7	The Galaxy Environment of the $z = 1.426$ Quasar	162
4.8	The Galaxy Environment of the $z = 1.230$ LQG Quasar	169
4.9	The Galaxy Environment of the $z = 1.306$ LQG Quasar	169
4.10	The Galaxy Environment of the $z = 1.226$ LQG Quasar	172
4.11	Comparison with Previous Studies	176
4.12	Consequences for the Evolution of Galaxy Clusters	180
4.13	The Galaxy Environments of $z \simeq 1.3$ Quasars	185
4.14	Evidence for a Large-Scale Structure at $z \simeq 1.3$	188
4.15	Summary	189
5	The Galaxy Environment of the $z = 1.226$ LQG Quasar	191
5.1	Introduction	191
5.2	Observations	193
5.3	Results — Galaxy Counts	197
5.4	Galaxy Colours	203
5.5	Photometric Redshift Estimation	206
5.5.1	Red Sequence Galaxies	214
5.5.2	Red Outlier Galaxies	216
5.6	Spatial Distribution of Galaxies	217
5.6.1	Red Sequence Galaxies	217
5.6.2	Clustering across Large-Scales	223
5.6.3	Blue Galaxies	225
5.7	The Immediate Environment of the Quasar	226
5.8	Discussion and Conclusions	228

5.8.1	A Possible Cluster Merging Event	230
5.8.2	Comparison with Other Work	231
5.8.3	Interpretation - Mechanisms for Quasar Formation	232
5.9	Summary	233
6	The Galaxy Environment of the $z = 1.306$ LQG Quasar	235
6.1	Introduction	235
6.2	Observations	236
6.3	Results — Galaxy Counts	241
6.4	Galaxy Colours	243
6.5	Photometric Redshift Estimation	246
6.6	Spatial Distribution of Galaxies	248
6.7	The Galaxy Environment of the $z = 1.306$ LQG Quasar	248
6.8	The $z \simeq 0.8$ Cluster	253
6.8.1	Early-type galaxies in the $z \simeq 0.8$ cluster	255
6.8.2	Star-forming Galaxies in the Cluster	258
6.8.3	Interpretation	258
6.9	Summary	260
7	Conclusions and Further Work	262
7.1	Summary of Conclusions	262
7.2	Future Work	270
	References	274

List of Figures

1.1	Galaxy power spectrum from the Las Campanas Redshift Survey . . .	6
1.2	Large-scale Structure in the Las Campanas Redshift Survey	12
1.3	The large-scale structure of the nearby universe	13
1.4	Evolution of the space density of quasars with redshift	15
1.5	Comparison of galaxy and quasar power spectra	23
1.6	Comparison of the distributions of AGN and galaxies at $z < 0.05$. . .	24
1.7	$I - K$ against $R - I$ colour-colour diagram for galaxies near the radio- loud quasar 1335+2834 from the $z \simeq 1.1$ Crampton et al. LQG	28
1.8	Large-scale structure traced by the $z \simeq 1.1$ Crampton et al. LQG . . .	30
1.9	Redshift distribution of MgII absorbers towards the LQG	32
2.1	The Clowes-Campusano LQG	36
2.2	Geometry of BTC CCD array	39
2.3	Optimal patterns of BTC pointings	40
2.4	Coverage of field by BTC patterns	41
2.5	Bias frame	43
2.6	Raw target V -band BTC image	44
2.7	Comparison of CCD sensitivities	45
2.8	Errors in registration of images	53
2.9	The effect of airmass on photometry	56
2.10	Overlaying of USNO catalogue sources on the BTC images	61
2.11	Sample false colour image	63
2.12	Resultant apertures from the source extraction process	66
2.13	RMS-noise map for the BTC V image	70
2.14	RMS-noise map for the BTC I image	71

2.15	Effect of star-galaxy classifier on BTC V, I images	74
2.16	Effect of averaging stellarity values	75
2.17	Completeness levels and magnitude errors for BTC V image	79
2.18	Completeness levels and magnitude errors for BTC I image.	80
2.19	Accuracy of aperture photometry as a function of V magnitude	82
2.20	Accuracy of aperture photometry as a function of I magnitude	83
2.21	V -band differential galaxy counts	87
2.22	I -band differential galaxy counts	88
3.1	Observed colour-magnitude diagram for Abell 2390	93
3.2	Evolution in time of the SED of a simple stellar population	94
3.3	Best fit to the average spectrum of an elliptical galaxy	95
3.4	Effect of metallicity on the SEDs of old stellar populations	96
3.5	Evolution of the zero-point of the colour-magnitude relation	98
3.6	Evolution of the slope of the colour-magnitude relation	99
3.7	Evolution of the cluster red sequence on a $V - I$ against I C-M diagram	102
3.8	Colour-magnitude diagram showing the redshift slices used	117
3.9	Galaxy surface densities for redshift slices from $0 < z \leq 0.15$	119
3.10	Galaxy surface densities for redshift slices from $0.15 < z \leq 0.30$	120
3.11	Galaxy surface densities for redshift slices from $0.30 < z \leq 0.45$	121
3.12	Galaxy surface densities for redshift slices from $0.45 < z \leq 0.60$	122
3.13	I -band image of the $z = 0.05$ cluster region	123
3.14	False colour image of the $z = 0.05$ cluster region.	123
3.15	Colour-magnitude diagram of galaxies near the $z = 0.05$ cluster	124
3.16	I -band image of the $z = 0.25$ cluster region	126
3.17	False colour image of the $z = 0.25$ cluster region.	126
3.18	Colour-magnitude diagram of galaxies near the $z = 0.25$ cluster	127
4.1	Evolution of $V - I$ colour as a function of galaxy type and redshift.	131
4.2	The co-added I -band EIS-DEEP image of the HDF-South field.	136
4.3	Comparison of $\omega(\theta)$ for red and $I < 23.5$ galaxies.	150
4.4	Spatial distribution of red galaxies in the BTC field ($\sigma = 0.75 h^{-1} \text{Mpc}$)	153
4.5	Spatial distribution of red galaxies in the BTC field ($\sigma = 0.35 h^{-1} \text{Mpc}$)	157

4.6	<i>I</i> -band image of high-redshift cluster candidates #70 and 71	159
4.7	False colour image of the same region, overlaid with contours showing the surface density of red galaxies	160
4.8	Colour-magnitude diagram of galaxies nearby clusters #70 and 71 . . .	162
4.9	<i>I</i> -band image of the clustering around the $z = 1.426$ quasar	163
4.10	False colour image of the same region, overlaid with contours showing the surface density of red galaxies	164
4.11	Colour-magnitude diagram of galaxies in the $z = 1.426$ quasar field .	166
4.12	<i>I</i> -band image of the $z = 1.230$ LQG quasar field	167
4.13	False colours image of the same region, overlaid with contours showing the surface density of red galaxies	168
4.14	<i>I</i> -band image of the $z = 1.306$ LQG quasar field	170
4.15	False colour image of the same region, overlaid with contours showing the surface density of red galaxies	171
4.16	<i>I</i> -band image of the $z = 1.226$ LQG quasar field	173
4.17	False colour image of the same region, overlaid with contours showing the surface density of red galaxies	174
4.18	Colour-magnitude diagram of galaxies in the $z = 1.226$ quasar field .	175
4.19	Radial distributions of red galaxies about the 4 $z \simeq 1.3$ quasars . . .	178
4.20	Radial distributions of $I < 23.5$ galaxies about the 4 $z \simeq 1.3$ quasars .	179
4.21	Cluster abundances as a function of redshift	183
5.1	<i>K</i> -band image of the $z = 1.226$ LQG quasar field	196
5.2	$I - K$ against $V - I$ colour-colour diagram of galaxies in the <i>K</i> image	204
5.3	Redshift probability distributions for four galaxies in the <i>K</i> image . .	213
5.4	$V - K$ and $I - K$ against <i>K</i> colour-magnitude diagrams	215
5.5	Spatial distribution of galaxies in the <i>K</i> image	218
5.6	<i>VIK</i> three-colour image of the $z = 1.226$ quasar field	219
5.7	Estimated density distribution of red galaxies in the quasar field . . .	222
5.8	Estimated density distribution of red galaxies showing the extent of the large-scale structure associated with the quasar	224
5.9	The angular cross-correlation between red and blue galaxies	226
5.10	The immediate environment of the $z = 1.226$ LQG quasar	227

6.1	<i>K</i> -band image of the $z = 1.306$ quasar field.	239
6.2	<i>K</i> -band image of the $z \simeq 0.8$ galaxy cluster field	240
6.3	Colour-colour diagram of galaxies in the <i>K</i> images	244
6.4	Redshift probability distributions for four galaxies in the <i>K</i> images	246
6.5	Spatial distribution of galaxies in the <i>K</i> images	249
6.6	<i>VIK</i> three-colour image of the combined $z = 1.306$ quasar and $z \simeq 0.8$ galaxy cluster fields	250
6.7	<i>K</i> -band image of the $z = 1.306$ quasar's immediate environment	251
6.8	<i>VIK</i> three-colour image of the $z \simeq 0.8$ galaxy cluster	254
6.9	Colour-magnitude diagram of galaxies in the $z \simeq 0.8$ cluster field	256

List of Tables

2.1	Quasars in the BTC field	38
2.2	Parameters of distortion model	52
2.3	Positions of quasars in the BTC images	59
2.4	Representation of the WCS in the fits header	60
2.5	Astrometric fits for each of the four quarter V, I images	62
2.6	5σ magnitude limits in V and I images	72
2.7	Completeness levels for the four deep I -band regions	81
2.8	Raw and corrected galaxy counts for V and I images	85
2.9	Summary of comparison deep surveys	86
4.1	Multi-colour optical- near-infrared catalogue of sources classed as red galaxies in the EIS-DEEP HDF-South field.	140
4.2	Photometric redshift estimates of sources in the EIS-DEEP HDF-South field classified as belonging to the high-redshift slice.	142
4.3	High-redshift cluster candidates in the BTC field.	155
4.4	Cluster abundances as a function of redshift for the BTC field.	182
5.1	Photometric properties of the images of the $z = 1.226$ quasar field	195
5.2	Total and $I - K > 3.75$ galaxy counts in the K image	198
5.3	Multi-colour optical- near-infrared catalogue of sources in the field centred on the $z = 1.226$ quasar covered by K -band imaging	199
5.4	Photometric redshift estimates of galaxies in the K image	210
5.5	Cluster membership analysis of the red sequence galaxies	221
6.1	Photometric properties of the images	241
6.2	Total and $I - K > 3.75$ galaxy counts in the K images	242

Acknowledgements

I wish firstly to thank my two supervisors Roger Clowes and Luis Campusano for their continued support throughout what has been a very rewarding project, and also Gordon Bromage for maintaining a friendly departmental environment, and for offering the opportunities to talk to the general public about our work, which in the end is what it is all about. I received financial support during this work from PPARC in the form of a research studentship and travel grants for an observing trip, conferences and a six month attachment in Chile. I wish to thank Prof. José Maza and the staff at Cerro Calán for their hospitality during my six month attachment, and the people of Chile for welcoming me to their beautiful country. The optical data were obtained using the 4-m Blanco telescope at CTIO which is part of the National Optical Astronomy Observatories (NOAO), and I wish to thank Malcolm Smith and the staff at CTIO for their hospitality during my three week stay there. I am very grateful to Andy Adamson for generously giving his Director's Discretionary time (and his personal time) to obtaining the near-infrared data. I acknowledge the use of facilities provided by the University of Central Lancashire and the PPARC STARLINK project, as well as the use of the IRAF software suite from NOAO, and the photometric redshift estimation software HYPERZ from Roser Pelló.

I wish to thank Ann and Allan for taking me into their home for the last three years, and for treating me as part of their family. Thanks to all my friends and colleagues in the department and elsewhere, for making my stay here a happy one, dragging me away from the office at regular intervals, and well for being you.

Finally I wish to give a special thankyou to my family for always being there when I needed them, and for believing in me.

The night was clear and filled with thousands of stars. One by one, they floated down from the sky and began to fly above our heads, and they were not stars but bejewelled birds, singing to celebrate the dawn of a new day.

Chapter 1

Introduction

1.1 Overview of the Thesis

This thesis describes the use of wide-field ultra-deep optical images in conjunction with near-infrared imaging to examine the galaxy environments of three quasars from the Clowes-Campusano Large Quasar Group (LQG) at $z \simeq 1.3$ and to search for indications of any associated large-scale structure. The remainder of this chapter describes the basic foundations of cosmology and structure formation used within this thesis, along with a summary of previous studies into the fields of quasars, their environments, and their clustering in the form of large quasar groups.

Chapter 2 describes the obtaining and reduction of ultra-deep optical images using the Big Throughput Camera (BTC) on the 4-m Blanco telescope at the Cerro Tololo Interamerican Observatory (CTIO) in Chile. The field covers a region of $30 \times 30 \text{ arcmin}^2$ containing three quasars from the Clowes-Campusano LQG, and reaches $V \simeq 26.5$, $I \simeq 26$, resulting in catalogues of $\simeq 10^5$ sources.

Chapter 3 describes the use of the Cluster Red Sequence method of Gladders & Yee (2000) to detect and characterise clusters as overdensities in the galaxy colour-magnitude-position three-space. The method is applied to the BTC field to identify clusters to $z \simeq 0.6$, resulting in two cluster candidates at $z \simeq 0.05$ and $z \simeq 0.25$.

Chapter 4 describes the examination of galaxy clustering at redshifts beyond 0.5 through the selection of galaxies redder than the expected colour of red sequence galaxies at $z = 0.5$. A 2σ excess of these galaxies is found in comparison to the EIS-DEEP HDF-South field, providing evidence for a high-redshift large-scale structure

encompassing the entire field. Four high-redshift cluster candidates are found, of which two appear associated with quasars, including one from the LQG.

Chapter 5 describes the addition of K imaging of a 2.25×2.25 arcmin² field around the $z = 1.226$ LQG quasar. Direct evidence for galaxy clustering associated with the quasar is found in the form of a population of galaxies with the colours expected for passively-evolving galaxies at $z = 1.2 \pm 0.1$, and which form clear red sequences at $V - K \simeq 6.9$ and $I - K \simeq 4.3$.

Chapter 6 describes the addition of K imaging of two adjacent 2.25×2.25 arcmin² fields: one containing the $z = 1.306$ LQG quasar and the other containing the most significant high-redshift cluster candidate of Chapter 4. The quasar itself appears to reside in a poor environment, indistinguishable from the field, whilst the cluster appears to be at $z = 0.8 \pm 0.1$. Finally, a summary of the conclusions of the thesis and an outline of future work are given in Chapter 7.

1.2 The Standard Cosmological Model

Gravity is the dominant force over large scales in the universe, and the foundation upon which cosmology is built is Einstein's General Theory of Relativity, which describes how the curvature of space is related to the distribution of mass. On scales from planets and stars, up to superclusters of galaxies, inhomogeneities are seen caused by the mutual attraction of matter under the action of gravity. However on larger scales above $100\text{--}200 h^{-1}\text{Mpc}$ the present universe becomes a homogeneous sponge-like structure, made up of walls and filaments of galaxies and galaxy clusters, separated by huge voids $\sim 50 h^{-1}\text{Mpc}$ across. This large-scale homogeneity is most apparent in the Cosmic Microwave Background (CMB), a thermal relic of the Big Bang, with an isotropic, near-perfect black-body spectrum at a temperature of 2.726K .

Such homogeneity is necessary to our current theories, as the basic premise upon which all cosmological models are founded is the Cosmological Principle which states that the universe is homogeneous and isotropic on sufficiently large-scales. From this comes the Robertson-Walker metric which describes the space-time geometry of the

universe,

$$ds^2 = (cdt)^2 - R(t)^2 \left[\frac{dr^2}{1 - kr^2} + r^2 d\psi^2 \right], \quad (1.1)$$

where r, ψ are comoving coordinates (constant for sources moving with the Hubble flow), ds is the space-time interval (zero for light paths), t is the proper time, $R(t)$ is the cosmic scale factor which describes the expansion of the universe, and k is a constant that takes the values $-1, 0,$ or 1 according to space being open, flat or closed.

General Relativity then gives us the Friedmann equations which relate mass with the geometry of space time through,

$$\ddot{R} = -\frac{4\pi}{3}G \left(\rho + 3\frac{p}{c^2} \right) R \quad (1.2)$$

$$\dot{R}^2 + kc^2 = \frac{8\pi}{3}G\rho R^2, \quad (1.3)$$

where ρ and p are the density and the pressure of the Universe. An examination of the second equation indicates a direct relation between the density of the universe and its geometry, with a critical density ρ_c separating closed and open universes,

$$\rho_c = \frac{3H(t)^2}{8\pi G}, \quad H(t) = \frac{\dot{R}(t)}{R(t)}, \quad (1.4)$$

where $H(t)$ is the Hubble parameter describing the rate of expansion of the universe. The density of the universe can be considered to be made up of three components, pressureless matter (both baryonic and non-baryonic; $\rho_M \propto R^{-3}$), radiation ($\rho_r \propto R^{-4}$), and vacuum energy ($\rho_\Lambda = \text{constant}$). For the post-recombination universe, the radiation density becomes negligible, allowing the evolution of $H(t)$ to be described as,

$$H(t)^2 = H_0^2 \left[\Omega_\Lambda + \Omega_M a^{-3} + (1 - \Omega_M - \Omega_\Lambda) a^{-2} \right], \quad (1.5)$$

where $H_0 = H(t = 0) = h \, 100 \, \text{km s}^{-1} \, \text{Mpc}^{-1}$ is the current expansion rate, $a(t) = R(t)/R(t = 0)$ is a dimensionless scale factor, and $\Omega_\Lambda = \rho_\Lambda/\rho_c$, $\Omega_M = \rho_M/\rho_c$ are the vacuum and matter density components normalised to the critical density.

The dimensionless scale-factor, $a(t)$, can be more usefully written in terms of the observable redshift, z , of the radiation from a source,

$$a(t) = \frac{\lambda_{emit}}{\lambda_{obs}} = \frac{1}{1 + z}. \quad (1.6)$$

The comoving distance of a source can then be related to its redshift through,

$$d_p = \int R dr = \int c dt = \int c \frac{dr}{R} = \frac{cdR}{RH(t)} = \frac{c}{H(z)} dz \quad (1.7)$$

$$= \frac{c}{H_0} \int \left[\Omega_\Lambda + \Omega_M(1+z)^3 + (1 - \Omega_\Lambda - \Omega_M)(1+z)^2 \right]^{-1/2} dz \quad (1.8)$$

For a matter-dominated model ($\Omega_\Lambda = 0$) this can be integrated analytically to produce Mattig (1958)'s formula,

$$d_p = \frac{2c}{H_0} \frac{\Omega_M z + (\Omega_M - 2)[\sqrt{1 + \Omega_M z} - 1]}{\Omega_M^2(1+z)} \quad (1.9)$$

Many of the largest cosmological studies have been aimed at constraining the three free parameters in the above equation, H_0 , Ω_M and Ω_Λ , through a variety of complementary approaches: the use of Cepheid variables (e.g. Freedman et al., 2000) and type 1a supernova (e.g. Perlmutter et al., 1999) as standard candles to measure the rate of expansion and deceleration (or acceleration) of the universe; the evolution of cluster abundances (e.g. Bahcall et al., 1997b) to examine the density of matter in the universe; and the power spectrum of the CMB anisotropies by MAXIMA-1 (Hanany et al., 2000) and BOOMERANG-98 (de Bernardis et al., 2000) which constrains the spatial geometry. By acting in orthogonal directions in the $\Omega_M - \Omega_\Lambda - H_0$ 3-dimensional parameter space, they combine to constrain the major cosmological parameters to (Jaffe et al., 2001),

Hubble's constant	$H_0 = 72 \pm 8 \text{ km s}^{-1} \text{ Mpc}^{-1}$,
the total energy density	$\Omega_0 = \Omega_M + \Omega_\Lambda = 1.1 \pm 0.07$,
the matter density	$\Omega_M = 0.37 \pm 0.07$,
the vacuum energy density	$\Omega_\Lambda = 0.71 \pm 0.05$,
the baryon density	$\Omega_b h^2 = 0.032 \pm 0.005$,
the power-law index of the power spectrum of mass fluctuations	$n = 1.01 \pm 0.08$.

These constraints support the main predictions of the inflation paradigm: that the geometry of the universe is flat; that the initial density perturbations are scale-invariant; and that the density of mass-energy of the universe is dominated by a form other than the ordinary baryonic matter that can be observed as stars and galaxies, with both components of dark (non-baryonic) matter ($\Omega_M - \Omega_b$) and vacuum energy (Ω_Λ) required to match observations.

Throughout the thesis, values of $H_0 = 75 \text{ km s}^{-1} \text{ Mpc}^{-1}$, $\Omega_M = 0.3$ and $\Omega_\Lambda = 0.7$ are assumed unless otherwise stated (usually for comparison with other studies), resulting in an age of the universe of $\simeq 12.6 \text{ Gyr}$.

1.3 Statistical Descriptors of Clustering

The effect of gravity on the growth of inhomogeneities is dependent on the matter content of the universe, producing clustering of characteristic strengths and scales. By examining the statistical properties of the observed distribution of matter, $\rho(\mathbf{x})$, it is possible to make predictions for the quantity and form of this matter.

The two most commonly used descriptors of the clustering of matter are the power spectrum, $P(k)$, and the two-point correlation function, $\xi(r)$, which measure the strength and scale of inhomogeneities of the density perturbation field

$$\delta(\mathbf{x}) = \frac{\rho(\mathbf{x}) - \langle \rho \rangle}{\langle \rho \rangle}. \quad (1.10)$$

The power spectrum measures the strength of clustering as a function of scale, and is defined as

$$P(k) = \langle |\delta_k|^2 \rangle, \quad (1.11)$$

$$\text{where } \delta_k = \frac{1}{V} \int \delta(\mathbf{x}) \exp(i\mathbf{k} \cdot \mathbf{x}) d^3x \quad (1.12)$$

is the Fourier transform of the density perturbation field $\delta(\mathbf{x})$. It is more commonly written in dimensionless form, as the variance of the density fluctuations per $\ln k$

$$\Delta^2(k) = \frac{d\langle \delta^2 \rangle}{d \ln k} = \frac{1}{(2\pi)^3} P(k) k^3 \quad (1.13)$$

As there is no physical motivation for any preferred length scale in the power spectrum, the most suitable choice for the spectrum is a featureless power law

$$P(k) \propto k^n, \quad (1.14)$$

where n is the spectral index and governs the balance between large- and small-scale power. The inflationary paradigm predicts a scale-invariant spectrum which implies that space has the same degree of structure on all scales, and corresponds to a value $n = 1$.

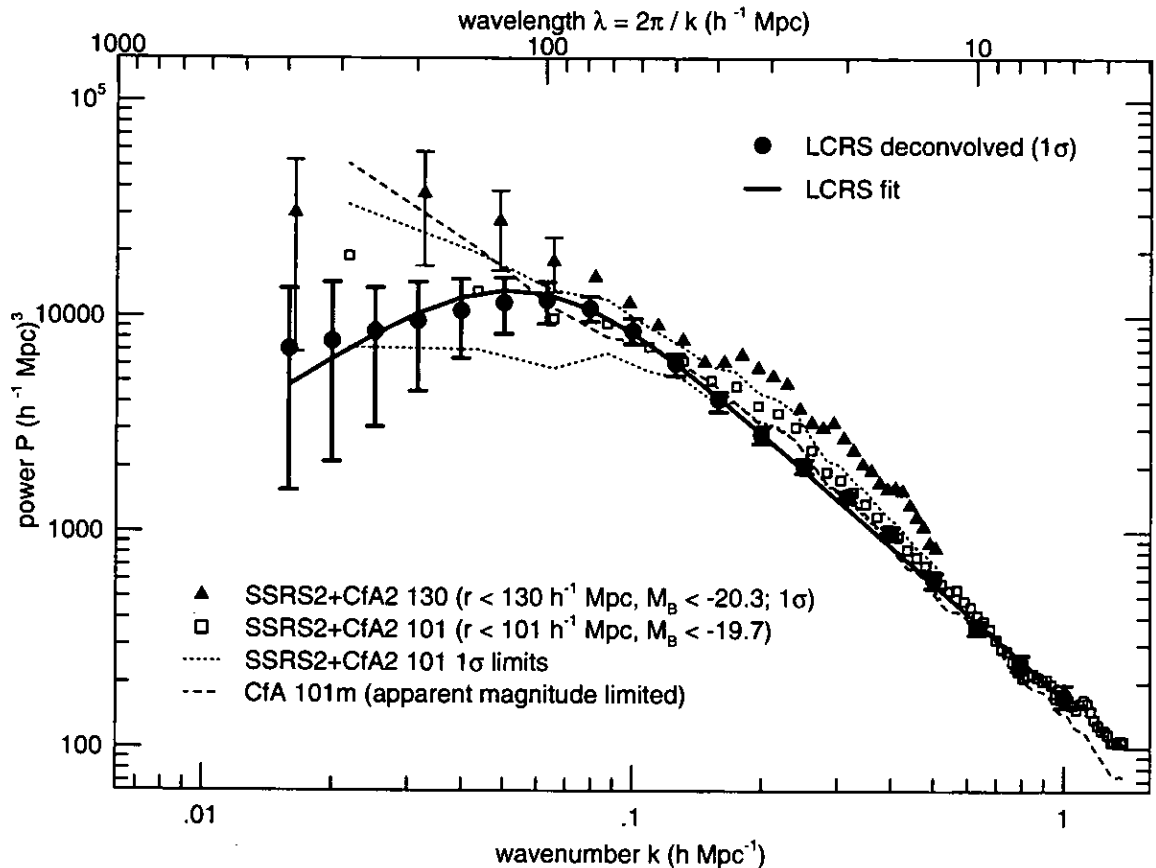


Figure 1.1: Deconvolved galaxy power spectrum (solid circles) and fit (solid line) from the Las Campanas Redshift Survey. For comparison the power spectra from the combined CfA and SSRS surveys are shown. Taken from Lin et al. (1996)

Figure 1.1 shows the galaxy power spectrum from the Las Campanas Redshift Survey (LCRS: Lin et al., 1996) of 23 697 galaxies. On small scales ($5\text{--}30 h^{-1}\text{Mpc}$) the power spectrum may be approximated by a power-law with $n = -1.8 \pm 0.1$. The clustering power appears to peak at a scale of $\simeq 100 h^{-1}\text{Mpc}$ which is a signature of the pattern of walls and voids apparent in large-scale galaxy redshift surveys, being the approximate separation between the large sheet-like structures apparent in the galaxy distribution. On larger scales the power spectrum is compatible with a spectral index of $n = 1$, although the errors are large, and it is possible that the power continues to increase beyond $100 h^{-1}\text{Mpc}$.

The two-point correlation function is basically described as the excess probability of finding a second overdensity at a distance r from a first

$$\xi(r) = \langle \delta(\mathbf{x})\delta(\mathbf{x} + \mathbf{r}) \rangle. \quad (1.15)$$

and is the inverse Fourier transform of the power spectrum

$$\xi(\mathbf{r}) = \frac{V}{(2\pi)^3} \int |\delta_{\mathbf{k}}|^2 \exp(-i\mathbf{k}\cdot\mathbf{r}) d^3k. \quad (1.16)$$

A power-law spectrum implies a power-law correlation function with

$$\xi(r) = \left(\frac{r}{r_0}\right)^{-\gamma}, \text{ with } \gamma = n + 3 \text{ (valid for } n < 0), \quad (1.17)$$

where r_0 is the correlation length. Results of galaxy redshift surveys (e.g., CNOC2: Carlberg et al. (2000); CfA: Davis & Peebles (1983); Las Campanas: Tucker et al. (1997)) indicate that $\gamma \simeq 1.8$ and $r_0 \simeq 5 h^{-1} \text{Mpc}$ for $1 \lesssim \xi(r) \lesssim 10^4$, implying that $n = -1.2$.

1.4 Structure Formation and Evolution

The standard cosmological paradigm has the structures observed in the present universe, such as galaxies and clusters, formed within dense halos of cold dark matter, which themselves have grown in a hierarchical manner from the small Gaussian perturbations in the initial density field, first observed as fluctuations in the Cosmic Microwave Background. These initial small-scale overdensities grow and progressively coalesce under the influence of gravity to form more massive structures, eventually becoming the clusters and superclusters seen today. The rate of evolution of structures is highly dependent on the cosmological parameters, particularly Ω_M as high-density universes will evolve much more rapidly than low-density ones. As a consequence, for a high-density universe, far fewer massive structures such as clusters or superclusters would be expected at early epochs than for a low-density universe. Hence by observing the evolution of massive structures it is possible to impose major constraints on any successful cosmological model.

There are two approaches to following the growth of structures in a cosmological framework — N-body simulations and analytical methods. Typical numerical simulations take a large volume filled with dark matter particles that are distributed in such a way as to represent the initial Gaussian density field observed at the epoch of recombination. These particles are then allowed to evolve under the influence of gravity into the non-linear regime where collections of the particles become gravitationally bound and collapse to form the massive dark matter halos that host galaxies

and clusters. More complex models involve the addition of gas particles which are affected by both gravitational and hydrodynamical forces, allowing the evolution of stars, galaxies and the hot gas of the intra-cluster medium to be described. Such simulations are highly computationally intensive, and although different cosmological models can be considered by varying the initial parameters, it is not trivial to relate the evolution observed back to the physical parameters.

The analytical approach allows in principle a deeper understanding of the effect of the various cosmological parameters on the evolution of structure, but faces two major difficulties. Firstly, the growth of density perturbations becomes highly non-linear as structures become gravitationally bound and begin to collapse, whereas analytical approaches are able to describe only the linear regime. Secondly, due to the immense complexities of the hydrodynamical physics involved in the evolution of galaxies, it is possible to describe analytically only the growth of the dark matter halos, which can be considered as collisionless particles. Hence, whereas the analytical model may follow the growth of dark matter halos, it is the evolution and growth of galaxies and clusters that is observed, and the effects of biasing of the distribution of galaxies and clusters with respect to the underlying mass distribution as described by the dark matter halos must be considered.

The standard analytical tool for describing the evolution of structure in a hierarchical universe is the Press-Schechter model (Press & Schechter, 1974), which despite not considering any non-linear dynamical effects, reproduces well the results from N-body simulations of the growth of dark matter halos.

In Press-Schechter theory the density field, $\rho(\mathbf{x})$, which is initially assumed to be a Gaussian random field, is smoothed by convolving with a filter function whose size is related to the mass M of interest. The density fluctuations, $\delta(\mathbf{x}) = [\rho(\mathbf{x}) - \langle\rho\rangle]/\langle\rho\rangle$, are assumed to grow linearly until they reach a critical overdensity, δ_c , at which point they are assumed to have collapsed into dark matter halos whose masses are determined from the maximum filtering scale at which the critical overdensity is reached.

The Press-Schechter approximation for the comoving number density of dark mat-

ter halos of mass M in the interval dM is given by

$$\frac{dn}{dM} = \left(\frac{2}{\pi}\right)^{\frac{1}{2}} \frac{\bar{\rho}}{M^2 \sigma(z, M)} \left| \frac{d \ln \sigma(z, M)}{d \ln M} \right| \exp\left(\frac{-\delta_c^2}{2\sigma(z, M)^2}\right), \quad (1.18)$$

where $\sigma(z, M)$ is the linear theory rms mass density fluctuation in spheres of mass M at redshift z , $\delta_c \simeq 1.68$ is the critical density contrast needed for collapse, and $\bar{\rho}$ is the mean density of the universe. The rms mass density fluctuation evolves with redshift as

$$\sigma(z, M) = \sigma_0(M) \frac{g(\Omega(z))}{g(\Omega)} \frac{1}{1+z} \quad (1.19)$$

where $g(\Omega)$ is the suppression factor of linear growth relative to that of a critical-density universe, where perturbations grow as $(1+z)^{-1}$, and is given by

$$g(\Omega_M, \Omega_\Lambda) = \frac{5}{2} \Omega_M \int_0^1 \frac{da}{a^3 H(a)^3}, \quad (1.20)$$

which for an $\Omega_\Lambda = 0$ universe is given by,

$$g(\Omega_M) = \frac{5}{2} \Omega_M \left[1 + \frac{\Omega_M}{2} + \Omega_M^{4/7} \right]^{-1} \quad (1.21)$$

and for a flat $\Omega_\Lambda = 1 - \Omega_M$ universe is well approximated by (Carroll et al., 1992)

$$g(\Omega_M, \Omega_\Lambda) = \frac{5}{2} \Omega_M \left[\frac{1}{70} + \frac{209\Omega_M}{140} - \frac{\Omega_M^2}{140} + \Omega_M^{4/7} \right]^{-1}, \quad (1.22)$$

and the redshift dependence of Ω_M is given by

$$\Omega_M(z) = \Omega_M \frac{1+z}{1+\Omega_M z} \quad (\Omega_\Lambda = 0) \quad (1.23)$$

$$\Omega_M(z) = \Omega_M \frac{(1+z)^3}{1-\Omega_M + (1+z)^3 \Omega_M} \quad (\Omega_\Lambda = 1 - \Omega_M) \quad (1.24)$$

$\sigma_0(M)$ is the present rms mass fluctuation within a sphere that on average has a mass M , and is related to the mass density power spectrum $P(k)$ through

$$\sigma_0^2(M) = \frac{1}{2\pi^2} \int dk k^2 P(k)^2 |f_k|^2, \quad (1.25)$$

where f_k is the Fourier transform of the volume's window function. If the power spectrum is approximated as a power law $P(k) \propto k^n$ around the $8h^{-1}\text{Mpc}$ scale then

$$\sigma_0(M) = \sigma_8 \left(\frac{M}{M_8} \right)^{-(n+3)/6}, \quad (1.26)$$

where M_8 is the mean mass within a sphere of radius $8h^{-1}\text{Mpc}$, and is proportional to Ω_M .

The mass of a typical rich cluster is contained within a Lagrangian radius of $6.5\Omega_M^{-1/3} h^{-1}\text{Mpc}$, close to the $8 h^{-1}\text{Mpc}$ value used to measure the rms mass fluctuations, and so by fitting the observed abundances of rich clusters with the Press-Schechter formalism it is possible to estimate σ_8 . By estimating the masses of the clusters either from their X-ray temperatures (e.g. Henry & Arnaud, 1991; Eke et al., 1996) or the velocity distributions of their member galaxies (White et al., 1993), the level of rms mass fluctuations has been estimated as

$$\sigma_8 \sim 0.5 \Omega_M^{0.5} \quad (1.27)$$

The dependence on Ω_M is due to clusters in low-density models requiring a greater degree of collapse to produce the same number of clusters of a given mass.

The amplitude of the mass fluctuations allows the relative distribution of mass and light in the universe to be compared, indicating whether the light observed from galaxies is a biased or unbiased tracer of mass on large scales. This biasing is quantified through the bias parameter (Kaiser, 1984) as

$$b = \frac{\sigma_8(\text{galaxies})}{\sigma_8(\text{mass})}. \quad (1.28)$$

Observations of the optical galaxy fluctuations (Davis & Peebles, 1983) indicate that $\sigma_8(\text{galaxies}) \simeq 1$, and so in order to produce an unbiased universe, where mass follows light on large scales, equation 1.27 implies a low-density universe with $\Omega_M \simeq 0.2\text{--}0.3$, whereas an $\Omega_M \simeq 1$ cosmology implies a highly biased universe with the distribution of light much more clustered than mass.

The $\Omega_M - \sigma_8$ degeneracy of equation 1.27 can be broken by examining the evolution of the abundance of rich clusters with redshift. For rich clusters where the exponential part of Equation 1.18 dominates the mass function, the total number density of dark matter halos of mass greater than M can be approximated as

$$\ln n(z, > M) \propto -\sigma(z, M)^{-2} = -\sigma_8^{-2} \Omega_M^{-(n+3)/3} \left(\frac{g(\Omega(z))}{g(\Omega)} \right)^{-2} M^{-(n+3)/3}. \quad (1.29)$$

Differentiating this with respect to redshift provides the rate of evolution of clusters of mass M

$$\frac{d(\ln n(z, > M))}{dz} \propto -\sigma_8^{-2} \Omega_M^{-(n+3)/3} \frac{d}{dz} \left(\frac{g(\Omega(z))}{g(\Omega)} \right)^{-2} M^{-(n+3)/3}. \quad (1.30)$$

The dominant factor in cluster evolution can be seen to be the rms mass fluctuation level σ_8 , and provides a powerful method for constraining σ_8 and hence Ω_M by comparing the abundance of rich clusters at high-redshifts with that of the present epoch (Fan et al., 1997).

For clusters of masses comparable to the Coma cluster ($\simeq 5.5 \times 10^{14} h^{-1} M_\odot$) the expected decrease in abundance from $z = 0$ to $z = 0.5$ is a factor of ~ 10 for unbiased, low-density models ($\Omega_M \simeq 0.2, \sigma_8 \simeq 1$), whilst for biased, high-density models ($\Omega_M = 1, \sigma_8 \simeq 0.5$) the cluster abundance evolves much more rapidly, with a decrease of a factor ~ 1000 expected.

Only a mild negative evolution of cluster abundances is observed in the cluster surveys that reach $z \simeq 0.5$ and beyond, in excellent agreement with unbiased, low-density models. The Canadian Network for Observational Cosmology Cluster Redshift Survey (CNOCC; Carlberg et al., 1996) provides a small but complete sample of massive clusters out to $z \simeq 0.5$, and the data show a mild decrease of a factor ~ 10 to $z \simeq 0.5$ for clusters of mass greater than $5.5 \times 10^{14} h^{-1} M_\odot$ (estimated from velocity distributions). The Palomar Distant Cluster Survey (PDCS; Postman et al., 1996) is a survey of distant clusters to $z \simeq 1$ found from deep imaging data over 5 deg^2 . By selecting moderately-rich clusters with $M > 1.5 \times 10^{14} h^{-1} M_\odot$ (based on the total luminosity of the member galaxies) only minimal negative evolution is observed, as expected for low-density, high- σ_8 models, but inconsistent with biased $\Omega_M = 1$ models which predict 10 times fewer clusters at $z \sim 1$ than that observed (see Figure 4.21).

The best-fitting value for σ_8 to the observed evolution of cluster abundances is $\sigma_8 = 0.83 \pm 0.15$ (Fan et al., 1997), implying a nearly unbiased universe where the mass follows the light. Combining this value with the $\Omega_M - \sigma_8$ relation of Equation 1.27 for local cluster abundances indicates a low-density, low-bias universe with $\Omega_M = 0.3 \pm 0.1$ (for $\Omega_\Lambda = 0$), and $\Omega_M = 0.34 \pm 0.13$ (for $\Omega_\Lambda = 1 - \Omega_M$).

1.5 Large Scale Structure at Low Redshifts

Over the last twenty years it has become possible for the first time to examine the large-scale structure of the universe and determine the characteristic scales at

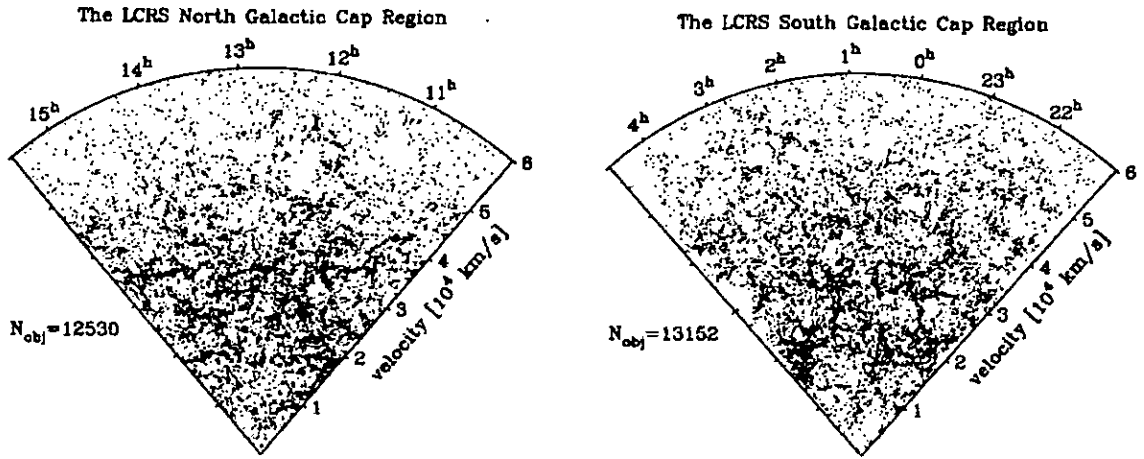


Figure 1.2: Large-scale structure in the Las Campanas Redshift Survey (Shectman et al., 1996). Velocity-right ascension pie diagrams for galaxies in the Las Campanas Redshift Survey: left, the North Galactic Gap data, composed of the $\delta = -3^\circ$, -6° , and -12° slices; right, the South Galactic Gap data, composed of the $\delta = -39^\circ$, -42° and -45° slices. Taken from Doroshkevich et al. (1996).

which the universe changes from being dominated by gravitationally-driven inhomogeneities such as galaxies and clusters to becoming homogeneous and isotropic, as theories and observations of the cosmic microwave background predict. Such progress has been made through the advent of surveys such as the CfA redshift survey (de Lapparent et al., 1986; Geller & Huchra, 1989) and the ACO (Abell et al., 1989) rich cluster catalogue of the 1980s, and the Las Campanas Redshift Survey (LCRS; Shectman et al., 1996; Doroshkevich et al., 1996; Tucker et al., 1997) of the 1990s, which have allowed the spatial distribution of galaxies and galaxy clusters to be examined out to distances of $\simeq 300 h^{-1} \text{Mpc}$.

The early surveys found evidence for inhomogeneities in the galaxy distribution on scales of $50\text{--}100 h^{-1} \text{Mpc}$: Kirshner et al. (1981) found evidence for a void in Boötes $60 h^{-1} \text{Mpc}$ across; and Geller & Huchra (1989) found a filamentary structure of galaxies $\sim 170 h^{-1} \text{Mpc}$ long in the CfA redshift survey, which they called the “Great Wall” (Figure 1.6(left)). In a pencil-beam galaxy redshift survey in the direction of the Galactic poles Broadhurst et al. (1990) found evidence for a periodicity in the galaxy distribution with a characteristic scale of $128 h^{-1} \text{Mpc}$ extending over $2000 h^{-1} \text{Mpc}$.

More recent surveys such as the LCRS (Shectman et al., 1996) have shown that

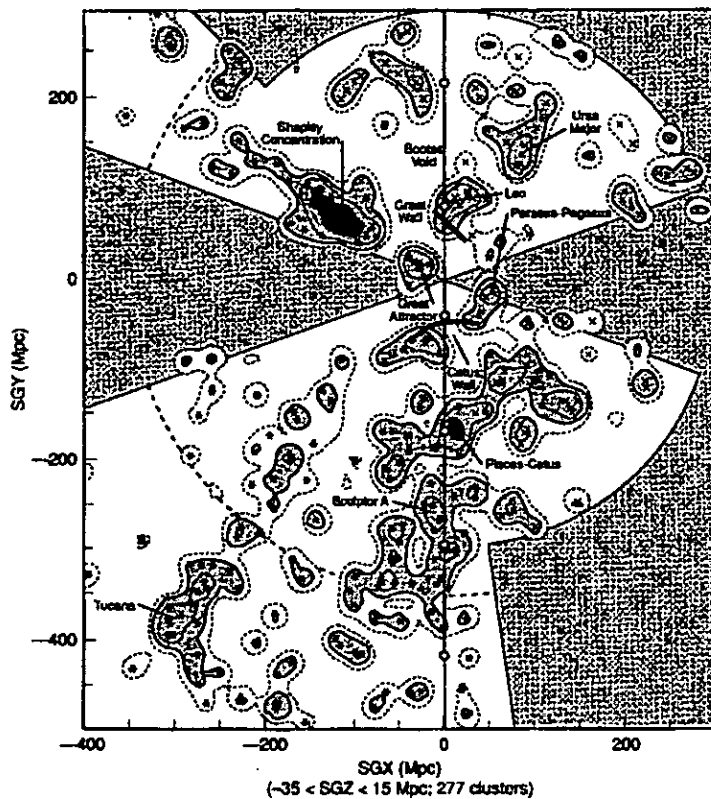


Figure 1.3: The large-scale structure of the local universe mapped by the spatial distribution of rich clusters from the Abell (1958) and ACO (Abell et al., 1989) catalogues. An SGX-SGY projection of a slab $50 h^{-1} \text{Mpc}$ thick. The distribution probed by the Broadhurst et al. (1990) pencil-beam survey is apparent as the vertical line passing through the origin, with the six cycle peaks indicated by white circles. The dashed-line and the first and second contour shade steps are at 0.5 , 1 and 3×10^{-3} clusters Mpc^{-2} . Taken from Tully et al. (1992).

the spatial distribution of galaxies in the universe becomes cellular or sponge-like on scales of $\simeq 100 h^{-1} \text{Mpc}$, with sheets and filaments of galaxies separated by huge voids similar to that found in Boötes (Kirshner et al., 1981). Figure 1.2 shows the large-scale structure of the universe mapped by the spatial distribution of galaxies from the LCRS. The pattern of filamentary structures of galaxies separated by regions almost devoid of galaxies is apparent across the whole of both the North and South Galactic cap regions, suggesting that the scale of homogeneity of the universe has been reached. This pattern of over- and under-dense regions (e.g., walls, filaments and voids) manifests itself in the power-spectrum (Figure 1.1: Lin et al., 1996) as the scale of maximum clustering power at $\simeq 100 h^{-1} \text{Mpc}$.

The large-scale structure of the universe has also been mapped by the spatial dis-

tribution of rich clusters and superclusters. By estimating the distances to clusters from the Abell (1958) and ACO (Abell et al., 1989) catalogues from the magnitudes of the third and tenth brightest cluster members (claimed to be accurate to 20% out to $\sim 300 h^{-1}\text{Mpc}$), Tully et al. (1992) map the large-scale structure of the local universe out to distances of $\simeq 400 h^{-1}\text{Mpc}$. Figure 1.3 shows the resultant map as a projection in the SGX-SGY plane of the region $-35 < SGZ < 15 h^{-1}\text{Mpc}$. Many of the features identified by earlier studies stand out as under- and over-densities in the rich cluster distribution, such as the Boötes void (Kirshner et al., 1981), the “Great Wall” (Geller & Huchra, 1989), the Great Attractor (Dressler, 1988, 1991), and the Shapley concentration (Scaramella et al., 1989). The region probed by the pencil-beam survey of Broadhurst et al. (1990) is shown as a vertical line passing through the origin, and the locations of the peaks (shown as white circles) can be seen to be coincident with several of the obvious features, including the “Great Wall”, the Cetus Wall (Fairall et al., 1990) and the Pisces-Cetus supercluster (Tully, 1987). Tully et al. (1992) also finds evidence for a concentration of rich clusters that extends along the supergalactic equator for $\sim 450 h^{-1}\text{Mpc}$.

More recent studies which take advantage of measured redshift distances to many of the Abell (1958) and ACO (Abell et al., 1989) clusters confirm many of the features of Figure 1.3. Einasto et al. (1994) examine the spatial distribution of the voids and network of superclusters, and estimate the mean diameter of voids as $85 h^{-1}\text{Mpc}$, and the mean distance between superclusters (on either side of a void) as $140 h^{-1}\text{Mpc}$.

It appears that the volumes covered by current redshift and cluster surveys have reached the scale of homogeneity, with repeated patterns of filaments, sheets and voids. The ongoing 2dF and SDSS (Sloan Digital Sky Survey) galaxy redshift surveys should confirm this by examining much greater volumes, reaching distances of $\sim 600 h^{-1}\text{Mpc}$ ($z \sim 0.2$).

1.6 Quasars — A Summary

Quasars were first identified nearly forty years ago (Hazard et al., 1963; Matthews & Sandage, 1963; Schmidt, 1963), and they have remained one of the most important

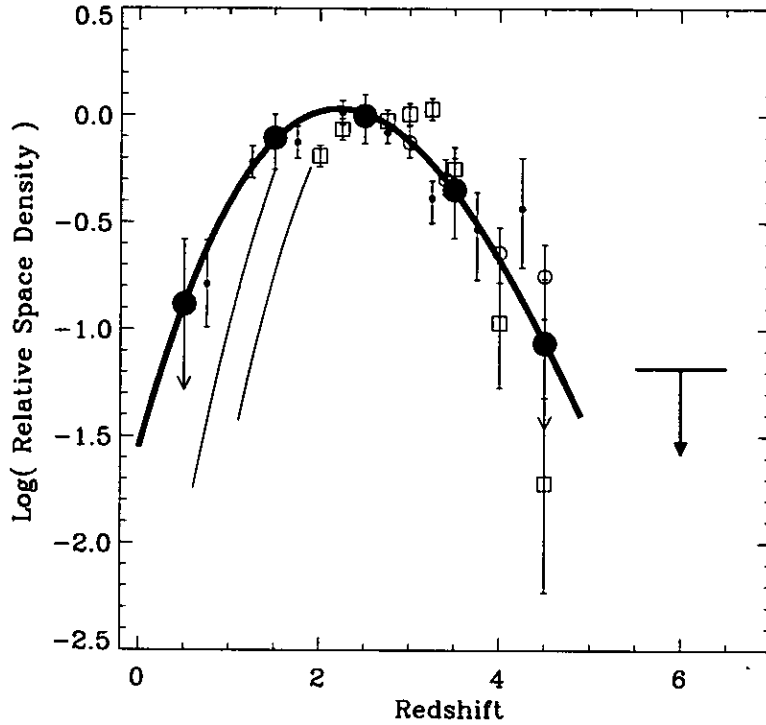


Figure 1.4: The quasar space density, normalised to $z \sim 2-3$ and plotted as a function of redshift. The data from Hook et al. (1999) for Parkes flat-spectrum radio-loud quasars with $P_{lim} > 7.2 \times 10^{26} \text{ W Hz}^{-1} \text{ sr}^{-1}$ are shown as solid circles. The upper limit for $5 < z < 7$ is taken from Shaver et al. (1996). Data from optically-selected quasar samples are also shown for Warren et al. (1994, open squares), Schmidt et al. (1995, open circles) and Hawkins & Veron (1996, small solid circles). Taken from Hook et al. (1999).

fields of study within cosmology. The basic model for a quasar (see Rees, 1984, for a review) is generally regarded to be a supermassive black hole ($M_{BH} \sim 10^6-10^{10} M_{\odot}$) which continuously accretes matter at the rate of $1-1000 M_{\odot} \text{ year}^{-1}$ resulting in a luminosity of 10^{39-41} W ($\simeq 100 L^*$, where L^* is the characteristic luminosity of galaxies).

The quasar population has evolved strongly with redshift, with the quasar space density a factor of ~ 150 greater at $z \simeq 1$ than at the present epoch (Schmidt, 1968). More recent studies indicate that the quasar space density continues to increase beyond $z \simeq 2$, peaks at $z \simeq 2-3$, before decreasing sharply beyond $z \simeq 3$ (e.g. Hartwick & Schade, 1990; Warren et al., 1994; Shaver et al., 1996; Hook et al., 1999) (Figure 1.4), although there are claims that this decrease at high-redshift is due mostly to a lack of sensitivity of quasar surveys to these high-redshift quasars (e.g. Wolf et al., 1999).

It is thought that the observed evolution is the result of many generations of quasars with lifetimes of the order 10^6 – 10^8 years, rather than a single generation of long-lived quasars whose luminosity changes with time. If the observed evolution were due to a small number of long-lived quasars, then as the mass of the black holes increases in relation to the total energy output by the quasar, a small fraction of the local galaxy population should be observed to harbour extremely massive remnant black holes ($M_{BH} \simeq 10^{12} M_{\odot}$; Cavaliere & Padovani, 1988). In contrast, observations indicate that most L^* class galaxies harbour quiescent black holes of mass $M_{BH} \sim 10^6$ – $10^9 M_{\odot}$ (Kormendy & Richstone, 1995; Magorrian et al., 1998). A strong correlation between the mass of the black hole and the bulge mass of the host galaxy is observed, indicating a causal connection between the formation evolution of the black hole and that of its galaxy host. Magorrian et al. (1998) construct dynamical models for a sample of 36 nearby galaxies with HST photometry and ground-based kinematics, and by modelling the dynamics in terms of a combination of compact massive object and an axisymmetric bulge find that for all but six galaxies the models require at the 95% confidence level a massive black hole with $M_{BH} \gtrsim 0.006 M_{bulge}$. Merritt & Ferrarese (2001) find that for a sample of 32 local early-type galaxies the frequency function $N[\log(M_{BH}/M_{bulge})]$ is reasonably well described as a Gaussian distribution with mean -2.90 and a standard deviation 0.45 . These results suggest that the majority of early-type galaxies undergo a short period of nuclear activity at some point during their evolution, and probably relatively early on, before their reservoirs of gas have been exhausted.

With the levels of angular resolution possible with the Hubble Space Telescope it has been possible over the last few years to establish the basic properties of the quasar host galaxies such as luminosity and morphology. Recent studies have found that the hosts of all luminous quasars ($M_V < -23.5$) are bright galaxies with $L > L^*$, and examinations of the host luminosity profiles have found them well fitted by a de Vaucouleurs $r^{1/4}$ -law spheroidal profile, establishing that, at low redshifts at least, the hosts of both radio-loud and radio-quiet quasars are unambiguously massive ellipticals (McLure et al., 1999; Dunlop, 2001), refuting the long-standing hypothesis that, like the majority of Seyferts, radio-quiet quasars lie in predominantly spiral galaxies (e.g. Smith et al., 1986).

There are thought to be two main mechanisms for the triggering of quasar activity: the accretion of hot gas during the process of galaxy formation (e.g. Efstathiou & Rees, 1988; Haehnelt & Rees, 1993), which is more likely to be the dominant mechanism for high-redshift ($z \gtrsim 1$) quasars; and the galaxy merger model whereby the merging event disrupts the galaxy host sufficiently to transport large amounts of gas onto the seed supermassive black hole (e.g. Roos, 1981, 1985a,b; Stockton, 1982; de Robertis, 1985; Carlberg, 1990), and which appears to be dominant at low redshifts.

In a newly forming dark matter halo, the central baryonic component of the protogalaxy collapses into a self-gravitating, rotationally-supported structure 100–1000 parsecs across. Unless all the gas can be converted into stars, dynamical friction results in a redistribution of angular momentum, leading to the formation of a self-gravitating, rotationally-supported baryonic object with a mass of around $10^8 M_\odot$ and a radius of a few parsec. Such an object rapidly collapses to form a supermassive black hole which then accretes the remainder of the gas, triggering the onset of quasar activity (Haehnelt & Rees, 1993). Such a mechanism is likely to dominate at high redshifts ($z \gtrsim 1$), and is supported by the coincidental epoch of quasar activity and the formation of galactic-size structures. If the correlation between black hole mass and bulge mass is due to physical processes involved in galaxy formation, then this correlation is unlikely to be epoch dependent. As the mass of the black hole needed to power the quasar is also likely to be independent of redshift, then so is the mass of the dark matter halo containing the quasar and its galaxy host.

In contrast, there is evidence that galaxy interactions and mergers have activated a significant fraction of low-redshift quasars. HST studies have found a wide variety of environments around low-redshift quasars, ranging from highly distorted or obviously interacting systems to apparently isolated, undisturbed systems (e.g. Hutchings & Neff, 1992; Disney et al., 1995; Bahcall et al., 1997a; McLure et al., 1999). In the Bahcall et al. (1997a) sample of 20 quasars at $z < 0.3$ they found three host galaxies undergoing major interactions, and 13 of the quasar hosts had close companions that may have recently interacted with the host. Of the sample of 15 $z < 0.3$ quasars, McLure et al. (1999) found that 11 showed signs of recent interactions. A number of the merging events appear to be between two large galaxies of

comparable size (e.g. QSO1613+658 from Hutchings & Neff, 1992; QSO0157+001 from McLure et al., 1999), but the vast majority appear to be interactions with a significantly smaller companion galaxy, and indeed many show no signs of interactions or companion galaxies whatsoever (e.g. QSO0244+194 from McLure et al., 1999). Many of the companion galaxies have been spectroscopically confirmed as having redshifts within 500 km s^{-1} of the quasar (e.g. Stockton, 1982; Canalizo & Stockton, 1997), and it has been suggested that these are tidally-stripped cores from galaxies that recently interacted with the quasar host galaxy, and provide an efficient fuelling mechanism for the quasar activity (e.g. Stockton, 1982; Bekki, 1999). Spectroscopic analysis of the companion to quasar PG 1700+518 (Canalizo & Stockton, 1997) finds evidence for both a star-burst event that occurred approximately 100 Myr earlier (and so could be coincident with the quasar activation), and a relatively old stellar population, likely to be from the merger progenitor disk. Whilst the fraction of quasars that has been triggered by some form of galaxy interaction remains open to debate, it appears certain that at least some of the low-redshift quasars have been activated by this mechanism.

1.7 The Galaxy Environments of Quasars

The environments of quasars have also been examined on much larger scales than those of typical host galaxies to determine whether quasars are located preferentially in rich environments such as clusters or are typically located in poor or field environments (Croom & Shanks, 1999; Ellingson et al., 1991a,b; Hall et al., 1998; Hall & Green, 1998; Hutchings et al., 1993, 1995; McLure & Dunlop, 2001; Sánchez & González-Serrano, 1999; Smith et al., 1995, 2000; Tanaka et al., 2000, 2001; Wold et al., 2000, 2001; Yamada et al., 1997; Yee & Green, 1984, 1987). Such studies can not only provide clues as to the triggering mechanisms of the quasars, but are important in cosmological terms by indicating how quasars trace mass, which is necessary if the quasar spatial distribution is to be used to trace galaxy clustering or large-scale structure at high redshifts.

The early studies examined the galaxy environments of both low- ($z \lesssim 0.3$) and intermediate-redshift ($z \simeq 0.5\text{--}0.8$) quasars. They often found evidence for galaxy

excesses in many of the quasar fields, but also found differences in the environments of radio-quiet and radio-loud quasars, finding the radio-quiet quasars in much poorer environments. Yee & Green (1984) obtained r imaging for a sample of 55 $z < 0.45$ quasars (18 radio-loud, 37 radio-quiet), and found them located preferentially in regions of higher than average density, comparable to poor groups and clusters, and found marginal evidence for radio-loud quasars being located in richer environments than radio-quiet quasars. Yee & Green (1987) examined the galaxy environments of 28 radio-loud quasars at $0.3 \lesssim z \lesssim 0.6$, through the spatial covariance amplitude, B_{gg} , which quantifies the overdensity of galaxies within $0.5 h^{-1} \text{Mpc}$ of the quasar. They found evidence for evolution of environment with redshift, finding the $z \simeq 0.6$ quasars in environments three times as dense as those of the $z \simeq 0.3$ quasars, with some $z \simeq 0.6$ quasars found in environments as rich as Abell class 1 clusters, a result which was confirmed by Ellingson et al. (1991b). In a comparable study of 36 radio-quiet quasars at $0.3 < z < 0.6$, Ellingson et al. (1991b) found their environments consistent with that of field galaxies, with none of them found in an environment as rich as an Abell class 1 cluster, a result confirmed by Smith et al. (1995), although in both cases it should be considered that these were relatively faint quasars with $M_V \sim -22$, fainter than the dividing line between quasars and Seyferts.

More recent observations have shed significant doubt on many of the above claims (e.g. Wold et al., 2000, 2001; McLure & Dunlop, 2001). In a study of 21 radio-loud quasars at $0.5 \leq z \leq 0.82$ Wold et al. (2000) find no epoch dependence for the environment of the quasars, finding them in a wide variety of environments, from undistinguished field regions to Abell class 1 clusters. On average they seem to prefer galaxy groups or clusters of approximately Abell class 0. In a comparable study of 20 radio-quiet quasars at $0.5 \leq z \leq 0.8$ Wold et al. (2001) find them located in environments indistinguishable from those of their radio-loud counterparts. As for the radio-loud quasars, the radio-quiet quasars are located preferentially in poor clusters of approximately Abell class 0, with a few located in environments as rich as Abell class 1–2 clusters, and others in environments comparable to the field. These results are confirmed by the study of 34 quasars (13 radio-loud and 21 radio-quiet) at $z \simeq 0.2$ of McLure & Dunlop (2001), which finds the radio-loud and radio-quiet populations to be located in indistinguishable environments, with both quasar

populations being preferentially located in Abell class 0 clusters, as for their higher redshift counterparts. These results confirm the lack of epoch dependence. McLure & Dunlop (2001) conclude that the distribution of cluster environments observed for the quasars from both their and Wold et al.'s studies is consistent with the quasar host galaxy being drawn at random from the massive elliptical population, indicating that the host galaxy is the dominant factor for quasar environments. Indeed, by considering the space density of Abell class $\simeq 0$ clusters and quasars at the epoch of peak quasar activity at $z \simeq 2.5$, McLure & Dunlop (2001) suggest that practically all Abell class $\simeq 0$ clusters contained an active galaxy at this epoch.

The discrepancy between the earlier and the later studies appears to be due to the observations. Whereas the later observations were based on imaging data through filters redder than the redshifted 4000\AA break, and so sensitive to old stellar populations at the quasar redshift, the earlier data were generally based on imaging data that did not go as deep, and which covered wavelengths that were sufficiently blue that, for galaxies at the upper end of the redshift range probed, the results could be affected by recent star-formation, introducing a redshift bias.

Hall et al. (1998) and Hall & Green (1998) have studied the environments of 31 $1 < z < 2$ radio-loud quasars using combined optical and near-infrared imaging to identify the extremely-red objects likely to be early-type galaxies at the quasar redshift. Hall et al. (1998) report a significant excess of $K \gtrsim 19$ galaxies in the quasar fields. Hall & Green (1998) examine the properties of this excess, and find that it occurs on two spatial scales. One component lies within 40 arcsec from the quasar and is significant compared to the galaxy surface density at greater distances for the same fields. The other component is an extended overdensity to 100 arcsec and is significant in comparison to field regions. The $r - K$ colour distribution of the excess galaxy populations are indistinguishable from one another, and are significantly redder than the colour distribution of the field population, and are consistent with being predominantly early-type galaxies at the quasar redshifts. The average level of excess observed corresponds to moderately rich clusters of Abell richness class $\sim 1.5 \pm 1.5$.

Sánchez & González-Serrano (1999) examined the galaxy environments of seven radio-loud quasars at $1.0 < z < 1.6$, and found excesses of faint galaxies ($B > 22.5$

and $R > 22.0$) on similar scales to those observed by Hall & Green (1998), with significant excesses within 35 arcsec of the quasars, and a more extended galaxy excess on scales out to 170 arcsec. The number of excess galaxies, their magnitudes, and the angular extensions of the excesses, are compatible with clusters of galaxies at the redshift of the quasars. As well as examining the radial distribution of galaxies around the quasars, they considered the density distribution on the sky, and found that the quasars were not in general located at the peaks of the galaxy density distributions, but at a projected distance of ~ 70 arcsec from it, suggesting that the quasars are preferentially located on the peripheries of the clusters.

This apparent avoidance of the densest cluster regions can be understood in the framework of both galaxy merger and galaxy formation quasar triggering mechanisms: (i) the encounter velocities of galaxies in the centre of clusters are much greater than the internal velocity distributions, and so galaxy mergers become much less efficient at triggering nuclear activity (Aarseth & Fall, 1980); and (ii) the cluster cores are filled with shock-heated virialised gas that does not easily cool and collapse (Blanton et al., 1999), inhibiting both the formation of stars and galaxies (Blanton et al., 2000), and hence inhibiting quasar formation as well (Haehnelt & Rees, 1993).

1.8 Quasar Clustering

Quasars currently offer a unique opportunity to examine the evolution of structure, and in particular large-scale structure, beyond the range of galaxy redshift surveys ($z \simeq 0.2$). Not only does the study of quasar clustering allow the evolution of clustering to be followed to much higher redshifts ($z \simeq 2-3$) than studies of the galaxy distribution, allowing the evolution of clustering to be examined, but it provides the only method of examining clustering on scales reaching $1000 h^{-1} \text{Mpc}$ and over a volume sufficiently large to be representative of the universe.

The largest quasar survey by an order of magnitude is the 2dF quasar redshift survey which aims to compile a homogeneous catalogue of $\sim 25\,000$ quasars over two $75^\circ \times 5^\circ$ regions. Quasar candidates are identified from broad-band UB_jR colours and then their spectra obtained using the 2-degree Field fibre-fed multi-object spectrograph on the Anglo-Australian Telescope (AAT). This selection of candidates by

their blue optical colour results in the survey being limited to $z \lesssim 2.2$, beyond which the colour-selection criterion rapidly becomes inefficient at detecting quasars. It also becomes highly inefficient at low-redshifts, as low-luminosity quasars ($M_B > -23$) whose colours are dominated by the host galaxy will be missed. However the survey is expected to be 90% complete for $0.3 \lesssim z \lesssim 2.2$ (Boyle et al., 2000). The survey is still underway, the observations not expected to be completed until February 2002, but the clustering of an interim catalogue of 10 681 quasars (the *10k catalogue*) has been examined through the two-point correlation function (Croom et al., 2000) and the power spectrum (Hoyle et al., 2001).

Croom et al. (2000) shows that the two-point redshift-space correlation function of quasars, $\xi_Q(r)$, follows a power law of the form $\xi_Q(r) = (r/r_0)^{-\gamma}$ on scales $r \simeq 1\text{--}35 h^{-1}\text{Mpc}$ similar to that observed for galaxies. The effect of the choice of cosmological parameters become important for drawing conclusions from the data as the separation of quasars increases significantly for Λ -dominated models compared with standard $\Omega_M = 1$ models, as the mean quasar redshift in the sample is 1.49. At this redshift the quasar separations for an $\Omega_M = 0.3, \Omega_\Lambda = 0.7$ cosmology are 70% greater than for an $\Omega_M = 1$ model. For the $\Omega_M = 1$ model, $\xi_Q(r)$ is best fit by a power law with $r_0 = 3.99_{-0.34}^{+0.28} h^{-1}\text{Mpc}$ and $\gamma = 1.55_{-0.09}^{+0.10}$, whereas for the Λ -dominated model ($\Omega_M = 0.3, \Omega_\Lambda = 0.7$) the power law extends to $\simeq 60 h^{-1}\text{Mpc}$ and is best fit by $r_0 = 5.69_{-0.50}^{+0.42} h^{-1}\text{Mpc}$ and $\gamma = 1.56_{-0.09}^{+0.10}$. The results are very similar to those observed for local optically selected galaxies indicating that quasars trace mass in a similar manner, which is unsurprising given their galaxy hosts.

To examine the evolution of quasar clustering with redshift, the quasar sample is split up into five redshift intervals from 0.3 to 2.9, and $\xi_Q(r, z)$ redetermined. There is no evidence for evolution of r_0 with redshift for an $\Omega_M = 1$ cosmology, and only a marginal increase of r_0 with redshift for the Λ -dominated model. It is difficult to draw any firm conclusions from the clustering evolution data as it is unclear what the biasing effects of quasar mechanisms are for models based on the growth of dark matter halos, particularly given that there are two likely quasar triggering mechanisms whose relative importance is likely to be redshift dependent. However the evolution of r_0 with redshift is consistent for a Λ -dominated cosmology with quasars being associated with dark matter halos of minimum mass $10^{13} M_\odot$,

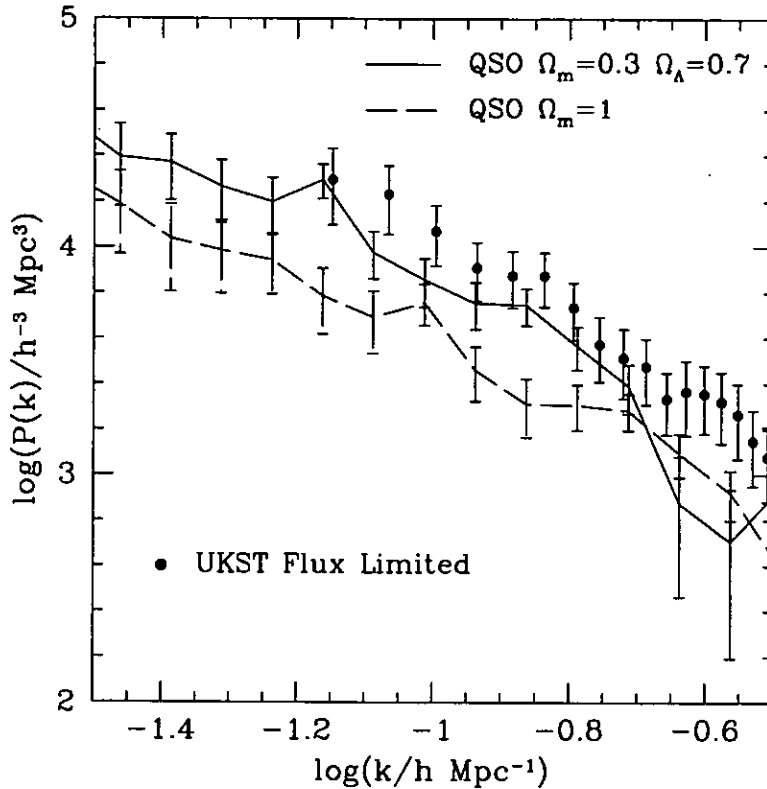


Figure 1.5: A comparison of galaxy and quasar power spectra. The lines show the power spectra of quasars from the 10k 2dF quasar catalogue for a Λ cosmology (solid-line) and $\Omega = 1$ cosmology (dashed-line). The circles show a flux limited power spectrum measured from the Durham/UKST Survey (Hoyle et al., 1999). Taken from Hoyle et al. (2001)

which suggests that the clustering signature is due to the relatively high masses of typical quasar host galaxies. As discussed previously, if the relationship between the black hole mass and the mass of the galaxy host is due to the physical processes of galaxy formation, then the mass of the dark matter halos associated with quasars is likely to be independent of epoch. Although the dark matter halo mass may remain constant, this does not imply that the effect of biasing does not change with redshift. At high redshifts, dark matter halos of mass $10^{13} M_{\odot}$ are likely to be due to the most significant perturbations in the initial density field, and so will be highly biased, whereas at low redshifts, the mass spectrum of dark matter halos has evolved significantly, so that $10^{13} M_{\odot}$ mass halos are due to much smaller perturbations in the initial density field, and so will have a different biasing effect.

Hoyle et al. (2001) present a power spectrum analysis of the same quasar sample from the 2dF 10k catalogue. Figure 1.5 shows the resultant power spectrum of the quasar sample on scales of 20–200 $h^{-1} \text{Mpc}$. The solid-line shows the power

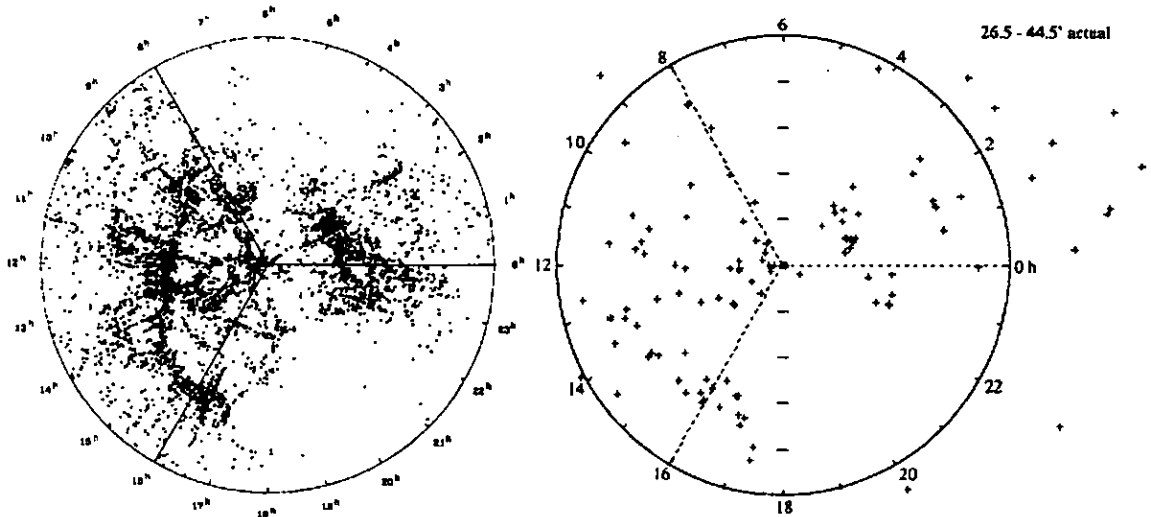


Figure 1.6: Distribution of normal galaxies found in the Centre for Astrophysics redshift survey (Geller & Huchra, 1989, — left) and the distribution of AGNs from the Veron-Cetty & Veron (1987) catalogue (right). The radial distance from the origins indicates the redshift z , with the outer circles corresponding to $z = 0.05$, or $cz = 15\,000\text{ km s}^{-1}$. The declination range for the galaxy distribution is $20^\circ \leq \delta \leq 40^\circ$ and the declination range for the AGN distribution is $26.5 \leq \delta \leq 44.5$. Taken from Longo (1991).

spectrum for an $\Omega_M = 0.3$, $\Omega_\Lambda = 0.7$ cosmology, and the dashed-line shows the power spectrum for an $\Omega_M = 1$ cosmology. For comparison the circles show the galaxy power spectrum from the Durham/UKST Survey (Hoyle et al., 1999). The quasar and galaxy power spectra have similar forms in the area of overlap, with both having $P(k) \propto k^{-1.4}$ on scales up to $50\text{--}100\ h^{-1}\text{Mpc}$, and is the same clustering signature as that manifested in the two-point correlation function (Croom et al., 2000). There is evidence of a spike feature at $\simeq 90\ h^{-1}\text{Mpc}$ assuming the Λ -dominated cosmology or $\simeq 65\ h^{-1}\text{Mpc}$ assuming an $\Omega_M = 1$ model. Although its significance is marginal, it may be the same manifestation of the average separation of galaxy walls and sheets apparent in the power spectrum of local galaxies (see Figure 1.1). However, the clustering power continues to increase beyond the spike to at least $300\text{--}400\ h^{-1}\text{Mpc}$, suggesting that the turnover in the power spectrum occurs at larger scales, and that the spike is the manifestation of another physical process, possibly the second baryon-radiation acoustic peak.

Both the power spectrum and the two-point correlation function confirm that the distribution of quasars is relatively unbiased with respect to that of galaxies,

and so quasars are likely to trace the same structures as galaxies.

This is confirmed by comparison of the spatial distribution of AGNs and galaxies at low redshifts (e.g. Longo, 1991; Mullis et al., 2001). Longo (1991) compared the spatial distribution of $z < 0.05$ AGN from the Veron-Cetty & Veron (1987) catalogue with that of normal galaxies from the CfA redshift survey (Geller & Huchra, 1989). A structure of 19 AGN was found that was spatially coincident with the “Great Wall” structure found in the distribution of galaxies, and other features observed in the galaxy survey were also apparent in the AGN distribution (see Figure 1.6). It was estimated that the probability of such a chance spatial coincidence between the quasar and galaxy distribution was $\lesssim 1\%$. Mullis et al. (2001) detected a supercluster at $z = 0.087$ in the ROSAT North Ecliptic Pole Survey, with 16 clusters identified in the redshift range $0.07 \leq z \leq 0.10$ whereas only 4–5 would be expected. In the same redshift range 12 AGN (the dominant class of X-ray emitters in the survey) were identified, whereas only 5.6 would be expected, a 2.2σ excess.

1.9 Large Quasar Groups

The previous discussion suggests that quasars sparsely sample the galaxy distribution, and so trace the same structures as galaxies. Given that superclusters at low-redshift are also manifested as regions containing an excess of AGN, it seems reasonable to propose that the converse is true also, that regions containing an excess of AGN indicate the presence of an underlying galaxy structure. This implies that if galaxy superstructures exist at redshifts beyond the current limits of galaxy redshift surveys, it should be possible to detect them as overdensities in the spatial distribution of quasars, or large quasar groups, and a number of studies have been made over the last twenty years to find such groupings within quasar surveys.

1.9.1 The Webster Large Quasar Group at $z \simeq 0.37$

The first group of quasars was found by Webster (1982) in the Cerro Tololo objective prism survey (Osmer & Smith, 1980) of 108 quasars. The vast majority of the quasars found have $z \gtrsim 2$, but of the six quasars with $z < 1$ three are found to have $z = 0.37$ and a fourth has $z = 0.36$. Not only are they clustered in redshift-space,

but they are also clustered in the sky, as although the survey covers an elongated region of size $71^\circ \times 5^\circ$ they all lie within a region 5° across, corresponding to a structure $\sim 100 h^{-1}\text{Mpc}$ across. The finding of such a cluster at this redshift by chance is very low, particularly as the spatial density of quasars at $z = 0.37$ is an order of magnitude below that at $z \simeq 2$. Webster (1982) estimated the probability of finding four of the six $z < 1$ quasars in such a cluster as 10^{-4} – 10^{-7} , indicating that this is a real structure. The shape of the structure outlined by the quasars appears flattened in the plane of the sky, the width in redshift space corresponding to $25 h^{-1}\text{Mpc}$, whereas the greatest angular width corresponds to $78 h^{-1}\text{Mpc}$. It is possible that there are other quasars associated with the cluster that lie outside the survey geometry, as the width in declination is small, and the cluster extends fully across it, indeed one lies on the nominal boundary. To date, no further studies have been made of this group, either to identify further members outside the original survey, or to examine its galaxy environment and determine whether it is associated with a supercluster.

1.9.2 The Crampton et al. Large Quasar Group at $z \simeq 1.1$

The second quasar group found, and currently the largest in terms of numbers, is that of Crampton et al. (1987, 1989) and consists of 23 quasars at $z \simeq 1.1$. The group was identified from the quasar survey of Crampton et al. (1985) which identified quasar candidates from Canada-France-Hawaii Telescope (CFHT) blue greys plates that were observed spectroscopically with the Multiple Mirror Telescope (MMT), resulting in 149 quasars over the 4.8 deg^2 1338+27 field. The 23 quasars have a mean redshift of $\bar{z} = 1.113$ and a dispersion of $\Delta z = 0.044$, which corresponds to $70 h^{-1}\text{Mpc}$, and the angular extent of the structure is $\sim 100 \text{ arcsec}$ corresponding to $80 h^{-1}\text{Mpc}$, making it comparable in size to the Webster (1982) group, and the expected scale-length of large-scale structures. There is evidence for sub-clustering on scales of $20 h^{-1}\text{Mpc}$ within the group, with two compact groups of 5 and 9 quasars apparent. As for the Webster (1982) group, the structure impinges on the survey boundaries, the group of five quasars located 6 arcmin from the nominal northern edge of the survey, leaving open the possibility that the structure is of even greater size.

There have been a number of studies (Hutchings et al., 1993, 1995; Yamada et al., 1997; Tanaka et al., 2000, 2001) that have examined the galaxy environments of quasars from the Crampton et al. (1989) large quasar group to search for evidence of any associated large-scale structure. Hutchings et al. (1993) and Hutchings et al. (1995) present broad- (R, I) and narrow-band (OII 3727 Å) imaging of 7×7 arcmin² fields of 11 members (10 radio-quiet) of the $z \simeq 1.1$ Crampton et al. (1989) LQG. Excesses of R - and I -selected galaxies are found for 10 out of 11 100×100 arcsec² subfields centred on the quasars, with an average excess of 15 galaxies over the background of 25, a result significant at $> 5\sigma$ level. Several of the quasars also have excesses of blue ($R - I < 1.0$) and emission-line galaxies indicating that the quasars are located in regions of enhanced star-formation, and Hutchings et al. (1995) suggested that most of the quasars are in compact groups of starbursting galaxies.

The largest excesses of blue and emission-line galaxies are observed for the $z = 1.086$ quasar 1335.8+2834, which Hutchings et al. (1995) classified as radio-quiet, but was confirmed later (Yamada et al., 1997) to be radio-loud from the VLA Faint Images of the Radio Sky at Twenty Centimeters (FIRST) survey catalogue as a 169 mJy radio source. In total nine emission-line galaxies and 15 blue galaxies (of which five are also emission-line galaxies) are identified in the 100×100 arcsec² field, and the total excess of R, I -selected galaxies is 17–20, significant at the 3.5σ level. Yamada et al. (1997) and Tanaka et al. (2000) obtained new deep optical (R, I) and near-infrared (K) imaging of the field of this quasar. The optical images cover an area of 8.8×8.8 arcmin² centred on the quasar and are complete to $I \sim 23.5$ and $R \sim 25$, whilst the K data cover a region of 5×3 arcmin² and are complete to $K \sim 19.5$ –20. Significant clustering of objects with very red optical- near-infrared colours of $4 \lesssim R - K \lesssim 6$ and $3 \lesssim I - K \lesssim 5$ is observed near the quasar. The colours and magnitudes of many of these objects are consistent with passively-evolving massive elliptical galaxies at the quasar redshift. This is confirmed by red sequences apparent at $R - K \simeq 5.3$ and $I - K \simeq 4.0$, close to that predicted by the Kodama & Arimoto (1997) model for $z = 1.1$.

The $I - K$ against $R - I$ colour-colour diagram for $K < 19$ sources in the field of quasar 1335+2834 is shown in Figure 1.7. Evidence for clustering of massive

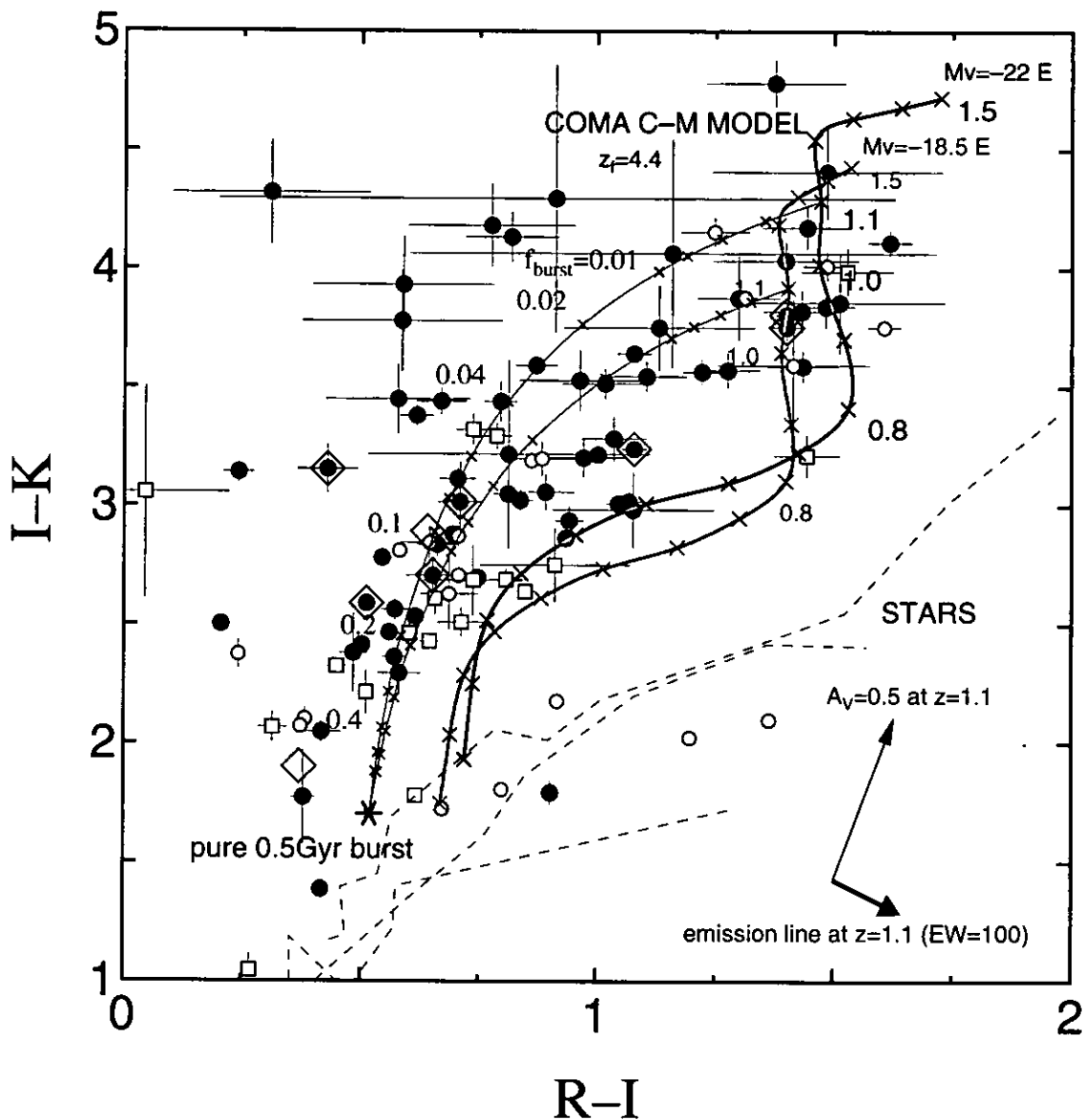


Figure 1.7: $I - K$ against $R - I$ colour-colour diagram for $K < 19$ galaxies near the radio-loud quasar 1335+2834 from the $z \simeq 1.1$ Crampton et al. (1989) LQG. The differing symbols indicate the location of the galaxy within the $5 \times 3 \text{ arcmin}^2$ field, with filled circles, open circles, and open boxes representing galaxies in the central third (centred on the quasar), the western third, and the eastern third of the field respectively. The sources indicated by large diamonds are the emission-line galaxies found by Hutchings et al. (1993). The Coma C-M evolutionary models of Kodama & Arimoto (1997) for passively-evolving elliptical galaxies with $M_V = -22$ and $M_V = -18.5$ (at $z = 0$) are indicated by solid red and orange curves respectively. Each track shows the colour evolution from $z = 1.5$ to $z = 0$ with crosses at 0.1 redshift intervals. The effect of adding a secondary burst of star-formation is shown by the thin blue curves, where f_{burst} indicates the mass fraction of the component that underwent a burst of star-formation 500 Myr before being observed. Taken from Tanaka et al. (2000)

ellipticals associated with the quasar is apparent in the form of sources near the quasar (shown as filled circles) with RIK colours consistent with the Kodama & Arimoto (1997) evolutionary model for massive elliptical galaxies at $z \simeq 1.1$. Many more galaxies still have relatively red optical- near-infrared colours, but also show a significant UV excess with respect to passive-evolution models (manifested as blue $V - I$ colours). These appear to be well described through the addition of a secondary star-forming component (shown as blue curve) to a $z \simeq 1.1$ passively-evolving population, suggesting that these are also galaxies at the quasar redshift, but with some recent star-formation. There are many more galaxies with the red optical- near-infrared colours expected of galaxies at the quasar redshift in the third of the field containing the quasar (shown as filled circles) than the other two thirds (open circles and boxes), indicating that the cluster is associated with the quasar. An examination of the spatial distribution of the red galaxies ($R - K > 4.5$) indicates that the cluster is centred not on the quasar but on the brightest member of the cluster red sequence (having $K = 17.27$), 20 arcsec (corresponding to $250 h^{-1} \text{kpc}$ at $z = 1.086$) to the west of the quasar (Yamada et al., 1997). The spatial distribution of the red galaxies appears as a filamentary structure extending in the north-south direction, about 30 arcsec wide and at least 150 arcsec ($\simeq 2 h^{-1} \text{Mpc}$) long, reaching the southern boundary of the K image. Indeed there is evidence of clustering beyond the K imaging from the spatial distribution of optically-red ($R - I > 1.3$) galaxies indicating that the filament extends further south, and another filamentary structure is apparent extending for $\sim 200\text{--}300$ arcsec along the southern edge of the K image (Tanaka et al., 2000). A comparison of the data of Hutchings et al. (1993) and Yamada et al. (1997) indicates that the emission-line galaxies are located preferentially along either side of the filament, just as the quasar is, suggesting that the quasar- and star-formation is restricted to the periphery of the clustering.

In a further study to identify signs of large-scale structure associated with the Crampton et al. (1989) LQG, Tanaka et al. (2001) present deep optical (R, I) imaging of a $48 \times 9 \text{ arcmin}^2$ ($35 \times 6.5 h^{-2} \text{Mpc}^2$) field containing five members of the Crampton et al. (1989) group. A colour-magnitude selection criterion of $1.2 < R - I < 1.6$ and $21 < I < 23.5$ is used to identify those sources likely to be passively-evolving galaxies associated with the group. Figure 1.8 shows the smoothed density map



Figure 1.8: Large-scale structure traced by the $z \simeq 1.1$ Crampton et al. (1989) Large Quasar Group. A smoothed density map of red galaxies with $21 < I < 23.5$ and $1.2 < R - I < 1.6$ across the whole $48 \times 9 \text{ arcmin}^2$ region studied by Tanaka et al. (2001), with the regions of high density indicated by yellow and red colours and regions of low density indicated by blue colours. The plotted contours indicate the 2σ , 3σ and 4σ significance levels of galaxy number density above the rms level. The locations of the five $z \simeq 1.1$ quasars from the Crampton et al. (1989) LQG are indicated by asterisks. Taken from Tanaka et al. (2001)

of these galaxies across the whole field, with high-density regions indicated by red and yellow colours and low-density regions indicated by blue colours. A filamentary structure is apparent along the southern edge of the field, made up of at least five clusters (indicated by labels *cl_1-cl_5*, extending for 20–30 arcmin ($14\text{--}22 h^{-1} \text{ Mpc}$)). Tanaka et al. (2001) classes four of the five clusters as of Abell richness class ~ 0 , with cluster *cl_2*, previously identified by Yamada et al. (1997) and Tanaka et al. (2000), classed as of richness class 2. The five $z \simeq 1.1$ quasars are indicated by asterisks, and it is notable how they trace the underlying large-scale structure of red galaxies. However, four of the five (all radio-quiet) quasars do not appear to be associated directly with any of the clusters/groups, and only the radio-loud quasar previously studied by Yamada et al. (1997) and Tanaka et al. (2000) appears associated with the rich cluster identified as *cl_2*, although as discussed previously, it is located on the periphery of the clustering rather than in the cluster core. The detected signature of a possible supercluster at $z \simeq 1.1$ may be the first direct indication of the association of large quasar groups with large-scale structure at high redshifts, although spectroscopic observations to determine the redshifts of the red galaxies which make up the apparent large-scale structure will be needed to confirm this picture.

1.9.3 The Clowes-Campusano Large Quasar Group at $z \simeq 1.3$

The third quasar group, and the largest spatially, is the Clowes-Campusano Large Quasar Group (Clowes & Campusano, 1991, 1994; Graham et al., 1995), and consists of 18 quasars at $z \simeq 1.3$. The UK Schmidt objective-prism plate UJ5846P of ESO/SERC field 927 (field centre $10^{\text{h}}40^{\text{m}}00^{\text{s}}$, $+05^{\circ}00'00''$) was examined and quasar candidates selected by, one or both of emission lines and ultraviolet excess, using the AQD (Automatic Quasar Detection — Clowes et al., 1984) method, for spectroscopic observations with the CTIO 4-m Blanco telescope, resulting in 118 quasars over the 25.3 deg^2 field (Clowes & Campusano, 1991, 1994; Clowes et al., 1999a), along with a further 27 that had been previously identified in the same field (Keable, 1987). The redshift distribution of the first half of the sample (56 from Clowes & Campusano (1991, 1994) and 5 from Keable (1987) that had been re-observed) shows a peak of 10 quasars at $1.2 \leq z < 1.4$, well away from the redshift range of $2 \lesssim z \lesssim 2.5$ where the survey is expected to find most quasars. These 10 quasars are found to be spatially correlated also, with nine of them located in one half of the field, above the north-west–south-east diagonal. A further three quasars with $1.2 \leq z < 1.4$ are identified in the data of Keable (1987), along with a further five in the second half of the quasar sample (Clowes et al., 1999a), taking the number of quasars in the group to 18. The spatial correlation is still observed after the addition of the eight other quasars, as can be seen in Figure 2.1 which shows the spatial distribution of the 18 quasars in relation to the survey boundaries. The quasars appear to form a large, elongated group with angular sizes $\sim 1^\circ$ and $\sim 2.5\text{--}5^\circ$, corresponding to $\sim 50h^{-1}\text{Mpc}$ and $\sim 120\text{--}240h^{-1}\text{Mpc}$ respectively at $z \sim 1.3$. The quasars have a mean redshift of $\bar{z} = 1.267$ and a redshift dispersion of $\Delta z = 0.056$ corresponding to a depth of $165h^{-1}\text{Mpc}$ in the redshift direction. As for the previous two quasar groups, the Clowes-Campusano LQG extends fully across the survey geometry, and so the full extent of the group is not yet clear, but even so it is comparable in size to any other structure known in the universe (e.g. Tully et al., 1992).

To date, apart from the work described in the remainder of this thesis, the only study to examine whether this quasar group traces an underlying mass distribution is that of Williger et al. (2000). The redshift distribution of MgII absorbers in the spectra of quasars behind the Clowes-Campusano LQG (i.e. in the same half-

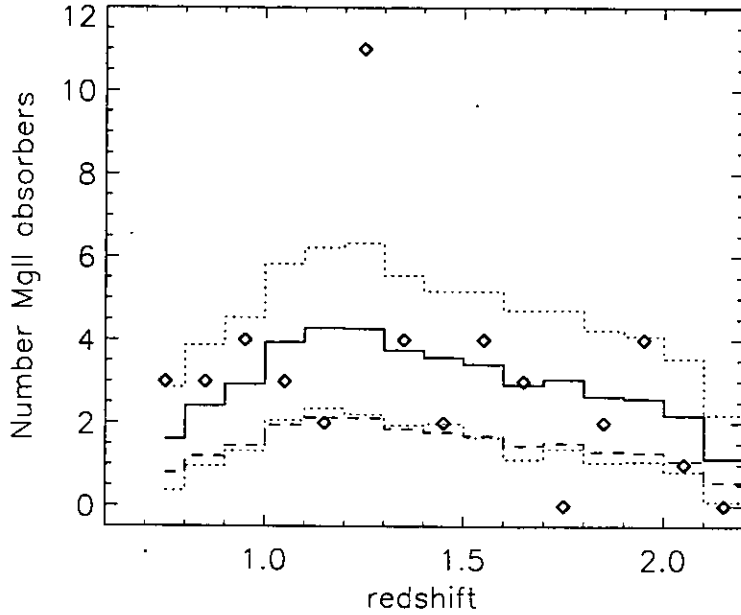


Figure 1.9: The redshift distribution of MgII absorbers towards the Clowes-Campusano LQG (shown as open diamonds). The expected redshift distribution, given the spectral coverage, and using the statistics of Steidel & Sargent (1992) for weak [$W_0(\text{MgII}\lambda 2796) \geq 0.3 \text{ \AA}$] absorbers is shown by the thin (lower) dashed line; it is half of the number detected, implying an overdensity of 5σ significance over the whole redshift range. The distribution normalised to the observations is shown by the thick (upper) solid line, with 1σ scatter determined from 200 random distributions of MgII absorbers shown by the dotted lines. Taken from Williger et al. (2000)

diagonal of the quasar survey of Clowes & Campusano (1991, 1994)) was examined to search for indications of gas associated with the quasar group. Evidence in favour of an excess of gas associated with the quasar group is found in the form of a 3.4σ overdensity for the redshift range $1.2 < z < 1.3$, with 11 absorbers detected whereas only 4 would be expected (see Figure 1.9). The Kolmogorov-Smirnov test rejects the null hypothesis that the observed redshift distribution is drawn from the Steidel & Sargent (1992) distribution at a level of significance of 0.003.

1.9.4 Other Large Quasar Groups

To establish the full extent of the Clowes-Campusano LQG, the Chile-UK Quasar Survey (CUQS) was undertaken. The survey aims to cover 140 deg^2 of sky centred on the Clowes-Campusano LQG in order to establish the full extent of the structure. Quasar candidates are selected by ultra-violet excess ($u_J - b_J < -0.3$) to a magnitude

limit of $b_J = 20$ and are observed using the 2.5-m du Pont telescope at Las Campanas Observatory in Chile. As part of this survey, Newman (1999) reports the discovery of a group of 13 quasars at $z \simeq 1.53$ with a spatial extent of $200 \times 120 \times 125 h^{-3} \text{ Mpc}^3$. The shape of the group resembles three intersecting filaments. The first filament runs approximately east-west at $z \simeq 1.49$, a second filament runs approximately north-south at $z \simeq 1.60$, and a third filament connects the first two.

To identify large quasar groups in other quasar surveys, Graham et al. (1995) describe and use a graph theoretical method, the minimal spanning tree (MST). Any distribution of points, such as the positions of quasars in redshift-space, has an associated unique network, called its minimal spanning tree, which is defined as the network that connects all the points with the minimum total length of edges (lines connecting two points). By progressively removing the edges in descending order of length until the number of structures (any set of connected points) is maximised, any significant structure still remaining is likely to be a real association. The significance and morphology of the remaining structures can be determined by comparing the mean and standard deviation of edge lengths with that for a Poisson distribution (Barrow et al., 1985). The minimal spanning tree structure finding algorithm was applied to six quasar surveys: Clowes & Campusano (1991, 1994); Crampton et al. (1987, 1989); Osmer & Smith (1980); Osmer & Hewett (1991); Cristiani et al. (1989); and Hawkins & Veron (1993). As a demonstration of the validity of the MST approach, the known quasar groups of Webster (1982), Clowes & Campusano (1991, 1994) and Crampton et al. (1989) are rediscovered. In the Osmer & Hewett (1991) quasar survey, a new quasar superstructure is identified of ten quasars at $z \simeq 1.9$, with a spatial extent of $170 \times 130 \times 30 h^{-3} \text{ Mpc}^3$. In the Cristiani et al. (1989) survey there is no significant structure among the quasars, but amongst the Seyfert galaxies there is a connected group of seven objects at $z \simeq 0.19$ forming a structure of extent $60 \times 30 \times 10 h^{-3} \text{ Mpc}^3$.

Komberg et al. (1996) applied the friends-of-friends structure finding algorithm to a combined list of quasar surveys, the Veron-Cetty & Veron (1991) catalogue of quasars. By selecting those structures detected that contained 10 or more quasars, and had a comoving quasar density twice that of the background one, they identified 12 candidate large quasar groups, including some that had been previously identified

(e.g. Crampton et al., 1989; Graham et al., 1995).

As a result of the observations of Hutchings et al. (1993, 1995), Komberg & Lukash (1994) and Komberg et al. (1996) suggested that as the individual quasars are associated with apparently young clusters of galaxies, then the groups are likely to be tracing the locations of enhanced-density regions which develop later into quasi-linear systems such as the local “Great Attractor” or Shapley concentration, and hence LQGs represent the progenitors of “Great Attractors” at high-redshifts. They also claim that not only were the LQGs of a comparable size to these local large-scale structures, but that the comoving number densities of LQGs and local superclusters are comparable. It is however difficult to draw many conclusions from the study of Komberg et al. (1996) regarding this claim given the significant heterogeneity of the Veron-Cetty & Veron (1991) catalogue. It will only be possible to estimate the statistical properties of LQGs in terms of number, size, and redshift distribution, once large homogeneous surveys such as the 2dF and SDSS quasar surveys are completed. It is not possible to use the recently released *10k catalogue* from the 2dF quasar survey for this purpose as the coverage is very patchy and inhomogeneous due to the observing strategy used, and even when the final catalogue is released, the elongated survey geometry is far from ideal for studying large quasar groups.

It has been suggested that the Large Quasar Groups could alternatively be merely regions of enhanced quasar formation that are not necessarily associated with any density enhancement (Silk & Weinberg, 1991). It does however appear unlikely that such a region of enhanced quasar formation would extend over such large scales if not associated with any underlying overdensity in terms of mass (Graham, 1997). The studies of the quasar two-point correlation function (Croom et al., 2000) and power spectrum (Hoyle et al., 2001), as well as those into the galaxy environments of quasars (e.g. Wold et al., 2000, 2001; Hall & Green, 1998), all indicate that quasars trace the galaxy distribution in a relatively unbiased manner, and are on an individual basis commonly associated with mass in the form of groups and clusters of galaxies. Finally, recent studies examining the association of large quasar groups with mass in the form of gas (Williger et al., 2000) and galaxies (Tanaka et al., 2001), support the hypothesis that large quasar groups trace an underlying structure extending over large-scales.

Chapter 2

Ultra-deep Imaging of the Clowes-Campusano Large Quasar Group

2.1 Introduction

The primary objective of this study is to determine the galaxy environment of quasars in the Clowes-Campusano LQG, and to examine the hypothesis that LQGs trace large-scale structures. To do this requires observations which satisfy the following requirements.

Detection The images have to be sufficiently deep to detect ‘typical’ galaxies at the redshift of the LQG. To put this in context, our Galaxy, if observed at a redshift of 1.3, would have $B \simeq 26.7$, $V \simeq 26.3$, $R \simeq 25.3$, $I \simeq 24.7$.

Identification There needs to be sufficient colour information to obtain photometric redshift estimates that at least allow the identification of high-redshift galaxies on a statistical basis, so that any associated clustering can be identified. The optimal choice of passbands for identifying quiescent galaxies are those which straddle the 4000 Å break, which at the LQG redshift correspond to I and K . The addition of further passbands with rest-frame wavelengths of 2000–10000 Å then improves the accuracy of the estimate. The technique of photometric redshift estimation will be described fully in chapter 4.

Width The field observed has to be sufficiently large to identify any large-scale structure associated with the LQG. In other words, it must be significantly

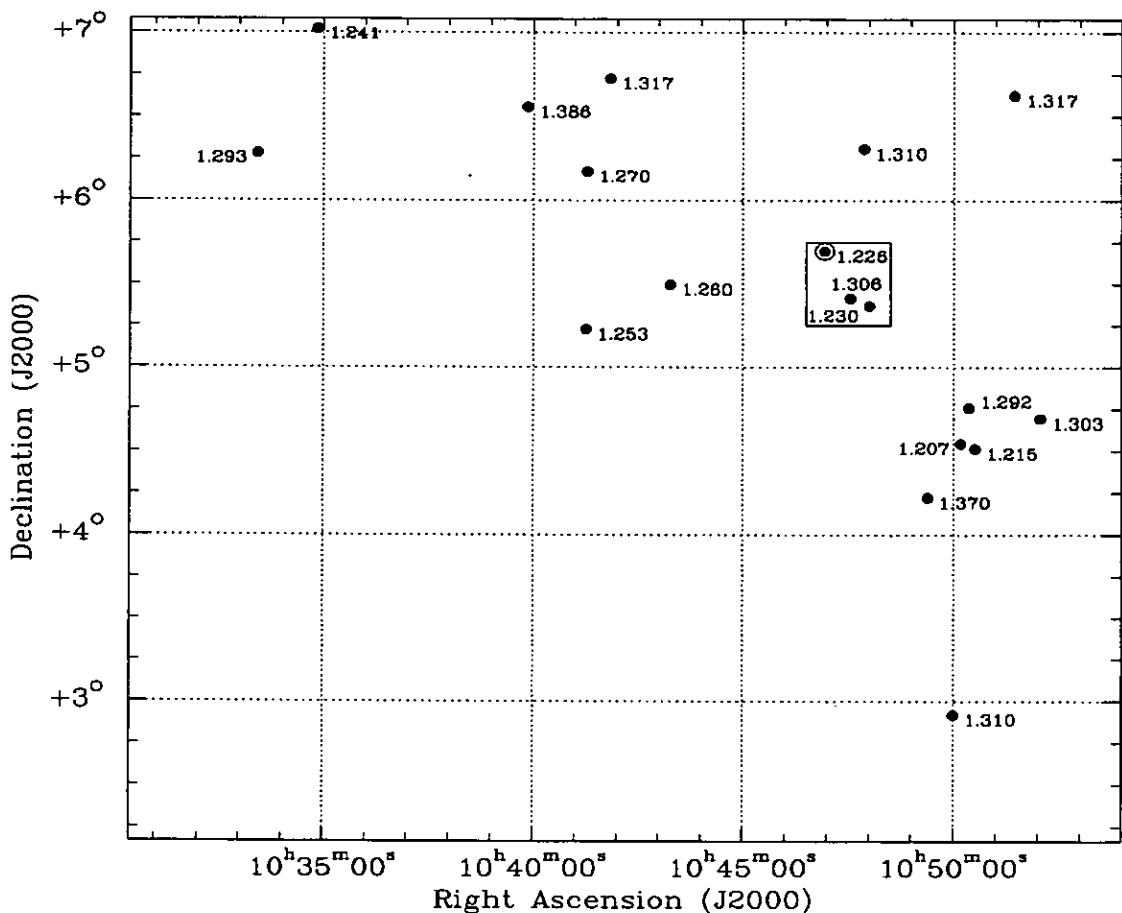


Figure 2.1: The Clowes-Campusano Large Quasar Group with each quasar labelled by its redshift. The 30×30 arcmin² region targeted for BTC imaging is indicated by the box, and the quasar for which K imaging has been obtained, the results of which are described in Chapter 5, is circled. The boundaries of the plot match the boundaries of the AQD survey of ESO/SERC field 927 (Clowes & Campusano, 1991, 1994; Clowes et al., 1999a).

larger than typical cluster sizes, giving us a minimum comoving field size of the order $10 h^{-1}$ Mpc.

This chapter describes the obtaining and reduction of ultra-deep wide-field optical images to meet these requirements. A 30×30 arcmin² field centred on $10^h 47^m 30^s$, $+05^{\circ} 32' 00''$ (J2000) and containing three of the quasars from the Clowes-Campusano LQG was observed on the nights of 21/22 and 22/23 April 1998, using the Big Throughput Camera (BTC) (Wittman et al., 1998) on the 4-m Blanco telescope at the Cerro Tololo Interamerican Observatory (CTIO) in Chile. One night was devoted to each optical broadband filter, reaching $V \simeq 26.5$ and $I \simeq 26.0$ in places, and resulting in catalogues of $\simeq 10^5$ sources.

Unfortunately, there are no near-infrared instruments comparable with the BTC, and so it has only been possible to obtain K imaging for selected subfields using the UFTI camera on the 3.8-m United Kingdom Infra-Red Telescope (UKIRT). In March 1999, a 2.25×2.25 arcmin² field centred on the $z = 1.226$ quasar at $10^{\text{h}}46^{\text{m}}56.70^{\text{s}}, +05^{\circ}41'50.5''$ was observed, reaching $K \simeq 20$. A second field, containing the $z = 1.306$ quasar at $10^{\text{h}}47^{\text{m}}33.17^{\text{s}}, +05^{\circ}24'54.9''$ was observed using the same camera in May 2000. The results and analysis of these data are described in Chapters 5 and 6.

2.2 BTC Observations

The Big Throughput Camera had, at the time of observing, the greatest throughput (in terms of flux) of any camera in the world, with a 30×30 arcmin² field on the 4-m Blanco telescope at CTIO, making it the ideal instrument for obtaining ultra-deep imaging (to $V \simeq 27$) for a cosmologically significant region. A particular example of its use has been in the Supernova Cosmology Project of Perlmutter et al. (1999) where its ability to combine depth with wide field has allowed the simultaneous observation of tens of thousands of galaxies, and made the multiple detection of high-redshift supernova feasible.

The first decision to be made regarding observing strategy is the selection of field. Although the BTC has the largest field of any 4-m telescope instrument, it is still an order of magnitude smaller than the 5×5 deg² region covered by the Clowes-Campusano LQG. The field centred on $10^{\text{h}}47^{\text{m}}30^{\text{s}}, +05^{\circ}32'00''$ (J2000) was chosen to be located near the centre of the LQG, and to contain three (the maximum possible in one field) quasars from the group. The size and location of the field in comparison with the LQG is shown in Figure 2.1. The chosen field also contains four background quasars from the quasar survey of ESO/SERC field 927 (Clowes & Campusano, 1991, 1994; Clowes et al., 1999a), although one of them (with $z = 1.738$) is within a few arcsec of the field's southern edge. The angular positions of the quasars are given in Table 2.1 along with their B magnitudes and redshifts.

The BTC optical observations took place on the nights of 21/22 and 22/23 April,

RA (J2000)	Dec (J2000)	m_B	z	Reference
$10^h46^m56.71^s$	$+05^\circ41'50.2''$	18.62	1.226	CC91
$10^h47^m33.17^s$	$+05^\circ24'54.9''$	17.87	1.306	CC91
$10^h48^m00.41^s$	$+05^\circ22'09.6''$	19.69	1.230	CC91
$10^h47^m21.58^s$	$+05^\circ13'48.4''$	19.33	1.738	CC91
$10^h48^m40.09^s$	$+05^\circ35'51.2''$	18.66	1.968	CC91
$10^h46^m42.83^s$	$+05^\circ31'07.1''$	19.18	2.682	CCG99
$10^h46^m31.85^s$	$+05^\circ20'09.8''$	19.98	1.426	N99

Table 2.1: List of quasars in the BTC field, including their B magnitudes and redshifts. The first three are the LQG quasars, and the remaining four are background quasars. The reference column indicates whether the data are taken from Clowes & Campusano (1991, 1994) [CC91], Clowes et al. (1999a) [CCG99], or Newman (1999) [N99].

1998. At that time of year, the field becomes too low in the sky to observe at 2am, giving a total observing window of only 5–6 hours per night. Given that at least 4 hours were needed to reach the required depths in each broadband filter, it was decided to spend one night each with the V and I filters. The reasons behind the choice of filters from the $UBVRI$ set are as follows:

- I was chosen above all others, as although all filters correspond to rest-frame wavelengths shortwards of the 4000 \AA break, the I filter is the reddest and so least affected by star-formation and is the optimal for photometric redshift estimation in combination with near-infrared photometry.
- U and B were rejected as they correspond to rest-frame UV, and the U was also rejected as the CCD is least sensitive at that wavelength resulting in prohibitive exposure times.
- V was chosen above R as the effect of redshift and star-formation on the $V - I$ colour are likely to be double that for $R - I$, and so the effect of photometric errors are halved.

The BTC is made up of four 2048×2048 CCDs which have pixels of size 0.43 arcsec , giving a field of view for each CCD of $14.7 \times 14.7 \text{ arcmin}^2$. The CCDs

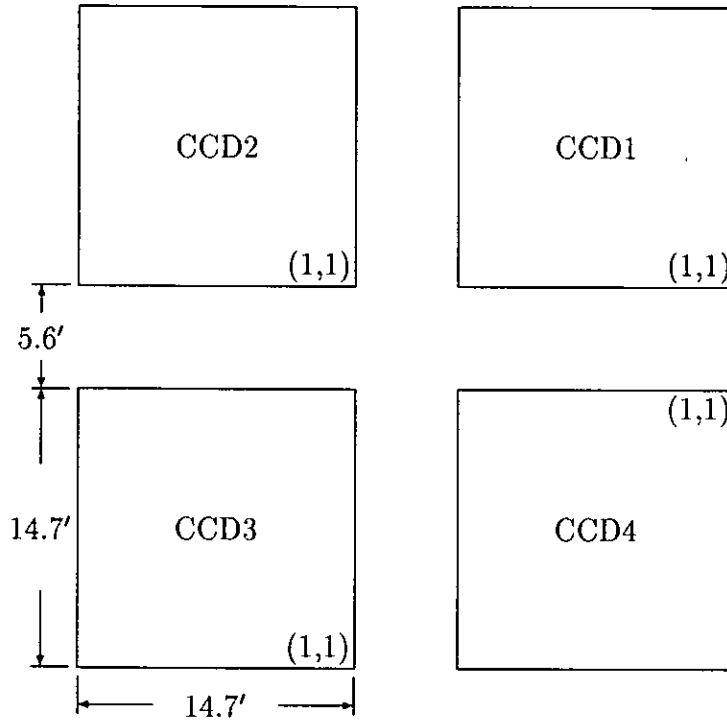


Figure 2.2: Geometry of BTC CCD array. For each CCD, the origin of the output image is represented in the figure by (1, 1) (CCD #4 is inverted). North is towards the top, and east is to the left.

are arranged in a 2 by 2 grid, and are separated by gaps of 5.6 arcmin, as shown in Figure 2.2.

As the camera does not have a contiguous field of view, it is necessary to shift the camera between exposures to obtain a contiguous image, and uniform coverage is impossible. However, after devising and comparing various observing strategies in which the camera is shifted between exposures, it was found that near-uniform coverage, over a 29.4×29.4 arcmin² field, could be attained from a 4 by 4 grid of pointings, with each pointing offset by the gap width to adjacent pointings, as shown in Figure 2.3 (left), with each pointing observed in the order indicated by its label.

This results in $\sim 75\%$ of the field being covered by exactly 9 out of the 16 pointings, as shown by Figure 2.4 (left). The pointing order was chosen to maximise the uniformity of the combined exposures to a given stage, in order to minimise the effect of incompleteness due to changes in weather conditions or telescope faults. However, given the 2 minute readout time between exposures, it was only feasible to complete one circuit of the 16 exposure pattern, and so a backup pattern was devised

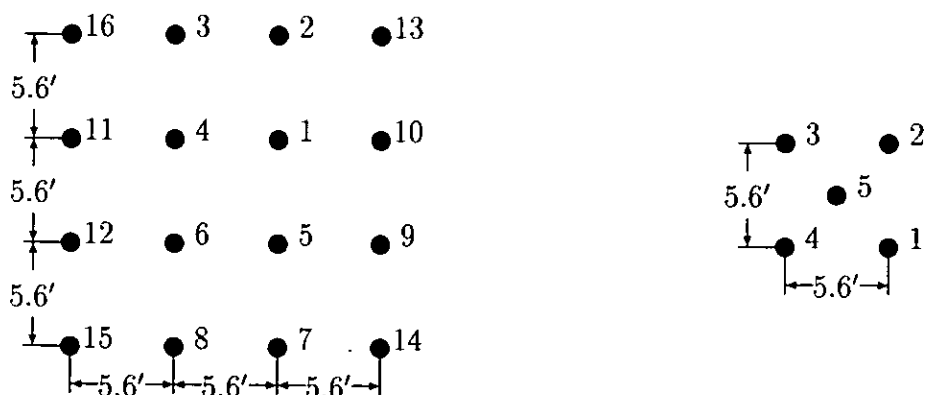


Figure 2.3: Relationship and order of pointings for both the original 4 by 4 grid pattern (left), and the reserve 5-pointing pattern (right).

in case of problems early on in the night. This could be completed several times during the night, thus reducing the effect of a significant loss of time on uniformity. The pattern involved 5 exposures, four forming a 2 by 2 grid of pointings, each separated by the CCD gap width, plus another in the centre of the grid, shown in Figure 2.3 (right). The coverage of the reserve pattern is shown in Figure 2.4 (right). Artifacts from the flat-fielding process can occur if the same source falls on the same pixel of a CCD in separate exposures, and so after each circuit of 5 pointings the telescope is shifted with respect to the centre by 30 arcsec in a random direction.

On the first night of observing the weather was good, and the *V* imaging was obtained using the original 4 by 4 grid pattern, with each exposure of 900 sec. Half-way through the night there were problems with the camera shutter not closing after an exposure and the software losing the data, and so approximately one hour was lost, and the last few target exposures were at very high airmasses (2–3). On the second night, thin cloud and more problems with the camera shutter caused a similar loss of one hour’s observing at the start of the night, and so it was decided to change to the reserve pattern for the *I* imaging in case of more problems. Fortunately, no more problems arose and we were able to complete three circuits of the 5 exposure pattern, producing 15 exposures of 1080 sec each.

Ten bias frames were produced before observations started each night. To calibrate the photometry, after the target field had set, the standard star fields PG1323–086, PG1633+099 and MARK A from Landolt (1992) were observed in

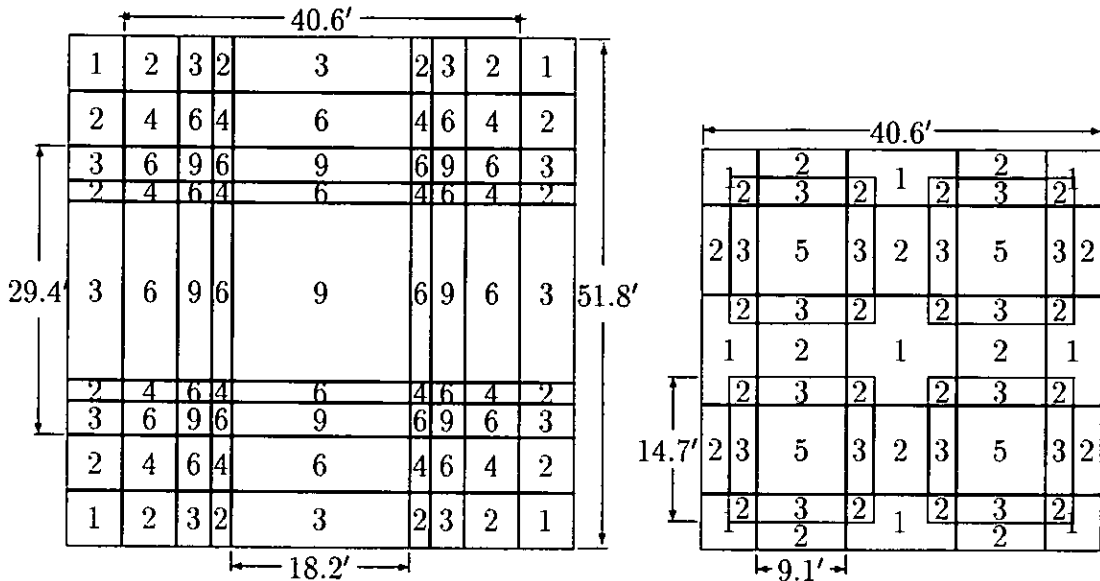


Figure 2.4: Coverage of the field by the 4 by 4 grid pattern (left), and for the reserve 5 exposure pattern (right). The numbers in each region represent the number of exposures per circuit which cover that region.

both filters, with 4×5 sec exposures positioned so that the field is centred on each of the four CCDs in turn. Each field contained four or five standard stars with ($12.0 < V < 16.0$), and fields were chosen to lie at varying airmasses (1.2–2.3) to allow the atmospheric extinction coefficient for each filter to be calculated. Finally, so that the distortions produced by the BTC camera optics could be modelled and removed, two USNO astrometric fields, centred at $16^h 13^m 44^s, -00^\circ 01' 50''$ and $18^h 47^m 44^s, -00^\circ 01' 05''$ were observed for 30 sec in both filters.

2.3 Reduction of the BTC Images

2.3.1 Summary

The images produced by CCD cameras are affected by the characteristics of the CCD and camera, such as biasing, spatial distortions, and sensitivity variations across the array, and so before any analysis of the data is possible, it is necessary to remove these instrumental signatures through data reduction.

The BTC has mostly the same generic characteristics as other cameras, and so the standard reduction tools of the IRAF software package were used to perform

much of the reduction, such as bias subtraction and flattening. However the BTC suffers from significant spatial distortions which required the use of astrometric fields to fit parameters to a distortion model supplied by the camera's development team (Dell'Antonio & Bernstein, 1997). Self-written code was developed to determine these parameters which then define the transformations which are applied to the images within IRAF. Throughout the reduction processes the images produced by each of the four BTC CCD arrays were considered separately.

2.3.2 Initial Reduction Steps

The IRAF `zerocombine` tool was used to combine the ten bias frames taken each night into a master bias frame, using the median value for each pixel after rejecting both the minimum and maximum values. This master bias frame is then subtracted from each of the target images. A regular narrow striping effect is noticeable in the bias frames, where the pixel counts are on average 5–8 ADU lower than the remainder of the bias image, and is shown in Figure 2.5. The horizontal position of the narrow stripes are not coincident from frame to frame, and so do not appear on the master bias. As a result they cannot be removed from the target frames, but the co-adding process should mean that the stripes do not appear in the final target image, and their effect on photometry should be negligible in any case.

The unilluminated rows and columns on the edge of each image were removed along with the overscan region (area that measures the changes in bias levels between images but which was not used here), using the IRAF `ccdproc` tool, with the trim data parameter set to [2:2047,2:2048] for all four CCDs, leaving an image of $2046 \times 2047 \text{ pix}^2$ for each CCD.

For each image a bad pixel file was generated, describing the location of the bad columns and regions, so that they can be interpolated across using `ccdproc`. As well as the bad columns/regions which are artifacts of the CCD and so constant throughout the night, the vertical lines apparent through the brightest stars are interpolated across. These lines are caused by the leakage of electrons along the readout axis from heavily saturated pixels. Their removal is mainly a cosmetic exercise, as the same area of sky tends to get affected on all exposures, so that the true data cannot be recovered. The number and extent of the vertical lines through

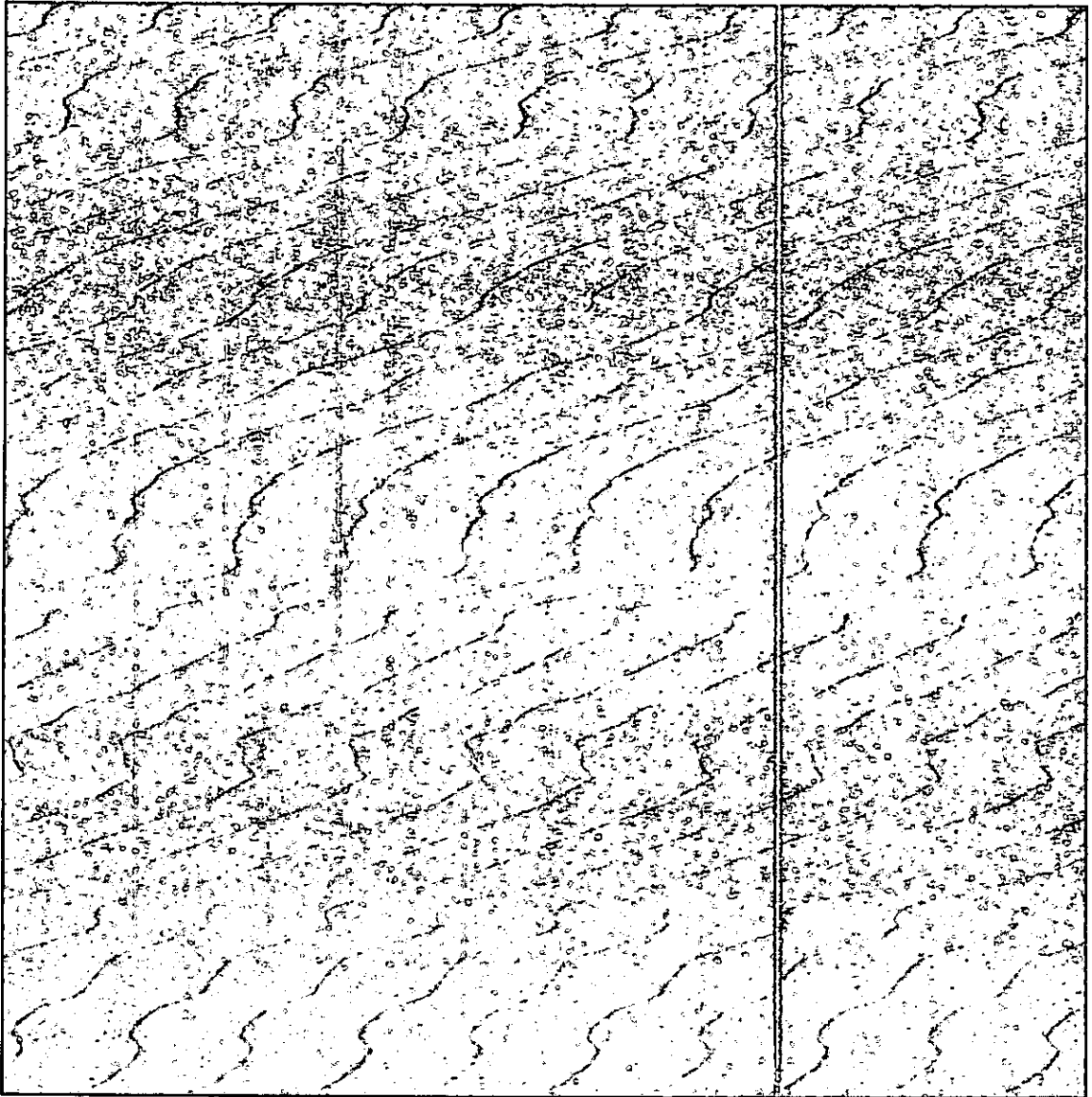


Figure 2.5: A bias frame taken from the first night with CCD #1. The white vertical line, two-thirds of the way to the right, is the same bad column as in Figure 2.6. The apparent regular black striping effect varies from frame to frame, and so cannot be removed from the individual target exposures.

bright stars are much greater for the *I*-band rather than the *V*-band exposures, as the background levels are much closer to the pixel saturation level of 65 000 ADU. The nature of both the bad columns and vertical lines through bright stars are apparent in the raw image shown in Figure 2.6.

It soon became apparent that CCD #1 was much worse than the other three. Figure 2.7 shows the count levels across the array (averaged over 10 rows) for each of the four CCDs from the first 900 sec *V*-band target exposure. It is clear that

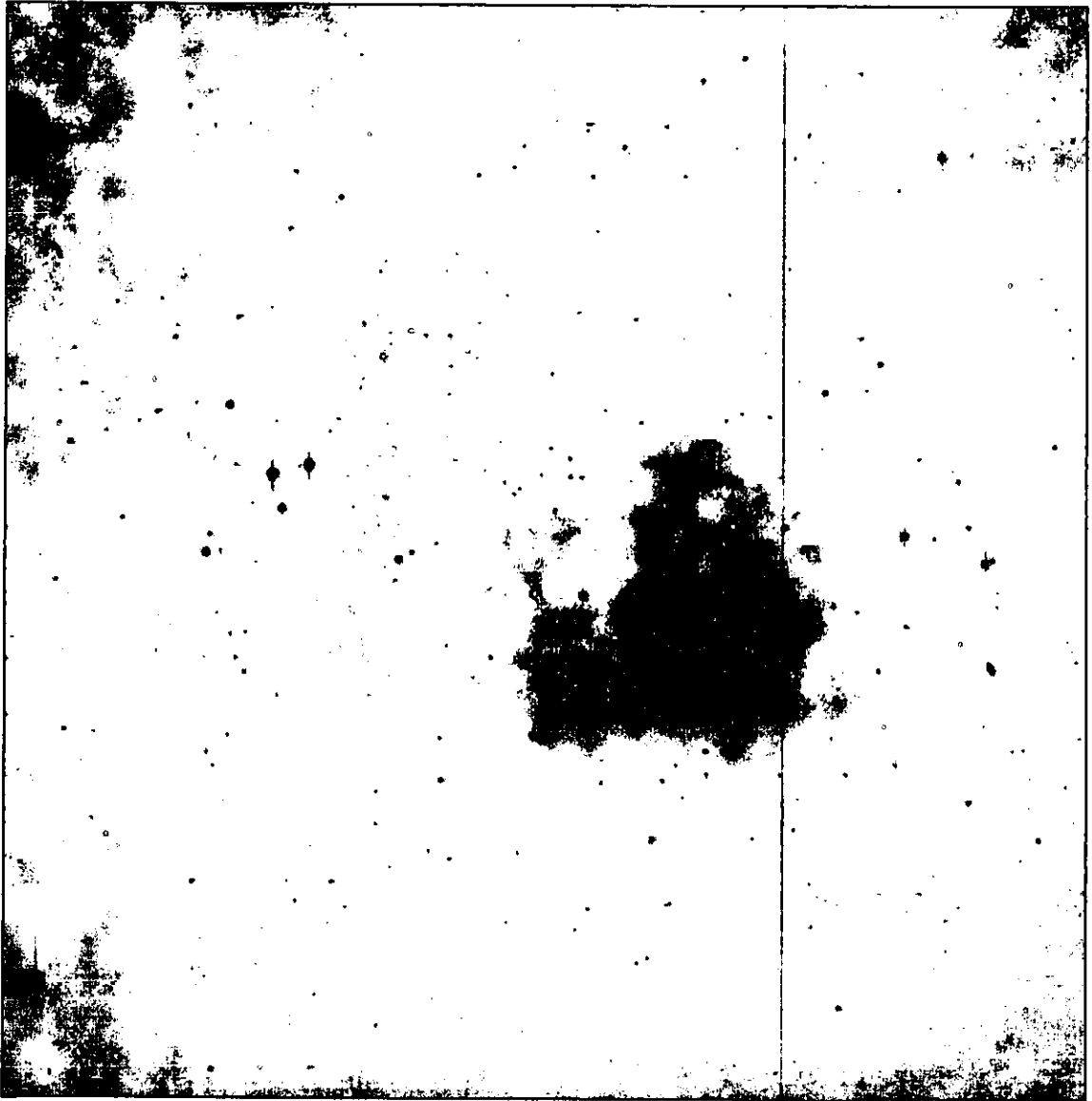


Figure 2.6: A raw BTC image of the quasar group, corresponding to a field of 14.7×14.7 arcmin². This is the first 900sec exposure of the target field taken by CCD #1 through the *V* filter. The large cloudy splodge in the centre of the image, and the cloudiness apparent towards the edges are purely CCD artifacts, and are removed during the flat-fielding process. The black vertical line, two-thirds of the way to the right is a bad column, which is removed by interpolating across it. The vertical lines through the brightest stars are due to leakage of electrons along the readout axis from heavily saturated pixels, and are also cosmetically removed by interpolation.

whereas CCDs #2-4 have typical count levels of 8000 ADU, and variations over the array of $\lesssim 5\%$, CCD #1's count levels are generally around 4000 ADU, with a $\simeq 50\%$ increase between columns 1000 and 1500 due to the cloudy splodge of Figure 2.6.

The loss in sensitivity of CCD #1 meant that those areas of the BTC field predominantly observed through CCD #1 had a reduction in magnitude limit, so

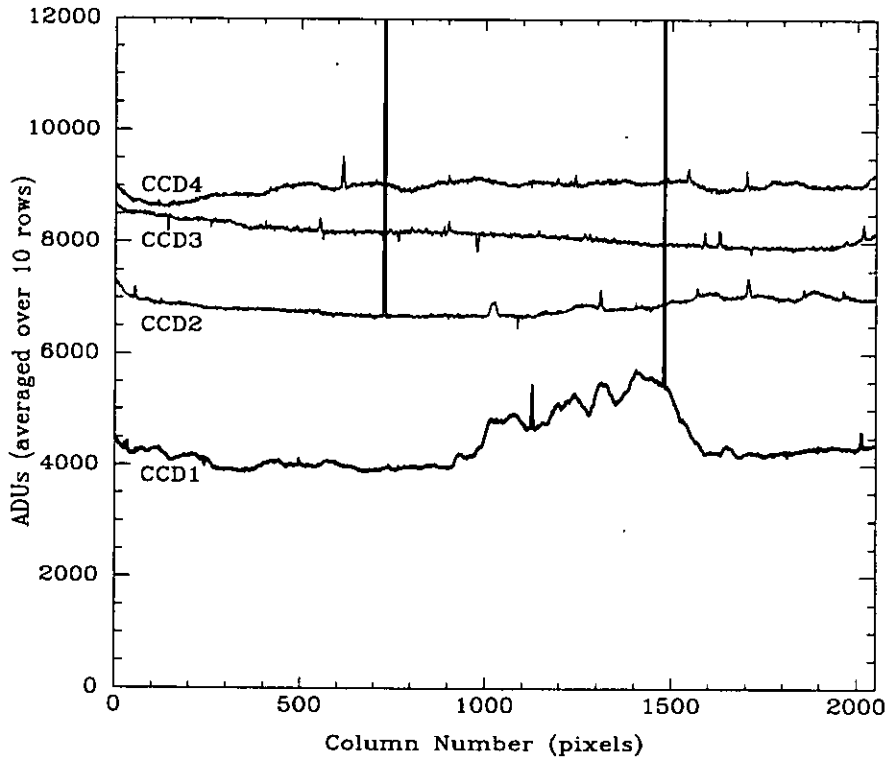


Figure 2.7: A comparison of sensitivity of the four CCD arrays. The curves correspond to the average ADUs of 10 adjacent rows in each of the four CCDs from the first 900 sec target V exposure (the raw image from CCD #1 is shown in Figure 2.6. The effect of bright stars (and in particular the vertical lines described earlier) can be seen as sharp peaks in the curves, the most obvious being that in CCD2 near column #720, and an attempt was made to minimise this contamination through the choice of rows. The sharp peak at column #1480 in CCD1 is due to the bad column visible in Figure 2.6.

that the desired uniformity over the BTC field is reduced, and the large variations in sensitivity across the array caused problems when it came to flat-fielding, as will be described later. The effect of CCD #1 on the I imaging was less severe, as the loss in sensitivity against the other CCDs was $\simeq 35\%$ rather than the 50% loss observed for the V images, and the variations across the CCD were much smaller, and were successfully handled by the flat-fielding procedure.

To remove the inter-pixel differences in sensitivity across the CCD, a flat-field image is required, which is an image of a uniformly illuminated field. As there were a sufficient number of exposures from differing pointings, the images themselves could be used to produce a *superflat* image using the IRAF `flatcombine` tool. Each image was scaled by its modal value to normalise the sky background levels, before

being combined by the median, with sigma clipping rejection (pixel values 3σ above the median are ignored) to remove stars, producing the superflat image. It was immediately apparent that the flat-fielding of the CCD #1 V -band images was not successful, with the cloudy structures of the raw image still visible. An examination of the images and their FITS headers indicated that the CCD temperature had changed significantly halfway through the night from 176 K to 188 K, at the same time as the problems with the shutter closure mechanism, and that this appeared to have affected the sensitivity of the CCD. To account for this, the CCD #1 images were separated according to their temperature, and two flat-field images produced. The temperature of the other three CCDs was found to change at the same time, but as the variations across the arrays were an order of magnitude smaller than CCD1, the temperature change had a negligible effect on the flat-fielding process.

Normally, at this point the images are flattened by dividing by the corresponding flat-field, but as the BTC has significant non-linear spatial distortions, these have to be transformed away before flattening to maintain image flatness.

2.3.3 Distortion modelling and removal

One of the problems inherent in using wide-field cameras such as the BTC is that the effect of non-linear distortions, produced by the camera optics, is no longer negligible. In order to successfully register images from different pointings these distortions must be first modelled and removed using transformations.

To do this requires a *control* image where the physical angular positions, (α, δ) , of a large number of stars are known to high accuracy. A distortion modelling program is then run which takes the (x, y) position of each source on the CCD, and determines the transformations which best map these (x, y) coordinates onto the (α, δ) coordinates.

To make this process possible, a number of astrometric fields spaced along the celestial equator have been observed by the United States Naval Observatory (USNO). The result is a catalogue of all the sources in the field with $m_V \leq 19.5$ with their angular positions determined to an accuracy of ~ 0.15 arcsec. During the observing run, two of these astrometric fields, centred at $16^h 13^m 44^s, -00^\circ 01' 50''$ and $18^h 47^m 44^s, -00^\circ 01' 05''$, were imaged in both V and I passbands.

The (x_{CCD}, y_{CCD}) positions of the $\simeq 300$ brightest sources in the CCD image are determined using `daophot`, which finds the centres and instrumental magnitudes of the sources through point-spread function fitting. The CCD image (with the sources labelled using `tvmark`) is visually compared with a Digitized Sky Survey (DSS) image of the same field, which is displayed using `GAIA` with the USNO catalogue (downloaded from the internet within `GAIA`) sources labelled upon it. The (x_{CCD}, y_{CCD}) and (α, δ) of each of the USNO sources labelled in the CCD images are stored as ordered lists in the form of eight text files, two for each CCD, named `BTC_CCD1_xy.txt`, `BTC_CCD1_usno.txt` etc., ready for input into the distortion modelling program `BTC_distortions.f`.

The causes of the distortions in the BTC are known, and can be modelled as a series of transformations with free parameters (Dell’Antonio & Bernstein, 1997), which are described below.

Place origin at Telescope Centre The CCD (x_{CCD}, y_{CCD}) and physical angular (α, δ) coordinates are related to one another by choosing a reference point, the telescope centre, and making that the origin for both coordinate systems. The four CCD arrays of the BTC are translated and rotated onto a common coordinate system, (x_3, y_3) , whose origin is taken to be the telescope centre, through the transformations

$$\begin{pmatrix} x_3 \\ y_3 \end{pmatrix} = \begin{pmatrix} \cos \theta^i & \sin \theta^i & x_{corner}^i \\ -\sin \theta^i & \cos \theta^i & y_{corner}^i \end{pmatrix} \begin{pmatrix} x_{CCD} \\ y_{CCD} \\ 1 \end{pmatrix}, \quad (2.1)$$

where θ^i is the clockwise rotation of CCD i , and $(x_{corner}^i, y_{corner}^i)$ is the translation vector from the bottom-right-hand corner of each CCD to the telescope centre in pixels.

A sine projection about the telescope centre, $(\alpha_{tel}, \delta_{tel})$ is constructed, so that the angular coordinates of the point, (α, δ) , relative to the telescope centre are given by

$$\begin{aligned} u &= \sin(\alpha - \alpha_{tel}) \cos \delta \\ v &= \sin(\delta - \delta_{tel}) + [1 - \cos(\alpha - \alpha_{tel})] \sin(\beta - \delta_{tel}) \cos \delta. \end{aligned} \quad (2.2)$$

CCD corrector lenses The BTC has corrector lenses above each of the CCDs to place the focal plane on the CCD arrays, the consequences of which are the magnification of each CCD image by the lens, and the distortion due to the breakdown of the thin lens approximation.

The combined CCD coordinates \mathbf{x}_3 are mapped onto the ideal focal plane coordinates \mathbf{x}_{FP} using the corrector lens transformation

$$(\mathbf{x}_{FP} - \mathbf{x}_L^i)(1 + s^i) = \mathbf{x}_3 - \mathbf{x}_L^i + \frac{(\eta - 1)}{\eta} \frac{|\mathbf{t}|^2}{2R_L^i} \mathbf{t} \left(1 + \frac{\eta^4 + \eta^2 - 2}{\eta^2 - 1} s^i\right) \quad (2.3)$$

$$\mathbf{t} \equiv (1 - s^i - 0.02) \mathbf{x}_3 - (1 - s^i) \mathbf{x}_L^i, \quad (2.4)$$

where \mathbf{x}_L^i are the locations of the corrector lens centres which are assumed to be at the centres of each CCD, and the R_L^i are their radii of curvature. The refractive index η of the lenses is taken to be 1.46, and the magnification, $1 + s^i$, of each of the CCD corrector lenses are known to be

$$\begin{aligned} CCD \#1 & 1.001673336 \\ CCD \#2 & 1.002482473 \\ CCD \#3 & 1.003383333 \\ CCD \#4 & 1.001731257 \end{aligned} \quad (2.5)$$

The R_L^i are related to each other by their magnifications through $R_L^i = R/(1 + s^i)$ leaving one free parameter, the radius of curvature constant R .

Telescope distortion The largest distortions produced in the images are due to the prime focus corrector optics, being around 60 pixels at the corners of the array. It is assumed that the telescope optics have an axis of symmetry (which is translated with respect to the telescope centre by the vector \mathbf{x}_{FA}), a plate scale, s , and that only the cubic (f_3) and quintic (f_5) distortion terms are of significance. The ideal focal plane coordinates, \mathbf{x}_{FP} are mapped onto the observed angular coordinates (u_{obs}, v_{obs}) by the transformation,

$$\mathbf{u}_{obs} = s \mathbf{x}_{FP} \left(1 + f_3 |\mathbf{x}_{FP} - \mathbf{x}_{FA}|^2 + f_5 |\mathbf{x}_{FP} - \mathbf{x}_{FA}|^4\right). \quad (2.6)$$

Differential atmospheric refraction Atmospheric refraction makes all sources in the sky appear closer to the zenith. If z_0 is the observed zenith angle, the true

zenith angle z_{true} is given by

$$\sin z_{true} = \eta \sin z_0, \quad (2.7)$$

where η is the index of atmospheric refraction.

The main effect of differential refraction is a slight stretch along the zenithal direction which can be modelled using the transformation

$$\begin{pmatrix} u_t \\ v_t \end{pmatrix} = \begin{pmatrix} 1 + \epsilon \sin^2 p & -\epsilon \cos p \sin p \\ -\epsilon \cos p \sin p & 1 + \epsilon \sin^2 p \end{pmatrix} \begin{pmatrix} u_{obs} \\ v_{obs} \end{pmatrix}, \quad (2.8)$$

where p is the parallactic angle of the telescope axis, and $\epsilon = (\eta - 1) \tan^2 z_0$.

The distortion modelling program The self-written FORTRAN distortion modelling program `BTC_distortions.f` takes as input the eight text files containing the CCD (x^i, y^i) and USNO (α^i, β^i) coordinates for each of the four CCDs. It then uses this data to iteratively optimise the distortion parameters by performing the above transformations, and minimising the error between the actual and transformed (u^i, v^i) .

In total there are 19 free parameters: 12 describe the four CCD positions and orientations relative to the telescope centre; five describe the distortions due to the prime focus camera optics (two define its axis of symmetry relative to the telescope centre, plus the plate scale, cubic and quintic distortion terms); one describes the radii of curvature of the corrector lenses; and one gives the refractive index of the atmosphere. Each of the 19 free parameters are given suitable initial values, p_0^j , and increments, δp_0^j .

For the n th iteration of the program, the (x^i, y^i) positions are transformed using the current values of parameters, p_n^j through each of the above transformations in turn, producing the transformed angular positions, (u_t^i, v_t^i) .

The rms error is determined to quantify how accurately the transforms match the actual distortions, through

$$E = \sqrt{\frac{1}{N} \sum_{i=1}^N (u^i - u_t^i)^2 + (v^i - v_t^i)^2}. \quad (2.9)$$

Each parameter is then varied in turn, so that the transforms are repeated using the values $p_n^j - \delta p_n^j$, p_n^j and $p_n^j + \delta p_n^j$, producing rms errors of $E(p_n^j - \delta p_n^j)$, $E(p_n^j)$

and $E(p_n^j + \delta p_n^j)$ respectively. By fitting a quadratic to the three points on the E versus p_n^j plot, an estimate of the optimal p^j value can be made as the minimum of the function

$$p_{opt}^j = \frac{E(p_n^j - \delta p_n^j) - E(p_n^j + \delta p_n^j)}{2E(p_n^j - \delta p_n^j) - 4E(p_n^j) + 2E(p_n^j + \delta p_n^j)}. \quad (2.10)$$

The new values for p^j and δp^j are taken to be

$$p_{n+1}^j = p_n^j + \frac{1}{3}(p_{opt}^j - p_n^j) \quad (2.11)$$

$$\delta p_{n+1}^j = \frac{1}{3}|p_{opt}^j - p_n^j|. \quad (2.12)$$

In other words, the p^j are moved one-third of the way to the estimated optimal value, before starting the next iteration.

The USNO astrometric catalogue was produced by digitising the photographic plates of the first Palomar Observatory Sky Survey (POSS I) using the Precision Measuring Machine (PMM). There are two key differences between the POSS I plates and the BTC images which are likely to affect the quality of the astrometric fit. Firstly, the USNO plates have a limiting magnitude of $O=21$, $E=20$ in comparison to the limiting magnitude of the individual BTC images of $V = 25.5$, $I = 24.5$. As a result, there are sources that could not be resolved in the POSS I plates but that are clearly resolved as double or extended sources by the higher quality BTC images. This means that the source centres as perceived by the source extraction software may not be due to the same source. The second source of error in any astrometric fit is due to the significant time difference between the two epochs of observation. The POSS I survey was carried out on the 48-in Oschin Schmidt Telescope at the Palomar Observatory between 1950 and 1957, whereas the BTC observations were made in 1998, a gap of 40–45 years. Most of the sources in the USNO catalogue are stars, some of which are presumably relatively nearby. As a result, a number of these sources will have proper motions that are large enough that, over the 40–45 years between observations, they have moved measurably across the celestial sphere (i.e. $\gtrsim 0.5$ arcsec). In order to minimise the error of the distortion model, once the parameters have been allowed to settle (after 800 iterations), these dubious sources (about 1% of the total) are removed by deleting those sources whose individual positional errors are greater than twice the rms error.

After 10 000 iterations the p^j are found to have stabilised to their optimal values, and so the program is terminated and the final values for the parameters output to the file `BTC_final_params.txt`, as shown in Table 2.2. A comparison of the relative sizes of the final values for p^j and δp^j confirm this stabilisation, with $\delta p^j/p^j \lesssim 10^{-5}$ for all of the parameters, and often at the 10^{-8} – 10^{-10} level. The resultant rms error in position of the sources in the BTC images relative to the USNO catalogue was $\simeq 0.3$ arcsec. This error includes the internal positional errors of the USNO catalogue (thought to be $\simeq 0.15$ arcsec), the errors due to the proper motion of the sources, as well as the internal errors due to the distortion model and the source extraction process. As will be shown later, the internal errors from the distortion model are only a small fraction of this value.

The parameters determined above can now be used to define the transformations that undistort each exposure that are to be performed using the IRAF `geotran` tool. The FORTRAN program `geo2.f` takes as input the distortion model parameter file `BTC_final_params.txt` and a short text file `imasename.txt` describing the time and location of observation for the image to be transformed, and creates the transformation files which can be read by `geomap`.

In total 12 transformations are defined, three for each of the four CCDs, as the full transformation has to be performed in three stages: the distortions due to the prime focus camera optics; the distortions due to the CCD corrector lenses; and the distortions due to atmospheric refraction. The transformation files produced for each CCD are called `imasename.CCD1_geo.dat`, `imasename.CCD1_geo.2.dat`, and `imasename.CCD1_geo.3.dat`. An IRAF script then runs the transformations which remove the distortions due to the camera optics (i.e. not the atmospheric refraction distortions) through `geomap` and `geotran` to produce the undistorted image. The images can then be flattened with the corresponding flat-field image which has also been undistorted using the same transformations.

Finally the atmospheric refraction transformation can be applied to the image, producing the final flattened, distortion-corrected image, `imasename.5.fits`. Being a linear transform, the atmospheric refraction transform does not affect the flatness of the image, and as it is image dependent, has to be carried out after the flat-fielding process.

Parameter	Final Value	Shift/Iteration
Telescope Centre X(CCD1)	0.24762849D+04	-0.37824707D-05
Telescope Centre Y(CCD1)	-0.36730508D+03	0.41376133D-05
CCD1 Angle	0.50924521D-03	0.31894649D-08
Telescope Centre X(CCD2)	-0.36614165D+03	0.24593362D-05
Telescope Centre Y(CCD2)	-0.36157846D+03	0.27733193D-05
CCD2 Angle	0.29145364D-02	0.33333333D-09
Telescope Centre X(CCD3)	-0.35598518D+03	0.39470715D-05
Telescope Centre Y(CCD3)	0.24470430D+04	-0.49457349D-05
CCD3 Angle	-0.24635815D-03	-0.36519606D-08
Telescope Centre X(CCD4)	0.24721950D+04	-0.23762401D-05
Telescope Centre Y(CCD4)	0.24540031D+04	-0.30179142D-05
CCD4 Angle	0.13559174D-02	-0.12935283D-08
Arcsecs per Pixel	0.43025539D+00	-0.10869774D-08
Cubic Distortion	-0.15427773D-08	-0.10000000D-14
Quintic Distortion	-0.59107636D-17	-0.51821574D-22
Refractive Index	0.10004057D+01	-0.69463099D-08
Focal Axis X Offset	-0.92505030D+02	-0.33945701D-04
Focal Axis Y Offset	-0.62506190D+01	0.22721372D-04
CCD Lens Radius Constant	0.77341952D+02	0.25226107D-03

Table 2.2: Typical output file from the distortion modelling program which contains the final values for the model's free parameters after 10 000 iterations.

Testing the Model and Registering the Images To determine the accuracy of fit of the distortion model, two *V*-band images from adjacent pointings in the 4 by 4 grid pattern (i.e. the pointings are separated by 5.6 arcmin) are transformed using the parametric distortion model, and then registered by allowing the second image to be translated and rotated relative to the first. To determine the registration transformation the source centres of about 300 bright (non-saturating) sources are found using the IRAF tool *daophot* in both images and written to two text files *imagename1.coo.txt* and *imagename2.coo.txt*. These are then loaded into the FORTRAN program *star_linker.f* which compares the two lists of source coordinates, and looks for the most common relative offset ($\delta x, \delta y$) between a point in the

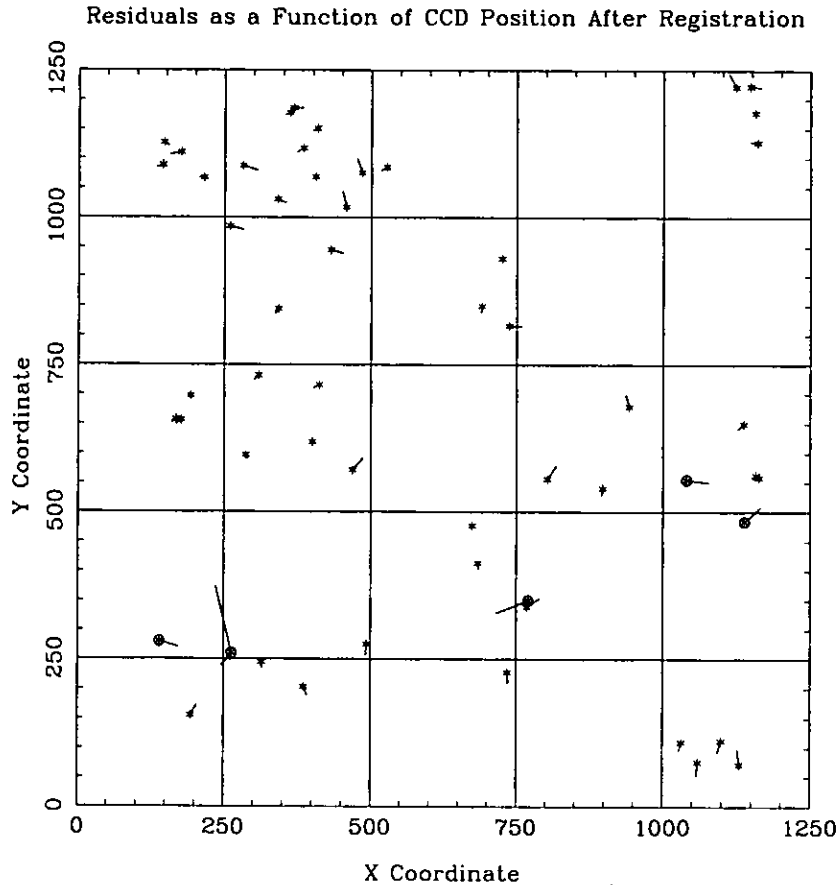


Figure 2.8: The errors in the registration of two images with pointings separated by 5.6 arcmin. Each point represents a source in the first image, and the arrow represents the registration error scaled by 100. The circled points have registration errors of 0.3 pixels or more, and are discarded from the linear registration fitting which produces rms errors of less than 0.1 pixels in X and Y, where (X,Y) is the position of the source in the CCD in units of pixels.

first coordinate list and a point in the second list, which it assumes to be due to the registration transformation. It then produces a list of coordinate pairs whose relative offsets are within 5 pixels of the most common offset, which can be read by `geomap` which finds the exact linear transformation to be performed using `register`.

Despite the large distortions involved, the images were successfully registered to an rms accuracy of ~ 0.1 pixels (0.05 arcsec) across all of the overlapping region, as shown in Figure 2.8. Other tests such as registering images from different CCDs, or images with larger pointing separations produced similarly good results, indicating that the model removed the distortions accurately. Having accepted the distortion model as sufficiently accurate, the individual exposures could be registered and stacked to produce the final *V* and *I* images. The image was built up iteratively,

using exposure #5 of the V images as a start-off point, and registering the four adjacent exposures (#1, 6, 7 and 9) first, and producing an intermediate stacked image. This intermediate image was then used as a start-off point, and the next batch of adjacent exposures were registered with respect to this image, and so on until all 16 exposures were registered.

The large effect of the distortions on the image were easily apparent in the undistorted images, as the image boundaries, which are obviously rectangular in the raw image, become visibly curved with the corner furthest from the centre of the BTC array clearly pulled inwards. The irregular shape of the distortion-corrected image causes problems for combining, as the boundary between image and non-image no longer lies precisely between pixels, but is now smeared over two pixel widths. Also, the registered images produced had sizes typically $5000 \times 5000 \text{ pix}^2$, most of which was blank, and so to regularise the shape of the images, and to save disc space, they were trimmed so that no blank space remained, and the relative offsets of the images stored in the file `offset_list`.

After examining the flattened and undistorted images, it became apparent that in $\sim 25\%$ of the images small gradients in the counts across the arrays remained. It is unclear what has produced these gradients, as the magnitude and orientation of the gradients vary from image to image in an apparently random manner, and also show no sign of the cloudy nature of the raw images, being of smooth appearance. To remove these gradients, the affected images were reflatened using a $63 \times 63 \text{ pix}^2$ median filter which modelled the gradients in the sky background, so that they could be subtracted from the image and replaced with a constant value. The median filter was affected by the large halos around bright stars, particularly in the I image, but given that they are heavily saturated anyway, this is not a major problem.

2.3.4 Photometric Calibration

The purpose of photometric calibration is the conversion of observed brightnesses in the form of instrumental magnitudes onto a standardised photometric system, thus allowing the comparison of data sets by different authors observed with different cameras and telescopes. This is achieved by the observation of “standard stars” whose magnitudes on a standard photometric system are accurately known,

and using their instrumental magnitudes to calibrate the remaining observations. The Johnson-Kron-Cousins broadband *UBVRI* photometric standard is the most commonly used at optical wavelengths, and uses the Landolt (1992) catalogue of standard stars whose *UBVRI* photometric magnitudes are known to an accuracy of 0.003 mag. This system has been adopted here, partly because of its widespread use, but also because the Landolt observations were made using the same telescope and passbands (but not the same filter set) as ours.

The aim of photometric calibration is to determine the free parameters of

$$m = m_{inst} - \alpha_\lambda \sec z + m_{zero} \quad (2.13)$$

where $m_{inst} = -2.5 \log(\text{counts})$ is the instrumental magnitude of a source, α_λ is the (wavelength-dependent) extinction coefficient, z is the zenith angle of the source, and the zero-point m_{zero} gives a reference point of the magnitude scale corresponding to the magnitude of a source that would be observed to have 1 count per second after accounting for the atmospheric extinction. The two values determined by photometric calibration are α_λ and the zero-point, the latter which has to be determined separately for each CCD. The effect of scattering by the atmosphere on a source's magnitude is proportional to the amount of atmosphere the light passes through on the way to the telescope, or $\sec z$, and so varies from exposure to exposure. For long exposures like these, where z changes significantly from the beginning to the end of the exposure, the best estimate of $\sec z$ is a "weighted" mean given by

$$\sec z = \frac{\sec z_0 + 4 \sec z_{1/2} + \sec z_1}{6} \quad (2.14)$$

where $\sec z_0$, $\sec z_{1/2}$ and $\sec z_1$ are respectively the airmasses at the beginning, midpoint and end of the exposure. The true magnitude of a source is defined as from above the atmosphere, i.e. zero airmass, and so each exposure has to be calibrated to zero airmass by multiplying by $10^{0.4 \times \alpha_\lambda \sec z}$.

As the positional shift between adjacent target exposures is 5.6 arcmin and the CCD width is 14.7 arcmin, there is significant overlap between adjacent images, so that many suitable sources are common to adjacent images. This meant that it was possible to estimate the atmospheric extinction coefficient α_λ using the target images themselves, by choosing two adjacent exposures observed with the same

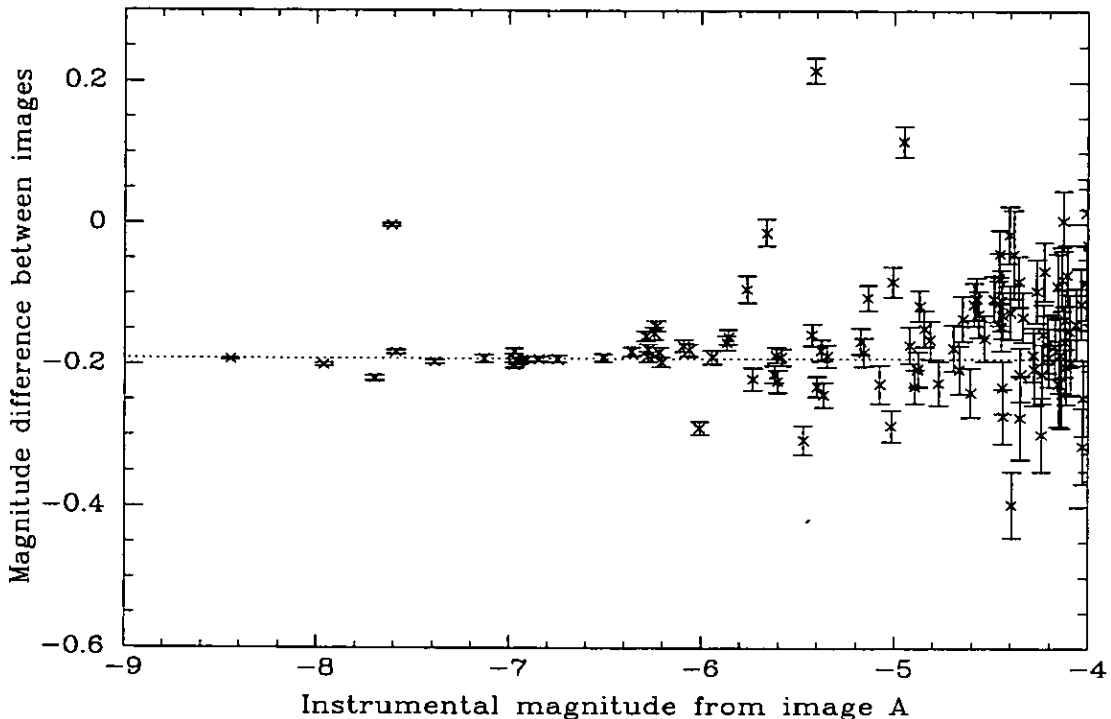


Figure 2.9: The effect of airmass on photometry: an estimate of the atmospheric extinction constant α_λ . The instrumental magnitudes of sources in two V -band images A and B (pointings #8 and #15 from CCD #4 respectively) which have differing airmasses (1.25 and 2.66 respectively) are compared. Aperture photometry is performed on both images using the same source positions determined using `daofind` on image A, and the difference between the two instrumental magnitudes of each source is represented by the y-axis. The mean change of instrumental magnitude from image A to image B (shown as a dotted line) due to the added atmospheric extinction is 0.1909 ± 0.0075 magnitudes, giving an estimate for α_V of 0.1356 ± 0.0053 .

CCD but at differing airmasses, and comparing the instrumental magnitudes of their common sources. Figure 2.9 shows an example comparison of two V -band images, one with an airmass of 1.25 and the other with an airmass of 2.66. The effect of the airmass difference between the two images is clear, with a weighted mean instrumental magnitude difference of 0.1909 magnitudes, giving a value for α_V of 0.1356 ± 0.0053 . In total five pairs of images were compared in each passband producing values for the atmospheric extinction coefficients of

$$\alpha_V = 0.1489 \pm 0.011 \quad (2.15)$$

$$\alpha_I = 0.0785 \pm 0.008. \quad (2.16)$$

The values of m_{zero} for each CCD and passband combination were estimated

from observations of the three standard star-fields PG1323-086, PG1633+099 and MARK A from the Landolt (1992) catalogue, after using the above values of α_λ to correct for atmospheric extinction. Both PG1323-086 and PG1633+099 fields contain five standard stars, whilst the MARK A field contains four. However one star from each field produced spurious results in comparison to the others, and so were discarded. Standard stars MARK A 1 and PG1633+099 A, which happened to be the faintest standard star in each field, produced zero-points that differed by 0.03–0.10 magnitudes from the other stars in the field, whereas the remaining stars typically agreed among themselves within 0.01 magnitudes. The standard PG1323-086 A was discarded as it turned out to be a variable star, which explained why its zero-points were 0.10 magnitudes different to the other four standards in the field.

Before images from different CCDs can be combined, it is necessary to equalise their zero-points. CCD #4 was considered the *standard* CCD, and the relative zero-points, m_{rel} of the remaining CCDs with respect to CCD #4 were determined, and each of the exposures from these CCDs were multiplied by the normalising factor $10^{0.4 \times m_{rel}(\text{CCD}n)}$. As a second estimate of the relative zero-points, m_{rel} , a similar method to that used to determine the α_λ was used, where the instrumental magnitudes of sources common to target exposures from differing CCDs were compared. These results agreed well with those from the standard stars, and so the mean of the values produced by the two methods were taken to be the final values of the m_{rel} ,

	$m_{rel}(V)$	$m_{rel}(I)$
CCD #1	0.8979 ± 0.018	0.4269 ± 0.011
CCD #2	0.2783 ± 0.015	0.2389 ± 0.012
CCD #3	0.1027 ± 0.021	0.0176 ± 0.007

This table quantifies the effect shown in Figure 2.7, with CCD #1 clearly much less sensitive than the remaining CCDs. The CCD #1 exposures had to be multiplied by 2.286 to normalise them to the sensitivity level of CCD #4. Finally the zero-points which normalise the instrumental magnitudes of sources in CCD #4, and also now the normalised exposures of the other CCDs are

$$m_{zero}(V) = 32.6785 \pm 0.026 \quad (2.17)$$

$$m_{zero}(I) = 32.1922 \pm 0.009 \quad (2.18)$$

where these values correspond to the magnitude of a source that would have 1 count in one of the target exposures, i.e. a 900s V or 1080s I exposure. Hence these are the values that are used during the photometric measurement of the sources.

2.3.5 Producing the Final Images

Having calibrated the photometry and then normalised the images to zero airmass and equalised the zero-points, and also having registered the images, it is now possible to co-add the images to produce the final V and I images using the IRAF tool `combine`. The process of co-adding the images involves: firstly registering each image using the values stored in the file `offset_list`; normalising the sky background levels of each image (taken to be the modal pixel value) to a constant level in an additive manner; and combining the images by the median, after rejecting all pixel values more than 3σ from the median (where σ is determined from the CCD readout noise and gain levels - the `ccdclip` rejection algorithm). The final images `V.fits` and `I.fits` have dimensions $5700 \times 5700 \text{ pix}^2$ and $5669 \times 5750 \text{ pix}^2$ respectively, where in order to register the V and I images there is a blank strip of width 800 pixels at the bottom of the I image. The reason that regions covered by the V and I images do not coincide exactly is due to way the I image was observed, as the first four pointings of the 5-pointing pattern used for the I image, correspond to pointings 1–4 in the 4 by 4 grid pattern of Figure 2.3 rather than the four central pointings, and this ensured that all three quasars were located within the deepest regions of the I image. The angular size of the exposed region common to both V and I images is $40.6 \times 35.0 \text{ arcmin}^2$.

2.3.6 Astrometric Calibration

The fits viewer GAIA allows images to be calibrated astrometrically in a transparent graphical fashion, and so this method was used. Unfortunately, at the time none of the computers in the department had sufficient memory to load the whole V or I image into GAIA (both fits files are 130 Mb), and so it was necessary to split the images up into quarters. The process of source extraction had also to be applied to the four quartered images for the same reason.

X_V	Y_V	X_I	Y_I	RA (J2000)	Dec (J2000)	z
1820.909	4768.753	1820.828	4768.740	$10^h46^m56.71^s$	$+5^\circ41'50.2''$	1.226
3090.208	2411.431	3090.322	2411.400	$10^h47^m33.17^s$	$+5^\circ24'54.9''$	1.306
4035.961	2029.467	4036.024	2029.500	$10^h48^m00.41^s$	$+5^\circ22'09.6''$	1.230
2690.967	862.173	2690.999	862.123	$10^h47^m21.58^s$	$+5^\circ13'48.4''$	1.738
5406.934	3941.169	5407.300	3941.192	$10^h48^m40.09^s$	$+5^\circ35'51.2''$	1.968
1342.471	3273.476	1342.441	3273.524	$10^h46^m42.83^s$	$+5^\circ31'07.1''$	2.682
963.952	1745.664	963.962	1745.729	$10^h46^m31.85^s$	$+5^\circ20'09.8''$	1.426

Table 2.3: Comparison of the quasars' (x, y) positions in the BTC images with the angular positions from Clowes & Campusano (1991, 1994), Clowes et al. (1999a) and Newman (1999).

The $5700 \times 5700 \text{ pix}^2$ V image was split into four images as follows:

$$\begin{aligned}
V_{\text{bl.fits}} &= V.\text{fits} [1:2900,1:2900] \\
V_{\text{br.fits}} &= V.\text{fits} [2801:5700,1:2900] \\
V_{\text{tl.fits}} &= V.\text{fits} [1:2900,2801:5700] \\
V_{\text{tr.fits}} &= V.\text{fits} [2801:5700,2801:5700]
\end{aligned}$$

i.e. the four quarter images were of size $2900 \times 2900 \text{ pix}^2$ and with overlaps of 100 pixels with one another.

The I image was also split up into four images as follows:

$$\begin{aligned}
I_{\text{bl.fits}} &= I.\text{fits} [1:2900,801:3600] \\
I_{\text{br.fits}} &= I.\text{fits} [2801:5669,801:3600] \\
I_{\text{tl.fits}} &= I.\text{fits} [1:2900,3501:5750] \\
I_{\text{tr.fits}} &= I.\text{fits} [2801:5669,3501:5750].
\end{aligned}$$

Note that the 800 pixel blank strip at the bottom of the I image is not carried over to the four quarter images, and that they are offset in declination with respect to the V quarter images.

GAIA requires the images to have an approximate astrometric calibration built into the fits header in order to be able to overlay the USNO guide stars upon the image. This first approximation was based upon the quasars themselves, as their CCD and actual angular positions are accurately known. As a byproduct of the

```

WCSDIM      = 2
EQUINOX     = 2000
CRPIX1      = 1820.909 ( $X_V$  of reference point - the  $z=1.226$  quasar)
CRPIX2      = 4768.753 ( $Y_V$  of reference point)
CRVAL1      = 161.7363104 (RA of reference point in degrees)
CRVAL2      = 5.697264901 (Dec of reference point in degrees)
XPIXELSZ    = 24 (size of pixels on CCD  $\mu\text{m}$ )
YPIXELSZ    = 24
PLTSCALE    = 17.92 (plate scale - arcsec per mm)
CTYPE1      = 'RA---CAR' (Type of projection - Cartesian cylinder)
CTYPE2      = 'DEC--CAR'
CUNIT1      = 'deg' (units used for CRVAL1 and CD1i)
CUNIT2      = 'deg' (units used for CRVAL2 and CD2i)
CD1_1       = 1.20131828E-4 ( $d\alpha/dX_V$  deg/pix)
CD1_2       = 2.65497529E-7 ( $d\alpha/dY_V$ )
CD2_1       = -2.2225703E-7 ( $d\delta/dX_V$ )
CD2_2       = 1.19552212E-4 ( $d\delta/dY_V$ )

```

Table 2.4: The portion of the fits header containing the World Coordinate System representation of the first approximation to the astrometric fit for the V -band BTC image.

removal of the image distortions using astrometric fields, the transformation from the CCD (x, y) to the angular (α, δ) coordinate systems must be linear, and so a simple linear regression fit between the two sets of coordinates should suffice.

Table 2.3 shows the data used to produce the first approximation to the astrometric fit, with the (x, y) positions of each of the quasars in the BTC images along with their angular positions taken from Clowes & Campusano (1991, 1994) and Clowes et al. (1999a). This linear fit is then written into the fits header as in Table 2.4.

Note that the values of CRPIX1 and CRPIX2 are only correct for the file `V.bl.fits`. The values for the other three fits images have to be corrected for the offsets in the image coordinates.

Having installed an approximate astrometric calibration from the quasars, the

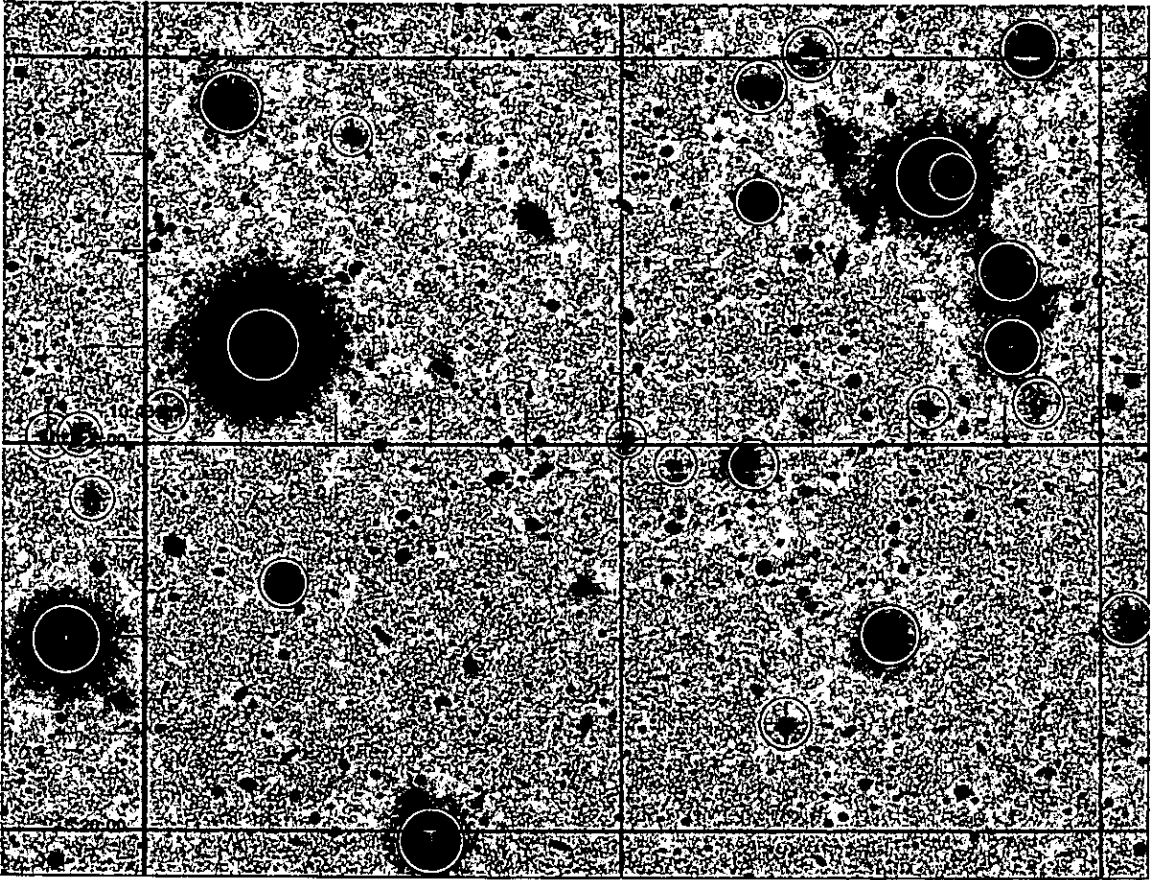


Figure 2.10: Region from the final BTC I -band image with USNO catalogue sources and resultant astrometric fit overlaid. The sources from the USNO catalogue are indicated by green crosses circumscribed by black/white circles whose radii increase with decreasing V magnitude. The problems in determining an accurate astrometric fit discussed in the text are apparent in the figure, with a number of catalogue positions out by an arcsec or more, and others corresponding to extended sources.

fits images can be loaded into GAIA and sources from the USNO astrometric catalogue overlaid upon the image as shown in Figure 2.10. Only sources fainter than $m_V = 16$ were selected, as the brighter sources were so heavily saturated that their centres on the BTC image could not be located accurately. This still left a catalogue of around 200 guide stars per quarter image to calibrate the astrometry. The astrometric fit was then obtained by centring these USNO guide stars upon their conjugates in the image, and determining the least-squares-error linear fit to the points. A small fraction ($\simeq 1\%$) of the USNO catalogue sources had clearly moved significantly since the production of the catalogue, or otherwise had inaccurate positions, and these sources were removed, before re-determining the fit. Due to a bug in the GAIA program related to the ‘unusual’ projection (it is a simple Cartesian

Image Name	V.bl.fits	V.br.fits	V.tl.fits	V.tr.fits
USNO sources used	185	249	149	181
rms error of fit (pix)	0.115	0.103	0.117	0.107
α (X=0,Y=0) (deg)	161.5167029	161.8527324	161.5170818	161.8533079
CD1.1($d\alpha/dX_V$) (°/pix)	1.200545E-4	1.201112E-4	1.201344E-4	1.202054E-4
CD1.2($d\alpha/dY_V$) (°/pix)	1.768723E-7	2.553850E-7	2.295687E-7	3.226733E-7
δ (X=0,Y=0) (deg)	5.127627615	5.127065674	5.462263224	5.461699242
CD2.1($d\delta/dX_V$) (°/pix)	-1.955586E-7	-2.714850E-7	-1.623995E-7	-2.418037E-7
CD2.2($d\delta/dY_V$) (°/pix)	1.195089E-4	1.195403E-4	1.195239E-4	1.195940E-4

Image Name	I.bl.fits	I.br.fits	I.tl.fits	I.tr.fits
α (X=0,Y=0) (deg)	161.5167468	161.8528750	161.5171875	161.8535525
CD1.1($d\alpha/dX_I$) (°/pix)	1.200959E-4	1.201236E-4	1.201403E-4	1.202108E-4
CD1.2($d\alpha/dY_I$) (°/pix)	2.151266E-7	2.813115E-7	2.466229E-7	2.954848E-7
δ (X=0,Y=0) (deg)	5.223116631	5.222693227	5.545913618	5.545451896
CD2.1($d\delta/dX_I$) (°/pix)	-1.589829E-7	-2.666298E-7	-1.538067E-7	-2.453403E-7
CD2.2($d\delta/dY_I$) (°/pix)	1.195735E-4	1.195302E-4	1.195268E-4	1.195789E-4

Table 2.5: The astrometric fits for each of the four quarter V and I images. The (X=0,Y=0) values indicate the fitted (α , δ) of the south-eastern corner of the images.

transformation after all), it miscalculates the linear fit, so the table of USNO guide star catalogue angular positions and (x , y) source positions were output to a file (e.g. `USNO_V.bl.txt`), and the astrometric calibration determined using a simple linear regression program.

The resultant astrometric fits and the rms errors for each of the four quarter V and I images are given in Table 2.5.

The rms accuracy of the linear astrometric fit over the whole 30×30 arcmin² image was 0.11 pixels, or 0.05 arcsec, which is about as accurate as attainable given the uncertainties in position of the USNO catalogue sources and the BTC's pixel size of 0.43 arcsec. This level of accuracy is more than sufficient to use as source positions for follow-up spectroscopy where 0.10–0.15 arcsec positional accuracy is required to locate the sources in the slits/fibres.

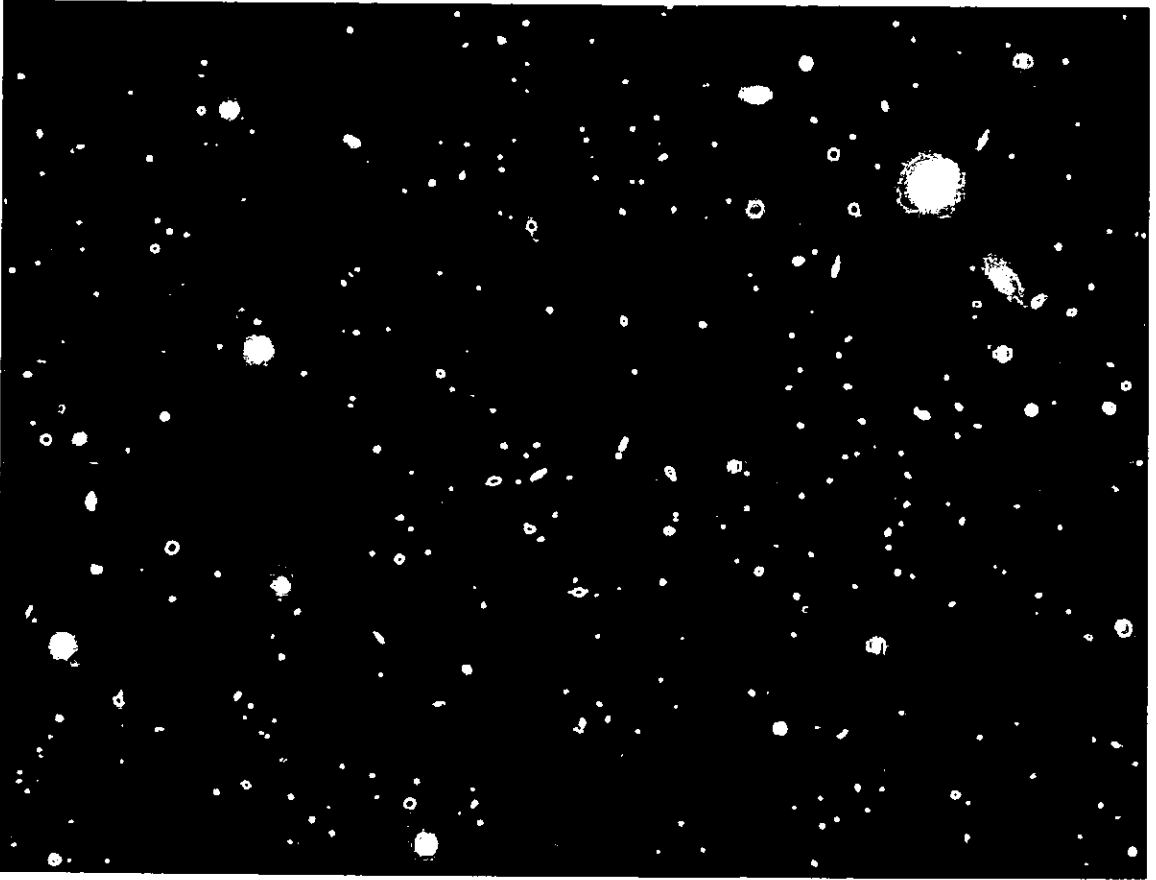


Figure 2.11: Region from the false colour image of the BTC field corresponding to the same region as Figure 2.10.

2.3.7 Production of a False Colour Image

The combination of two or more registered broad-band filter images into a single false colour image has produced many impressive looking posters and images, particularly the Hubble Deep Field and other HST images. Admittedly, this is usually more of a publicity exercise than a scientific one, but it does allow the easy visual inspection of images in search of 'interesting' sources. The colour information of a generic raster image is stored in three components: red, green and blue, which take values from 0 to 255. White for example has values of 255 for red, green and blue, and yellow say has values of 255 for red and green, and 0 for blue. In the ideal case then, there would be three registered images, taken through filters that broadly match red, green and blue, i.e. R , V , and B . However in this case, there are only two filters, neither covering blue wavelengths, and so a little trial and error was necessary to produce suitable colours:

$$\begin{aligned}\text{red} &\propto \log(I - I_0), \\ \text{green} &\propto \log(V - V_0), \\ \text{blue} &\propto \log[1.5(V - V_0) - 0.5(I - I_0)],\end{aligned}$$

where V, I are the pixel values in the V and I BTC images, and V_0, I_0 are the mean background pixel values across the V and I images, in order that the background appears black. The IRAF tool `export` can be used to produce a raster image from the two BTC fits images.

2.4 Source Extraction — Producing the Final Catalogue

The software tool used to extract source catalogues from the BTC images was `SEXTRACTOR` (Bertin & Arnouts, 1996). The `SEXTRACTOR` tool is particularly oriented towards reduction of large-scale galaxy survey data, and has several features which made it the optimal choice for this data set, rather than `DAOPHOT` for example. The final catalogue was much improved by the key features of this package including: its handling of extended sources; using weight maps to model the varying rms noise levels across images; and the in-built neural-network-based star-galaxy classifier.

The process of extracting sources from the image is controlled through the configuration file `default.sex`, and the list of parameters output to the catalogue is stored in the parameter file `default.param`. Many of the configuration file parameters are self-explanatory and their values are either known or can be determined from the image. The choice of value for some of the parameters is not obvious, and required some trial and error to obtain the best results. The configuration parameters are split into subsections corresponding to the stage of source extraction they are involved with, e.g., extraction, photometry, background, and the same subsections are used here to describe the decision processes used to find the optimal values.

2.4.1 Extraction

For normal astronomical images, the optimal method of source extraction is to firstly filter the image by convolving it with the point-spread function, and then

select sources with $\simeq \text{FWHM}^2$ pixels over some threshold, usually around 1σ above background.

The power spectrum of the noise and the superimposed signal are usually significantly different, and the process of filtering is used to maximise the signal-to-noise level and hence optimise the detection of sources. Assuming the signal has the same power spectrum as the point-spread function, and that the noise is white, the optimal convolution kernel for detecting sources is then the point-spread function inverted in both the x and y directions. This is less efficient at detecting extended objects such as elliptical or low-surface brightness galaxies, but in this case, most of the faint sources of interest should be relatively small, due to their distance, making the point-spread function the optimal choice of convolution kernel.

The source detection process was performed using a thresholding method, in which a detection was classified as any group of 4 connected pixels 0.8σ over the background level. This choice of values was based on trial and error, by examining the output catalogue and corresponding check image, and try to maximise the number of *real* detections and minimise the contamination due to noise.

The result of the extraction process can be seen in Figure 2.12. The top figure shows a region of the BTC I image within the area covered by all 15 exposures of CCD #4, and hence is one of the deepest sections of the BTC field. The lower figure shows the same image with apertures overlaid corresponding to each of the sources detected, i.e. with 4 connected pixels 0.8σ over the background level. Virtually all sources apparent in the upper image have been detected, and there are few spurious detections due to random noise, indicating a suitable choice of parameters. There are two apertures per detection: an adaptive elliptical aperture used to estimate the total apparent magnitude; and a 2.5 arcsec diameter circular aperture used to ascertain the source's colour (see below). 501 sources are detected in this 3.55×1.72 arcmin² image, corresponding to a mean density of 295 000 deg².

2.4.2 Photometry

The total apparent magnitude of a source is the most physically relevant photometric parameter to extract directly from pixel data. For stellar sources this is relatively simple, as the point-spread function is known, and so a suitably sized circular aper-

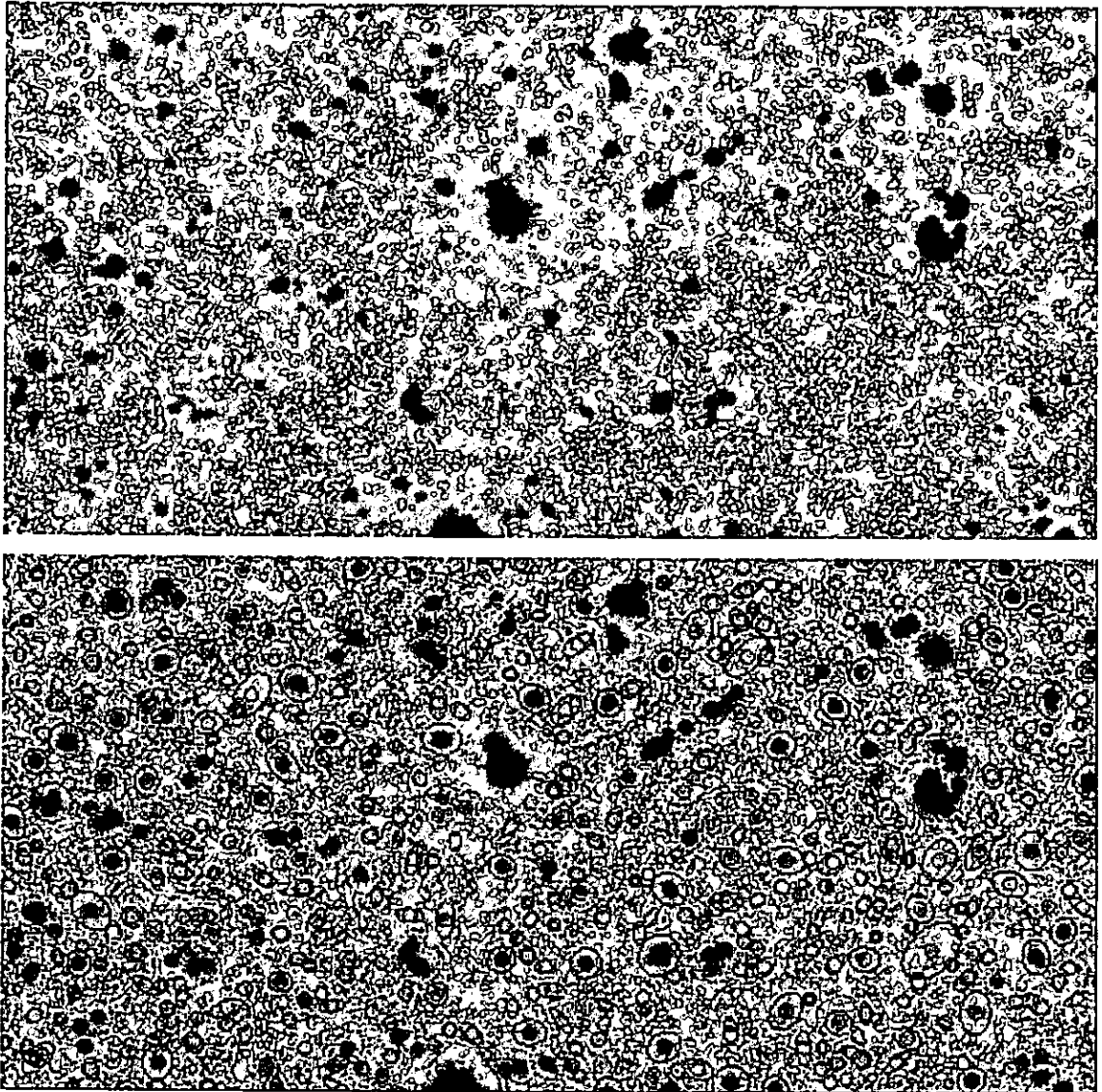


Figure 2.12: Resultant apertures from the source extraction process applied to a section from the BTC *I* image. The top figure shows a $496 \times 240 \text{ pixel}^2$ ($3.55 \times 1.72 \text{ arcmin}^2$) subsection of the BTC *I* image within the deep region covered by all the CCD #4 exposures. The bottom figure shows the same image with the apertures corresponding to each of the detections overlaid. Both the adaptive apertures used to determine the total magnitude, and the 2.5 arcsec circular apertures used to determine the sources' colours are shown.

ture will suffice, with a small correction to consider the flux outside the aperture. It becomes somewhat more complex when dealing with non-stellar sources whose size and morphology can only be estimated from the pixel data itself.

There are two main approaches to determining total apparent magnitudes for generic extended sources: adaptive apertures and corrected isophotes.

Adaptive aperture magnitudes. The adaptive aperture photometry routine of

SEXTRACTOR is based on the “first moment” algorithm of Kron (1980). The second order moments of the object profile ($\sigma_x^2 = \sum x^2 I(x) / \sum I(x)$, σ_{xy} and σ_y^2) are used to define an equivalent bivariate Gaussian profile with mean standard deviation σ . An elliptical aperture defined by these moments and scaled to 6σ is then determined for the source. Within this aperture the first moment r_1 is then computed with $r_1 = \sum r I(r) / \sum I(r)$. Kron (1980) and Infante (1987) have shown that for star and galaxy profiles convolved with Gaussian seeing an almost constant fraction of the flux is expected to lie within a circular aperture of radius kr_1 (and also for elliptical apertures with ϵkr_1 and kr_1/ϵ as the principal axes), independently of their magnitude. Empirically, a balance between systematic and random errors is achieved for $k \approx 2$. This method is known to be less biased than isophotal photometry, but only works in non-crowded regions.

Corrected isophotal magnitudes If we make the assumption that the intensity profiles of sources are roughly Gaussian with a width σ and a peak density p , then the total flux from the source can be considered as

$$I_{tot} = 2\pi\sigma^2 p. \quad (2.19)$$

Using a threshold density t , the corresponding flux I_{iso} and area A_{aper} , are then

$$I_{iso} = 2\pi\sigma^2(p - t) = 2\pi\sigma^2 p \left(1 - \frac{t}{p}\right) \quad (2.20)$$

$$A_{aper} = 2\pi\sigma^2 \ln\left(\frac{p}{t}\right). \quad (2.21)$$

By rearranging these equations, then the fraction $\eta = I_{iso}/I_{total}$ of the total flux enclosed within a particular isophote is given by

$$\left(1 - \frac{1}{\eta}\right) \log(1 - \eta) = \frac{A_{aper} t}{I_{iso}}, \quad (2.22)$$

where A_{aper} is the area and t is the isophote threshold (Maddox et al., 1990).

Thus given A , t and I_{iso} it is possible to calculate η and then I_{tot} . This approximation clearly works best with stars, but it proves to be reasonably accurate with disk galaxies, although it can result in large errors with the broad wings of spheroidal galaxy profiles.

SEXTRACTOR uses the following procedure to give the best estimate for the total magnitude (MAG_BEST) for an object: the adaptive aperture method is taken, except

if a neighbour is suspected to bias the magnitude by more than 0.1 mag in which case the corrected isophotal magnitude is taken.

As well as determining the total magnitude of a source in the V and I images, it is necessary to determine its $V - I$ colour. At first glance, this may seem a trivial task, and in the case of stellar sources it is. However galaxies can look completely different when observed through different filters. For example one filter may trace the recent star-formation within a galaxy, whilst the other traces the old stellar population. Hence galaxy sizes and morphologies can vary greatly between images, and so the isophote or adaptive aperture for a galaxy can also change with wavelength, with the result being that you are not always considering the same source. The usual way to determine the colour of an object is to use a circular aperture whose diameter is 2–3 times the FWHMs of a point-source. SExtractor is then used in two-image mode to obtain the aperture magnitudes (MAG_APER) corresponding to the same circular aperture in each of the images, from which the colour can be determined. The FWHM of the V and I images are 1.30 and 1.15 arcsec respectively, and so a circular aperture of diameter 2.5 arcsec was used to determine the colour of each source.

The corresponding errors for both the total magnitudes and colours were determined for each source by assuming Poisson noise through the equation

$$\Delta m = \Delta(2.5 \log F_{tot}) = \frac{2.5}{10} \left(\frac{\Delta F_{tot}}{F_{tot}} \right) = 1.0857 \frac{\sqrt{A_{aper} \sigma^2 + \frac{F_{tot}}{g}}}{F_{tot}}, \quad (2.23)$$

where A_{aper} is the aperture area, σ is the rms noise of the background, F_{tot} is the total flux, and $g = N_{exp} g_{CCD}$ is the gain of the image (which is equal to the CCD gain multiplied by the number of exposures used to build the final image).

2.4.3 Background Modelling and Weight Maps

The value measured at each pixel is a sum of a *background* signal and flux from each of the sources. To be able to detect and measure these sources, an accurate estimate of the background level at all points across the image is required — a *background map*. SExtractor produces a background map by splitting the image up into a grid of 16×16 pix² meshes (the size of the meshes is a free parameter, BACK_SIZE). For each mesh, a local background level is calculated by clipping the background

histogram at $\pm 3\sigma$ around its median, and then taking the mean value. For crowded fields (a mesh is taken to be crowded if the clipping process changes the mean value by more than 20%) the background level is taken to be the mode, which is estimated as

$$\text{Mode} = 2.5 \times \text{Median} - 1.5 \times \text{Mean}. \quad (2.24)$$

Once the grid is set up, a median filter can be applied to suppress possible local overestimations due to bright stars. The size of the median filter can be controlled using the parameter `BACK_FILTERSIZE`. The choice of the mesh size (`BACK_SIZE`) is very important. If it is too small, the background estimation is affected by the presence of sources and random noise, and also part of the flux of the more extended sources can be absorbed into the background map. If the mesh size is too large, it cannot reproduce the small scale variations of the background. For reasonably sampled images, with $\text{FWHM} \approx 2\text{--}3$ pixels, a width of 32 to 256 pixels works well, with smaller sizes possible in conjunction with filtering. It took some considerable trial and error to determine the optimal values for the mesh and filter size, using the output check images to examine how well the background is modelled and the sources detected.

In parallel with the making of the background map, an *RMS-background map* — that is, a map of the background noise in the image — is produced. This is particularly useful in this case, as the background noise levels vary greatly across the image, and so by setting the `WEIGHT_TYPE` parameter to `BACKGROUND` the threshold for detection of sources can be varied across the image by using the RMS-background map to model $\sigma(x, y)$. This allows the extraction to work efficiently both in the deep regions where a low threshold is necessary, and in the shallower regions where a higher threshold is needed to limit the number of spurious detections due to random noise.

The RMS-background maps for the final *V* and *I* BTC images are shown in Figures 2.13 and 2.14. The effect of the structure in coverage due to the exposure patterns, and the differing sensitivities of the four CCDs are evident in both maps.

To give an indication of the effect of the CCDs differing sensitivities the background rms-noise maps can be used to determine 5σ magnitude limits. In the case of the *V* image the central 29.4×29.4 arcmin² region was planned to be an almost

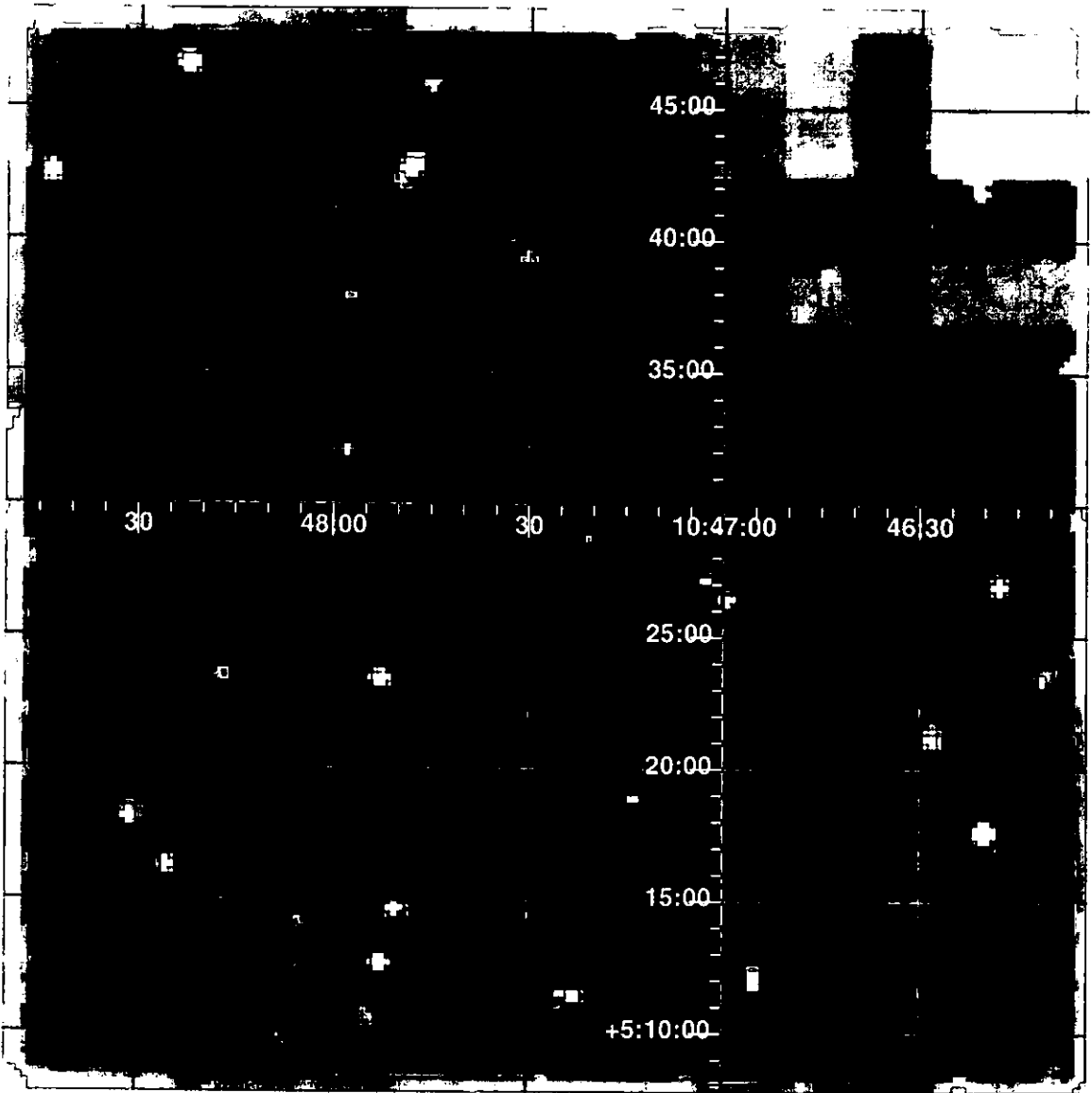


Figure 2.13: RMS-noise map for BTC V image. The dark colours correspond to those regions with low RMS-noise levels ($\sigma \simeq 20 \text{ ADU pix}^{-1}$), with the mid-range colours corresponding to moderate noise levels ($\sigma \simeq 35 \text{ ADU pix}^{-1}$) and light colours corresponding to high noise levels ($\sigma \simeq 50 \text{ ADU pix}^{-1}$) due to bright stars. The effect of the loss in sensitivity of CCD #1 (top-right) is clear, as is the “tartan” striping effect produced by the 4 by 4 grid exposure pattern (cf. Figure 2.4 [left]).

uniform deep field (see Figure 2.4-left). For the purposes of comparing the four CCDs, this area is subdivided into quarters, assigned to the appropriate CCD, and the modal rms-noise level determined. In the case of the I image, the areas considered are the four $9.1 \times 9.1 \text{ arcmin}^2$ deep regions that were built up of all 15 exposures from one CCD only, thus indicating the maximum depths reached.

An examination of Table 2.6 and Figure 2.13 indicates that the observing strategy

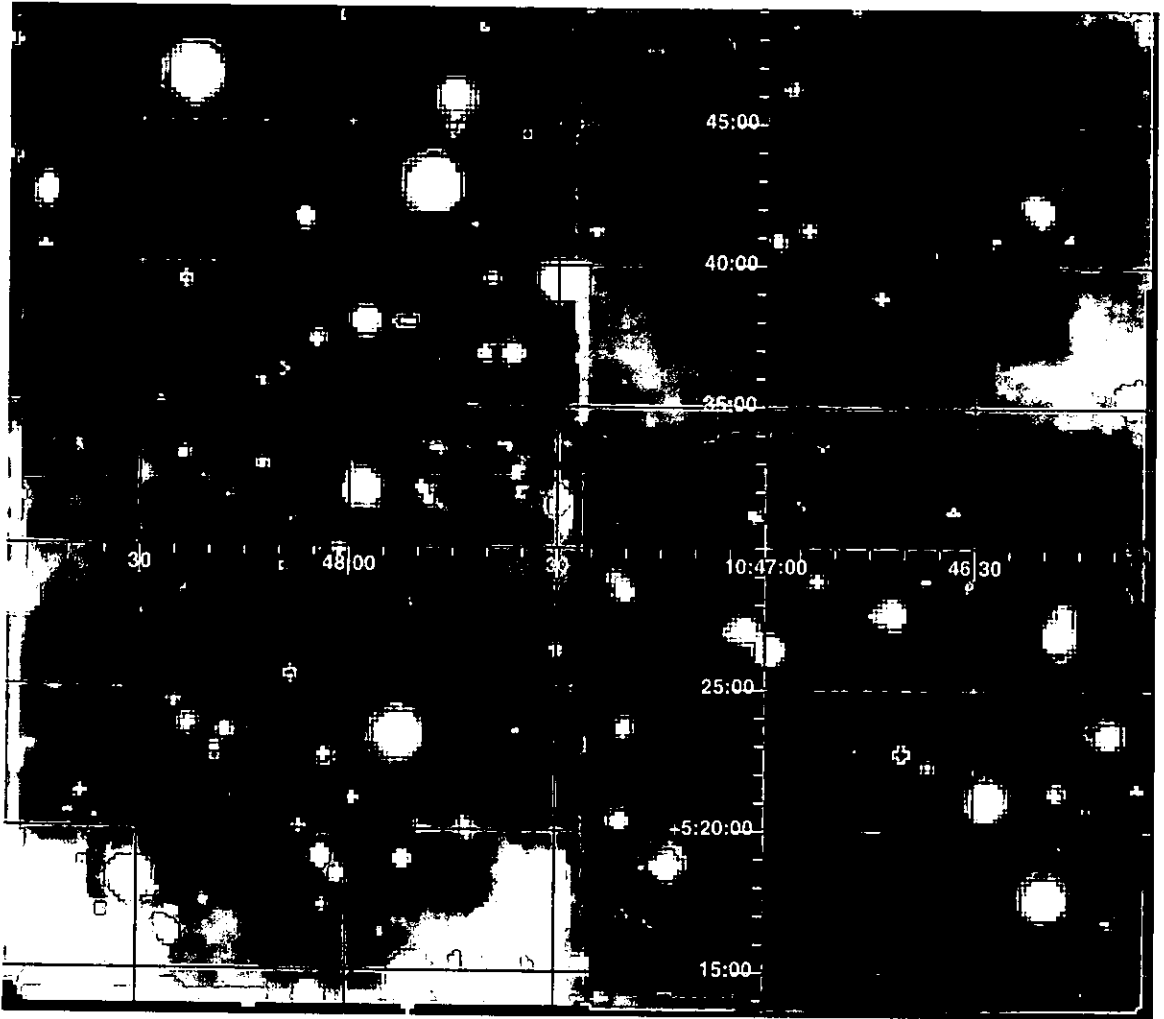


Figure 2.14: RMS-noise map for BTC *I* image. The dark colours correspond to those regions with low RMS-noise levels ($\sigma \simeq 20 \text{ ADU pix}^{-1}$), with the mid-range colours corresponding to moderate noise levels ($\sigma \simeq 40 \text{ ADU pix}^{-1}$) and light colours corresponding to high noise levels ($\sigma \simeq 100 \text{ ADU pix}^{-1}$) due to bright stars. The effect of the differing sensitivities of the four CCDs is clear, with those regions always covered by CCDs #2 (top-left) and #4 (bottom-right) having noise levels of $\sigma \simeq 20 \text{ ADU pix}^{-1}$ whilst CCDs #3 (bottom-left) and #1 (top-right) having noise levels of $\sigma \simeq 35 \text{ ADU pix}^{-1}$. The effect of the exposure pattern is clear, with the structure of the coverage pattern of Figure 2.4 (right) apparent in the rms noise levels, with the four deep regions that are covered by all 15 exposures.

of the 4 by 4 grid pattern has resulted in an almost uniformly deep image across the central $29.4 \times 29.4 \text{ arcmin}^2$ region of the *V* BTC image ($10^{\text{h}}46^{\text{m}}27^{\text{s}} < \alpha < 10^{\text{h}}48^{\text{m}}25^{\text{s}}$, $+05^{\circ}13'22'' < \delta < +05^{\circ}42'46''$), with three of the four quarter subregions producing 5σ magnitude limits within 0.03 magnitudes of one another.

The effect of the less sensitive CCD #1 does not appear as significant as feared, with an increase of 10% in the rms noise levels across the quarter covered mainly

<i>V</i> image	boundaries of region (α, δ) (J2000)	rms-noise (ADU/pix)	5σ mag.arcsec ⁻²
CCD1	10:46:27.1–10:47:26.3, +5:28:04–5:42:47	25.81	26.49
CCD2	10:47:26.3–10:48:25.3, +5:28:03–5:42:45	23.27	26.60
CCD3	10:47:26.3–10:48:25.3, +5:13:21–5:28:03	22.65	26.63
CCD4	10:46:27.1–10:47:26.3, +5:13:23–5:28:04	22.76	26.62
<i>I</i> image	boundaries of region (α, δ) (J2000)	rms-noise (ADU/pix)	5σ mag.arcsec ⁻²
CCD1	10:46:29.8–10:47:02.6, +5:39:46–5:47:43	38.55	25.56
CCD2	10:47:50.5–10:48:23.2, +5:39:39–5:47:39	21.33	26.21
CCD3	10:47:50.2–10:48:22.9, +5:19:53–5:27:52	36.51	25.62
CCD4	10:46:30.1–10:47:02.8, +5:19:50–5:27:48	23.02	26.12

Table 2.6: Comparison of the model rms noise levels and the resultant 5σ magnitude limits for the areas covered by the four CCDs in both the *V* and *I* BTC images

by that CCD. In contrast the *I* BTC image is much less uniform, partly a result of the observing strategy, but also a variation in sensitivity of the four CCDs. The 5σ magnitude limits of the deep regions covered by all 15 exposures of each of the four CCDs vary considerably, with CCDs #2 and #4 reaching $\simeq 0.5$ magnitudes deeper than CCDs #1 and #3. The loss in sensitivity of CCD #1 was expected, but the reason for the high noise levels in CCD #3 is unclear as it is 99% as sensitive as CCD #4, and 20% more sensitive than CCD #2 according to the photometric calibrations based on the standard star observations.

2.4.4 Star - Galaxy Separation

One of the most useful aspects of the *SExtractor* package is its in-built stellerity classifier which uses a neural-network-based algorithm to separate stars and galaxies by morphology. Previous simple classifiers have used 2-parameter spaces such as magnitude- isophotal-area, magnitude- peak-intensity or magnitude- surface-brightness. These do not use all the information available in the intensity profile, and have difficulties when dealing with merged or close sources. If each source is

considered a vector of parameters, classifying stars and galaxies optimally is nothing more than finding the best frontier hypersurface between the two classes in parameter-space, a task particularly suited to neural networks. They can easily handle problematic cases such as merged sources as long as they have learned to recognise them. This is achieved by using a training set of artificial stars and galaxies. Modern CCDs produce images which have many common properties: a linear intensity scale; essentially white background noise; and an approximately Gaussian point-spread function due to atmospheric blurring. This means that by scaling the image intensity and seeing/pixel size suitably, one can use the artificial images to train the neural network to classify sources for any well-sampled CCD data. The input parameters used to describe each source are eight isophotal areas corresponding to different threshold levels (the lowest being the detection threshold), the peak intensity, and a control parameter, the seeing, which is used to scale the isophotal areas and hence tune the neural network. The neural network then produces a single output parameter for each source, the stellarity index (`CLASS_STAR`) which, by definition, will equal 0 for galaxies and 1 for stars, but in practice produces a value somewhere in between, a confidence level of the classification. The key to producing the best results from this classifier, is the correct value for the `SEEING_FWHM` control parameter. At high signal-to-noise levels, most sources' stellarity indexes should be close to either 0 or 1, and at the lowest signal-to-noise levels, unresolved sources should produce an even spread of stellarities between 0 and 1.

The effect of the star-galaxy classifier on sources in the BTC V and I images is shown in Figure 2.15. The two graphs plot the stellarity index of sources as a function of V and I total magnitudes, with those sources classified as stars having indexes approaching 1, and those sources classified as galaxies having indexes approaching 0. It is clear that at high signal-to-noise levels the classifier is separating stars and galaxies efficiently, (the V image in particular) with most sources having indexes either less than 0.1 (i.e. classed as galaxies) or more than 0.9 (i.e. classed as stars) to $V \simeq 23.5$, $I \simeq 23$. At the very brightest magnitudes ($V < 16$, $I < 18$) there are a number of sources with indexes between 0.6 and 0.85; these are all heavily saturated stars. At the faintest levels there appears an even spread of stellarity indexes from 0 to 1. These are all sources which cannot be resolved due to their low signal-to-

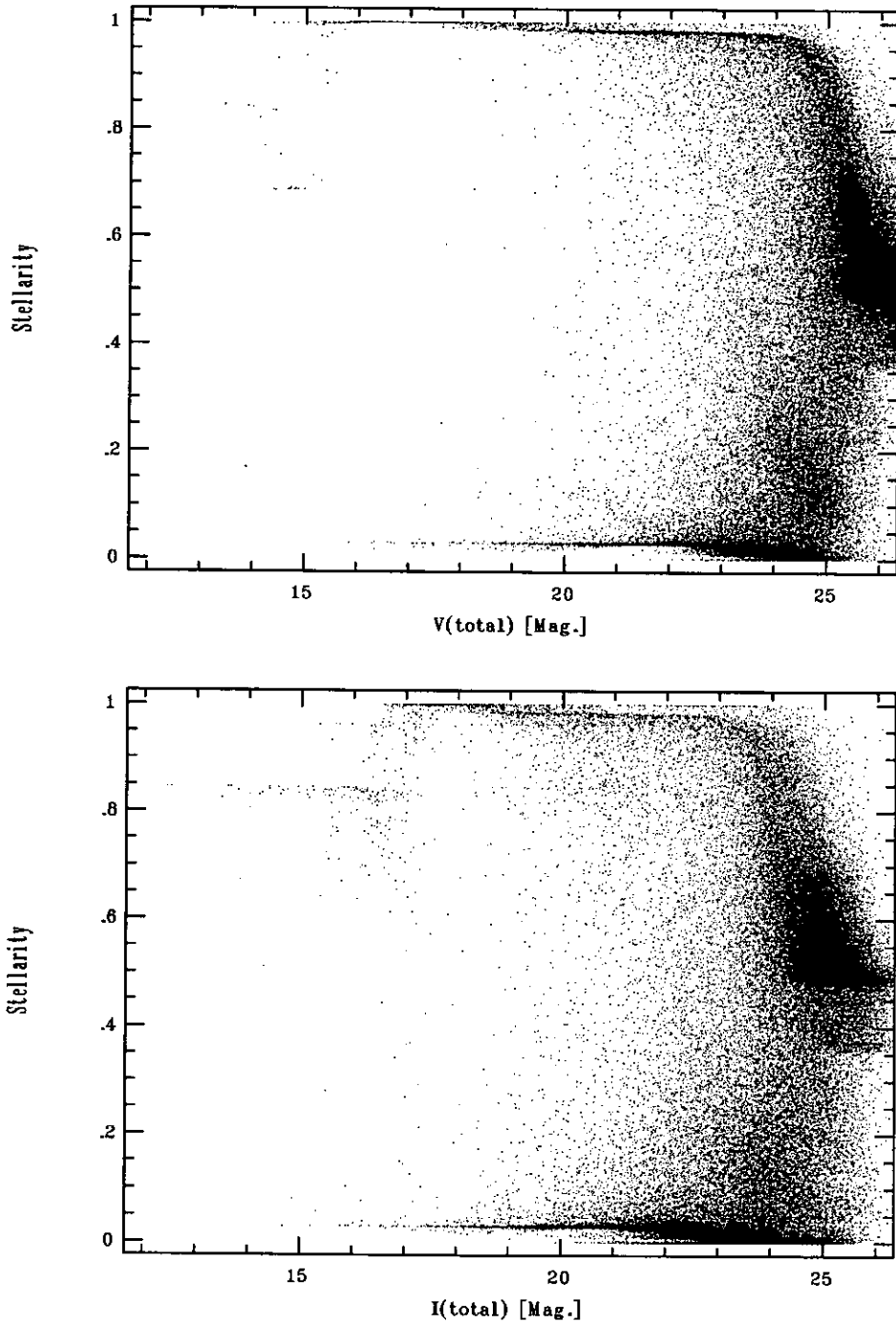


Figure 2.15: Effect of the star-galaxy classifier on sources in the BTC V and I images. The stellarity index is plotted as a function of V and I total magnitudes, with those sources classified as stellar having indexes approaching 1, and those sources classified as galaxies having indexes approaching 0. The classifier can be seen to separate stars and galaxies efficiently to $V \simeq 24$ and $I \simeq 23.5$. At fainter magnitude the classifier breaks down, but nearly all sources at these magnitudes are likely to be galaxies anyway. At the brightest magnitudes ($V \lesssim 16$, $I \lesssim 18$) there are a number of sources with stellarities around 0.6–0.8; these are heavily saturated stars.

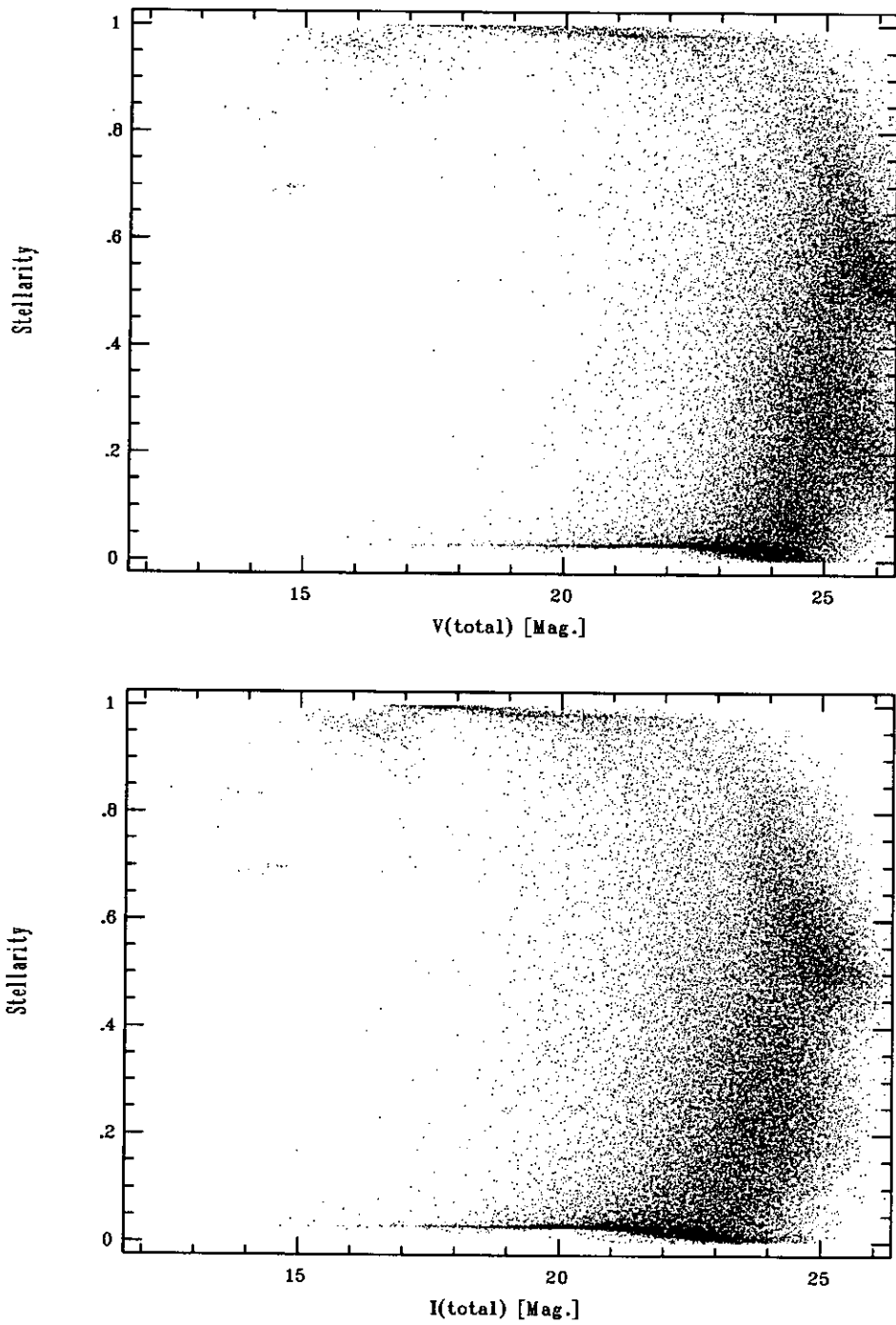


Figure 2.16: Effect of the star-galaxy classifier on sources in the BTC V and I images after averaging the two values. The stellarity index is plotted as a function of V and I total magnitudes, with those sources classified as stellar having indexes approaching 1, and those sources classified as galaxies having indexes approaching 0.

noise levels. Nearly all sources at these magnitudes ($V \gtrsim 24, I \gtrsim 23.5$) are likely to be galaxies, particularly as the field is at high galactic latitude.

As there are two independent measures of each source's stellarity, the two values can be averaged to give an improved classification. As the classification efficiency improves with increased signal-to-noise, the two values are weighted according to the signal-to-noise levels, using the inverse of the magnitude error

$$\text{CLASS_STAR_IMPROVED} = \frac{\frac{\text{CLASS_STAR}(I)}{\Delta\text{MAG_BEST}(I)} + \frac{\text{CLASS_STAR}(V)}{\Delta\text{MAG_BEST}(V)}}{\frac{1}{\Delta\text{MAG_BEST}(I)} + \frac{1}{\Delta\text{MAG_BEST}(V)}} \quad (2.25)$$

The results of averaging the two stellarity values can be seen in Figure 2.16. A relatively successful separation of the loci of sources classed as stars and galaxies is apparent, with a concentration of sources (which are presumably stellar) having $\text{CLASS_STAR_IMPROVED}$ greater than 0.95 for $17 \lesssim I \lesssim 23$, and the remaining sources (presumably galaxies) having $\text{CLASS_STAR_IMPROVED}$ less than 0.1 at bright magnitudes, and less than ~ 0.8 at $I \gtrsim 22$. As a result the selection criteria used to separate stars and galaxies in the final source catalogues are

$$\text{Source} \in \begin{cases} \text{Stars} & \text{if} \begin{cases} \text{CLASS_STAR_IMPROVED} > 0.6 \text{ and } I < 18 \\ \text{or} \\ \text{CLASS_STAR_IMPROVED} > 0.95 \text{ and } I > 18 \end{cases} \\ \text{Galaxies} & \text{otherwise} \end{cases} \quad (2.26)$$

This classification of sources into stars and galaxies is clearly approximate, and to an extent arbitrary, and so cannot be more than a guide, but it is efficient at removing those sources which are clearly stellar, at the expense of losing a few unresolved faint galaxies.

2.4.5 Source Parameters Output to the Final Catalogue

The `SEXTRACTOR` package leaves the choice of source parameters stored in the final catalogue to the user through the parameter file `default.param`. It is possible to extract up to 102 parameters for each source, but many of these are interdependent or irrelevant, and so to prevent the catalogue being unwieldy, only 17 are used in the catalogues:

NUM_I Source number
 I_APER *I*-band source magnitude through 2.5 arcsec diameter aperture
 IERR_APER Error in aperture magnitude
 FLUX_BEST Total flux of source in ADU
 I_BEST Source I_{total} magnitude
 IERR_BEST Error in total magnitude
 I_THRESHOLD Detection threshold level at source's position (0.8σ rms-noise level).
 I_MAX Maximum surface brightness (mag. arcsec⁻²)
 X_I Source's X position in BTC image (pixels) — centre of adaptive aperture
 Y_I Source's Y position in BTC image (pixels)
 A_I Semi-major axis length of adaptive aperture (arcsec)
 E_I Ellipticity of adaptive aperture/source
 FWHM_I Full-width half-maximum of source (arcsec)
 FLAGS_I Internal flags produced during source extraction — indicates whether a source is truncated/saturated/blended etc
 STAR_I Stellarity of source
 RA_I_J2000 Right Ascension (J2000) of source based on astrometric fit
 DEC_I_J2000 Declination (J2000) of source

Note that these names do not correspond exactly to those used in the SEXTRACTOR literature. The names here correspond to those used in the source catalogue extracted from the *I* image, and the corresponding names for the *V*-band catalogue simply replace the *I* identifier with *V*. The catalogues are output by SEXTRACTOR in FITS format, but for analysis within IRAF, and the TABLES tools in particular, they are converted into the TABLES format using the TABLES tool `fitsio.strfits`.

2.5 Sources in the BTC images

2.5.1 Magnitude Limits

Having produced the ultra-deep V and I BTC images, and extracted source catalogues from them, before examining the source catalogue for ‘interesting’ sources, it is necessary to establish to what extent the information contained within the catalogue is reliable. The major problem that has to be considered when dealing with such deep images is the non-detection, misidentification and errors in determining the flux of the faintest sources. At the faintest magnitudes incompleteness and the Eddington bias (produced as magnitude errors scatter the plentiful faint objects to brighter magnitude levels) affect significantly the number of galaxies detected.

To determine the level of confidence we can have in the information stored within the source catalogues, the levels of non-detection and magnitude errors are estimated as a function of magnitude using Monte Carlo simulations. To do this numerous artificial sources, whose magnitudes are known beforehand, are added into the BTC images and the same source extraction processes applied as to the original images. From this the completeness levels of the image as a function of magnitude are estimated by determining the fraction of sources detected at a given magnitude, and the rms magnitude errors of sources as a function of magnitude are estimated by comparing the extracted source magnitudes with their actual values.

For each of the BTC images a sub-image was chosen to be representative of the whole image. In the case of the V image a $4000 \times 1000 \text{ pix}^2$ region was taken from an area within the central $29.4 \times 29.4 \text{ arcmin}^2$ region that was observed mostly by CCDs #3 and #4 ($10^{\text{h}}46^{\text{m}}30^{\text{s}} < \alpha < 10^{\text{h}}48^{\text{m}}25^{\text{s}}$, $+05^{\circ}15'00'' < \delta < +05^{\circ}22'00''$ — see Figure 2.13), and is representative of the three-quarters of the central deep region not covered by CCD #1. Given the large amount of variation in noise levels across the I image, it is not possible to select an area to be representative of the whole image, but by selecting one of the four deep regions, at least an area of uniform coverage and depth can be considered, from which the properties of the remaining deep areas can be extrapolated by comparison with the 5σ magnitude limits of Table 2.6. For this reason the $1136 \times 1110 \text{ pix}^2$ deep region covered by all 15 CCD #4 exposures ($10^{\text{h}}46^{\text{m}}30.1^{\text{s}} < \alpha < 10^{\text{h}}47^{\text{m}}02.8^{\text{s}}$, $+05^{\circ}19'50'' < \delta < +05^{\circ}27'48''$

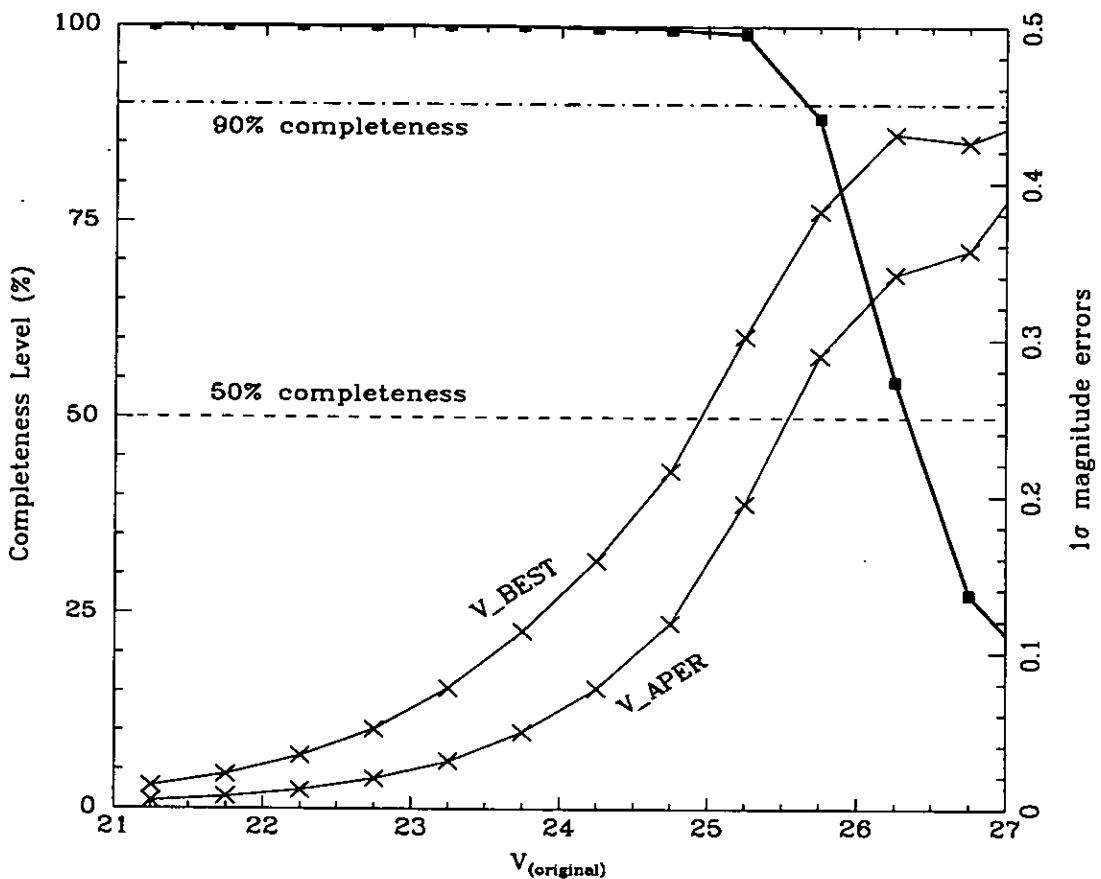


Figure 2.17: Completeness levels and magnitude errors for a sample region from the BTC V image that is representative of the sensitivities reached by three-quarters of the central 30×30 arcmin² image, i.e. not the quarter covered by CCD #1. The red curve indicates the completeness level of the image as a function of magnitude, with the blue horizontal dashed- and dot-dashed-lines indicating the 50% and 90% completeness levels respectively. The green and magenta lines indicate the 1σ magnitude errors produced by the adaptive (V_BEST) and 2.5 arcsec apertures (V_APER).

— see Figure 2.14) was chosen to be the representative area for the I -image.

For each image we consider the photometric properties of galaxies in magnitude bins of width 0.5 mags from $21 < I < 27$ and $21 < V < 27$. For each image and magnitude bin, artificial galaxies are created by dimming a bright galaxy by $\simeq 2.5$ magnitudes. Then 500 copies of the artificial galaxy are created with specified magnitudes having the following probability distribution:

$$P(\text{galaxy has magnitude } m) = \begin{cases} 0 & m < m_{min} \\ \propto m^{0.4} & m_{min} < m < m_{max} \\ 0 & m > m_{max} \end{cases}, \quad (2.27)$$

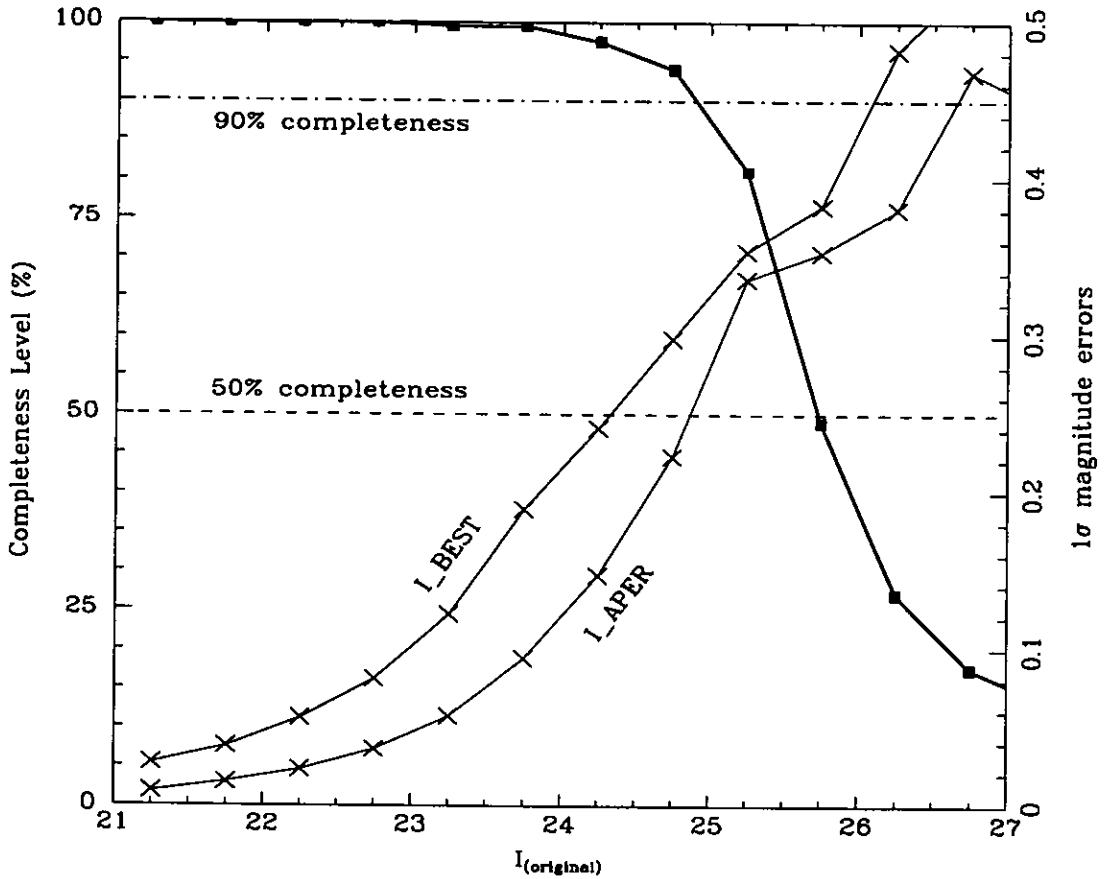


Figure 2.18: Completeness levels and magnitude errors for the 8×8 arcmin² deep region of the BTC *I*-band image, covered by CCD #4 for all 15 1080sec exposures, giving a total exposure time of 16 200sec. The red curve indicates the completeness level of the image as a function of magnitude, with the blue horizontal dashed and dot-dashed lines indicating the 50% and 90% completeness levels respectively. The green and magenta lines indicate the 1σ magnitude errors produced by the adaptive apertures (*I_BEST*) and 2.5 arcsec apertures (*I_APER*).

and added to the image at random positions. The false colour image of Figure 2.11 shows extended red halos around bright stars, indicating problems in modelling the background levels in the *I* image around these sources. This affects the ability of the source extraction process to detect and analyse any sources in these halos, and so these areas are removed from this analysis.

The images with the added artificial sources are then processed by the source extraction routine in the same manner as the original images, and the photometric properties of those artificial sources detected by the extraction process are compared with their actual values, resulting in completeness levels and magnitude errors for

CCD covering deep region	5σ mag arcsec ⁻²	90% completeness level (mag)	50% completeness level (mag)
CCD #1	25.56	24.59	25.29
CCD #2	26.21	25.24	25.94
CCD #3	25.62	24.65	25.35
CCD #4	26.12	25.15	25.85

Table 2.7: Estimation of 90% and 50% completeness levels for each of the four deep regions from the BTC *I*-band image through extrapolation from the values of the CCD #4 deep region.

each magnitude bin (Figures 2.17 and 2.18).

Figure 2.17 shows the completeness levels and magnitude errors (both aperture and total) for the sample *V*-band image. An analysis of the artificial source detection levels indicates that the source catalogue is essentially complete to $V \simeq 25.5$, 90% complete to $V \simeq 25.80$, and 50% complete to $V \simeq 26.35$.

The two fractional completeness levels, 90% and 50%, are commonly used as measures of the depth of the catalogue, with the 90% level indicating the limit of reliable photometry in a catalogue, and the 50% level indicating the maximum magnitude limit beyond which incompleteness and Eddington bias render any error measurements meaningless.

The figure also shows the rms magnitude errors (both aperture and total) for sources in each magnitude bin. For each bin, the total magnitude (*V*_BEST) error (shown as green curve) is $\sim 50\%$ greater than that of the 2.5 arcsec aperture magnitude (*V*_APER) error (shown as magenta curve). This is due to the fact that the apertures used to determine the total magnitudes are larger than 2.5 arcsec on average, and so the errors due to background noise are increased.

Figure 2.18 shows the completeness levels and magnitude errors as a function of magnitude for the sample deep region from the *I*-band image. An analysis of the artificial source detection levels indicate that the source catalogue is essentially complete to $I \simeq 24.80$, 90% complete to $I \simeq 25.15$, and 50% complete to $I \simeq 25.85$. By assuming that the completeness levels and 5σ magnitude limits are simply related, the completeness levels for each of the four deep regions can be determined by extrapolation of Table 2.6 as shown in Table 2.7.

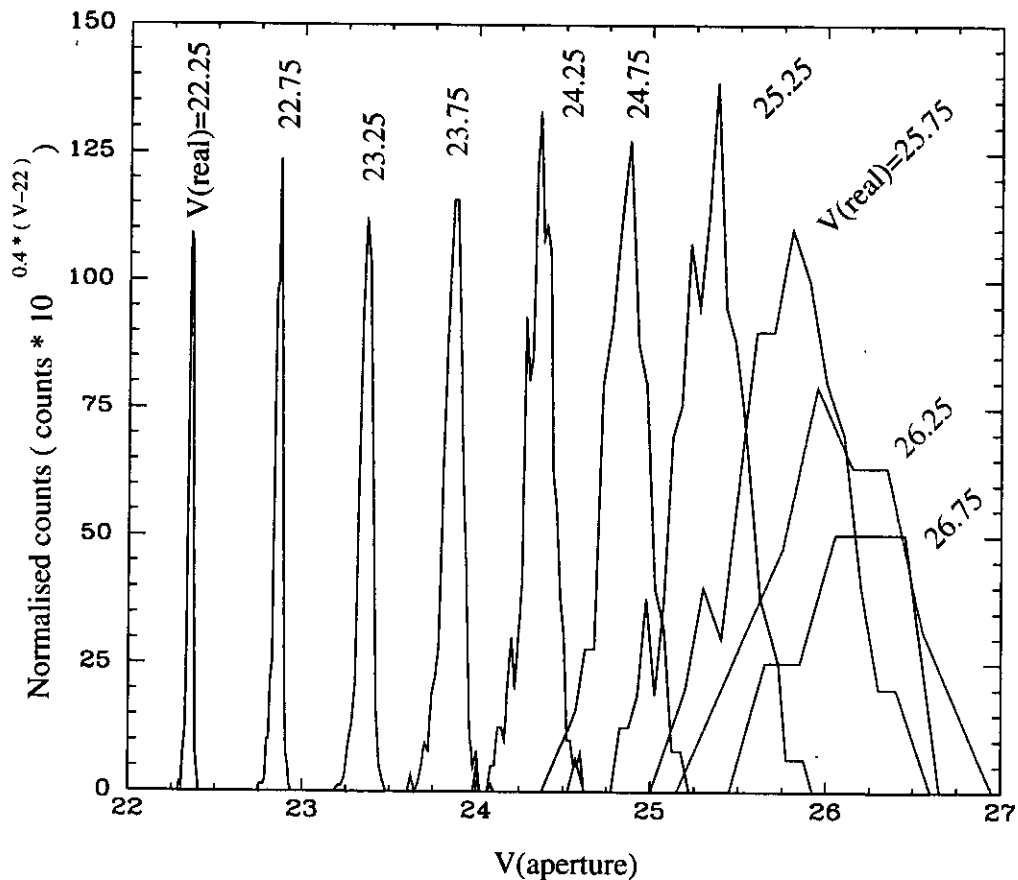


Figure 2.19: Histograms showing the effects on aperture photometry of the source extraction processes in the sample deep region of the BTC V-band image as a function of magnitude.

To demonstrate the effect of Eddington biasing at faint levels, histograms of the aperture magnitudes of the artificial stars for each magnitude bin are shown in Figures 2.19 and 2.20. So that the width of the histogram of extracted aperture magnitudes reflects the rms photometric errors for sources in a particular magnitude bin, each aperture magnitude is corrected so that the actual magnitudes of all the sources in the bin are equal to the mid-point of the magnitude bin (e.g. $V=22.25$, 22.75 , 23.25 , 23.75 etc.), rather than distributed across the whole bin, i.e.

$$\text{MAG_CORR} = \text{MAG_APER} - \text{MAG_REAL} + \text{MAG}(\text{mid-point}).$$

Eddington bias is due to the fact that there are many more faint galaxies in an image than brighter sources for any given magnitude level, whereas equal numbers of artificial galaxies have been added for each magnitude bin. To correct for this each histogram of MAG_CORR counts is multiplied by a normalising factor, so that the number of artificial sources in each magnitude bin is proportional to the expected

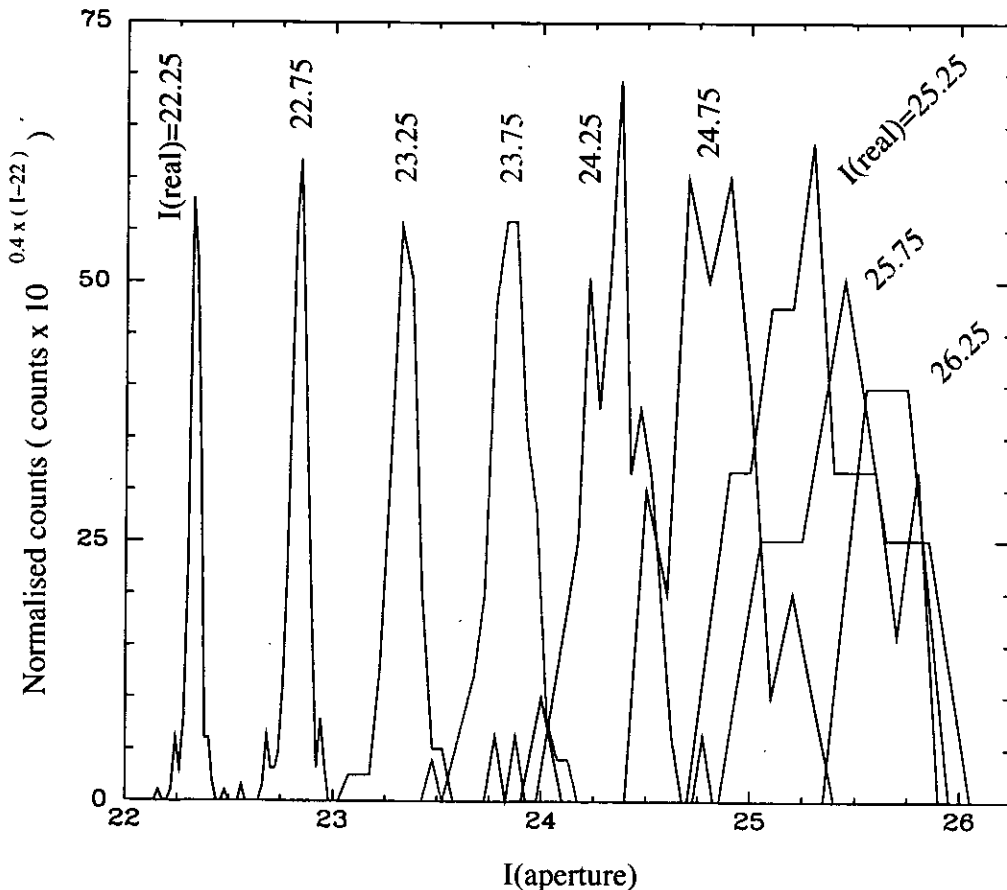


Figure 2.20: Histograms showing the effects on aperture photometry of the source extraction processes in the sample deep region of the BTC *I*-band image as a function of magnitude.

galaxy number density in the bin. In previous deep surveys, the galaxy counts at these magnitudes form a simple power law, $\text{Galaxies}(m) \propto 10^{\alpha m}$, where $\alpha \simeq 0.4$ for both *V* and *I* passbands at these magnitudes (e.g. Smail et al., 1995); and so the normalising factor used in these plots is $10^{0.4(m-22)}$. Another consequence of using this normalising factor is that if the rms errors are proportional to $10^{0.4 \times m}$ (i.e. inversely proportional to the flux) then the histogram widths should increase in the same manner, and so the histogram peak heights should be proportional to the completeness level of each bin, i.e. constant at bright magnitudes.

At magnitudes brighter than the 90% completeness levels ($V \lesssim 25.5, I \lesssim 25.0$) the aperture magnitudes produced by the source extraction process appear well behaved, with the 1σ errors increasing as $10^{0.4 \times m}$ as expected, and the histogram peak heights approximately constant. There is an offset of $\simeq 0.10$ mag between the median aperture magnitude and the real magnitude for each magnitude bin.

This is due to the fact that the artificial galaxies are larger than the 2.5 arcsec aperture and so some of the flux is lost. However this offset appears constant with magnitude and passband, and so the resultant $V - I$ colour should not be affected. At fainter magnitudes the effects of Eddington bias become apparent as faint galaxies are scattered up to brighter magnitude bins by the large photometric errors. For example, $\simeq 25\%$ of sources with aperture magnitudes of $25.5 < V < 26.0$ or $25.0 < I < 25.5$ are expected to be faint sources scattered into the magnitude bin by photometric errors, and whose actual magnitudes are more than 0.25 magnitudes fainter than that measured. As a consequence the flux levels of many galaxies in the faintest magnitude bins may be significantly overestimated.

A particular consequence of Eddington biasing may be the apparent bluing of faint intrinsically-red sources. For example, consider a galaxy with $I = 23.5$, $V = 26.5$, i.e. $V - I = 3.0$, magnitudes and colours typical of passively-evolving galaxies at $z \gtrsim 1$. The galaxy should be easily detectable in the I -image, resulting in accurate photometry. However, it is on the detection limit of the V -image, and if detected its flux levels may well be significantly overestimated, resulting in an apparent V magnitude as much as 0.5–1.0 mag too bright, hence producing a $V - I$ colour 0.5–1 mag too blue.

2.5.2 Galaxy Counts

One of the motivations behind ultra-deep surveys to date has been to test cosmological models via the classical number-magnitude relations, or in other words, *how many galaxies are there?* Hence as a result, the plot most synonymous with deep fields is that of galaxy counts as a function of magnitude. With the building of larger and larger telescopes and the constantly improving quality and collecting area of CCD cameras, surveys have been able to go deeper and cover greater angular areas, obtaining more accurate results. However to date, interpretation has always been hampered by the difficulty of disentangling the effects of galaxy selection and evolution from the cosmological effects we wish to probe. Although the survey undertaken here is not nearly as deep, or as wide, or has as many passbands, as other surveys recently completed or in progress (e.g. HDF-North and South, Canada-France Deep Fields Survey, EIS) it is still a useful exercise to produce such galaxy

V	Raw	Galaxies	$\sigma(N_{cor})$	I	Raw	Galaxies	$\sigma(N_{cor})$
mag	counts	(deg ⁻² .mag ⁻¹)		mag	counts	(deg ⁻² .mag ⁻¹)	
20.25	25	880	175	20.25	82	4700	520
20.75	50	1750	250	20.75	148	8480	700
21.25	91	3190	330	21.25	183	10480	770
21.75	125	4380	390	21.75	283	16210	960
22.25	187	6550	480	22.25	378	21650	1100
22.75	315	11040	620	22.75	549	31400	1300
23.25	491	17200	780	23.25	804	46300	1900
23.75	841	29500	1000	23.75	1019	58650	2100
24.25	1374	48250	1400	24.25	1251	73500	2900
24.75	1781	62700	1700	24.75	1521	92700	3800
25.25	2196	77700	2000	25.25	1983	140200	6300
25.75	2575	102300	3300	25.75	1930	225600	9000
26.25	2603	167100	5300	26.25	758	160800	7000
26.75	1247	159500	5400	26.75	21		

Table 2.8: Raw and corrected galaxy counts for the $4000 \times 1000 \text{ pixel}^2$ (205.44 arcmin^2) deep region of the BTC V image, and the combined CCD #2 and CCD #4 deep regions (125.72 arcmin^2 in total) of the BTC I image.

number-magnitude plots and compare the results with existing data, if only as a validation method to show that there is nothing seriously awry with the photometric calibration and source extraction process.

As discussed in the previous subsection, before determining the galaxy counts, a correction for incompleteness at faint magnitudes has to be applied, otherwise the counts at faint magnitudes would be significantly underestimated. The completeness levels for subsections of the V and I BTC images were determined in the previous subsection. However given the non-uniformity of depth of both the V and I images, these levels are not valid over the whole image, and so only those regions similar in depth to those used in the previous section can be considered. In the case of the V image, only the $4000 \times 1000 \text{ pix}^2$ region used to determine the completeness levels of Figure 2.17 is considered, giving a total area of 205.44 arcmin^2 . In the

Survey name	Reference	Area (arcmin ²)	$m_{lim}(50\%)$
BTC images	This thesis	205.44(V)	$V = 26.3$
		125.73(I)	$I = 25.9$
Deep Keck Images	Smail et al. (1995)	54.8(V)	$V = 27.0$
		76.3(I)	$I = 25.8$
NTT SUSI Deep Field	Arnouts et al. (1999)	5.62	$V = 26.5, I = 25.3$
HDF - North	Williams et al. (1996)	5.3	$V = 29.5, I = 28.5$
HDF - South	Casertano et al. (2000)	5.1	$V = 29.4, I = 28.0$
Herschel Deep Field	Metcalfe et al. (2000)	52.2	$I = 25.2$
	Lilly et al. (1991)	4.1	$I = 25.0$

Table 2.9: Summary of the deep surveys used for comparison with the differential galaxy counts from the BTC images.

case of the I image, as well as using the deep region covered by all 15 CCD #4 exposures, the comparable deep region covered by CCD #2 is also used, as their 5σ magnitude limits are similar, and thus doubling the area available for analysis to 125.73 arcmin².

For each of the regions the raw galaxy counts are determined for bins of width 0.5 magnitude, after discounting those sources classified as stellar. The classification of stars and galaxies has been shown to be efficient at bright magnitudes ($I < 22$, $V < 23$), and at fainter magnitudes the fraction of sources classified as stellar becomes negligible ($< 1\%$). The counts are then corrected for incompleteness by simply dividing by the fraction of artificial sources detected at each magnitude level. Note that this analysis does not include the Eddington bias and can thus overestimate the correction factor.

In Figures 2.21 and 2.22 the corrected differential galaxy counts are plotted as a function of magnitude, and the raw and corrected number counts are reported in Table 2.8. The errors determined are Poisson and include the uncertainty in the completeness level at each magnitude.

The differential galaxy counts produced by other deep surveys are shown on the two figures for comparison. A summary of the size and magnitude limits of each

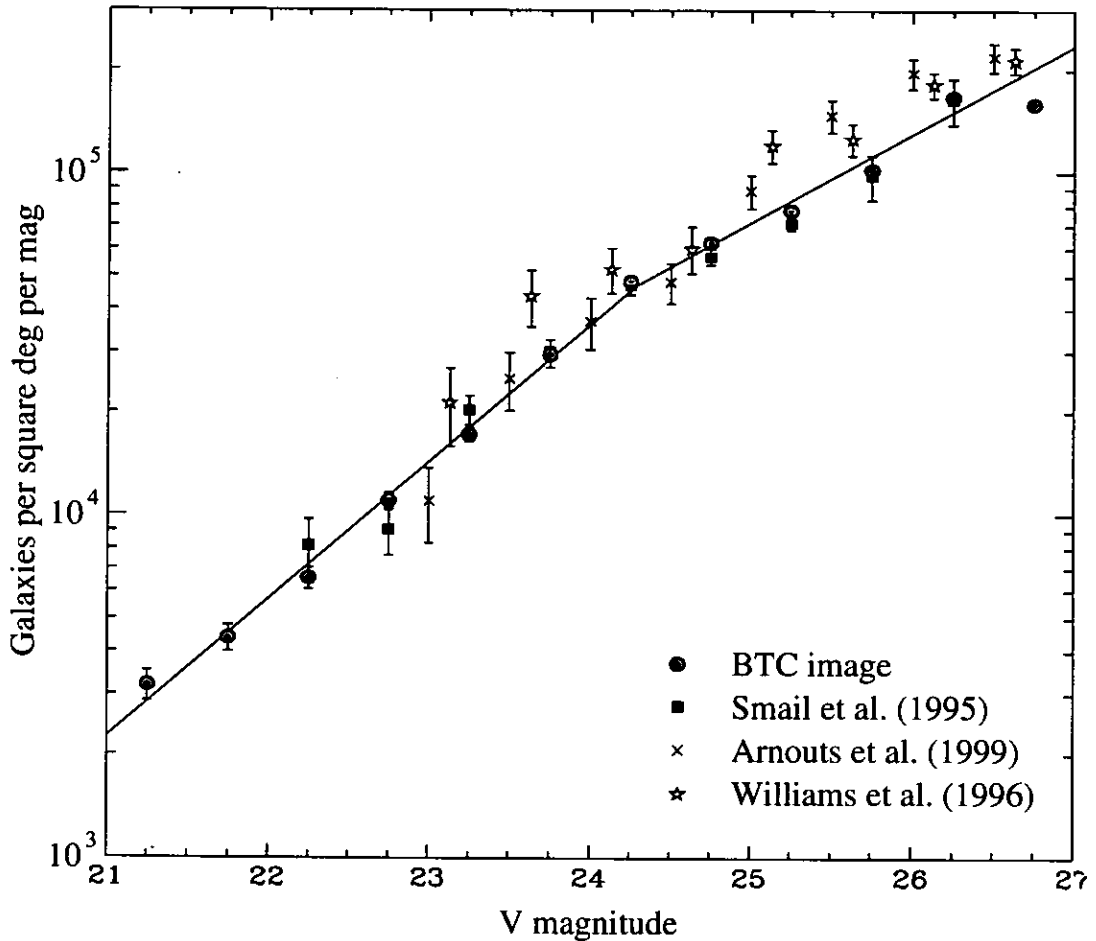


Figure 2.21: Differential galaxy counts as a function of V magnitude for a representative $4000 \times 1000 \text{ pix}^2$ (205.4 arcmin^2) deep region from the BTC V -band image. The corrected V -band galaxy counts are represented by red-filled circular symbols. The errors shown consider the both the Poisson uncertainties from the raw galaxy counts and also the uncertainties in the completeness corrections given the number of artificial sources added and detected. The two-component least-squares linear fits to the galaxy counts are shown by solid red lines. The other symbols represent the galaxy counts observed in other ultra-deep surveys: (Smail et al., 1995, green filled squares), the NTT SUSI deep field (Arnouts et al., 1999, magenta crosses), and the Hubble Deep Field North (Williams et al., 1996, blue stars).

of the surveys is given in Table 2.9. It can be seen immediately that our V and I galaxy counts are in good agreement with the other deep surveys, in particular that of Smail et al. (1995) which is the most comparable both in terms of area covered, and the filter set used. The HDF galaxy counts for example have been converted from the WFPC2 filter set and AB magnitude system to the standard ground based Johnson-Kron-Cousins $UBVRI$ photometric system adopted in this study, by the

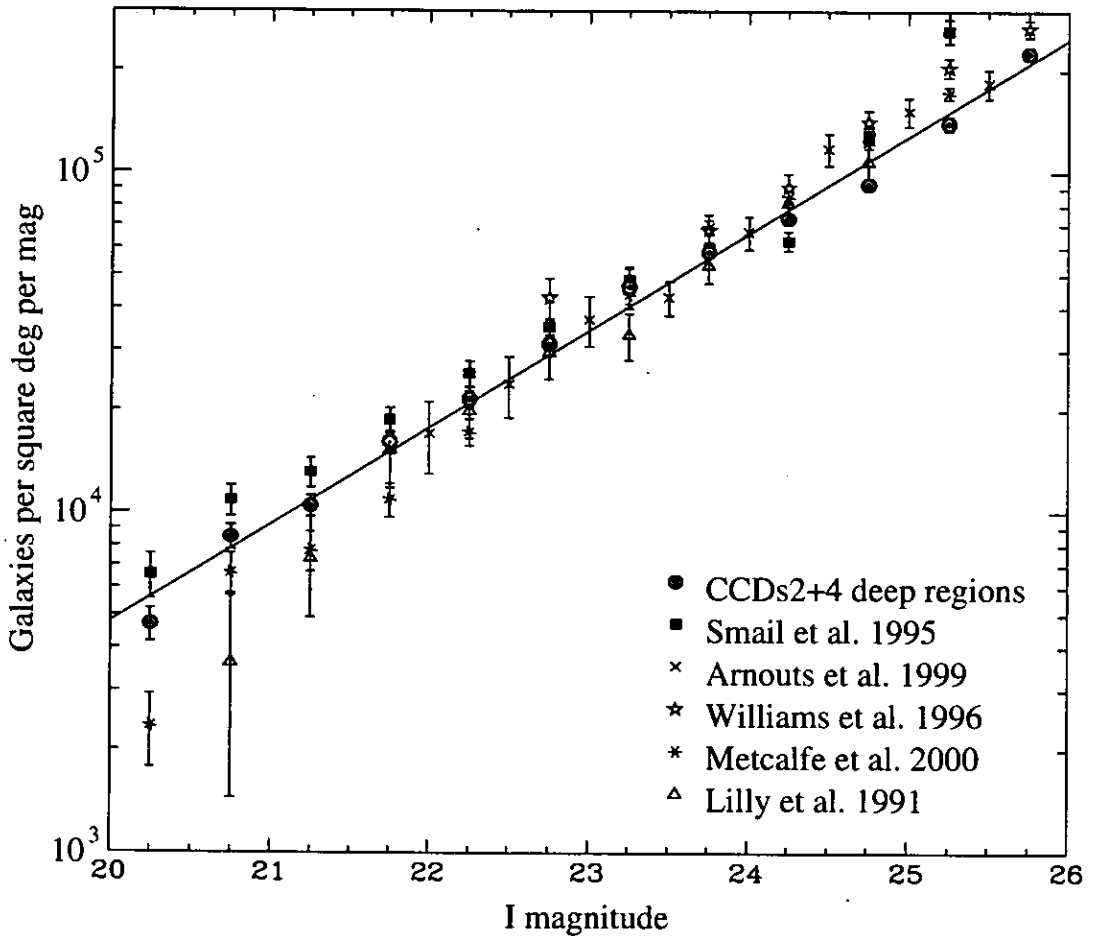


Figure 2.22: Differential galaxy counts as a function of I magnitude for the deep regions covered by CCD #2 and CCD #4 (125.7 arcmin^2 in total) from the BTC I -band image. The corrected I -band galaxy counts are represented by red-filled circular symbols. The errors shown consider the both the Poisson uncertainties from the raw galaxy counts and also the uncertainties in the completeness corrections given the number of artificial sources added and detected. The least squares linear fit to the galaxy counts is shown by a solid red line. The other symbols represent the galaxy counts observed in other ultra-deep surveys: Smail et al. (1995, green filled squares), the NTT SUSI deep field (Arnouts et al., 1999, magenta crosses), the combined Hubble Deep Fields North and South (Williams et al., 1996; Casertano et al., 2000, blue stars), the Herschel Deep Field (Metcalf et al., 2000, cyan asterisks), and Lilly et al. (1991, black triangles).

relations $V_{AB} = V$, $I_{AB} = I + 0.47$.

The slopes of the corrected V and I -band galaxy counts are estimated using linear regression, and are shown as red lines on corresponding figures. For the V band, the slope of galaxy counts is measured as $\alpha_V = 0.402 \pm 0.012$ for $V=21-24$, before a pronounced break in the slope at $V \simeq 24.25$, and a significant flattening

to $\alpha_V = 0.258 \pm 0.017$ for $V = 24\text{--}26$. Evidence of this break and flattening has been already produced by previous works. Smail et al. (1995) report a slope of $\alpha_V = 0.404 \pm 0.015$ for $V = 22\text{--}24.5$, then a break at $V \sim 24.5$, and a flattening of galaxy counts to $\alpha_V = 0.28 \pm 0.05$ at fainter magnitudes. There is no evidence of a break in the I -band count slope. Indeed the galaxy counts are fitted extremely well by a single line of slope $\alpha_I = 0.286 \pm 0.006$ for $I = 20\text{--}26$. Again these results are in excellent agreement with previous studies with Smail et al. (1995) and Arnouts et al. (1999) reporting values for the slopes of $\alpha_I = 0.271 \pm 0.009$ for $I = 19.5\text{--}25.5$ and $\alpha_I = 0.31 \pm 0.02$ for $I = 22.5\text{--}25.5$ respectively.

2.6 Summary

In this chapter the obtaining and reduction of ultra-deep optical images using the Big Throughput Camera (BTC) on the 4-m Blanco telescope at the Cerro Tololo Interamerican Observatory (CTIO) is described. The observations were made on the nights of 21/22 and 22/23 April 1998, the first night devoted to obtaining V imaging, and the second night devoted to obtaining I imaging. The resultant images cover a 40.6×34.9 arcmin² region containing three quasars from the Clowes-Campusano LQG, as well as four background quasars. The process of removing the spatial distortions inherent in the BTC optics is shown, and the validity of the resultant model is demonstrated by the linear astrometric fit being accurate to $\simeq 0.05$ arcsec across the whole field. The photometric calibration is performed using the standard stars of Landolt (1992) and is believed to be accurate to $\Delta m \simeq 0.02$.

The SExtractor package is used to extract the sources from the final images, resulting in catalogues of $\approx 10^5$ sources that are 50% complete to $V \simeq 26.35$ and $I \simeq 25.85$ in the fully exposed regions. The differential galaxy counts are determined and compared with other deep surveys, and are found to be in excellent agreement. The galaxy counts increase logarithmically with magnitude, with the slopes measured for the V -band as $\alpha_V = 0.402 \pm 0.012$ for $V = 21\text{--}24$, flattening to $\alpha_V = 0.258 \pm 0.017$ for $V = 24\text{--}26$, and for the I -band as $\alpha_I = 0.286 \pm 0.006$ for $I = 20\text{--}26$.

Chapter 3

Analysis of Galaxy Clustering in the BTC Images

3.1 Introduction

The detection and characterisation of clusters of galaxies is one of the most crucial aspects of observational cosmology, providing important constraints for both cosmological models and galaxy evolution. For example, the evolution of cluster number density as a function of redshift is highly dependent on the cosmological parameters Ω_M and Ω_Λ , with clusters forming much more rapidly in high-density universes. Indeed the fact that rich clusters have been observed at $z \gtrsim 1$ virtually rules out the $\Omega_M = 1, \Omega_\Lambda = 0$ universe. Extensive observational work has also established that the star-formation and morphological properties of galaxies in rich clusters differ significantly from those of field galaxies, with star-formation rates lower in cluster environments than the field for galaxies of the same class, and elliptical and S0 galaxies more abundant in clusters.

As a consequence of the importance of galaxy clusters, numerous galaxy cluster surveys have been undertaken in recent years, in many wavebands (e.g. the Palomar Distant Cluster Survey, Postman et al. (1996); the ROSAT Distant Cluster Survey, Rosati et al. (1998)), and numerous algorithms have been developed to detect and classify galaxy clusters from imaging or redshift data, each method being more appropriate to one kind of data than another.

This chapter describes one such algorithm, the Cluster Red Sequence method

of Gladders & Yee (2000) which uses the observation that the bulk of early-type galaxies in clusters lie along a tight, linear colour-magnitude relation — the red sequence — to maximise the signal from a cluster in imaging data and to estimate its redshift. This algorithm is then applied to the BTC V and I imaging data, allowing the detection and characterisation of clusters in the BTC field out to $z \simeq 0.6$.

3.2 The Cluster Red Sequence Method

The basic premise of all optical-infrared cluster finding algorithms is that galaxies are a reliable (although possibly biased) tracer of mass, and so an overdensity in the galaxy distribution is a signature of the underlying mass overdensity. The most likely complication to this approach would be the presence of dark clusters, but to date there appears little evidence to indicate that such objects are common. Ongoing and forthcoming observations of *cosmic shear* should clarify the relationship between the galaxy and mass distributions as the statistical properties of weak gravitational lensing of background galaxies are used to reveal the underlying mass distribution (e.g. Wittman et al., 2000b). Current results from eight clusters at $z \simeq 0.2$ suggest that the mass follows the light very closely on scales of $0.2\text{--}2 h^{-1}\text{Mpc}$ (Wittman et al., 2000a). On the basis of this premise, each cluster finding algorithm then attempts to identify the real galaxy overdensities in redshift-space in typically two-dimensional imaging data, by using some assumed property of clusters to maximise the signal.

A popular approach is the matched-filter technique (Postman et al., 1996; Kepner et al., 1999) which filters the image by a model cluster galaxy luminosity function and spatial distribution. This allows it to improve the detection sensitivity to true clusters (while at the same time being less sensitive to random projections), but by its parametric and filtering nature, it is biased towards clusters which conform to the models, i.e. virialised clusters. As a result, at the higher redshifts which we wish to probe, this approach is likely to become less efficient as the clusters are less dynamically evolved, and have more irregular morphologies. Another disadvantage of this approach is that to obtain accurate redshift estimates for the clusters and also to determine cluster membership properties, a significant amount of colour

information is required to obtain photometric redshift estimates of sufficient quality. Given the very limited colour information available from the BTC images, it would be highly unwise to make any cluster redshift or membership estimates through this approach.

Instead of using assumptions about the morphology or luminosity function of clusters, the approach used here is based upon the assumption that the presence of a red sequence of early-type galaxies is a universal signature of a galaxy cluster. What appears at first sight to be a dubious assumption, given the large variety of galaxy populations from one cluster to another, is in fact well supported by the current observational evidence, and provides a powerful and efficient method for detecting clusters, and making accurate redshift estimates, based on imaging data obtained using as few as two filters.

3.2.1 The Red Sequence in Nearby Clusters

The observation that rich clusters have a population of early-type galaxies that follow a tight, linear colour-magnitude ($C-M$) relation was made over forty years ago (Baum, 1962), and confirmed later for the Virgo and Coma clusters (Sandage, 1972), but it has only been over the last ten years that the physical processes behind the relation have been sufficiently understood that its use in observational cosmology has been established.

An example colour-magnitude relation is shown in Figure 3.1, which shows the measured colour-magnitude relation for the $z = 0.231$ cluster Abell 2390, from the HST data of Gladders et al. (1998). It shows a population of early-type galaxies (shown as asterisks) following a linear colour-magnitude relation over a range of 5–6 magnitudes with little scatter (~ 0.05 mag). A corollary of the small observed photometric scatter is that the early-type galaxies within a cluster must form a homogeneous population, i.e. they must have similar ages and star-formation histories. Bower et al. (1992) obtained precision photometry of early-type galaxies in the Coma and Virgo clusters and concluded that the two populations were indistinguishable, even though the clusters are of completely different types: the Coma cluster is rich, massive, centrally-concentrated, elliptical-rich and X-ray luminous; whilst the Virgo cluster is relatively poor, much less massive, irregular and spiral-rich. López-Cruz &

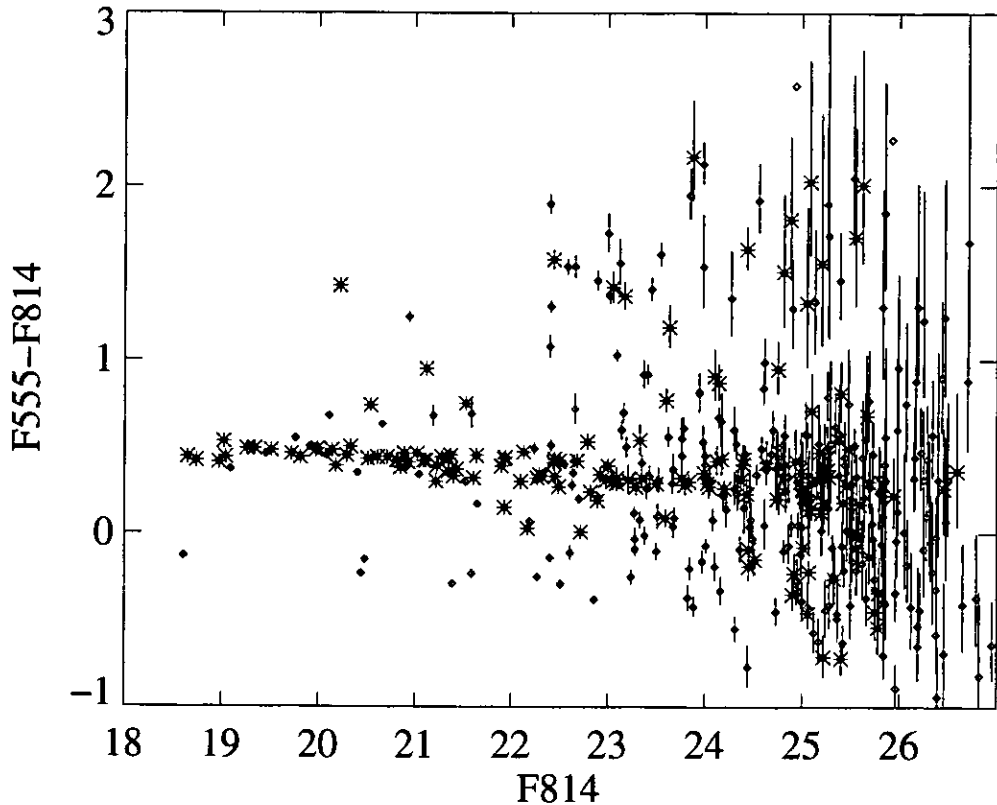


Figure 3.1: The observed colour-magnitude diagram for Abell 2390, based on two-filter HST imaging of the cluster core. The asterisks indicate galaxies morphologically selected as early-types, and diamonds indicate other galaxies in the image. Taken from Gladders & Yee (2000).

Yee (2000) have examined an extensive sample of 45 X-ray selected Abell clusters, encompassing a wide range of optical richnesses. Despite this heterogeneity, every cluster in the sample has a red sequence, and the k -corrected slopes, scatters and colours of these red sequences are indistinguishable. This indicates that the early-type galaxies which make up the red sequences form a homogeneous population, not only within each cluster, but from cluster to cluster, and also that red sequences are universal and homogeneous features of galaxy clusters, at least at $z \lesssim 0.2$.

Figure 3.2 shows the evolution with time of the spectral energy distribution (SED) of a simple stellar population (i.e. one that formed in an instantaneous burst) for the Salpeter initial mass function (IMF). This shows that for ages less than ~ 4 Gyr the SED changes rapidly with time, the galaxy initially dominated by the short-lived luminous blue stars, before reddening as those stars complete their evolution and disappear, leaving the galaxy dominated by stars in the advanced

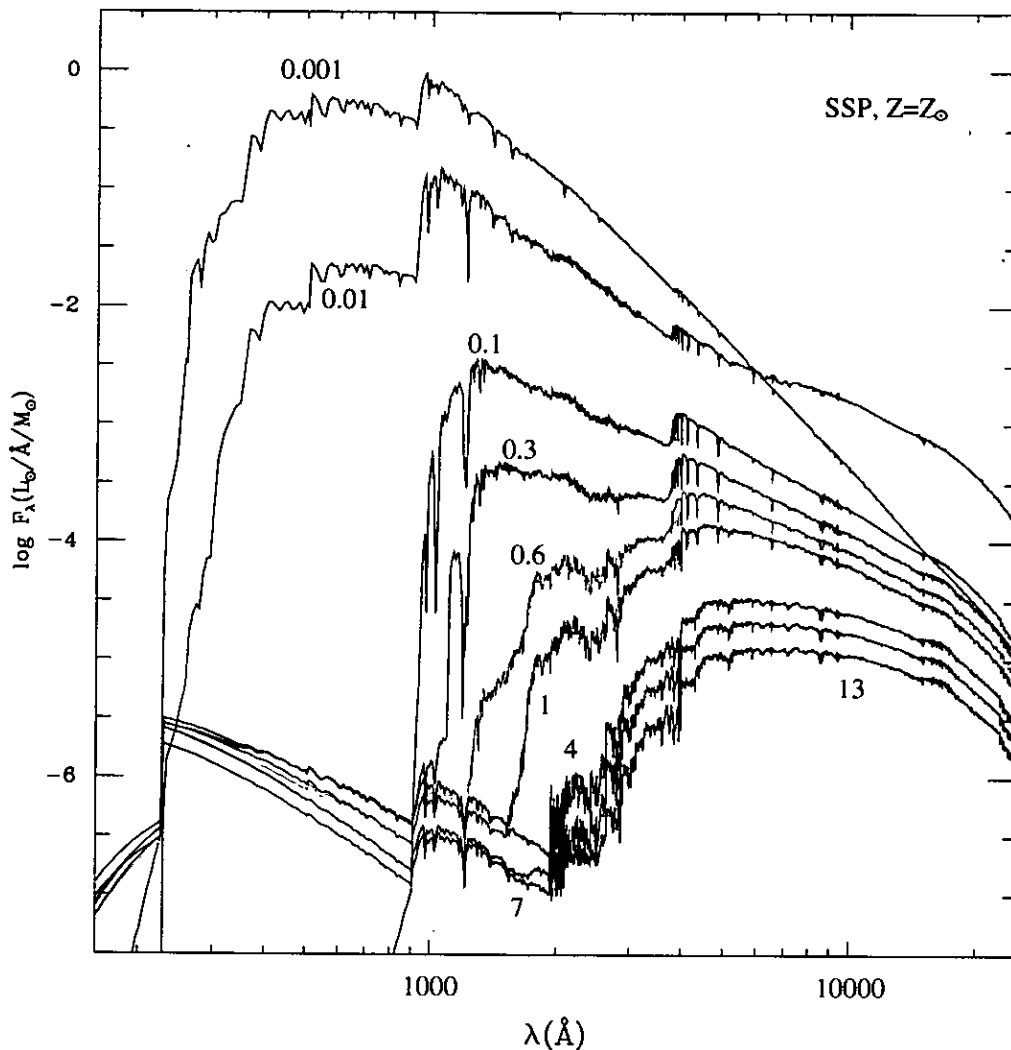


Figure 3.2: Evolution in time of the spectral energy distribution (SED) of a simple stellar population computed for the Salpeter IMF ($m_L = 0.1 M_\odot$, $m_U = 125 M_\odot$) using the Bruzual & Charlot (2000) evolutionary code. The age in Gyr is indicated next to each spectrum. Taken from Bruzual (2000).

stages of stellar evolution, and the long-lived low-mass stars. For ages greater than ~ 4 Gyr the SED changes much less as only the long-lived stars remain, resulting in colour changes less than ~ 0.05 magnitudes per Gyr.

We can use this model to transform between age and colour variations as the observed scatter of galaxy colours in a cluster is equal to the rate of change of galaxy colour measured at the mean galaxy age, multiplied by the scatter in the star-formation epoch. For example, if early-type galaxies were formed in a single-burst of star-formation about 10 Gyr ago, with a scatter in the time of formation of

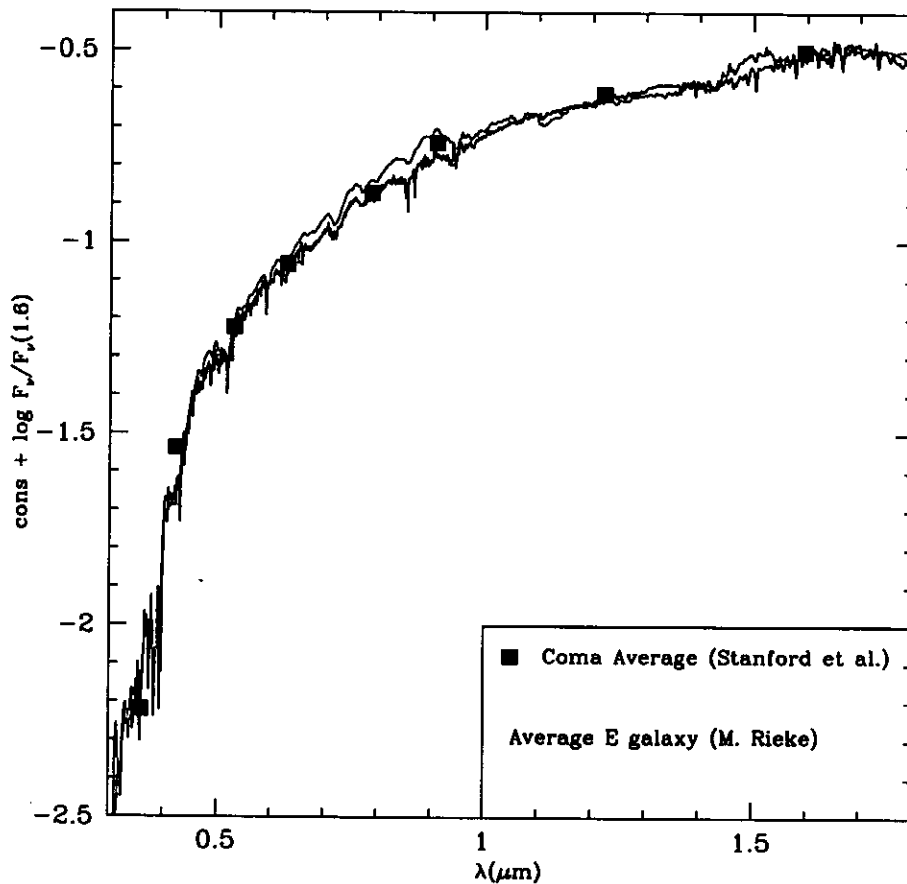


Figure 3.3: Best fit to the average spectrum of an elliptical galaxy (shown as red line). The model SED (black line) corresponds to a 10 Gyr old $Z=Z_{\odot}$ simple stellar population computed for the Salpeter IMF ($m_L = 0.1 M_{\odot}$, $m_U = 125 M_{\odot}$). The broad-band fluxes representing the average of elliptical galaxies in the Coma cluster are shown as blue squares. Taken from Bruzual (2000).

~ 1 Gyr, then this would result in an intrinsic colour scatter of 0.025 mag. However, if they were formed only 5 Gyr ago, to produce the same intrinsic colour scatter, the spread of galaxy formation time would have to be less than 300–400 Myr. Given the great distances between clusters, such a high level of synchronisation for the formation of early-type galaxies appears unlikely, meaning that these galaxies, or at least their stellar populations, are probably older than 5 Gyr. This argument is confirmed by the spectra of the red sequence galaxies, as they are best fit by simple stellar populations of ages 9–12 Gyr (see Figure 3.3).

A second notable feature of the red sequence of Figure 3.1 is its apparent slope, with the colour becoming progressively bluer towards fainter magnitudes. The two conventional explanations for this gradient are that it is caused by a progressive

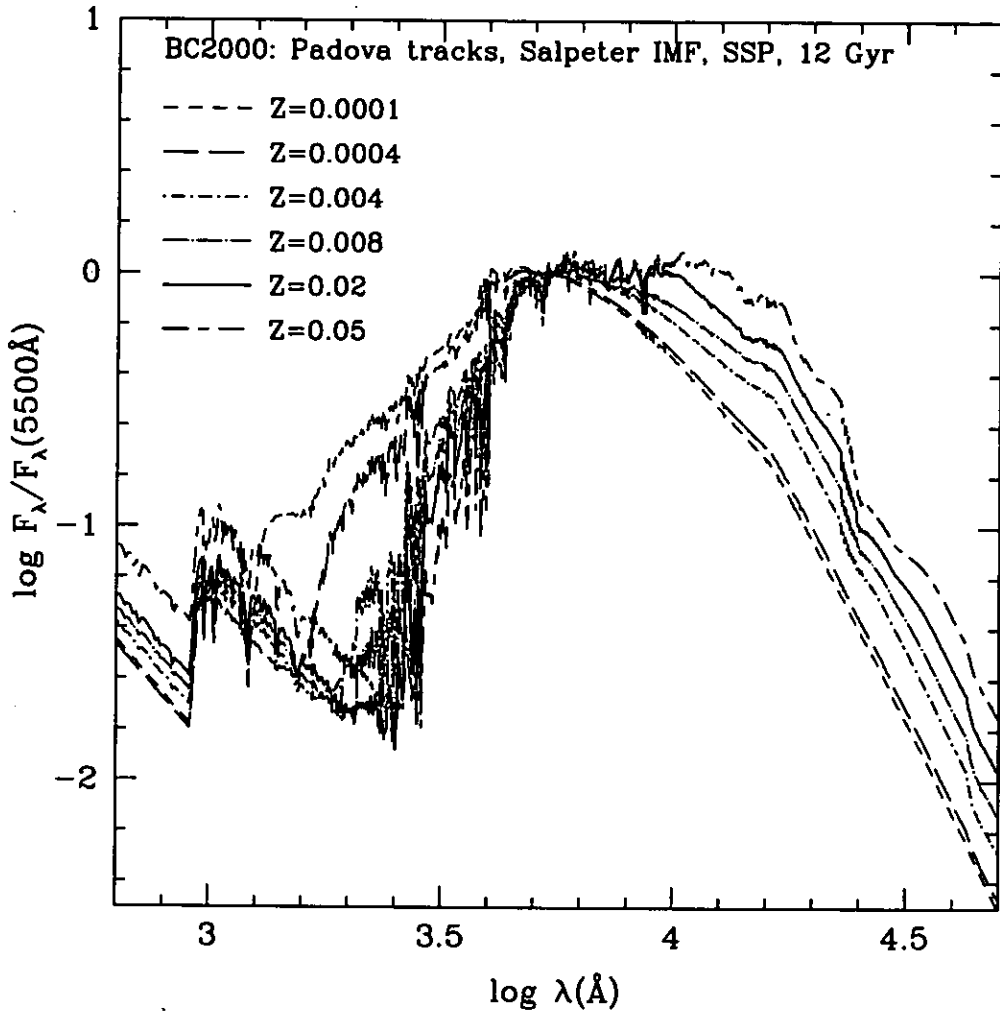


Figure 3.4: Effect of metallicity on old stellar populations. Each line represents a simple stellar population model galaxy SED of age 12 Gyr, produced using the Bruzual & Charlot (2000) evolutionary code, with a different metallicity, as indicated inside the frame. All the models shown were computed for the Salpeter IMF ($m_L = 0.1 M_\odot$, $m_U = 125 M_\odot$), and the SEDs normalised at $\lambda = 5000 \text{ \AA}$. Taken from Bruzual (2000).

increase of either a mean stellar metallicity or a mean effective age with increasing galaxy luminosity.

The effect of age on galaxy colour was shown previously (see Figure 3.2) with galaxies becoming increasingly red with age. The effect of metallicity on the colour of evolved galaxies (12 Gyr old) can be seen in Figure 3.4, which shows the galaxies becoming increasingly red as the metallicity is increased from $Z = 0.0001$ (magenta dashed-line) to $Z = 0.05$ (red dot-dashed-line).

The conventional explanation for an increase of metallicity with luminosity/mass

is that the more massive galaxies have deeper potential wells, and so are better able to retain their metals when the galactic wind, triggered by the heating of the interstellar medium by supernovae in the initial star-burst, ejects the remaining gas, and ends the epoch of star-formation.

This dual interpretation of the red sequence slope is well known as the age-metallicity degeneracy of old stellar populations, and it is difficult to break this degeneracy as long as one considers only photo-spectroscopic data from nearby clusters. However, by considering the evolution of the red sequence with redshift it is possible to break this degeneracy, as the slope should remain relatively constant with redshift if it is a metallicity effect, whereas if it is caused by age differences, the slope will increase rapidly as the formation epoch of the fainter (and hence younger) galaxies is approached.

3.2.2 Evolution of the Cluster Red Sequence

The photometric evolution of early-type galaxies in higher redshift clusters (to $z \simeq 1.2$) has been examined by a number of authors (e.g. Aragón-Salamanca et al., 1993; Ellis et al., 1997; Stanford et al., 1998; Kodama et al., 1998).

Aragón-Salamanca et al. (1993) examined the evolution of galaxies, selected using near-infrared imaging, in the fields of 10 rich clusters at $0.5 < z < 0.9$. They detected a clear and systematic trend with redshift in the optical- near-infrared colours of the red cluster sequence galaxies, in which they become increasingly blue in a manner consistent with the passive ageing of stellar populations formed before $z_f \simeq 2$. It does have to be noted that this survey did suffer the flaw that the galaxies were selected by colour rather than morphology, increasing the possibility of contamination from other galaxy types.

Morphological selection of distant cluster galaxies became possible with the HST, and Ellis et al. (1997) analysed the colour-magnitude relations of three clusters at $z \simeq 0.54$ using HST photometry and morphological selection. They found relatively small dispersions in the relations even at these higher redshifts, indicating a high formation redshift ($z_f \simeq 3$) for the stellar populations. They also did not detect a significant change in the slopes of the relations with respect to the Coma data, and found modest colour evolution in agreement with earlier studies.

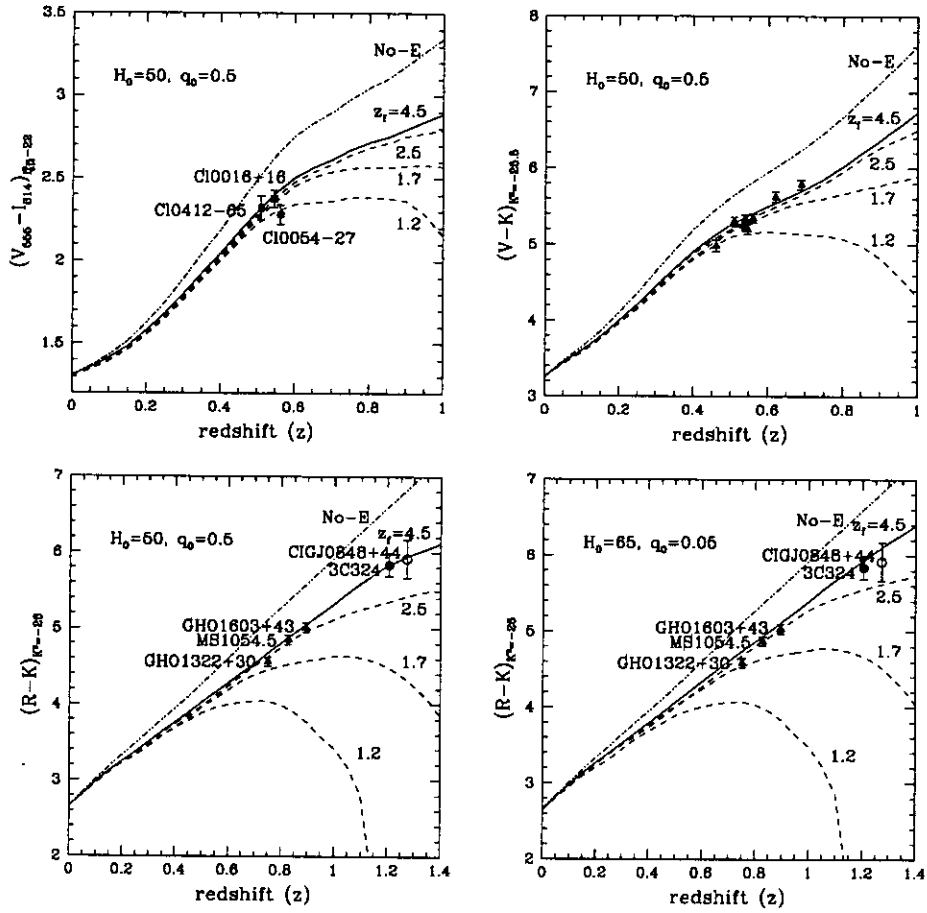


Figure 3.5: Evolution of the zero-point of the C-M relation. The blue dotted-line indicates the no-evolution model. The red solid-lines represent the metallicity sequence model of Kodama & Arimoto (1997) with $z_f = 4.5$ ($\text{Age}_G = 12 \text{ Gyr}$). The green dashed-lines correspond to $z_f \simeq 2.5$, 1.7 and 1.2, ($\text{Age}_G = 11, 10$ and 9 Gyr) from top to bottom respectively. $H_0 = 50 \text{ km s}^{-1} \text{ Mpc}^{-1}$ and $q = 0.5$ is assumed unless otherwise stated. Taken from Kodama et al. (1998)

Stanford et al. (1998) presented optical- near-infrared colour-magnitude relations for morphologically-selected (using HST imaging data) early-type (E+S0) galaxies in 19 clusters out to $z \simeq 0.9$. They observed no significant change in either the slope or the scatter of the colour-magnitude relationship as a function of redshift out to $z \simeq 0.9$. By comparing the optical- near-infrared colours of the C-M relations to that of the Coma cluster, they observed a progressive blueing with increasing redshift of the early-type cluster galaxies in a manner consistent with the passive evolution of an old stellar population formed in a burst at an early cosmic epoch ($z_f > 2$).

Kodama et al. (1998) investigated the evolution of the colour-magnitude relations

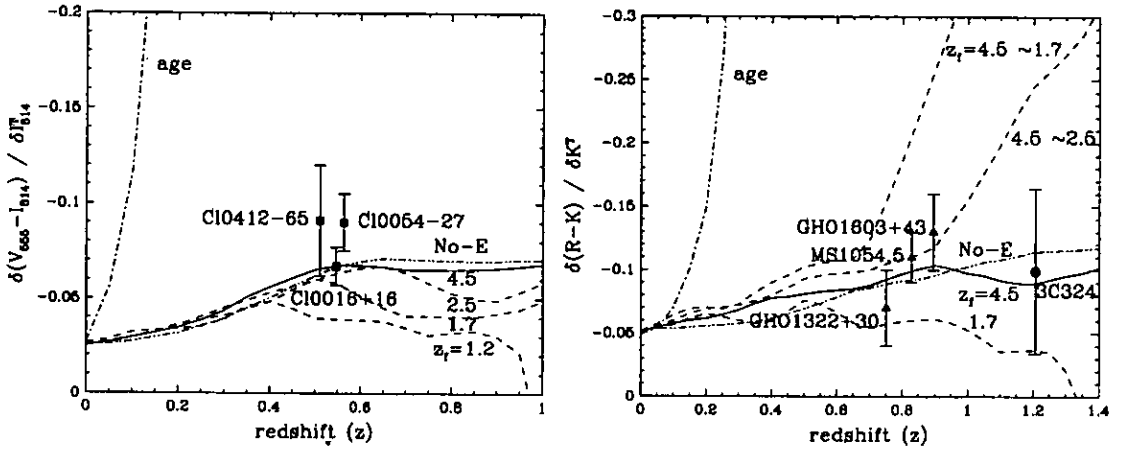


Figure 3.6: Evolution of the slope of the C-M relation. The blue dotted-line indicates the no-evolution model. The red solid-lines represent the metallicity-sequence model of Kodama & Arimoto (1997) with $z_f=4.5$ ($\text{Age}_G=12$ Gyr). The green long-dashed lines show the models that change z_f as a function of galaxy luminosity for the brightest three mag range (brighter galaxies form earlier). The magenta dot-dash lines show the extreme age-sequence models of Kodama & Arimoto (1997). The results from the Ellis et al. (1997), Stanford et al. (1998), and Barger et al. (1996) samples are indicated by filled squares, triangles and circles respectively. Taken from Kodama et al. (1998)

for morphologically-selected early-type galaxies in 17 clusters at $0.31 < z < 1.27$, using the Kodama & Arimoto (1997) evolutionary model for elliptical galaxies. This model assumes that elliptical galaxy formation occurs in a monolithic collapse accompanied by a galactic wind. Star formation is burst-like with star-formation and gas-infall time-scales set to be 0.1 Gyr, followed by a galactic wind which occurs less than 0.5 Gyr from the start of galaxy formation. The model is calibrated to the C-M relation of the Coma cluster, by changing either the mean stellar metallicity or the mean age of the galaxies as a function of luminosity/mass. In Figure 3.5 the zero-points (colour of the C-M relation at a fixed absolute magnitude) of the C-M relations of the 17 clusters are compared with the models for various formation epochs. At redshifts below 0.6, the differences between the zero-points for the model C-M relations are too small to provide significant constraints on the formation epoch. By considering the relations of higher redshift clusters, particularly those beyond $z \sim 1$, the formation epoch of these early-type galaxies can be constrained to $z_f > 3$.

The evolution of the C-M relation slope with redshift is shown in Figure 3.6. It was found to be also in good agreement with the metallicity-sequence model, with

little increase with redshift even beyond $z = 1$, certainly much less than would be expected if the slope were produced as a result of age differences. Both the evolution of the C-M relation zero-point and slope with redshift were found to be best fit by a metallicity-sequence model in which the epoch of major star-formation was $z_f = 4.5$. The effect of a non-zero value for Ω_Λ is to move the galaxy-formation redshift in order to produce the same galaxy ages at $z \simeq 1$, and so for the $\Omega_M = 0.3$, $\Omega_\Lambda = 0.7$ model used here, the galaxy-formation redshift is reduced to $z_f = 3.5$.

3.2.3 Motivation for using the Cluster Red Sequence Method

The basic premise motivating the use of the Cluster Red Sequence method is the observation that all rich clusters have a population of early-type galaxies which follow a strict colour-magnitude relation. To date there is no evidence for a population of clusters not having a red sequence for $z < 1$, and although the universality of the red sequence in clusters at $z > 1$ has not been thoroughly tested, due mainly to the lack of known clusters at these redshifts, it is striking that all the high-redshift clusters studied so far have red sequences.

All the current observational evidence (discussed in the previous two subsections) indicates that red sequence galaxies form remarkably homogeneous populations, both within a single cluster, and between clusters. Studies following the evolution of this population with redshift indicate that the stellar population of early-type galaxies is formed in a synchronous manner at high redshifts ($z_f > 3$). Finally, each of the properties of the C-M relation, its slope, scatter, and zero-point, for all the studied clusters to $z \simeq 1.2$, can be successfully described by a single model, in which the epoch of major star-formation was $z_f = 4.5$, and the slope is a product of the increase in metallicity with galaxy mass/luminosity.

Beyond the homogeneity of its population, and the ability to model its properties, there are numerous other observational reasons for using the red sequence as a tool for cluster finding. Firstly, the red sequence galaxies generally dominate the bright end of the cluster luminosity function, and so are the easiest cluster members to detect, and will also have the smallest photometric errors. Secondly, these galaxies are concentrated in the densest regions of clusters (as described by the density-morphology relation; Dressler, 1980), thus presenting a higher contrast against the

background. For regular, core-dominated clusters, they tend to be more concentrated in the core than other morphological types, and even in irregular clusters, they still trace the highest density regions.

A key advantage of the cluster red sequence method results from the relative ages of the stellar populations of the early-type and other galaxies. As discussed previously, the early-type galaxies can be successfully modelled by a simple stellar population formed at an early epoch ($z_f > 3$). In contrast, the spectra of other morphological types of galaxies show signs of recent or ongoing star-formation, and are dominated by relatively young stellar populations. An examination of Figure 3.2 shows that the addition of even small amounts of recent star-formation results in a large increase in flux at short wavelengths, causing the galaxy to appear bluer at optical wavelengths.

Figure 3.7 shows model colour-magnitude tracks, from $z = 0.1$ to $z = 1.0$, for galaxies of various spectral types (from Coleman et al., 1980), as well as the expected location of the cluster red sequence at the same redshift, using the evolutionary model of Kodama & Arimoto (1997). Since the early-type galaxies which make up the cluster red sequences are likely to represent the oldest stellar populations in the universe, they must be as red or redder than any other galaxies at a given redshift.

A particularly noticeable feature in the spectra of early-type galaxies is the strong break at 4000 \AA , emphasised by the absence of young blue stars. By selecting the filters to cover this break, the cluster red sequence is as red or redder than other galaxies at a given redshift, and all lower redshifts. This has huge consequences for the use of this method to identify high redshift clusters. As the cluster red sequence galaxies at high redshifts are redder than all nearer galaxies, it is possible to eradicate the problem of foreground contamination by removing those galaxies bluer than the cluster red sequence at a given redshift. As can be seen in Figure 3.7, the bulk of the contaminant galaxies to a cluster red sequence will then be intrinsically bluer galaxies at still higher redshifts. Moreover, since it is possible to remove foreground galaxies, projection effects due to two clusters at differing redshifts will be minimised, as the nearer cluster will have a bluer red sequence than the farther one, so the two can be separated.

The final motivation for using the cluster red sequence is that the colour of the

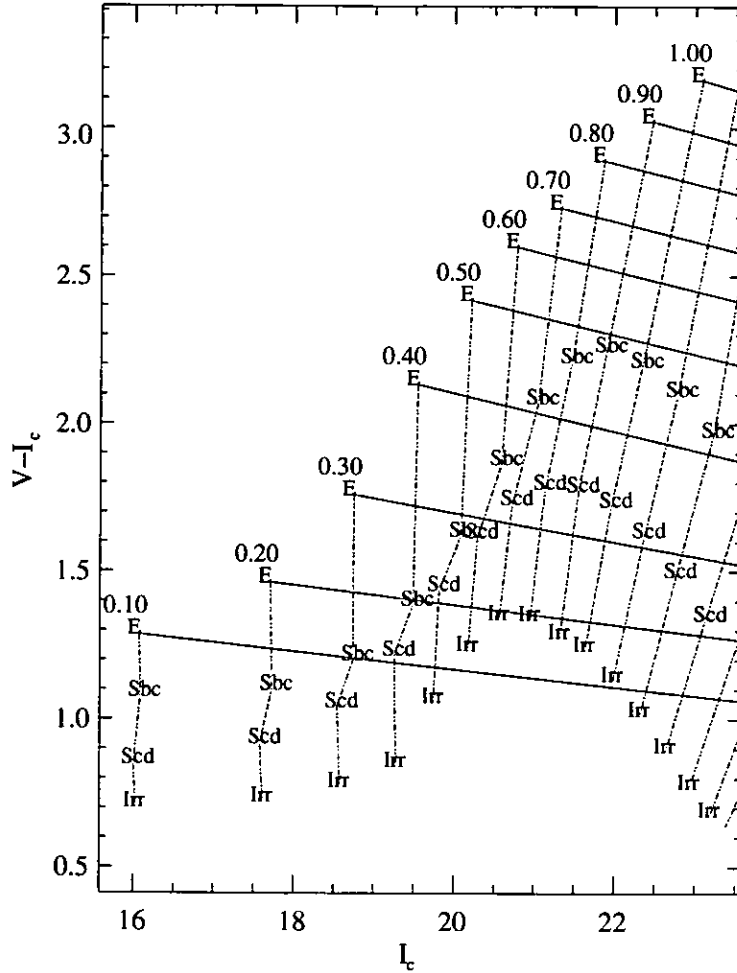


Figure 3.7: A simulated $V - I$ versus I colour-magnitude diagram. Model apparent magnitudes and colours for the differing galaxy morphologies at redshifts from 0.1 to 1.0 at a fixed absolute magnitude of $M_I = -22$ are shown. The blue dotted lines connect galaxies at the same redshift. The cluster red sequences are shown for redshifts from 0.1 to 1.0 in increments of 0.1 as near-horizontal red solid-lines. Adapted from figure in Gladders & Yee (2000).

observed cluster red sequence can be used as an extremely precise redshift indicator. This is due partly to the homogeneity of the red sequence galaxy population between clusters so that the red sequences of two clusters at the same redshift will have the same colour. Secondly, it is possible to determine the zero-points of the cluster red sequences to a high level of precision, due to the small intrinsic colour scatter of galaxies about the relation, and the reduction in photometric errors by averaging over many galaxies. By selecting filter bands carefully, so that the rate of increase of cluster red sequence colour with redshift is maximised, redshift estimates accurate to $\Delta z \simeq 0.02$ are possible, comparable to the best results attainable using other

methods in conjunction with photometry for four or more bands. Gladders & Yee (2000) reported a mean redshift error of $\Delta z = 0.026$ for 23 $z < 0.5$ clusters from the CNOc2 redshift survey when applying the cluster red sequence algorithm to V, I imaging data.

3.2.4 Basic Implementation of the Cluster Red Sequence method to Identify Clusters

The basic implementation of the cluster red sequence algorithm is to split the galaxy catalogue into a series of redshift *slices* by selecting the subset of galaxies whose colours and magnitudes are consistent with the colour-magnitude relation at that redshift. Effectively the galaxy catalogue is split into colour slices, centred on the colour-magnitude relation for a given redshift, and whose widths are equal to the width of the redshift slice, with allowances for the intrinsic colour scatter of cluster red sequence galaxies and photometric errors. For each slice the galaxy surface density is estimated using the adaptive kernel method discussed in the next section. Significant peaks in each redshift slice are then identified as cluster candidates at that redshift.

3.3 Cluster Analysis Methods

The finding of clusters, associations or patterns amongst a set of data points is one of the most important problems of analysis across all scientific disciplines, and has produced a vast array of methods. Many of these methods have been translated into a cosmological framework to address a particularly well discussed problem, the detection and analysis of clusters and subclusters amongst a catalogue of galaxy positions. The methods of cluster analysis can be broadly divided into two families: parametric methods, which search for clusters of some pre-determined form and which have been widely used in astronomy; and non-parametric methods, which use only the data points themselves and until recently have largely been neglected. The other main factor to consider when performing cluster analysis is the type of data produced by the galaxy survey: from purely two-dimensional (2D) imaging surveys using angular position only; to three-dimensional (3D) redshift surveys; and

in between multi-band imaging surveys with photometric redshift estimates based on galaxy colours and magnitudes ($2\frac{1}{2}D$).

3.3.1 Parametric Methods

The critical feature of parametric methods of cluster analysis is their dependence on the choice of parameters that define the properties of a hypothetical cluster. A typical example is the automated clusterfinding method of Kepner et al. (1999): the adaptive matched filter. This uses cluster luminosity and radial profiles to produce a filter which is convolved with the data to produce cluster probability maps. The cluster luminosity and radial profiles are allowed to vary with redshift so that a cluster redshift estimate can be made, and the magnitude of any peak found allows the cluster richness to be estimated. The advantage of using filters in cluster finding algorithms is that they maximise the signal of a cluster, and that quantitative information of the clusters detected, such as their richness, can be extracted in an objective manner over a large survey. A problem with using a parametric approach is that by making assumptions of cluster shape and luminosity function, the survey becomes biased towards such clusters, whereas clusters in reality do not conform to the parametric forms of the filter, but often have significant substructure or asymmetry, and the luminosity function and galaxy type fractions vary greatly from cluster to cluster, particularly at high redshifts. Hence parametric approaches are most suited to large surveys containing a statistically significant number of clusters, where such asymmetries are averaged out. Another problem is the author dependency of the analyses due to their choice of parameters, meaning that different authors may obtain results that disagree significantly, despite using the same set of data because their parameters were chosen differently.

3.3.2 A non-parametric approach to cluster analysis

Some of the problems of parametric methods, can be addressed by using a method which, as far as possible, avoids making any assumptions about the structures, taking as its input, only the data points themselves.

In this section a non-parametric method for cluster analysis is described, that

minimises the number of assumptions used, and gives an objective estimate of the clustering of a data sample. The method, proposed by Pisani (1993) for the univariate case, and then extended to analyse multivariate data by Pisani (1996), is based on estimating the probability density function underlying the data sample, and the assumption that the maxima of this probability density function indicates the presence of a cluster. The cluster analysis thus has two stages: the first is the estimation of the probability density function underlying the data; and the second is the cluster (i.e. maxima) identification and analysis.

3.3.3 Estimating the probability density function

The estimation of the probability density function, $F(\mathbf{r})$, for a data set D is a well-known problem in statistics, and there exist a variety of methods for tackling it (see Silverman, 1986, for detailed discussion). Here we consider only the adaptive kernel estimator, which is widely considered to be the best behaved method for a general set of data, and which also requires no assumption about the true probability density. It is an extension of the fixed kernel estimator, in which each data point is smoothed by a kernel of fixed width (usually a Gaussian), and which is analogous to the simple counts-in-cells method, a commonly used statistical tool in astronomy.

At this point it is worth noting the distance and separation formulae for points with angular positions $r_1 = (\alpha_1, \delta_1)$ and $r_2 = (\alpha_2, \delta_2)$ for the 2-dimensional case, and with redshifts z_1 and z_2 for the 3-dimensional case.

The angular separation θ of two points on a sphere is given by

$$\cos \theta = \sin \delta_1 \sin \delta_2 + \cos \delta_1 \cos \delta_2 \cos(\alpha_2 - \alpha_1). \quad (3.1)$$

The proper distance to a source at redshift z for an $\Omega_\Lambda = 0$ universe is (Mattig, 1958)

$$s = \frac{2c}{H_0} \frac{\Omega_M z + (\Omega_M - 2)[\sqrt{1 + \Omega_M z} - 1]}{\Omega_M^2(1 + z)}, \quad (3.2)$$

and the proper separation of two points $|r_1 - r_2|$ is found using the cosine rule

$$|r_1 - r_2| = (s_1^2 + s_2^2 - 2s_1s_2 \cos \theta)^{1/2}. \quad (3.3)$$

The adaptive kernel can also be applied to $2\frac{1}{2}$ -dimensional data, where photometric redshift estimates exist, through the use of redshift slices (see e.g. Yee, 1998)

which, by considering those galaxies likely to lie at a specific redshift, increases the signal of any clustering, and gives an approximate cluster redshift. For example, the photometric redshift estimator HYPERZ produces redshift probability distributions which could be used as weighting factors allowing a series of slices at various redshifts to be produced.

Now consider a data-set D_N of N points in a d -dimensional space, with position vectors $\mathbf{r}_i \in \mathfrak{R}^d (i = 1, \dots, N)$, weighting factors ω_i , and which has a true underlying probability density function $F(\mathbf{r})$ which we wish to estimate.

In the adaptive kernel estimator, the i th point is mapped by a kernel of width σ_i , and the adaptive kernel density estimate $f_{ak}(\mathbf{r})$ is given by

$$f_{ak}(\mathbf{r}) = \frac{1}{\sum_{i=1}^N \omega_i} \sum_{i=1}^N K(\mathbf{r}_i, \sigma_i; \mathbf{r}) \omega_i, \quad (3.4)$$

where $K(\mathbf{r}_i, \sigma_i; \mathbf{r})$ is the kernel function of the i th data point at the position vector \mathbf{r} . The choice of kernel function is not unique for a given $\mathbf{r}_i, \sigma_i, \mathbf{r}$, but the requirement that $f_{ak}(\mathbf{r})$ is a good estimator of $F(\mathbf{r})$ produces a number of conditions for the kernel function, namely:

- $K(\mathbf{r}_i, \sigma_i; \mathbf{r})$ is non-negative and real;
- it is bounded;
- it is absolutely integrable in \mathfrak{R} ;
- and it is normalised so that $\int_{\mathfrak{R}} K(\mathbf{r}_i, \sigma_i; \mathbf{r}) d\mathbf{r} = 1$.

All these conditions are satisfied by the standard Gaussian kernel,

$$K(\mathbf{r}_i, \sigma_i; \mathbf{r}) = \frac{1}{(\sqrt{2\pi}\sigma_i)^d} \exp\left(-\frac{1}{2} \frac{|\mathbf{r}_i - \mathbf{r}|^2}{\sigma_i^2}\right). \quad (3.5)$$

This is the kernel function adopted for this analysis, although there are alternative functions such as the Epanechnikov kernel which performs marginally better in estimating $F(\mathbf{r})$ (Silverman, 1986), and for the 2-dimensional case is given below

$$K(\mathbf{r}) = \begin{cases} 2/9\pi (3 - |\mathbf{r}_i - \mathbf{r}|^2/\sigma_i^2) & \text{if } |\mathbf{r}_i - \mathbf{r}| \leq \sqrt{3}\sigma_i \\ 0 & \text{otherwise.} \end{cases} \quad (3.6)$$

However the Epanechnikov kernel is not differentiable over all of its domain, a property which is critical in the peak finding process as will be seen later.

The crucial aspect of estimating $F(\mathbf{r})$ is not the precise shape of the kernel function, rather the choice of σ_i . Too small a value will tend to over-model the noise of the data rather than $F(\mathbf{r})$, while too large a value will over-smooth $F(\mathbf{r})$, hiding its true features. In typical data-sets there are high-density regions where narrow kernels are required so that the detail of the clustering pattern is not smoothed out, but also low-density regions where more smoothing is required. This dependence of local density on the optimal amount of smoothing required is the aspect which fixed-width kernels cannot model, and hence the desire for adaptive kernels is clear.

The estimate of the kernel widths σ_i is done through a two-step procedure:

- In the first step a pilot estimate, $f_p(\mathbf{r})$, of the probability density function, $F(\mathbf{r})$, is made in which the kernel widths, σ_i , are fixed at σ . Parzen (1962) has shown that there exists a method to obtain an asymptotically optimal estimate of the kernel size σ that works by minimising the integrated square error of the fixed-width kernel density estimate, $f_k(\mathbf{r})$

$$ISE(f_k) = \int_{\mathbb{R}} [F(\mathbf{r}) - f_k(\mathbf{r})]^2 d\mathbf{r} = \int_{\mathbb{R}} F^2(\mathbf{r}) d\mathbf{r} + \int_{\mathbb{R}} f_k^2(\mathbf{r}) d\mathbf{r} - 2 \int_{\mathbb{R}} F(\mathbf{r}) f_k(\mathbf{r}) d\mathbf{r} \quad (3.7)$$

Since the first term does not depend on the fixed-width kernel density estimate $f_k(\mathbf{r})$, it is possible to show Silverman (1986) that the minimisation of $ISE(f_k)$ is equivalent to the minimisation of the cross-validation $M(f_k)$ defined by

$$M(f_k) = \int_{\mathbb{R}} f_k^2(\mathbf{r}) d\mathbf{r} - 2 \int_{\mathbb{R}} F(\mathbf{r}) f_k(\mathbf{r}) d\mathbf{r}. \quad (3.8)$$

It is possible to show that, under mild assumptions (see Pisani, 1993, and references therein), $M(f_k)$ can be expressed as a function of the sample data positions \mathbf{r}_i and kernel widths σ_i , which for a Gaussian kernel is given by

$$M(f_k) = \frac{1}{(\sum_{i=1}^N \omega_i)^2} \sum_{i=1}^N \sum_{j=1}^N \frac{\omega_i \omega_j}{[2\pi(\sigma_i^2 + \sigma_j^2)]^{d/2}} \exp\left(-\frac{1}{2} \frac{|\mathbf{r}_i - \mathbf{r}_j|^2}{\sigma_i^2 + \sigma_j^2}\right) - \frac{2}{\sum_{i=1}^N \sum_{j \neq i} \omega_i \omega_j} \sum_{i=1}^N \sum_{j \neq i} \frac{\omega_i \omega_j}{(\sqrt{2\pi}\sigma_j)^d} \exp\left(-\frac{1}{2} \frac{|\mathbf{r}_i - \mathbf{r}_j|^2}{\sigma_j^2}\right). \quad (3.9)$$

Thus by calculating $M(f_k)$ and iteratively varying σ until the minimum of $M(f_k)$ is reached the optimal value of σ for the fixed-kernel estimator $f_k(\mathbf{r})$ can be obtained.

- Having obtained a fixed-kernel estimate of the probability density function $f_k(\mathbf{r})$, we use this to adapt the kernel widths σ_i to suit the local density $f_k(\mathbf{r}_i)$ so that high-density regions have narrower kernels than low-density regions. This is achieved by setting $\sigma_i = \sigma \lambda_i$ where λ_i is a ‘local bandwidth factor’ defined as

$$\lambda_i = \left[\frac{f_k(\mathbf{r}_i)}{g} \right]^{-0.5}, \log g = \frac{1}{\sum_{i=1}^N \omega_i} \sum_{i=1}^N \omega_i \log[f_k(\mathbf{r}_i)], \quad (3.10)$$

where g is the geometric mean of the local densities $f_k(\mathbf{r}_i)$. Thus the adaptive kernel estimate of the probability density function is given by

$$f_{ak}(\mathbf{r}) = \frac{1}{\sum_{i=1}^N \omega_i} \sum_{i=1}^N K(\mathbf{r}_i, \lambda_i \sigma; \mathbf{r}) \omega_i. \quad (3.11)$$

- It is then possible to iteratively recalculate the adaptive kernel estimator by re-optimising the value of σ using the cross-validation method with $\sigma_i = \sigma \lambda_i$ and producing a new pilot estimate with adaptive kernels rather than fixed kernels, which can then be used to recalculate the λ_i and so on. The effect of successive iterations on the λ_i generally become negligible after 10–20 iterations.
- Although the value of σ may be the optimal choice in the purely mathematical sense, because it is dependent on the distribution of data points, its value will change from one set to another. However it soon became clear that it was desirable to have control over this value, so that the amount of smoothing could be kept constant for two different sets of data, or so that the value of σ could be maintained at a fixed value, for example so that for two sets of points in different redshift slices, the proper angular distance corresponding to σ could be maintained at a constant level. As a result it was decided to make σ a free parameter which could be chosen by the user, rather than being determined by the cross-validation method, although the λ_i values are still estimated in an iterative manner.

3.3.4 Cluster Identification and Analysis

Having produced the adaptive kernel estimator of the probability density function, clusters are identified using the assumption that they correspond to local maxima

in the density distribution. The local maxima are found by solving for each of the data points ($i = 1, N$) the iterative equation

$$\mathbf{r}_{m+1,i} = \mathbf{r}_{m,i} + \frac{d}{\sum_{i=1}^N [\nabla f_{ak}(\mathbf{r}_i)/f_{ak}(\mathbf{r}_i)]^2} \frac{\nabla f_{ak}(\mathbf{r}_{m,i})}{f_{ak}(\mathbf{r}_{m,i})}, \quad (3.12)$$

where $\mathbf{r}_{1,i} = \mathbf{r}_i$ is the original position of the i th galaxy. This equation defines a path from each galaxy to a limiting point along the maximum gradient of the function $f_{ak}(\mathbf{r})$. The limiting point $\mathbf{r}_{\infty,i} = \lim_{m \rightarrow \infty} \mathbf{r}_{m,i}$ is taken to be the location of the cluster. Although this may be a mathematically rigorous approach it is also computationally intensive, and so instead $f_{ak}(\mathbf{r})$ was stored as an array of discrete values, and the local maxima identified as points in the array with values of $f_{ak}(\mathbf{r})$ greater than or equal to those of all of their neighbouring points. Each galaxy was then identified with a local maxima, by starting at the point corresponding to the galaxy location, and iteratively moving to the neighbouring point with the highest value of f_{ak} until a local maxima is reached.

The cluster C_μ can then be defined as the set of all the members i_μ of D_N whose limiting points $\mathbf{r}_{\infty,i_\mu}$ correspond to the same local maxima in $f_{ak}(\mathbf{r})$ and containing $n_\mu > 1$ points:

$$C_\mu = \{\mathbf{r}_i : \mathbf{r}_{\infty,i_\mu} \simeq \mathbf{r}_{\infty,\mu}; n_\mu > 1\} \quad (3.13)$$

with $i = 1, \dots, N$ and $\mu = 1, \dots, \nu$ where ν is the number of clusters present within D_N .

The set of local maxima that are associated with only single data points form the population of isolated points C_0 . Thus all points in D_N are members of one of the clusters C_μ or are isolated points. However, some points which lie in the tails of clusters and so are initially classified as cluster members, are actually more likely to be isolated or background points. These are known as *interlopers*, and the processes described below have to be repeated: the first pass identifies the interlopers and the second pass recalculates the cluster membership probabilities having reassigned the interlopers to the group of isolated points C_0 .

The contribution to the local density $f_{ak}(\mathbf{r})$ due to the μ th cluster is the sum of the kernels of its member galaxies i_μ , hence

$$F_\mu(\mathbf{r}) = \frac{1}{\sum_{i=1}^N \omega_i} \sum_{i_\mu} K(\mathbf{r}_i, \lambda_i \sigma; \mathbf{r}) \omega_i. \quad (3.14)$$

The contribution of background or isolated points to the local density is initially estimated (i.e. on the first pass) through

$$F_0(\mathbf{r}) = \frac{1}{N} K(\mathbf{r}, \sigma_0; \mathbf{r}), \quad (3.15)$$

where σ_0 is the average width of the kernels associated with isolated or background data points, or is set so that $F_0(\mathbf{r})$ equals the known value of the background contribution.

Having located the clusters from the density peaks, it is possible to consider their member galaxies on an individual basis through the relative contributions of the background and cluster local densities at the galaxy position. The probability that a given point is isolated, and hence due to the background component, can then be defined as

$$P(i \in 0) = \frac{F_0(\mathbf{r}_i)}{f_{ak}(\mathbf{r}_i)}. \quad (3.16)$$

In the first pass, the interlopers are assigned to one of the ν clusters, and so the total density estimate $f_{ak}(\mathbf{r})$ has not accounted for the background contribution. Hence, for the first pass, the probability that a point is a member of the μ th cluster is the fractional contribution of the cluster to the local density, after considering the background contribution

$$P(i \in \mu) = \{1 - P(i \in 0)\} \frac{F_\mu(\mathbf{r}_i)}{f_{ak}(\mathbf{r}_i)}. \quad (3.17)$$

The interlopers for each cluster $\mu = 1, \dots, \nu$ can now be identified as the members which satisfy

$$P(i_\mu \in 0) \geq P(i_\mu \in \mu). \quad (3.18)$$

Each of the interlopers is now reassigned to the group of isolated points, C_0 , so all points are now assigned to their most likely group, either the group of isolated points or one of the clusters.

The background density $F_0(\mathbf{r})$ can now be estimated as the sum of the kernels for the members i_0 of the group C_0

$$F_0(\mathbf{r}) = \frac{1}{\sum_{i=1}^N \omega_i} \sum_{i \in C_0} K(\mathbf{r}_i, \lambda_i \sigma; \mathbf{r}) \omega_i, \quad (3.19)$$

and the contribution to the local density $f_{ak}(\mathbf{r})$ due to the μ th cluster can be recalculated using equation 3.14 but not counting the kernels of the points defined as interlopers.

All the density in $f_{ak}(\mathbf{r})$ has now been accounted for in the background and clusters, as each kernel is counted once, so that

$$f_{ak}(\mathbf{r}) = F_0(\mathbf{r}) + \sum_{\mu=1}^{\nu} F_{\mu}(\mathbf{r}). \quad (3.20)$$

Hence the cluster membership probabilities $P(i \in \mu)$ can easily be calculated as the fractional contribution of $F_{\mu}(\mathbf{r}_i)$ to the local density

$$P(i \in \mu) = \frac{F_{\mu}(\mathbf{r}_i)}{f_{ak}(\mathbf{r}_i)}. \quad (3.21)$$

For each member $i_{\mu} \in C_{\mu}$, the estimates $P(i_{\mu} \in 0)$ and $P(i_{\mu} \in \lambda)$, with $\lambda = 1, \dots, \nu$ can be made, and then used to obtain detailed information about the cluster and its membership. The probable number of galaxies in each cluster, n_{μ} , for example is given by

$$n_{\mu} = \sum_{i=1}^N P(i \in \mu). \quad (3.22)$$

We can consider a cluster to be compact and well defined if for a large fraction of its members i_{μ} the probability that they belong to it, $P(i_{\mu} \in \mu)$, is greater than 0.90.

It is possible to determine the statistical significance S_{μ} of the μ th cluster, by measuring the effect of the presence of the μ th cluster in increasing the local density, and hence the sample likelihood L_N , over that which one would have if the members of the μ th cluster were all isolated and hence belonging to the background component, as described by L_{μ} where

$$L_N = \prod_i \left[\sum_{\mu=0}^{\nu} F_{\mu}(\mathbf{r}_i) \right], \quad (3.23)$$

$$L_{\mu} = \prod_i \left[f_{ak}(\mathbf{r}_i) - F_{\mu}(\mathbf{r}_i) + \frac{1}{\sum_{i=1}^N \omega_i} \sum_{j \in i_{\mu}} K(\mathbf{r}_j, \sigma_0; \mathbf{r}_j) \omega_j \right], \quad (3.24)$$

$$S_{\mu} = -2 \ln \left(\frac{L_{\mu}}{L_N} \right). \quad (3.25)$$

The cluster significance S_{μ} is distributed as chi-squared with one degree of freedom, and so the values of S_{μ} for the μ th group to be significant at the 5%, 1%, and 0.1% levels are 3.8, 6.6 and 11.0 respectively. However care must be made in interpreting these results, as they are affected by the choice of background level.

It is also interesting to examine the overlap or contact between clusters. A cluster μ can be said to be in contact with a second cluster $\lambda (\neq \mu)$ if there is at least one

member of the μ th cluster that could have been classified as being a member of the λ th cluster, or

$$P(i_\mu \in \lambda) \geq P(i_\mu \in 0) \text{ for some } i_\mu \in C_\mu. \quad (3.26)$$

Two clusters which are close together may share several members, so that there is significant overlap. The amount of overlap or contact can be measured by

$$\mathcal{L}(\mu, \lambda) = \sum_{i_\mu \in C_\mu} P(i_\mu \in \lambda) \omega_{i_\mu} + \sum_{i_\lambda \in C_\lambda} P(i_\lambda \in \mu) \omega_{i_\lambda}. \quad (3.27)$$

If significant overlap between two or more clusters is observed, the possibility that a single elongated cluster has been misidentified as a multimodal structure should be investigated. The theorem of Fukunaga (1972) proves that the optimal kernel shape for a unimodal structure is the same as that of the structure, i.e. the optimal kernel shape for investigating an elongated structure is also elongated along the same major axis. As a result a circular or spherical kernel is not the optimal kernel shape for an elongated cluster, and so may misidentify it as a multimodal system.

In the case of contact between two or more clusters, where there is a possibility of misidentification, a second analysis using the optimally shaped kernels will clarify the situation.

To determine the locally optimal kernel, for the two clusters μ and λ , calculate the covariance matrix \mathbf{A} , which for example in the 2-dimensional Cartesian coordinate system (x, y) is

$$\mathbf{A} = \begin{pmatrix} \text{var}(X) & \text{cov}(XY) \\ \text{cov}(XY) & \text{var}(Y) \end{pmatrix}, \quad (3.28)$$

in which the variances and covariances are calculated after weighting each data point by the probability that it is a member of one of the two clusters, $P(i \in \mu) + P(i \in \lambda)$.

The eigenvectors of this matrix are parallel to the major axes of the best-fitting ellipsoid for the structure, and the eigenvalues correspond to the axes lengths squared. The area of this ellipsoid is equal to $\pi(\det \mathbf{A})^{1/2}$, and so to be the optimal kernel this has to be normalised for each point to equal $\pi\sigma_i^2$, i.e. the area of the Gaussian kernel of width σ_i . The locally optimal kernel is then given by

$$K_{opt}(\mathbf{r}_i, \sigma_i; \mathbf{r}) = \frac{1}{(\sqrt{2\pi}\sigma_i)^d} \exp \left[-\frac{1}{2} \frac{(\mathbf{r} - \mathbf{r}_i)^T \mathbf{A}^{-1} (\mathbf{r} - \mathbf{r}_i)}{(\det \mathbf{A})^{1/2} \sigma_i^2} \right]. \quad (3.29)$$

If after smoothing the data with the locally optimal kernels the cluster system remains multimodal, then it may be that one of the clusters included in the sub-catalogue is spurious and has biased the estimate of the locally optimal kernel, but if this is not the case then the system must be a set of separate, although close, clusters. Otherwise if the system is unimodal the final density estimate can be found by using the locally optimal kernels for the members of the merged system, and the original radially-symmetric kernels for the non-merged and the points not included in the sub-catalogue

$$f_{ak-opt}(\mathbf{r}) = \frac{1}{\sum_{i=1}^N \omega_i} \sum_{i=1}^N \frac{\omega_i}{(\sqrt{2\pi}\sigma_i)^d} \exp \left[-\frac{1}{2} \frac{(\mathbf{r} - \mathbf{r}_i)^T \mathbf{A}_i^{-1} (\mathbf{r} - \mathbf{r}_i)}{(\det \mathbf{A}_i)^{1/2} \sigma_i^2} \right] \quad (3.30)$$

where \mathbf{A}_i is set to the covariance matrix \mathbf{A} for the members of the merged system, and \mathbf{A}_i is set to the identity matrix \mathbf{I} for the remaining points.

The use of non-radially symmetric kernels is equivalent to the approach suggested by Fukunaga (1972) of firstly ‘pre-whitening’ the data by linearly transforming them to have unit covariance matrix, next smoothing using a radially symmetric kernel, and finally transforming back. Hence the process of using non-radially symmetric kernels is termed ‘whitening’.

3.3.5 Estimating the Significance of Substructure

The previous analyses give a qualitative feel for whether substructure is real, but some method of obtaining a quantitative significance level is desirable. The question that needs to be answered is ‘*What is the probability of the null hypothesis that the galaxies belonging to the substructures are drawn instead from a single cluster?*’ One method for examining the null hypothesis is the likelihood ratio test statistic (LRTS) (Ashman et al., 1994; Kriessler & Beers, 1997) which evaluates the improvement in fitting the data of a two-component model over a single elliptical Gaussian probability density function.

Consider again the data-set D_N to which the adaptive kernel estimator has been applied from which the clusters A and B have been identified, and we wish to determine the probability that the galaxies in the two clusters are drawn from a unimodal distribution. The best-fitting single- and double-elliptical Gaussian probability density functions are determined using the means and covariance matrices of the data

points weighted by their cluster membership probabilities $P(i \in A)$ and $P(i \in B)$.

The centres of the one- and two-component Gaussians for example are given by

$$\bar{\mathbf{r}}_{(2A)} = \frac{1}{n_A} \sum_{i=1}^N P(i \in A) \mathbf{r}_i \quad (3.31)$$

$$\bar{\mathbf{r}}_{(2B)} = \frac{1}{n_B} \sum_{i=1}^N P(i \in B) \mathbf{r}_i \quad (3.32)$$

$$\bar{\mathbf{r}}_{(1)} = \frac{1}{n_A + n_B} \sum_{i=1}^N \{P(i \in A) + P(i \in B)\} \mathbf{r}_i. \quad (3.33)$$

The best-fit one- and two-component models, $f_{(1)}$, and $f_{(2)}$, are thus given by

$$f_{(1)}(\mathbf{r}) = \frac{(n_A + n_B)(\det \mathbf{A}_{(1)})^{-1/2}}{(2\pi)^{d/2}} \exp \left[-\frac{1}{2}(\mathbf{r} - \bar{\mathbf{r}}_{(1)})^T \mathbf{A}_{(1)}^{-1}(\mathbf{r} - \bar{\mathbf{r}}_{(1)}) \right] \quad (3.34)$$

$$f_{(2)}(\mathbf{r}) = \frac{n_A(\det \mathbf{A}_{(2A)})^{-1/2}}{(2\pi)^{d/2}} \exp \left[-\frac{1}{2}(\mathbf{r} - \bar{\mathbf{r}}_{(2A)})^T \mathbf{A}_{(2A)}^{-1}(\mathbf{r} - \bar{\mathbf{r}}_{(2A)}) \right] \quad (3.35)$$

$$+ \frac{n_B(\det \mathbf{A}_{(2B)})^{-1/2}}{(2\pi)^{d/2}} \exp \left[-\frac{1}{2}(\mathbf{r} - \bar{\mathbf{r}}_{(2B)})^T \mathbf{A}_{(2B)}^{-1}(\mathbf{r} - \bar{\mathbf{r}}_{(2B)}) \right] \quad (3.36)$$

The measure of the fits by the one- and two-component models are evaluated through the log-likelihood values

$$\ln L_C(1) = \sum_{i=1}^N \{P(i \in A) + P(i \in B)\} f_{(1)}(\mathbf{r}_i) \quad (3.37)$$

$$\ln L_C(2) = \sum_{i=1}^N \{P(i \in A) + P(i \in B)\} f_{(2)}(\mathbf{r}_i), \quad (3.38)$$

and the improvement in going from a single to a double elliptical Gaussian fit is then evaluated by the LRTS

$$\lambda = -2 \ln \left(\frac{L_C(2)}{L_C(1)} \right). \quad (3.39)$$

Except for the simple univariate case where comparison with the chi-squared distribution will suffice, the only way to reliably assess the statistical significance of a particular value of the LRTS is a bootstrap estimation. This is achieved by generating bootstrap catalogues under the null hypothesis that the data points assigned to clusters A and B are drawn from the best-fitting single-elliptical Gaussian probability density function with mean $\bar{\mathbf{r}}_{(1)}$ and covariance matrix $\mathbf{A}_{(1)}$. Each bootstrap catalogue thus contains N data points, made up of those points from the original catalogue not assigned to clusters A and B, and the remainder drawn from the null hypothesis distribution. The applied kernel estimator is applied to each bootstrap

sample, and for those catalogues in which bimodality is again observed, a value of λ is obtained. The value of λ from the actual data can then be compared to the null distribution of λ values calculated from the bootstrap samples to find the level of significance, by considering the probability that a null sample produces a larger value of λ (i.e. a more significant substructure) than the actual data. Conventionally, a probability less than 5% indicates that the null hypothesis is strongly inconsistent with the data, whereas probabilities between 5% and 10% indicates marginal inconsistency.

The terms and methods described in this section will become clearer when applied to actual data in the remainder of the thesis.

3.4 Applying the Cluster Red Sequence Method to the BTC Images

In the previous sections the scientific justification for the use of the cluster red sequence method to finding galaxy clusters using imaging data was discussed, as well as its basic implementation, before going into the theory of the adaptive kernel estimator of the galaxy surface density. In this section the details of their application to finding galaxy clusters in the BTC images, both at low and high redshifts, are described.

3.4.1 Definition of the Redshift Slices

The first step is to determine the expected photometric behaviour of the red sequence as a function of redshift. For this, the Kodama & Arimoto (1997) evolutionary model is used as discussed earlier, with the the metallicity sequence calibrated to the Coma cluster, and the formation epoch set to $z_f = 4.5$, i.e. the best fitting model to the data of Kodama et al. (1998).

It was decided to divide the data into photometric redshift slices of width $\Delta z = 0.025$ from $z = 0.05$ to $z = 0.6$. At these redshifts, an increase in redshift of 0.025 corresponds to an increase in the $V - I$ C-M relation colour of $\simeq 0.05$, comparable to the intrinsic scatter of the relation and the typical photometric errors. This

results in colour slices of width $\Delta(V - I) \simeq 0.1$, and means that each galaxy would be in two slices on average. The upper redshift limit of $z = 0.6$ was necessary, as beyond this, the efficiency of the C-M relation algorithm at determining accurate redshifts decreases, due to the choice of filters, and the increased photometric errors as the galaxies become fainter and redder. Instead, a single high redshift slice is considered for all galaxies redder than the $z = 0.5$ C-M relation, the results of which will be discussed later. Another redshift slice is considered for all clusters nearer than $z = 0.05$, by considering all galaxies bluer than the $z = 0.05$ C-M relation.

For each redshift slice, bounding red sequences were determined so that the width of the slice in the colour-magnitude plane included both the intrinsic scatter of the C-M relation, and the photometric errors. For the redshift slice centred on a redshift z , the upper and lower bounding red sequences were given by

$$[V - I]_+(I) = [V - I](z, I) + \left(\Delta[V - I](V - I, I)^2 + \Delta RS^2\right)^{1/2} \quad (3.40)$$

$$[V - I]_-(I) = [V - I](z, I) - \left(\Delta[V - I](V - I, I)^2 + \Delta RS^2\right)^{1/2}, \quad (3.41)$$

where $[V - I](z, I)$ is the colour of the red sequence at a given redshift and magnitude, $\Delta[V - I](V - I, I)$ is the photometric colour error of galaxies at a given colour and magnitude, and δRS is the intrinsic colour scatter seen in cluster red sequences. A value of $\Delta RS = 0.075$ is used here (Gladders & Yee, 2000; Stanford et al., 1998).

A faint magnitude limit is also applied to each redshift slice, an absolute magnitude limit of $M_V = -17$, or $I = 23.5$, whichever is brightest. A faint absolute limit is applied as red sequence galaxies are intrinsically more luminous than $M_V = -17$, and so beyond this level only noise is being added. The limit of $I = 23.5$ is applied as the red sequence galaxies at this magnitude limit are only just detected in the V image, and so the resultant photometric errors become much larger than the width of the redshift slices. Figure 3.8 is a colour-magnitude diagram that shows the positions of the red sequences for each redshift slice, with each galaxy plotted as a point whose colour indicates the redshift slice to which it has been assigned, if any.

3.4.2 Estimating the Galaxy Surface Density

Having determined the upper and lower bounding C-M relations, and set a faint magnitude limit for each redshift slice, subsets of the galaxy catalogue satisfying

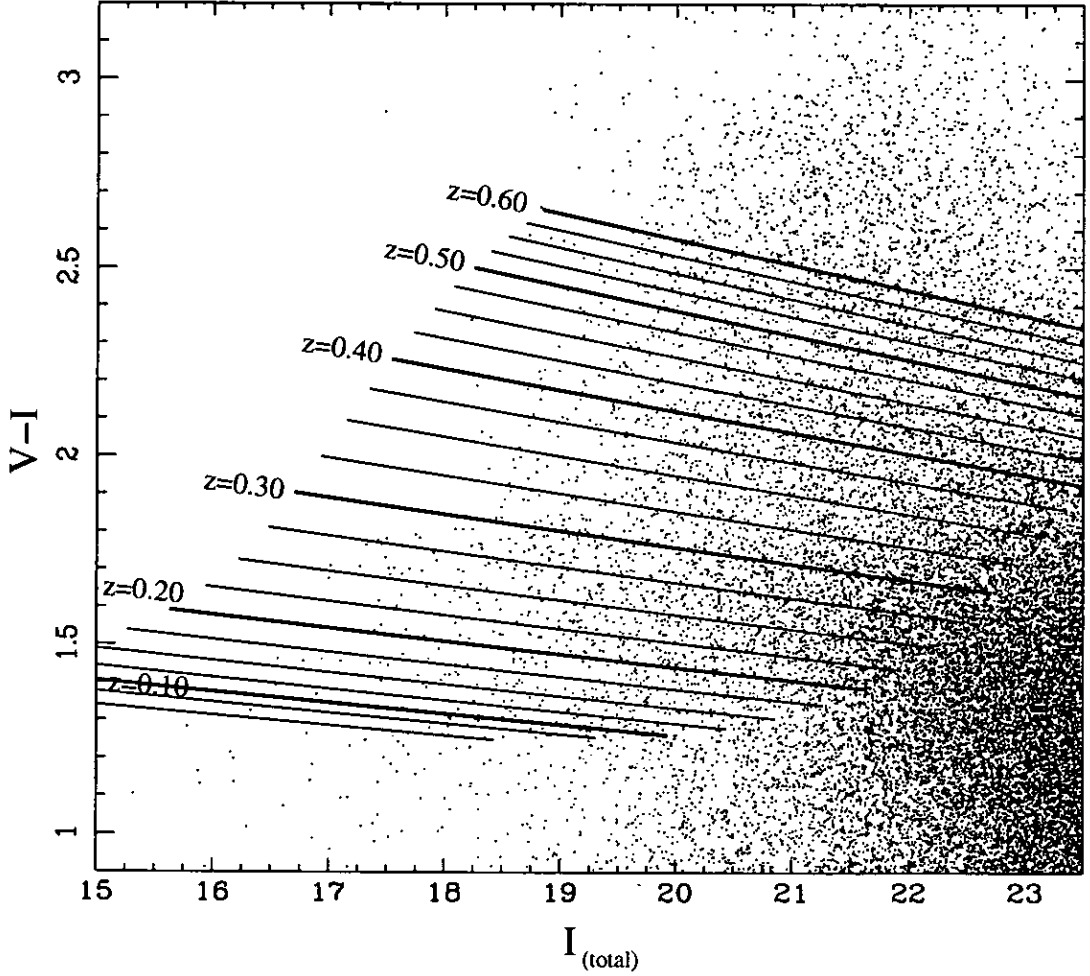


Figure 3.8: Colour-magnitude diagram showing the positions and contents of the redshift slices. Each cluster red sequence from $z = 0.05$ to $z = 0.60$ in increments of $\Delta z = 0.025$ is shown as a near-horizontal red line whose endpoints are defined as $M_V = -23$ and $M_V = -17$ at the sequence redshift. Each galaxy from the BTC image is plotted as a point whose colour indicates the redshift slices (if any) the galaxy has been assigned to. Note that although many galaxies are assigned to two or more redshift slices, due to the way in which the points are plotted, the colour corresponds to the lowest redshift slice to which the galaxy is assigned. Black points indicate that the galaxy is not assigned to any redshift slice due to failing the $M_V < -17$ absolute magnitude selection criterion. The blue points at the bottom of the diagram are those assigned to the $z < 0.05$ redshift slice, and the red points at the top of the diagram are those assigned to the high redshift slice, being redder than the $z = 0.50$ cluster red sequence.

the selection criteria are created for each slice.

To estimate the galaxy surface density for each redshift slice, the adaptive kernel estimator is applied. As discussed earlier, instead of determining the optimal kernel width, σ , through the cross-validation method, it was decided to set this manually, to a constant proper angular scale of $0.35 h^{-1}\text{Mpc}$ (for an $\Omega_M = 0.3$, $\Omega_\lambda = 0.7$ universe). This is similar to values used by other authors (Gladders & Yee, 2000, use $0.33 h^{-1}\text{Mpc}$), and appears close to optimal for all redshift slices. Note that in terms of an observed angular size, this results in a much greater smoothing for lower redshift slices than for higher redshift slices.

The density maps for each redshift slice, $f_{ak}(\mathbf{r}, z)$ must be transformed to a single standard measure (such as σ of detection), before comparing one slice with another, or combining the slices into a three-dimensional density map. This is necessary because the meaning of a given density value changes between the slices, due to the change in mean density, and the apparent size of the kernel, from one redshift slice to another. The natural approach is to consider the significance of a given density level by estimating the background galaxy density and standard deviation for each slice. These values can in principle be easily extracted from the $f_{ak}(\mathbf{r}, z)$, but the possible effect of any clusters should be considered first. The presence of a galaxy cluster in a redshift slice is likely to affect the σ of the $f_{ak}(\mathbf{r})$ through the resulting region of high density values. However, as the clusters will occupy only a small fraction of the total surface area of any map, it is possible to effectively remove them from the statistics by excluding some fraction of the highest valued regions (and lowest to preserve symmetry) from the map. Hence the background galaxy density level and standard deviation are taken to be the mode and standard deviation of $f_{ak}(\mathbf{r})$, after excluding the 5% highest and lowest density values from the statistics.

The resultant normalised redshift slices are shown in Figures 3.9–3.12. In each image regions with galaxy densities 1.5σ below background level or lower are indicated by black colours, and regions with galaxy densities greater than 10σ above the background level indicated by white colours.

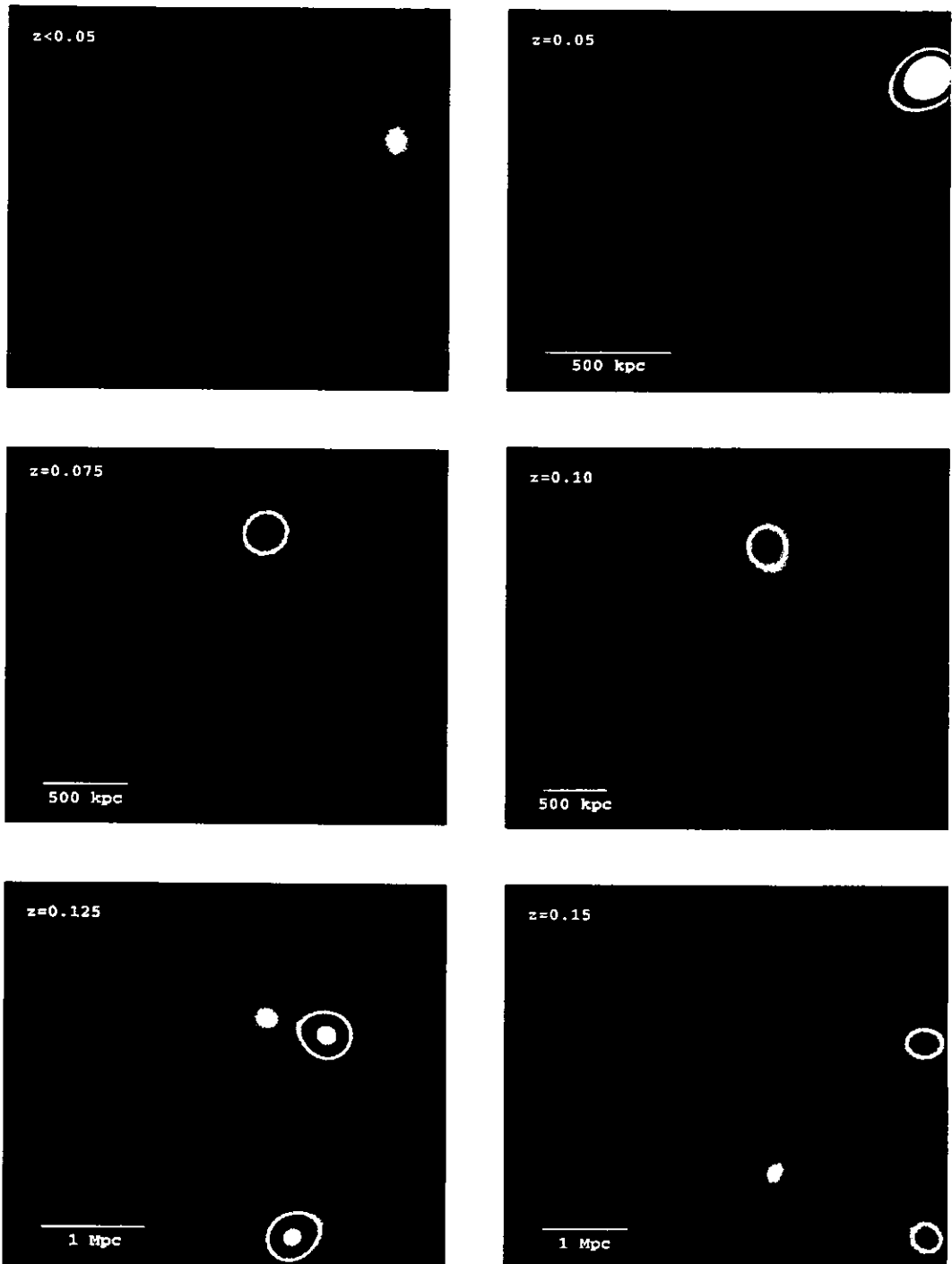


Figure 3.9: The galaxy surface densities of the lowest six redshift slices ($0 < z \leq 0.15$) from the BTC images. The lowest density regions are indicated by blue and black colours, whilst the highest density regions are indicated by red and white colours. A physical angular distance of $500 h^{-1} \text{kpc}$ at the central redshift is indicated for each map. A cluster at $z \simeq 0.05$ is apparent as a significant high-density region in the top-right corner of the $z = 0.05$ redshift slice.

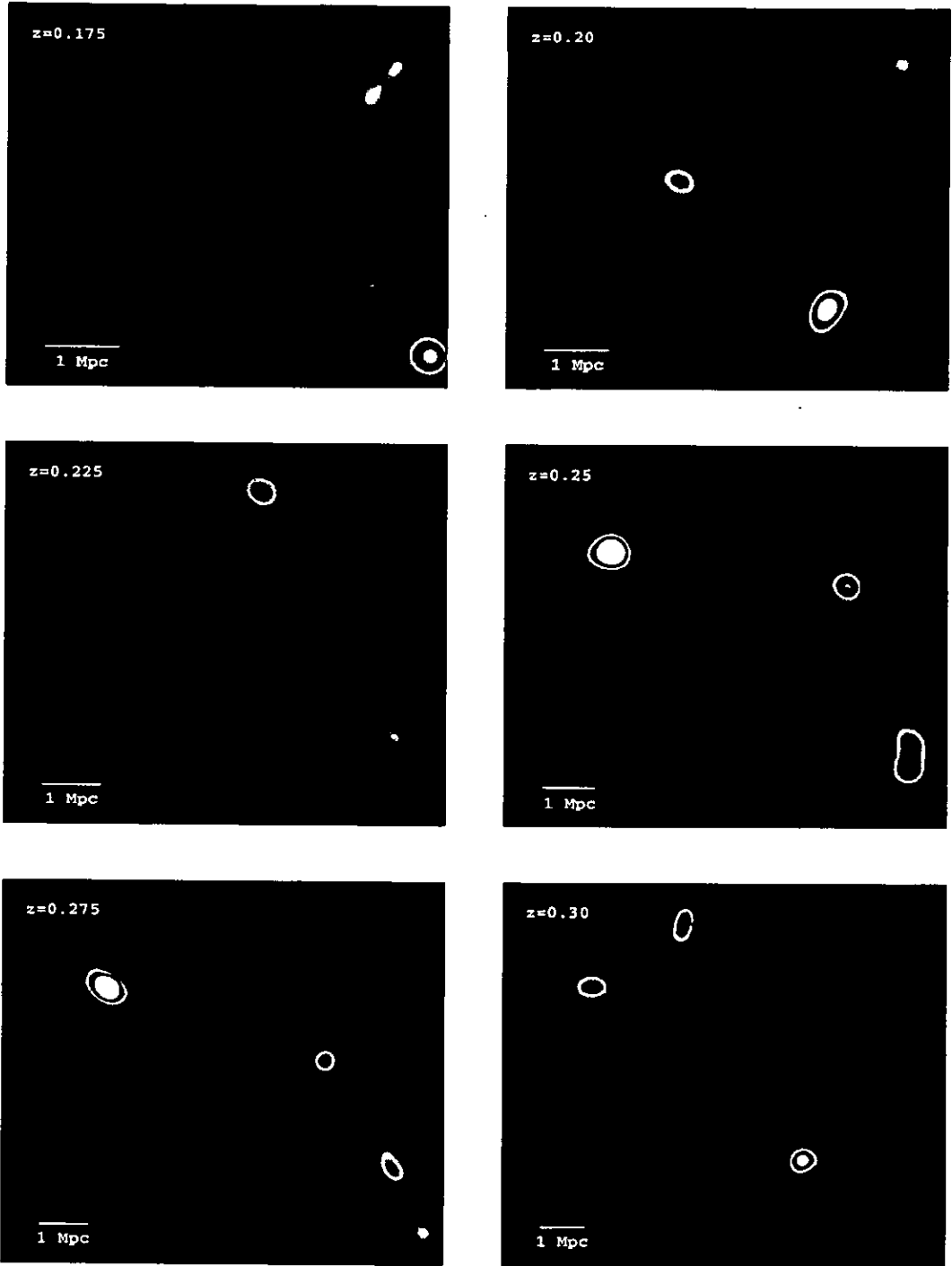


Figure 3.10: The galaxy surface densities of the next six redshift slices ($0.15 < z \leq 0.30$) from the BTC images. The lowest density regions are indicated by blue and black colours, whilst the highest density regions are indicated by red and white colours. A physical angular distance of $1 h^{-1} \text{Mpc}$ at the central redshift is indicated for each map. A cluster at $z \simeq 0.25$ is apparent as the coincident high-density regions in the top-left corners of each of the $z = 0.25$, $z = 0.275$ and $z = 0.30$ slices.

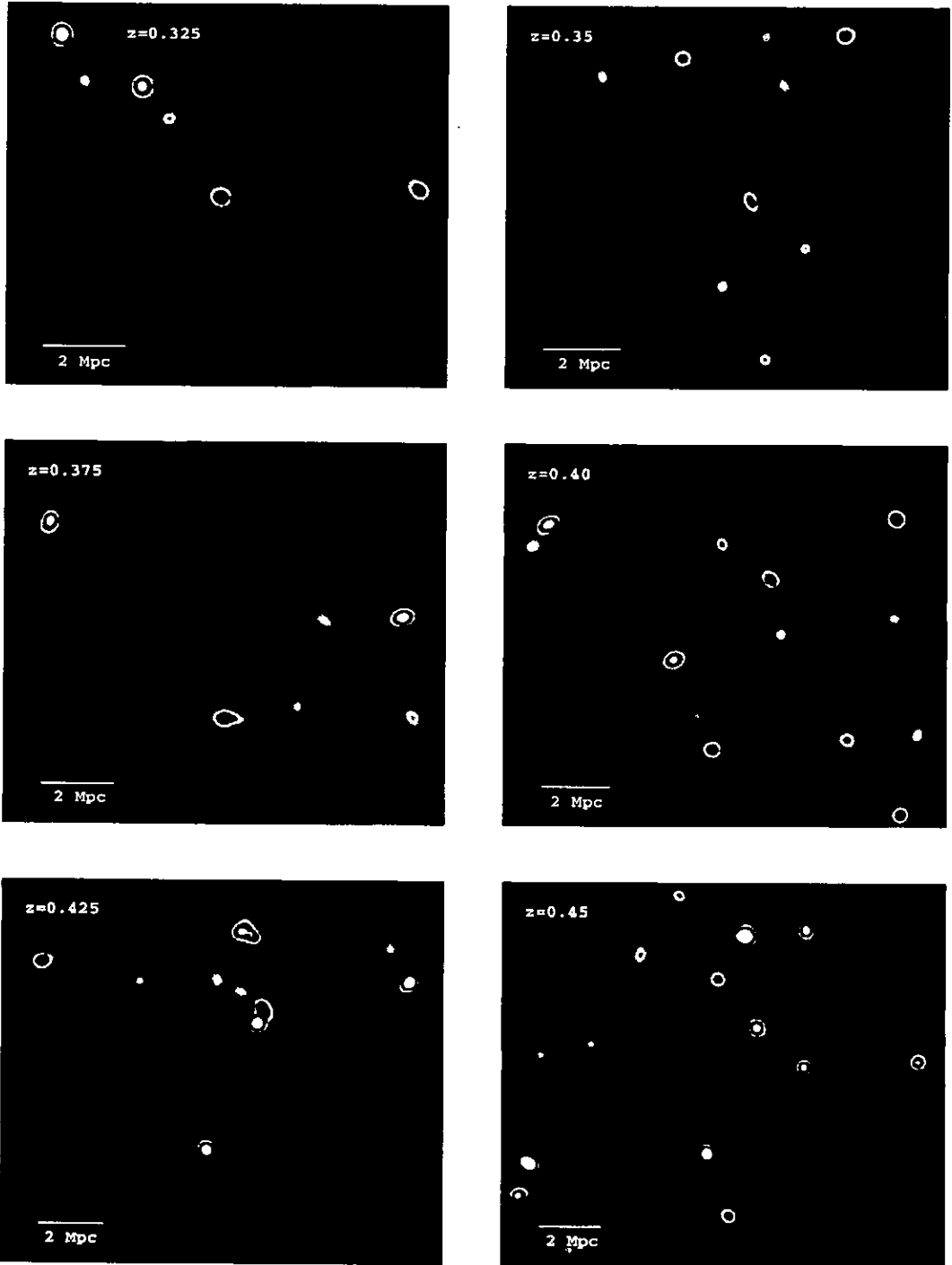


Figure 3.11: The galaxy surface densities of six intermediate-redshift slices ($0.30 < z \leq 0.45$) from the BTC images. The lowest density regions are indicated by blue and black colours, whilst the highest density regions are indicated by red and white colours. A physical angular distance of $2 h^{-1} \text{Mpc}$ at the central redshift is indicated for each map.

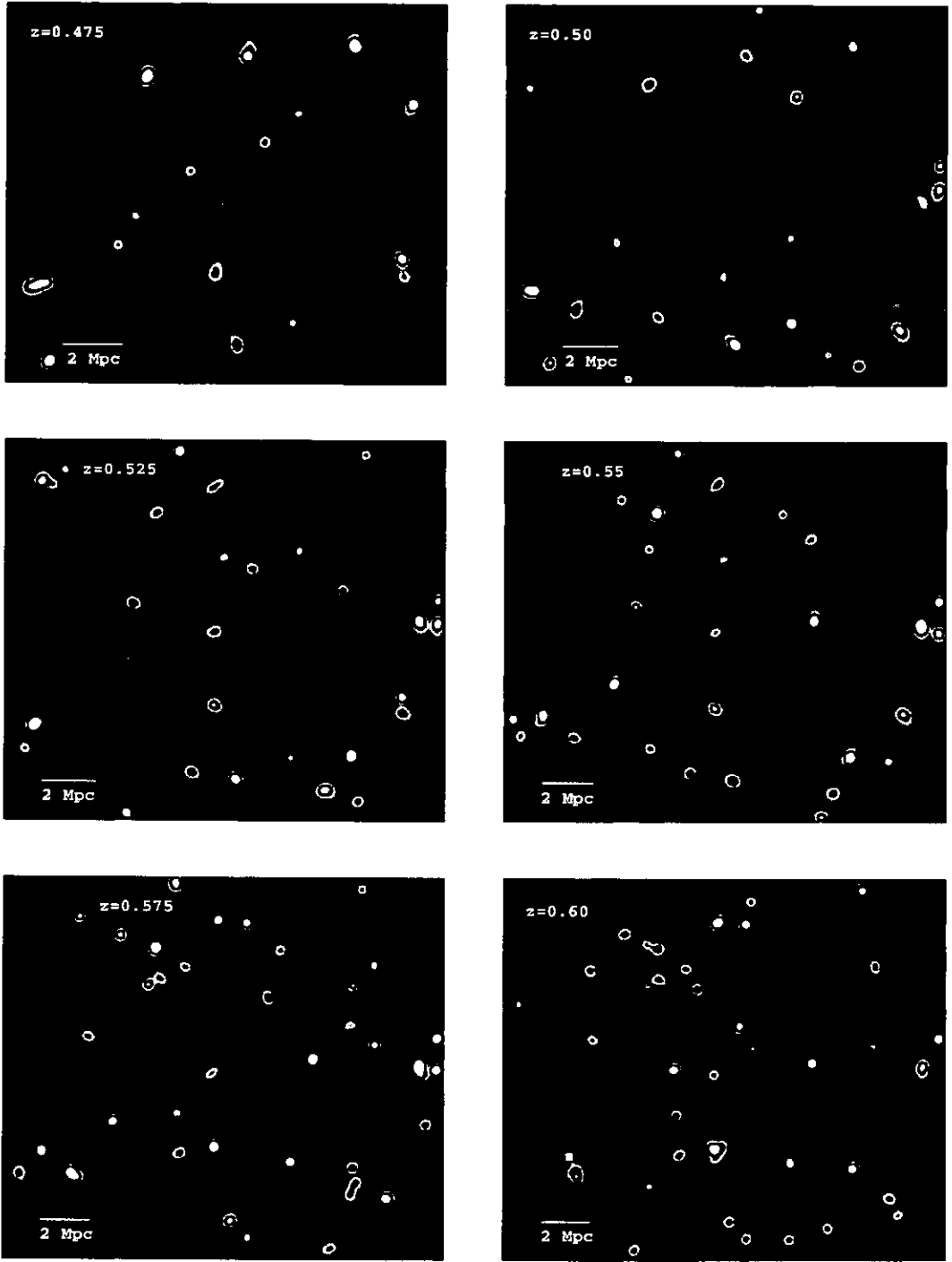


Figure 3.12: The galaxy surface densities of the highest six redshift slices ($0.45 < z \leq 0.60$) from the BTC images. The lowest density regions are indicated by blue and black colours, whilst the highest density regions are indicated by red and white colours. A physical angular distance of $2 h^{-1} \text{Mpc}$ at the central redshift is indicated for each map.

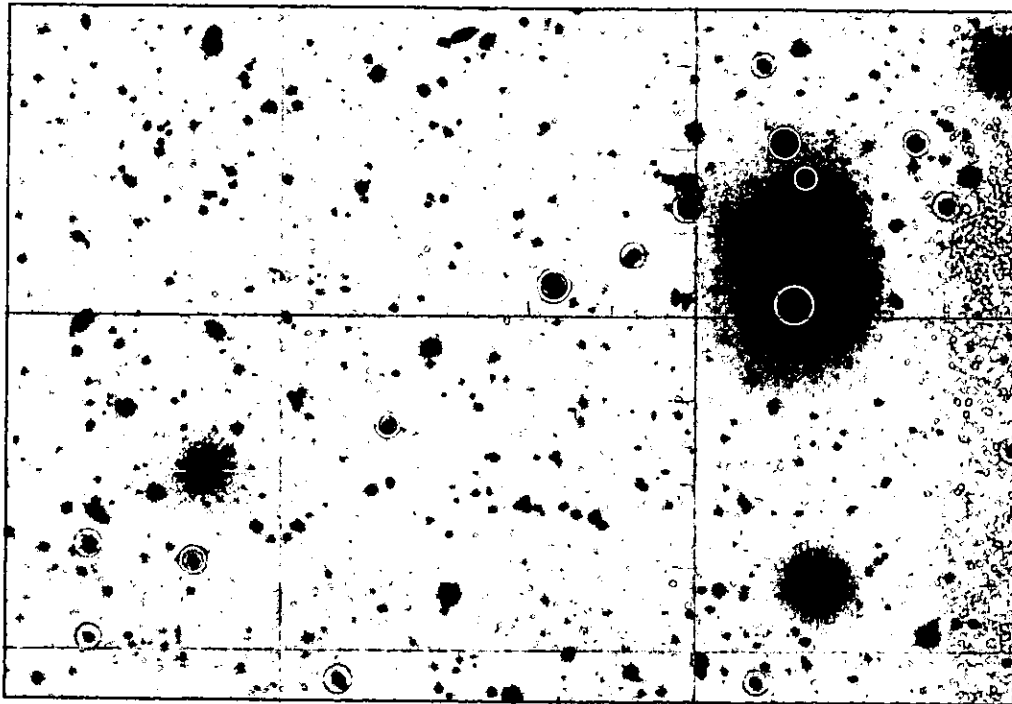


Figure 3.13: *I*-band image of a 6.1×4.2 arcmin² region containing the galaxy clustering apparent in the $z = 0.05$ redshift slice of Figure 3.9. Galaxies from the $z < 0.05$, $z = 0.05$, $z = 0.075$ and $z = 0.10$ redshift slices are indicated by green, yellow, orange and red circles respectively whose radii indicate their *I* magnitudes.

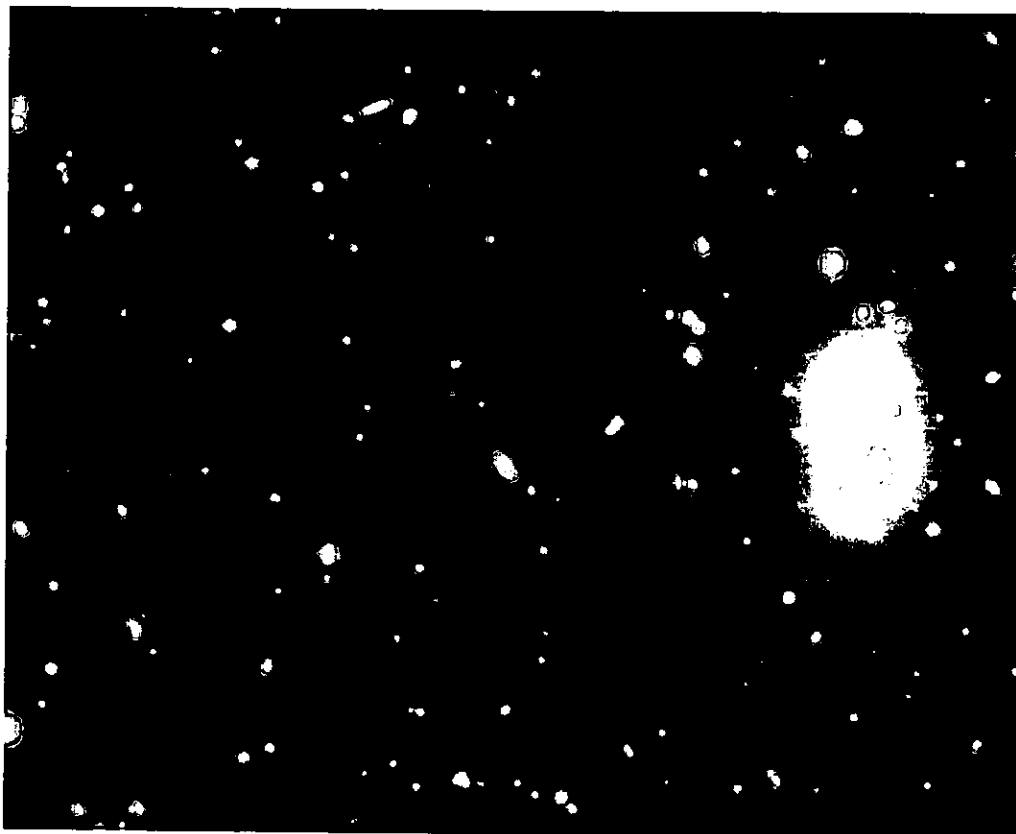


Figure 3.14: False colour image of the $z = 0.05$ cluster region.

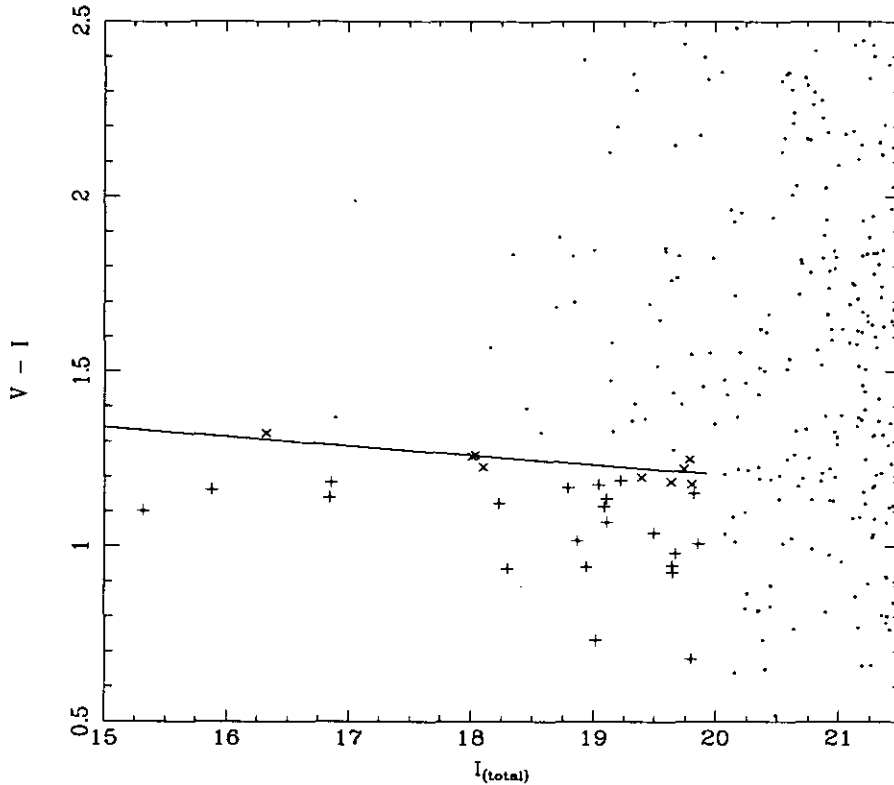


Figure 3.15: Colour-magnitude diagram of galaxies within $250h^{-1}\text{kpc}$ (at $z = 0.05$) of the central bright galaxy from the $z = 0.05$ cluster. Galaxies within the $z = 0.05$ and $z < 0.05$ redshift slices are indicated by \times and $+$ signs respectively. The Kodama & Arimoto (1997) model red sequence at $z = 0.05$ is indicated by a near-horizontal line.

3.5 Example Clusters from the Redshift Slices

As a demonstration of the validity of the cluster red-sequence method as applied to the BTC images, two example low-redshift clusters found by the method are presented here.

The most significant detection in the first six redshift slices ($0 < z \leq 0.15$) of Figure 3.9 is that apparent in the top-right corner of the $z = 0.05$ redshift slice. Figure 3.13 shows the I -band image of the cluster region with the galaxies from the $z < 0.05$, $z = 0.05$, $z = 0.075$ and $z = 0.10$ redshift slices indicated by green, yellow, orange and red circles respectively, and whose radii indicate their I magnitudes.

A poor, compact group is apparent, centred on a bright galaxy ($I = 15.32$ — $\alpha = 10^{\text{h}}48^{\text{m}}42.58^{\text{s}}$, $\delta = +5^{\circ}42^{\text{m}}29.3^{\text{s}}$), which is unfortunately close to a bright star. Figure 3.14 shows the false colour image of the same region. The red sequence

galaxies are apparent as bright white-coloured galaxies. Figure 3.15 is the colour-magnitude diagram of galaxies within $250h^{-1}\text{kpc}$ (at $z = 0.05$) of the bright central galaxy. Galaxies within the $z = 0.05$ and $z < 0.05$ redshift slices are indicated by \times and $+$ signs respectively. The Kodama & Arimoto model red sequence at $z = 0.05$ is indicated by a near-horizontal line. A red sequence is apparent, although the two brightest galaxies do not lie particularly close to it, probably due to the effect of the nearby bright star on the I -band photometry. Although the cluster appears relatively poor, and despite the effect of the bright star, a red sequence is apparent, and is clearly detected by the cluster red sequence method.

At higher redshifts, the most significant detection is that observed in the top-left of both the $z = 0.25$ and $z = 0.275$, and to a lesser extent the $z = 0.30$, redshift slices of Figure 3.10.

Figure 3.16 shows the $7.1 \times 4.5 \text{ arcmin}^2$ (corresponding to $1.5 \times 0.9 h^{-1}\text{Mpc}$ at $z = 0.25$) I -band image of the cluster region with the galaxies from the $z = 0.225$, $z = 0.250$, $z = 0.275$ and $z = 0.30$ redshift slices indicated by green, yellow, orange and red circles respectively, and whose radii indicate their I magnitudes.

A cluster, somewhat richer than that of the $z = 0.05$ slice, is apparent, centred on a compact clump of galaxies around what is presumably the brightest cluster galaxy. Figure 3.17 shows the false colour image of the same region, with the red sequence galaxies apparent as bright yellow-coloured galaxies. Figure 3.18 is the colour-magnitude diagram of galaxies within $500 h^{-1}\text{kpc}$ (at $z = 0.25$) of the bright central galaxy. Galaxies within the $z = 0.250$ and $z = 0.275$ redshift slices are indicated by \times and $+$ signs respectively. The best fitting red sequence from the Kodama & Arimoto (1997) evolutionary model is shown as a near-horizontal line, and corresponds to a redshift of $z = 0.263$. The red sequence is very clear with 65 galaxies from the two redshift slices within $500 h^{-1}\text{kpc}$ of the cluster centre, whereas elsewhere in the BTC image 19.73 galaxies would be expected for a same sized region. The intrinsic photometric scatter of the red sequence is small with $\Delta(V - I) = 0.045$, corresponding to an error in redshift of 0.013. Note that this is the best fitting *model* red sequence, and so the slope is constrained, and not fit by linear regression, only the C-M relation's zero-point is a free parameter. This cluster would be detected by a simple cluster finding algorithm, as an overdensity of

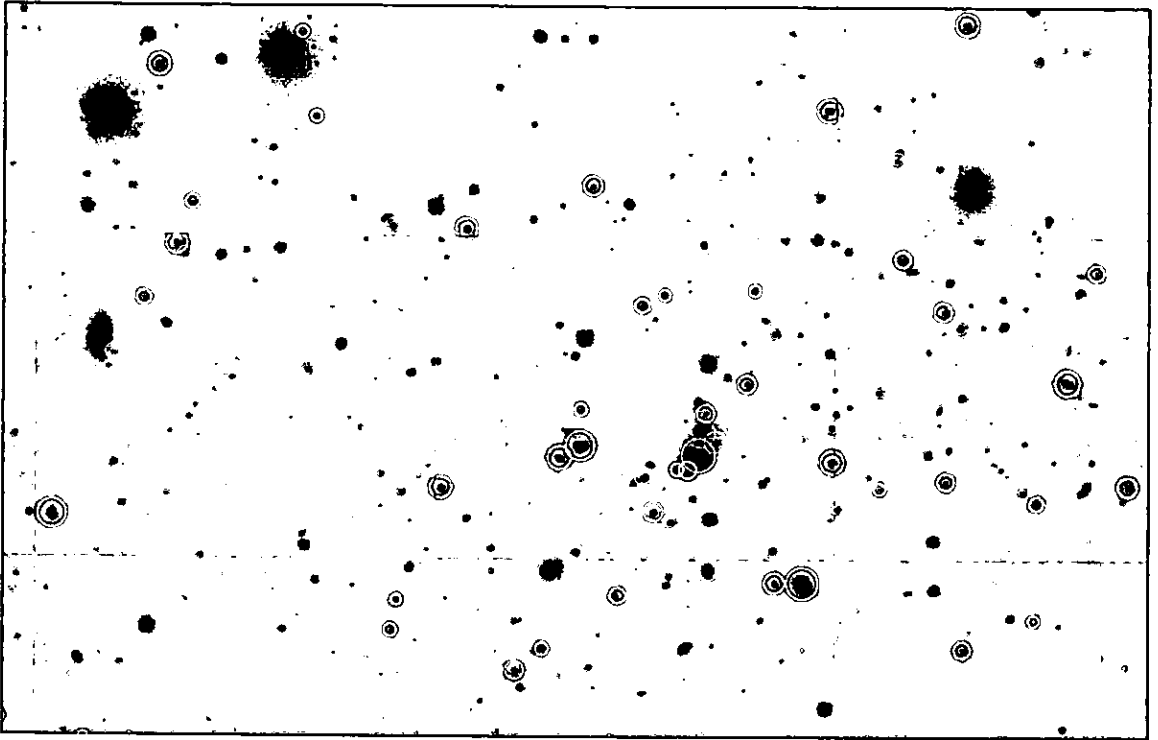


Figure 3.16: I -band image a 7.1×4.5 arcmin² region containing the galaxy clustering apparent in the $z = 0.25$ and $z = 0.275$ redshift slices of Fig. 3.10. Galaxies from the $z = 0.225$, $z = 0.250$, $z = 0.275$ and $z = 0.30$ redshift slices are indicated by green, yellow, orange and red circles respectively whose radii indicate their I magnitudes.

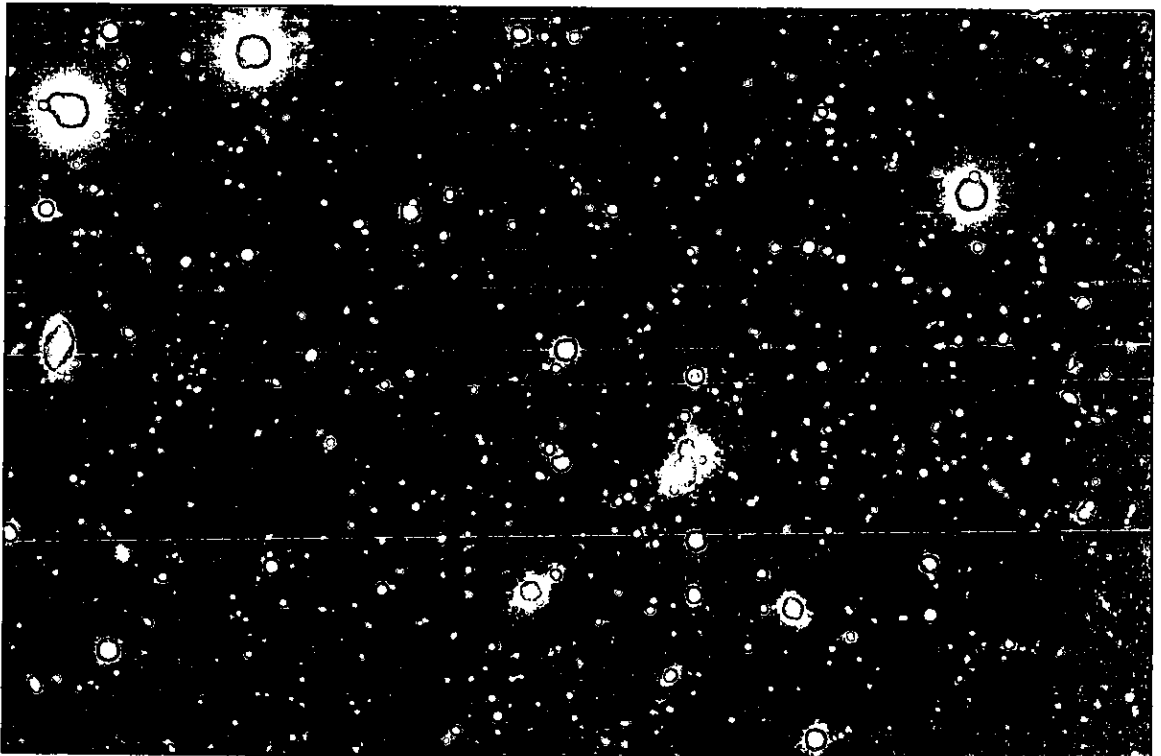


Figure 3.17: False colour image of the $z = 0.25$ cluster region.

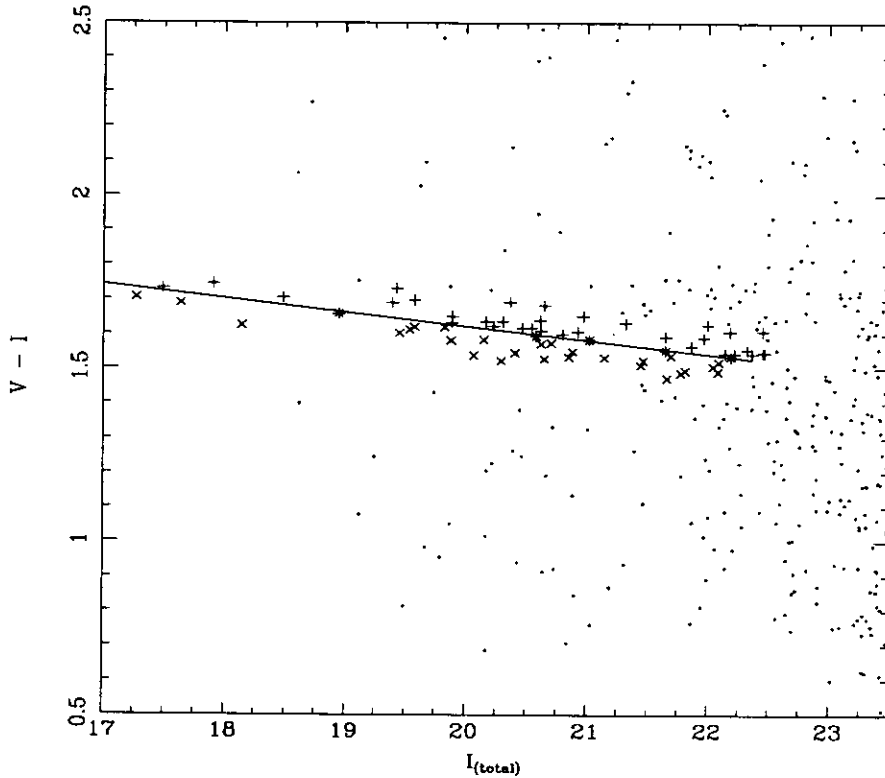


Figure 3.18: Colour-magnitude diagram of galaxies within $500h^{-1}\text{kpc}$ (at $z = 0.25$) of the central bright galaxy from the $z = 0.25$ cluster. Galaxies within the $z = 0.25$ and $z = 0.275$ redshift slices are indicated by \times and $+$ signs respectively. The best-fitting Kodama & Arimoto model red sequence, corresponding to $z = 0.263$, is indicated by a near-horizontal line.

bright I -band galaxies, 111 $I < 21$ galaxies are found within the $500h^{-1}\text{kpc}$ radius whereas, in 100 000 circular regions of the same radius taken at random from the BTC image, only 74.13 ± 15.09 are found, a 2.44σ excess.

These two examples demonstrate the validity of applying the cluster red sequence method to finding low-redshift clusters in the BTC images, and estimating their redshifts. Both examples would be detected using conventional approaches based on simple galaxy overdensities, but this method has the advantage of being able to estimate their redshifts in an accurate manner in theory, although given that no spectroscopic confirmation exists to date, this accuracy has yet to be tested. Finally, the detection of clear red sequences in the BTC image is not only a validation of the method, but also an internal consistency check of the photometry, as the average error in the measurement of the sources' $V - I$ colours must be less than the observed scatter in the red sequence.

3.6 Summary

One of the most important aspects of observational cosmology is the detection and characterisation of galaxy clustering, by providing important constraints for both cosmological models and galaxy evolution. Numerous algorithms have been developed to perform this procedure in both wide field imaging and redshift surveys.

In the case of the BTC images, where the information pertaining to each galaxy is limited to magnitude, position and one colour ($V - I$), the most appropriate choice of cluster detection algorithm is the Cluster Red Sequence method of Gladders & Yee (2000). This chapter describes this method, and the motivation behind using it for this type of imaging data. This is based on the fact that the bulk of early-type galaxies in all rich clusters, and at all observed redshifts, lie along a tight linear colour-magnitude relation, commonly referred to as the cluster red sequence. This red sequence appears homogeneous from cluster to cluster at the same redshift, and its colour evolves with redshift in a predictable manner, allowing an accurate cluster redshift estimate to be obtained, a feature which makes it much more powerful than other algorithms. By selecting only those galaxies which lie on the red sequence corresponding to a particular redshift it is possible to obtain a redshift *slice*. Candidate clusters in each redshift slice can then be identified as density peaks in the galaxy number density.

The Cluster Red Sequence method is then applied to the BTC images, producing redshift slices from $z = 0.05$ to $z = 0.6$. The use of the adaptive kernel method to estimate the surface density of galaxies in each redshift slice is described, and a number of candidate low redshift clusters are identified as density maxima in the slices. By considering the properties of two clusters found using this approach, the validity of applying the cluster red sequence method to finding clusters in the BTC images is demonstrated.

Chapter 4

The Identification of Galaxy Clustering Associated with the Clowes-Campusano Large Quasar Group.

4.1 Introduction

The main objective behind obtaining the ultra-deep BTC V and I images was to identify galaxy clustering associated with the Clowes-Campusano Large Quasar Group at $z \simeq 1.3$, and in particular, the three members of the group contained in the images. Although the Cluster Red Sequence method of Gladders & Yee (2000) is not ideally suited to identifying galaxy clustering at such high redshifts in the BTC images, the principles described in the previous chapter can be applied and the properties of the red sequences at high redshifts can be used to find evidence of any associated galaxy clustering.

In ideal circumstances near-infrared imaging would be used in conjunction with the optical images to allow the cluster red sequence to be followed accurately to such high redshifts. Such imaging would allow redshift estimates accurate to $\Delta z \lesssim 0.05$, sufficient to identify any clustering associated with the quasars, and would provide a definitive answer as to whether the group traces large scale structure, and provide insights into how the quasars trace the clustering. However, at present there are no

near-infrared cameras with fields comparable in size to the BTC; indeed they are an order of magnitude or more smaller in area, making a near-infrared survey of the whole field impossible at the present time.

This chapter describes the examination of galaxy clustering at high redshifts in the BTC field through the selection of galaxies redder than the colour expected of red sequence galaxies at $z = 0.5$. The properties of these optically-red galaxies can be examined through comparison with the EIS-DEEP HDF-South field. This covers 27 arcmin^2 and has $UBVRIJHK_s$ photometry which reaches comparable depths as the BTC field in the V and I bands, allowing the same selection of red galaxies to be made. The properties of these galaxies can then be examined in terms of number density to see if the BTC field has an overall excess as would be expected if it contains a high-redshift large-scale structure associated with the quasar group; and accurate photometric redshift estimates to confirm whether they are indeed high-redshift early-type galaxies.

4.2 High Redshift Galaxies in the BTC images

As discussed previously, the BTC images are not ideal for identifying high-redshift ($z > 0.5$) clusters using the cluster red sequence method. Firstly, the choice of filters means that beyond $z \approx 0.5$ the rate at which the cluster red sequence becomes redder with redshift slows markedly, thus reducing the accuracy of any redshift estimate. Secondly, at these high redshifts, the red sequence galaxies are approaching the detection limit in the V -band image, due to a combination of distance and red colour, and so the increased photometric errors will smooth out any red sequence in the colour direction and hence decrease its detectability.

However, the red sequence galaxies of any high-redshift clusters will remain amongst the optically-reddest galaxies, and the foreground contamination can be minimised by removing those galaxies bluer than the $z = 0.50$ cluster red sequence. One advantage of the increased distance to these clusters, in terms of their detectability, is that the angular size of the clustering will be reduced, resulting in a more compact and dense clump of galaxies and a higher contrast against the background. Hence by broadening the redshift slice, the ability to detect high-redshift

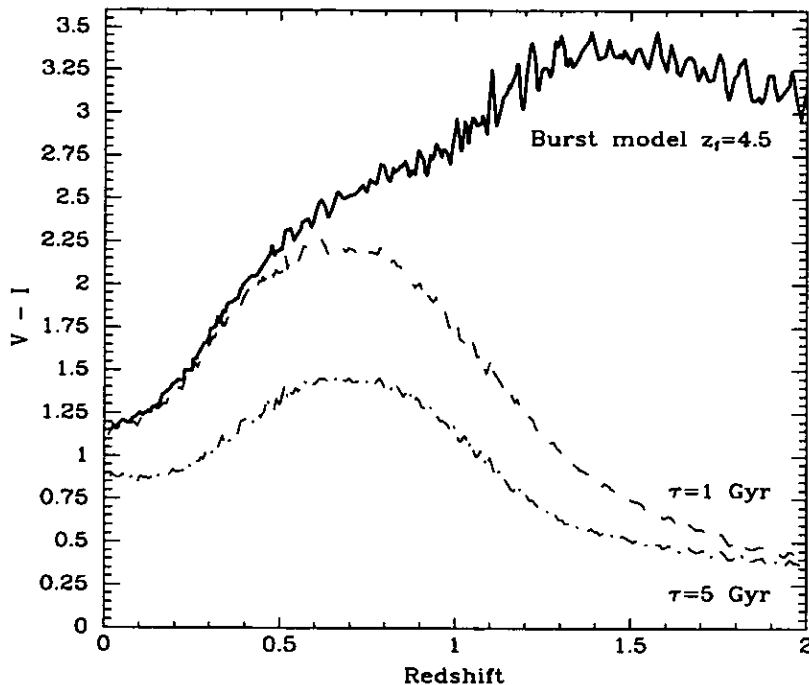


Figure 4.1: Evolution of galaxies' $V - I$ colours as a function of galaxy type and redshift. The solid red curve corresponds to a simple stellar population formed in an instantaneous burst at $z_f = 4.5$ (11 Gyr ago), and is thought to represent the colour evolution of massive ellipticals. The dashed green and dot-dashed blue curves correspond to stellar populations with exponentially-decaying star-formation rates with time-scales (τ) of 1 and 5 Gyr respectively, and are thought to represent the colour evolution of disk-dominated galaxies.

clustering is increased at the expense of accuracy in the redshift estimate.

Galaxies are selected to belong to the high-redshift slice if they are redder than the $z = 0.50$ cluster red sequence, and brighter than the $I = 23.5$ faint magnitude limit, resulting in the following selection criteria

$$V - I > 3.6891 - 0.06517 \times I_{total}, \quad (4.1)$$

$$I_{total} < 23.50 \quad (4.2)$$

$$\text{CLASS_STAR} < 0.95. \quad (4.3)$$

All galaxies passing the above selection criteria, and hence belonging to the high-redshift slice, will hereafter be described as *red galaxies*.

Figure 4.1 plots model galaxy $V - I$ colours as a function of galaxy type and redshift. The models are built using the Bruzual & Charlot evolutionary code (GISSEL98; Bruzual & Charlot, 1993) and assume solar metallicity, a Miller & Scalo

(1979) IMF and no internal reddening, and the galaxy ages for each model are calculated for a $H_0 = 75 \text{ km s}^{-1} \text{ Mpc}^{-1}$, $\Omega_M = 0.3$, $\Omega_\Lambda = 0.7$ universe. The solid red curve corresponds to a simple stellar population formed in an instantaneous burst at $z_f = 4.5$ (11 Gyr ago), and is thought to represent the colour evolution of massive ellipticals. The dashed green and dot-dashed blue curves correspond to stellar populations with exponentially-decaying star-formation rates with time-scales (τ) of 1 and 5 Gyr respectively, and are thought to represent the colour evolution of disk-dominated galaxies.

All galaxies classed as belonging to the high-redshift slice have $V - I > 2.1576$. It is clear from Figure 4.1 that the selection of galaxies with $V - I > 2.1576$ is an efficient means of identifying early-type galaxies at $z \gtrsim 0.5$ as, neither galaxies at $z \lesssim 0.5$ of any star-formation history, or late-type galaxies (as represented by the dashed green and dot-dashed blue curves) at any redshift, can be sufficiently red without the effect of internal extinction.

In total 2616 sources detected in both the V and I images satisfy the above criteria and are classed as red galaxies. However when examining these sources in the I -band image it is apparent that a significant fraction ($\sim 10\%$) are false detections, making it necessary to inspect each source visually and removing the spurious detections by hand. The bulk of these contaminant sources are due to either the wide wings of heavily saturated stars' point spread functions boosting the I -band flux of faint sources, or random noise events near the field edges. Given that the faint magnitude limit of $I = 23.5$ is considerably brighter than the detection threshold of the BTC I -band images, it is relatively easy to distinguish between real and spurious sources for the vast majority of cases. After visually inspecting each source on two separate occasions, 263 sources were deemed spurious and discarded, leaving 2359 real detections of galaxies classed as belonging to the high-redshift slice. The process of classifying sources as real or spurious on the basis of a visual inspection is inevitably subjective, and hence there must be a certain amount of uncertainty about the final figure. However, given the relative ease of distinguishing the two classes of sources, the level of uncertainty is only likely to be about 10% of the number of sources discounted or ~ 25 , i.e. $\sim 1\%$ of the total of real sources.

As well as those sources detected in both V and I images, there is a considerable

number of sources which are detected in the I image only and which are brighter than the faint magnitude limit of $I = 23.5$. Given that the V -band source catalogue is 90% complete to $V = 25.8$, 2.3 magnitudes fainter, any source brighter than the faint magnitude limit in I , but not detected in V is almost certainly sufficiently red to be classified as belonging to the high-redshift slice. In total 3278 sources are brighter than $I = 23.5$, but remain undetected in the V -band image. Of course, the most likely cause of a source not being detected in V -band image is that it is due to random noise or the result of a defect in the I -band image, and indeed the vast majority of these sources are spurious. The bulk of these contaminant sources is due to heavily saturated stars in the I -band image, with the sources found either in the wide wings of the stars' point spread functions, or along the diffraction or saturation spikes. They are then easily identified by position. Other spurious sources are due to defects in the image from cosmic rays or satellite trails (only in the regions covered by 1–3 exposures), or are the result of random noise fluctuations. After visually inspecting each source on two separate occasions, 658 sources were classified as being red galaxies. Again this process is by its nature subjective, which results in an uncertainty in the final figure of around 10%.

In total 3017 sources in the 1417.98 arcmin^2 region covered by both V and I BTC images are classified as galaxies redder than the $z = 0.5$ cluster red sequence, and hence can be described as *red* galaxies. This corresponds to a mean galaxy number density of 2.13 galaxies per arcmin^2 . The uncertainty in this figure due to the process of classifying sources as real or spurious is $\simeq 0.05$, and so even a conservative classification, in which only sources that are certainly real are considered, will not result in a figure significantly lower than that obtained.

The most significant source of contamination of the red galaxies is likely to be from red point-sources, presumably red dwarfs. Even though the star-galaxy classifier has been shown to work reasonably efficiently to $I \simeq 22$ (Figure 2.16), due to the relatively poor seeing levels in which the images were obtained (the last exposures of each night in particular), some stellar sources are likely to be misclassified as galaxies, especially near the faint magnitude limit. Indeed the most extreme red sources, with $V - I > 3$, are likely to be red dwarfs. The reddest that a galaxy can be at any given redshift, without resorting to internal dust extinction,

can be modelled by a solar-metallicity, simple stellar population formed at very early epochs ($z_f \simeq 4.5$). The $V - I$ colour evolution of such a stellar population is shown as the thick red curve on Figure 4.1, and it can be seen that this model galaxy population never becomes redder than $V - I \simeq 3.3$ at any redshift. In contrast, stars at the very low-mass end of the main sequence ($M_* \lesssim 0.10 M_\odot$) can have colours considerably redder than ($V - I = 3$). Evolutionary models predict that a 5 Gyr old, solar-metallicity red dwarf will have a $V - I$ colour of 3.27 at a mass of $0.10 M_\odot$, reaching $V - I = 4.55$ at the hydrogen-burning mass limit of $0.08 M_\odot$ (Baraffe et al., 1998). There is evidence for contamination by these very low-mass red dwarfs in the sources classed as high-redshift galaxies in the form of a population of ~ 75 extremely red sources with $V - I > 3$, and stellarities close to the level at which sources would be classed as stars ($0.80 \lesssim \text{CLASS_STAR} < 0.95$).

Having ascertained that a contamination of red dwarfs is likely, the problem now is to estimate the level of this contamination, given that there are no spectral data which could verify how well the stellarity index is classifying stars and galaxies at these magnitude levels. Two approaches are considered: one is to consider all sources belonging to the high-redshift slice with ambiguous stellarity classifications to be contaminant red dwarfs; and another is to assume that the most extreme red sources with $V - I > 3.2$ are all contaminant sources, and extrapolate to bluer colours using the colour distribution of sources classified as stars based on their stellarity index.

In Figure 2.16 stellarity is plotted against I_{total} . Two loci are apparent, one at stellarities greater than 0.95 which presumably is due to stellar sources which have been successfully classified, and the other at stellarities below 0.8 where the classifier is identifying galaxies efficiently. In between, there are a number of sources which do not obviously belong to either set, and for which there is some ambiguity in classification. Hence, an upper limit to the contamination by the red dwarf population can be made by considering all of the sources classified as high-redshift galaxies, but with ambiguous stellarity classifications, to be red dwarfs. In total 248 sources in the high-redshift slice have stellarities between 0.8 and 0.95 and so the overall contamination from red dwarfs will be less than this value, and probably closer to 150 given that many of these ambiguous sources will be indeed high-redshift

galaxies.

As a second estimate of the red dwarf contamination, the colour distribution of sources classified as stars by the stellarity index is used to estimate the fraction of stars redder than $V - I > 3.2$ out of those redder than the $z = 0.5$ cluster red sequence. Out of those sources classified as stars on the basis of morphology, 16% of those redder than the $z = 0.5$ red sequence also have $V - I > 3.2$. If it is assumed that all of the 28 sources from the high-redshift galaxy slice with $V - I > 3.2$ and stellarities between 0.8 and 0.95 are contaminant sources, and that the colour distribution can be extrapolated to these sources, this results in a total contamination by red dwarfs of 175.

Certainly both estimates are based on crude assumptions, but both produce similar results which do not appear unreasonable, and so it is likely that the contamination due to red dwarfs is in the range of 100–250, i.e. less than 10% of the total.

4.3 Comparison with the ESO Imaging Survey of the Hubble Deep Field South

The ESO Imaging Survey (EIS; Renzini & da Costa, 1997) programme is a major public survey that was undertaken in preparation for the operation of the VLT. One of the main goals of the EIS was to carry out deep, multi-colour observations in the optical and near-infrared wavebands over a relatively large area (~ 200 arcmin²) to produce faint galaxy samples (EIS-DEEP), and then use photometric redshift techniques to identify interesting targets for follow-up spectroscopic observations with the VLT, such as Lyman-break candidates or EROs. One contributory factor behind this and other deep public surveys are the remarkable results produced by the Northern Hubble Deep Field (HDF). Such was the success of the HDF-North that the STScI completed a similar campaign in a second field, the HDF-South, which was accessible from southern-hemisphere sites. In response to these observations, ESO selected as one of their EIS-DEEP fields a 25 arcmin² region including the HDF-South WFPC2 field. Deep optical and near-infrared observations carried out at the ESO 3.5-metre New Technology Telescope (NTT), reaching 90% completeness

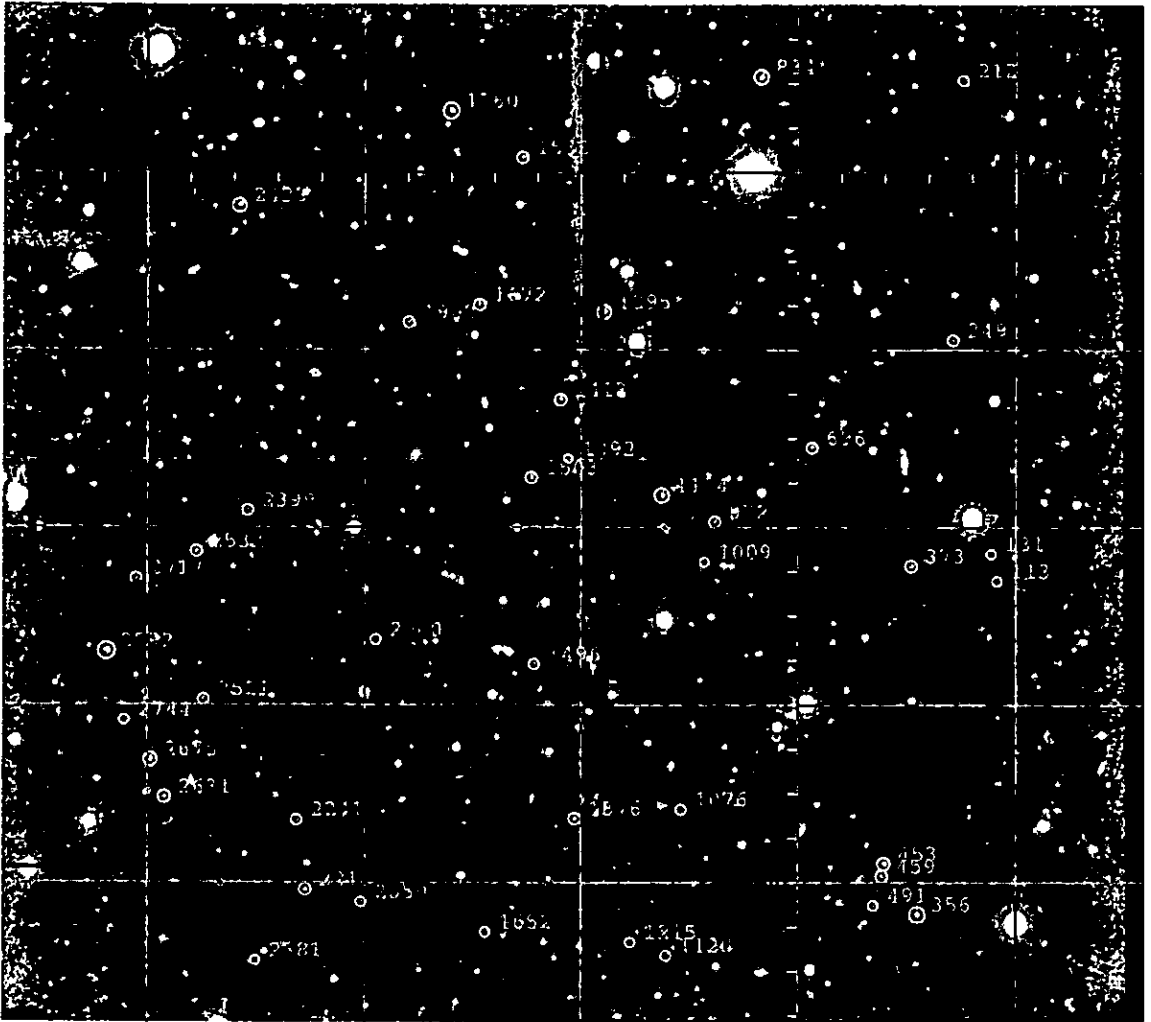


Figure 4.2: The co-added I -band EIS-DEEP image of the HDF-South field. The region also covered by the near-infrared images is indicated by the green border. The WFPC2 HST field is indicated by the blue border. The points labelled by yellow circles are those sources classified as belonging to the high-redshift slice, and the corresponding number indicates the source's identification number in the multi-colour optical catalogue of Table 4.1.

limiting magnitudes of $U \sim 26$, $B \sim 26.5$, $V \sim 26$, $R \sim 26$ and $I \sim 24.5$ in the optical, and $J \sim 24$, $H \sim 22.5$ and $K \sim 22$ in the near-infrared (da Costa et al., 1998).

The optical observations were carried out using the SUperb-Seeing Imager (SUSI2) camera which is made up of two thinned, anti-reflection coated, $2k \times 4k$ CCDs with the long side aligned in the north-south direction, producing a field of view of $5.46 \times 5.46 \text{ arcmin}^2$ with a gap between the CCDs of 8 arcsec. A dithering pattern was used to cover this gap, but sources in this region and around the edges of the field were not considered. Even so, the noise levels around the edges of

the optical field are somewhat higher than for the centre, and this has resulted in a number of false detections due to noise near the field edges. The field centre for the optical images is $22^{\text{h}}32^{\text{m}}42.4^{\text{s}}$, $-60^{\circ}33'50''$, and the total effective area is $5.1 \times 5.3 \text{ arcmin}^2$. The near-infrared images were obtained using the Son of ISAAC (SOFI) camera which has a Rockwell $1024 \times 1024 \text{ pix}^2$ detector and a field of view of $4.9 \times 4.9 \text{ arcmin}^2$, slightly smaller than that of the SUSI2 camera. The near-infrared images were offset from the optical images in order to cover both the WFPC2 and STIS HDF-South regions, having a field centre of $22^{\text{h}}33^{\text{m}}00.0^{\text{s}}$, $-60^{\circ}33'30''$, which resulted in only half the optical EIS-DEEP field being covered by the near-infrared observations. The co-added *I*-band EIS-DEEP image of the HDF-South field is shown in Figure 4.2, with the regions also covered by the near-infrared and WFPC2 HST images indicated by green and blue borders respectively.

Although the EIS-DEEP HDF-South field is unfortunately small in comparison with the BTC field for use as a control field, it is currently the largest publicly available survey with comparably deep *V*, *I* imaging and catalogues. The main objective of using this survey as a control field is to examine the properties of galaxies that pass the *V*, *I* colour-magnitude selection criteria used to create the red galaxy subset for the BTC field. Firstly, a comparison of the galaxy number density in the BTC and EIS HDF-South fields may provide tentative evidence for large-scale structure associated with the quasar group in the form of an excess of high-redshift galaxies. However, given the small size of the EIS-DEEP field, only a few dozen galaxies are likely to pass the criteria resulting in a low significance for any result. A second aspect that can be examined by the EIS field is the redshift distribution of the selected galaxies, taking advantage of the *UBVRI*, or in some cases *UBVRIJK_s*, photometry to obtain redshift estimates and to confirm whether the selection criteria is finding the desired high-redshift galaxies.

ESO have made public both the reduced images for each of the filters, and the source catalogues, both single-filter, and multi-colour, which in principle should allow the extraction of the red galaxies in a simple and straightforward manner by applying the same selection criteria as used for the BTC field. The multi-colour catalogues are created by detecting sources in a reference image that is formed from the co-adding of all the broadband images and using this reference to define a single

aperture used to measure the photometric properties of the source in each of the passbands. This ensures that the colour information for each source is accurate, but does not imply that the magnitude determined for a single passband includes all the flux from the source, as the extent of a source may vary greatly from one passband to another. Hence the total magnitude for a source in a given passband is most accurately estimated using apertures determined from the corresponding filter's image, in other words the single-filter catalogues. Hence where possible, the source's total magnitude is taken from the single-filter catalogues, whilst its colours are taken from the multi-colour catalogues. The source detection is performed using the same SExtractor tool as used for the BTC images, and so the MAG_BEST value is taken to be the total magnitude in the *I*-band catalogue. As discussed earlier, the SExtractor package provides a star-galaxy classifier that produces a stellarity index, which is approximately the probability that a source is a point source. The paper describing the survey (da Costa et al., 1998) defines stars to be sources with a stellarity index greater than 0.85 in the *I*-band. Nearly all the sources classed as stellar lie close to the model stellar tracks, suggesting that these sources are indeed stars. However there does appear to remain some stellar contamination of sources classed as extended, as several of these sources have stellar colours and an examination of the HDF-South image that covers some of the EIS-DEEP region confirms that some of these "extended" sources are in fact stellar.

Given that the intention of the survey was that it should be used by the general astronomical community, it would be hoped that the published catalogues would be complete and relatively free of noise detections, particularly given that there are fewer than 3 000 sources in the catalogues. However, after an initial inspection this was shown to not be the case, with numerous false detections in the *I*-band catalogue, particularly around the field edges where the noise levels are higher, as well as several bright sources missed. The multi-colour catalogues appear to be complete at the magnitude levels of interest, although the problem of false detections persists. As sources which are detected only in the *I*-band image satisfy the red galaxy selection criteria, it is clearly vital to ensure that the false detections are removed. Despite the use of a faint magnitude limit of $I = 23.5$ for the red galaxy subset that is a magnitude brighter than the completeness limit of the survey, a

significant number of false detections remain, necessitating a visual inspection of each source classed as a red galaxy.

In total 39 non-stellar (based on having stellarity indices less than 0.85) sources in the 27.03 arcmin² field are classed as red galaxies, of which 37 are in both the single *I*-band and multi-colour optical catalogues, one is in the multi-colour optical catalogues only, and one is in the single *I*-band catalogue only. For the source found only in the multi-colour optical catalogue the I_{total} magnitude is taken to be the I_{aper} magnitude, as this is the only value available. Given that the source is significantly brighter than the $I = 23.5$ faint magnitude limit, this should not affect the results in any way. There are no real sources that could have met the criterion based on their I_{aper} magnitude, but not their I_{total} magnitude. Each source was visually verified, and there is no reason to believe that this subcatalogue is either incomplete or contains false detections. There is a possible effect of an offset between the photometric systems in terms of the $V - I$ colour, as five more sources would meet the criterion if the $V - I$ colour is shifted bluewards by 0.05 magnitudes, the stated level of accuracy of the EIS *I*-band photometric calibration, although no sources fail the $I = 23.5$ magnitude limit by less than 0.05 magnitudes. Of the 39 high-redshift galaxies in the optical image, 14 are also found in the near-infrared images and the multi-colour optical- near-infrared catalogues, providing full *UBVRIJK_s* photometry, and four are covered by the WFPC2 HST images.

The full photometric and astrometric data for each of the sources in the multi-colour catalogue is given in Table 4.1. The first column gives the identification number for the source in the optical multi-colour catalogue, followed by the corresponding number in the optical- near-infrared multi-colour catalogue if included. The starred source (ID #1295) is the one which is not found in the single *I*-band catalogue, and hence has no value for I_{total} . The next two columns give the right ascension and declination (J2000) of the source as determined from the reference image. The next eight columns give the magnitude and error of the source in each of the eight passbands (*UBVRIJK_s*) as determined using the single reference aperture, from which the galaxy colours can be determined. Those sources not detected through a particular filter are given corresponding apparent magnitudes of 99.99 ± 9.99 . The next two columns give the $V - I$ colour and I_{total} magnitude of

ID	RA(J2000)	Dec(J2000)	m_U	m_B	m_V	m_R	m_I	m_J	m_H	m_K	$V - I$	I_{tot}	Star
113	22:32:20.87	-60:34:18.1	99.99 ± 9.99	99.99 ± 9.99	26.92 ± 0.24	25.19 ± 0.13	23.89 ± 0.07	-	-	-	3.03 ± 0.25	23.13 ± 0.09	0.35
181	22:32:21.14	-60:34:08.9	99.99 ± 9.99	99.99 ± 9.99	26.75 ± 0.21	25.12 ± 0.12	23.92 ± 0.07	-	-	-	2.83 ± 0.22	23.11 ± 0.07	0.36
212	22:32:22.43	-60:31:28.8	99.99 ± 9.99	27.50 ± 0.47	25.98 ± 0.11	24.87 ± 0.10	23.59 ± 0.05	-	-	-	2.39 ± 0.12	23.25 ± 0.08	0.12
249	22:32:22.89	-60:32:56.6	99.99 ± 9.99	27.76 ± 0.57	25.66 ± 0.09	24.64 ± 0.08	23.21 ± 0.04	-	-	-	2.45 ± 0.10	22.73 ± 0.08	0.49
366	22:32:24.52	-60:36:10.7	99.99 ± 9.99	25.36 ± 0.21	23.11 ± 0.03	21.42 ± 0.02	20.67 ± 0.01	-	-	-	2.44 ± 0.03	20.65 ± 0.01	0.15
373	22:32:24.90	-60:34:13.0	99.99 ± 9.99	26.55 ± 0.19	25.25 ± 0.06	24.08 ± 0.05	22.69 ± 0.03	-	-	-	2.66 ± 0.07	22.38 ± 0.03	0.75
453	22:32:26.05	-60:35:53.5	27.19 ± 0.69	26.22 ± 0.15	24.66 ± 0.04	23.34 ± 0.03	22.07 ± 0.02	-	-	-	2.59 ± 0.04	21.44 ± 0.02	0.15
459	22:32:26.14	-60:35:57.7	99.99 ± 9.99	26.50 ± 0.19	25.08 ± 0.08	23.90 ± 0.04	22.48 ± 0.02	-	-	-	2.60 ± 0.06	21.53 ± 0.02	0.02
491	22:32:26.53	-60:36:07.6	26.99 ± 0.34	26.66 ± 0.21	25.86 ± 0.10	24.53 ± 0.07	23.59 ± 0.05	-	-	-	2.29 ± 0.11	23.22 ± 0.07	0.36
696	22:32:29.35	-60:33:33.0	26.38 ± 0.44	27.00 ± 0.29	25.19 ± 0.06	24.02 ± 0.05	22.95 ± 0.03	-	-	-	2.24 ± 0.07	22.56 ± 0.04	0.66
972	22:32:35.52	-60:33:58.1	26.35 ± 0.44	26.73 ± 0.23	25.17 ± 0.06	24.02 ± 0.05	22.92 ± 0.03	-	-	-	2.25 ± 0.07	22.58 ± 0.04	0.17
1009	22:32:35.31	-60:34:11.6	99.99 ± 9.99	99.99 ± 9.99	27.16 ± 0.30	25.87 ± 0.24	24.15 ± 0.08	-	-	-	3.01 ± 0.31	23.33 ± 0.08	0.36
1076	22:32:35.38	-60:35:35.2	26.68 ± 0.60	26.76 ± 0.34	26.15 ± 0.13	25.18 ± 0.13	23.51 ± 0.05	-	-	-	2.64 ± 0.14	22.93 ± 0.06	0.03
1120	22:32:36.06	-60:36:24.6	99.99 ± 9.99	27.83 ± 0.63	26.19 ± 0.14	25.62 ± 0.20	23.59 ± 0.06	-	-	-	2.60 ± 0.15	23.18 ± 0.09	0.51
1134	22:32:36.27	-60:33:49.1	25.51 ± 0.22	25.69 ± 0.10	24.11 ± 0.03	22.41 ± 0.03	21.10 ± 0.02	-	-	-	3.01 ± 0.04	21.10 ± 0.02	0.30
1215	22:32:37.73	-60:36:20.1	99.99 ± 9.99	99.99 ± 9.99	26.03 ± 0.21	25.86 ± 0.26	23.79 ± 0.07	-	-	-	2.70 ± 0.19	22.83 ± 0.08	0.35
1376	22:32:40.20	-60:35:38.3	26.03 ± 0.21	26.56 ± 0.32	25.25 ± 0.07	22.60 ± 0.02	21.71 ± 0.02	-	-	-	2.60 ± 0.30	-	0.38
1392	22:32:40.59	-60:33:36.7	99.99 ± 9.99	27.71 ± 0.32	26.95 ± 0.17	25.80 ± 0.14	24.46 ± 0.08	-	-	-	2.54 ± 0.08	22.35 ± 0.04	0.70
1413	22:32:40.95	-60:33:16.8	99.99 ± 9.99	26.74 ± 0.27	25.38 ± 0.08	24.31 ± 0.07	22.69 ± 0.03	-	-	-	2.49 ± 0.19	22.54 ± 0.08	0.49
1496/50	22:32:42.19	-60:34:45.0	99.99 ± 9.99	99.99 ± 9.99	99.99 ± 9.99	25.50 ± 0.19	23.47 ± 0.07	21.70 ± 0.10	21.45 ± 0.16	20.96 ± 0.11	2.43 ± 0.08	23.36 ± 0.04	0.62
1609/57	22:32:42.31	-60:33:43.0	99.99 ± 9.99	26.69 ± 0.26	25.31 ± 0.10	23.95 ± 0.06	22.72 ± 0.04	21.23 ± 0.08	20.26 ± 0.07	19.68 ± 0.05	2.39 ± 0.08	22.36 ± 0.04	0.47
1532/76	22:32:42.72	-60:31:54.8	99.99 ± 9.99	26.28 ± 0.19	25.12 ± 0.09	23.92 ± 0.05	22.70 ± 0.04	21.50 ± 0.09	21.00 ± 0.11	20.73 ± 0.10	2.77 ± 0.15	22.96 ± 0.07	0.55
1652	22:32:44.43	-60:39:16.6	99.99 ± 9.99	99.99 ± 9.99	26.59 ± 0.14	25.60 ± 0.16	23.82 ± 0.08	-	-	-	2.27 ± 0.07	22.24 ± 0.04	0.16
1672/175	22:32:44.72	-60:32:44.6	25.87 ± 0.37	26.09 ± 0.17	25.01 ± 0.08	24.05 ± 0.06	22.88 ± 0.05	21.34 ± 0.08	20.29 ± 0.07	19.47 ± 0.05	3.37 ± 0.03	20.39 ± 0.01	0.22
1760/246	22:32:46.01	-60:31:39.2	99.99 ± 9.99	24.86 ± 0.15	23.02 ± 0.04	21.75 ± 0.02	20.50 ± 0.02	18.94 ± 0.03	18.03 ± 0.03	17.22 ± 0.02	2.45 ± 0.13	22.71 ± 0.09	0.52
2000/433	22:32:49.48	-60:34:37.3	26.33 ± 0.51	26.80 ± 0.29	25.98 ± 0.16	25.09 ± 0.13	23.91 ± 0.10	22.12 ± 0.12	21.26 ± 0.13	20.60 ± 0.09	2.60 ± 0.15	23.47 ± 0.08	0.35
2050	22:32:50.18	-60:36:06.5	99.17 ± 9.99	27.49 ± 0.45	26.30 ± 0.13	25.01 ± 0.12	23.70 ± 0.07	-	-	-	2.63 ± 0.07	23.27 ± 0.04	0.76
2217	22:32:52.74	-60:36:02.3	99.17 ± 9.99	27.04 ± 0.30	26.20 ± 0.05	23.98 ± 0.05	22.57 ± 0.03	-	-	-	2.69 ± 0.15	23.47 ± 0.08	0.35
2399/735	22:32:55.04	-60:36:25.2	99.17 ± 9.99	27.65 ± 0.47	26.30 ± 0.13	25.58 ± 0.18	23.99 ± 0.08	-	-	-	2.31 ± 0.15	23.17 ± 0.10	0.15
2429/753	22:32:55.40	-60:33:54.5	99.99 ± 9.99	28.02 ± 0.79	26.73 ± 0.30	25.14 ± 0.14	23.35 ± 0.06	21.67 ± 0.10	20.92 ± 0.10	20.97 ± 0.11	3.14 ± 0.15	22.77 ± 0.06	0.59
2521/831	22:32:57.44	-60:32:11.2	25.82 ± 0.39	25.54 ± 0.12	23.19 ± 0.04	22.05 ± 0.03	21.00 ± 0.02	19.78 ± 0.04	18.87 ± 0.04	18.26 ± 0.03	2.43 ± 0.04	20.87 ± 0.02	0.57
2637/842	22:32:57.76	-60:34:08.2	27.19 ± 0.97	27.02 ± 0.38	26.82 ± 0.14	24.75 ± 0.10	23.38 ± 0.06	20.85 ± 0.07	19.80 ± 0.06	19.15 ± 0.04	2.45 ± 0.10	22.91 ± 0.06	0.62
2675/950	22:32:59.57	-60:35:18.3	25.35 ± 0.55	26.71 ± 0.31	23.42 ± 0.05	22.22 ± 0.03	21.01 ± 0.02	20.75 ± 0.09	20.75 ± 0.09	20.73 ± 0.10	2.87 ± 0.11	22.65 ± 0.05	0.69
2717/985	22:33:00.55	-60:34:17.3	26.06 ± 0.42	27.82 ± 0.69	26.10 ± 0.18	24.78 ± 0.10	23.46 ± 0.07	21.52 ± 0.09	20.84 ± 0.09	20.26 ± 0.08	2.66 ± 0.04	21.01 ± 0.02	0.09
2744/1006	22:33:01.07	-60:35:05.1	99.99 ± 9.99	99.99 ± 9.99	26.61 ± 0.27	25.42 ± 0.18	23.84 ± 0.09	21.62 ± 0.09	21.03 ± 0.11	20.82 ± 0.10	2.53 ± 0.11	22.71 ± 0.05	0.67
2792/1040	22:33:01.88	-60:34:41.8	24.51 ± 0.33	24.17 ± 0.10	22.38 ± 0.03	21.15 ± 0.02	19.97 ± 0.01	18.56 ± 0.02	17.61 ± 0.02	16.87 ± 0.02	2.63 ± 0.27	23.33 ± 0.10	0.36

Table 4.1: Multi-colour optical- near-infrared catalogue of sources in the EIS-DEEP HDF-South field classified as belonging to the high-redshift slice.

the source from which the source selection was made. The final column gives the stellarity of the source as determined from the *I*-band image.

To estimate the photometric redshifts of each of the sources from its *UBVRI* (and if possible *JHK_s*) photometry, the HYPERZ code of Bolzonella et al. (2000) has been used (discussed in more detail in the next chapter). This uses the Bruzual & Charlot evolutionary code (GISSEL98; Bruzual & Charlot, 1993) to build synthetic template galaxies. It has stellar populations with eight star-formation histories, roughly matching the observed properties from E to Im type: an instantaneous burst; six exponentially decaying SFRs with time-scales τ from 1 to 30 Gyr; and a constant star-formation rate. The models assume solar metallicity and a Miller & Scalo (1979) IMF, with internal reddening considered through the Calzetti et al. (2000) model with A_V allowed to vary between 0 and 1 mag. The HYPERZ software then produces a photometric redshift probability distribution through a chi-squared minimisation process, allowing for all possible galaxy ages, star-formation histories and A_V s. Hence instead of a single best-fitting redshift for a galaxy, a range of compatible redshifts is produced.

Table 4.2 shows the resultant photometric redshift estimates determined by the HYPERZ code for each of the sources classed as red galaxies. The table is split into two, with those sources covered by the optical observations only in the top section, and those sources covered by both the optical and the near-infrared observations in the lower section. The first column gives the entry number of each source in the multi-colour optical catalogue, followed by the entry number in the multi-colour optical- near-infrared catalogue for those sources in both. The z_{best} column indicates the most probable redshift based on the photometry of the source, i.e. the one that gives the best fit. The z_{mean} is the mean redshift estimate produced by weighting by the redshift probability distribution. $P(z_{best})$ is the probability of the redshift estimate associated with the chi-squared value of the fit at z_{best} . The next column gives the stellarity of the source as determined from the *I*-band image. For the four sources covered by the HST WFC2 images a simple visual inspection allows the classification of the sources as point sources or galaxies, and the next column indicates this classification as a (S)tar or (G)alaxy. The value in the spectral class column indicates the star-formation history of the best fitting template galaxy, with

ID	z_{best}	z_{mean}	$P(z_{best})$ (%)	Class		HST S/G	Spectral Class	Galaxy Age (Gyr)	Δy (best)	z_{min} (99%)		z_{max} (99%)		z_{min} (90%)		z_{max} (90%)		z_{min} (68%)		z_{max} (68%)		MV (z_{best})
				Star	0.35					0.399	2.800	0.472	1.433	0.858	1.344	0.359	2.800	0.472	1.433	0.858	1.344	
113	1.080	1.344	100.0	0.35	1	1	2.3000	0.00	0.399	2.800	0.472	1.433	0.858	1.344	0.472	1.433	0.858	1.344	0.858	1.344	-20.81	
131	2.044	2.184	100.0	0.36	1	1	1.0152	0.80	0.349	2.800	1.854	2.279	1.939	2.184	1.854	2.279	1.939	2.184	1.939	2.184	-24.66	
212	1.378	1.485	99.51	0.12	1	1	0.7187	0.80	0.388	1.966	1.199	1.603	1.292	1.485	1.199	1.603	1.292	1.485	1.292	1.485	-22.35	
249	0.776	0.877	94.57	0.49	1	1	1.7000	0.00	0.513	1.048	0.597	0.931	0.607	0.877	0.597	0.931	0.607	0.877	0.607	0.877	-19.91	
356	2.358	2.376	00.22	0.15	1	1	0.7187	0.00	2.246	2.408	2.298	2.388	2.331	2.376	2.298	2.388	2.331	2.376	2.331	2.376	-27.37	
373	0.894	0.953	65.10	0.75	1	1	0.7187	0.50	0.678	1.133	0.735	1.030	0.848	0.953	0.735	1.030	0.848	0.953	0.848	0.953	-20.92	
453	1.304	1.342	96.87	0.15	1	1	1.0152	0.00	1.166	1.402	1.230	1.366	1.265	1.342	1.230	1.366	1.265	1.342	1.265	1.342	-23.31	
459	0.854	0.912	71.38	0.02	1	1	0.7187	0.50	0.626	1.072	0.681	0.969	0.801	0.912	0.681	0.969	0.801	0.912	0.801	0.912	-20.75	
491	0.676	0.718	79.78	0.36	1	1	0.3602	0.70	0.432	0.769	0.501	0.747	0.638	0.718	0.501	0.747	0.638	0.718	0.638	0.718	-18.92	
696	0.670	0.707	99.30	0.66	1	1	1.0152	0.00	0.321	0.767	0.512	0.732	0.627	0.707	0.512	0.732	0.627	0.707	0.627	0.707	-19.63	
972	0.682	0.727	91.78	0.17	1	1	1.0152	0.00	0.359	0.796	0.485	0.754	0.638	0.727	0.485	0.754	0.638	0.727	0.638	0.727	-19.66	
1009	1.590	1.894	99.97	0.35	1	1	1.4340	0.30	0.487	2.800	0.585	2.009	1.346	1.894	0.585	2.009	1.346	1.894	1.346	1.894	-22.45	
1076	1.038	1.085	50.59	0.03	1	1	0.5088	0.90	0.745	1.157	0.869	1.119	0.935	1.085	0.869	1.119	0.935	1.085	0.935	1.085	-20.69	
1120	1.570	1.661	05.42	0.51	1	1	1.0152	0.50	1.373	1.841	1.439	1.742	1.500	1.661	1.439	1.742	1.500	1.661	1.500	1.661	-22.89	
1134	1.022	1.098	03.40	0.30	1	1	1.0152	0.80	0.906	1.239	0.951	1.170	0.976	1.098	0.951	1.170	0.976	1.098	0.976	1.098	-23.32	
1215	1.612	1.726	30.91	0.35	1	1	1.0152	0.80	1.321	1.909	1.424	1.814	1.493	1.726	1.424	1.814	1.493	1.726	1.493	1.726	-23.03	
1295	0.644	0.714	99.00	0.38	1	1	1.7000	0.80	0.475	0.945	0.553	0.799	0.592	0.714	0.553	0.799	0.592	0.714	0.592	0.714	-21.22	
1376	0.800	0.897	19.51	0.70	2	2	5.5000	0.30	0.609	1.026	0.658	0.960	0.699	0.897	0.658	0.960	0.699	0.897	0.699	0.897	-20.63	
1392	1.128	1.280	99.89	0.49	1	1	0.5088	0.90	0.491	1.597	0.815	1.432	0.710	1.280	0.815	1.432	0.710	1.280	0.710	1.280	-20.18	
1413	0.894	0.945	20.17	0.72	1	1	0.5088	0.90	0.893	1.130	0.757	1.043	0.859	0.945	0.757	1.043	0.859	0.945	0.859	0.945	-20.79	
1652	1.612	1.760	86.09	0.58	1	1	1.0152	0.80	1.307	1.925	1.406	1.836	1.470	1.760	1.406	1.836	1.470	1.760	1.470	1.760	-23.00	
2050	1.346	1.447	100.0	0.35	1	1	0.7187	0.90	0.344	1.985	0.527	1.529	1.183	1.447	0.527	1.529	1.183	1.447	1.183	1.447	-22.16	
2217	1.396	1.444	99.91	0.76	1	1	1.0152	0.20	1.276	1.569	1.326	1.488	1.355	1.444	1.326	1.488	1.355	1.444	1.355	1.444	-23.23	
2381	1.490	1.619	75.51	0.15	1	1	0.7187	0.70	0.598	1.838	1.334	1.703	1.403	1.619	1.334	1.703	1.403	1.619	1.403	1.619	-22.18	
1495/50	0.894	0.973	00.00	0.62	1	1	1.0152	0.10	0.758	1.108	0.812	1.077	0.856	0.973	0.812	1.077	0.856	0.973	0.856	0.973	-20.48	
1503/57	0.938	0.991	90.94	0.47	1	1	1.0152	0.10	0.464	1.023	0.732	1.005	0.855	0.991	0.732	1.005	0.855	0.991	0.855	0.991	-21.05	
1632/78	0.758	0.785	00.08	0.55	1	1	0.7187	0.00	0.687	0.828	0.719	0.803	0.738	0.785	0.719	0.803	0.738	0.785	0.738	0.785	-20.09	
1672/176	0.676	0.703	53.12	0.16	2	2	3.5000	0.90	0.518	0.809	0.580	0.736	0.643	0.703	0.580	0.736	0.643	0.703	0.643	0.703	-19.86	
1760/246	0.884	0.910	33.58	0.22	1	1	1.7000	0.00	0.340	0.956	0.817	0.940	0.854	0.910	0.817	0.940	0.854	0.910	0.854	0.910	-23.11	
2000/433	1.152	1.206	85.03	0.52	1	1	0.5088	0.30	1.013	1.335	1.080	1.247	1.121	1.206	1.080	1.247	1.121	1.206	1.121	1.206	-20.70	
2399/735	0.862	0.946	00.00	0.59	S	S	1.0152	0.20	0.708	1.005	0.785	0.971	0.819	0.946	0.785	0.971	0.819	0.946	0.819	0.946	-20.06	
2423/753	0.594	0.621	17.98	0.57	G	G	2.3000	0.00	0.538	0.680	0.559	0.631	0.577	0.621	0.559	0.631	0.577	0.621	0.577	0.621	-21.32	
2521/831	1.602	1.629	32.36	0.62	1	1	1.0152	0.00	1.324	1.683	1.409	1.651	1.518	1.629	1.409	1.651	1.518	1.629	1.518	1.629	-22.83	
2537/842	0.934	0.943	00.00	0.69	S	S	1.0152	0.00	0.790	0.991	0.840	0.962	0.875	0.943	0.840	0.962	0.875	0.943	0.875	0.943	-20.95	
2675/950	0.676	0.720	54.20	0.09	1	1	1.4340	0.60	0.444	0.814	0.555	0.745	0.616	0.720	0.555	0.745	0.616	0.720	0.616	0.720	-21.73	
2717/986	0.742	0.767	58.09	0.67	G	G	6.5000	0.10	0.491	1.112	0.605	0.785	0.681	0.767	0.605	0.785	0.681	0.767	0.681	0.767	-19.59	
2744/1006	1.094	1.126	00.00	0.36	1	1	1.0152	0.00	0.962	1.629	1.031	1.153	1.059	1.126	1.031	1.153	1.059	1.126	1.059	1.126	-21.14	
2792/1040	0.486	0.497	52.00	0.06	2	2	6.5000	0.50	0.354	0.871	0.403	0.617	0.460	0.497	0.403	0.617	0.460	0.497	0.460	0.497	-21.74	

Table 4.2: Photometric redshift estimates of sources in the EIS-DEEP HDF-South field classified as belonging to the high-redshift slice.

a value of 1 indicating an instantaneous burst model or simple stellar population, values of 2–7 indicating exponentially-decaying star-formation rates with characteristic time-delays, τ , of 1, 2, 3, 5, 15 and 30 Gyr respectively, and a value of 8 indicating a template with a constant star-formation rate. The next two columns indicate the age and level of internal reddening (A_V) of the best-fitting galaxy template. The next six columns give the 99% (3σ), 90% (2σ) and 68% (1σ) confidence levels for the redshift estimate, and the final column gives the absolute magnitude, M_V of the best-fitting template galaxy.

It is immediately apparent that these sources, classified as belonging to the high-redshift slice from their red $V-I$ colour and $I_{total} < 23.5$ magnitude alone, are indeed high-redshift early-type galaxies as suggested. Even at the 99% confidence level, all of them are constrained to redshifts above $z = 0.34$, and indeed most are constrained at this level as being at $z > 0.5$. The typical redshift range of these galaxies appears to be $0.7 \lesssim z \lesssim 1.5$, just the redshift range that the selection is aimed at probing. Secondly, the best-fitting templates are almost all the simple stellar populations that would be expected of early-type galaxies that formed in a monolithic collapse, with the remaining four sources being best fit by an exponentially-decaying star-formation rate with a characteristic time-delay of 1 Gyr. None of the sources are best fit by the models with higher characteristic time-delays or constant star-formation rates that are used to describe late-type galaxies.

It is also clear that not all of these sources are galaxies, despite the star-galaxy separation applied using the stellarity classifier. A number of stars remain in the catalogue, presumably all red dwarfs given their red colour and faint magnitudes. Indeed of the four sources in the WFPC2 field, two are clearly point-sources, and a comparison of the stellarity values of the two stars and the two red galaxies in the field indicates that the stellarity value is not a good distinguisher between the two. Indeed, source #2717 which in the WFPC2 image is clearly a galaxy, has a higher stellarity index than source #2399 which when observed with the much greater resolution of the HST is certainly a star. Although the stellarity index may not be a good separator of stars and galaxies in this subset, the photometric redshift estimator does provide a means of classifying them on the basis that stars and galaxies form separate colour loci, and so given sufficient colour information, stars should stand

out by not being fit by any galaxy template at any redshift. Indeed the two stars in the WFPC2 field both have zero probabilities of being fit by any template model. However a low peak probability of fit does not imply that a source is not a galaxy, as the models are limited in their nature, and for example a galaxy undergoing a secondary burst of star-formation with large amounts of dust extinction is unlikely to be fit by any of the simple star-formation history models, and neither would a galaxy with an AGN. Source #2423 is evidently a galaxy from the WFPC2 image, but has a best-fitting probability of only 17.98%, although it does not lie near the model predictions for stellar sources, having a $J - K$ colour of 1.52, 0.5 magnitudes redder than that predicted for any star. By comparing the colours of those sources not well fit by the photometric redshift software with the predictions for stellar sources, the separation of stars and unusually coloured galaxies should be possible at least for those sources with near-infrared data where stars are much bluer than high-redshift galaxies. By doing this three further sources can be confidently categorised as stars from their near-infrared colours, sources #1496, #1532, and #2744. These have the lowest fitting probabilities outside the WFPC2 region, and all have relatively blue near-infrared colours ($J - K \sim 0.7$, $I - K \sim 2-3$) in comparison to those expected of high-redshift galaxies ($J - K \sim 1.8$, $I - K \simeq 3.5$). For those poorly-fit sources with only optical data, it is not possible to conclude definitively whether they are stars or galaxies from their colours, and so they are left in the catalogue.

In total 34 sources remain classified as red galaxies in the 27.03 arcmin² EIS-DEEP field, giving a number density of 1.258 galaxies per arcmin². In comparison, over the 1417.98 arcmin² field covered by both V and I BTC imaging, 3017 red galaxies are observed, producing a galaxy number density of 2.128 galaxies per arcmin², almost twice that observed in the EIS-DEEP field, or an excess of 1200 red galaxies in the BTC field.

It has to be remembered that the EIS-DEEP field is much smaller than the BTC field, and given that many of these galaxies are expected to be massive ellipticals and hence the most clustered and biased tracers of mass, cosmic variance is likely to reduce the significance of this result greatly. To estimate the effect of cosmic variance, subregions of the BTC field with the same dimensions as the EIS-DEEP field (5.3×5.1 arcmin²) are selected at random and the number of red galaxies in

each subregion counted. By considering a large number of subregions and examining the statistical likelihood of finding 34 or fewer red galaxies in a field of the same size as the EIS-DEEP field, the significance of the observed excess can be estimated. After examining 100 000 randomly-positioned subregions (of course with a great deal of mutual overlap) 58.86 ± 12.58 red galaxies would be expected in a region with the same dimensions as the EIS-DEEP field, resulting in an excess significant at the 1.976σ level. The distribution of counts in each of the random fields is not normally distributed, as clusters within the BTC field will produce abnormally high counts for those regions containing them, skewing the distribution and increasing the variance. Instead by considering the fraction of regions containing 34 or fewer red galaxies, the probability that the red galaxy densities in EIS-DEEP and BTC fields are drawn from the same distribution can be estimated. Out of the 100 000 randomly-positioned EIS-DEEP field-sized subregions, only 1591 contain 34 or fewer red galaxies, meaning that the observed excess in the BTC field is significant at the 98.4% level.

Another possible cause for the observed excess of red galaxies in the BTC image could be a relative offset of the photometric systems between the BTC and EIS-DEEP data. There is certainly no evidence for a problem in the photometric calibration in either set of data, as both sets of galaxy counts are consistent with the other major surveys. One possible cause for a discrepancy is the different filter sets used, the BTC data using the standard V , I Bessell filters, and the EIS-DEEP data using the SUSI Bessell V , I filters (ESO #812 and #814). In fact, the peak wavelengths of the BTC V and I filters are 5% closer than for the SUSI V and I filters, which could result in sources which are intrinsically red appearing redder in the EIS-DEEP V , I images, and so should counteract the observed effect. Another possible discrepancy could be the different sized apertures used: whereas the sources' colours are determined through a fixed 2.5 arcsec diameter aperture in the BTC images, in the EIS-DEEP images they are determined through apertures whose sizes and shapes vary between sources. Given though that the apertures are constant for each source, this should not affect the colour, and the observed small scatter of the cluster red sequence of Figure 3.18 indicates that the colour determination in the BTC images is internally consistent.

However it is unlikely that any photometric offset will be greater than 0.1 magnitudes, and so to examine the effect of such an offset on the number of high-redshift galaxies, the colour boundary is shifted redder by 0.1 magnitudes, and the faint magnitude limit is brightened to $I = 23.4$, and the number of sources in the BTC images recounted. After this tightening of the selection criteria by 0.1 magnitudes, 2517 red galaxies remain, or 1.775 galaxies per arcmin², reducing the expected number of galaxies in a field of the same size as the EIS-DEEP field to 47.98. By considering the effect of both cosmic variance, and a photometric offset of 0.1 magnitudes, the significance of the observed excess is reduced from 1.976σ to 1.621σ .

Other possible contributory causes of the observed excess could be a contaminant population of stars or noise events in the BTC data. As discussed earlier, some contamination by stellar sources is likely, but due to the relatively high efficiency of the star-galaxy classifier at these magnitude levels, this contamination should be of the order 100–250 sources, and certainly much smaller than the total observed excess. In fact, despite comparable FWHMs for the point-spread functions of the BTC and EIS-DEEP images, the differentiation of stars and galaxies in the BTC images is much easier than in the EIS-DEEP images, as the point-spread function is circular and has a consistent radial profile across the whole BTC field, presumably due to the accuracy of the distortion model and of the registration process. This is surprising given the much wider field of the BTC camera in comparison with the SUSI2 camera, and the scale of the initial distortions for the BTC images. There is also evidence for further stellar contamination in the EIS-DEEP images in the region not covered by the near-infrared imaging. As discussed earlier, five sources in the region covered by the near-infrared imaging could be confidently classed as stars on the basis of their $UBVR_{IJK}$ photometry or their morphology in the WFPC2 imaging, whereas it was not possible to classify sources as stars confidently in the remainder of the EIS-DEEP field. However, several of the sources classed as red galaxies in the region not covered by near-infrared imaging do have very low probabilities of any photometric redshift, indicating that there are probably 2–5 stars remaining in the catalogue.

The possible effect of noise events is substantial given that both catalogues had contamination levels of around 30%, and necessitated the visual inspection of each

source in order to remove those sources which were clearly noise events. However given that the faint magnitude limit of $I = 23.5$ is a magnitude or more above the detection threshold in both images, it is relatively easy to discern between real and noise events for the vast majority of sources, and as discussed earlier, the uncertainty in the total number of sources in each catalogue is of the order of 5%.

There are two possible astrophysical explanations for the observed excess of high-redshift galaxies in the BTC image with respect to the EIS-DEEP HDF-South field. Either the BTC image contains more high-redshift galaxies than average, or the EIS-DEEP field is deficient in galaxies which belong to the high-redshift slice, or a combination of the two. Of course, it is impossible to say whether the EIS-DEEP field has such an unusual deficiency. It is only a comparatively small field, and as these galaxies are more highly clustered than normal galaxies, such a chance event is always possible. Only comparison with other deep surveys will confirm this.

The potentially much more interesting explanation is that the BTC field contains of the order of 1000 more early-type galaxies in the redshift range $0.7 \lesssim z \lesssim 1.5$ than normal. Clearly, given that this redshift range includes that of the three quasars from the Clowes-Campusano Large Quasar Group in the BTC field, at $1.2 \lesssim z \lesssim 1.3$, this excess of optically-red galaxies could be the result of a large-scale structure associated with the quasar group.

Assuming that the observed excess of red galaxies is real, then their spatial distribution should provide some clues as to their nature. Firstly, if these sources are the high-redshift early-type galaxies predicted they should be significantly more clustered than normal galaxies selected by I -band magnitude only, because as these are the most massive galaxies, they should be associated with the most massive dark matter halos, which in turn are most likely to have formed around the rarest overdensities in the early universe. Secondly, if this excess is due to a large-scale structure associated with the quasar group, a spatial correlation between the galaxies and the individual quasars should be observed.

4.4 Clustering of the Red Galaxies

The most frequently used (and misused) statistical tool for measuring the extent of galaxy clustering is the angular two-point correlation function, $\omega(\theta)$. This is defined as the excess probability over a Poisson distribution of finding galaxies separated by the angular distance θ .

Numerous methods exist for estimating $\omega(\theta)$ from a set of object positions, but the estimator that suffers least from biases on large scales and has the lowest levels of variance is the Landy & Szalay (1993) estimator

$$\hat{\omega}(\theta) = \frac{\text{DD} - 2\text{DR} + \text{RR}}{\text{RR}} \quad (4.4)$$

where DD, DR and RR are the number of galaxy-galaxy, galaxy-random and random-random object pairs at angular separations $\theta \pm \delta\theta$. Each of these counts has to be first normalised by dividing by the total number of pairs in each of the three samples, respectively $\frac{1}{2}N_g(N_g - 1)$, $N_g N_r$, and $\frac{1}{2}N_r(N_r - 1)$. The variance of this estimator can be considered to be the normal Poisson counting errors

$$\text{Var}(\hat{\omega}(\theta)) = \frac{N_{gg}(\theta)}{N_{rr}(\theta)^2}. \quad (4.5)$$

For the purpose of estimating $\omega(\theta)$, 100 random catalogues are created, each containing the same number of objects as the compared galaxy catalogue, and given the same spatial geometry. Contamination by effects such as the large halos around bright stars and the low levels of signal to noise around the image edges would result in biases in the estimate of $\omega(\theta)$, and so these regions are removed from both the galaxy and random catalogues.

The estimator $\hat{\omega}(\theta)$ satisfies the integral constraint

$$\int \int \hat{\omega}(\theta) \delta\Omega_1 \delta\Omega_2 \simeq 0 \quad (4.6)$$

(Groth & Peebles, 1977), resulting in an underestimate of the angular correlation function. To remove this bias from the correlation function, the term

$$\omega(\theta)_\Omega = \frac{1}{\Omega^2} \int \int \omega(\theta) \delta\Omega_1 \delta\Omega_2 \quad (4.7)$$

is added to the estimate of the correlation function. This term, requires an assumption of the form of the correlation function to estimate correctly the value of the

correlation function. However, previous studies have shown that the angular correlation function is well approximated by a power law of the form $\omega(\theta) = A_\omega \theta^{-\delta}$ for the angular scales examined here (e.g. Maddox et al., 1996). From the results of numerous large surveys (e.g. Groth & Peebles, 1977; Efstathiou et al., 1991) the index of the power-law is found to be $\delta \simeq 0.8$. Assuming such a power law for the form of the angular correlation function, the level of bias can be estimated using the random-random sample

$$C = \frac{\omega(\theta)_\Omega}{A_\omega} = \frac{\sum N_{rr}(\theta)\theta^{-\delta}}{\sum N_{rr}(\theta)}. \quad (4.8)$$

The amplitude and power index of the real two-point correlation function $\omega(\theta)$ can be estimated by fitting to the measured $\hat{\omega}(\theta)$ the function

$$\hat{\omega}(\theta) = A_\omega(\theta^{-\delta} - C). \quad (4.9)$$

The angular two-point correlation functions have been determined for the red galaxy subset and also for comparison the subset containing all galaxies brighter than $I = 23.5$ using the Landy & Szalay (1993) estimator. To minimise biasing due to areas of low signal-to-noise levels, the edges of the BTC field have been discarded along with regions affected by the halos of bright stars, resulting in a total area considered of 1354.55 arcmin^2 . In this area there are 24 483 galaxies brighter than $I = 23.5$ of which 2 978 are also classified as red galaxies. By assuming a power-law correlation function, $\omega(\theta) \propto \theta^{-0.8}$ the integral constraint term C is found to be 0.00472 for the $I < 23.5$ galaxies. For the red galaxies however, $\omega(\theta)$ cannot be well fitted by a power-law of index -0.8, requiring a somewhat steeper index. By instead assuming a power-law index of -1.0, the integral constraint term C is found to be 0.001335 for the red galaxy subset.

Figure 4.3 shows the angular two-point correlation functions for the red galaxy subset (shown as filled red squares), and for comparison the set of all galaxies brighter than $I = 23.5$ (shown as filled green circles). The significant difference of clustering strength, A_ω , and the power-law index, δ , between the two samples is immediately apparent, with the clustering of the red galaxies greater than that of $I < 23.5$ galaxies for all separations, the difference becoming an order of magnitude at small separations ($\lesssim 10 \text{ arcsec}$). The best fitting power-law to the red galaxy

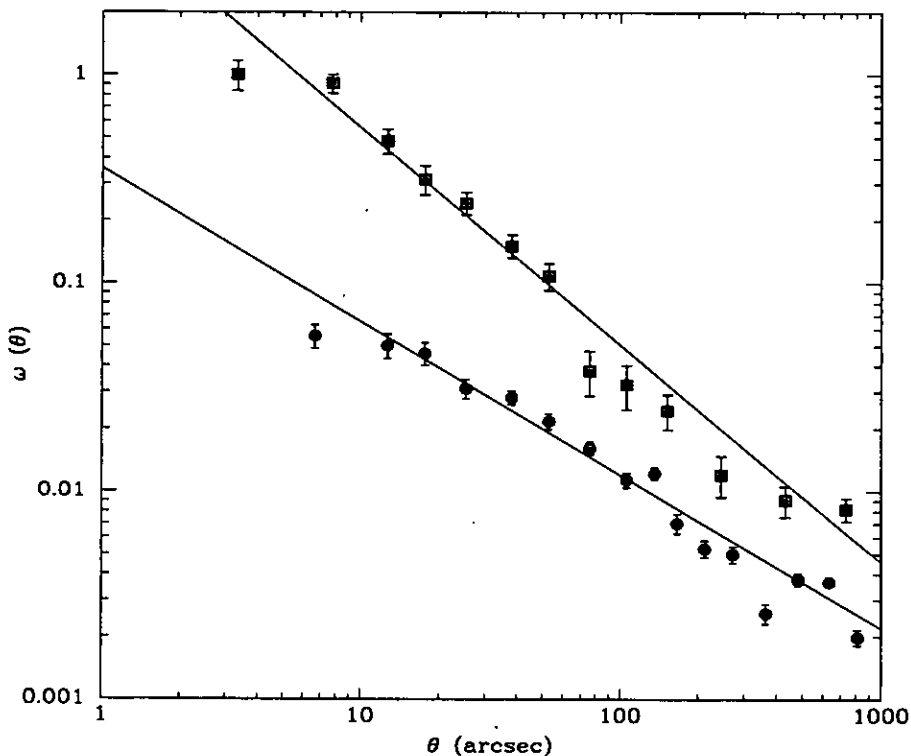


Figure 4.3: The angular two-point correlation functions for all $I < 23.5$ galaxies (green filled circles) and the red galaxy subset (red filled squares). The errors shown assume Poisson count errors. The best fitting power-laws to each of the correlation functions are shown as magenta (for the red galaxy subset) and blue (for all $I < 23.5$ galaxies) lines. The red galaxy subsample shows stronger clustering and a higher value of δ , consistent with the strong clustering of elliptical and early-type galaxies at high-redshifts.

angular two-point correlation function has $A_{\omega}^{red}(1'') = 6.23 \pm 0.71$ and a power-law index of -1.045 . In contrast the best fitting power-law for the $I < 23.5$ galaxy sample has a much smaller clustering strength of $A_{\omega}^{I < 23.5}(1'') = 0.356 \pm 0.03$ and a shallower power-law index of -0.736 .

There is no evidence for the level of clustering in the $I < 23.5$ control sample being abnormally low. Both the clustering strength and the power-law index are comparable to results from other I -band magnitude limited surveys. To compare this result with published data, $\omega(\theta)$ is redetermined for a fixed power index of -0.8 , giving a clustering strength of $A_{\omega}(1'')$ of 0.61 ± 0.07 . Woods & Fahlman (1997) in comparison obtain $A_{\omega}(1'') = 0.627 \pm 0.116$ for $19 \leq I \leq 23.5$ galaxies in three $\simeq 49$ arcmin² fields. Figure 3 of McCracken et al. (2000) plots the logarithm of the amplitude of the angular correlation function $\omega(\theta)$ at one degree as a function of

sample median I -band magnitude. The median I magnitude of the $I < 23.5$ sample is 22.51, and its clustering strength is $\log A_\omega(1^\circ) = -3.06 \pm 0.11$, placing it centrally among the results at comparable median I magnitudes (Lidman & Peterson, 1996; Postman et al., 1998; McCracken et al., 2000).

The observation that red galaxies are more strongly clustered than galaxies selected on magnitude only has been made in previous studies (Brown et al., 2000; Daddi et al., 2000).

In an attempt to examine the relative clustering strengths of early- and late-type galaxies at low redshifts ($z \lesssim 0.4$) Brown et al. (2000) created two subsets, a red and blue subsample, from a catalogue of bright $B_J < 21.5$ galaxies from two $5^\circ \times 5^\circ$ fields, using both $U - B_J$ and $B_J - R_F$ colours to separate the two subsets. The two-point angular correlation functions of the red and blue subsamples, taken to contain mostly early- and late-type galaxies respectively, were estimated and compared. The red subsample (early-type galaxies) was observed to be significantly more clustered at separations less than one degree than the blue subsample (late-types), the difference reaching a factor of ~ 5 at separations of 1 arcmin.

In contrast to the low redshifts probed by the previous study, Daddi et al. (2000) examined the clustering properties of Extremely Red Objects (EROs) selected to have $R - K_s > 5$. The red colours of EROs are consistent with being either old, passively-evolving early-type galaxies at $z \gtrsim 1$, or strongly dust-reddened star-forming galaxies also at high redshifts, and observations have shown that both classes of galaxies are present among the ERO population. If the dominant ERO population were star-forming galaxies, then it would be expected that EROs would be weakly clustered as firstly, IRAS-selected star-forming galaxies have very low intrinsic clustering (Fisher et al., 1994) and secondly, the red colours are dependent much more on the amount of dust extinction rather than the redshift, resulting in a wide redshift distribution which should dilute the observed clustering strength. In contrast if the ERO population is dominated by early-type galaxies at $z \gtrsim 1$, then a strong clustering signal should be observed, as they should be found in the most massive dark matter halos which should be highly clustered as they due to being formed at only the rarest density peaks (Kauffmann et al., 1999).

Daddi et al. (2000) obtained R, K_s imaging over a 700 arcmin^2 region, reach-

ing $K_s \simeq 19$ and $R \simeq 26$, detecting 400 EROs with $R - K_s > 5$. The clustering of the ERO subsample was compared with the K_s -selected sample in the same magnitude range, and the EROs were found to be of an order of magnitude more strongly clustered, with $A_\omega(1^\circ) = 0.022 \pm 0.003$ for the $K_s < 18.5$ ERO subsample, and $A_\omega(1^\circ) = 0.0016 \pm 0.0003$ for the comparable K_s -selected sample, both assuming $\delta = 0.8$. This observed strong clustering of EROs is direct evidence that a large fraction of these sources are high-redshift early-type galaxies. It explained the conflicting results of previous studies in determining the density of high-redshift ellipticals in terms of strong field-to-field variations.

The wavelength and redshift range covered by this study of red galaxies is intermediate between the two previous studies, this study having $\lambda_{med} \sim 700$ nm and $0.6 \lesssim z \lesssim 1.5$, in comparison to $\lambda_{med} \sim 450$ nm and $z \lesssim 0.4$ for the study of Brown et al. (2000), and $\lambda_{med} \sim 1400$ nm and $z \gtrsim 1$ in the case of Daddi et al. (2000). The observed increases in clustering strengths of the red galaxies to the magnitude-selected galaxies are comparable, with the effect becoming greater at higher redshifts, presumably due to the dark matter halos sufficiently large to contain an early-type galaxy becoming increasingly rare at earlier epochs.

This observation that the red galaxies in the BTC field are more clustered than magnitude-selected galaxies in conjunction with the results of the photometric redshift study of red galaxies in the EIS-DEEP field serves to support that a large fraction of the red galaxies are indeed early-type galaxies at $0.6 \lesssim z \lesssim 1.5$.

4.5 Spatial Distribution of the Red Galaxies

The previous section demonstrated that the red galaxies are early-type galaxies at $0.6 \lesssim z \lesssim 1.5$. As a result any galaxy clustering associated with the Clowes-Campusano Large Quasar Group should be evident among this subsample. The observed excess of red galaxies in the BTC images hints at the possibility of a large-scale structure associated with the quasar group, but to probe this possibility further, the spatial distribution of red galaxies needs to be determined, allowing the relationship between the red galaxies and the group's quasars to be examined.

As in the previous chapter, to estimate the surface density of red galaxies, the

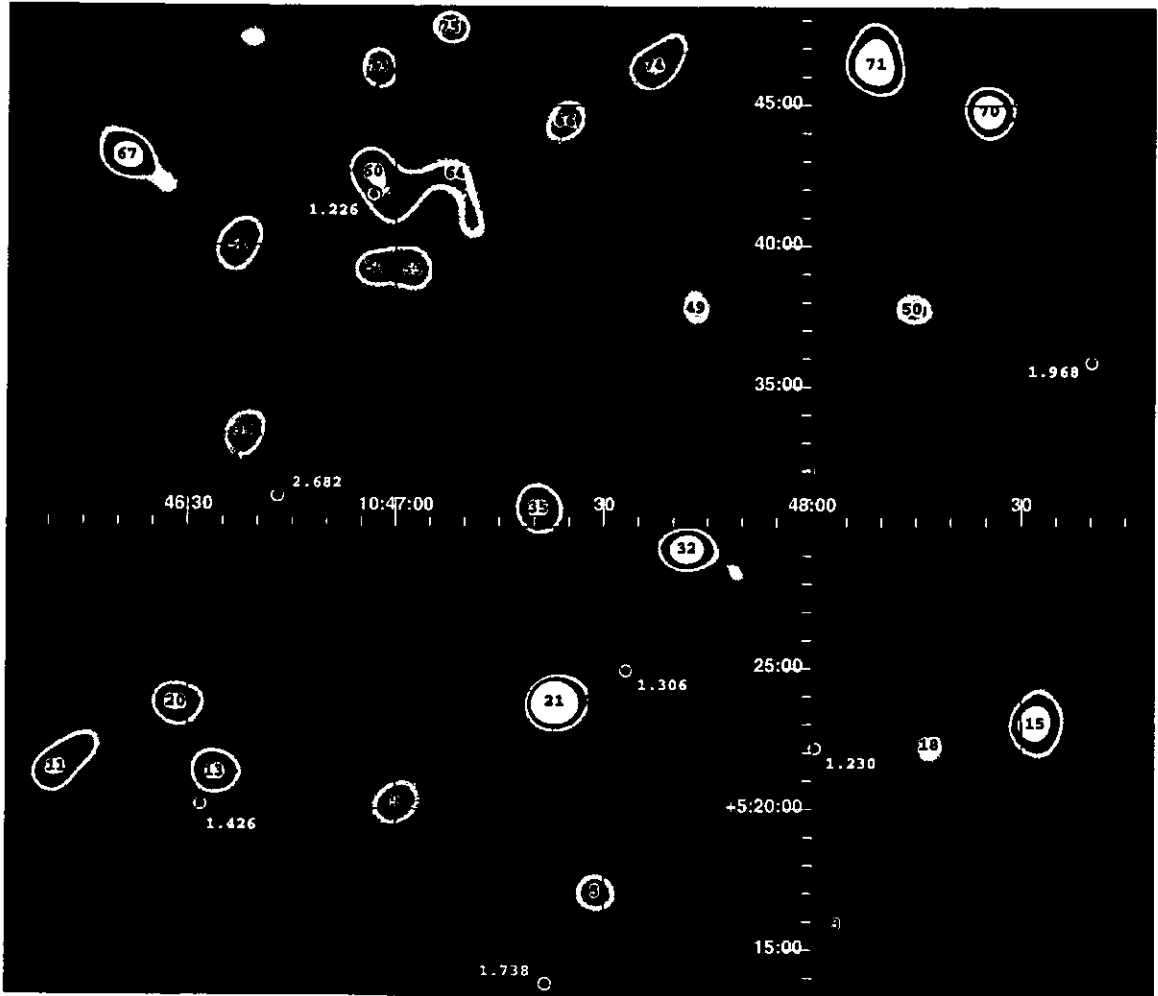


Figure 4.4: The spatial distribution of red galaxies in the BTC images. The galaxy surface density is estimated using the adaptive kernel estimator with $\sigma = 0.75 h^{-1} \text{Mpc}$. The low-density regions are indicated by black and blue colours, whilst the high-density regions are indicated by red and white colours. The positions of the high-redshift cluster candidates of Table 4.3 are indicated in black by their ID number. Each of the known quasars in the field are indicated by black/white circles labelled by the quasar redshift. The region shown corresponds to a proper size of $33.0 \times 28.4 h^{-1} \text{Mpc}$ at $z = 1.3$.

adaptive kernel estimator is applied. At the redshifts of interest any galaxy clustering is likely to be rather more amorphous and diffuse than compact and virialised, and so to detect these structures more efficiently, along with signs of any large-scale structure, a greater level of smoothing should be applied than previously. The geometric mean kernel width, σ , is set to an angular distance of $0.75 h^{-1} \text{Mpc}$ (for an $\Omega_M = 0.3$, $\Omega_\Lambda = 0.7$ universe), instead of the $0.35 h^{-1} \text{Mpc}$ value used for the low-redshift slices.

Figure 4.4 shows the spatial distribution of red galaxies in the BTC image as

determined by the adaptive kernel estimator with $\sigma = 0.75 h^{-1}\text{Mpc}$. The known quasars in the field are indicated by circles labelled by the quasar redshift. The region shown has an apparent angular size $40.85 \times 35.12 \text{ arcmin}^2$ which corresponds to a proper angular size of $33.0 \times 28.4 h^{-1}\text{Mpc}$ at $z = 1.3$. Black/blue colours indicate low-density regions with less than 2 red galaxies per square arcmin, whilst red and white colours indicate high-density regions with more than 5 red galaxies per square arcmin. The positions of the high-redshift cluster candidates of Table 4.3 are indicated in black by their ID number.

The first thing that should be said about the red galaxy distribution is that on the very largest scales it is fairly homogeneous, that is to say that there are no apparent trends from one half of the field to the other, and no obvious structure due to the varying rms noise levels across the field. This is reassuring as it suggests that there are not significant numbers of sources in the subsample due to the larger photometric errors in the regions covered by fewer exposures, such as in the centre of the *I*-band image.

The second feature apparent in the red galaxy distribution is the number of high-density regions, that are apparent over the whole BTC field, and are candidate high-redshift galaxy clusters. It is these structures that have produced the strong clustering shown in the red galaxy two-point correlation function of Figure 4.3. There is no evidence for a single supercluster or filamentary structure as the cause of the clustering signal; the individual clusters appear separate and evenly distributed across the field. The most likely large-scale structure is a wavy filamentary structure across the top of the field, but even this is rather unconvincing.

There are also some notable low-density regions apparent in Figure 4.4. The low-density regions around the edges of the BTC field are merely boundary effects due to the smoothing of the density field, and are not physical voids. There are however several regions, well away from the field boundaries, that are almost devoid of red galaxies. Some, such as that apparent at $10^{\text{h}}47^{\text{m}}50^{\text{s}}$, $+05^{\circ}45'$, are the result of the halos of bright stars, but most appear to be simply regions devoid of red galaxies, the most notable being the one located to the south of the $z = 1.426$ quasar.

In total 77 maxima of the red galaxy surface density were found over the BTC field, of which 26 were found to have 6 or more red galaxies within 37.13 arcsec

ID	RA	Dec	ρ_{max}	S_{μ}	N(gals) _{red}		N(gals) _{I<23.5}	
	(J2000)	(J2000)	(/□")		(^a)	(^b)	(^a)	(^b)
21	10:47:22.5	+05:23:51	20.41	21.33	18 (16)	51 (30)	48 (27)	285 (97)
32	10:47:41.8	+05:29:15	9.05	10.61	12 (10)	35 (14)	26 (5)	185 (-3)
70	10:48:24.9	+05:44:50	9.13	10.50	14 (12)	37 (16)	38 (17)	232 (44)
20	10:46:28.3	+05:23:48	6.77	8.96	11 (9)	29 (8)	30 (9)	183 (-5)
60	10:46:56.9	+05:42:35	6.77	8.40	11 (9)	46 (25)	27 (6)	190 (2)
71	10:48:08.4	+05:46:30	9.99	7.79	10 (8)	46 (25)	32 (11)	230 (42)
75	10:47:07.9	+05:47:47	5.32	7.19	12 (10)	29 (8)	35 (14)	157 (-31)
15	10:48:31.4	+05:23:06	8.26	6.56	13 (11)	41 (20)	33 (12)	264 (76)
13	10:46:33.9	+05:21:21	6.55	6.51	10 (8)	37 (16)	34 (13)	231 (43)
52	10:46:37.3	+05:40:09	5.85	6.44	6 (4)	38 (17)	29 (8)	233 (45)
35	10:47:20.4	+05:30:42	6.53	6.13	9 (7)	30 (9)	40 (18)	207 (19)
39	10:46:38.1	+05:33:20	5.54	5.83	9 (7)	35 (14)	35 (14)	221 (33)
11	10:46:11.2	+05:21:24	6.45	5.45	12 (10)	38 (17)	30 (8)	226 (38)
73	10:46:57.5	+05:46:19	5.90	5.38	10 (8)	29 (8)	26 (5)	165 (-23)
50	10:48:14.3	+05:37:49	4.87	5.03	7 (5)	29 (8)	30 (9)	230 (42)
57	10:46:57.0	+05:39:15	5.46	4.68	11 (9)	36 (14)	40 (19)	213 (25)
53	10:47:01.8	+05:39:17	5.58	4.18	7 (5)	40 (19)	31 (10)	218 (30)
9	10:47:00.2	+05:20:14	5.61	4.01	9 (7)	36 (15)	27 (6)	194 (6)
66	10:47:24.3	+05:44:28	5.31	4.00	9 (7)	36 (15)	22 (1)	191 (3)
74	10:47:37.2	+05:46:24	6.45	3.58	9 (7)	35 (14)	32 (11)	220 (32)
18	10:48:16.7	+05:22:10	4.47	3.34	6 (4)	28 (7)	33 (12)	242 (54)
49	10:47:43.1	+05:37:47	4.65	3.28	8 (6)	31 (10)	28 (7)	218 (30)
64	10:47:07.4	+05:42:32	4.74	1.83	8 (6)	43 (22)	36 (15)	201 (13)
67	10:46:21.5	+05:43:12	7.89	1.30	10 (8)	39 (18)	23 (2)	190 (2)
3	10:48:04.0	+05:16:05	3.98	-0.01	9 (7)	26 (5)	37 (16)	202 (14)
5	10:47:28.7	+05:17:04	5.25	-7.95	10 (8)	28 (7)	33 (12)	181 (-7)

^a total (and excess) galaxies within $500 h^{-1}$ kpc (at $z = 1.3$) of the cluster centre

^b total (and excess) galaxies within $1.5 h^{-1}$ Mpc (at $z = 1.3$) of the cluster centre

Table 4.3: High-redshift cluster candidates in the BTC field.

($500 h^{-1}\text{kpc}$ at $z = 1.3$), corresponding to a 2σ excess. The properties of the most significant high-redshift cluster candidates in the BTC field are shown in Table 4.3.

The first column indicates the ID number given to the cluster candidate by the cluster finding algorithm, and is used to label each candidate in Figure 4.4. The next two columns give the Right Ascension and Declination of each density maximum, and the next column gives the red galaxy surface density at that point. S_μ is the significance of the cluster as determined from the using the formulae described in the previous chapter with the background kernel width, $\sigma_0 = \sigma = 750 h^{-1}\text{kpc}$. The final columns give the number of red and $I < 23.5$ galaxies within 37.13arcsec ($500 h^{-1}\text{kpc}$ at $z = 1.3$) and 111.39arcsec ($1.5 h^{-1}\text{Mpc}$), with the excess given in parentheses.

The background number of red and $I < 23.5$ galaxies for each column is taken to be the modal number of galaxies within $100\,000$ circular subfields of the corresponding radius positioned at random within the BTC field. The red galaxy background counts were found to be 1.81 ± 2.05 and 20.5 ± 7.4 for the $500 h^{-1}\text{kpc}$ and $1.5 h^{-1}\text{Mpc}$ circular regions, resulting in 3σ significance levels of 8 and 42 red galaxies respectively. For the $I < 23.5$ galaxies, the background counts were found to be 20.5 ± 5.9 and 188 ± 22 for $500 h^{-1}\text{kpc}$ and $1.5 h^{-1}\text{Mpc}$ circular regions, with corresponding 3σ significance levels of 38 and 254 galaxies.

The most significant density maximum by some considerable margin is #21, in the bottom-centre of Figure 4.4, which has a maximal density more than twice that found anywhere else in the field, and has highly significant excesses ($> 3\sigma$) of red and $I < 23.5$ galaxies within both $500 h^{-1}\text{kpc}$ and $1.5 h^{-1}\text{Mpc}$ of the cluster centre.

The next most significant cluster candidates appear to be the three density maxima (#11, 13 and 20) in the lower-left corner near to the $z = 1.426$ quasar, the extended clustering around the $z = 1.226$ quasar (comprising density maxima #53, 57, 60, and 64), the two density maxima (#70 and 71) in the upper-right corner, and density maximum #15 in the lower-right corner.

The fact that three out of the five most significant cluster candidates show signs of substructure, even though the galaxy surface density has been smoothed on $750 h^{-1}\text{kpc}$ scales, suggests that galaxy clustering at these high redshifts is much more amorphous, with clusters still being built up from the progressive coalescence

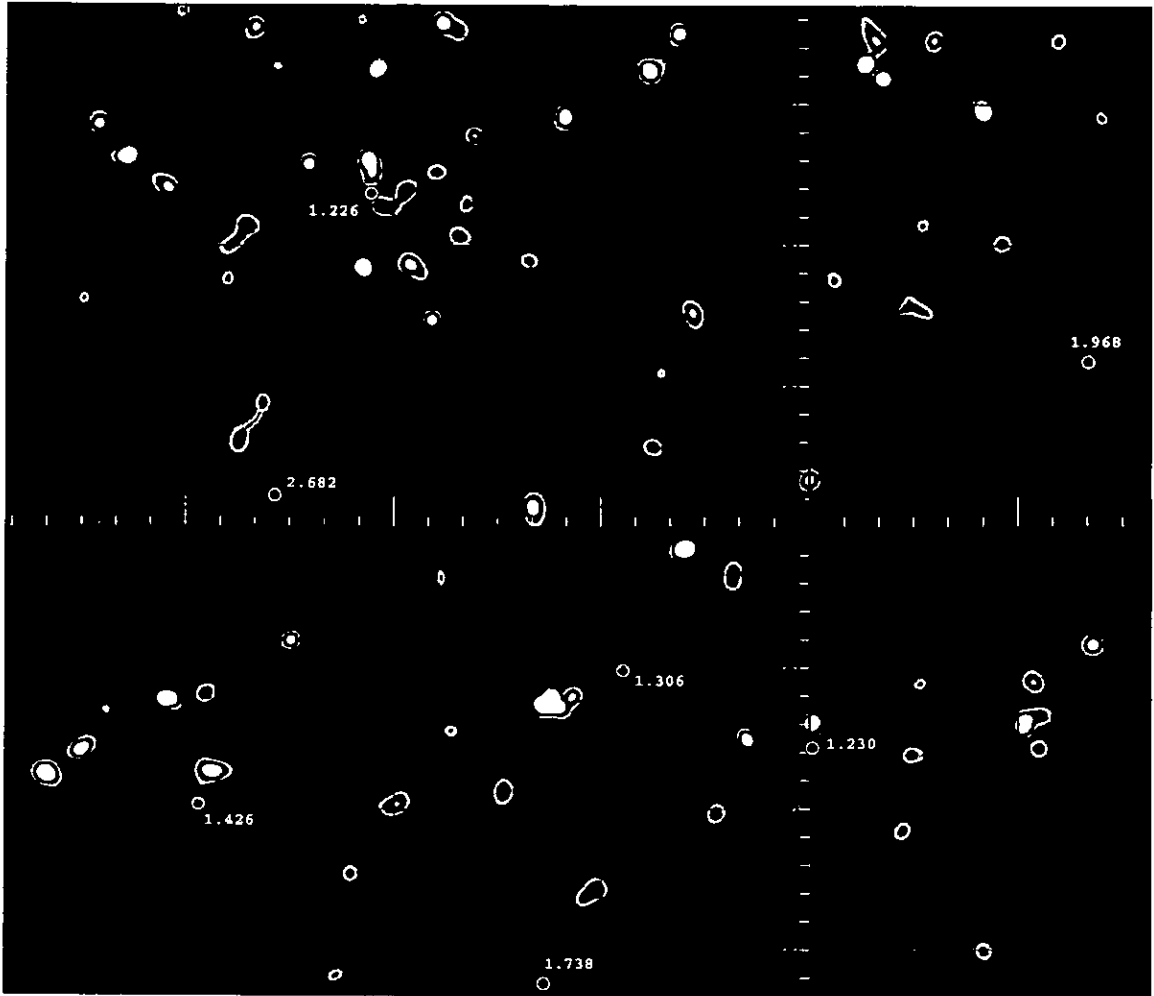


Figure 4.5: The spatial distribution of red galaxies in the BTC images. The galaxy surface density is estimated using the adaptive kernel estimator with $\sigma = 0.35 h^{-1}\text{Mpc}$. The low-density regions are indicated by black and blue colours, whilst the high-density regions are indicated by red and white colours. Each of the known quasars in the field is indicated by a black/white circle labelled by the quasar redshift. The region shown corresponds to a proper size of $33.0 \times 28.4 h^{-1}\text{Mpc}$ at $z = 1.3$.

of sub-clusters. This picture is confirmed if the surface density of red galaxies is re-estimated using kernels of mean width $\sigma = 0.35 h^{-1}\text{Mpc}$, the same width as used for the low-redshift slices. The density map of red galaxies in the BTC field as re-determined using this narrower kernel is shown in Figure 4.5. Many of the significant clusters which appeared as single density maxima in Figure 4.4 have been resolved into two or more components. The cluster candidate associated with the single density maximum #15 in Figure 4.4, appears now to be made up of three subclusters, as does density maximum #71.

Three of the five most significant cluster candidates are also located nearby

quasars. The most significant cluster candidate #21 is 170 arcsec ($2.3 h^{-1}\text{Mpc}$ at the quasar redshift) from the $z = 1.306$ LQG quasar, although the quasar itself appears in a low-density region. The $z = 1.226$ quasar appears to be fairly centrally located within an extended region of galaxy clustering (comprising density maxima #53, 57, 60 and 64), although it appears to lie between the density maxima, rather than associated with one particular peak. The $z = 1.426$ quasar appears to be associated with a region of galaxy clustering, lying on the edge of density maxima #13, although it should be remembered that this quasar is not considered to be a member of the quasar group. This certainly suggests that some of the galaxy clustering is directly associated with the quasars, and would appear to confirm the hypothesis that the excess of red galaxies is due to a large-scale structure associated with the LQG. In contrast, none of the higher redshift quasars ($z = 1.738$, $z = 1.968$ and $z = 2.682$) appears to be associated with any galaxy clustering. This is more likely to be due to the fact that the criteria used to select red galaxies is not efficient at identifying galaxies at such high redshifts, rather than their having poor environments.

The galaxy environments of each of the quasars will be examined in detail in later sections and the next two chapters, but first the properties of the two other significant cluster candidates will be examined, firstly the clustering associated with the density maxima #70 and 71, and secondly the clustering associated with density maximum #21.

4.6 Galaxy Clustering Around Density Maxima #70 and #71

The two density maxima #70 and 71 of Table 4.3 are among the most significant cluster candidates across the BTC field, and as they are separated by just 4.4 arcmin ($3.56 h^{-1}\text{Mpc}$ at $z = 1.3$) it appears likely that they are physically related. Both maxima are manifested by large excesses of both red and $I < 23.5$ galaxies within $1.5 h^{-1}\text{Mpc}$, confirming that they are likely to be real high-redshift clusters. Indeed the combined excesses are 41 red and 86 $I < 23.5$ galaxies within $1.5 h^{-1}\text{Mpc}$ of either maxima.

Figure 4.6 shows a $6.6 \times 4.6 \text{ arcmin}^2$ (corresponding to $5.3 \times 3.7 h^{-1}\text{Mpc}$ at

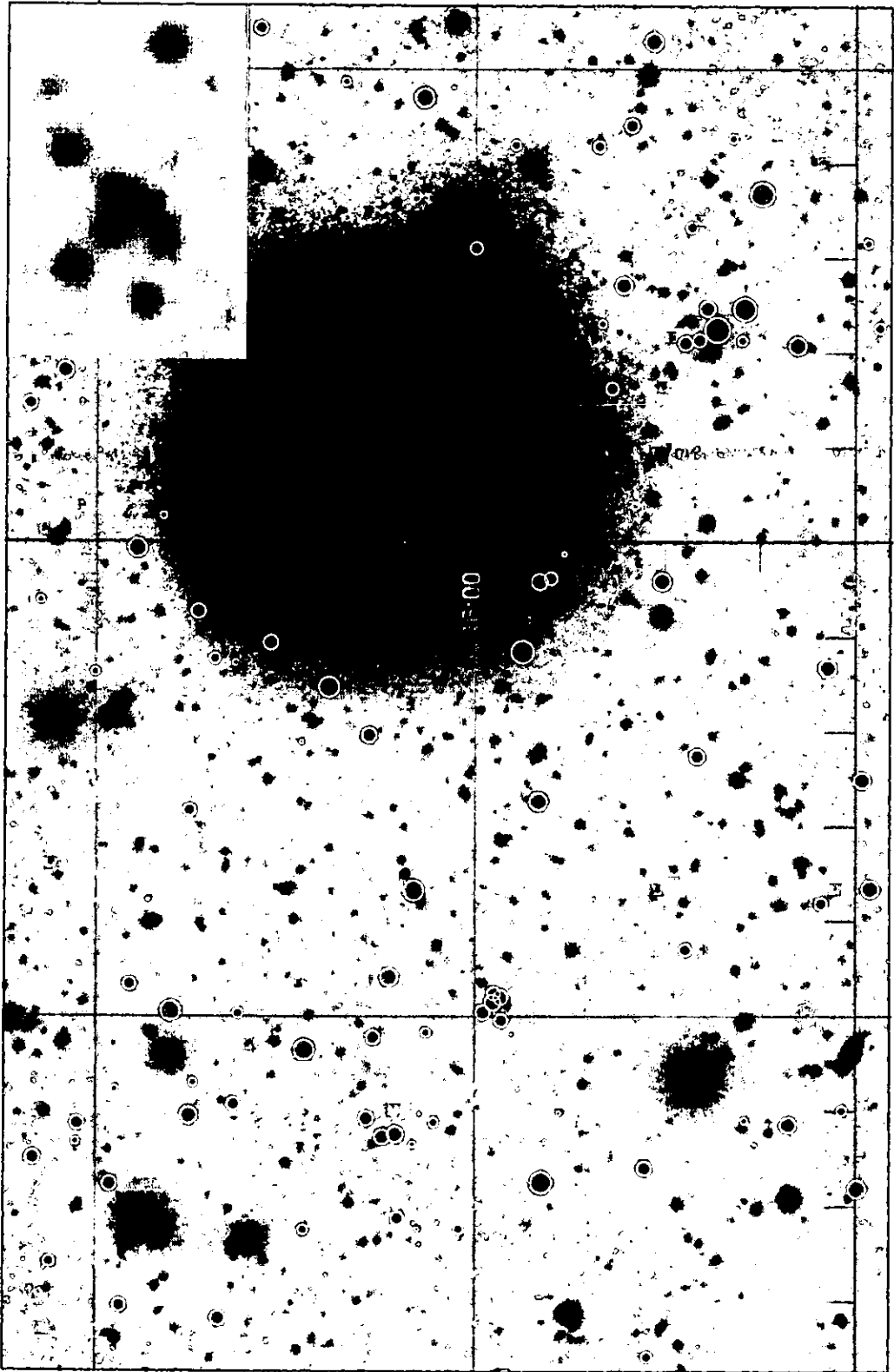


Figure 4.6: *I*-band image of a $6.6 \times 4.6 \text{ arcmin}^2$ ($5.3 \times 3.7 h^{-1} \text{ Mpc}$ at $z = 1.3$) region around the high-redshift cluster candidates #70 and 71. Red galaxies detected in both *V* and *I* images are indicated by yellow circles whose radii indicate the I_{total} magnitude. Red galaxies detected in the *I* image only are indicated by red squares. The inset shows an expanded view of the dense group of galaxies at the core of cluster candidate #71.

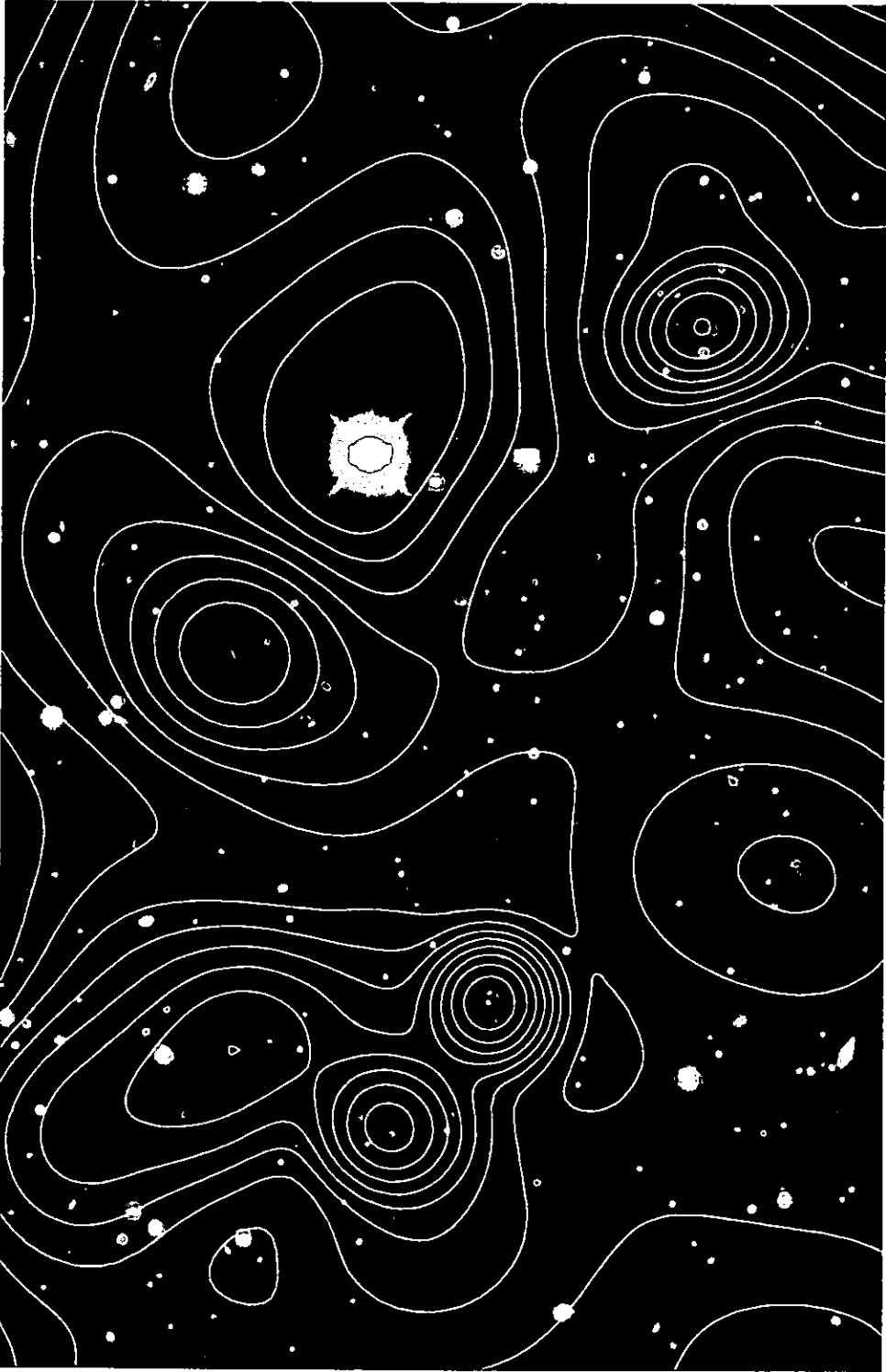


Figure 4.7: False colour image of the region around the high-redshift cluster candidates #70 (top-right) and #71 (bottom-centre), overlaid with contours showing the surface density of red galaxies. The galaxy density is estimated using the adaptive kernel estimator with $\sigma = 350 h^{-1} \text{kpc}$ at $z = 1.3$. The contours increase logarithmically with separation $\sqrt{2}$, with the yellow contour set to 2 red galaxies per arcmin^2 .

$z = 1.3$) I -band image of the region around the density maxima #70 and 71 in the red galaxy surface density. Red galaxies detected in both V and I images are indicated by yellow circles whose radii indicate the I_{total} magnitude. Red galaxies detected in the I image only are indicated by red squares.

Figure 4.7 shows the false colour image of the same region. It is overlaid with contours showing the surface density of red galaxies as estimated using the adaptive kernel estimator with $\sigma = 350 h^{-1} \text{kpc}$ and taken from the corresponding region of Figure 4.5. The contours increase logarithmically with separation $\sqrt{2}$, with the yellow contour set to 2 galaxies per square arcmin, which is approximately the mean density across the whole BTC field.

Density maximum #70 can be seen as the single, compact peak in the top-right corner, whilst density maximum #71 can be seen as the triple-peaked structure in the lower-centre of the figure.

It is clear from the figures that the clusters are unfortunately close to one of the brightest stars in the BTC field, GSC00260-00481 with $m_B = 11.2$, $m_V = 10.0$. Its extensive halo in the I image meant that no source within 55 arcsec of it could be considered as a red galaxy, resulting in the low-density region centred on the star in Figure 4.7.

Both density maxima appear centred on compact groups of ≈ 6 red galaxies within a region $\lesssim 10$ arcsec across. Indeed the group of red galaxies which produces the most significant of the maxima of the triple-peaked structures are barely resolved by the I image (Figure 4.6-inset), being separated by $\approx 2-3$ arcsec ($11-17 h^{-1} \text{kpc}$ at $z = 1.3$). Each of the group members have $I \sim 21-22$, making them L^* galaxies for the redshift range probed. Given their relative proximity, and their early epoch, it seems likely that they will have merged in the intervening time between then and now, forming a single very massive and luminous galaxy, perhaps comparable to the cD galaxies observed at the present epoch. These galaxies are commonly found at the centres of rich clusters, and are thought to have been built into some of the most luminous and massive galaxies in the universe from the multiple merging and cannibalism of galaxies.

Beyond the two dense central cores, the remainder of the red galaxies appear to form a diffuse, extended distribution between the two clusters which suggests

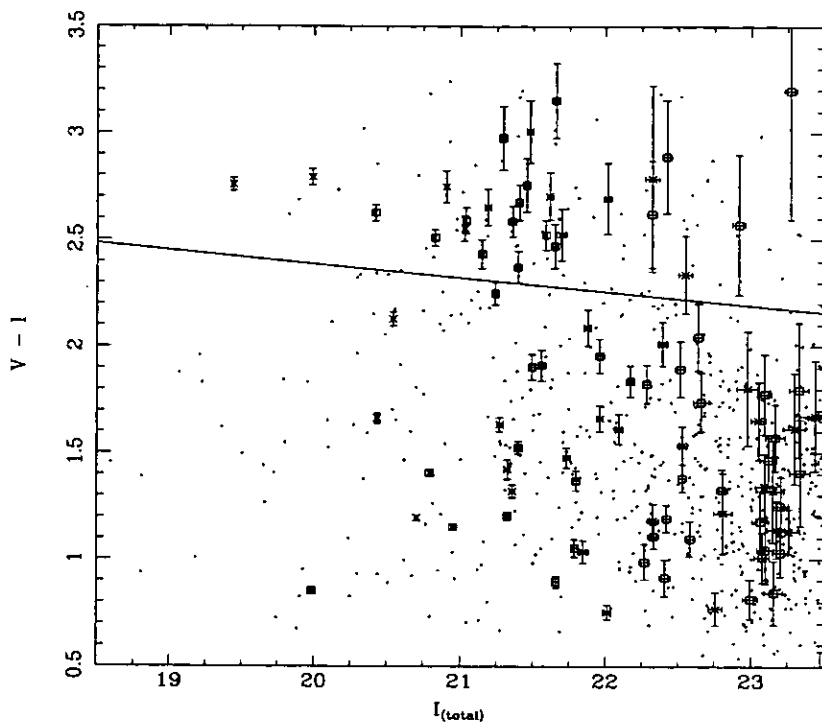


Figure 4.8: Colour-magnitude diagram of galaxies in the region covered by Figures 4.6 and 4.7. Galaxies within $500 h^{-1} \text{kpc}$ (at $z = 1.3$) of the density peak #70 are indicated by crosses, whilst galaxies within $500 h^{-1} \text{kpc}$ of the density maximum #71 are indicated by squares. The red galaxy colour-magnitude selection criterion is indicated by the near-horizontal line.

that the two clusters are physically related to one another. This appears to be confirmed by Figure 4.8 — the colour-magnitude diagram of all galaxies in the region covered by Figures 4.6 and 4.7. Galaxies within the central $500 h^{-1} \text{kpc}$ of the clusters marked by density maxima #70 and 71 are indicated by crosses and square-symbols respectively. There are no apparent differences between the colour distributions of the red galaxies associated with the two density maxima, and indeed when viewed as a single set, there is a suggestion of a red sequence at $2.6 \lesssim V - I \lesssim 2.8$.

4.7 The Galaxy Environment of the $z = 1.426$ Background Quasar

Although the $z = 1.426$ quasar may not be classed as a member of the Clowes-Campusano LQG, it is within the redshift range probed by the red galaxy selection criteria, and so any associated clustering should be detectable as an overdensity of

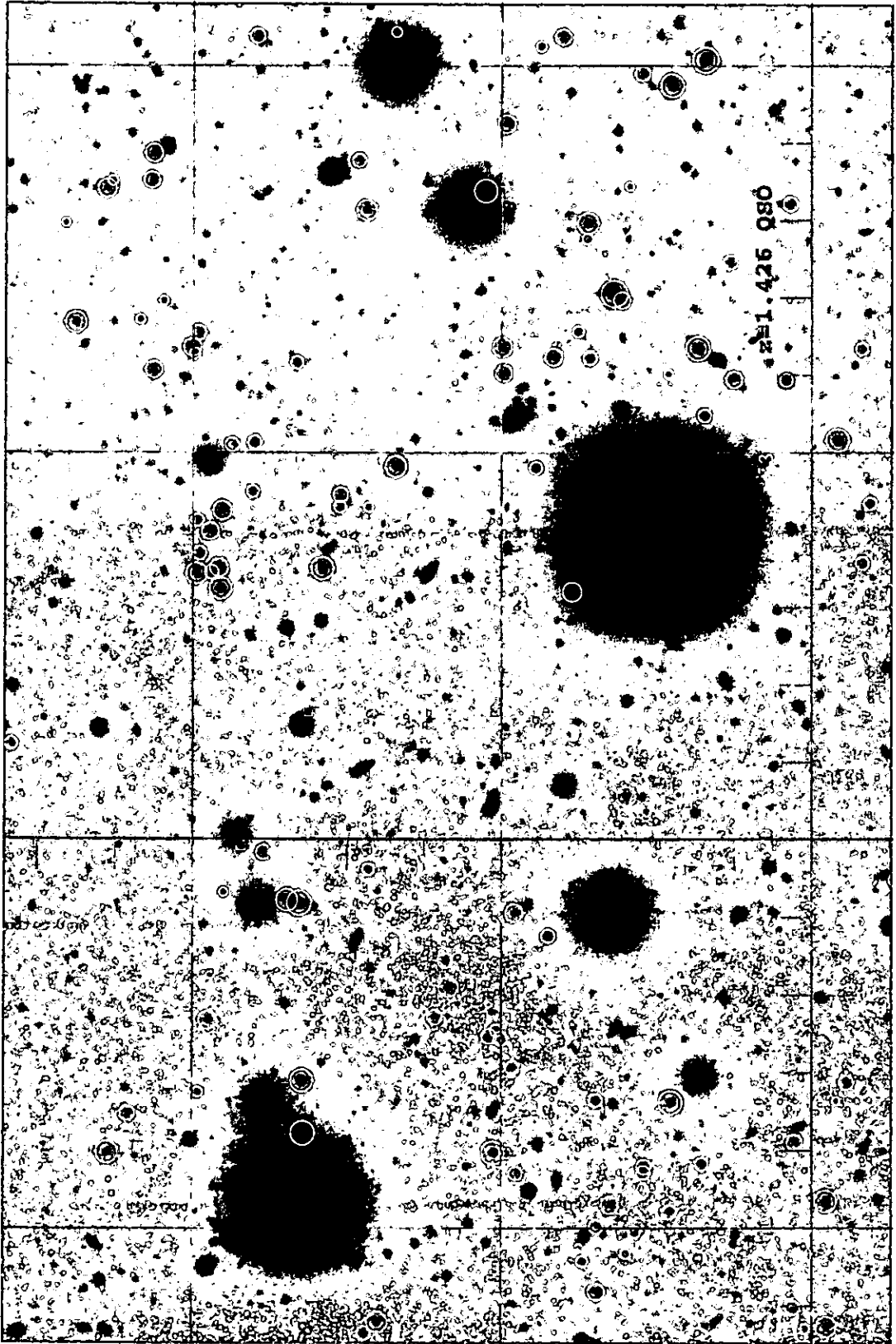


Figure 4.9: I -band image of an $8.6 \times 5.8 \text{ arcmin}^2$ ($7.4 \times 5.0 h^{-1} \text{ Mpc}$ at $z = 1.426$) region around the high-redshift cluster candidates #11, 13, and 20 in the vicinity of the $z = 1.426$ quasar. Red galaxies detected in both V and I images are indicated by yellow circles whose radii indicate the I_{total} magnitude. Red galaxies detected in the I image only are indicated by red squares.



Figure 4.10: False colour image of the region around the high-redshift cluster candidates #11 (bottom-centre), #13 (top-right), and #20 (centre-left) in the vicinity of the $z = 1.426$ quasar. It is overlaid with contours showing the surface density of red galaxies, which is estimated using the adaptive kernel estimator with $\sigma = 350 h^{-1} \text{kpc}$ at $z = 1.3$. The contours increase logarithmically with separation $\sqrt{2}$, with the yellow contour set to 2 red galaxies per arcmin^2 .

red galaxies in the vicinity of the quasar. Figure 4.4 indicates that there may be associated galaxy clustering, with three of the significant red galaxy density maxima of Table 4.3 located near the quasar.

Figure 4.9 shows a $8.6 \times 5.8 \text{ arcmin}^2$ (corresponding to $7.4 \times 5.0 h^{-1} \text{ Mpc}$ at $z = 1.426$) *I*-band image containing the $z = 1.426$ quasar and the three nearby density maxima, #11, 13, and 20, in the red galaxy surface density. Red galaxies detected in both *V* and *I* images are indicated by yellow circles whose radii indicate the I_{total} magnitude. Red galaxies detected in the *I* image only are indicated by red squares.

Figure 4.10 shows the false colour image of the same region. It is overlaid with contours showing the surface density of red galaxies as estimated using the adaptive kernel estimator with $\sigma = 350 h^{-1} \text{ kpc}$ and taken from the corresponding region of Figure 4.5. The contours increase logarithmically with separation $\sqrt{2}$, with the yellow contour set to 2 galaxies per square arcmin, which is approximately the mean density across the whole BTC field.

An inspection of Figures 4.9 and 4.10 suggests that the quasar is associated with the red galaxy clustering marked by density maximum #13 of Table 4.3. Not only is the quasar just 79 arcsec (corresponding to $1.13 h^{-1} \text{ Mpc}$ at the quasar redshift) from the cluster centre, but the red galaxy clustering appears from Figure 4.10 to extend in the direction of the quasar.

Just as in the previous section where there was clear substructure in the surface density of red galaxies, the red galaxy spatial distribution in the field of the $z = 1.426$ quasar appears bimodal. Only 170 arcsec ($2.4 h^{-1} \text{ Mpc}$ at $z = 1.426$) to the north-west of density maximum #13, is a second significant cluster of red galaxies, identified by density maximum #20. There are also a number of red galaxies in between the two density maxima, suggesting that the two are physically related. In a second similarity between this galaxy clustering and that of the previous section, at the core of density maximum #13 is a very compact group of 4 red galaxies within a few arcsec of one another.

The colour-magnitude diagram of galaxies in the $z = 1.426$ quasar field is shown in Figure 4.11 and lends further credence to the hypothesis that the clustering of red galaxies is associated with the quasar. Galaxies within $1 h^{-1} \text{ Mpc}$ of the density

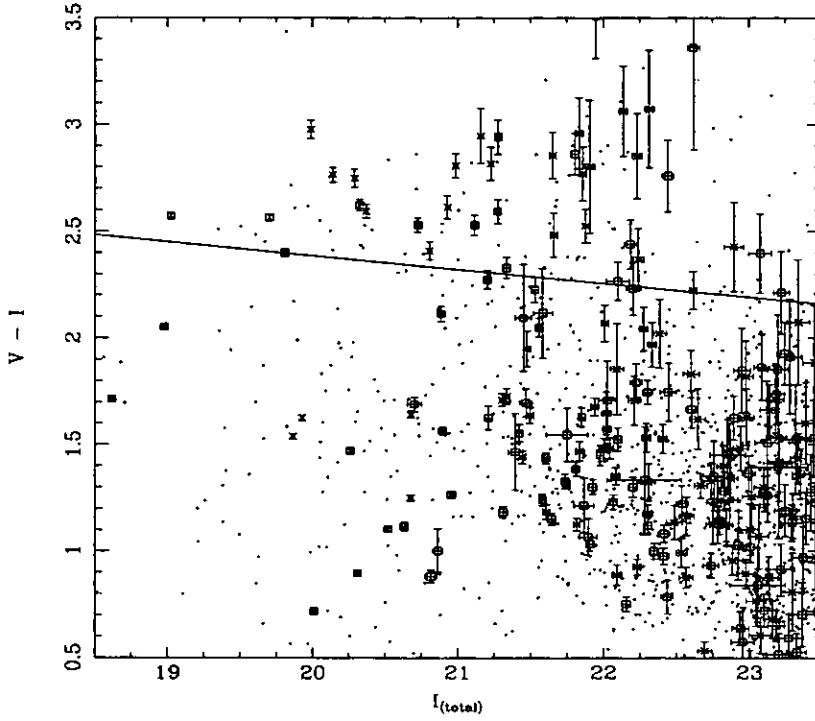


Figure 4.11: Colour-magnitude diagram of galaxies in the region covered by Figures 4.9 and 4.10. Galaxies within $1 h^{-1}\text{Mpc}$ (at $z = 1.3$) of the density peak #13 are indicated by crosses, whilst galaxies within $1 h^{-1}\text{Mpc}$ of the density maximum #20 are indicated by squares. The red galaxy colour-magnitude selection criterion is indicated by the near-horizontal line.

peaks #13 and 20 are indicated by crosses and square symbols respectively, with the remaining galaxies in the $8.6 \times 5.7 \text{ arcmin}^2$ region covered by Figures 4.9 and 4.10 indicated by single points. If the clustering of red galaxies is to be associated with the quasar, then the galaxies should be significantly redder than the $z = 0.5$ red sequence used as the red galaxy colour selection criterion. An inspection of Figure 4.1 indicates that such galaxies should have $V - I \simeq 3$. This is observed for the $z = 1.426$ quasar field, with in particular 13 galaxies within $1 h^{-1}\text{Mpc}$ of density maximum #13 having $V - I \simeq 3$ along with 3 from cluster #20, and 15–20 from the remainder of the field, possibly combining to form a weak red sequence.

The galaxy environment of the $z = 1.426$ quasar appears rich, with the combined excess of red and $I < 23.5$ galaxies within $1.5 h^{-1}\text{Mpc}$ of either density maxima #13 or #20 being 24 and 38 respectively. Assuming that this clustering is indeed associated with the quasar, and hence at $z = 1.426$, then it means that any similar levels of clustering should be detected by this approach for the three LQG quasars

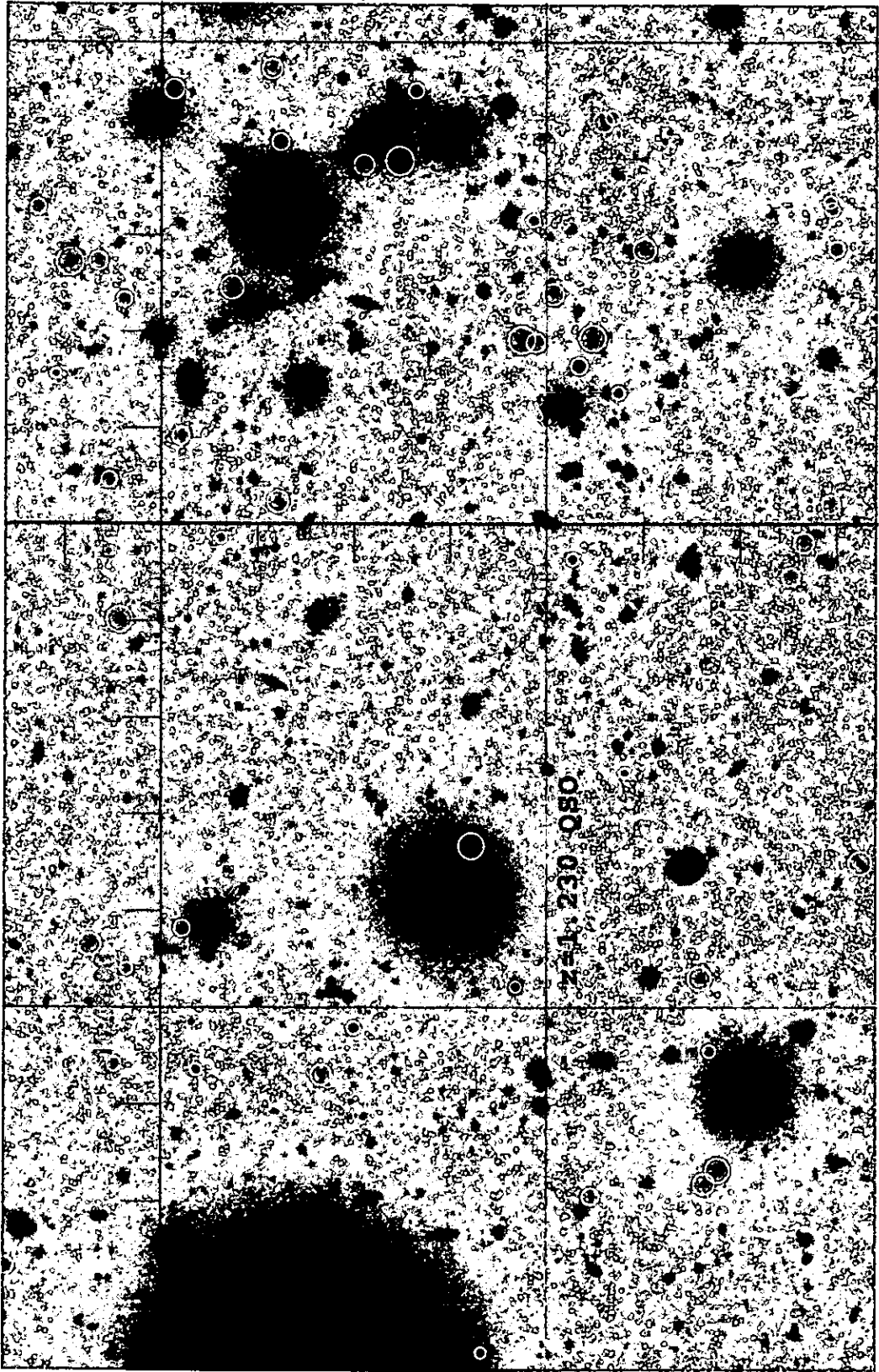


Figure 4.12: I -band image of a $7.0 \times 4.5 \text{ arcmin}^2$ ($5.5 \times 3.5 h^{-1} \text{ Mpc}$ at $z = 1.230$) field containing the $z = 1.230$ LQG quasar. Red galaxies detected in both V and I images are indicated by yellow circles whose radii indicate the I_{total} magnitude. Red galaxies detected in the I image only are indicated by red squares.



Figure 4.13: False colour image of the region around the $z = 1.230$ LQG quasar. It is overlaid with contours showing the surface density of red galaxies, which is estimated using the adaptive kernel estimator with $\sigma = 350 h^{-1} \text{kpc}$ at $z = 1.3$. The contours increase logarithmically with separation $\sqrt{2}$, with the yellow contour set to 2 red galaxies per arcmin^2 .

at slightly lower redshifts.

4.8 The Galaxy Environment of the $z = 1.230$ LQG Quasar

An inspection of Figure 4.4 finds little evidence for galaxy clustering associated with the $z = 1.230$ LQG quasar, with only a weak overdensity of red galaxies apparent 1–2 arcmin to the north. This appears confirmed by the higher resolution of Figure 4.5 which suggests that the overdensity is due to a poor, compact group of galaxies.

Figure 4.12 shows a 7.0×4.5 arcmin² (corresponding to $5.5 \times 3.5 h^{-1}$ Mpc at $z = 1.230$) *I*-band image containing the $z = 1.230$ LQG quasar, with the red square- and yellow circular-symbols indicating the positions of red galaxies as in Figures 4.6 and 4.9.

Figure 4.13 shows the false colour image of the same region, with the surface density of red galaxies indicated by contours as in Figures 4.7 and 4.10.

It is apparent from the two figures that the weak overdensity apparent in Figures 4.4 and 4.5 is due to a compact group of just five faint red galaxies located 1 arcmin to the north of the quasar. There is no evidence that the quasar lies in anything but an unremarkable field region, with no sign of even a single L^* class galaxy associated with the quasar (not including the host galaxy). The nearest clustering of red galaxies is the amorphous, extended clustering apparent 4–5 arcmin ($3\text{--}4 h^{-1}$ Mpc at $z = 1.230$) to the east of the quasar in Figures 4.12 and 4.13.

4.9 The Galaxy Environment of the $z = 1.306$ LQG Quasar

Figures 4.4 and 4.5 suggest the possibility of a rich galaxy cluster associated with the $z = 1.306$ LQG quasar, with the most significant density maximum #21 located just 165 arcsec to the west of the quasar. However at the quasar redshift this corresponds to a distance of $2.24 h^{-1}$ Mpc, and the quasar itself appears to lie in a low-density

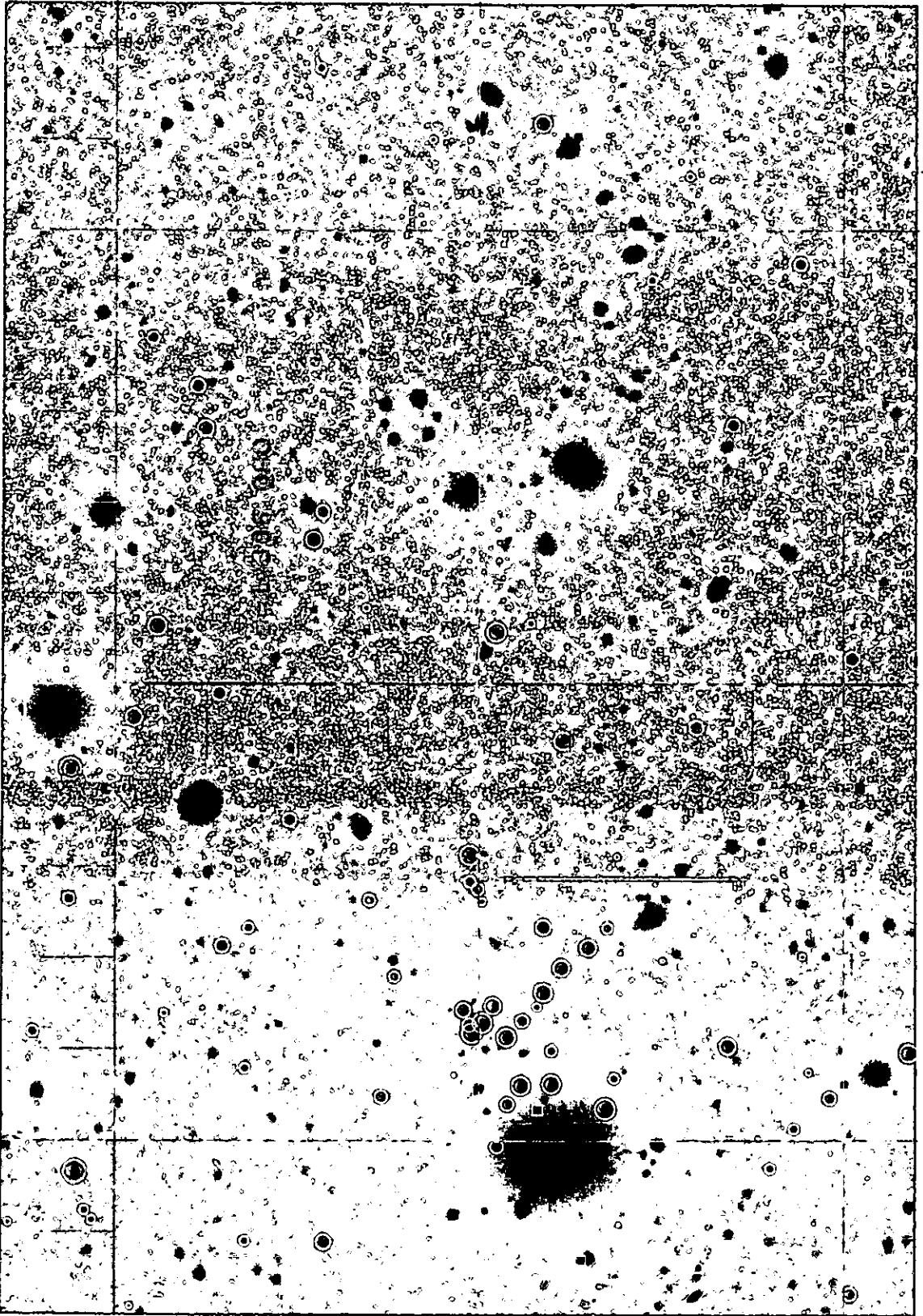


Figure 4.14: I -band image of the $7.2 \times 5.1 \text{ arcmin}^2$ ($5.8 \times 4.1 h^{-1} \text{ Mpc}$ at $z = 1.306$) region around the $z = 1.306$ LQG quasar and the high-redshift cluster candidate #21. Red galaxies detected in both V and I images are indicated by yellow circles whose radii indicate the I_{total} magnitude. Red galaxies detected in the I image only are indicated by red squares.



Figure 4.15: False colour image of the region around the $z = 1.306$ LQG quasar and the high-redshift cluster candidate #21. Overlaid is a contour map showing the surface density of red galaxies, which is estimated using the adaptive kernel estimator with $\sigma = 350 h^{-1}\text{kpc}$ at $z = 1.3$. The contours increase logarithmically with separation $\sqrt{2}$, with the yellow contour set to 2 red galaxies per arcmin^2 .

region, and so even if the galaxy clustering is at the quasar redshift, the quasar and the galaxy clustering may not be directly related.

Figure 4.14 shows a 7.2×5.1 arcmin² (corresponding to $5.8 \times 4.1 h^{-1}$ Mpc at $z = 1.306$) *I*-band image containing both the $z = 1.306$ quasar and the galaxy clustering associated with density maximum #21, with the red square- and yellow circular-symbols indicating the positions of red galaxies as before.

Figure 4.15 shows the false colour image of the same region, with the surface density of red galaxies indicated by contours as in Figure 4.7.

It is apparent that the density maximum #21 is caused by a compact, dense cluster of 10–15 red galaxies within 30 arcsec, with a comparable number of bluer galaxies interspersed. It is perhaps the most striking region of the whole BTC image, with a central galaxy density significantly higher than anywhere else in the field. For this reason, and also due to its proximity to the LQG quasar, follow-up *K*-band imaging was obtained in May 2000. The results and analysis of these observations are described in Chapter 6, and so the discussion here will be limited to results based solely on the optical data.

The galaxy clustering associated with density maximum #21 appears extended beyond the central, compact core, and is highly significant with excesses of 51 red and 97 $I < 23.5$ galaxies within $1.5 h^{-1}$ Mpc (at $z = 1.3$), indicating a rich high-redshift cluster.

The quasar, in contrast, appears to reside in a relatively poor environment with no excess of red or $I < 23.5$ galaxies within $1.5 h^{-1}$ Mpc observed.

4.10 The Galaxy Environment of the $z = 1.226$ LQG Quasar

Figures 4.4 and 4.5 suggest that the $z = 1.226$ LQG quasar is the most likely of the quasars to be associated with a rich galaxy cluster, it being located within a region of extended clustering of red galaxies.

Figure 4.16 shows a 6.8×5.7 arcmin² (corresponding to $5.3 \times 4.3 h^{-1}$ Mpc at $z = 1.226$) *I*-band image containing the $z = 1.226$ quasar and the extended clustering comprising density maxima #53, 57, 60 and 64 in the red galaxy surface density.

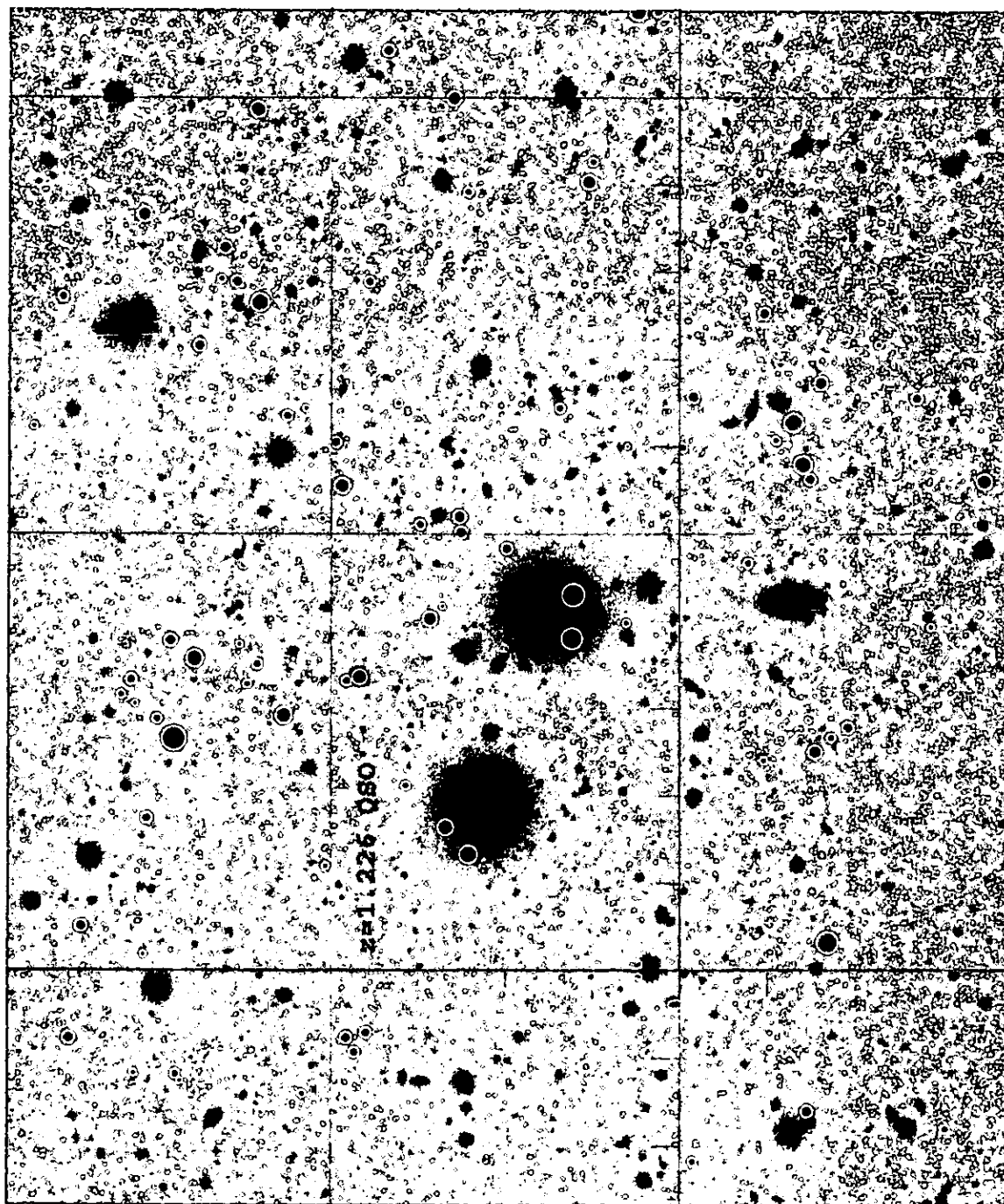


Figure 4.16: I -band image of the $6.8 \times 5.7 \text{ arcmin}^2$ ($5.3 \times 4.3 h^{-1} \text{ Mpc}$ at $z = 1.226$) region of extended red galaxy clustering around the $z = 1.226$ LQG quasar, comprising density maxima #53, 57, 60 and 64. Red galaxies detected in both V and I images are indicated by yellow circles whose radii indicate the I_{total} magnitude. Red galaxies detected in the I image only are indicated by red squares.

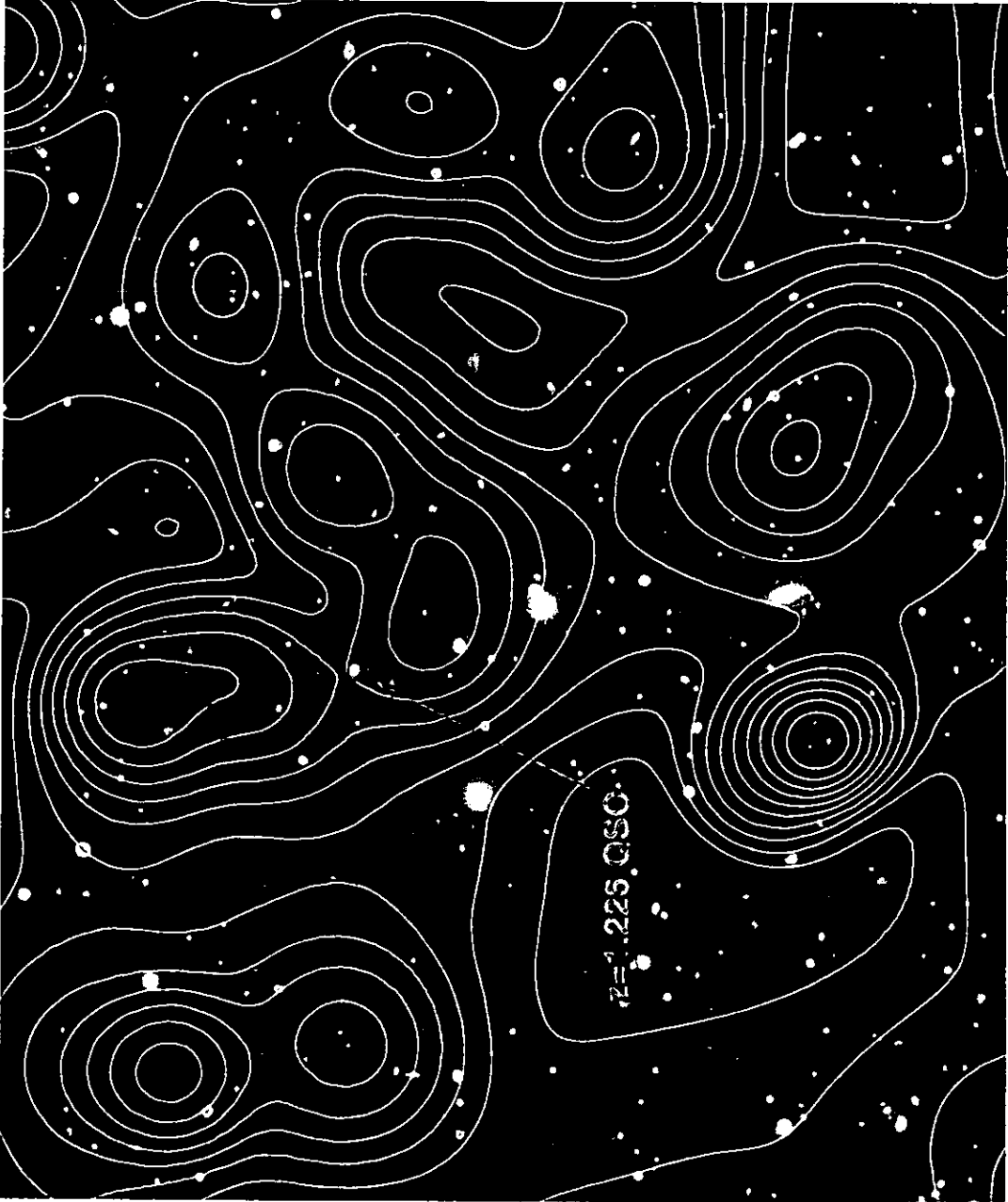


Figure 4.17: False colour image of the region around the $z = 1.226$ LQG quasar, showing the extended clustering associated with density maxima #53, 57, 60 and 64. Overlaid is a contour map showing the surface density of red galaxies, which is estimated using the adaptive kernel estimator with $\sigma = 350 h^{-1} \text{kpc}$ at $z = 1.3$. The contours increase logarithmically with separation $\sqrt{2}$, with the yellow contour set to 2 red galaxies per arcmin^2 .

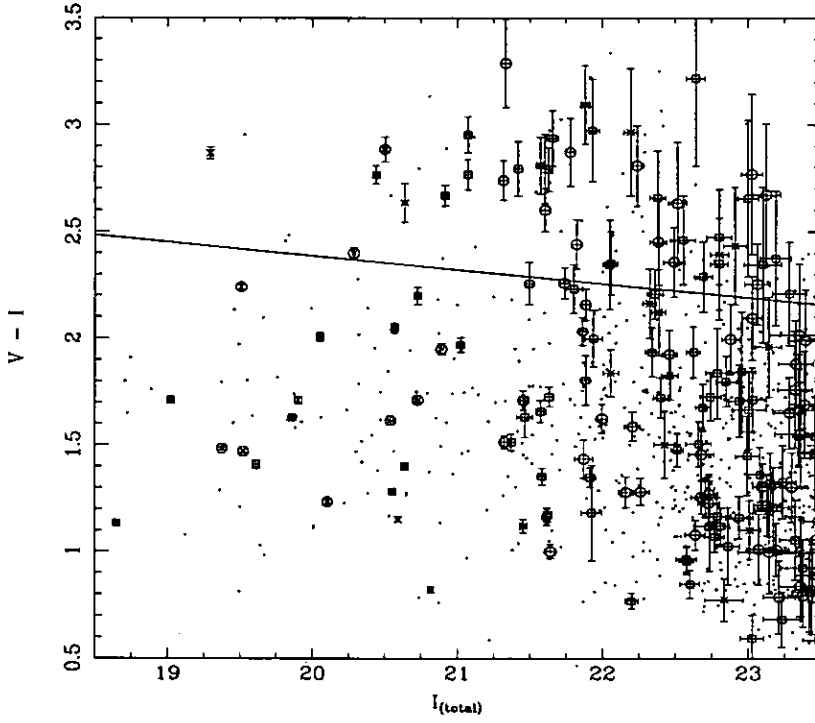


Figure 4.18: Colour-magnitude diagram of galaxies in the region covered by Figures 4.16 and 4.17. Galaxies within $500 h^{-1}\text{kpc}$ (at $z = 1.226$) of the density peak #64 are indicated by squares, galaxies within $500 h^{-1}\text{kpc}$ of the density maximum #60 are indicated by crosses, and galaxies within $500 h^{-1}\text{kpc}$ of the density maxima #53 and #57 are indicated by circles. The red galaxy colour-magnitude selection criterion is indicated by the near-horizontal line.

Red galaxies detected in both V and I images are indicated by yellow circles whose radii indicate the I_{total} magnitude. Red galaxies detected in the I image only are indicated by red squares.

Figure 4.17 shows the false colour image of the same region. It is overlaid with contours showing the surface density of red galaxies as estimated using the adaptive kernel estimator with $\sigma = 350 h^{-1}\text{kpc}$ and taken from the corresponding region of Figure 4.5. The contours increase logarithmically with separation $\sqrt{2}$, with the yellow contour set to 2 galaxies per square arcmin, which is approximately the mean density across the whole BTC field.

A significant number of red galaxies are apparent in the field around the $z = 1.226$ quasar, forming an amorphous and extended structure. There is circumstantial evidence that it is associated with the quasar in the form of a number of red galaxies within 5 arcsec of the quasar. It was because of these galaxies in close proximity to the quasar that it was considered the most likely of the three LQG quasars to be in

a rich environment, resulting in K imaging of being obtained at the 3.8-m United Kingdom Infra-Red Telescope (UKIRT) in March 1999. The results and analysis of this data are described in Chapter 5, and so the discussion here will be limited to the optical data.

The colour-magnitude diagram of galaxies in the 6.8×5.7 arcmin² region covered by Figures 4.16 and 4.17 is shown in Figure 4.18. Galaxies within $500 h^{-1}$ kpc (at $z = 1.226$) of the density peak #64 are indicated by squares, galaxies within $500 h^{-1}$ kpc of the density maximum #60 are indicated by crosses, and galaxies within $500 h^{-1}$ kpc of the density maxima #53 and #57 are indicated by circles. There are a significant number of galaxies with $2.7 \lesssim V - I \lesssim 3.0$, from each of the density maxima, suggesting that the clustering around each of the density maxima is associated, and may be at the quasar redshift.

Assuming the extended clustering is associated, the combined structure must have a considerable mass, comparable to that of the Coma cluster ($\simeq 6 \times 10^{14} M_{\odot}$), with an excess of 100–150 red galaxies (depending on the choice of background level) within 5 arcmin ($3.9 h^{-1}$ Mpc) of the quasar.

4.11 Comparison with Previous Studies

The most obvious result from this study of four quasars at $z \simeq 1.3$ is that they reside in a wide variety of galaxy environments: both the $z = 1.306$ and $z = 1.230$ LQGs appear to reside in poor environments, with no signs of galaxy clustering within $2 h^{-1}$ Mpc; the $z = 1.426$ quasar is located on the edge of a moderately-rich cluster; and the $z = 1.226$ quasar is within a region of extended galaxy clustering comprised of a number of sub-clusters, but rather than being located at one of the peaks of the red galaxy surface density, it appears to lie between two of the substructures.

In a comparable study of the galaxy environments of seven radio-loud quasars at $1.0 < z < 1.6$, Sánchez & González-Serrano (1999) find excesses of faint ($B > 22.5$ and $R > 22.0$) galaxies on scales of $r < 170$ and $r < 35$ arcsec around the quasars, whose numbers, magnitudes and angular extensions are compatible with being clusters of galaxies at the quasar redshifts. In particular, however, they find that the quasars are not located at the peaks of the density distribution, lying at a projected

distance of 40–100 arcsec from them, placing the quasars on the cluster *peripheries*.

The observation that those quasars which have associated galaxy clustering are located on the cluster peripheries rather than in the cluster cores, has important consequences for many of the previous studies of quasar galaxy environments. This is because the standard statistical approach used for examining quasar environments is the radial distribution of galaxies about the quasar, or equivalently, the two-point angular quasar-galaxy cross-correlation function, $\omega_{Qg}(\theta)$ (e.g. Hall & Green, 1998). Clearly the radial distribution of galaxies about a quasar will be significantly different if the quasar is located on the periphery of a cluster rather than its core, the mean distance to the galaxies will be increased, and as a result because the radial distribution averages over all angles the significance of the excess will be reduced greatly. An additional problem of quasars being located typically 40–100 arcsec from the cluster centre arises for many of the quasar environment studies as the fields observed are sufficiently small that a significant fraction of any associated galaxy clustering will be outside the field of view. The Hall & Green (1998) study has images of size $\lesssim 3 \times 3$ arcmin² centred on each of the quasars, and so for example would miss much of the clustering associated with the $z = 1.426$ quasar.

To demonstrate these problems, and to allow direct comparison with previous studies the radial distributions of red and $I < 23.5$ galaxies about the four $z \simeq 1.3$ quasars are shown in Figures 4.19 and 4.20.

Figure 4.19 shows that the clustering of red galaxies is most significant about the $z = 1.226$ quasar, which is expected given that the combined excess of red galaxies from the extended clustering is $\simeq 100$ –150, depending on the choice of background level. The signal is particularly high due to the central location of the quasar within the extended galaxy clustering, with high densities out to 90 arcsec, with a more extended distribution out to 200 arcsec and beyond.

Given the previous discussion it would be expected that the next most significant clustering signal in the radial distribution would be that of the $z = 1.426$ quasar due to its location on the periphery of a cluster of red galaxies. However, there is no significant difference in the red galaxy radial distributions about the $z = 1.426$ quasar and the $z = 1.230$ quasar, which, from the previous discussion, shows no sign of associated clustering. An excess of red galaxies is observed for $\theta < 120$ arcsec

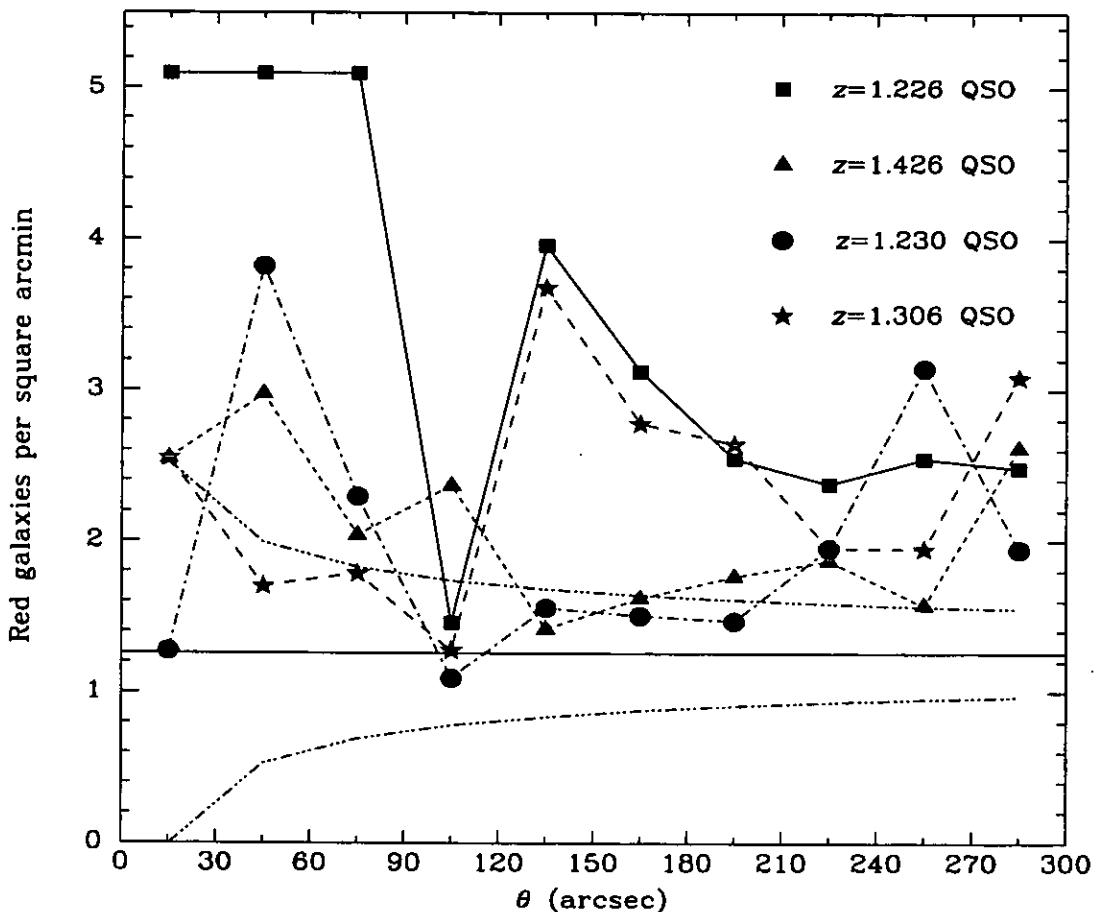


Figure 4.19: Radial distributions of red galaxies about each of the four $z \simeq 1.3$ quasars in bins of width 30 arcsec. The four radial distributions are indicated by red squares ($z = 1.226$ quasar), magenta triangles ($z = 1.426$ quasar), green circles ($z = 1.230$ quasar) and blue stars ($z = 1.306$ quasar). The mean red galaxy surface density (1.258 galaxies per square arcmin) of the EIS-DEEP HDF-South field is indicated by the black horizontal line, and the black dot-dashed curves indicate the 1σ errors for each bin.

around the $z = 1.426$ quasar, but it not as significant as would be expected. This is due to a combination of effects, firstly as the galaxy clustering is concentrated on one side of the quasar the galaxies are further from the quasar on average than if the quasar was centrally located, and they are shared between a larger number of bins. Secondly, on the opposite side of the quasar from the cluster is a region relatively devoid of red galaxies (Figure 4.5) which because the radial distribution averages over all angles, effectively cancels out the galaxy cluster.

The improvement in the clustering signal by considering red galaxies as against I -band selected galaxies is clear by comparison with Figure 4.20. Whereas for the

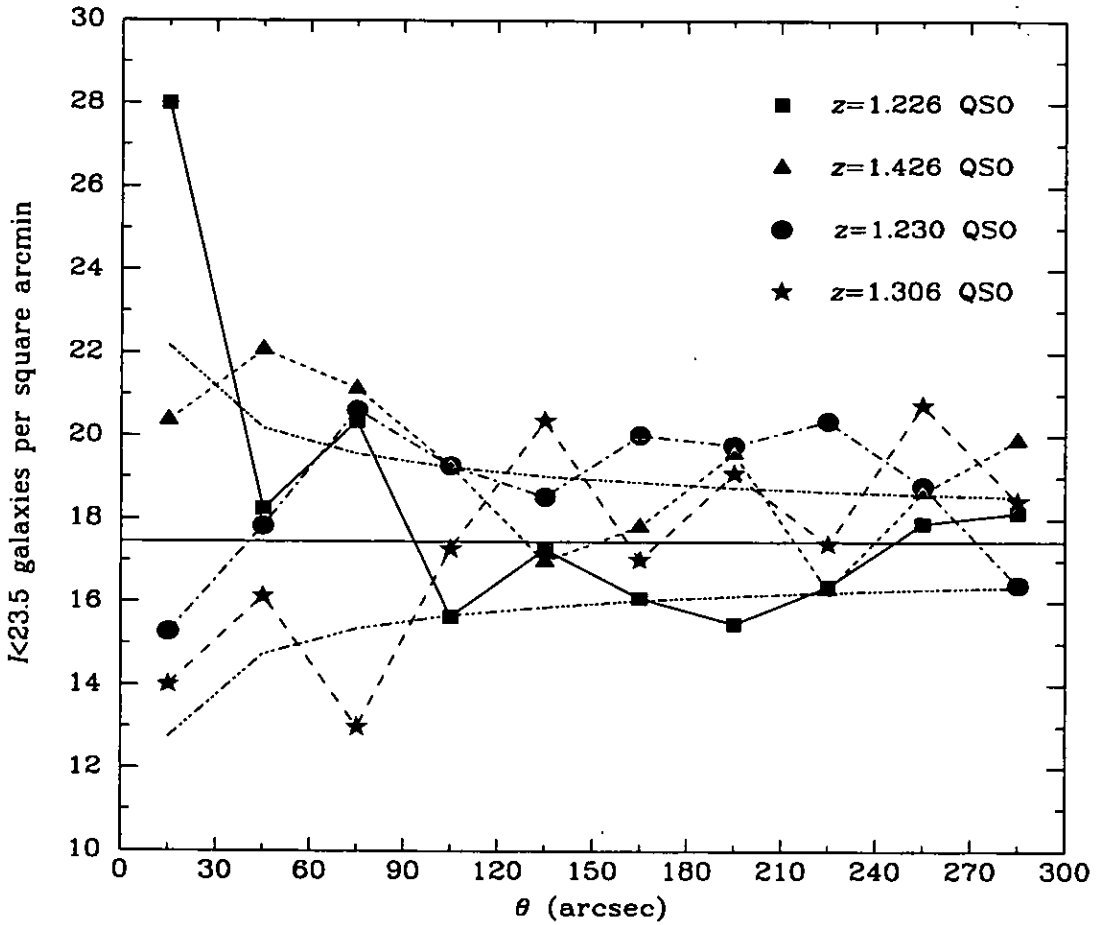


Figure 4.20: Radial distributions of $I < 23.5$ galaxies about each of the four $z \simeq 1.3$ quasars in bins of width 30 arcsec. The four radial distributions are indicated by red squares ($z = 1.226$ quasar), magenta triangles ($z = 1.426$ quasar), green circles ($z = 1.230$ quasar) and blue stars ($z = 1.306$ quasar). The mean $I < 23.5$ galaxy surface density determined from the remainder of the BTC field (17.452 galaxies per square arcmin) is indicated by the black horizontal line, and the black dot-dashed curves indicate the 1σ errors for each bin.

radial distribution of red galaxies about the $z = 1.226$ quasar a clustering signal is apparent both at $\theta < 90$ arcsec and $120 < \theta < 200$ arcsec scales, the radial distribution of $I < 23.5$ galaxies only shows a clustering signal at the shortest scales with $\theta < 30$ arcsec, and for $\theta \gtrsim 90$ arcsec there is actually a deficit of $I < 23.5$ galaxies. This appears due to an unfortunate coincidental lack of foreground bright galaxies in the same region, but it does indicate the necessity of colour-selection to identify high-redshift clusters, not only to remove foreground clusters, but also as in this case to remove foreground voids.

Hall & Green (1998) examined the galaxy environments of 31 radio-loud quasars

at $1 < z < 2$, and found them on average in moderately-rich environments. In particular they report excesses of $K \gtrsim 19$ galaxies on two spatial scales. One component is within 40 arcsec of the quasar, and is significant compared to the galaxy surface density at greater distances for the same fields. The other component is an extended overdensity at $\theta \approx 100$ arcsec, and is significant in comparison to field regions.

Sánchez & González-Serrano (1999) examined the galaxy environments of seven radio-loud quasars at $1.0 < z < 1.6$, and found excesses of faint galaxies ($B > 22.5$ and $R > 22.0$) on similar scales to those observed by Hall & Green (1998), with significant excesses within 35 arcsec of the quasars, and a more extended galaxy excess on scales out to 170 arcsec.

An examination of Figures 4.19 and 4.20 in conjunction with the known spatial distribution of red galaxies from Figures 4.10, 4.13, 4.15 and 4.17 suggests an explanation for the two spatial scales observed for the galaxy excesses.

Short-scale excesses are apparent for both the $z = 1.226$ and $z = 1.426$ quasars, and are due to both quasars being associated with galaxy clusters, although being located on the peripheries the signal is smeared out. The large-scale excesses are due to the fact that both the clusters that produce the short-scale excess are part of a large-scale structure. In the case of the $z = 1.226$ quasar, there is the filamentary structure marked by density maximum #64, plus the two clusters (#53 and #57) to the south of the quasar. In the case of the $z = 1.426$ quasar, there is the second cluster (#20) on the far side of the first. The large-scale excess is also partly due to the quasars being located on the cluster peripheries, as the signal from the cluster is smeared over scales reaching 100–150 arcsec.

4.12 Consequences for the Evolution of Galaxy Clusters

As discussed in Chapter 1, one of the primary aims for the identification and study of high-redshift clusters is to estimate the evolution of cluster abundances, from which Ω_M and Ω_Λ can be constrained. The growth of high-mass clusters depends strongly on cosmology, mainly Ω_M and σ_8 . In low-density models, density fluctuations evolve and freeze out at early times, thus producing little evolution to $z \simeq 1$,

whereas in an $\Omega_M = 1$ universe, the fluctuations only start growing recently producing strong evolution of cluster abundances. Indeed by $z = 1$ the number density of $M(r < 1 h^{-1} \text{Mpc}) \geq 1.5 \times 10^{14} h^{-1} M_\odot$ clusters (corresponding to a total cluster luminosity of $L \geq 50 L^*$) is of an order of magnitude greater in an $\Omega_M = 0.4, \Omega_\Lambda = 0.6$ model than in an $\Omega_M = 1$ model.

From the whole BTC image, there are four excellent high-redshift cluster candidates discussed in the previous section, each of which can be considered to have $M > 1.5 \times 10^{14} h^{-1} M_\odot$ from the combined luminosity of its member red galaxies alone ($L \gtrsim 50 L^*$). Out of the four cluster candidates: the extended clustering around the $z = 1.226$ LQG quasar will be shown in Chapter five to be associated with the quasar, and so at $z > 1$; the clustering located near the $z = 1.426$ quasar is made up of galaxies with similar $V - I$ colours to the previous cluster, and so is likely to be at a similar redshift, and presumably associated with the quasar; the clustering manifested by density maximum #21 will be shown in Chapter six to be at $z \simeq 0.8 \pm 0.1$; and the clustering associated with density maxima #70 and #71 could be either above or below a redshift of unity. To be conservative as regards examining the evolution of cluster abundances, just the one cluster associated with the $z = 1.226$ quasar is classed as $z > 1.0$, with the remainder placed at $0.5 < z < 1.0$, although it should be stated once again that this does not imply that they are at these redshifts. In addition to the four high-redshift clusters, there is the low-redshift cluster candidate at $z = 0.26$, giving one $z < 0.5$ cluster as a conservative level.

By determining the volumes probed by the BTC field for each of the redshift bins $z < 0.5$, $0.5 < z < 1.0$, and $1.0 < z < 1.5$, for differing cosmological models, a conservative cluster number density can be determined, and compared with the cluster abundance evolution models of Bahcall et al. (1997b). Two cosmological models are considered, the Standard Cold Dark Matter (SCDM; $\Omega_M = 1$), and a low-density, Λ -dominated CDM model (LCDM; $\Omega_M = 0.4, \Omega_\Lambda = 0.6$). Table 4.4 shows the cluster abundances for the BTC field based on the conservative cluster redshift distribution discussed previously for the different volumes probed by the BTC field in the two cosmological models.

Figure 4.21 compares the observed cluster abundances as a function of redshift for clusters with mass $M(r < 1.0 h^{-1} \text{Mpc}) \geq 1.5 \times 10^{14} h^{-1} M_\odot$ with those predicted for

Redshift	Clusters	$\rho(h^3 \text{ Mpc}^{-3})$	$\rho(h^3 \text{ Mpc}^{-3})$
Range	$M(r < 1.0 h^{-1} \text{ Mpc}) >$ $1.5 \times 10^{14} h^{-1} M_{\odot}$	$(\Omega_M = 1,$ $\Omega_{\Lambda} = 0)$	$(\Omega_M = 0.4,$ $\Omega_{\Lambda} = 0.6)$
$z < 0.5$	1	1.87×10^{-5}	1.20×10^{-5}
$0.5 < z < 1.0$	3	1.83×10^{-5}	8.97×10^{-6}
$1.0 < z < 1.5$	1	4.72×10^{-6}	1.98×10^{-6}

Table 4.4: Cluster abundances as a function of redshift for the BTC field.

a number of cosmological models by numerical simulations (Bahcall et al., 1997b). The data are from the Palomar Distant Cluster Survey (PDCS; Postman et al., 1996) indicated by the black symbols, and the BTC field which are indicated by the red symbols. The different symbols represent the observed number densities for $\Omega_M = 1$ (filled circles), $\Omega_M = 0.35, \Omega_{\Lambda} = 0$ (open circles), and $\Omega_M = 0.4, \Omega_{\Lambda} = 0.6$ (filled triangles) cosmologies.

The evolution of the cluster abundance with redshift has been modelled by Bahcall et al. (1997b) for four different cosmologies using large-scale numerical simulations. The different cosmological models considered are: a biased Standard Cold Dark Matter (SCDM) model with $\Omega_M = 1$; a low-density, Λ -dominated CDM model (LCDM) with $\Omega_M = 0.4, \Omega_{\Lambda} = 0.6$; a low-density, open CDM model (OCDM) with $\Omega_M = 0.35, \Omega_{\Lambda} = 0$; and a mixed, hot and cold dark matter model (MDM) with $\Omega_M = 1, \Omega_{\text{HDM}} = 0.3$. Each of the models is constrained to be consistent with the present-day abundance of rich clusters by adjusting $\sigma_8(\text{mass})$, the fractional rms mass fluctuations in a sphere of radius $8 h^{-1} \text{ Mpc}$, to satisfy $\sigma_8 \Omega_M^{0.5} \simeq 0.5 \pm 0.05$ (Henry & Arnaud, 1991; Viana & Liddle, 1996). The parameter σ_8 effectively measures the bias in the distribution of mass versus light observed as galaxies, since $\sigma_8(\text{galaxies}) \simeq 1$. Hence the SCDM model which has $\sigma_8 = 0.5$ is highly biased, with mass distributed more widely than light. All models except for the biased SCDM model are also consistent with the COBE microwave background fluctuations.

Only a mild negative evolution of cluster abundances with redshift is observed for both sets of data, in excellent agreement with the low-density bias-free models (OCDM, LCDM). They are highly inconsistent with the biased high-density models (SCDM), with the observed number of clusters an order of magnitude greater than

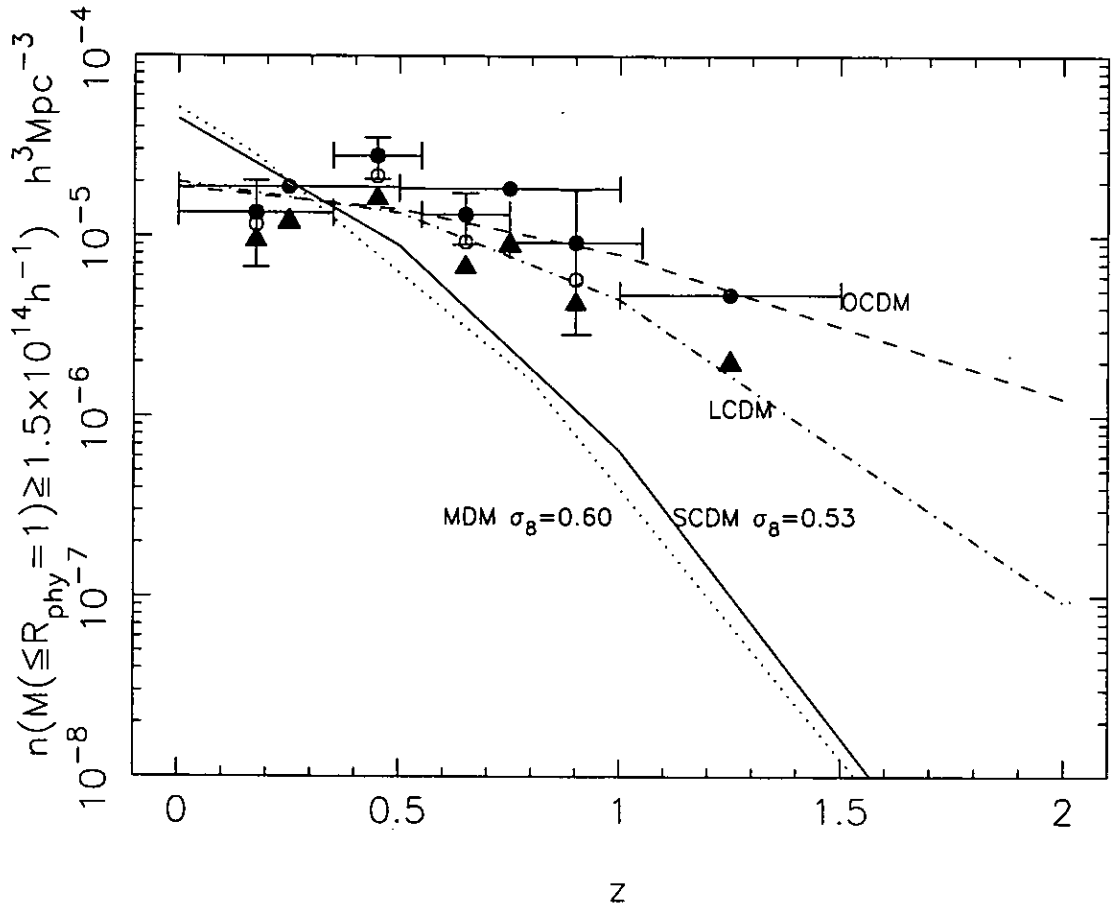


Figure 4.21: Comparison of observed and model cluster abundances as a function of redshift for clusters with mass $M(r < 1.0 h^{-1} \text{Mpc}) \geq 1.5 \times 10^{14} h^{-1} M_{\odot}$. The data are from the PDCS (Postman et al., 1996, - black symbols) and the BTC field (red symbols). The different symbols represent the observed number densities for $\Omega_M = 1$ (filled circles), $\Omega_M = 0.35$, $\Omega_{\Lambda} = 0$ (open circles), and $\Omega_M = 0.4$, $\Omega_{\Lambda} = 0.6$ (filled triangles) cosmologies. Adapted from Figure 13 of Bahcall et al. (1997b).

predicted at $0.5 < z < 1.0$, and a factor of ~ 100 greater at $1.0 < z < 1.5$. The finding of any $z > 1$ clusters is highly unlikely in $\Omega_M = 1$ cosmologies, and given that numerous $z > 1$ clusters have now been found (e.g. this thesis; Dickinson, 1995; Stanford et al., 1997; Yamada et al., 1997; Rosati et al., 1999) such biased high-density cosmologies can be all but ruled out.

It should be considered that the BTC field is biased towards high-redshift clusters, in the sense that it was selected for its high-density of $z \simeq 1.3$ quasars. However this does not affect the conclusion that the data are inconsistent with an $\Omega_M = 1$ cosmology, as either the three clusters in the $0.5 < z < 1.0$ redshift bin are at these

redshifts, and hence unrelated to the quasar structure and selected in a bias-free manner, or one or more of them are related to the quasar group, implying that a large-scale structure is in place at $z \simeq 1.3$ containing more than one rich cluster, something that would be even more inconsistent with an $\Omega_M = 1$ universe. The problem is even worse for the $\Omega_M = 1$ model if the mass of the cluster associated with the $z = 1.226$ quasar is significantly greater than the conservative $1.5 \times 10^{14} h^{-1} M_\odot$ used in the models, as the predicted abundances of $1 < z < 1.5$ clusters are reduced by several orders of magnitude for masses ($\simeq 6 \times 10^{14} h^{-1} M_\odot$) comparable to that of the Coma cluster.

One factor that was not considered in the previous discussion was the substructure observed for three of the four clusters. Certainly the clustering nearby the $z = 1.426$ quasar and that marked by density maxima #70 and #71 appears highly bimodal, and the clustering associated with the $z = 1.226$ quasar shows a great deal of substructure with several compact clumps of galaxies connected by a more diffuse and extended distribution. Such substructure in the galaxy clustering appears relatively common at high redshifts. Using deep Chandra X-ray imaging data Stanford et al. (2000) detect spatially-extended X-ray emission from cluster RX J0848+4453 at $z = 1.27$ (Stanford et al., 1997) due to hot gas in its intra-cluster medium, that appears amorphous and bimodally distributed. They suggest that this cluster is in the process of merging, as the bimodality is also apparent in the distribution of red galaxies.

It should not be surprising that a large fraction of clusters at $z \gtrsim 1$ show signs of substructure or merging, as in a hierarchical clustering model galaxy clusters are formed by the progressive coalescence of subclusters. It is also interesting that many of the high-redshift structures apparent in the BTC field have dense, compact cores surrounded by a diffuse, extended galaxy structure. This suggests that at these redshifts clusters are still in the process of forming with only the cores dynamically settled, and that over the next few gigayears the clusters will increase in size through the progressive absorbing of galaxies from the extended distribution.

4.13 Interpretation — The Galaxy Environments of $z \simeq 1.3$ Quasars

The primary result of studies of the galaxy environments of quasars at $1 \lesssim z \lesssim 1.5$ (e.g. this thesis; Hall & Green, 1998; Sánchez & González-Serrano, 1999) are that the quasars are found in a wide variety of environments, from those comparable to field regions, to others as rich as Abell class 1–2 clusters, but on average they reside in poor clusters, making them biased tracers of mass compared to galaxies. Also, those quasars which have associated galaxy clustering are located on the peripheries of the clusters rather than in the centres.

These observations are entirely consistent with, and can be explained by, our current understanding of quasars, their galaxy hosts, and their triggering mechanisms. They also indicate that large-scale environmental factors do not play a dominant role in the activation of quasars, as can be seen simply by the fact that quasars are found in such diverse environments, although there is one important proviso to this statement as will be discussed later.

The dominant factor in determining the galaxy environment of a quasar appears to be the host galaxy. As discussed in the introduction, recent HST-based studies have been able to establish the basic properties of the quasar host galaxies, finding that they are bright galaxies with $L > L^*$ and have luminosity profiles that are well described by a de Vaucouleurs $r^{1/4}$ -law spheroidal profile, establishing that, at low redshifts at least, the hosts of both radio-loud and radio-quiet quasars are massive elliptical galaxies (McLure et al., 1999; Dunlop, 2001).

The requirement for a massive galaxy host for a quasar to be activated appears related to the observation of a correlation between the mass of the central black hole and the bulge mass of the host galaxy (Magorrian et al., 1998; Merritt & Ferrarese, 2001), implying a causal link between the formation and evolution of the black hole and its galaxy host. This suggests that the finding of quasars in massive galaxy hosts with $M_{\text{host}} \simeq 10^{12} M_{\odot}$ is the combined result of this observed correlation and the requirement for a black hole mass of $M_{\text{BH}} \gtrsim 10^9 M_{\odot}$ to power luminous quasars with $M_V < -23.5$.

The observation that the hosts of quasars are the most luminous and massive

galaxies appears confirmed by the quasar two-point redshift-space correlation function from the 2dF QSO Redshift Survey, which is found to be comparable to results for local optically-selected galaxies, and evolves with redshift in a manner consistent with quasars residing in dark matter halos with masses of $M_{DMH} \gtrsim 10^{12-13} M_{\odot}$ (Croom et al., 2000).

The observation that quasars are found in a wide variety of environments, but are on average found in overdense regions, hence can be fully explained by the quasar host being a massive elliptical galaxy, which traces mass in the same biased manner as described by the density-morphology relation of Dressler (1980). Whilst massive elliptical galaxies are found preferentially in cluster environments, they are also found in field regions.

As mentioned previously, there is one particular environmental factor which may affect quasar formation. That is the apparent avoidance by quasars of the high-density regions of cluster cores (e.g. this thesis; Sánchez & González-Serrano, 1999). This observation can be understood in terms of both the quasar triggering mechanisms described in the introduction: the accretion of gas during the process of galaxy formation (e.g. Efstathiou & Rees, 1988; Haehnelt & Rees, 1993); and galaxy interactions (e.g. Roos, 1981, 1985a,b; Stockton, 1982).

If quasars are activated as the result of the accretion of gas during galaxy formation (Haehnelt & Rees, 1993), then they are unlikely to form in the cluster cores, as these regions are filled with shock-heated virialised gas that does not easily cool and collapse (Blanton et al., 1999), thus inhibiting the formation of both stars and galaxies (Blanton et al., 2000). If instead, galaxy interactions and mergers are the dominant quasar triggering mechanism, then as the encounter velocities of galaxies in the centres of clusters are much greater than the internal velocity distribution of galaxies of $\approx 200 \text{ km s}^{-1}$, galaxy encounters become much less effective at producing galaxy mergers and triggering nuclear activity (Aarseth & Fall, 1980). As discussed in the introduction, the vast majority of those interactions likely to have triggered quasar activity appear to be minor mergers involving dwarf companion galaxies. Just as there is a density-morphology relation for early-type galaxies (Dressler, 1980), there is a comparable relation for the dwarf galaxy population, with dwarfs more common in low-density environments away from the centres of

rich clusters (Phillipps et al., 1998). The need for a potential source of gas to fuel the quasar activity may also play a part in the preferential location of quasars on the cluster peripheries, as galaxies in the centres of clusters have previously lost most or all of their gas, by having had it stripped off by ram-pressure from the intra-cluster medium (Evrard, 1991), or by tidal forces from close encounters with other galaxies (galaxy harassment; Moore et al., 1996), or by consuming the gas in a starburst during its first infall into the cluster.

This avoidance of the high-density cluster cores by quasars should be redshift dependent with the effect greatest for low-redshift clusters as they are more massive and have had more time to virialise than their high-redshift counterparts, and so the inhibitory effect of the hot intra-cluster medium will be that much greater. At high redshifts ($z \gtrsim 2$) the effect should disappear, as the clusters are less massive on average and are still in the process of forming, and also the effective biasing of quasars will be much greater, as those dark matter halos sufficiently massive to host a quasar are associated with the most significant overdensities in the initial density perturbation field.

In a counter argument to the preferential location of quasars on the cluster peripheries, it should be noted that there is a selection effect in favour of finding quasars on the peripheries rather than the centres of clusters, in terms of the relative volumes of the cluster peripheries and centres, i.e. the volume of space with $r_0 < r < 2r_0$ is seven times greater than that with $r < r_0$. Hence given the small sample involved (the two in this paper and the seven of Sánchez & González-Serrano, 1999) it cannot be conclusively ruled out that quasars show no preference with regard to their location within a cluster.

The observations of the galaxy environments of quasars appear to confirm the consensus view of the framework of quasar activity being triggered by the infall of gas onto a seed black hole. Quasars also appear to be biased tracers of mass, located preferentially in overdense regions. This is the reason why quasars are such excellent probes of high-redshift galaxy clustering, and lends credence to the hypothesis that large quasar groups trace the most massive superclusters in the universe.

4.14 Evidence for a Large-Scale Structure Associated with the Clowes-Campusano Large Quasar Group at $z \simeq 1.3$

The observation of a 2σ excess of red galaxies across the whole BTC field in comparison to the EIS-DEEP HDF-South field is significant evidence in favour of a high-redshift large-scale structure crossing the field. The observed 50–70% excess of red galaxies may seem at first sight unlikely, but a comparison with the redshift distribution of MgII absorbers for quasars behind the Clowes-Campusano LQG indicates that such a result is reasonable. Williger et al. (2000) observe 11 MgII absorbers at $1.2 < z < 1.3$ whereas only 4 would be expected, a 3.4σ overdensity or an excess of 175%. To compare this result with the observed red galaxy excess, consider a redshift distribution for the red galaxies that is uniform for $0.6 < z < 1.4$. By then adding a 175% excess of galaxies with $1.2 < z < 1.3$, this would produce a total red galaxy excess of 22%. This is clearly a crude estimate, but it does suggest that large fractional excesses would be expected for any large-scale structure associated with the Clowes-Campusano Large Quasar Group. If one then considers that the BTC field was chosen to cover a particularly dense region of the group containing three quasars, it is easy to see how excesses of the order observed are possible, and indeed likely.

Given the relatively small size of the EIS-DEEP field used for comparison, it is not possible to be certain that the observed excess is real. It could be just that the EIS-DEEP field is a particularly underdense region, although the random placement of same-sized fields in the BTC image are found to contain as few red galaxies less than 2% of the time. It would still be desirable to consider further comparison fields as and when they become publicly available.

Further evidence in favour of a large-scale structure associated with the Clowes-Campusano LQG comes in the form of the spatial distribution of the red galaxies, and in particular the observed extended clustering around the $z = 1.226$ quasar. From the optical images alone, it appears likely that this clustering is indeed associated with the quasar, and as will be discussed in Chapter 5 the additional

near-infrared imaging confirms this. The extent of clustering associated with this quasar appears significant, with an excess of 100–150 red galaxies within 5 arcmin (corresponding to $3.8 h^{-1}\text{Mpc}$ at $z = 1.226$) of the quasar.

If the overall red galaxy excess, the clustering associated with the $z = 1.226$ quasar, and the excess of MgII absorbers at the LQG redshift are considered together, the evidence for the Clowes-Campusano Large Quasar Group tracing a large-scale structure at $z \simeq 1.3$ becomes highly convincing. These results are paralleled by those of Tanaka et al. (2000, 2001) who find evidence for a large-scale structure $\simeq 20 h^{-1}\text{Mpc}$ across that is traced by five quasars from the Crampton et al. (1989) LQG at $z \simeq 1.1$ (Tanaka et al., 2001), with one of the quasars located on the periphery of a rich cluster (Tanaka et al., 2000).

4.15 Summary

In this chapter galaxy clustering at redshifts beyond 0.5 is examined by considering the spatial distribution of the reddest galaxies in the BTC images, with $I < 23.5$ and $V - I > 3.6891 - 0.0651 \times I_{total}$. By selecting galaxies using the same criteria in a comparably deep field, the EIS-DEEP HDF-South field covering 27 arcmin^2 , and taking advantage of its $UBVRIJHK_s$ photometry to estimate the red galaxies' redshifts and star-formation histories, it is demonstrated that these are early-type galaxies at $0.6 \lesssim z \lesssim 1.5$. This is confirmed by the two-point angular correlation function of the red galaxies in the BTC field which finds the clustering strength of red galaxies to be an order of magnitude greater than I -band selected galaxies.

A 2σ excess of red galaxies is found in the BTC field in comparison to the EIS-DEEP HDF-South control field, corresponding to ~ 1000 extra red galaxies over the BTC field. It is suggested that this excess is due to a high-redshift large-scale structure encompassing the whole field, which supports the hypothesis that the Clowes-Campusano Large Quasar Group traces a large-scale structure at $z \simeq 1.3$.

Four high-redshift cluster candidates are apparent in the BTC field, of which two appear associated with quasars. The $z = 1.226$ quasar is located within a region of amorphously-distributed galaxy clustering extending over several megaparsecs and which appears to be a very rich environment with an excess of 100–150 red

galaxies observed. The $z = 1.426$ quasar is located on the periphery of a cluster of red galaxies, with a second cluster $2.4 h^{-1}\text{Mpc}$ from the first. It appears that at this epoch, galaxy clusters are still in the process of forming and coalescing, as three of the four high-redshift cluster candidates have significant substructure, either bimodal or more complex. The finding of so many clusters at high-redshifts indicates a mild negative evolution of cluster abundance with redshift that is highly inconsistent with an $\Omega_M = 1$ universe where clusters are predicted to form later and evolve much more rapidly.

Chapter 5

The Galaxy Environment of the $z = 1.226$ LQG Quasar

5.1 Introduction

As discussed in the previous chapter, to determine whether LQGs trace large-scale structure requires observations capable of identifying the quiescent galaxies that mark out any associated supercluster, in particular the massive ellipticals which dominate cluster cores. These are both the most luminous and the reddest galaxies in nearby clusters, and form a homogeneous population with very tight, linear colour-magnitude relations known as *red sequences* (Bower et al., 1992), indicative of old (11–12 Gyr) stellar populations. This red sequence has been followed in the optical for clusters out to $z \sim 0.9$ (Aragón-Salamanca et al., 1993; Stanford et al., 1998) and is consistent with the passive evolution of galaxies that formed in a monolithic collapse at $z \gtrsim 3$ (Eggen et al., 1962). At these low and intermediate redshifts the location of the red sequence on optical colour-magnitude diagrams can be used as an accurate indicator of redshift. However at $z \gtrsim 1$ the 4000 Å break has been redshifted into the *I* band, and so the accuracy of redshift estimates based on optical data alone is reduced: as (i) the rate at which the red sequence colour reddens with redshift slows markedly; and (ii) the red sequence galaxies are intrinsically faint in the optical and so have greater photometric errors, smoothing out any red sequence in the colour direction.

The cluster red sequence method can be applied successfully to the detection and

redshift estimation of clusters beyond $z \simeq 1$ through the addition of near-infrared imaging. By straddling the 4000 \AA break, which at these redshifts is passing through the I -band, the $I - K$ colour can be used as an excellent identifier of $z \gtrsim 1$ early-type galaxies. These should be characterised by extremely-red optical- near-infrared colours with $I - K \simeq 4$, much redder than all foreground galaxies except for a few extremely dust-enshrouded starbursting galaxies. Good contrasts of $z \gtrsim 1$ clusters over the background are possible as field $I - K \simeq 4$ galaxies appear rare: the Hawaii K -band survey finds no galaxies with $I - K > 4$ for $K < 18$ over an area of 86.7 arcmin^2 (Cowie et al., 1994; Songaila et al., 1994).

Several $z \simeq 1.2$ clusters have been found by searching for galaxies with $I - K \simeq 4$ in fields around both targeted high-redshift AGN (Dickinson, 1995; Yamada et al., 1997) and regions of extended X-ray emission (Stanford et al., 1997; Rosati et al., 1999). These galaxies are found to have the optical- near-infrared colours ($I - K \simeq 4$, $R - K \simeq 6$) expected for passively-evolving galaxies which are 2–3 Gyr old, in good agreement with the monolithic-collapse model predictions. Dickinson (1995) also finds a red sequence for the $z = 1.2$ cluster around the radio-galaxy 3C324 with $R - K \simeq 5.9$ and an rms scatter of only 0.07 mag, suggesting that these galaxies formed within 300 Myr of one another.

As described in the previous chapter, on the basis of the spatial distribution of red galaxies in the BTC field, the $z = 1.226$ quasar appeared to be the most likely of the three quasars from the Clowes-Campusano LQG to have associated galaxy clustering on $\simeq 1 h^{-1} \text{ Mpc}$ scales. It was located within a region of red galaxy clustering extending over $\gtrsim 5 \text{ arcmin}$ ($\gtrsim 4 h^{-1} \text{ Mpc}$ at $z = 1.226$) resulting in an excess of 100–150 red galaxies. It was thus an excellent candidate for follow-up near-infrared imaging to confirm the redshift of the clustering, and to examine the properties of galaxies in the cluster environment in more detail, by allowing those galaxies with some recent star-formation to be identified as well as the passively-evolving ellipticals.

The initial motivation for examining the field of this quasar in preference to the other two LQG quasars, was in fact its immediate environment as, at the time the decision was made, the V and I images had not been registered and combined, and so the distribution of red galaxies was not yet known. Of the three LQG

quasars in the BTC field, the $z = 1.226$ quasar had the most interesting immediate environment with several galaxies within 5 arcsec indicating that it was likely to be in an interacting system.

This chapter details the results and analysis of K imaging of a 2.25×2.25 arcmin² field (corresponding to $1.75 \times 1.75 h^{-2}$ Mpc² at the quasar redshift) centred on the $z = 1.226$ quasar at $10^h 46^m 56.70^s$, $+05^\circ 41' 50.5''$ (J2000). The quasar is classed as being radio-quiet on the basis of not being detected at the 1 mJy level by the VLA Faint Images of the Radio Sky at Twenty-centimetres (FIRST) Survey.

5.2 Observations

K imaging was obtained for a 2.25×2.25 arcmin² field centred on the $z = 1.226$ LQG quasar using the UKIRT Fast-Track Imager (UFTI) camera on the 3.8-m United Kingdom Infra-Red Telescope (UKIRT). The near-infrared observations took place on the night of 20/21 March 1999, obtained using the Director's Discretionary Time of Andy Adamson, who was also the observer on the night.

The UFTI camera is a cooled 1–2.5 μ m instrument with a 1024×1024 HgCdTe array. The plate scale is 0.091 arcsec per pixel, giving a field of view of 92×92 arcsec². A standard 9-point jitter pattern was used, with each 1 minute exposure offset by 20 arcsec relative to adjacent exposures, the nine pointings forming a 3 by 3 grid. A dark frame was obtained between each set of jitters, and subtracted before self-flattening the set. In total 7 circuits of the jitter pattern were completed, resulting in a total exposure time of 63 minutes. The exposures were registered by considering the relative position of the quasar in each of the images, as it was the only source apparent in all of the individual exposures. As a result the effect of any rotation between images was not considered, but this does not appear to have affected the results. Due to the use of the jitter pattern, the size of the field observed is increased to 2.25×2.25 arcmin², although the 20 arcsec wide strips at the edges of the field have only one-third of the exposure time. However, as many of the sources identified in the previous chapter as red galaxies are located near the edges of the field, the strips have been retained, with each source checked visually, and separate magnitude limits determined.

The resultant K image has a FWHM of 0.6 arcsec, a typical level of seeing for UKIRT data, but significantly better than for the BTC images. To allow galaxy colours to be determined using a single fixed aperture, the K image was convolved to the same seeing as the I image (1.15 arcsec) using a Gaussian kernel of FWHM = 0.86 arcsec ($\sigma = 4$ pixels).

The K image was then registered with the optical image through comparison of the positions of 40 bright sources ($K < 19$) in the K and I images using the IRAF tools `geomap` and `register`, resulting in the simple linear transformation

$$X_{reg} = 1982.3106 - 0.2116363 \times X_K - 0.0034551 \times Y_K \quad (5.1)$$

$$Y_{reg} = 4617.3771 - 0.0032378 \times X_K + 0.2127302 \times Y_K, \quad (5.2)$$

where (X_K, Y_K) is the position of the source in the K image, and (X_{reg}, Y_{reg}) is the corresponding position in the I image after registration.

The photometric calibration of the K image was performed through observation of the UKIRT faint standard fs20 (G163-50; $\alpha = 11^h06^m59.93^s$, $\delta = -05^\circ09'26.1''$) which has $K = 13.503 \pm 0.010$ (Hawarden et al., 2001). Five 20 second observations were obtained for the standard star, using differing parts of the detector, which resulted in a zero-point for the K image of 25.546 ± 0.021 .

Object detection was carried out using SExtractor (Bertin & Arnouts, 1996) with sources identified as having 150 ($\simeq \text{FWHM}^2$) contiguous pixels over the 1.6σ detection threshold. As the K image had been previously convolved to the seeing of the optical images, a Gaussian filter was not used in the detection process. The total magnitudes were taken to be the `MAG_BEST` output from SExtractor, and colours were determined using fixed apertures of diameter 2.5 arcsec. The magnitude errors are determined in SExtractor by considering the rms noise levels in the image. However, in this case these levels have been artificially reduced by convolving the image before the source detection process, and hence are significantly lower than they should be.

Instead of using the errors as determined by SExtractor, they are calculated for each source by assuming Poisson noise through the equation

$$\delta m_K = \delta(2.5 \log F_{source}) = \frac{2.5}{\ln 10} \left(\frac{\delta F_{source}}{F_{source}} \right) = 1.0857 \frac{\sqrt{A \frac{F_{back}}{N_{exp9}} + \frac{F_{source}}{N_{exp9}}}}{F_{source}}, \quad (5.3)$$

Filter band (subfield)	Exposure time (sec)	Seeing FWHM (arcsec)	Completeness	
			limits (mag)	
			90%	50%
<i>K</i> (centre)	3780	0.60	19.25	19.95
<i>K</i> (edge)	1260	0.60	18.82	19.53
<i>I</i>	16200	1.15	24.68	25.39
<i>V</i>	8100	1.30	25.40	25.95

Table 5.1: Photometric properties of the images, including exposure times and completeness levels. The *V* and *I* values are for the area covered by the *K* image, rather than for the whole BTC field.

where A is the aperture area in units of square pixels, $F_{back} = 1320.4$ is the background flux level, N_{exp} is the number of 60 second exposures that the source is covered by, F_{source} is the flux level of the source, and $g = 7.172$ is the gain of the detector (Bertin, 1996, p. 12).

Star-galaxy separation of each source was performed using a combination of morphology (using the stellarity classifier in SExtractor) and a comparison of $V - I$ and $I - K$ colours with model stellar and galaxy tracks. Stellarities of sources in both *V* and *I* images were obtained and the weighted mean used for classification as discussed in Chapter 2. Most of the sources classified as stars by morphology, also had colours that lay near the model stellar tracks, but a number of sources had the colours of blue galaxies, and were reclassified as such.

Figure 5.1 shows the convolved *K*-band image of the 2.25×2.25 arcmin² field centred on the $z = 1.226$ LQG quasar. Each source detected by SExtractor and visually-verified is labelled by the identification code used in Table 5.3. The differing colours and symbols indicate the morphological classification of the source, and whether it is detected in the optical BTC images: yellow circles indicate that the source is classified as a galaxy and is detected in all three images (*V*, *I* and *K*); green circles indicate that the source is classified as a galaxy and is detected in the *K* and *I* images only; red squares indicate that the source is classified as a galaxy and is detected in the *K* image only; and blue circles indicate that the source is classified as stellar.

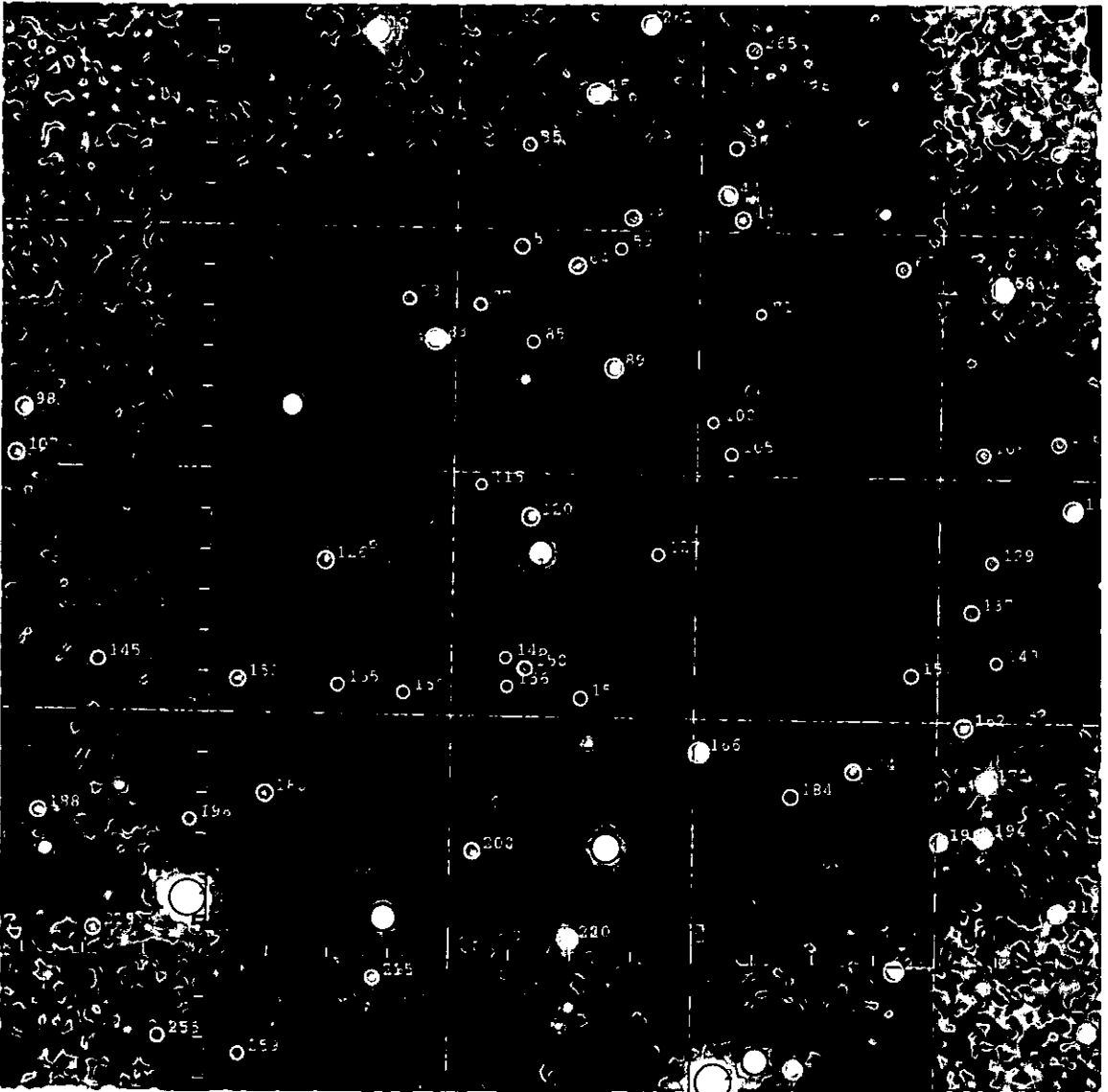


Figure 5.1: *K*-band image of the 2.25×2.25 arcmin² field centred on the $z = 1.226$ LQG quasar (source #121). Each source detected by SExtractor and visually verified is labelled by the identification code used in Table 5.3. The differing colours and symbols indicate the morphological classification of the source, and whether it is detected in the optical BTC images: yellow circles indicate that the source is classified as a galaxy and is detected in all three images (*V*, *I* and *K*); green circles indicate that the source is classified as a galaxy and is detected in the *K* and *I* images only; red squares indicate that the source is classified as a galaxy and is detected in the *K* image only; and blue circles indicate that the source is classified as stellar.

Completeness levels were determined for the K image in a similar manner as for the optical BTC images, by dimming a bright galaxy to a specified magnitude and adding 100 copies to the image at random positions, and then processing through SExtractor in the usual way. The 50% and 90% completeness levels are estimated as the magnitude for which 50 and 90 galaxies out of the 100 are recovered. As the exposure levels vary considerably across the K image, two separate completeness levels were determined, one for the centre of the image where all 63 exposures are used, and one for the 20 arcsec wide strips at the edges of the image where only one-third of the exposures are used. The resulting completeness levels are shown in Table 5.1 with in addition the corresponding completeness levels for the BTC V and I optical images for the same region.

5.3 Results — Galaxy Counts

In total 100 sources are detected in the K image, of which 95 have counterparts in the I image, and 79 have counterparts in both V and I images. Each source has been visually-verified, in particular if the source is not detected in either of the optical images, as a number of sources only detected in the K image are spurious noise events towards the edges of the images and have to be removed. Fourteen of the 79 sources are classified as stars, leaving 86 galaxies in the 2.25×2.25 arcmin² field. Of the five sources detected in the K image only, two are the close companion galaxies of the quasar which could not be separated from the quasar point-spread function by SExtractor in the V and I images, and the three others must have $I - K > 3.75$ to remain undetected in I .

Table 5.2 shows the comparison of galaxy counts for the K image with those expected from a field region (Songaila et al., 1994). Excesses of galaxies are observed in all magnitude bins, even in the last bin where incompleteness should reduce any excess. By considering a magnitude limit of $K < 19$ (an L_K^* galaxy at $z = 1.226$ has $K \simeq 19.05$) for which both the data are essentially complete and the photometry is accurate, then a 3.5σ excess is observed, with 40 galaxies observed whereas only 19 would be expected. The significance of this result takes into account the effect on galaxy statistics of the two-point angular correlation function, which is taken to be

Magnitude	Observed		Expected	
	Total	I-K>3.75	Total	I-K>3.75
$15 < K \leq 16$	1	1	0.533	0
$16 < K \leq 17$	3	1	2.186	0
$17 < K \leq 18$	13	5	4.204	0.050
$18 < K \leq 19$	23	16	11.36	1.939
$19 < K \leq 20$	39	23	21.81	1.896
Total	79	46	41	4

Table 5.2: A comparison of total and extremely-red ($I - K > 3.75$) galaxy counts in the K image, binned by magnitude, and those expected for the same-sized region in the field (Songaila et al., 1994). The numbers include those observed only in the K image, with the two companions to the quasar assumed to have $I - K < 3.75$, and the other three sources to have $I - K > 3.75$.

$\omega(\theta) = 1.13\theta''^{-0.8}$ (Roche et al., 1999) for $K < 19$ galaxies, through

$$\sigma^2 = N_{exp} + N_{exp}^2 \frac{\int \int \omega(\theta_{12}) d\Omega_1 d\Omega_2}{\int \int d\Omega_1 d\Omega_2} \quad (5.4)$$

where N_{exp} is the expected number of galaxies in the field. By considering only those galaxies with $I - K > 3.75$ then the excess is much more significant, with 23 galaxies observed instead of the expected 2. Even though the clustering amplitude of extremely-red galaxies is a factor of ten greater than that of K -selected field galaxies (Daddi et al., 2000), a 9σ excess is still observed. It is clear that the total excess is due entirely to these extremely-red galaxies, indicating a likely cluster at $z \gtrsim 0.8$, and so all $I - K > 3.75$ galaxies are considered to be cluster members.

The multi-colour optical- near-infrared catalogue of sources detected in the K -image is presented in Table 5.3.

ID The identification number given to each source by the SExtractor software, as indicated by the labelling in Figure 5.1.

RA, Dec The Right Ascension and Declination (J2000) for each source calculated for the position of the source in the K image.

ID	RA (J2000)	Dec (J2000)	X_{QSO}	Y_{QSO}	K_{total}	I_{total}	V_{total}	$I - K$	$V - I$	$V - K$	STAR
4	10:46:58.827	5:40:47.202	31.86	-62.94	17.740 ± 0.105	19.584 ± 0.018	21.477 ± 0.013	2.788 ± 0.100	1.422 ± 0.020	4.211 ± 0.020	0.02
12	10:46:55.287	5:42:54.062	-21.20	63.81	15.745 ± 0.029	19.263 ± 0.007	22.081 ± 0.030	3.883 ± 0.015	2.876 ± 0.025	6.760 ± 0.025	E1
15	10:46:57.107	5:42:46.845	6.28	56.69	17.048 ± 0.062	20.569 ± 0.017	23.277 ± 0.097	4.310 ± 0.046	2.610 ± 0.087	6.920 ± 0.087	E3
29	10:47:00.904	5:42:40.198	62.89	49.95	18.918 ± 0.237	22.936 ± 0.078	24.776 ± 0.207	3.948 ± 0.326	1.787 ± 0.162	5.736 ± 0.162	0.75
35	10:46:56.558	5:42:40.442	-1.96	50.30	19.467 ± 0.208	23.808 ± 0.146	25.245 ± 0.367	3.613 ± 0.375	1.314 ± 0.207	4.928 ± 0.207	0.31
36	10:46:58.260	5:42:40.324	23.25	50.16	19.234 ± 0.227	23.000 ± 0.077	24.440 ± 0.161	3.923 ± 0.312	1.092 ± 0.142	5.015 ± 0.142	0.32
44	10:46:58.322	5:42:31.485	24.38	41.43	18.495 ± 0.108	21.670 ± 0.023	23.362 ± 0.059	3.176 ± 0.116	1.942 ± 0.062	5.119 ± 0.062	0.36
47	10:46:58.195	5:42:34.482	22.55	44.29	17.540 ± 0.059	21.021 ± 0.016	22.615 ± 0.037	3.509 ± 0.050	1.747 ± 0.036	5.256 ± 0.036	0.03
53	10:46:57.412	5:42:31.579	11.17	41.33	18.593 ± 0.108	22.749 ± 0.063	25.626 ± 0.238	4.341 ± 0.131	2.455 ± 0.308	6.796 ± 0.308	0.16
57	10:46:56.506	5:42:27.884	-2.47	38.69	18.946 ± 0.103	22.414 ± 0.076	24.241 ± 0.107	3.835 ± 0.162	1.526 ± 0.154	5.362 ± 0.154	0.04
59	10:46:57.320	5:42:27.751	9.60	37.75	19.936 ± 0.176	22.890 ± 0.078	24.821 ± 0.176	3.624 ± 0.403	1.922 ± 0.270	5.546 ± 0.270	0.07
62	10:47:01.124	5:42:26.865	65.74	36.80	19.829 ± 0.511	21.816 ± 0.036	24.011 ± 0.150	4.045 ± 0.605	1.774 ± 0.118	5.820 ± 0.118	0.02
64	10:46:56.963	5:42:25.592	4.37	35.18	18.354 ± 0.100	22.072 ± 0.045	25.256 ± 0.169	4.142 ± 0.105	2.498 ± 0.244	6.641 ± 0.244	0.12
65	10:46:59.647	5:42:25.685	44.25	35.56	19.045 ± 0.155	21.755 ± 0.027	23.056 ± 0.053	3.013 ± 0.219	1.533 ± 0.054	4.547 ± 0.054	0.15
68	10:47:00.461	5:42:23.329	56.60	33.15	16.558 ± 0.044	19.905 ± 0.006	21.537 ± 0.016	3.454 ± 0.029	1.708 ± 0.011	5.163 ± 0.011	0.31
73	10:46:55.583	5:42:21.227	-16.55	31.00	19.619 ± 0.147	23.165 ± 0.077	25.981 ± 0.315	3.754 ± 0.275	2.333 ± 0.365	6.088 ± 0.365	0.76
77	10:46:56.170	5:42:20.663	-7.72	30.22	19.792 ± 0.179	23.327 ± 0.105	24.317 ± 0.160	3.535 ± 0.287	1.224 ± 0.123	4.760 ± 0.123	0.43
81	10:46:58.484	5:42:19.939	27.69	29.47	20.685 ± 0.345	23.921 ± 0.169	24.465 ± 0.156	3.524 ± 0.799	0.427 ± 0.151	3.951 ± 0.151	0.14
83	10:46:55.806	5:42:16.279	-13.17	26.10	16.969 ± 0.030	20.720 ± 0.014	23.266 ± 0.059	3.983 ± 0.022	2.805 ± 0.067	6.788 ± 0.067	E2
85	10:46:56.609	5:42:16.150	-1.03	25.69	19.736 ± 0.086	25.053 ± 0.287	26.208 ± 0.422	4.961 ± 0.480	0.728 ± 0.518	5.689 ± 0.518	0.53
89	10:46:57.272	5:42:13.083	8.71	22.89	17.655 ± 0.045	20.940 ± 0.019	22.725 ± 0.045	3.450 ± 0.040	1.924 ± 0.033	5.374 ± 0.033	0.02
98	10:46:52.424	5:42:07.027	-64.02	16.50	18.182 ± 0.096	22.459 ± 0.049	24.144 ± 0.119	4.420 ± 0.111	1.435 ± 0.090	5.855 ± 0.090	0.02
100	10:46:58.099	5:42:06.519	20.64	16.32	20.366 ± 0.108	24.750 ± 0.384	24.601 ± 0.133	4.459 ± 0.532	0.510 ± 0.316	4.969 ± 0.316	0.23
105	10:46:58.254	5:42:02.613	23.63	11.91	19.733 ± 0.152	21.568 ± 0.034	23.191 ± 0.065	2.157 ± 0.273	1.670 ± 0.051	3.827 ± 0.051	0.02
106	10:47:00.938	5:42:04.383	64.10	14.35	19.093 ± 0.186	23.138 ± 0.102	25.611 ± 0.244	4.331 ± 0.273	2.397 ± 0.312	6.728 ± 0.312	0.11
107	10:46:52.366	5:42:01.400	-64.95	11.71	18.494 ± 0.139	22.597 ± 0.054	25.983 ± 0.368	4.401 ± 0.143	2.714 ± 0.294	7.116 ± 0.294	0.09
108	10:47:00.320	5:42:02.931	54.37	12.87	19.198 ± 0.172	22.684 ± 0.063	25.231 ± 0.220	3.755 ± 0.269	2.347 ± 0.171	6.103 ± 0.171	0.80

Table 5.3: Multi-colour optical- near-infrared catalogue of sources in the K -image centred on the $z = 1.226$ quasar. Page 1 of 4. Each source on this page is detected in all three passbands, and is classified as a galaxy.

ID	RA (J2000)	Dec (J2000)	X_{QSO}	Y_{QSO}	K_{total}	I_{total}	V_{total}	$I - K$	$V - I$	$V - K$	STAR
115	10:46:56.200	5:41:58.469	-7.57	7.89	20.464 ± 0.066	23.787 ± 0.194	24.080 ± 0.135	3.624 ± 0.510	0.376 ± 0.169	4.201 ± 0.169	0.15
116	10:47:01.062	5:41:56.217	65.69	6.02	17.464 ± 0.067	20.911 ± 0.015	23.702 ± 0.076	3.594 ± 0.055	2.673 ± 0.050	6.267 ± 0.050	0.58
120	10:46:56.606	5:41:54.566	-1.33	4.42	18.121 ± 0.060	22.213 ± 0.044	24.254 ± 0.096	4.296 ± 0.068	2.021 ± 0.116	6.318 ± 0.116	0.03 E10
126	10:46:54.916	5:41:48.837	-26.65	-1.01	18.252 ± 0.073	22.858 ± 0.071	24.551 ± 0.149	4.322 ± 0.087	1.574 ± 0.105	5.896 ± 0.105	0.64
127	10:46:57.660	5:41:50.190	14.69	-0.33	19.858 ± 0.117	23.568 ± 0.117	23.755 ± 0.086	3.496 ± 0.288	0.546 ± 0.094	4.043 ± 0.094	0.09
129	10:47:00.403	5:41:49.735	55.88	-0.25	19.745 ± 0.243	23.792 ± 0.160	24.899 ± 0.236	4.211 ± 0.439	1.197 ± 0.194	5.409 ± 0.194	0.30
137	10:47:00.241	5:41:43.600	53.59	-6.78	19.030 ± 0.194	21.614 ± 0.031	22.739 ± 0.040	2.874 ± 0.218	1.168 ± 0.033	4.043 ± 0.033	0.03
145	10:46:53.062	5:41:36.267	-53.80	-14.66	19.338 ± 0.198	24.209 ± 0.200	25.373 ± 0.212	4.666 ± 0.321	1.218 ± 0.264	5.885 ± 0.264	0.73
146	10:46:56.417	5:41:37.237	-4.02	-12.98	20.014 ± 0.105	22.769 ± 0.056	23.862 ± 0.068	2.667 ± 0.327	1.128 ± 0.084	3.796 ± 0.084	0.72
149	10:47:00.447	5:41:37.403	56.24	-13.14	19.940 ± 0.283	22.765 ± 0.067	23.858 ± 0.086	2.997 ± 0.547	1.066 ± 0.072	4.063 ± 0.072	0.55
150	10:46:56.575	5:41:35.980	-1.78	-14.16	19.062 ± 0.106	22.976 ± 0.070	24.490 ± 0.123	4.173 ± 0.153	1.726 ± 0.167	5.899 ± 0.167	0.02
151	10:46:59.754	5:41:35.679	45.96	-14.26	19.259 ± 0.160	22.578 ± 0.047	23.624 ± 0.052	3.292 ± 0.222	0.955 ± 0.064	4.247 ± 0.064	0.33
152	10:46:54.206	5:41:34.105	-37.29	-15.90	18.718 ± 0.104	22.327 ± 0.052	25.552 ± 0.295	3.610 ± 0.119	2.823 ± 0.195	6.433 ± 0.195	0.41
155	10:46:55.030	5:41:33.614	-24.98	-16.46	19.567 ± 0.123	22.947 ± 0.078	24.967 ± 0.192	3.346 ± 0.248	2.021 ± 0.147	5.368 ± 0.147	0.75
156	10:46:56.431	5:41:33.721	-4.03	-16.35	20.010 ± 0.088	23.179 ± 0.080	24.654 ± 0.124	3.348 ± 0.351	1.323 ± 0.159	4.672 ± 0.159	0.69
158	10:46:55.576	5:41:32.777	-16.75	-16.92	19.710 ± 0.118	22.442 ± 0.073	23.283 ± 0.080	3.274 ± 0.276	0.807 ± 0.073	4.081 ± 0.073	0.02
159	10:46:57.035	5:41:32.368	5.10	-17.48	19.327 ± 0.080	22.934 ± 0.102	24.653 ± 0.171	3.147 ± 0.188	1.649 ± 0.172	4.797 ± 0.172	0.46
162	10:47:00.187	5:41:29.398	52.31	-20.91	18.087 ± 0.119	21.977 ± 0.039	24.432 ± 0.111	4.336 ± 0.116	2.329 ± 0.143	6.665 ± 0.143	0.10 E9
166	10:46:58.017	5:41:25.955	19.91	-24.26	17.243 ± 0.030	21.023 ± 0.018	23.694 ± 0.091	4.061 ± 0.027	2.934 ± 0.082	6.996 ± 0.082	0.33 E4
171	10:47:00.379	5:41:22.704	55.30	-27.13	16.724 ± 0.056	20.002 ± 0.010	22.088 ± 0.023	3.663 ± 0.032	2.012 ± 0.020	5.675 ± 0.020	0.02
174	10:46:59.291	5:41:23.823	38.71	-26.27	18.584 ± 0.125	22.221 ± 0.048	24.492 ± 0.169	3.679 ± 0.129	2.253 ± 0.116	5.932 ± 0.116	0.03
180	10:46:54.443	5:41:20.086	-33.81	-30.52	18.416 ± 0.093	21.340 ± 0.062	24.107 ± 0.165	3.711 ± 0.130	1.966 ± 0.129	5.677 ± 0.129	0.01
184	10:46:58.779	5:41:20.599	30.95	-29.81	18.875 ± 0.088	25.274 ± 0.310	25.376 ± 0.293	5.187 ± 0.408	0.395 ± 0.449	5.583 ± 0.449	0.49
188	10:46:52.589	5:41:17.559	-61.75	-32.54	18.730 ± 0.156	22.168 ± 0.080	24.015 ± 0.084	3.925 ± 0.187	1.859 ± 0.105	5.785 ± 0.105	0.08
194	10:47:00.362	5:41:15.868	54.97	-34.36	17.598 ± 0.087	21.421 ± 0.024	24.194 ± 0.111	4.271 ± 0.075	2.893 ± 0.137	7.165 ± 0.137	0.02 E7
196	10:46:59.994	5:41:15.283	49.60	-34.92	18.013 ± 0.102	21.553 ± 0.028	23.346 ± 0.085	4.246 ± 0.103	2.858 ± 0.165	7.105 ± 0.165	0.02 E8
198	10:46:53.828	5:41:16.714	-42.48	-33.44	19.692 ± 0.249	22.517 ± 0.077	22.758 ± 0.054	2.973 ± 0.443	1.422 ± 0.104	4.395 ± 0.104	0.07

Table 5.3 continued: Multi-colour optical- near-infrared catalogue of sources in the K -image centred on the $z = 1.226$ quasar. Page 2 of 4. Each source on this page is detected in all three passbands, and is classified as a galaxy.

ID	RA (J2000)	Dec (J2000)	X_{QSO}	Y_{QSO}	K_{total}	I_{total}	V_{total}	$I - K$	$V - I$	$V - K$	STAR
200	10:46:56.163	5:41:13.405	-8.33	-36.97	18.678 ± 0.110	24.291 ± 0.199	26.740 ± 0.449	5.470 ± 0.217	1.891 ± 0.468	7.362 ± 0.468	0.44
215	10:46:55.349	5:40:57.699	-19.97	-52.88	19.352 ± 0.330	23.459 ± 0.167	25.128 ± 0.299	4.697 ± 0.351	2.023 ± 0.299	6.721 ± 0.299	0.15 E18
216	10:47:00.969	5:41:06.677	63.97	-43.64	17.842 ± 0.106	20.361 ± 0.010	21.389 ± 0.015	2.966 ± 0.109	1.27 ± 0.0120	4.236 ± 0.012	0.03
219	10:46:53.052	5:41:03.265	-54.85	-46.88	18.814 ± 0.174	21.689 ± 0.056	24.129 ± 0.098	3.468 ± 0.282	2.131 ± 0.119	5.600 ± 0.119	0.06
220	10:46:56.959	5:41:02.731	4.12	-47.37	17.260 ± 0.058	19.489 ± 0.014	21.464 ± 0.015	3.014 ± 0.040	1.636 ± 0.012	4.650 ± 0.012	0.02
239	10:46:59.641	5:40:59.411	44.11	-50.66	17.523 ± 0.092	22.005 ± 0.075	24.004 ± 0.124	4.658 ± 0.083	2.088 ± 0.100	6.746 ± 0.100	0.02 E6
254	10:47:01.223	5:40:52.134	67.86	-58.11	17.626 ± 0.111	20.841 ± 0.015	23.041 ± 0.052	3.505 ± 0.116	2.203 ± 0.035	5.709 ± 0.035	0.04
255	10:46:53.591	5:40:50.127	-47.57	-60.76	19.412 ± 0.246	23.294 ± 0.238	23.831 ± 0.094	3.988 ± 0.500	0.657 ± 0.133	4.645 ± 0.133	0.06
259	10:46:54.247	5:40:48.085	-36.57	-62.11	19.498 ± 0.263	22.660 ± 0.086	24.053 ± 0.119	3.341 ± 0.401	1.593 ± 0.105	4.934 ± 0.105	0.52
261	10:46:57.540	5:42:55.404	12.49	64.95	17.516 ± 0.080	21.575 ± 0.028	24.218 ± 0.180	4.226 ± 0.070	2.819 ± 0.132	7.045 ± 0.132	0.10 E5
265	10:46:58.394	5:42:52.398	25.59	62.25	18.916 ± 0.137	23.204 ± 0.103	25.464 ± 0.301	3.439 ± 0.275	2.000 ± 0.244	5.439 ± 0.244	0.17
21	10:46:54.069	5:42:42.746	-38.76	53.50	19.040 ± 0.192	24.605 ± 0.208		5.280 ± 0.389	> 0.460	> 5.739	0.63
39	10:46:52.651	5:42:37.457	-59.92	47.75	19.640 ± 0.354	24.590 ± 0.211		5.094 ± 0.687	> 0.632	> 5.726	0.54
42	10:46:54.480	5:42:36.257	-33.33	46.09	19.447 ± 0.237	24.345 ± 0.307		5.148 ± 0.421	> 0.758	> 5.906	0.21
50	10:46:52.386	5:42:32.558	-65.12	42.90	19.298 ± 0.265	25.370 ± 0.365		6.148 ± 0.655	> -0.114	> 6.034	0.51 E17
60	10:47:00.801	5:42:27.758	61.97	37.67	19.243 ± 0.269	23.719 ± 0.099		4.670 ± 0.363	> 1.363	> 6.032	0.20
93	10:46:58.412	5:42:10.449	25.23	19.93	19.968 ± 0.117	24.343 ± 0.245		4.370 ± 0.402	> 0.904	> 5.274	0.05
104	10:46:52.843	5:42:02.975	-57.95	12.94	19.056 ± 0.164	24.527 ± 0.213		5.099 ± 0.304	> 0.806	> 5.905	0.68
135	10:46:55.830	5:41:53.184	-13.23	3.76	19.853 ± 0.138	23.865 ± 0.289		4.481 ± 0.337	> 0.889	> 5.370	0.49
165	10:46:57.107	5:41:26.884	6.16	-23.31	18.973 ± 0.097	23.084 ± 0.092		4.327 ± 0.142	> 2.033	> 6.360	0.02 E15
193	10:46:57.447	5:41:10.605	11.23	-39.55	19.649 ± 0.170	21.873 ± 0.031		2.322 ± 0.298	> 3.189	> 5.512	0.11
201	10:46:54.745	5:41:12.299	-30.07	-38.28	20.532 ± 0.409	22.814 ± 0.099		3.720 ± 0.794	> 1.303	> 5.024	0.00
202	10:46:59.108	5:41:11.928	35.61	-38.21	19.186 ± 0.135	24.086 ± 0.198		4.520 ± 0.287	> 1.094	> 5.613	0.73
208	10:46:55.260	5:41:11.192	-21.57	-39.24	19.556 ± 0.186	24.300 ± 0.306		5.113 ± 0.377	> 0.595	> 5.708	0.74
236	10:46:54.415	5:40:58.740	-33.78	-51.99	19.608 ± 0.234	22.553 ± 0.101		4.291 ± 0.430	> 1.296	> 5.587	0.00
242	10:46:58.137	5:40:58.446	22.04	-52.37	20.498 ± 0.340	21.035 ± 0.034		2.666 ± 0.807	> 2.102	> 4.768	0.00
250	10:46:56.891	5:40:52.194	2.81	-58.19	18.696 ± 0.123	23.615 ± 0.119		4.461 ± 0.232	> 1.574	> 6.035	0.94

Table 5.3 continued: Multi-colour optical- near-infrared catalogue of sources in the K -image centred on the $z = 1.226$ quasar. Page 3 of 4. Each source on this page is classified as a galaxy and is detected in both I and K bands, and the first 11 sources are detected in the V band also.

ID	RA (J2000)	Dec (J2000)	X_{QSO}	Y_{QSO}	X_{QSO}	Y_{QSO}	K_{total}	K_{total}	STAR
45	10:46:58.385	5:42:34.014	25.29	43.80	18.651 ± 0.135	0.76			
46	10:46:58.474	5:42:31.456	26.62	41.24	19.383 ± 0.181	0.02			
119	10:46:56.853	5:41:52.693	2.32	2.48	20.037 ± 0.127	0.06			
122	10:46:56.575	5:41:47.815	-1.85	-2.40	19.091 ± 0.074	0.42			
125	10:46:55.302	5:41:51.085	-20.96	0.87	20.194 ± 0.188	0.50			

ID	RA (J2000)	Dec (J2000)	X_{QSO}	Y_{QSO}	K_{total}	I_{total}	V_{total}	$I - K$	$V - I$	$V - K$	STAR
1	10:46:58.511	5:40:48.124	27.20	-62.06	15.391 ± 0.020	16.967 ± 0.002	17.380 ± 0.001	1.740 ± 0.013	0.379 ± 0.001	2.12 ± 0.001	0.99
2	10:46:58.168	5:40:45.518	22.00	-64.80	11.922 ± 0.001	15.448 ± 0.001	14.830 ± 0.001	4.834 ± 0.001	-0.793 ± 0.001	4.041 ± 0.001	0.97
51	10:46:59.479	5:42:32.415	42.03	42.03	18.135 ± 0.093	20.301 ± 0.009	22.562 ± 0.033	2.441 ± 0.105	2.279 ± 0.027	4.72 ± 0.027	0.88
91	10:46:56.541	5:42:11.510	-2.31	21.26	18.403 ± 0.069	21.920 ± 0.034	24.990 ± 0.195	3.573 ± 0.080	2.922 ± 0.149	6.496 ± 0.149	0.96
95	10:46:54.618	5:42:07.911	-31.13	17.70	16.126 ± 0.016	18.500 ± 0.001	20.506 ± 0.005	2.433 ± 0.010	2.108 ± 0.003	4.541 ± 0.003	0.99
121	10:46:56.691	5:41:50.206	0.00	0.00	15.461 ± 0.007	17.556 ± 0.001	18.120 ± 0.001	2.189 ± 0.004	0.636 ± 0.001	2.826 ± 0.001	0.99
128	10:46:55.483	5:41:49.282	-18.14	-0.88	19.790 ± 0.102	21.915 ± 0.030	23.637 ± 0.071	2.383 ± 0.273	1.543 ± 0.050	3.926 ± 0.050	0.83
141	10:46:57.378	5:41:41.102	10.18	-9.12	20.371 ± 0.168	23.340 ± 0.098	25.121 ± 0.207	2.931 ± 0.421	2.014 ± 0.215	4.946 ± 0.215	0.85
179	10:46:53.245	5:41:20.766	-51.82	-29.52	18.514 ± 0.146	21.427 ± 0.049	24.472 ± 0.278	3.562 ± 0.181	3.079 ± 0.188	6.641 ± 0.188	0.02
192	10:46:57.261	5:41:13.995	8.48	-36.19	14.372 ± 0.004	16.922 ± 0.001	17.567 ± 0.001	2.780 ± 0.002	0.568 ± 0.001	3.348 ± 0.001	0.99
199	10:46:52.644	5:41:13.007	-60.89	-37.46	17.739 ± 0.085	20.447 ± 0.020	23.224 ± 0.070	2.954 ± 0.080	3.771 ± 0.106	6.726 ± 0.106	0.80
206	10:46:53.821	5:41:07.084	-43.20	-43.18	12.034 ± 0.001	15.433 ± 0.001	15.065 ± 0.001	4.750 ± 0.001	-0.846 ± 0.001	3.904 ± 0.001	0.97
214	10:46:55.435	5:41:05.050	-18.93	-45.12	15.300 ± 0.011	17.763 ± 0.001	20.193 ± 0.003	2.537 ± 0.006	2.529 ± 0.002	5.066 ± 0.002	0.99
249	10:46:56.963	5:40:54.230	3.99	-55.79	18.289 ± 0.129	20.981 ± 0.026	23.476 ± 0.071	2.609 ± 0.131	2.593 ± 0.053	5.203 ± 0.053	0.84

Table 5.3 continued: Multi-colour optical- near-infrared catalogue of sources in the K -image centred on the $z = 1.226$ quasar. Page 4 of 4. The first table lists those sources detected in the K image only, and the second table lists those sources classified as stellar sources.

X_{QSO}, Y_{QSO} The position of the source relative to the quasar in units of arcsecs, with east and north the directions of increasing X and Y respectively.

K_{total}, I_{total}, V_{total} The total magnitudes (and errors) of each source in the *K*, *I* and *V* images according to the MAG_BEST output of SExtractor.

I-K, V-I, V-K The colours (and errors) of each source as determined through a single 2.5 arcsec diameter aperture. For those sources not detected in one of the bands, a lower limit is given which is taken to be the 90% completeness level for the non-detection band.

STAR The stellarity of the source based on the combined *V* and *I* data if possible. For those sources detected in *K* and *I* only, the stellarity is taken from the *I* data, and for those sources detected in the *K* image only, the stellarity is taken from the *K* data.

Comments Where given the comment indicates whether the source is either the quasar, indicated by 'QSO', or one of the early-type galaxies which make up the cluster red sequence. These are indicated by E1–18 in order of increasing *K* magnitude, and correspond to the sources of Table 5.5 and Figure 5.7.

The first two and a half pages of the table lists the 65 sources detected in all three passbands and which are classified as galaxies, whilst the remaining 16 sources on the third page are those detected in both *K* and *I* images, but not the *V* image, and are also classified as galaxies. The fourth page of the table lists the five galaxies detected in the *K* image only, and also the 14 sources classed as stars from a combination of their morphology and colour.

5.4 Galaxy Colours

The *I* – *K* versus *V* – *I* colour-colour diagram for sources in the *K* image is shown in Figure 5.2. Those galaxies whose colours are well described by the $z_f = 3.5$ burst model at $z \simeq 1.2$ are shown as filled red squares. Those galaxies whose colours are well described by galaxies at $z \simeq 1.2$ with some recent star-formation are shown as filled green circles, and the remainder of sources classified as galaxies are shown as

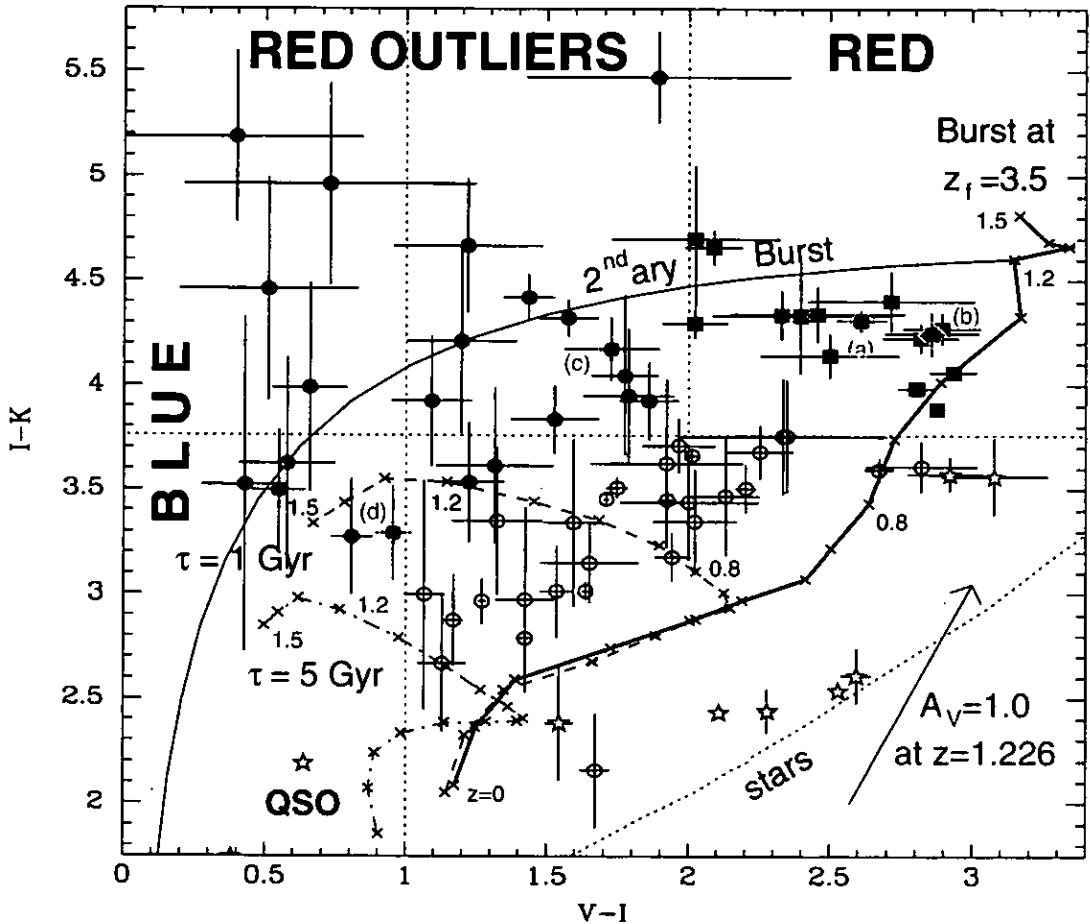


Figure 5.2: $I - K$ against $V - I$ colour-colour diagram for sources in the K image. Those galaxies whose colours are well described by the $z_f = 3.5$ burst model at $z \simeq 1.2$ are shown as red solid squares, those whose colours are well described by galaxies at $z \simeq 1.2$ with some recent star-formation are shown as green solid circles, and the remainder of sources classified as galaxies are shown as open circles. Those sources classified as stars are shown as blue star-symbols, and the model track for main sequence stars is shown as a blue dotted-line. The four galaxies whose redshift probability distributions are shown in Figure 5.3 are indicated by superimposed, labelled yellow diamonds. For comparison, model tracks are shown for an instantaneous burst at $z_f = 3.5$ (solid red line), and exponentially-decaying star-formation rate models with time-scales of 1 Gyr (green dashed-line) and 5 Gyr (magenta dot-dashed-line). Each track shows the colour evolution from $z = 1.5$ to $z = 0$ with crosses at 0.1 redshift intervals. The effect of adding a secondary burst of star-formation to the passively-evolving component is shown by the blue curve. The effect of internal extinction at $z = 1.226$ at the level of $A_V = 1.0$ is indicated by an arrow in the bottom-right corner.

open circles. The four galaxies whose redshift probability distributions are shown in Figure 5.3 are indicated by superimposed, labelled yellow diamonds.

For comparison, Figure 5.2 also has model tracks showing the colour evolution of the different galaxy types. The model curves correspond to stellar populations formed in an instantaneous burst (red solid-line), and stellar populations with exponentially-decaying SFRs with time-scales (τ) of 1 Gyr (green dashed-line) and 5 Gyr (magenta dot-dashed-line), and are thought to approximate the colour evolution of massive elliptical and disk-dominated galaxies respectively. Lilly et al. (1998) showed that the colours of disk-dominated galaxies at $z = 0.65\text{--}0.87$ are broadly fitted by similar models with $\tau = 5$ Gyr. The formation epoch of each model is set to $z_f = 3.5$, and each track shows the colour evolution from $z = 1.5$ to $z = 0$ with crosses at 0.1 redshift intervals. The galaxy ages are determined for an $H_0 = 75 \text{ km s}^{-1} \text{ Mpc}^{-1}$, $\Omega_M = 0.3$, $\Omega_\Lambda = 0.7$ universe, but most reasonable cosmologies do not affect the tracks significantly at these redshifts.

By considering the effects of redshift and star-formation on the colour of galaxies, it is possible to select galaxies of a particular type and redshift through colour selection. The $I - K$ colours of the model tracks increase monotonically with redshift to $z \simeq 1.3$, and it is clear that $I - K \simeq 4$ is a good indicator of galaxies at $z \gtrsim 1$ with predominantly old stellar populations. As a result, those galaxies with $I - K > 3.75$ (above the red dotted-line) are the most likely to be at $z \simeq 1.2$ and so this selection criterion is used to identify cluster candidates.

The effect of a recent secondary burst of star-formation on a high-redshift galaxy that had been previously evolving passively is shown by the blue curve. The secondary-burst model curve is created by taking the passively-evolving galaxy model in which the stellar populations form in an instantaneous burst at $z_f = 3.5$, to which are added increasing amounts of recent star-formation in the form of a 200 Myr long burst of constant star-formation, and are then observed at $z = 1.226$. The colour of the two-population model is then dependent on the mass ratio between the star-forming and passively-evolving components. It is clear that the effect of a recent burst of star-formation is to make the optical $V - I$ colour significantly bluer, without greatly affecting the $I - K$ colour. The relative mass fraction involved in the star-formation can be quite small, with only one percent of the total mass

required to be undergoing star-formation to produce a $V - I$ colour of $\simeq 1$, and only $\sim 0.1\%$ required to produce a $V - I$ colour of $\simeq 2.2$. Given that the effect of star-formation is predominantly in the $V - I$ direction, by selecting galaxies by their $V - I$ colour, star-forming and passively-evolving cluster members can be separated, and so a selection boundary of $V - I = 2.00$ (shown as green dotted-line) is used to classify galaxies as either passively-evolving (hereafter labelled *red*) or star-forming (hereafter labelled *red outliers*).

Galaxies dominated by star-formation are likely to have blue $V - I$ colours whatever the redshift, and so the selection of *blue* galaxies having $V - I < 1$ (left of cyan dotted-line) is used to identify these starbursting galaxies.

The effect of internal extinction at $z = 1.226$ at the level of $A_V = 1.0$ is indicated by an arrow in the bottom-right corner. It can be seen that the effect of internal dust-extinction in galaxies at the quasar redshift is to predominately increase the $I - K$ colour, and appears necessary to explain some of the more extreme red outlier galaxies with $I - K \simeq 5$.

The sources classified as stars by morphology and colour are shown as blue star-symbols. For comparison the model stellar track of Baraffe et al. (1998) is shown as a blue dotted-line. The models are for low-mass main sequence stars with solar-metallicity and an age of 5 Gyr. It is apparent that there is a good separation between the colours of stars and galaxies, with stars having much bluer optical-near-infrared colours than galaxies for a given $V - I$ colour, and so by selecting by both colour and morphology, stars and galaxies can be efficiently classified, as has been done here. Most of these stars are likely to be red dwarfs, given that the colour of a 5 Gyr old, $0.20 M_\odot$ main sequence star is $V - I = 2.41$, and also the stars' faint apparent magnitudes ($V \gtrsim 20$).

5.5 Photometric Redshift Estimation

Photometric redshift estimation, is the estimation of the redshift of a galaxy from colours obtained through multi-band photometry. The concept has been around for some considerable time; Baum (1962) originally applied it to measuring the redshifts of elliptical galaxies in distant clusters. However, the technique was not developed

until the nineties, when interest in the method increased with the advent of large- and deep-field surveys, and in particular the Hubble Deep Fields, where the galaxies are too faint to obtain spectroscopic redshifts.

There are two basic approaches to photometric redshift estimation: the empirical training set method; and the fitting of the observed spectral energy distribution (SED) by synthetic template spectra. The first approach uses a subsample of objects, with both photometry and measured spectroscopic redshifts, as a training set to estimate the remainder of the objects, for which only the photometry is known. This method can produce excellent results, and has the advantage of not making any assumptions concerning galaxy spectra or evolution, but is highly dependent on the quality of the sample used. This is particularly a problem at $z \gtrsim 1$ where only a few of the brightest galaxies have been observed spectroscopically, resulting in samples dominated by massive ellipticals.

The alternative approach takes a set of reference spectra which are allowed to evolve with redshift, before being multiplied by the filter set used, and the resultant colours compared with those of the observed galaxies. The photometric redshift of a given object then corresponds to the redshift of the best-fitting template spectra. The usual source of reference spectra are synthetic stellar populations which are given some initial mass function (IMF) and are then allowed to evolve, producing template galaxies of varying ages, star-formation histories, metallicities, and levels of internal dust-extinction, from which model galaxy colours can be calculated.

Given the large number of parameters involved, the key to obtaining accurate photometric redshift estimates is the ability to detect and identify strong spectral features, usually either the 4000 Å break for evolved galaxies, or the Lyman break for star-forming galaxies (see Figure 3.2). Estimates based on observations with filter sets that straddle one of these spectral features at the redshift range of interest will produce the most robust and accurate measurements. Much of the controversy involving the use of photometric redshift estimates has been due to the use of filter sets that are inappropriate for the redshift range considered, resulting in degenerate solutions and catastrophic errors where follow-up spectroscopic observations have found the photometric redshift estimate to be completely inaccurate. Another possible cause of significant errors in the photometric redshift estimate of a source is

the insensitivity of the broad-band filters to emission-lines, particularly those due to AGN. However, by using four or five appropriate passbands which cover the 4000 Å break at the redshift range of interest, it is possible to obtain results accurate to $\Delta z \simeq 0.1$ for all galaxy types, and even three passbands (as in this case) can constrain the redshifts and star-formation histories sufficiently to be of scientific value.

To estimate the photometric redshifts of each galaxy from its *VIK* colours, and to produce the model colour tracks of Figure 5.2, the HYPERZ code of Bolzonella et al. (2000) has been used. It builds synthetic template galaxies using the Bruzual & Charlot evolutionary code (GISSEL98; Bruzual & Charlot, 1993). It has stellar populations with eight star-formation histories roughly matching the observed properties of local galaxies from E to Im type: an instantaneous burst; a constant star-formation rate; and six exponentially-decaying star-formation rates with time-scales, τ , from 1 to 30 Gyr chosen to match the sequence of colours from E-S0 to Sd galaxies. The models assume solar metallicity and a Miller & Scalo (1979) initial mass function with upper and lower mass-limits for star-formation of $125 M_{\odot}$ and $0.1 M_{\odot}$ respectively. Internal reddening is also considered through the Calzetti et al. (2000) model with A_V allowed to vary between 0 and 0.5 mag.

For each redshift interval, the HYPERZ code determines the photometric properties of galaxies as a function of age, star-formation history, and A_V , and through a chi-squared minimisation process finds the best-fitting template at that redshift, which can then be converted to a probability that the galaxy is at that redshift. By repeating this for all redshift intervals, a redshift probability distribution, $P(z)$, is produced, rather than a single best-fitting redshift estimate for a galaxy. This is a particularly important feature of the software, as given the limited colour information available a wide range of redshifts may be compatible, as well as degenerate solutions, and so knowing the range of compatible redshifts is much more appropriate than a single best-fitting value.

The results of applying the HYPERZ photometric redshift estimation code to the *VIK* galaxy catalogue is shown in Table 5.4.

ID The identification number given to the source by SEXTRACTOR. This is the same as for Table 5.3 and Figure 5.1.

z_{best} The most probable redshift based on the source's photometry.

z_{mean} The mean redshift estimate produced by weighting the probability redshift distribution, i.e. $z_{\text{mean}} = \int z P(z) dz / \int P(z) dz$.

$P(z_{\text{best}})$ The probability of the redshift estimate associated with the chi-squared value of the fit at z_{best} .

Galaxy Class The identification number of the star-formation history of the best-fitting template galaxy. A value of 1 indicates the instantaneous burst model or single stellar population thought to represent the evolution of elliptical galaxies; values of 2–7 indicate exponentially-decaying star-formation rates with characteristic time-delays, τ , of 1, 2, 3, 5, 15 and 30 Gyr respectively used to model the evolution of E-S0 through to Sd galaxies; and a value of 8 indicates a template with a constant star-formation rate used to represent irregular galaxies.

Galaxy Age (Gyr) The age of the best-fitting template galaxy in Gyr.

$A_V(\text{best})$ The level of internal reddening for the best-fitting template galaxy.

$z_{\text{min, max}}(99, 90, 68\%)$ These six columns indicate the 99% (3σ), 90% (2σ) and 68% (1σ) confidence levels for the redshift estimate.

$P(z_{\text{QSO}})$ The probability of the redshift estimate associated with the chi-squared value of the fit at the redshift of the quasar.

$M_V(z_{\text{QSO}})$ The absolute magnitude of the source if placed at the quasar redshift, assuming an $\Omega_M = 0.3$, $\Omega_\Lambda = 0.7$, $H_0 = 75 \text{ km s}^{-1} \text{ Mpc}^{-1}$ cosmology.

Comments Where given the comment indicates whether the source is either the quasar, indicated by 'QSO', or one of the early-type galaxies which make up the cluster red sequence. These are indicated by E1–18 in order of increasing K magnitude, and correspond to the sources of Table 5.5 and Figure 5.7.

ID	z_{best}	z_{mean}	$P(z_{best})$ (%)	Gal. Class	Galaxy Age (Gyr)	A_V (best)	z_{min} (99%)	z_{max} (99%)	z_{min} (90%)	z_{max} (90%)	z_{min} (68%)	z_{max} (68%)	$P(z_{QSO})$ (%)	M_V (z_{QSO})
4	0.200	0.588	99.98	3	10.5000	0.40	0.049	1.223	0.077	0.612	0.100	0.539	3.64	-23.74
12	0.896	0.842	98.41	1	6.5000	0.05	0.748	0.970	0.758	0.911	0.890	0.903	3.16	-24.83 E1
15	1.240	1.329	99.99	1	1.0152	0.40	1.102	1.589	1.224	1.490	1.234	1.409	42.82	-23.41 E3
29	1.082	1.206	99.99	2	4.5000	0.10	0.191	1.838	0.822	1.765	0.907	1.179	67.02	-21.40
35	1.118	1.180	99.89	2	2.6000	0.40	0.000	2.053	0.858	1.835	0.962	1.707	86.33	-20.89
36	1.330	1.933	99.97	2	3.5000	0.05	0.951	2.800	1.087	2.056	1.128	1.513	99.36	-20.93
44	0.716	0.592	99.99	3	6.5000	0.35	0.257	0.950	0.273	0.903	0.286	0.867	5.95	-22.71
47	0.944	0.951	99.99	3	5.5000	0.45	0.846	1.054	0.873	1.026	0.896	1.009	72.44	-23.16
53	1.526	1.291	99.83	1	1.0152	0.10	0.814	1.717	0.859	1.689	1.223	1.628	66.34	-21.76 E13
57	1.470	1.310	99.97	1	0.5088	0.15	0.876	1.769	0.956	1.630	1.244	1.589	41.81	-21.46 E14
59	1.220	0.963	99.99	1	0.5088	0.20	0.130	1.771	0.230	1.629	0.631	1.535	96.59	-21.14
62	1.608	1.089	99.99	1	0.7187	0.00	0.154	1.909	0.225	1.780	1.481	1.712	75.93	-21.70
64	1.312	1.204	99.92	1	1.0152	0.15	0.778	1.621	0.841	1.559	1.106	1.522	74.40	-22.07 E11
65	0.920	0.676	99.86	3	3.5000	0.35	0.076	1.288	0.128	1.239	0.785	1.007	62.39	-22.33
68	1.234	1.219	99.69	1	0.5088	0.00	1.122	1.345	1.150	1.289	1.186	1.266	75.23	-24.20
73	1.172	0.949	99.99	1	0.7187	0.30	0.270	1.632	0.357	1.492	0.662	1.320	94.15	-21.35
77	1.416	1.341	99.99	1	0.3602	0.15	0.843	1.849	0.962	1.718	1.027	1.599	68.56	-21.19
81	2.072	1.541	99.91	2	2.3000	0.05	0.000	2.800	0.000	2.800	0.958	2.800	69.53	-19.38
83	1.176	0.990	99.92	1	1.4340	0.00	0.754	1.271	1.126	1.226	1.167	1.191	37.65	-23.62 E2
85	1.718	1.951	89.00	2	4.5000	0.20	1.005	2.800	1.226	2.731	1.504	2.316	23.14	-19.51
89	0.886	0.874	99.65	2	3.5000	0.45	0.695	1.005	0.784	0.968	0.821	0.954	42.70	-23.45
98	1.344	1.529	99.49	2	4.5000	0.15	1.140	1.913	1.213	1.476	1.291	1.415	34.72	-21.81

Table 5.4: Photometric redshift estimates of galaxies in the K image based on their VIK colours.

ID	z_{best}	z_{mean}	$P(z_{best})$ (%)	Gal. Class	Galaxy Age (Gyr)	A_V (best)	z_{min} (99%)	z_{max} (99%)	z_{min} (90%)	z_{max} (90%)	z_{min} (68%)	z_{max} (68%)	$P(z_{QSO})$ (%)	M _V (z_{QSO})
100	2.076	1.879	99.33	2	3.5000	0.20	0.000	2.800	1.242	2.800	1.628	2.610	22.77	-19.49
105	0.576	0.720	99.82	1	0.3602	0.20	0.256	1.101	0.394	1.044	0.436	1.024	0.00	-22.27
106	1.564	1.267	99.99	1	1.0152	0.00	0.395	1.829	0.808	1.764	1.190	1.694	69.97	-21.26 E16
107	1.304	1.249	99.96	1	1.0152	0.40	0.810	1.715	0.856	1.628	1.105	1.547	79.45	-21.99 E12
108	1.118	0.932	99.99	1	0.7187	0.45	0.340	1.557	0.391	1.426	1.103	1.256	89.50	-22.09
115	2.544	1.766	100.0	2	2.6000	0.15	0.000	2.800	0.097	2.800	1.263	2.800	48.52	-20.06
116	0.740	0.823	99.97	1	4.5000	0.35	0.559	1.116	0.591	1.106	0.598	0.863	0.28	-23.70
120	1.490	1.334	99.96	1	0.7187	0.35	1.006	1.638	1.311	1.625	1.382	1.586	25.49	-22.36 E10
126	1.258	1.495	99.64	2	4.5000	0.15	1.113	1.855	1.149	1.351	1.198	1.306	81.91	-21.99
127	2.226	2.077	99.99	2	2.0000	0.25	0.960	2.800	1.282	2.800	1.442	2.800	10.48	-20.55
129	2.498	1.802	99.99	1	0.3602	0.25	0.000	2.800	1.009	2.800	2.084	2.800	96.67	-20.76
137	1.020	1.110	99.93	5	3.5000	0.20	0.780	1.400	0.924	1.307	0.954	1.277	96.45	-22.06
145	1.552	1.956	99.99	2	4.5000	0.35	1.007	2.800	1.145	2.800	1.288	2.626	44.88	-20.57
146	1.020	0.648	99.96	5	1.4340	0.35	0.000	1.449	0.000	1.309	0.936	1.264	85.23	-21.15
149	1.062	0.855	99.97	5	3.5000	0.20	0.000	1.778	0.000	1.632	0.951	1.497	97.59	-21.05
150	1.140	1.415	99.95	2	4.5000	0.15	0.946	1.849	1.016	1.821	1.107	1.228	68.41	-21.61
151	1.200	1.418	99.85	3	2.3000	0.35	1.018	1.859	1.088	1.771	1.114	1.289	95.59	-21.58
152	0.786	0.832	99.62	1	6.5000	0.15	0.502	1.230	0.574	1.110	0.597	0.863	10.04	-22.36
155	0.790	0.763	99.96	3	6.5000	0.45	0.244	1.422	0.273	0.979	0.300	0.955	42.95	-21.85
156	1.100	0.983	99.99	2	2.0000	0.45	0.000	1.826	0.834	1.628	0.940	1.489	94.10	-20.82
158	1.280	1.911	100.0	4	1.7000	0.45	0.492	2.800	1.116	2.070	1.148	1.909	98.87	-21.33
159	0.870	0.732	99.97	4	6.5000	0.30	0.112	1.349	0.170	1.268	0.674	1.011	65.90	-21.13

Table 5.4 continued: Photometric redshift estimates of galaxies in the K image based on their VIK colours. Page 2 of 3.

ID	z_{best}	z_{mean}	$P(z_{best})$ (%)	Gal. Class	Galaxy Age (Gyr)	A_V (best)	z_{min} (99%)	z_{max} (99%)	z_{min} (90%)	z_{max} (90%)	z_{min} (68%)	z_{max} (68%)	$P(z_{QSO})$ (%)	M _V (z_{QSO})
162	1.552	1.318	99.92	1	1.0152	0.05	0.873	1.708	1.262	1.659	1.451	1.626	13.53	-22.13 E9
166	0.844	0.997	99.73	1	6.5000	0.45	0.791	1.237	0.810	0.919	0.817	0.873	54.13	-23.51 E4
171	1.158	1.219	99.98	1	0.5088	0.40	1.105	1.415	1.142	1.283	1.152	1.245	65.53	-23.98
174	1.222	0.982	99.70	1	0.7187	0.10	0.389	1.382	1.095	1.304	1.113	1.233	82.90	-22.32
180	1.164	1.164	99.89	1	0.5088	0.40	0.750	1.578	1.080	1.486	1.150	1.290	90.92	-22.10
184	1.718	1.956	37.57	2	4.5000	0.25	1.235	2.709	1.521	2.314	1.634	1.719	1.07	-19.86
188	1.262	1.282	99.96	1	0.5088	0.40	0.793	1.705	1.195	1.627	1.228	1.313	59.66	-22.12
194	1.040	1.125	99.93	1	3.5000	0.00	0.820	1.507	0.852	1.456	0.859	1.314	87.67	-22.95 E7
196	1.140	1.130	99.97	1	1.4340	0.30	0.801	1.529	0.841	1.467	0.855	1.318	92.02	-22.85 E8
198	0.940	0.680	100.0	5	6.5000	0.20	0.000	1.620	0.000	1.343	0.052	1.286	78.41	-21.65
200	2.174	2.080	99.97	1	0.7187	0.40	1.160	2.800	1.687	2.565	1.829	2.383	9.34	-21.28
215	1.264	1.802	99.99	2	5.5000	0.25	0.280	2.800	0.950	1.910	1.102	1.274	96.62	-21.55 E18
216	0.980	1.087	99.89	7	5.5000	0.30	0.864	1.305	0.924	1.117	0.950	1.097	87.72	-23.50
219	0.852	0.829	99.92	2	4.5000	0.25	0.283	1.456	0.315	0.980	0.585	0.943	67.11	-22.32
220	0.898	0.595	99.61	2	2.3000	0.40	0.190	1.010	0.638	0.965	0.753	0.948	7.37	-23.95
239	2.616	2.618	98.73	1	0.5088	0.15	2.478	2.728	2.537	2.696	2.574	2.680	84.74	-22.71 E6
254	0.868	0.735	99.77	2	5.5000	0.00	0.354	0.967	0.676	0.942	0.719	0.905	54.98	-23.49
255	2.312	1.836	100.0	2	2.6000	0.40	0.000	2.800	1.182	2.800	1.340	2.800	39.64	-20.83
259	0.980	0.826	99.94	2	2.6000	0.45	0.056	1.592	0.140	1.486	0.783	1.276	94.53	-21.84
261	1.060	1.119	99.98	1	2.0000	0.30	0.814	1.477	0.849	1.416	0.858	1.317	93.02	-23.12 E5
265	1.116	0.826	99.84	1	0.5088	0.30	0.197	1.557	0.254	1.370	1.050	1.261	78.32	-21.36

Table 5.4 continued: Photometric redshift estimates of galaxies in the K image based on their VIK colours. Page 3 of 3.

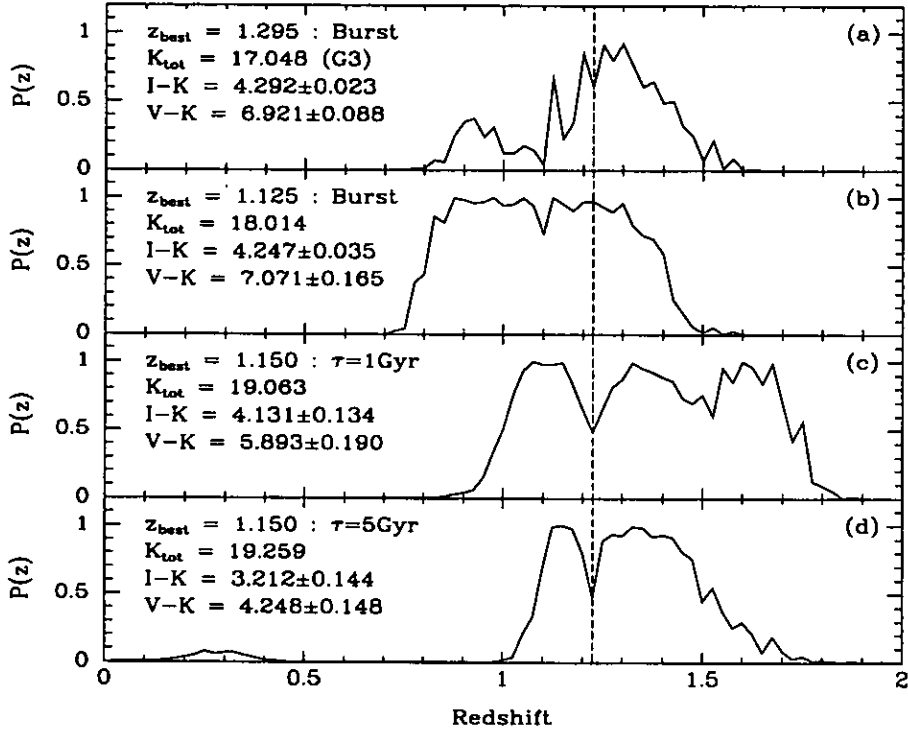


Figure 5.3: Redshift probability distributions for four galaxies in the K image based on their VIK colours. The best fitting model is described by its redshift z_{best} and star-formation history, which is either an instantaneous burst or an exponentially-decaying star-formation rate with time-scale τ . The vertical dashed-line indicates the redshift of the quasar.

In Figures 5.3a–d the redshift probability distributions, $P(z)$, are shown for four galaxies which are compatible with being at the quasar redshift, incompatible with being at $z \lesssim 0.8$, and which represent the differing classes of galaxies discussed in the text below. For each of the galaxies, the best-fitting model is described by its redshift, z_{best} , and star-formation history, which is either an instantaneous burst or an exponentially-decaying star-formation rate with time-scale τ . The vertical dashed-line indicates the redshift of the quasar.

Distributions (a) and (b) correspond to two *red* galaxies, IDs #15 and #196. These are galaxies with colours close to those predicted for stellar populations formed in an instantaneous burst at $z_f = 3.5$ and observed at $z \simeq 1.2$ (Figure 5.2). They also help make up the observed red sequences in both the $V-K$ and $I-K$ against K colour-magnitude plots of Figure 5.4. The colours of both galaxies are best described by the $z_f = 3.5$ burst model at $z \simeq 1.2$, and galaxy (a) in particular has a tight range of compatible redshifts, being constrained to $1.1 \lesssim z \lesssim 1.4$.

Redshift probability distribution (c) corresponds to a ‘red outlier’ galaxy, ID #150. It has a similarly red $I - K$ colour to galaxies (a) and (b), and it is this that constrains its redshift to $z \gtrsim 1$. Its optical $V - I$ colour is much bluer, indicating more recent star-formation, and results in it being best fitted by a $\tau = 1$ Gyr exponentially-decaying model. An examination of Figure 5.2 suggests that the combination of blue optical colour and extremely-red optical- near-infrared colour may be better explained by a two-component star-formation model in which a secondary burst of star-formation is added to a dominant old passively-evolving stellar population. However, given the limited colour information available the only conclusions that should be drawn are that the galaxy is at high-redshift, has a dominant old stellar population, and some recent star-formation.

Redshift probability distribution (d) corresponds to a blue ($V - I < 1$) galaxy, ID #151. It is bluer in both $V - I$ and $I - K$ colours than galaxy (c), but has a similar redshift probability distribution. The difference in their colours appears due to an increased fraction of recent star-formation in galaxy (d) which is manifested by it being fitted best by a $\tau = 5$ Gyr model.

It appears from an examination of Figures 5.3a–d that it is possible to identify galaxies at $z \gtrsim 1$ on the basis of their VIK colour information alone, irrespective of their star-formation history. Although insufficient to say definitively whether an individual galaxy is associated with the $z = 1.226$ quasar, it is possible to identify suitable candidates for follow-up spectroscopy in a manner relatively unbiased with respect to star-formation history.

5.5.1 Red Sequence Galaxies

There are 15–18 galaxies (hereafter labelled ‘red’) whose extremely-red colours ($I - K > 3.75$, $V - I > 2.00$) are consistent with being passively-evolving galaxies at $z \simeq 1.2$ (indicated by red squares in Figure 5.2). These red galaxies can be seen (as red squares again) in the $V - K$ and $I - K$ against K colour-magnitude diagrams of Figure 5.4 to form ‘fingers’ at $V - K \simeq 6.9$ and $I - K \simeq 4.3$, comparable in form to the red sequences observed in lower redshift clusters, and in colour to other clusters at the same redshift. The $z \simeq 1.2$ clusters of Dickinson (1995), Stanford et al. (1997), and Rosati et al. (1999) are all observed to have red sequences

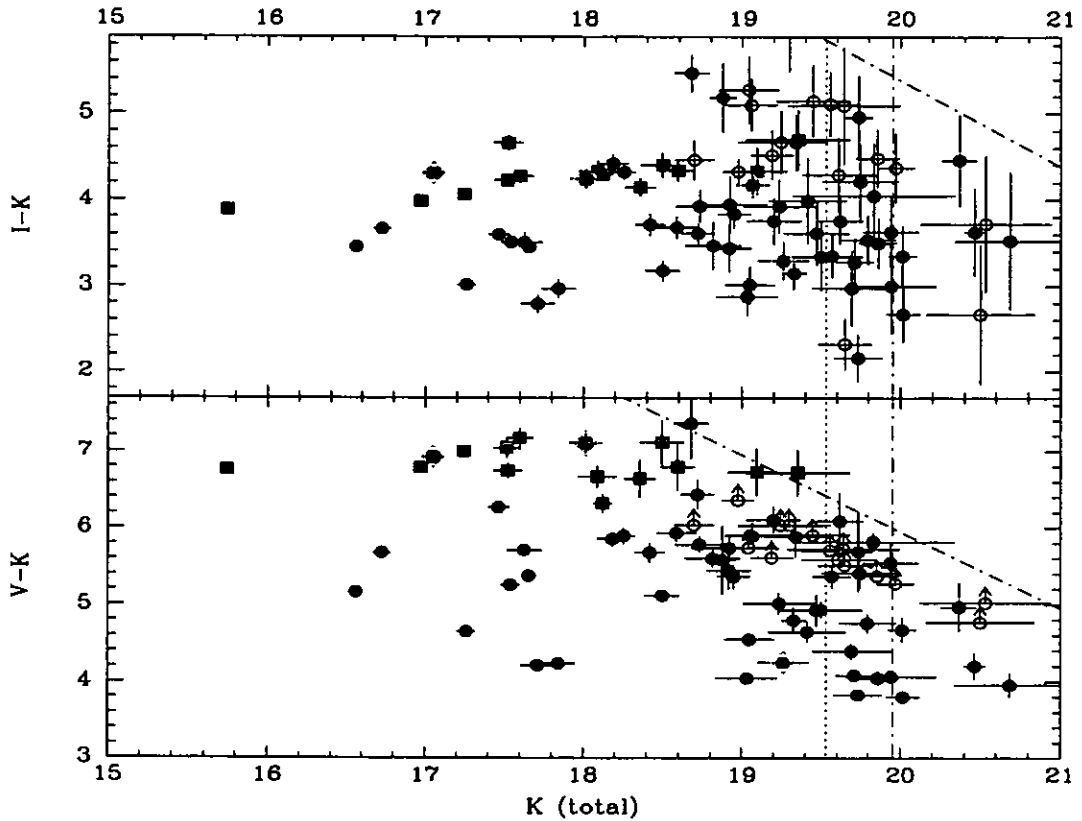


Figure 5.4: $V - K$ against K and $I - K$ against K colour-magnitude diagrams of galaxies in the 2.25×2.25 arcmin² K image centred on the $z = 1.226$ LQG quasar. The solid symbols represent those galaxies detected in all three bands. The empty symbols represent those galaxies detected in I and K only. Galaxies whose colours are well described by the $z_f = 3.5$ burst model at $z \simeq 1.2$ are indicated by red squares. The four galaxies whose redshift probability distributions are shown in Figure 5.3 are indicated by yellow diamonds. The green and blue dot-dashed-lines indicate the 50% completeness levels for each filter in the centre of the image, with the magenta dotted-line indicating the completeness level in K for the edge of the image.

at $R - K \simeq 5.9$, each with $\gtrsim 4$ members spectroscopically confirmed as being at the cluster redshift. The red sequence galaxy colours can be compared directly for the Rosati et al. (1999) cluster where $I - K$ colour data exist, and the four spectroscopically confirmed red sequence members all have $4 < I - K < 4.4$, in good agreement with the red sequence members observed here. The colours of these red sequence galaxies are well described by the passively-evolving monolithic-collapse models of elliptical galaxies, and both their spectra and morphologies (from HST data) are similar to present-day ellipticals (Dickinson, 1997). Red sequence galaxies are usually the most luminous cluster members, the massive ellipticals, and this also

appears to be the case here, with the 10 brightest galaxies with $I - K > 3.75$ also having $V - K \simeq 6.9$. Given that these are both the reddest and most luminous galaxies, these should provide the tightest redshift estimates, and Figure 5.3a shows that the third brightest of these galaxies (G3) has $1.2 \lesssim z \lesssim 1.4$.

The mean $I - K$ colour of the red galaxies is 4.25 with an intrinsic dispersion of 0.15 mag, and is best fit by a 2 Gyr old burst with a corresponding age dispersion of 400 Myr. The colour distribution seen in the red sequence is comparable to that seen in the cluster of Tanaka et al. (2000) (0.22 mag in $R - K$), but is larger than that seen in the cluster associated with the radio galaxy 3C 324 at $z = 1.206$ (Dickinson, 1995) which has an rms scatter of 0.07 mag in $R - K$, suggesting that this cluster is less dynamically evolved than that of Dickinson (1995).

5.5.2 Red Outlier Galaxies

Only half of the excess of $I - K > 3.75$ galaxies is accounted for by the red sequence members, and comparable numbers (15–20) of $K \gtrsim 19$ galaxies are observed (hereafter labelled ‘red outliers’) with both $I - K > 3.75$ and $V - I < 2.00$. They appear to fit neither the passively-evolving nor exponentially-decaying star-formation galaxy models (Figure 5.2), but are better described by a two-component model in which a secondary burst of recent star-formation is added to a dominant old stellar population.

Galaxies with similar colours and magnitudes have been observed in other clusters at $z \simeq 1.2$ (e.g. Tanaka et al., 2000; Kajisawa & Yamada, 1999; Kajisawa et al., 2000). They have also been observed at $20 \lesssim K \lesssim 22$ in deep optical- near-infrared surveys (e.g. Moustakas et al., 1997), and appear common (several per square arcminute) at these fainter magnitudes. Much of the discussion (see e.g. Moustakas et al., 1997) of these objects has been limited to speculation due to lack of spectroscopic observations, but a widely held view is that they are probably high-redshift objects ($1 \lesssim z \lesssim 2$) which are undergoing significant star-formation and whose extremely-red $I - K$ colours are caused by a combination of dust and dominant old stellar populations. There is also some spectroscopic evidence that some $z \simeq 1.2$ cluster ellipticals are undergoing star-formation, such as O II emission-lines seen in object #4 of Rosati et al. (1999) and object #237 of Stanford et al. (1997),

both of which appear bluer in optical colours than the other red sequence galaxies in the clusters. Some extreme members of this population have been observed with $I - K > 6$ (e.g. Hu & Ridgway, 1994), and one has since been spectroscopically confirmed as an ultra-luminous infrared galaxy at $z = 1.44$ with significant ongoing star-formation that is heavily obscured by dust (Graham & Dey, 1996; Dey et al., 1999). Given that both star-formation and dust are likely to have affected the colours of these ‘red outliers’ significantly, it is not possible to constrain the galaxy redshifts beyond $z \gtrsim 1$ (Fig. 5.3c), but their prevalence in the vicinity of other high-redshift clusters, and the relative rarity of field $I - K > 3.75$ galaxies, suggests that many are associated with the cluster.

5.6 Spatial Distribution of Galaxies

The spatial distribution of galaxies detected in the K image, is shown in Figure 5.5 with the $z = 1.226$ quasar indicated by the central green triangle. The solid red symbols indicate the locations of the members of the observed red sequence and which are likely to be massive ellipticals at the quasar redshift. The solid green and blue star symbols indicate the red outlier and blue ($V - I < 1$) galaxies respectively, whilst the open symbols indicate the remaining sources in the image that are likely to be low-redshift foreground galaxies.

For comparison, the VIK three-colour image of the 2.25×2.25 arcmin² field covered by the K -band data is shown in Figure 5.6. The red sequence members are apparent as orange-red sources concentrated towards the top-centre and bottom-right of the image. The quasar is apparent as the central, bright, blue-white, point-like source. The red structures apparent in each corner, and along the edges of the field, are due to the relative exposure levels produced by the 9-point jitter pattern. The *band* of enhanced star-formation discussed later is apparent in the form of a concentration of blue-violet sources across the centre of the image.

5.6.1 Red Sequence Galaxies

The red galaxies appear to be distributed across the K image (the field corresponds to $1.75 \times 1.75 h^{-2}$ Mpc² at $z = 1.226$) with no concentration towards the quasar.

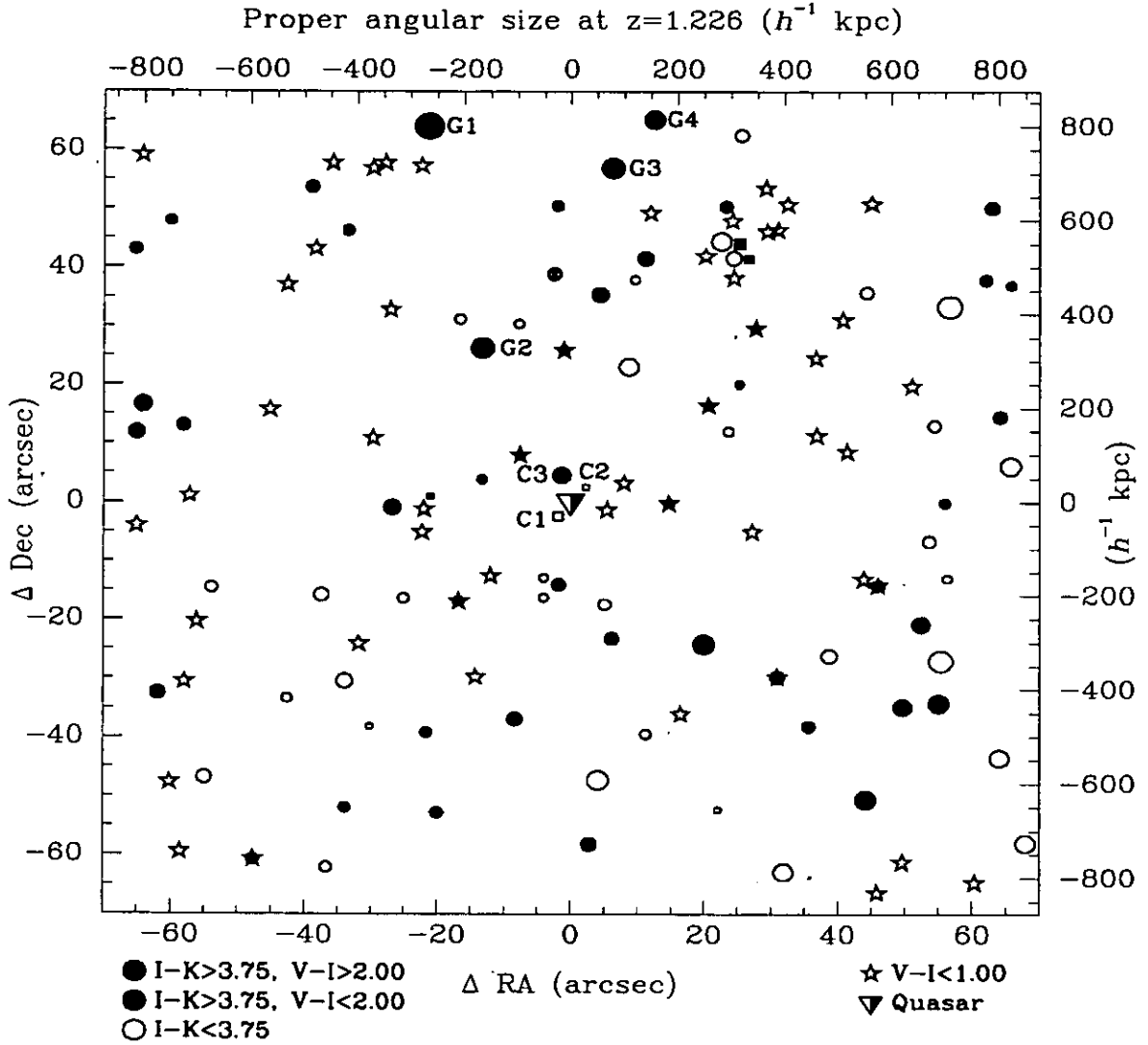


Figure 5.5: Spatial distribution of galaxies in the field of the $z = 1.226$ LQG quasar. The different symbols indicate the galaxies' colours, with circles (squares) indicating those galaxies detected (not detected) in I . Solid red symbols indicate the red ($I - K > 3.75, V - I > 2.00$) galaxies which could be early-type galaxies at the quasar redshift. Solid green symbols indicate the red outlier ($I - K > 3.75, V - I < 2.00$) galaxies which are likely to be high-redshift galaxies with some recent star-formation. The blue star-symbols indicate the blue ($V - I < 1.00$) galaxies which are probably undergoing significant star-formation. The size of the symbols (except stars) indicates the K_{total} magnitude.

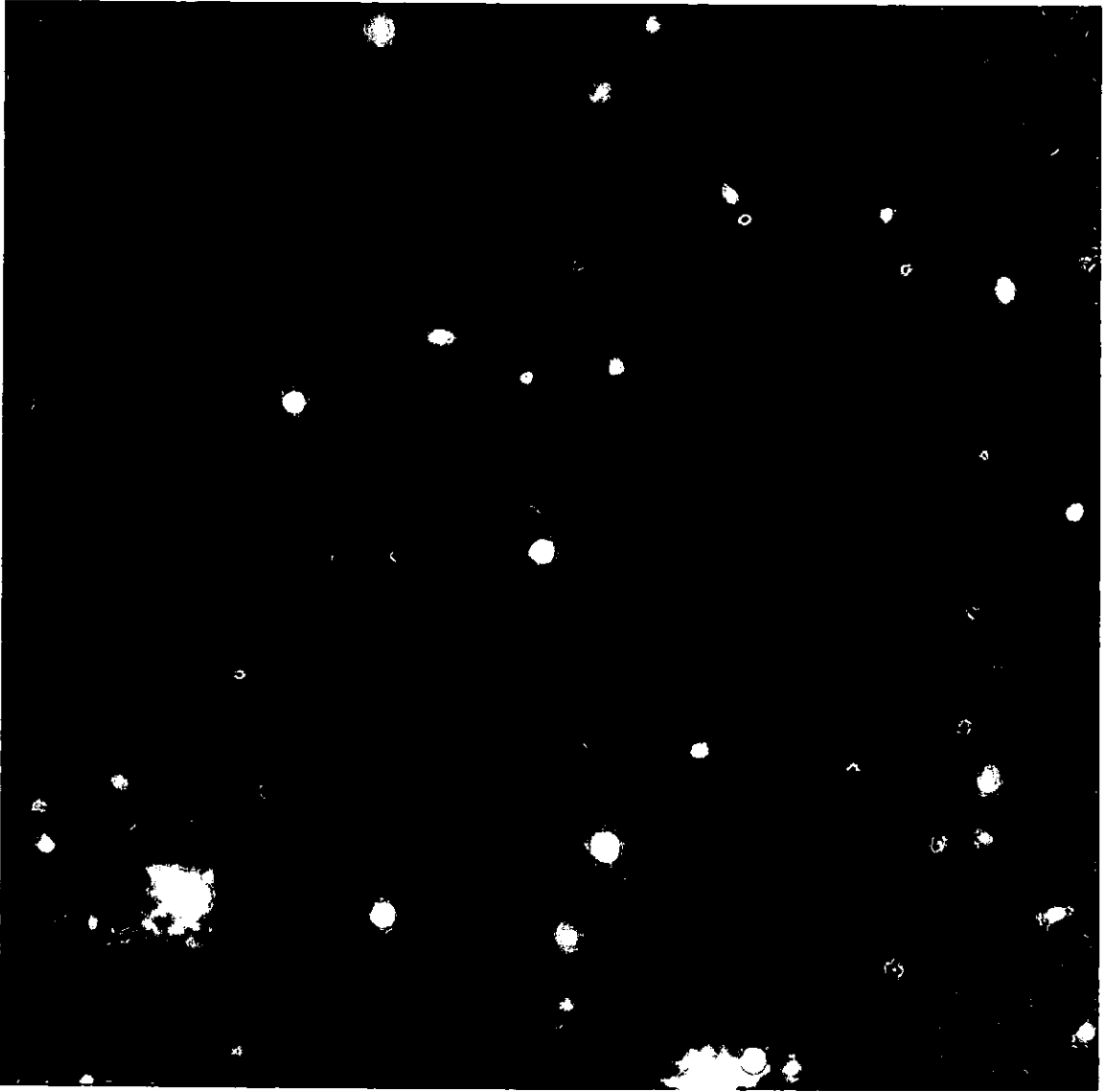


Figure 5.6: False-colour image produced from the combination of the V (blue component), I (green) and K (red) images. The $z = 1.226$ quasar is apparent as the blue-white point-like source in the centre of the image. The red galaxies likely to be massive ellipticals at the quasar redshift can be seen as orange-red sources, and are concentrated towards the top-centre and bottom-right of the image. The *band* of enhanced star-formation is apparent in the form of a concentration of blue-violet sources across the centre of the image.

However, the ten most luminous red galaxies (which, as indicated earlier, are probably massive ellipticals at the quasar redshift) are concentrated in two compact groups, one towards the top-centre of the image (along with a number of fainter members), and the other in the south-eastern corner. This suggests that the galaxy excesses and red sequences could be due to two clusters at similar redshifts.

Assuming that the brightest of the red galaxies, G1, is a quiescent galaxy at the quasar redshift, then it has $L \approx 14L_K^*$, and is more luminous in K , by almost a magnitude, than any of the galaxies from other $z \sim 1.2$ clusters (Dickinson, 1995; Stanford et al., 1997; Rosati et al., 1999). It is also a radio emitter, being the only source in the K image detected by the VLA FIRST 20cm survey, having an integrated flux of 2.63 ± 0.15 mJy, which suggests that it has an active nucleus. It is common for the brightest cluster galaxy (which is what this is assumed to be) to be also a radio source, although it is not as spectacular an example as 3C 324 which is at a similar redshift, but is 1000 times more luminous in the radio. If this galaxy is comparable to 3C 324 then it may also display narrow-line emission, in particular OII and MgII, and this may explain why it appears bluer than the other red sequence galaxies, as the emission-lines boost the optical flux. The brightest cluster galaxy is usually located near the cluster centre, and it appears to be the case here too if Figures 5.5 and 5.8 are compared.

To examine the significance of any substructure for the red galaxies the non-parametric cluster analysis method of Pisani (1993, 1996) and described in Chapter 3 is applied. The probability density estimate of red galaxies, $f_{ak}(\mathbf{x})$ is determined using the cross-validation method to estimate the mean kernel width, σ , and is shown in Figure 5.7 with the two density peaks, labelled A and B, assumed to mark the two cluster centres.

Having produced the probability density estimate, each galaxy is assigned membership to one of the clusters by following a path from the original position \mathbf{x}_i along the maximum gradient of $f_{ak}(\mathbf{x})$ until it reaches the local maximum A or B. The contribution to the local density from each cluster, $f_A(\mathbf{x}), f_B(\mathbf{x})$, is then taken to be the sum of the kernels for galaxies assigned to that cluster.

The expected background contamination from red field galaxies, $f_0(\mathbf{x})$, is unknown, and so it has been estimated to be half that of the $I - K > 3.75$ field galaxies

ID	K_{tot}	A/B	$P(i \in 0)$	$P(i \in A)$	$P(i \in B)$
1	15.75	A	0.0827	0.9075	0.0098
2	16.97	A	0.0324	0.9259	0.0417
3	17.05	A	0.0259	0.9626	0.0115
4	17.24	B	0.0562	0.1172	0.8266
5	17.52	A	0.0391	0.9468	0.0142
6	17.52	B	0.0438	0.0128	0.9434
7	17.60	B	0.0319	0.0159	0.9522
8	18.01	B	0.0306	0.0164	0.9529
9	18.09	B	0.0357	0.0298	0.9345
10	18.12	A	0.0583	0.6754	0.2663
11	18.35	A	0.0188	0.9582	0.0230
12	18.50	A	0.6440	0.2716	0.0844
13	18.59	A	0.0200	0.9595	0.0205
14	18.95	A	0.0191	0.9641	0.0167
15	18.97	B	0.0732	0.2129	0.7139
16	19.09	B	0.1860	0.2110	0.6030
17	19.24	A	0.2852	0.3465	0.3683
18	19.35	B	0.2512	0.1011	0.6477

Table 5.5: Results from the cluster membership analysis of the red galaxies. Column A/B indicates whether a galaxy was assigned to cluster A or B, and the last three columns show the probabilities that a galaxy is isolated or a member of cluster A or B.

or 0.5 galaxies per square arcminute, as about half the $I - K > 3.75$ galaxies are also classified as red ($I - K > 3.75, V - I > 2.00$). The probability that each galaxy is isolated, and hence due to the background component, is just the contribution of the background density as a fraction of the local density $P(i \in 0) = f_0/f_{ak}(\mathbf{x}_i)$. The probability that galaxy i is a member of cluster A is then the fractional contribution of cluster A to the local density, after considering the background contribution $P(i \in A) = (1 - P(i \in 0))f_A(\mathbf{x}_i)/f_{ak}(\mathbf{x}_i)$, and for each of the red galaxies these probabilities are shown in Table 5.5. Looking at this table and Figure 5.7 it appears that the two clusters are well defined, with 11 out of the brightest 14 galaxies having probabilities greater than 0.90 of having been assigned correctly to cluster A or B. Only galaxies #4 and #10 have significant doubt over cluster assignment, and #12 appears to be isolated, whilst the four faintest red galaxies show no clear

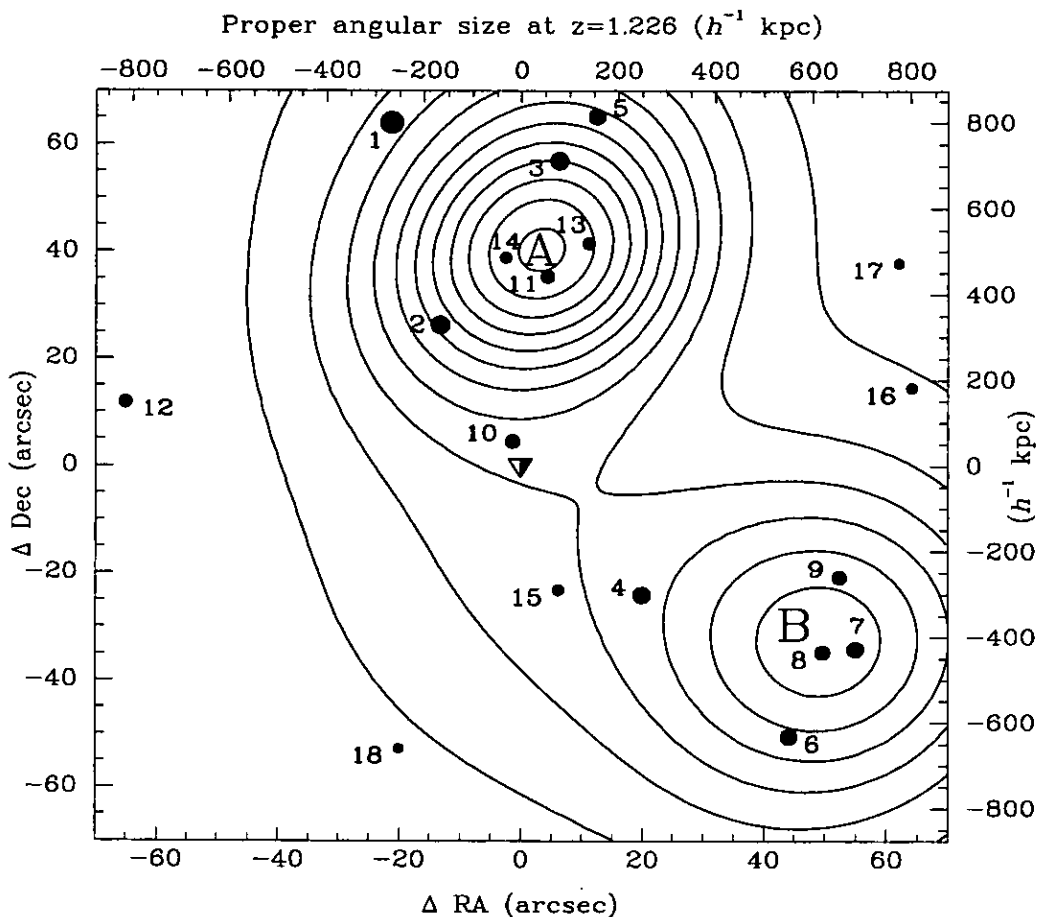


Figure 5.7: Estimated density distribution of the red galaxies in the field of the $z = 1.226$ LQG quasar. The first contour corresponds to a density of 1 galaxy per square arcminute, and the separation of successive contours is also 1 galaxy per square arcminute. The quasar and red galaxies are marked as in Figure 5.5, and the labels correspond to the galaxy IDs of Table 5.5, which are numbered in order of increasing K magnitude.

membership of either cluster, and may be only part of the combined structure.

As a second estimate of the significance of the substructure, the null hypothesis that the galaxies are all members of a single cluster is examined, using the likelihood ratio test statistic (LRTS) described in Chapter 3 (Ashman et al., 1994; Kriessler & Beers, 1997) which evaluates the improvement in fitting the data of a two-component model over a single elliptical Gaussian probability density function. The best-fit single elliptical Gaussian $f_{(1)}(\mathbf{x})$ to the data is found, and this unimodal probability density function is used to create 10000 bootstrap catalogues of 18 galaxies each. The adaptive kernel estimator is applied to each bootstrap catalogue in the same way as the original data, and for those catalogues where bimodality is observed, the

best-fitting double elliptical Gaussian model is determined. The measure of the fit by the g-component model is evaluated through the likelihood value

$$L_C(g) = \prod_{i=1}^N \left(\sum_{\mu=1}^g f_{(g;\mu)}(\mathbf{x}_i) \right)^{1-P(i \in 0)}. \quad (5.5)$$

The evaluation of the improvement in going from a single- to a double-Gaussian fit is then given by the LRTS $\lambda = -2 \ln\{L_C(2)/L_C(1)\}$. The significance of the substructure observed is estimated by the probability that a null hypothesis bootstrap catalogue produces a value of λ greater than the observed value. For the observed distribution, using 10000 bootstrap catalogues, the substructure is found to be marginally inconsistent with the null hypothesis at the 8.88% significance level. The low level of significance is due to the small number of galaxies involved, as many of the more significant substructures among the bootstrap catalogues were due to just three or four points that were within a few arcsec of one another.

5.6.2 Clustering across Large-Scales

As both groups are located near the edges of the K image, and so may suffer from truncation, the full extent of clustering associated with the quasar is estimated by considering the distribution of galaxies in the BTC V and I images. As discussed in Chapter 4 and as shown by Figure 5.2, any passively-evolving galaxy associated with the cluster should be amongst the reddest galaxies in $V - I$, and so by selecting these red galaxies, the density contrast due to any clustering at $z \simeq 1.2$ should be maximised. In Chapter 4, high-redshift passively-evolving galaxies were identified by being redder than the cluster red sequence at $z = 0.5$, resulting in a high-redshift slice in the colour-magnitude diagram. Figure 5.8 shows the surface density of galaxies belonging to this high-redshift slice for a 6.8×5.7 arcmin² (corresponding to $5.3 \times 4.3 h^{-1}$ Mpc at the quasar redshift) field containing the $z = 1.226$ quasar, which is estimated as in Chapter 4 using the adaptive kernel estimator with $\sigma = 350 h^{-1}$ kpc. The field is the same as that for Figures 4.16 and 4.17, and the density map shown here is exactly the same as that of Figure 4.17. The contours increase logarithmically with separation $\sqrt{2}$, with the red contour set to 2 galaxies per arcmin², which is approximately the mean density across the whole BTC field. The area covered by K imaging is indicated by the black box. The two density

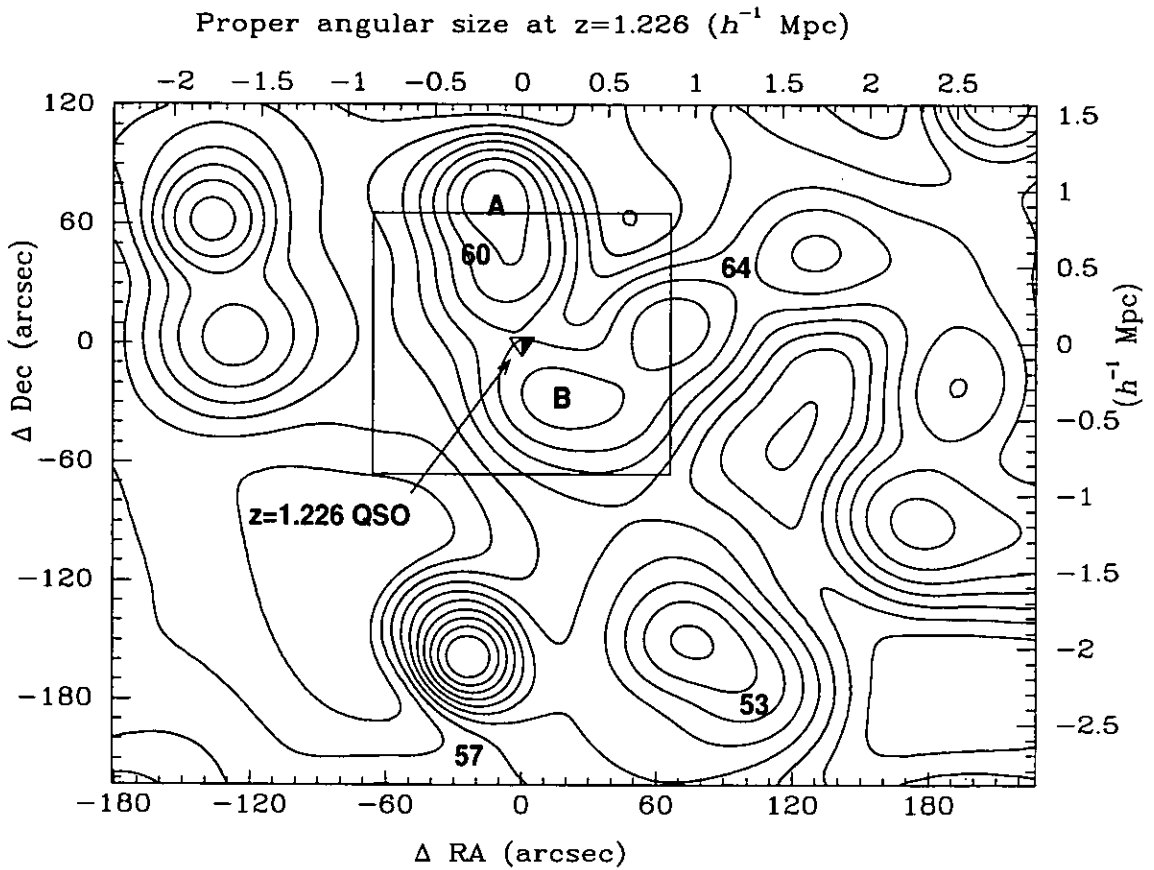


Figure 5.8: Contour plot of the estimated density distribution of galaxies redder than the $z = 0.5$ cluster red sequence (including all C-M relation members) in a $6.8 \times 5.7 \text{ arcmin}^2$ (corresponding to $5.3 \times 4.3 h^{-2} \text{ Mpc}^2$ at $z = 1.226$) field around the quasar. The contours increase logarithmically with separation $\sqrt{2}$, with the red contour set to 2 galaxies per arcmin^2 . The quasar is marked as previously, and the box centred on the quasar corresponds to the field of the K image.

maxima identified in the previous section as clusters A and B are indicated in red, and the density maxima identified in Chapter 4 are indicated in green.

It is clear from this figure that the clustering extends well beyond the K image. Cluster A now appears to be centred on the northern edge of the K image and corresponds to density maximum #60 of the previous chapter. Cluster B appears part of an elongated, filamentary structure which extends 2–3 arcmin to the north-east that was identified in the previous chapter as density maximum #64. Two further groups (identified in the previous chapter as density maxima #53 and #57), each of 6–10 optically-red galaxies, are apparent 3 arcmin south of the quasar and 1.5 arcmin apart. The significance of the substructure formed by clusters A and B appears to be much higher now, as the density peaks are moved further apart. A

re-examination of the null hypothesis, after including the red galaxies outside the K image, finds the substructure to be inconsistent with the null hypothesis at the 1.86% significance level. The increase in significance suggests that the clusters were truncated by the boundaries of the K image, but the increase is also partly due to the larger galaxy sample.

As stated in the previous chapter, the total excess of galaxies belonging to the high-redshift slice within 5 arcmin (corresponding to $3.9 h^{-1} \text{Mpc}$ at the quasar redshift) is $\simeq 100\text{--}150$. Given that an L^* galaxy at $z = 1.226$ has $I \simeq 23.5$, the total luminosity of the structure can be estimated as $100\text{--}150 L^*$, which for an average cluster mass-to-luminosity ratio of $M/L \approx 300 h M_{\odot}/L_{\odot}$, corresponds to a conservative mass estimate of $M_{cl} \gtrsim 3\text{--}4.5 \times 10^{14} M_{\odot}$, suggesting that the overall cluster mass is comparable to that of the Coma cluster with $M_{Coma} \simeq 6 \times 10^{14} M_{\odot}$.

5.6.3 Blue Galaxies

To compare this quasar field with the results of Hutchings et al. (1995) the distribution of blue ($V - I < 1$) galaxies for $I < 25$ (indicated by star-symbols in Figure 5.5) has also been examined. A concentration of blue galaxies within 30 arcsec ($290 h^{-1} \text{kpc}$) of the quasar is observed, which appears to be extended towards the north-east, forming a ‘band’ that bisects the two groups of red galaxies. The band presumably corresponds to a region of enhanced star-formation. Few, however, are found near the centres of either group of red galaxies. In comparison with adjacent fields (over a $7 \times 7 \text{ arcmin}^2$ region) in the optical images no excess of blue galaxies is found. In fact 51 are observed whereas 60 would be expected, suggesting that the avoidance of the two red groups by the blue galaxies is at least as significant as the bisecting ‘band’.

To examine the relative spatial distribution of red and blue galaxies, the angular cross-correlation function, $\omega_{rb}(\theta) = N_{rb}(\theta)/N_{rR} - 1$, is determined (see Figure 5.9), where $N_{rb}(\theta)$ is the number of red-blue galaxy pairs with separation θ , and $N_{rR}(\theta)$ is the expected number of pairs with one member from the red catalogue and the other from one of 10 000 randomly distributed catalogues.

At small separations ($\theta < 20 \text{ arcsec}$) the red and blue galaxies are strongly anti-correlated at the 3σ level, confirming the apparent avoidance of the red groups by

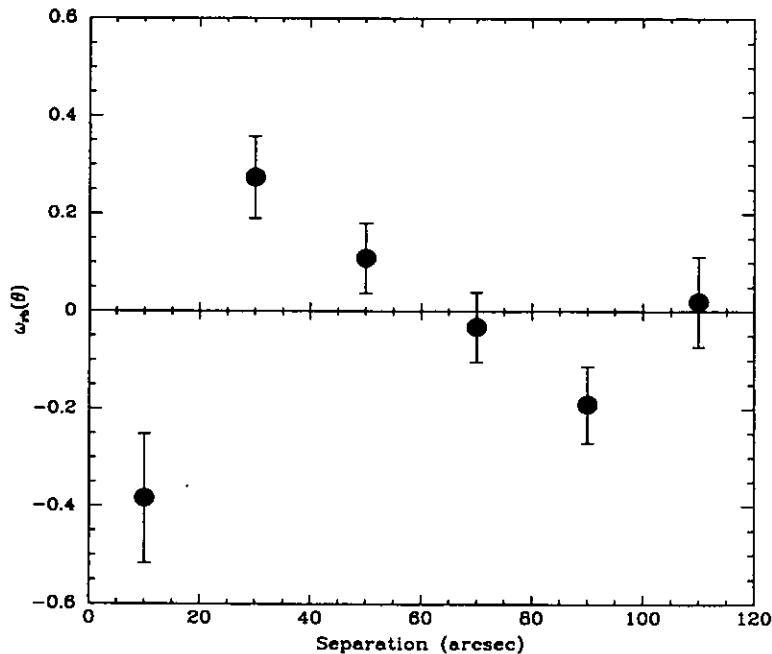


Figure 5.9: The angular cross-correlation, $w_{rb}(\theta)$, between red ($V - I > 2.00$, $I - K > 3.75$) and blue ($V - I < 1.00$) galaxies in the field covered by the K image. Poisson count errors are assumed with variance $N_{rR}(\theta)$.

the blue galaxies in Figure 5.5. In contrast, for $20 < \theta < 60$ arcsec, there is a correlation at the 3σ level between red and blue galaxies, which is due to the ‘band’ of blue galaxies that bisects the two groups of red galaxies.

The blue galaxies do not contribute to the excess of galaxies observed at $K < 19$, as only 9 of 51 are detected in K , the brightest having $K = 18.87$. These nine all have the red $I - K$ colours indicative of $z \gtrsim 1$ galaxies (e.g. Figure 5.3d), of which six help make up the concentration $\lesssim 30$ arcsec from the quasar, which suggests that this at least is real. However, given that the $V - I$ colour is affected much more by recent star-formation than redshift, nothing can be said about the likely redshift of the remaining blue galaxies.

5.7 The Immediate Environment of the Quasar

Figure 5.10 shows the immediate environment of the $z = 1.226$ quasar. The V (left), I (centre) and K (right) images are of size 30×30 arcsec², corresponding to $390 \times 390 h^{-2}$ kpc² at the quasar redshift.

The immediate environment of the quasar appears congested, with five galaxies

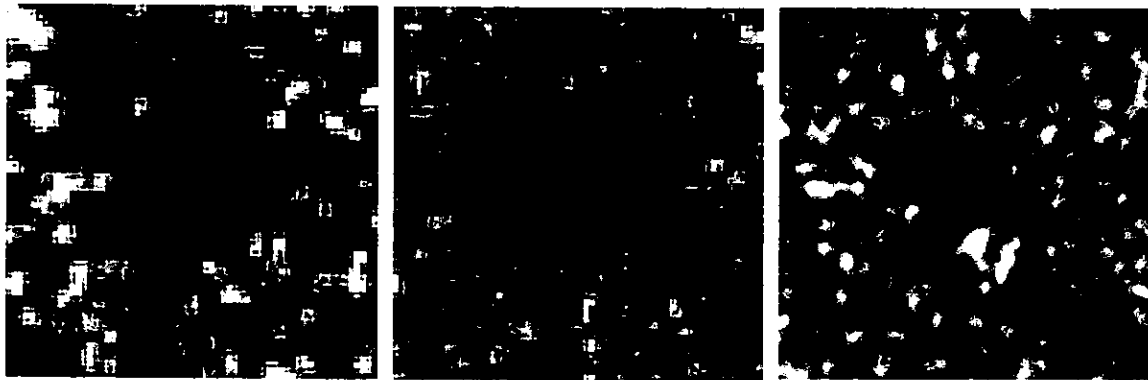


Figure 5.10: The immediate environment of the $z = 1.226$ LQG quasar. The V (left), I (centre) and K (right) images are of size $30 \times 30 \text{ arcsec}^2$, corresponding to $390 \times 390 h^{-2} \text{ kpc}^2$ at the quasar redshift.

within 7 arcsec (corresponding to an angular diameter distance of $40 h^{-1} \text{ kpc}$) apparent in the I image. The brightest of these in the K image is 5 arcsec to the north of the quasar (labelled C3 in Figure 5.5 and E10 in Tables 5.3 and 5.4), and is a member of the cluster red sequences apparent in the colour-magnitude diagrams of Figure 5.4, with $K_{tot} = 18.12$, $I - K = 4.30$ and $V - K = 6.32$. It is thus likely to be a passively-evolving massive elliptical galaxy at the quasar redshift, having $M_V = -22.36$, and its proximity to the quasar confirms that the clustering of the red sequence galaxies is almost certainly associated with the quasar.

There are two more galaxies (labelled C1 and C2 in Figure 5.5) apparent in the K image that are even closer to the quasar, being located only 3 arcsec ($17.4 h^{-1} \text{ kpc}$) to the north-east and south-west of the quasar. Given their proximity to the quasar, they may well be companion galaxies that have recently interacted with the quasar host. They have $K_{tot} = 19.09$ (C1) and $K_{tot} = 20.04$ (C2), and appear bluer than the red sequence galaxy C3 in the false-colour image of Figure 5.6, possibly the result of a recent episode of star-formation caused by the interaction process.

Compact companions are found for a significant fraction ($\approx 40\%$) of quasars, (e.g. Bahcall et al., 1997a) and spectroscopic observations confirm that many have stellar populations and redshifts within 500 km s^{-1} of the quasar (e.g. Stockton, 1982; Canalizo & Stockton, 1997). It has been suggested (e.g. Stockton, 1982; Bekki, 1999) that these companion objects are tidally-stripped cores from galaxies that have recently interacted with the quasar host galaxies, and that this interaction provides an efficient fuelling mechanism for quasar activities. Spectroscopic analysis of the

companion to quasar PG 1700+518 (Canalizo & Stockton, 1997) finds evidence for both a starburst event that occurred roughly 100 Myr ago (and so could be coincident with the quasar activation), and a relatively old stellar population likely to be from the merger progenitor disk.

There are also a number of blue ($V - I < 1$) galaxies apparent in Figure 5.10 that are likely to be undergoing significant star-formation, and may be part of the *band* of star-formation apparent between the two clusters. The galaxies are apparent as sources, in the top-left corner, the bottom-left corner, and just to the right of the quasar, that are much brighter in the V image than the I image, and are not apparent in the K image.

5.8 Discussion and Conclusions

A 3.5σ excess of $K < 19$ galaxies is found in the 2.25×2.25 arcmin² field around the $z = 1.226$ radio-quiet quasar 104420.8+055739 from the Clowes-Campusano LQG. The excess is due entirely to a factor ~ 11 overdensity of red ($I - K > 3.75$) galaxies, which must have $z \gtrsim 0.8$ to explain their colour. In particular, cluster red sequences of 15–18 galaxies are found, in the $I - K$ and $V - K$ against K colour-magnitude diagrams at $I - K \simeq 4.3$, $V - K \simeq 6.9$, comparable in both colour and magnitudes to red sequences observed for other $z \simeq 1.2$ clusters. These red sequences suggest a population of massive ellipticals at the quasar redshift. In the area of the K image tentative evidence of substructure amongst these galaxies is found, with two groups apparent 40 arcsec to the north and 60 arcsec to the south-east of the quasar. An examination of the optical images over a 6.8×5.7 arcmin² area indicates that this substructure is significant at the 2% level, and that the clustering extends well beyond the K image, forming a large-scale structure $2\text{--}3 h^{-1}$ Mpc across. The overall structure is suggestive of being the early stages of formation of a cluster through the progressive coalescence of subclusters.

Only half of the excess of $I - K > 3.75$ galaxies is accounted for by the red sequence members, and comparable numbers (15–20) of ‘red outlier’ galaxies with both $I - K > 3.75$ and $V - I < 2.00$ are found, which appear to fit neither the passively-evolving nor exponentially-decaying star-formation rate galaxy models (Figure 5.2).

Although it is only possible to say that they are likely to be dusty star-forming galaxies at $1 \lesssim z \lesssim 2$, given that such galaxies are found around other $z \simeq 1.2$ clusters (e.g. Tanaka et al., 2000; Kajisawa & Yamada, 1999; Kajisawa et al., 2000), and given their comparative rarity in field regions, it seems reasonable to assume that they are associated with the cluster. This would suggest that the Butcher-Oemler effect observed in intermediate-redshift ($z \simeq 0.4$) clusters (Butcher & Oemler, 1978, 1984) increases in strength to higher redshifts, with $\gtrsim 50\%$ of likely cluster members exhibiting the blue colours of recent star-formation.

A concentration of blue ($V - I < 1$) galaxies is also found within 30 arcsec ($130 h^{-1} \text{kpc}$) of the quasar, with many having the red $I - K$ colours of $z \gtrsim 1$ galaxies, which suggests that the quasar lies in a region of enhanced star-formation, in agreement with the results of Hutchings et al. (1995). This concentration appears extended in such a way as to separate the two groups of red galaxies, and it is also notable how the blue galaxies appear to avoid the centres of red galaxy clustering.

Some foreground contamination of the blue galaxies is likely, but given that such concentrations appear common around LQG quasars at this redshift, and the highly significant spatial interrelation between the blue and red galaxies, then one can be reasonably confident that this concentration is real, and is associated with the quasar. However spectroscopic observations of these and the other cluster candidates will be required to confirm cluster membership, and to provide more quantitative information about their star-formation histories, such as their approximate ages and current star-formation rates.

Recent studies of intermediate- and high-redshift clusters to examine the Butcher-Oemler effect have observed this morphological segregation of red and blue galaxies. Ellingson et al. (2001) and Balogh et al. (1999) examine the fraction of red and blue galaxies as a function of clustercentric radius for clusters from the CNOC1 sample of rich X-ray luminous clusters at $0.18 < z < 0.55$. They observe that whereas the cluster cores (within $\simeq 250 h^{-1} \text{kpc}$) are dominated by early-type galaxies which make up $\gtrsim 80\%$ of the population, as the clustercentric radius is increased, so does the fraction of blue galaxies, making up 50% of the population at $\simeq 1 h^{-1} \text{Mpc}$, and 70–80% of the population at $\simeq 2 h^{-1} \text{Mpc}$. They find star-formation rates significantly diminished in the cluster cores, and find no evidence for an excess of star-

formation above field levels at any clustercentric radius. Their results imply that the cluster environments are not responsible for inducing starbursts, and indeed inhibit star-formation, and that the infall of galaxies into the cluster produces a gradual truncation of star-formation by ram-pressure from the intra-cluster medium.

This suggests that the blue band is made up of galaxies on the edges of the two clusters whose star-formation has not yet been inhibited by the cluster environment. This would mean that the band is not an area of excess star-formation, but of average star-formation that only appears blue in contrast to the diminished star-formation found in the centres of the two clusters. This is supported by the observations of Ellingson et al. (2001) and Balogh et al. (1999) described above, and also by the lack of an overall excess of blue galaxies over the whole 2.25×2.25 arcmin² field covered by the *K* imaging.

5.8.1 A Possible Cluster Merging Event

The relative distribution of red and blue galaxies can also be explained as the early stages of merger of the two clusters of red galaxies, which has triggered both the band of enhanced star-formation and possibly the quasar itself. A comparable distribution has been observed for the Coma cluster (Caldwell et al., 1993) with a band of post-starburst or 'E+A' galaxies located between the Coma cluster centre and a secondary X-ray peak. Dynamical studies (Burns et al., 1994) indicated that these galaxies had passed through the centre of the Coma cluster about 2 Gyr ago, coincident with the epoch of starbursting predicted from the spectra of the post-starburst galaxies. Unusually high blue galaxy fractions have been observed for a number of low-redshift clusters with bimodal X-ray surface brightness profiles (Metevier et al., 2000), implying that cluster mergers can induce starbursts simultaneously in a large fraction of cluster galaxies, and they could be a major contributor to the Butcher-Oemler effect. Several mechanisms have been suggested that could cause firstly the triggering and then the termination of a secondary burst of star-formation in a galaxy, as a subcluster passes through a cluster. These include ram-pressure from the intra-cluster medium (Evrard, 1991), shocks due to collisions between the two intra-cluster media (Roettiger et al., 1996), and the effect of close galaxy encounters (Moore et al., 1996). As the 'band' of blue galaxies is likely to be undergoing or has

recently undergone star-formation, and because the two groups are relatively close together, this would suggest that this system is being observed at an earlier epoch of the cluster merger process than that of Caldwell et al. (1993), either just before or just after core passage, and that the star-formation has been triggered by the interaction of galaxies with the shock fronts produced by the collision of the two intra-cluster media (see Roettiger et al., 1996).

Cluster merging events are predicted to be relatively common at high redshifts ($z \gtrsim 1$) in hierarchical clustering models (e.g. Press & Schechter, 1974; Bahcall et al., 1997b; Percival & Miller, 1999). Examples of possible merging clusters at high redshifts are the CL0023+00423 groups at $z = 0.8274$ and 0.8452 which, according to a dynamical study, have a 20% chance of merging (Lubin et al., 1998), and the Rosati et al. (1999) and Stanford et al. (1997) clusters which are separated by only $2.5 h^{-1} \text{Mpc}$. Of the four candidate high-redshift clusters in the BTC field, three show indications of significant substructure: the galaxy clustering around the $z = 1.226$ quasar described in this chapter; the galaxy clustering near the $z = 1.426$ quasar (Figure 4.10); and the galaxy clustering marked by density maxima #70 and #71 (Figure 4.7).

5.8.2 Comparison with Other Work

As discussed in the previous chapter, Sánchez & González-Serrano (1999) find evidence for associated galaxy clustering for a sample of seven radio-loud quasars at $1.0 < z < 1.6$, but that the quasars are in general not located at the peaks of the density distribution, but are found on the cluster peripheries, at a projected distance of 40–100 arcsec from the cluster centres, just as the $z = 1.226$ LQG quasar appears to be located 40 and 60 arcsec from two clusters. This observation of an apparent avoidance of the high-density regions of the cluster cores by quasars, despite cluster cores being generally dominated by the massive elliptical galaxies that typically host the quasars, is understandable in terms of either quasar triggering mechanism as discussed in the previous chapter. The shock-heated virialised gas that fills the cluster centres inhibits quasar activation through the formation of galaxies (Haehnelt & Rees, 1993); galaxies in the cluster centres have previously lost most or all of their gas, by having had it stripped of by ram-pressure from the intra-cluster medium or

by tidal forces from close encounters with other galaxies, or by consuming the gas in a starburst during its first infall into the cluster; and the encounter velocities of galaxies in the cluster centres are too great to allow the galaxies to merge (Aarseth & Fall, 1980) and trigger a quasar through that mechanism.

In a comparable study of the galaxy environment of the radio-loud $z = 1.086$ quasar 1335.8+2834 from the $z \sim 1.1$ Crampton et al. (1989) LQG, Tanaka et al. (2000) obtain results which have several similarities to those described here. This quasar had been part of the Hutchings et al. (1995) study, and was known to lie in a band of blue and emission-line galaxies. Using deep R , I and K observations, a number of extremely-red objects with the colours of passively-evolving galaxies at the quasar redshift were found, forming a cluster which lies to one side of both the quasar and the band of blue and emission-line galaxies. They also find a similar population of ‘red outliers’ and estimate the blue galaxy fraction as 60–80%. They also find an indication that this cluster is part of a larger structure with groupings of optically-red ($R - I > 1.3$) galaxies, similar to the clustering near the quasar, found across the $8 \times 8 \text{ arcmin}^2$ ($4.7 \times 4.7 h^{-2} \text{ Mpc}^2$ at $z = 1.086$) R , I optical images.

5.8.3 Interpretation - Mechanisms for Quasar Formation

As several of the Hutchings et al. (1995) quasars were found in regions of enhanced star-formation, and as both the quasar of Tanaka et al. (2000) and this chapter are located in ‘bands’ of enhanced star-formation, a causal link between the quasar and star-formation is proposed, whereby both are triggered by the same mechanism: the interaction between the galaxy and the intra-cluster medium.

If a galaxy can be disrupted sufficiently by its passage through the intra-cluster medium to cause it to undergo starbursting, then if it also contains a supermassive black hole, enough gas may be channelled onto the nucleus to trigger a phase of quasar activity. Such a mechanism explains the finding of quasars in regions of enhanced star-formation more naturally than the galaxy merger model, as it allows many galaxies to be affected simultaneously, although there is good evidence that a significant fraction of quasars have been triggered by galaxy mergers. If there is a connection between the quasar and star-formation activation, then it is likely that these quasars are found preferentially in clusters with high blue galaxy fractions,

and that these are not representative of $z \simeq 1.2$ clusters as a whole.

There is, however, significant evidence to suggest that this is not the quasar triggering mechanism in this specific case. Firstly, the immediate environment of the quasar is congested, with two companion galaxies within 3 arcsec of the quasar that may be the remnants of a recent interaction with the quasar host galaxy, indicating that the most likely trigger for the activation of the quasar is a galaxy merging event. Secondly, as discussed previously, the blue ‘band’ may not in fact be a region of enhanced star-formation, but merely a region of average levels of star-formation that would be expected for galaxies on the cluster peripheries before their first infall into the cluster, but that appears enhanced relative to the diminished levels of star-formation in the cluster cores.

This work and previous studies show that searching for sources with the optical-near-infrared colours ($I - K > 3.75$) characteristic of quiescent galaxies at $z \gtrsim 1$ is an efficient means of locating $z \gtrsim 1$ clusters. By adding a second optical band it is then possible to obtain qualitative information on the star-formation history of these galaxies. Using this information along with the relative spatial distribution of quiescent and star-forming galaxies, a more complex picture arises in which the evolution of galaxies, quasars and clusters are all interrelated.

5.9 Summary

This chapter describes the results of K imaging of a 2.25×2.25 arcmin² field centred on the $z = 1.226$ radio-quiet quasar from the Clowes-Campusano LQG. From an examination of the optical data, this quasar appeared the most likely of the three LQG quasars in the BTC field to have associated galaxy clustering, being located within a region of clustering of optically-red galaxies extending over ≈ 5 arcmin.

Photometric redshift estimates based on the VIK photometry allows the galaxy environment of the quasar to be examined by identifying those galaxies likely to be at $z \simeq 1.2$. Galaxies at these redshifts are distinguished by their extremely-red colours, with $I - K > 3.75$, and a factor ~ 11 overdensity of such galaxies is found in the K image. In particular, 15–18 galaxies with colours consistent with being a population of passively-evolving massive ellipticals at the quasar redshift are found.

They form red sequences in the $V - K$ against K and $I - K$ against K colour-magnitude plots at $V - K \simeq 6.9$, $I - K \simeq 4.3$ comparable to those observed in other $z \simeq 1.2$ clusters. There is suggestive evidence for substructure among the red sequence galaxies in the K image, in the form of two compact groups, 40 arcsec to the north, and 60 arcsec to the south-east of the quasar. An examination of the wider optical images indicates that this substructure is significant, and that the clustering extends to form a large-scale structure $2-3 h^{-1} \text{Mpc}$ across.

There is evidence for a high ($\gtrsim 50\%$) fraction of blue galaxies in this system, in the form of 15-20 'red-outlier' galaxies with $I - K > 3.75$ and $V - I < 2.00$, indicating that they are probably dusty, star-forming galaxies at the quasar redshift. Within 30 arcsec of the quasar a concentration of blue ($V - I < 1$) galaxies is found, forming a band that bisects the two groups of red sequence galaxies. This band of blue galaxies is similar to those regions of enhanced star-formation apparent around many of the $z \simeq 1.1$ quasars of the Hutchings et al. (1993, 1995) studies, suggesting that this band also corresponds to a region of enhanced star-formation. However, no overall excess of blue galaxies is observed, and it may be that this band has star-formation levels typical of field galaxies before they are absorbed into the clusters and have their star-formation truncated by ram-pressure from the intra-cluster medium. The observed distribution of galaxies in the K image is explained as the early-stages of a cluster merger, and the wider distribution is suggestive of the formation of a rich cluster from the progressive coalescence of subclusters.

The quasar appears to have been activated as the result of a recent galaxy interaction. The immediate environment of the quasar is congested with five sources within 7 arcsec, one of which is a member of the cluster red sequence confirming that the galaxy clustering is associated with the quasar. Two galaxies are found just 3 arcsec ($17.4 h^{-1} \text{kpc}$) from the quasar, and may well be companion galaxies that have recently interacted with the quasar host. They appear somewhat bluer than the galaxy from the cluster red sequence, and it is suggested that this is the result of a recent episode of star-formation caused by the interaction process.

Chapter 6

The Galaxy Environment of the $z = 1.306$ LQG Quasar

6.1 Introduction

Having had the success of finding galaxy clustering associated with the $z = 1.226$ LQG quasar through the addition of near-infrared imaging, it was decided to obtain further K imaging to examine the galaxy environments of one of the remaining LQG quasars in the BTC field. As discussed previously, the addition of K -band photometry to the existing V and I data allows the identification of high-redshift galaxies irrespective of star-formation history, and also provides qualitative star-formation histories, thus enabling a detailed examination of the quasar environment to be made.

As described in Chapter 4, of the two remaining LQG quasars, the quasar at $z = 1.306$ appeared the most likely to have associated galaxy clustering. Although its immediate environment (within $1 h^{-1}\text{Mpc}$) does not appear promising, as it lies in a low-density region of red galaxies, it is located just 165 arcsec from the most significant high-redshift cluster candidate in the BTC field, density maximum #21. Irrespective of whether the galaxy clustering marked by density maxima #21 is associated with the quasar or not, the cluster warrants further interest because of its richness and compact size.

This chapter details the results and analysis of K -band imaging of two adjacent 2.25×2.25 arcmin² UFTI fields, one containing the $z = 1.306$ LQG quasar, and the

other containing the galaxy clustering associated with density maximum #21.

6.2 Observations

K imaging was obtained for two 2.25×2.25 arcmin² field using the UKIRT Fast-Track Imager (UFTI) camera on the 3.8-m United Kingdom Infra-Red Telescope (UKIRT). The field containing the $z = 1.306$ was centred on $10^{\text{h}}47^{\text{m}}32.8^{\text{s}}$, $+05^{\circ}25'57''$ (J2000), and the field containing the cluster of red galaxies was centred on $10^{\text{h}}47^{\text{m}}24.9^{\text{s}}$, $+05^{\circ}24'22''$ (J2000). The near-infrared observations took place on the nights of 14/15 and 15/16 May, 2000, obtained as 3 hours of PATT allocated time as part of the UKIRT Service programme. The observations of the field containing the quasar were made on the first night, and the observations of field containing the cluster of red galaxies were made on the second night.

The UFTI camera is a cooled $1\text{--}2.5\mu\text{m}$ instrument with a 1024×1024 HgCdTe array. The plate scale is 0.091 arcsec per pixel, giving a field of view of 92×92 arcsec². A standard 9-point jitter pattern was used, with each 1 minute exposure offset by 20 arcsec relative to adjacent exposures. A dark frame was obtained during each night, and subtracted before self-flattening the set. In total 6 circuits of the jitter pattern were completed for each of the fields, resulting in total exposure times of 54 minutes each. The exposures were registered by considering the relative position of a bright source apparent in each of the images. In the case of the quasar field, the quasar itself was used, and in the case of the field containing the red cluster, the galaxy labelled as source #1280 in Figure 6.2 was used. As a result the effect of any rotation between images was not considered, but this does not appear to have affected the results. Due to the jitter pattern used to flatten the images, the size of the field observed is increased to 2.25×2.25 arcmin² although the 20 arcsec wide strips at the edges of the field have only one third of the exposure time. The separation of the two fields in the Right Ascension direction is 118 arcsec, and means that the fields overlap sufficiently so that the 20 arcsec wide strip on the western side of the quasar field is also covered by the 20 arcsec wide strip on the eastern side of the field containing the cluster of red galaxies. Hence there is a contiguous field covering both the quasar and the clustering of red galaxies (allowing for the vertical

offset between the two fields) covered by at least two-thirds of the total 54 minute exposure time.

The resulting K images each have FWHMs of 0.6 arcsec, a typical level of seeing for UKIRT data, but significantly better than the BTC images. To allow galaxy colours to be determined using a single fixed aperture, the K image was convolved to the same seeing as the I image (1.15 arcsec) using a Gaussian kernel of FWHM=0.86 arcsec ($\sigma = 4$ pixels).

The K images were then registered with the optical image through comparison of the positions of ~ 40 bright sources ($K < 19$) in the K and I images using the IRAF tools `geomap` and `register`, resulting in the simple linear transformations for the quasar field

$$X_{reg} = 3232.4092 - 0.2111109 \times X_K - 0.0034030 \times Y_K \quad (6.1)$$

$$Y_{reg} = 2271.6090 - 0.0032148 \times X_K + 0.2126044 \times Y_K, \quad (6.2)$$

and the field containing the cluster of red galaxies

$$X_{reg} = 2959.0412 - 0.2112882 \times X_K - 0.0027995 \times Y_K \quad (6.3)$$

$$Y_{reg} = 2185.3242 - 0.0032065 \times X_K + 0.2124531 \times Y_K, \quad (6.4)$$

where (X_K, Y_K) is the position of the source in the K image, and (X_{reg}, Y_{reg}) is the corresponding position in the I image after registration.

The photometric calibrations of the K images were obtained through observation of the same UKIRT faint standard fs20 as previously (G163-50 : $\alpha = 11^h 06^m 59.93^s$, $\delta = -05^\circ 09' 26.1''$ (J2000)) which has $K = 13.503 \pm 0.010$ (Hawarden et al., 2001). Five 40 second observations were obtained for the standard star at three separate points during the first night, and at one further point on the second night. Each of the five sets of observations was dark-subtracted, flattened and registered as for the target frames, and then combined, resulting in zero-points for the first night of 25.833 ± 0.020 , and 25.807 ± 0.023 for the second night.

Object detection was carried out using SExtractor (Bertin & Arnouts, 1996) for objects with 150 ($\simeq \text{FWHM}^2$) contiguous pixels over the 1.6σ detection threshold. As the K images had been previously convolved, a Gaussian filter was not used in the detection process. The total magnitudes were taken to be the `MAG_BEST`

output from `SEXTRACTOR`, and colours were determined using fixed apertures of diameter 2.5 arcsec. The magnitude errors are determined in `SEXTRACTOR` by considering the rms noise levels in the image. However, in this case these levels have been artificially reduced by convolving the image before the source detection process. Consequently, the noise levels are significantly lower than they should be, and so are recalculated for each source by assuming Poisson noise in the same manner as in the previous Chapter.

Star-galaxy classification of each source was performed using a combination of morphology (using the stellarity classifier in `SEXTRACTOR`) and a comparison of $V - I$ and $I - K$ colours with model star and galaxy tracks. Stellarities of sources in both V and I images were obtained and the weighted mean used for classification as discussed in Chapter 2. Most of the sources classified as stars morphologically, also had colours that lay near the model star tracks, but a number of sources had the colours of blue galaxies, and were reclassified as such.

Figure 6.1 shows the convolved K -band image of the 2.25×2.25 arcmin² field containing the $z = 1.306$ LQG quasar. Each source detected by `SEXTRACTOR` and visually verified is labelled by its identification code. The differing colours and symbols indicate the source's morphological classification and whether it is detected in the optical BTC images: yellow circles indicate that the source is classified as a galaxy and is detected in all three images (V , I and K); green circles indicate that the source is classified as a galaxy and is detected in the K and I images only; and blue circles indicate that the source is classified as stellar.

Figure 6.2 shows the convolved K -band image of the 2.25×2.25 arcmin² field containing the cluster of red galaxies (apparent in the bottom-left of the figure). Each source detected and visually verified is labelled by its identification code, to which 1000 has been added to differentiate them from the sources in the quasar field. The differing colours and symbols indicate the morphological classification and optical detections for each source as for Figure 6.1. The area of overlap between the two fields is apparent towards the top-right of the figure with $\alpha > 10^h 47^m 28^s$ and $\delta > +05^\circ 23' 55''$, as the exposures from the field containing the quasar that overlap this field have been included in the figure.

Completeness levels were determined for the K image in a similar manner as for

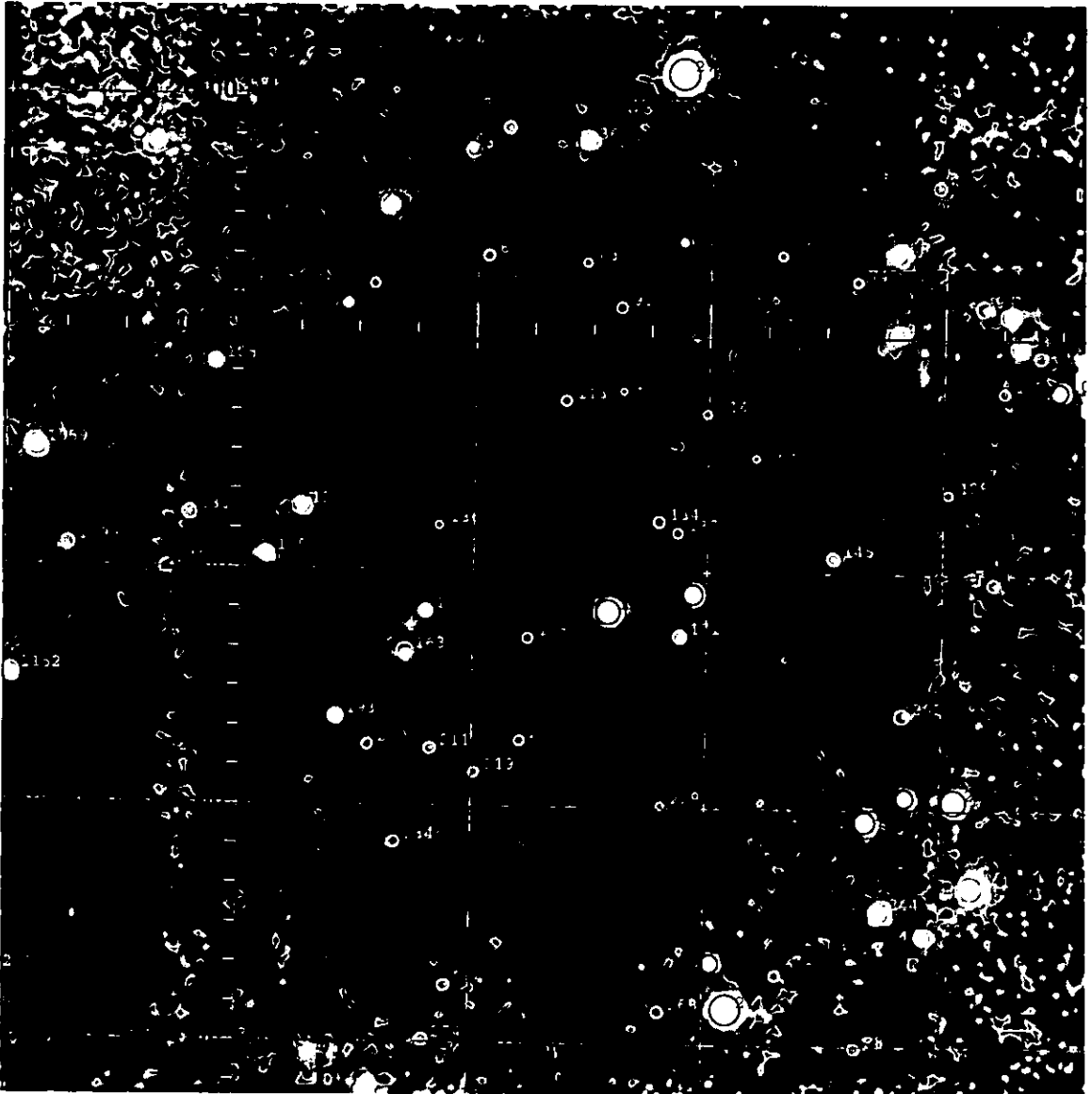


Figure 6.1: K -band image of the 2.25×2.25 arcmin² field containing the $z = 1.306$ quasar (source #157). Each source detected by SExtractor and visually verified is labelled by its identification code. The differing colours and symbols indicate the sources morphological classification and whether it is detected in the optical BTC images: yellow circles indicate that the source is classified as a galaxy and is detected in all three images (V , I and K); green circles indicate that the source is classified as a galaxy and is detected in the K and I images only; and blue circles indicate that the source is classified as stellar.

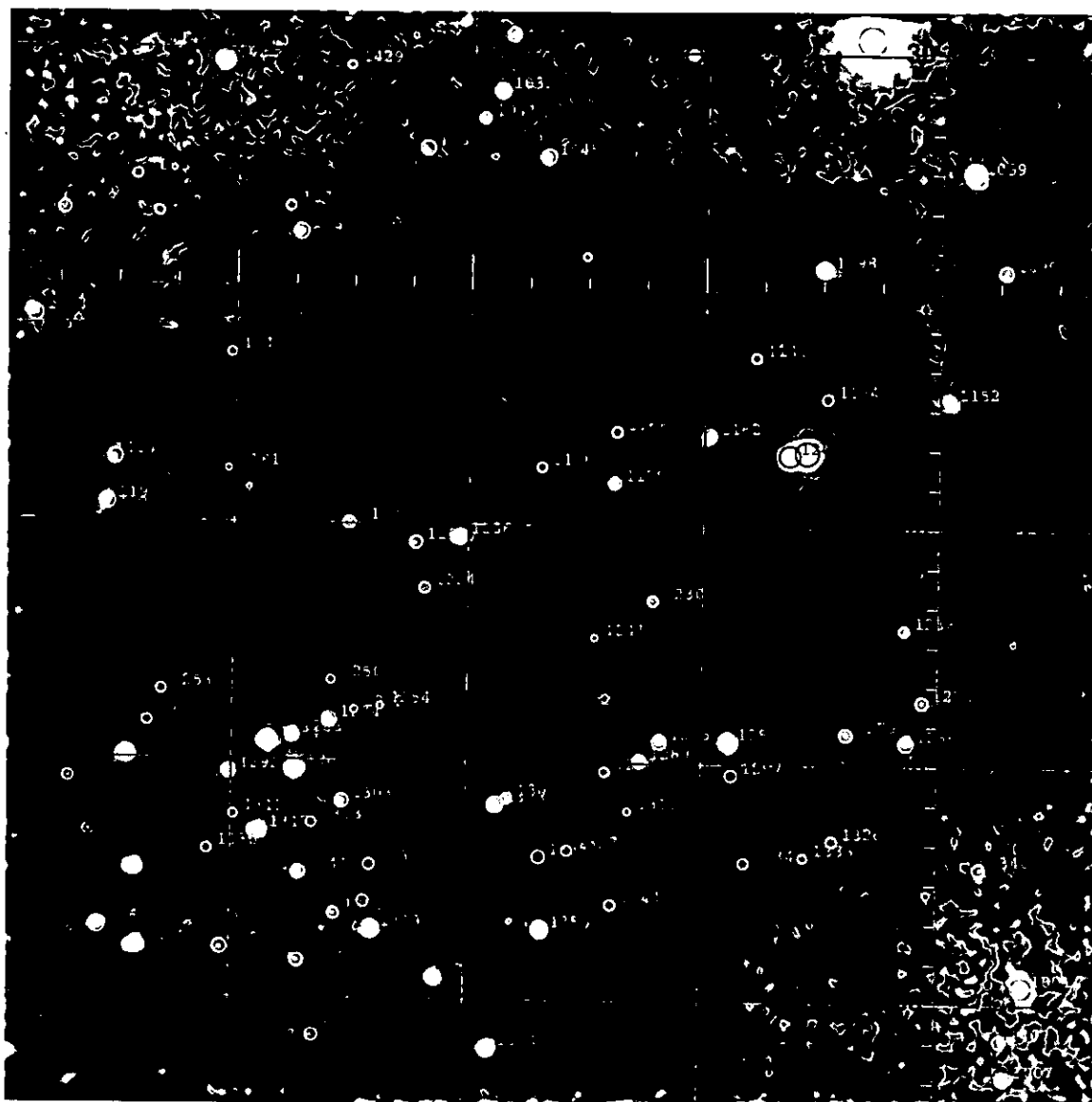


Figure 6.2: *K*-band image of the 2.25×2.25 arcmin² field containing the cluster of red galaxies (apparent in the bottom-left corner). Each source detected by SExtractor and visually verified is labelled by its identification code to which 1000 has been added to differential these sources from those of Figure 6.1. The differing colours and symbols indicate the morphological classification of the source, and whether it is detected in the optical BTC images: yellow circles indicate that the source is classified as a galaxy and is detected in all three images (*V*, *I* and *K*); green circles indicate that the source is classified as a galaxy and is detected in the *K* and *I* images only; and blue circles indicate that the source is classified as stellar.

Filter	Exposure	Seeing	Completeness	
Band	time	FWHM	limits (mag)	
(subfield)	(sec)	(arcsec)	90%	50%
<i>K</i> (centre)	3240	0.60	19.60	20.35
<i>K</i> (edge)	1080	0.60	19.15	19.80
<i>I</i>	6480	1.15	24.50	25.20
<i>V</i>	8100	1.30	25.55	26.10

Table 6.1: Photometric properties of the images, including exposure times and completeness levels. The *V*, *I* figures are for the area covered by the *K* image, rather than for the whole BTC field.

the optical BTC images, by dimming a bright galaxy (ID #58, $K_{tot} = 17.47$) to a specified magnitude and adding 100 copies to the image at random positions, and the processing through SExtractor in the usual way. The 50% and 90% completeness levels are estimated as the magnitude for which 50 and 90 galaxies out of the 100 are recovered. As the exposure levels vary considerably across the *K* image, two separate completeness levels were determined, one for the centre of the image where all 54 exposures are used, and one for the 20 arcsec wide strips at the edges of the image where only one third of the exposures are used. The resulting completeness levels are shown in Table 6.1 with in addition the corresponding completeness levels for the BTC *V* and *I* optical images for the same region.

The fields are located in a region covered by only two out of every five *I*-band exposures, lying midway between the deep regions covered by CCDs #3 and #4. As a result, the total exposure time through the *I* filter is reduced to 6480 s, and the magnitude limits are brighter by 0.2 mag. The effective decrease in sensitivity by the loss of exposure time is partially offset by the fact that the $z = 1.226$ quasar was covered by the less efficient CCD #1.

6.3 Results — Galaxy Counts

In total 173 sources were detected in the two *K* images, all of which had counterparts in the *I* image, and 168 had counterparts in both *V* and *I* images. Each of these

Magnitude	Observed				Expected	
	Total		$I - K > 3.75$		Total	$I - K > 3.75$
	QSO	Red	QSO	Red		
$15 < K \leq 16$	1	0	0	0	0.533	0
$16 < K \leq 17$	1	1	0	1	2.186	0
$17 < K \leq 18$	8	13	1	1	4.204	0.050
$18 < K \leq 19$	10	20	1	2	11.36	1.939
$19 < K \leq 20$	16	21	2	1	21.81	1.896
Total	36	55	4	4	41	4

Table 6.2: A comparison of total and extremely-red ($I - K > 3.75$) galaxy counts in the two K images, binned by magnitude, and those expected for the same-sized region in the field (Songaila et al., 1994). The columns labelled “QSO” indicate the results for the field containing the $z = 1.306$ quasar, and the columns labelled “red” indicate the results for the field containing the clustering of red galaxies.

sources has been visually verified, as a number of sources in the K image only were spurious noise events towards the edges of the images and had to be removed. 22 of the 168 sources were classed as stars, leaving 151 galaxies in the combined field of total area 9.96 arcmin^2 .

Table 6.2 shows the comparison of galaxy counts seen in the two K images, with those expected from a field region (Songaila et al., 1994). The columns labelled “QSO” indicate the results for the field containing the $z = 1.306$ quasar, and the columns labelled “red” indicate the results for the field containing the clustering of red galaxies. There are three sources found in both the “QSO” and “red” fields, and these have been counted twice.

There is no excess of K -selected or $I - K > 3.75$ galaxies in the field containing the $z = 1.306$ quasar in comparison to that expected from the Hawaii K -band survey of Songaila et al. (1994). This appears to confirm the suspicion of Chapter 4 that the quasar is located in a low-density region indistinguishable from the field.

For the field containing the cluster of red galaxies there is an excess of 14 $K < 20$ galaxies over that expected for a field region, corresponding to a significance level of 1.3σ (accounting for the effect on galaxy statistics of the two-point angular correla-

tion function for K selected galaxies as in the previous chapter). However there is no excess of $I - K > 3.75$ galaxies for the same field which, given that any clustering associated with the quasar should manifest itself as an excess of $I - K > 3.75$ galaxies, indicates that the galaxy clustering must be at a significantly lower redshift than the quasar, presumably at $0.6 \lesssim z \lesssim 1.0$ given that it was not identified by the cluster red sequence method at the low-redshifts examined in Chapter 3.

6.4 Galaxy Colours

The $I - K$ versus $V - I$ colour-colour diagram for sources in the K image is shown in Figure 6.3. Those galaxies whose colours are well described by the $z_f = 3.5$ burst model at $z \simeq 1.3$ are shown as filled red squares, whilst those galaxies whose colours are well described by the same burst model, but at $z \simeq 0.8$ are shown as filled yellow circles. Those whose colours are well described by galaxies at $z \simeq 1.3$ with some recent star formation are shown as filled green circles, and the remainder of sources classified as galaxies are shown as open circles. The four galaxies whose redshift probability distributions are shown in Figure 6.4 are indicated by superimposed, labelled yellow diamonds.

For comparison, Figure 6.3 also has model tracks showing the colour evolution of different galaxy types. The model curves correspond to stellar populations formed in an instantaneous burst (solid red line), and stellar populations with exponentially-decaying SFRs with time-scales (τ) of 1 Gyr (dashed green line) and 5 Gyr (dot-dashed magenta line), and are thought to approximate the colour evolution of massive elliptical and disk-dominated galaxies respectively. Lilly et al. (1998) showed that the colours of disk-dominated galaxies at $z = 0.65\text{--}0.87$ are broadly fitted by similar models with $\tau = 5$ Gyr. The formation epoch of each model is set to $z_f = 3.5$, and each track shows the colour evolution from $z = 1.5$ to $z = 0$ with crosses at 0.1 redshift intervals. The galaxy ages are determined for an $H_0 = 75 \text{ km s}^{-1} \text{ Mpc}^{-1}$, $\Omega_M = 0.3$, $\Omega_\Lambda = 0.7$ universe, but most reasonable cosmologies do not affect the tracks significantly at these redshifts.

By using the effects of redshift and star-formation on the colour of galaxies, it is possible to select galaxies of a particular type and redshift through colour selection.

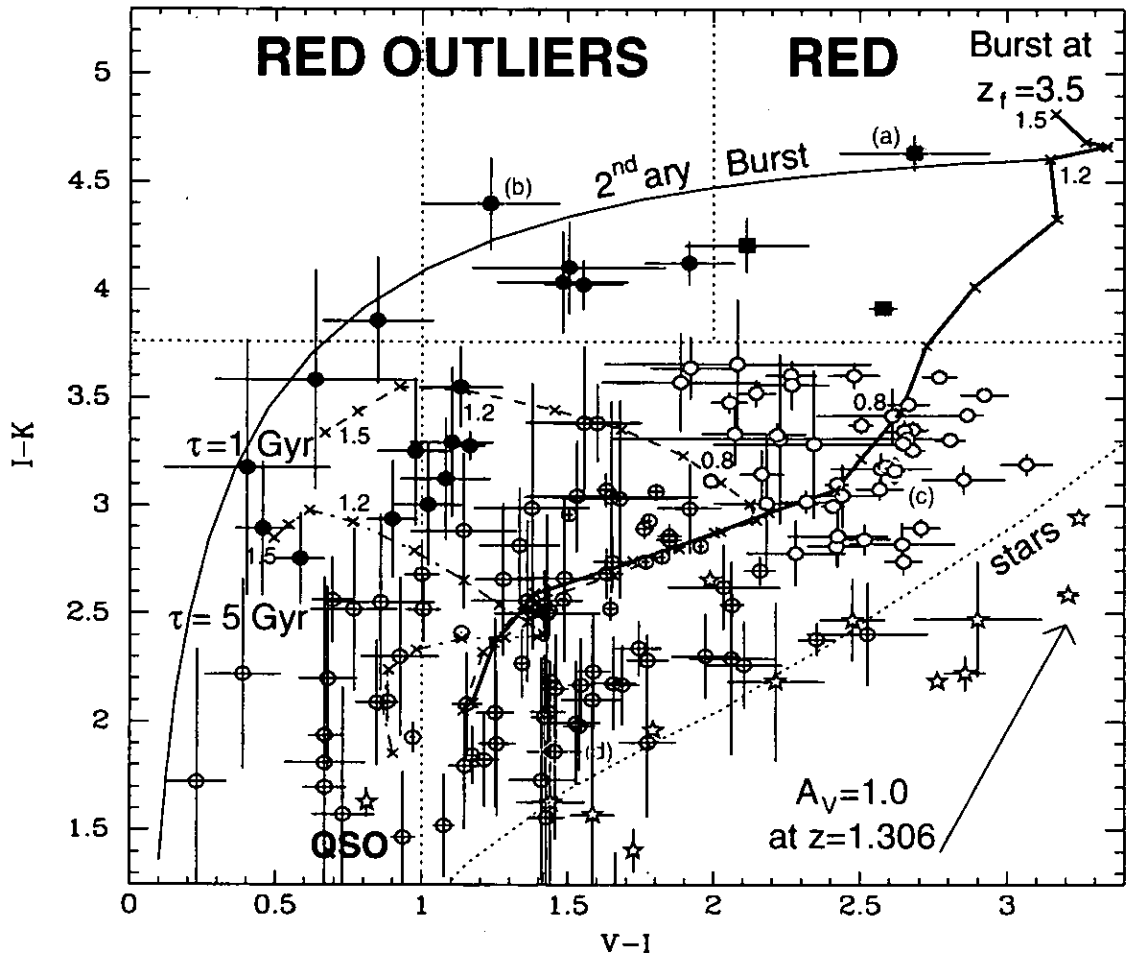


Figure 6.3: $I - K$ against $V - I$ colour-colour diagram of all galaxies in the K image. Those galaxies whose colours are well described by the $z_f = 3.5$ burst model at $z \simeq 1.3$ are shown as filled red squares; those whose colours are well described by galaxies at $z \simeq 1.3$ with some recent star formation are shown as filled green circles; those sources whose colours are well described by the burst model at $z \simeq 0.8$ are shown as filled yellow circles; and the remainder of sources classified as galaxies are shown as open circles. Those sources classified as stars are shown as blue star symbols, and the model track for main sequence stars is shown as a dotted blue line. For comparison, model tracks are shown for an instantaneous burst at $z_f = 3.5$ (solid red line), and exponentially-decaying star-formation rate models with time scales of 1 Gyr (dashed green line) and 5 Gyr (dot-dashed magenta line). The effect of adding a secondary burst of star-formation to the passively-evolving old component is shown by the solid blue curve. The effect of internal extinction at $z = 1.306$ at the level of $A_V = 1.0$ is shown as an arrow in the bottom-right corner.

The $I - K$ colours of the model tracks increase monotonically with redshift to $z \simeq 1.3$, and it is clear that $I - K \simeq 4$ is a good indicator of galaxies at $z \gtrsim 1$ with predominantly old stellar populations. As a result, those galaxies with $I - K > 3.75$ (above the red dotted-line) are most likely to be at $z \simeq 1.3$ and so this selection criterion is used to identify galaxies that could be associated with the quasar.

The effect of a recent secondary burst of star-formation on a high-redshift galaxy that had previously been evolving passively is shown by the blue curve. The secondary burst model curve is created by taking the $z = 1.306$ passively-evolving galaxy model and adding increasing amounts of recent star-formation in the form of a 200 Myr long burst of constant star-formation. The colour of the two-population model is then dependent on the mass ratio between the star-forming and passively-evolving components. Given that the effect of star-formation is predominantly in the $V - I$ direction, by classifying galaxies by their $V - I$ colour, star-forming and passively-evolving galaxies at the quasar redshift can be separated, and so a selection boundary of $V - I = 2.00$ (shown as green dotted-line) is used to classify galaxies as either passively-evolving (hereafter labelled *red*) or star-forming (hereafter labelled *red outliers*).

The effect of internal extinction at $z = 1.306$ at the level of $A_V = 1.0$ is shown as an arrow in the bottom-right corner. It can be seen that the effect of internal dust extinction in galaxies at the quasar redshift is to increase the $I - K$ colour.

The sources classified as stars from their morphology and colour are shown as blue star symbols. For comparison the model stellar track of Baraffe et al. (1998) is shown as a blue dotted line. The models are for low-mass main sequence stars with solar-metallicity and an age of 5 Gyr. It is apparent that there is a good separation between the colours of galaxies and stars with stars having much bluer optical- near-infrared colours than galaxies for a given $V - I$ colour, and so by selecting by both colour and morphology, stars and galaxies can be efficiently classified, as has been done here.

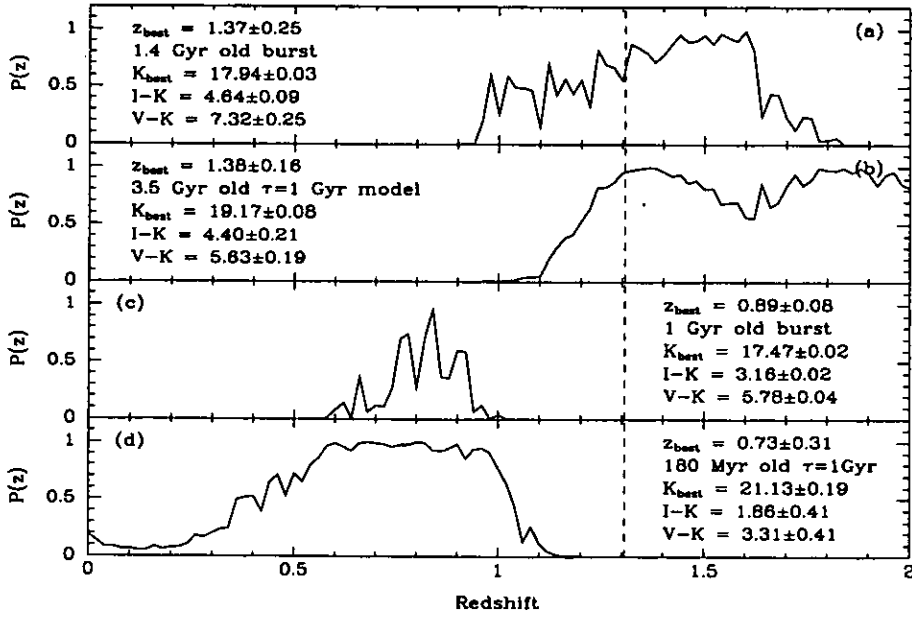


Figure 6.4: Redshift probability distributions for four galaxies in the K image based on their VIK colours. The best fitting model is described by its redshift z_{best} and star-formation history, which is either an instantaneous burst or an exponentially decaying star-formation rate with time-scale τ . The vertical dashed line indicates the redshift of the quasar. Distributions (a) and (b) correspond to two galaxies which may be at the redshift of the quasar, being classed as being *red* and *red outlier* galaxies respectively. Galaxy (c) is a typical member of the compact clump of red galaxies marked by density maximum #21, and galaxy (d) is also close to the centre of the clump, but has much bluer colours indicating recent star-formation.

6.5 Photometric Redshift Estimation

To estimate the photometric redshifts of each galaxy from its VIK colours, and to produce the model colour tracks of Figure 6.3, the HYPERZ code of Bolzonella et al. (2000) has been used as described in the previous chapter.

In Figures 6.4(a)–(d) the redshift probability distributions, $P(z)$, are shown for two galaxies which are the most promising candidates for being associated with the $z = 1.306$ quasar, and two galaxies from the cluster of red galaxies marked by density maximum #21. For each of the galaxies, the best-fitting model is described by its redshift z_{best} and star-formation history, which is either an instantaneous-burst or an exponentially-decaying star-formation rate with time-scale τ . The vertical dashed-line indicates the redshift of the quasar.

Distribution (a) corresponds to galaxy ID #1152, which is one of only three

galaxies classed as *red*, and has the VIK colours closest to those predicted for stellar populations formed in an instantaneous burst at $z_f = 3.5$ and observed at $z \simeq 1.3$ (Figure 6.3).

Redshift probability distribution (b) corresponds to a ‘red outlier’ galaxy, ID #201. It has a similarly red $I - K$ colour to galaxy (a), and it is this that constrains its redshift to $z \gtrsim 1$. Its optical $V - I$ colour is much bluer, indicating more recent star-formation, and results in it being best fitted by a $\tau = 1$ Gyr exponentially-decaying model. An examination of Figure 6.3 suggests that the combination of blue optical colour and extremely-red optical- near-infrared colour may be better explained by a two-component star-formation model in which a secondary burst of star-formation is added to a dominant old passively-evolving stellar population. However, given the limited colour information available the only conclusions that should be drawn are that the galaxy is at high-redshift, has a dominant old stellar population, and some recent star-formation.

Redshift probability distribution (c) corresponds to one of the galaxies (ID #1284) from the core of the cluster of red galaxies marked by density maximum #21. Its colours are typical of many members of the cluster as can be seen from Figures 6.3 and 6.5. The galaxy colour can be seen to be close to that predicted for the $z_f = 3.5$ burst model at $z \simeq 0.8$. The redshift probability distribution confirms this, and indicates that it is tightly constrained about this redshift to $0.7 \lesssim z \lesssim 0.9$. It is highly incompatible with being at the quasar redshift, and indicates that the clustering of red galaxies is at $z \simeq 0.8 \pm 0.1$.

Redshift probability distribution (d) corresponds to galaxy ID #1256 which is also found close to the core of the cluster of red galaxies, but has much bluer colours indicating that if associated with the cluster it must have affected by significant amounts of recent star-formation. Its photometric redshift estimate suggests that it may well be associated with the cluster, being constrained to $0.5 \lesssim z \lesssim 1$.

It appears from an examination of Figures 6.4(a-d) that although there are a number of galaxies that have redshift estimates compatible with that of the quasar, the cluster of red galaxies is at a much lower redshift, with $0.7 \lesssim z \lesssim 0.9$.

6.6 Spatial Distribution of Galaxies

The spatial distribution of galaxies detected in the two K images, is shown in Figure 6.5 with the $z = 1.306$ quasar indicated by the green triangle towards the top-centre of the image. The blue dashed-lines indicate the boundaries of the region covered by the K imaging. The solid red symbols indicate the locations of the *red* galaxies likely to be early-type galaxies at the quasar redshift. The solid green symbols indicate those galaxies classed as *red outliers* having the $I - K \gtrsim 3.5$ and $V - I < 2.00$ colours which are best described by galaxies at $z \gtrsim 1$ with some recent star-formation. The yellow symbols indicate those galaxies with colours well described by the instantaneous burst model at $z \simeq 0.8$ having $2.75 < I - K < 3.75$ and $V - I > 2.00$. The blue star symbols indicate galaxies with $V - I < 1$ which are likely to be undergoing significant star-formation.

For comparison, Figure 6.6 is the VIK three-colour image of the field covered by the K imaging data. The areas not covered by the K images are apparent by the blue-green coloured regions to the top-right and bottom-left of the image. North is to the left, and east is towards the top of the page. The $z = 1.306$ quasar is apparent as the lower/brighter of the two blue-white point-like sources in the top-centre of the image. The few galaxies likely to be at the quasar redshift are apparent as orange-red sources, whilst those galaxies likely to be early-type galaxies associated with the $z \simeq 0.8$ cluster towards the bottom-right of the image, appear as yellow-coloured sources. The inset shows an expanded view of galaxy ID #163, a red outlier galaxy located 25 arcsec to the west of the quasar.

6.7 The Galaxy Environment of the $z = 1.306$ LQG Quasar

The addition of K imaging around the $z = 1.306$ LQG quasar confirms the tentative result of Chapter 4 that the quasar is located in a poor environment, indistinguishable from the field. The K -band and $I - K > 3.75$ galaxy counts for the 2.25×2.25 arcmin² field containing the quasar find no excess in either case in comparison with the Hawaii K -band survey of Songaila et al. (1994). Given the rarity

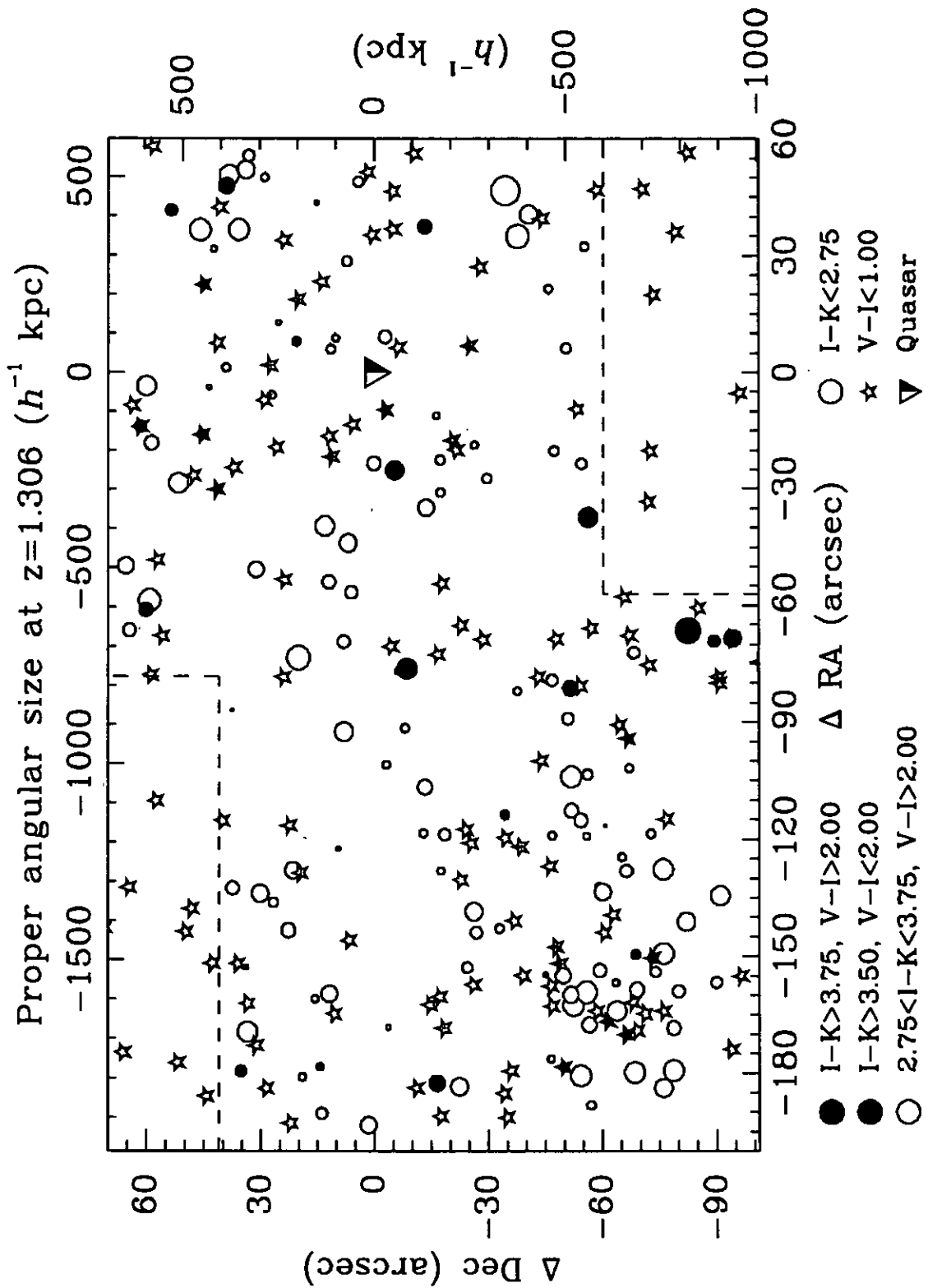


Figure 6.5: Spatial distribution of galaxies in the field of the $z = 1.306$ LQG quasar covered by the combined K images. The different symbols indicate the colours of the galaxies, with circles (squares) indicating those galaxies detected (not detected) in I . The blue dashed-lines indicate the boundaries of the region covered by the K imaging. The size of the symbols (except stars) indicate the K_{total} magnitude.

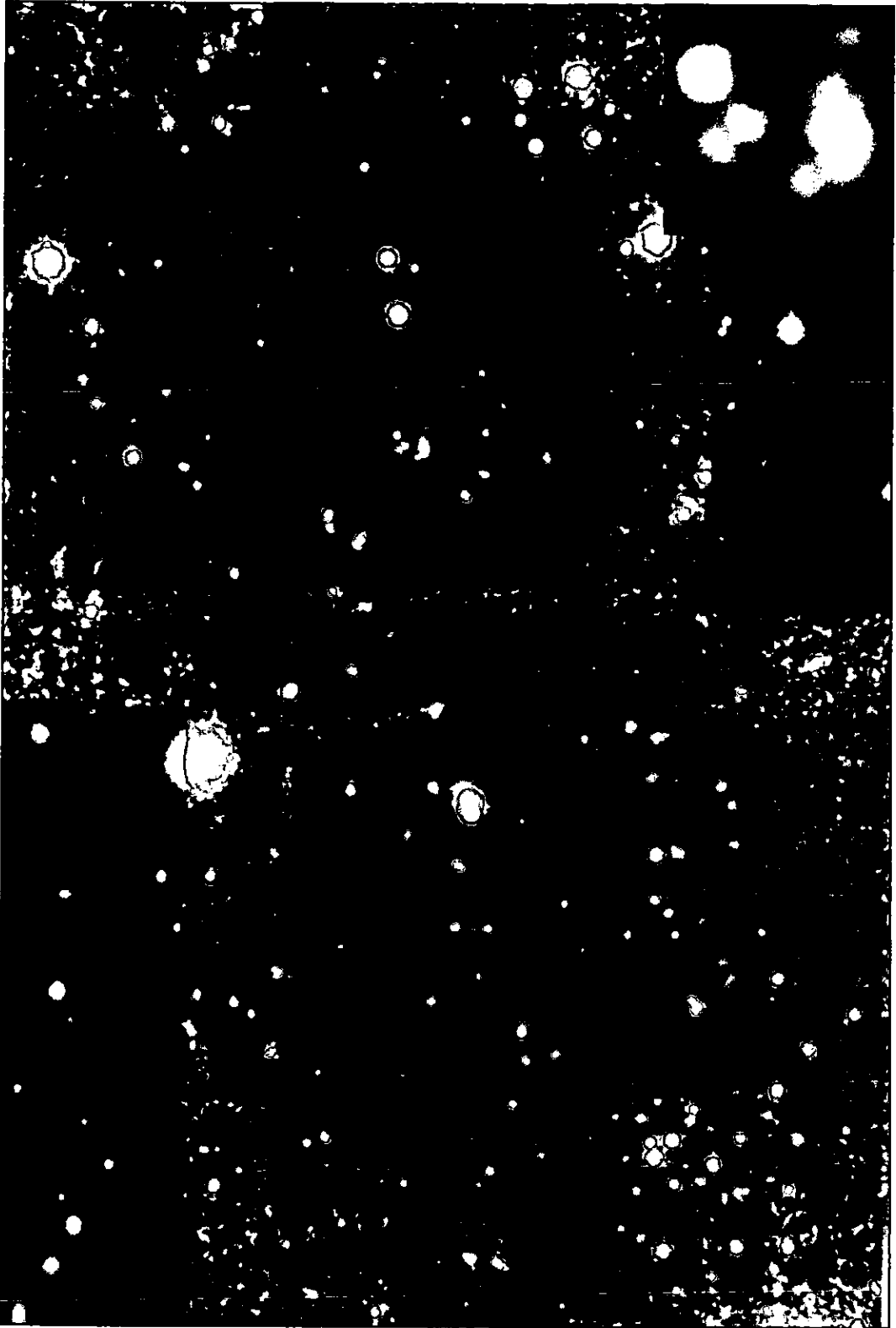


Figure 6.6: False-colour image of the $z = 1.306$ LQG quasar field, produced from the combination of the V (blue component), I (green) and K (red) images. The quasar is apparent as the lower of the two blue-white point-like sources in the top-centre of the image. The blue-green regions towards the top-right and lower-left corners have not been observed in the K band. North is to the left, and east is to the top. The inset shows an expanded view of galaxy ID #163.

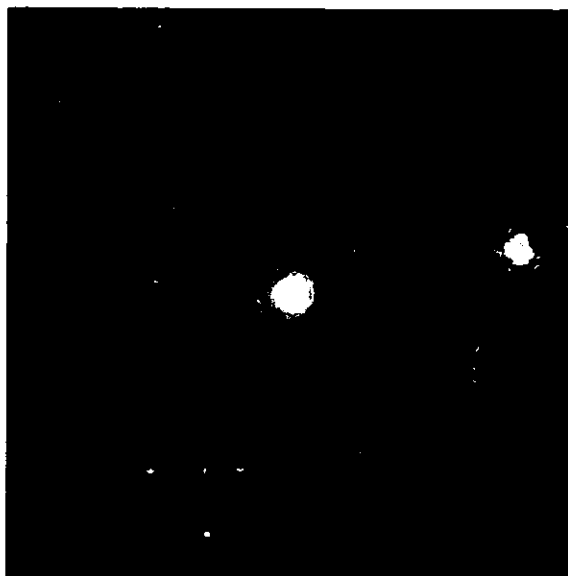


Figure 6.7: K -band image of the immediate environment of the $z = 1.306$ LQG quasar. The image is 30×30 arcsec² across, corresponding to $400 h^{-1}$ kpc at the quasar redshift. The three sources apparent are the $z = 1.306$ quasar (centre), source #156 which is a UV-excess point-like source which is the brighter of the two sources to the right, and galaxy #171 just below.

of field $I - K > 3.75$ galaxies, even a poor group associated with the quasar would be detectable as a significant excess of $I - K > 3.75$ galaxies.

Of the sources most likely to be at the redshift of the quasar, galaxy #163 is the nearest of any brightness ($K_{tot} = 18.26 \pm 0.04$) being located 25 arcsec to the west of the quasar. It is classed as a red outlier, and is shown as the extended red structure to the right of Figure 6.6(inset). The galaxy appears extended in all three bands, and in the K -band in particular there is evidence of a tail extending to the north-west, which is also apparent in the I image, but not the V image. The colours measured may have been affected by a chance projection which is apparent as the blue tinge to the eastern edge of the galaxy, and which is apparent as a separate source in both optical images. There is also apparent a second compact red source 3 arcsec to the north of galaxy #163, which is identified in the K image as galaxy #164, with $K_{tot} = 19.55$, but could not be separated from the source 1.5 arcsec to the north-west which is much brighter in the optical images. The morphology of galaxy #163 appears complex, with signs of an interaction, possibly with galaxy #164.

The immediate environment of the $z = 1.306$ LQG quasar is shown in Figure 6.7,

the K -band image of size 30×30 arcsec² centred on the quasar which has been convolved with a Gaussian kernel of width $\sigma = 1$ pix, to reduce the background noise levels without smoothing out the sources significantly.

The most notable source in the vicinity of the quasar is the bright point-like source (ID #156) located 11 arcsec to the east of the quasar, to the right of Figure 6.7. It can be seen from the false-colour image of Figure 6.6 to have the same blue-white colour as the quasar itself, and it was thus suggested that it may also be a quasar. The $z = 1.306$ quasar was observed as part of the Chile-UK Quasar Survey (Newman, 1999), where candidates selected on the basis of their $U - B < -0.3$ colour were observed using the multi-object spectrograph on the 2.5-m du Pont telescope at Las Campanas Observatory in Chile (the quasar had been identified previously by Keable (1987) using the AQD method). The second blue-white source passed the colour selection criterion (just), having $U - B = -0.33$, but was not observed as: firstly not all candidates could be observed in the time available, and so preference was given to those with the bluest colours; and secondly the minimum separation of fibres on the spectrograph was 55 arcsec so that both the quasar and the blue-white source could not be observed simultaneously.

If the source is indeed a quasar, then it would be a remarkable quasar pair, particularly given the relatively poor galaxy environment. It is certainly not a double image of a single quasar due to a gravitational lens, which would be unlikely anyway given the wide separation and no apparent lensing object, as their colours are significantly different, the quasar has $I - K = 2.27$, $V - I = 0.09$ whilst the blue-source has $I - K = 0.85$, $V - I = 0.59$, $V_{tot} = 18.36$. The VIK colours of the blue-white source in fact indicate that it is likely to be a white dwarf (however unfortunately located) having the colours expected from models of white dwarf cooling sequences (Chabrier et al., 2000) and those found from optical- near-infrared photometry of a sample of white dwarfs (e.g. Leggett et al., 1998). There is also marginal evidence of a proper motion of the source with respect to the quasar from the USNO catalogue where the relative position of the source with respect to the quasar in Right Ascension and declination in units of arcsec is (11.07,2.54) whereas in the BTC field it is (10.91,2.33), a change of 0.26 arcsec.

There is no evidence of any close companion galaxies or extended structure of the

galaxy host to the quasar in the K image of Figure 6.7 at all. The nearest source is galaxy #171, a $K_{tot} = 19.30$ galaxy 9.7 arcsec (corresponding to $130 h^{-1} \text{kpc}$ at $z = 1.306$) to the south-east, and whose colours are not those expected for a galaxy at $z \simeq 1.3$, with $I - K = 2.4$, $V - I = 2.3$. There is no evidence for any source closer to the quasar than this brighter than $K = 22.3 \text{ mag arcsec}^{-2}$ (3σ background fluctuation level). Given the relatively poor resolving ability of the images, it is possible that there are companion galaxies within ~ 1 arcsec ($\sim 10 h^{-1} \text{kpc}$) that cannot be resolved from the much brighter quasar.

If the quasar has not been triggered by a recent galaxy merger or interaction, then alternatively it may be the result of the accretion of hot gas during the process of galaxy formation (Haehnelt & Rees, 1993). As a protogalaxy collapses, the gas in the inner regions of the galaxy must fall inward and form a central black hole unless all the material is converted into stars. Further gas then accretes onto the central nucleus triggering the onset of the quasar. The triggering of quasars during galaxy formation is thought to be the dominant mechanism at high redshifts ($z \gtrsim 1$) and explains the correlation between the mass of the central black hole and the bulge mass of the host galaxy (e.g. Merritt & Ferrarese, 2001).

If the quasar luminosity is related in any way to the mass of the host galaxy or the environment, in that more luminous quasars are associated with more massive host galaxies or richer environments, then it is surprising that this quasar is in an apparently isolated environment. Of the four $z \simeq 1.3$ quasars, it is the most luminous with $M_V = -26.98$ (assuming a spectral index of $\alpha = -1$, $H_0 = 50 \text{ km s}^{-1} \text{ Mpc}^{-1}$ and $\Omega_M = 1$ for comparison with other studies), making it a relatively bright quasar. In comparison the $z = 1.226$ LQG quasar which was shown in the previous chapter to reside in a rich cluster environment, and had a number of companion galaxies, has $M_V = -26.60$.

6.8 The $z \simeq 0.8$ Cluster

Figure 6.8 is an expanded VIK three-colour image of the $z \simeq 0.8$ galaxy cluster, with north to the left, and east to the top of the page. The image has dimensions $63.7 \times 45.5 \text{ arcsec}^2$, corresponding to a proper angular size of $600 \times 430 h^{-2} \text{ kpc}^2$ at

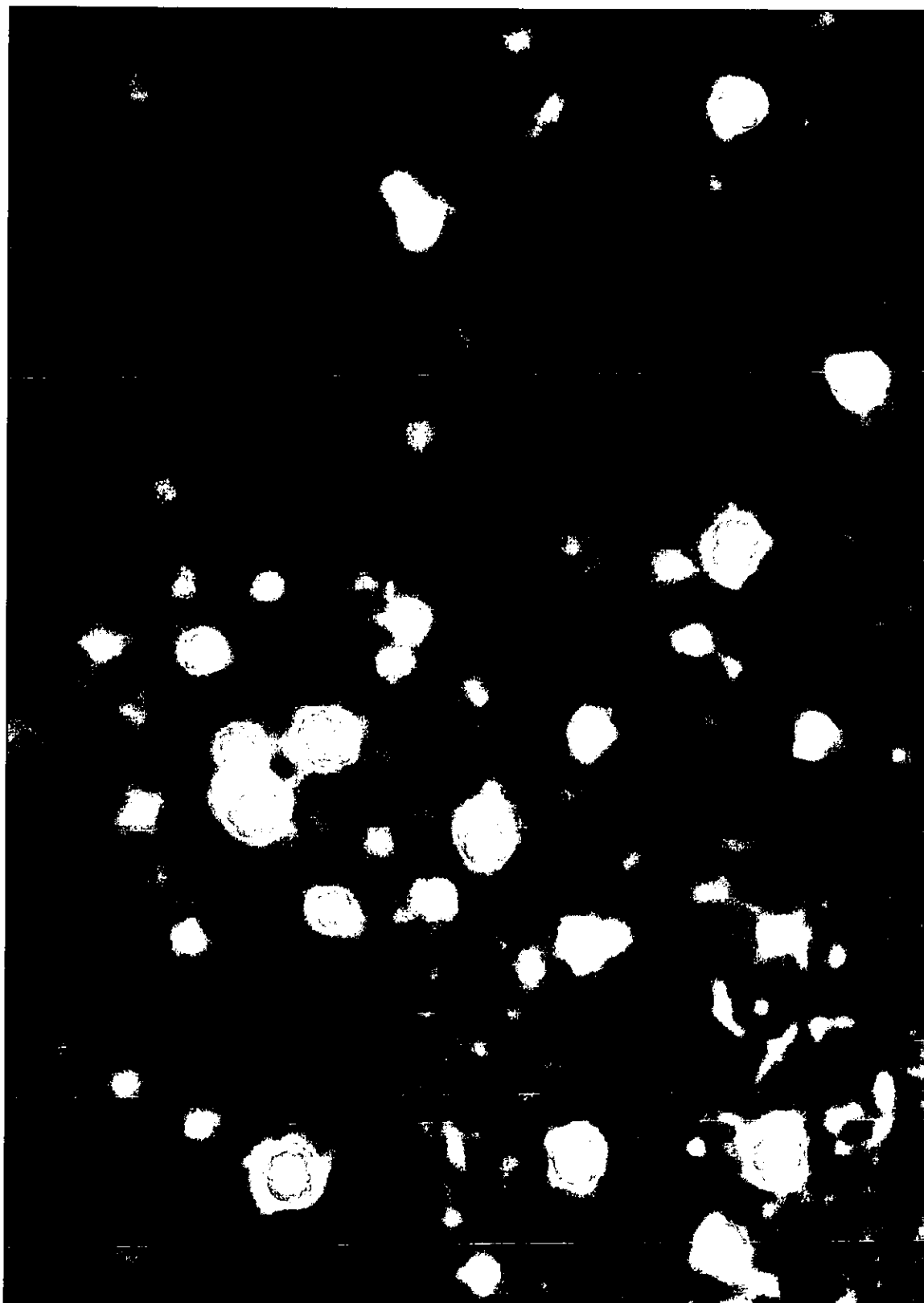


Figure 6.8: False-colour image of the $z \simeq 0.8$ galaxy cluster, produced from the combination of the V (blue component), I (green) and K (red) images. The galaxies whose colours are well described by the burst model at $z \simeq 0.8$ appear as orange-yellow sources, whilst the galaxies undergoing star-formation appear blue.

$z = 0.8$.

There are two notable features of the galaxy clustering apparent from the image. Firstly, there is a highly compact, dense core of the cluster containing 20–25 galaxies within a region $\sim 250 h^{-1} \text{kpc}$ across. Secondly, the cluster is made up of two very distinct populations: half the galaxies appear orange-yellow in the image, and have colours well described by the $z_f = 3.5$ burst model at $z \simeq 0.8$ (Figure 6.3); and the remainder of the galaxies appear blue in the image, indicating that they have undergone significant recent star-formation.

6.8.1 Early-type galaxies in the $z \simeq 0.8$ cluster

Figure 6.3 shows that there is a significant number of galaxies (indicated by solid yellow circles) with colours well described by an instantaneous burst at $z_f = 3.5$ and observed at $z \simeq 0.8$, having $2.75 < I - K < 3.75$ and $V - I > 2.00$. An examination of the spatial distribution of these galaxies in Figure 6.5 finds them highly concentrated towards the cluster in the bottom-right corner of the field. Figure 6.4(c) shows the redshift probability distribution for galaxy #1284, which having $I - K = 3.16$ and $V - I = 2.62$ has colours typical of this galaxy class, and is located in the central core, being the lowest of the three yellow-orange sources forming a small right-angled triangle in Figure 6.8. Its colours constrain its redshift and star-formation history, to an early-type galaxy at $0.7 \lesssim z \lesssim 0.9$. The photometric redshift estimates for the other yellow-orange sources produce similar results, indicating a population of early-type galaxies at $z \simeq 0.8$.

A large spread of colours, both $V - I$ and $I - K$, is observed for these galaxies, which is surprising given that they appear to be early-type galaxies and are presumably at the same redshift. Some of this spread may well be due to problems with photometry due to the high density of sources in the cluster core, making it difficult to determine the background levels, but even for those galaxies which are sufficiently isolated for this to not be an issue, this spread exists. The only other explanation is that there are small amounts of recent star-formation affecting the colours of many of these galaxies, and may well be related to the compact nature of the cluster, and also the finding of comparable numbers of star-forming galaxies.

Figure 6.9 shows the $V - K$ and $I - K$ against K colour-magnitude diagrams

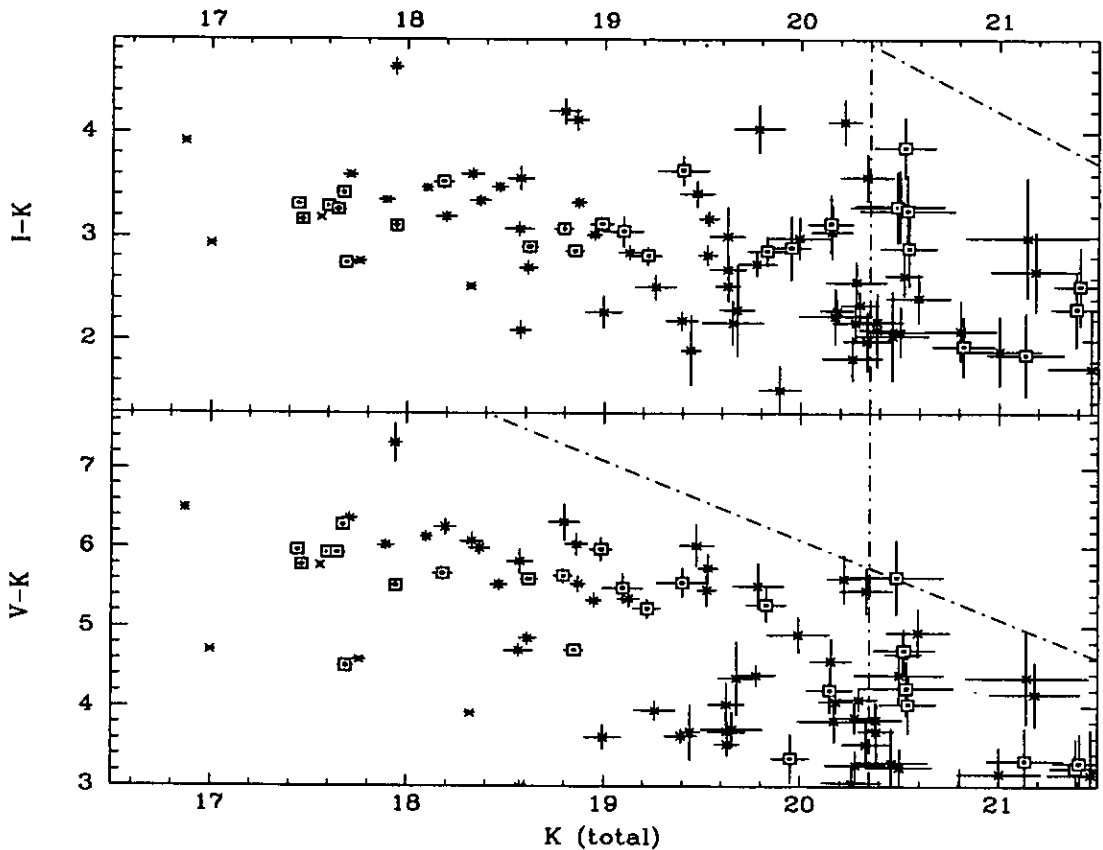


Figure 6.9: Colour-magnitude diagrams of galaxies in the 2.25×2.25 arcmin² K -band image containing the $z \simeq 0.8$ cluster. Those galaxies within $250 h^{-1}$ kpc (at $z = 0.8$) of the cluster centre are indicated by yellow squares, whilst the remainder are indicated by crosses. The dot-dashed green and blue lines indicate the 50% completeness levels for each filter in the image.

for galaxies in the 2.25×2.25 arcmin² K -band image containing the $z \simeq 0.8$ cluster. Those galaxies within $250 h^{-1}$ kpc of the centre of the cluster (taken to be the position of density maximum #21) are indicated by yellow squares, whilst the remainder are indicated by crosses. The dash-dotted green and blue lines indicate the 50% completeness levels for each filter in the image.

Red sequences are apparent at $I - K \simeq 3.4$ and $V - K \simeq 6$ and are particularly obvious if only galaxies within $250 h^{-1}$ kpc of the cluster centre are considered, although there appear a significant number of galaxies in the remainder of the image that lie on the same colour-magnitude relation. The observation of the red sequences confirms that these galaxies are early-type galaxies in a high redshift cluster, and a comparison of the zero-points of the red sequences and the model predictions of Kodama & Arimoto (1997) shown in Figure 3.5 confirms that the cluster is likely

to be at $z \simeq 0.8$. There are notable slopes in both red sequences, as the galaxies become progressively bluer with increasing magnitudes, reaching $I - K \simeq 3.0$ and $V - K \simeq 5.4$ at $K = 20.5$, suggesting slopes of $\delta(I - K)/K \simeq -0.13$ and $\delta(V - K)/K \simeq -0.20$, which are somewhat steeper than predicted by metallicity sequence models (values of -0.07 and -0.12 respectively). There appears a relatively high scatter about the red sequences of $\simeq 0.2$ mag, although this is less than would be expected from the colour-colour diagram. This large scatter is probably related to the high fraction of star-forming galaxies in the cluster.

The galaxies all appear relatively compact, and there is no single dominant galaxy in the cluster. It is clear from Figure 6.8 that all the early-type galaxies in the cluster are fairly similar, both in terms of morphology and luminosity, with no dominant central galaxy. The brightest of the galaxies has $K_{tot} = 17.44$ which corresponds to an absolute magnitude of $M_V = -22.17$ or $\sim L^*$. The fifth brightest galaxy is only 0.2 magnitudes fainter, having $K_{tot} = 17.68$, and all five have $2.6 < V - I < 2.9$ and $3.1 < I - K < 3.5$ indicating that these galaxies at least are not responsible for the observed wide spread of colours. The value of $M_V^* = -22.03$ is based on Lilly et al. (1995)'s estimation of the Canada-France Redshift Survey luminosity function in the $0.75 \leq z \leq 1.00$ redshift range as $M_{AB}^*(B) = -21.24$, which is then converted to our photometric system using $B_{AB} = B - 0.17$, and to the V band using the colours of a typical zero redshift E galaxy, $B - V = 0.96$ (Fukugita et al., 1995).

Their compact nature is apparent from Figure 6.8, and their FWHMs in the convolved K image are $\simeq 1.4$ arcsec in comparison to $\simeq 1.25$ arcsec for sources of comparable magnitudes classed as stars, suggesting their intrinsic FWHMs are $\simeq 0.6$ - 0.8 arcsec. In comparison, galaxy #1001, whose magnitude of $K_{tot} = 16.87$ extremely-red colours $I - K = 3.92$ and $V - I = 2.58$ indicate that it is likely to be a massive elliptical galaxy at $z \simeq 1$, appears both much more luminous than the early-type galaxies in the cluster, and an examination of Figure 6.6, where it is apparent as the extremely-red galaxy in the centre-right of the image, indicates that it is clearly extended.

It appears remarkable that given the relative proximity of the galaxies in the cluster core, that there is no evidence of galaxy interactions or mergers whatsoever in the form of tidal tails or galaxies with apparent substructure in any of the the V ,

I or *K* images.

6.8.2 Star-forming Galaxies in the Cluster

In stark contrast to the early-type galaxies in the cluster which are well described by passively-evolving stellar populations with little or no recent star-formation, the remainder of the galaxies appear dominated by star-formation, appearing as blue sources in Figure 6.8. Unfortunately, due to their blue colour, most of these galaxies are too faint to have been detected in the *K* image, and the few that have been are at or near the detection limit at $K \simeq 21$.

The photometric redshifts of those blue galaxies from Figure 6.8 that are detected in the *K* image tend to result in few constraints in terms of redshifts as their colours $I - K \simeq 2$ and $V - I \lesssim 1$ can be modelled by star-forming galaxies at virtually any redshift, although galaxy #1256 does appear constrained to $0.5 \lesssim z \lesssim 1$ from Figure 6.4(d). However, by making the assumption that these galaxies are associated with the cluster, which seems likely given that both the concentrations of blue and early-type galaxies are spatially coincident, then all of them are best described by 100–400 Myr old bursts of star-formation. These galaxies are probably irregular galaxies with small intrinsic masses, and are only visible due to their young stellar populations. An examination of Figure 3.2 indicates that the *V*-band luminosity of a stellar population decreases by an order of magnitude as a simple stellar population ages from 200 Myr to 2 Gyr.

Perhaps the most remarkable sign of star-formation in the cluster is the bright blue galaxy below and to the right of the cluster core ($\alpha = 10^{\text{h}}47^{\text{m}}21.89^{\text{s}}$, $\delta = +5^{\circ}23'45.4''$), which, despite being the brightest galaxy near the cluster core in the *V*-band image, having $V = 21.86$, and also $I = 21.17$, is not detected in the *K* image. There is also evidence of structure in this galaxy, with a tail extending away from the cluster core.

6.8.3 Interpretation

A comparison of the *VIK* three-colour image of the $z \simeq 0.8$ cluster in Figure 6.8 with the two-colour optical and three-colour *VIK* images of the other high-redshift

clusters in the BTC field (Figures 4.7, 4.10 and 5.6) suggest that the $z \simeq 0.8$ cluster is unusual. Firstly, it appears much more compact than the others, which by itself is not remarkable, as it is likely to be at the lowest redshift, and hence has had more time to collapse and virialise. Secondly, in the densest regions of the other high-redshift clusters there is no evidence of star-formation at all. Indeed for the clustering around the $z = 1.226$ quasar the star-formation rate appears to be anti-correlated spatially with the galaxy surface density, whereas in the $z \simeq 0.8$ cluster, despite it being the most compact and apparently densest of the cluster environments, there are signs of significant star-formation.

The high star-formation rate observed for this cluster is in contrast to studies of the blue galaxy population in other distant clusters (e.g. Oemler et al., 1997; Kodama & Bower, 2001). They observe a radial- and density-dependence for the star-formation in which star-formation is inhibited by high-density regions, and the blue galaxy fractions are lowest in the cluster cores. The effects are observed to be particularly strong for compact, dense clusters (Oemler et al., 1997) like this one. This is due to the densest cluster regions becoming filled with shock-heated, virialised gas which does not easily cool and collapse to form galaxies (Blanton et al., 1999) or new stars, inhibiting star-formation (Blanton et al., 2000).

It does not appear that the star-formation has been triggered as the result of galaxy interactions and mergers (Lavery & Henry, 1988), as there is no evidence of any galaxy interactions or mergers in the cluster whatsoever, despite their presumed close proximity. More recent evidence suggests that this mechanism is not a major contributor to the Butcher-Oemler effect, as observations of blue galaxies in a cluster at $z \simeq 0.4$ indicate that they are predominantly normal late-type spirals and that most of them were not undergoing dynamical interactions (Dressler et al., 1994). An examination of the *VIK* three-colour image of the galaxy clustering around the $z = 1.226$ cluster (Figure 5.6) finds that the blue galaxies appear isolated and show no signs of having had their star-formation triggered by interactions with another galaxy.

It is possible that the star-formation has been triggered by the ongoing infall of the galaxies into the cluster as a result of ram pressure from the intra-cluster medium (Evrard, 1991). Although star-formation is inhibited by the dense environment of

the cluster core, as the gas is heated up and ultimately stripped from the galaxy, as the galaxy approaches the cluster centre, the star-formation rate can be temporarily increased (by up to a factor of 2) as ram-pressure from the passage of the galaxy through the intra-cluster medium compresses the molecular gas of the galaxy (Fujita & Nagashima, 1999).

The observed high rate of star-formation in this cluster is probably a very temporary phenomenon, as the passage through the dense cluster core by the blue galaxies will rapidly truncate star-formation in them over a period of a few hundred Myr. The fact that the blue galaxy fraction is so high is probably due to a coincidental infall of a number of field galaxies onto the cluster, which may have had their star-formation rate boosted by the effects of ram pressure, or may just have the typical star-formation rates of field galaxies.

6.9 Summary

This chapter describes the results of K imaging of two adjacent 2.25×2.25 arcmin² fields, one containing the $z = 1.306$ LQG quasar, and the second containing the most significant high-redshift cluster candidate associated with density maximum #21. Photometric redshift estimates based on the VIK photometry allow the galaxy environment of the quasar to be examined by identifying those galaxies likely to be at $z \simeq 1.3$. There is no evidence of any galaxy clustering associated with the quasar, with no excess of $I - K > 3.75$ galaxies observed in either field, indicating that the quasar is located in a poor environment indistinguishable from the field. There is also no evidence of any companion galaxies or interactions associated with the quasar host, with no galaxy detected to $K \simeq 21$ ($M_K^* + 2$) within $100 h^{-1}$ kpc.

The addition of K imaging allows the confirmation that the clustering of red galaxies associated with density maximum #21 is indeed a high-redshift cluster. Red sequences are apparent at $I - K \simeq 3.4$ and $V - K \simeq 6$, indicative of a population of 15–25 early-type galaxies at $z \simeq 0.8$. The constraints produced by the photometric redshift estimates indicate that this cluster is certainly not associated with the quasar group, as the VIK colours of the red sequence members are incompatible with such high redshifts. There is evidence for significant star-formation

occurring in the cluster in the form of comparable numbers of faint blue ($V - I < 1$) galaxies concentrated around the cluster centre, whose colours are probably due to very young stellar populations ($\simeq 200$ Myr old). Despite the galaxy density in the cluster centre being particularly high, and the observation of numerous star-forming galaxies, there is no evidence of galaxy interactions or mergers, which suggests that this star-formation has not been triggered by such events, but is the result of the infall of the galaxies into the cluster.

Chapter 7

Conclusions and Further Work

In this chapter, the main findings of this thesis are summarised. Some of the work, in particular that described in Chapter 5, has been published in refereed journals (Haines et al., 2001), and presented at conferences (Clowes et al., 1999b; Haines et al., 2000a,b,c). Many of the conclusions presented in this thesis are limited by being able to estimate the distance and properties of sources from their colour, and so this chapter also describes a number of avenues open for future work that could clarify these issues.

7.1 Summary of Conclusions

The BTC Field

Chapter 2 describes the obtaining and reduction of ultra-deep optical images using the Big Throughput Camera (BTC) on the 4-m Blanco telescope at the Cerro Tololo Interamerican Observatory (CTIO). The observations were made over two nights in April 1998, resulting in ultra-deep V and I imaging of a 40.6×34.9 arcmin² region that contains three quasars from the $z \simeq 1.3$ Clowes-Campusano Large Quasar Group, as well as four background quasars.

The astrometry was calibrated through the comparison of the positions of $\simeq 800$ sources from the USNO catalogue, and is believed to be accurate to $\simeq 0.05$ arcsec. The photometric calibration was performed by using the standard stars of Landolt (1992) and the zero-point is believed to be accurate to $\simeq 0.02$ mag whilst the pho-

tometric errors due to random noise are believed to be ≈ 0.1 mag at $V \simeq 24.75$ and $I \simeq 23.75$.

The SEXTRACTOR package was used to extract the sources from the final images, resulting in catalogues of $\approx 10^5$ sources that are 50% complete to $V \simeq 26.35$ and $I \simeq 25.85$ in the fully exposed regions. The differential galaxy counts have been determined and compared with other deep surveys and are found to be in excellent agreement. The galaxy counts increase logarithmically with magnitude, with the slopes measured for the V -band as $\alpha_V = 0.402 \pm 0.012$ for $V = 21$ – 24 , flattening to $\alpha_V = 0.258 \pm 0.017$ for $V = 24$ – 26 . The slope for the I -band galaxy counts is measured as $\alpha_I = 0.286 \pm 0.006$ for $I = 20$ – 26 .

The Cluster Red Sequence Method

Chapter 3 describes the use of the Cluster Red Sequence method of Gladders & Yee (2000) to detect and characterise clusters in the BTC field. The method is motivated by the observation that the bulk of early-type galaxies in all rich clusters, and at all observed redshifts, lie along a tight, linear colour-magnitude relation — the cluster red sequence. This red sequence appears homogeneous from cluster to cluster at the same redshift, and its colour evolves with redshift in a manner predicted for the galaxies being described as simple stellar populations formed at $z_f \simeq 3$ – 5 which then evolve passively. This allows accurate cluster redshift estimates to be obtained from imaging data with as few as two filters, as is the case for the BTC data. By selecting only those galaxies which lie on the red sequence corresponding to a particular redshift, it is possible to obtain a redshift *slice*, from which candidate clusters can be identified as density peaks in the galaxy number density. The method was applied to the BTC data, and two candidate low-redshift clusters identified, one at $z \simeq 0.05$, and another at $z \simeq 0.25$. An examination of the properties of the $z \simeq 0.25$ cluster in particular demonstrates the validity of applying the cluster red sequence to the BTC images, as it is clearly a cluster from an examination of the images themselves: a 2.4σ excess of $I < 21$ galaxies within $500 h^{-1}$ kpc of the cluster location predicted by the cluster red sequence algorithm is observed; and an examination of the colour-magnitude diagram of galaxies within $500 h^{-1}$ kpc of the cluster centre shows the clear red sequence due to the presence of the cluster.

Galaxy Clustering Associated with the $z \simeq 1.3$ Clowes-Campusano LQG

Chapter 4 describes the examination of galaxy clustering at redshifts beyond $z \simeq 0.5$ through the selection of galaxies redder than the expected colour of red sequence galaxies at $z = 0.5$. By applying these selection criteria to galaxies in a comparably deep field, the EIS-DEEP HDF-South field covering 27 arcmin^2 , and taking advantage of its $UBVRIJHK$, photometry to estimate the red galaxies' redshifts and star-formation histories, it is demonstrated that these are early-type galaxies at $0.6 \lesssim z \lesssim 1.5$. This is confirmed by the two-point angular correlation function of the red galaxies in the BTC field which finds the clustering strength of red galaxies to be an order of magnitude greater than for I -band selected galaxies, as would be expected if the red galaxies are on average more massive, and hence more biased tracers of mass, than galaxies selected by magnitude alone.

In total 3017 red galaxies are found in the BTC field, corresponding to a mean galaxy density of $2.13 \text{ galaxies per arcmin}^2$. In contrast, there are only 34 sources classified as red galaxies in the EIS-DEEP HDF-South control field, corresponding to a mean galaxy density of $1.26 \text{ galaxies per arcmin}^2$. The excess is found to be significant at the 98.4% by considering the fraction of EIS-DEEP field-sized regions in the BTC field that contain as few red galaxies as observed in the EIS-DEEP field. Even after considering the possibility of contamination of the red galaxy number by misclassified stellar objects, the excess is estimated to be significant at the 1.6σ level. The observed excess corresponds to ≈ 1000 extra red galaxies over the BTC field, and it is suggested that this is due to the presence of a high-redshift large-scale structure encompassing the whole field. Given that the BTC field was chosen to cover a dense region of the Clowes-Campusano Large Quasar Group, it seems reasonable to suggest that this excess of red galaxies is evidence for a large-scale structure traced by the quasar group. A crude estimate of the expected excess of red galaxies, given the observed excess of MgII absorbers at $1.2 < z < 1.3$ in the region of the quasar group (Williger et al., 2000), indicates that excesses of the order of 20–50% are possible.

If the overall red excess, the clustering associated with the $z = 1.226$ quasar, and the excess of MgII absorbers at the LQG redshift are considered together, the evidence for the Clowes-Campusano Large Quasar Group tracing a large-scale struc-

ture at $z \simeq 1.3$ becomes highly convincing. These results are paralleled by those of Tanaka et al. (2000, 2001) who find evidence for a large-scale structure $\simeq 20 h^{-1} \text{Mpc}$ across that is traced by five quasars from the Crampton et al. (1989) LQG at $z \simeq 1.1$ (Tanaka et al., 2001), with one of the quasars located on the periphery of a rich cluster (Tanaka et al., 2000).

The evidence in favour of LQGs tracing large-scale structures at high-redshift has become much stronger over the last few years, and opens the possibility of them being used as probes of large-scale structure beyond the range of galaxy redshift surveys. With the prospect of large, homogeneous quasar surveys, such as the 2dF, becoming publicly available over the coming years, it should be possible to determine the statistical properties of LQGs, such as number density, redshift evolution, and to use these to deduce properties of the evolution of the underlying large-scale structure. However, any mapping of the spatial distribution of quasars onto an underlying mass distribution will be complicated by the uncertainty of the biasing effects of the quasar triggering mechanisms, and the likely redshift dependency of this bias.

High-redshift Galaxy Clusters

Four high-redshift cluster candidates are apparent in the BTC field, of which two appear associated with $z \simeq 1.3$ quasars.

The $z = 1.226$ LQG quasar is located within a region of amorphously-distributed galaxy clustering extending over several megaparsecs. This appears to be a very massive system, with an excess of 100–150 red galaxies within 5 arcmin of the quasar, suggesting a total mass of $M_{cl} \approx 5 \times 10^{14} h^{-1} M_{\odot}$, comparable to that of the Coma cluster. The $z = 1.426$ quasar is located on the periphery of a region of clustering of red galaxies, made up of two clusters separated by $\sim 2.4 h^{-1} \text{Mpc}$. A similar bimodal distribution of red galaxies is observed for another cluster candidate, with two compact groups of ≈ 6 red galaxies separated by 4.4 arcmin, the intervening region being filled with a diffuse, extended distribution of red galaxies.

The most significant (in terms of the cluster finding algorithm) high-redshift cluster candidate is located just 165 arcsec (corresponding to $2.2 h^{-1} \text{Mpc}$ at the quasar redshift) from the $z = 1.306$ LQG quasar, and so K imaging was obtained in May 2000 to estimate its redshift, as described in Chapter 6. Red sequences

are apparent at $I - K \simeq 3.4$ and $V - K \simeq 6$, indicative of a population of 15–25 early-type galaxies at $z = 0.8 \pm 0.1$. There is evidence for significant star-formation occurring in the cluster in the form of comparable numbers of faint blue ($V - I < 1$) galaxies concentrated around the cluster centre, whose colours are probably due to very young stellar populations ($\simeq 200$ Myr old). Despite the galaxy density in the cluster centre being particularly high, and the observation of numerous star-forming galaxies, there is no evidence of galaxy interactions or mergers, which suggests that this star-formation has not been triggered by such events, but is the result of the infall of the galaxies into the cluster.

Three of the four high-redshift cluster candidates have significant substructure, either bimodal or more complex, with only the $z \simeq 0.8$ cluster appearing dynamically evolved. Such substructure appears relatively common at these redshifts: X-ray imaging data of the $z = 1.27$ cluster of Stanford et al. (1997) finds the spatial distribution of the emission from the hot gas of the intra-cluster medium both amorphous and bimodal (Stanford et al., 2000). This suggests that at $z \simeq 1$ galaxy clusters are still in the process of forming and coalescing, as would be expected from the hierarchical clustering model. Many of the high-redshift structures apparent in the BTC field have dense, compact cores surrounded by a diffuse, extended galaxy structure, suggesting that at these redshifts only the cores of clusters have formed, and that over the next few gigayears the clusters will increase in size through the progressive absorbing of galaxies from the extended distribution.

The finding of so many clusters at high-redshifts indicates a mild negative evolution of cluster abundance with redshift that is highly inconsistent with an $\Omega_M = 1$ universe where clusters are predicted to form later and evolve much more rapidly, but is in good agreement with that predicted by low-density cosmological models, with or without a cosmological constant.

The Galaxy Environment of Quasars at $z \simeq 1.3$

Chapters 5 and 6 describe near-infrared imaging for fields around two of the three LQG quasars in the BTC field. K imaging of 2.25×2.25 arcmin³ fields around the $z = 1.226$ and $z = 1.306$ LQG quasars was obtained using the UKIRT Fast-Track Imager (UFTI) camera on the 3.8-m United Kingdom Infra-Red Telescope

(UKIRT) in March 1999 and May 2000, reaching $K \simeq 20$. The addition of K imaging allows the identification of galaxies likely to be associated with the quasars through photometric redshift estimation methods, with $I - K \simeq 4$ colours being a particularly good indicator of galaxies at these redshifts.

The clustering of optically-red galaxies around the $z = 1.226$ quasar is confirmed (in the region covered by K imaging at least) to be at the quasar redshift, in the form of a factor ~ 11 excess of galaxies with $I - K > 3.75$ in the 2.25×2.25 arcmin² field. In particular, 15–18 galaxies with colours consistent with being a population of passively-evolving massive ellipticals at $z = 1.2 \pm 0.1$ are found. They form red sequences in the $V - K$ against K and $I - K$ against K colour-magnitude diagrams at $V - K \simeq 6.9$, $I - K \simeq 4.3$ comparable to those observed in spectroscopically-confirmed $z \simeq 1.2$ clusters (e.g. Dickinson, 1995; Stanford et al., 1997; Rosati et al., 1999). There is suggestive evidence for substructure amongst these red sequence galaxies in the K image, in the form of two compact groups, 40 arcsec to the north, and 60 arcsec to the south-east of the quasar. An examination of the wider optical images indicates that this substructure is significant at the 98% level, and that the clustering extends well beyond the K image, forming a large-scale structure $2\text{--}3 h^{-1}\text{Mpc}$ across.

There is evidence for a high ($\gtrsim 50\%$) fraction of blue galaxies in this system in the form of 15–20 ‘red-outlier’ galaxies with $I - K > 3.75$ and $V - I < 2.00$. Such galaxies are rare in field regions indicating that they are likely to be associated with the $z \simeq 1.2$ cluster, and their colours are best described by a two-component model in which a secondary burst of recent star-formation is added to a dominant old, passively-evolving stellar population. Within 30 arcsec of the quasar a concentration of blue ($V - I < 1$) galaxies is found, forming a *band* that bisects the two groups of red sequence galaxies. This band is similar to regions of enhanced star-formation apparent around many of the $z \simeq 1.1$ quasars of the Hutchings et al. (1995) study, suggesting that this band also corresponds to a region of enhanced star-formation. However, no overall excess of blue galaxies is observed, and it may be that this band is in fact a region of average star-formation levels, that only appears blue in contrast to the diminished star-formation found in the centres of the two clusters. This is supported by the observations of Balogh et al. (1999) and Ellingson et al.

(2001) which examine the galaxy morphology fractions and star-formation rates as a function of clustercentric radius, and find that star-formation rates are significantly diminished in the cluster cores which are dominated by early-type galaxies, and find no evidence of an excess of star-formation at any clustercentric radius. Their results imply that the cluster environments are not responsible for inducing starbursts, and indeed inhibit star-formation, and that the infall of galaxies into the cluster produces a gradual truncation of star-formation by ram-pressure from the intra-cluster medium.

The immediate environment of the quasar suggests that it has been activated by a recent galaxy interaction event, as there are two sources within 3 arcsec, that may be companion galaxies to the quasar host. Such compact companions are found for a significant fraction ($\approx 40\%$) of quasars (e.g. Bahcall et al., 1997a; McLure et al., 1999), and spectroscopic observations have confirmed that many have stellar populations and redshifts within 500 km s^{-1} of the quasar (e.g. Stockton, 1982) and in one case have found evidence for a recent star-burst event that may be coincident with the quasar activation (Canalizo & Stockton, 1997).

In complete contrast, there is no evidence of any galaxy clustering associated with the $z = 1.306$ LQG quasar, with no excess of $I - K > 3.75$ or $K < 20$ galaxies in the $2.25 \times 2.25 \text{ arcmin}^2$ K -image containing the quasar, indicating that the quasar is located in a poor environment that is indistinguishable from the field. There is also no evidence of any companion galaxies or interactions associated with the quasar host, with no galaxy detected to $K \simeq 21 (M_K^* + 2)$ within $100 h^{-1} \text{ kpc}$. There is no evidence of galaxy clustering associated with the $z = 1.230$ LQG quasar either from the BTC data, it being located in a low-density region of optically-red galaxies.

The $z = 1.426$ quasar which, although not classed as belonging to the Clowes-Campusano LQG, is at a similar redshift, and has associated galaxy clustering, it being located on the periphery of a cluster of optically-red ($V - I \simeq 3$) galaxies, with a second cluster $2.4 h^{-1} \text{ Mpc}$ beyond the first.

The four $z \simeq 1.3$ quasars are found in a wide variety of galaxy environments, from those indistinguishable from the field, to being associated with rich clusters, although it is notable that they are located on the cluster peripheries rather than in the cores. These results are similar to those of other studies of quasar environments

at these redshifts (e.g. Hall & Green, 1998; Sánchez & González-Serrano, 1999), which find the quasars in a wide variety of environments, but on average are in overdense regions comparable to poor clusters, making them biased tracers of mass compared to galaxies. Sánchez & González-Serrano (1999) also observe that the quasars are not located in the highest density regions of the galaxy clustering, but are found on the cluster peripheries, at a projected distance of 40–100 arcsec from the cluster centres.

The wide variety of environments observed for quasars, and the bias towards over-dense regions, is consistent with the quasars being hosted by massive ellipticals, which trace mass in the same biased manner as described by the density-morphology relation of Dressler (1980). This is confirmed by recent HST-based studies that have found that the host galaxies of all low-redshift, luminous ($M_V < -23.5$) quasars are bright galaxies with $L > L^*$, and have luminosity profiles that are well described by a de Vaucouleurs $r^{1/4}$ -law spheroidal profile (McLure et al., 1999; Dunlop, 2001). This is also confirmed by the quasar two-point redshift-space correlation function from the 2dF QSO Redshift Survey, which is found to be comparable to results for local optically-selected galaxies, and evolves with redshift in a manner consistent with quasars residing in dark matter halos with masses of $M_{DMH} \gtrsim 10^{12-13} M_\odot$.

Given that massive ellipticals tend to dominate the galaxy population in the cores of clusters, the apparent avoidance by quasars of these high-density regions must be the result of the quasar triggering mechanism rather than the host galaxy. This avoidance of the high-density regions can indeed be understood in the framework of both galaxy merger and galaxy formation quasar triggering mechanisms: the encounter velocities of galaxies in the centre of clusters are much greater than the internal velocity distributions, and so galaxy mergers become much less efficient at triggering nuclear activity (Aarseth & Fall, 1980); and the cluster cores are filled with shock-heated virialised gas that does not easily cool and collapse (Blanton et al., 1999), inhibiting both the formation of stars and galaxies (Blanton et al., 2000), and hence inhibiting quasar formation as well (Haehnelt & Rees, 1993).

7.2 Future Work

One of the recurring themes of this thesis has been the limitation of many conclusions due to having to estimate galaxy redshifts from their colour alone, rather than having any definite redshift value. Hence, the most imperative avenue for future work is to obtain improved redshift data for those galaxies thought to be of most interest. There are two sets of observations that will provide improved redshift and star-formation history data for galaxies in the BTC field: further near-infrared imaging; and multi-object spectroscopy.

Chapters 5 and 6 demonstrated the power of combined optical and near-infrared imaging in discriminating between galaxies associated with the $z \simeq 1.3$ LQG quasars and foreground galaxies, with the $I - K$ colour in particular being able to constrain galaxy redshifts efficiently at these redshifts, and the $V - I$ colour allowing separation between passively-evolving and star-forming galaxies.

Near-infrared imaging (J, K) of fields centred on the high-redshift cluster candidates would allow estimates of their redshifts accurate to a few percent using the cluster red sequence method. Any clustering of passively-evolving galaxies associated with the quasar group should manifest itself as red sequences at $V - K \simeq 7$, $I - K \simeq 4.3$ and $J - K \simeq 2$. It should also be possible to examine the star-formation properties of galaxies in these clusters by identifying candidate late-type cluster members from their VIK , or preferably $VIJK$, colours through photometric redshift estimation methods. Such galaxies are likely to have a wide range of $V - I$ colours, making it impossible to identify them from the BTC data alone, but they should still have relatively red optical- near-infrared colours at $z \simeq 1.3$ allowing them to be distinguished from foreground galaxies.

The most suitable instrument for obtaining near-infrared imaging of high-redshift cluster candidates is the SOFI infrared imaging camera on the 3.5-m New Technology Telescope (NTT) at La Silla in Chile, which has a 4.9×4.9 arcmin² field of view and can reach 5σ magnitude limits of $K = 20.9$ and $J = 22.9$ in one hour. The field of view is sufficiently large to cover most or all of the clustering associated with each of the high-redshift cluster candidates (Figures 4.7, 4.10, and 4.17) in one exposure, and so J, K imaging of sufficient depth to detect typical cluster galaxies

could be obtained in 2–3 hours per cluster candidate. As well as observing each of the high-redshift cluster candidates, it may be worth observing a field region within the BTC image to examine the properties of the optically-red galaxies belonging to the high-redshift slice and to see if the observed excess could be due to a large-scale structure at $z \simeq 1.3$.

Although near-infrared observations can provide useful constraints on galaxy redshifts and star-formation histories, definite redshifts and star-formation rates can only be obtained using spectroscopic data. By using multi-object spectrographs on 8-m class telescopes it is now possible to obtain high-quality spectra for a large sample of $I \simeq 23$ galaxies in a few hours. The Visible Multi-Object Spectrograph (VIMOS) on the 8-m Melipal Very Large Telescope (VLT - UT3) at the Paranal Observatory in Chile for example, is able to define masks with $\simeq 500$ slits over a field of 14×16 arcmin², allowing the spectra of hundreds of $I \simeq 23$ galaxies to be obtained in a single observation of ≈ 4 hours, and is likely to be available to astronomers from late 2001.

Instruments such as VIMOS would allow a follow-up spectroscopic study of a large ($\gtrsim 100$) sample of the optically-red galaxies from the high-redshift slice and determine if the observed excess of these galaxies is due to a large-scale structure at $z \simeq 1.3$, in which case a sharp peak would be apparent in the redshift distribution at $1.2 \lesssim z \lesssim 1.3$. Such a study would also naturally provide a large sample of high-redshift early-type galaxies allowing their evolution to be examined.

As well as a wide-field spectroscopic study of the optically-red galaxies, concentrated spectroscopic studies of the high-redshift cluster candidates would be desirable. Such studies could not only establish the redshift and galaxy membership of the clusters, but could also estimate the mass of the clusters through the velocity dispersion of the galaxies. Chapters 5 and 6 have speculated on the effects of the cluster environment on star-formation in the galaxies, in particular the ‘band’ of blue galaxies near the $z = 1.226$ quasar, and it would be particularly interesting to obtain spectra of these galaxies, and examine the spatial distribution of star-formation in the cluster neighbourhood. To identify these star-forming cluster members requires at least the *VIK* colour data described in Chapters 5 and 6, and so before any detailed spectroscopic survey of the clusters, near-infrared imaging should be obtained

to allow the selection of candidate cluster members in a manner as free from bias with respect to star-formation history as possible.

A service observing proposal to obtain spectra of 57 galaxies in the vicinity of the $z = 1.226$ quasar using the FOcal Reducer / Low Dispersion Spectrograph (FORs1) on the 8-m Antu Very Large Telescope (VLT - UT1) was submitted in September 1999 for the April-September 2000 semester (period 65), and was accepted with the highest priority level.

The FORs instrument allows multi-object spectroscopy through 19 slitlets which can be positioned in a limited manner over a 6.8×4 arcmin² field. Three sets of 19 cluster candidates were identified for spectroscopic observations, with exposure times of 1 hour (for the brightest sources), 3 hours and 4 hours, making up the total of 8 hours given to the proposal. Exposure times of 3–4 hours are needed to reach continuum signal-to-noise levels of 5 for $I \simeq 23$ galaxies, and are comparable to the exposure times used in spectroscopic studies of other $z \simeq 1.2$ clusters (e.g. Dickinson, 1995; Stanford et al., 1997; Rosati et al., 1999). The candidates were selected to contain as many of the 15–18 galaxies from the $V - K \simeq 6.9$ and $I - K \simeq 4.3$ cluster red sequences as possible, as well as members of the blue ‘band’ and the quasar companion galaxies, and the remainder of the slits were filled with optically-red galaxies from the surrounding large-scale structure. The wavelength range to be observed is 6 000–11 000 Å covering the redshifted 4 000 Å break and OII 3727 Å emission-line of galaxies at the quasar redshift, allowing the ages and star-formation rates of the galaxies to be estimated. There were several objectives of the proposal: to confirm the redshift and extent of the large-scale structure of galaxies with the colours of early-type galaxies at $z \simeq 1.2$, and whether it is associated with the quasar as believed; to examine the nature of the blue ‘band’ by firstly confirming whether it is associated with the quasar and the clustering of early-type galaxies, and then ascertaining whether it is a region of average or enhanced star-formation levels; and confirming whether the two galaxies 3 arcsec from the quasar are indeed companion galaxies, and search for indications of a recent starburst that could indicate that the quasar was triggered by an interaction of the host galaxy with one of the companion galaxies.

It was hoped to include the analysis of these observations in this thesis, as they

may have produced many interesting results. Unfortunately, despite the service proposal being successful, and given the highest priority level, it remains only partly completed a year after the observations would have been expected to have taken place.

There are further avenues for future work, such as HST-based imaging of the galaxy clustering around the $z = 1.226$ LQG quasar, using its unique resolving capabilities to examine the morphologies of the cluster galaxies, and the immediate environment of the quasar to discern the host galaxy and the companion galaxies. There are also other interesting objects that may merit HST imaging, such as the $z \simeq 0.8$ cluster to search for signs of galaxy mergers or gravitationally-lensed objects, or the compact group of galaxies at the heart of density maximum #71 that may be the progenitor of a cD galaxy.

Finally, the hot gas from the intra-cluster media of the high-redshift clusters could be observed directly through X-ray imaging by the XMM or Chandra satellites. Recent Chandra X-ray observations of clusters at $z \simeq 1.2$ finds spatially extended X-ray emission that clearly shows that a hot intra-cluster medium exists in clusters at these redshifts (Stanford et al., 2000). It would be particularly interesting to obtain comparable data for the clustering around the $z = 1.226$ quasar as one of the possible explanations of the 'blue' band was that it was triggered by shocks in the intra-cluster medium produced by the merging of the two clusters on either side, and so these shocks, if they exist, should be directly observable in the X-ray data.

It is hoped that over the next few years many of the results and conclusions presented in this thesis will be confirmed by improved data, and that the idea of using Large Quasar Groups as cosmological probes will be advanced.

References

- Aarseth, S. J. & Fall, S. M. 1980, *ApJ*, 236, 43
- Abell, G. O. 1958, *Astrophys. J. Suppl. Ser.*, 3, 211
- Abell, G. O., Corwin, H. G., & Olowin, R. P. 1989, *Astrophys. J. Suppl. Ser.*, 70, 1
- Aragón-Salamanca, A., Ellis, R. S., Couch, W. J., & Carter, D. 1993, *Mon. Not. R. Astron. Soc.*, 262, 764
- Arnouts, S., D'Odorico, S., Cristiani, S., Zaggia, S., Fontana, A., & Giallongo, E. 1999, *Astron. Astrophys.*, 341, 641
- Ashman, K. A., Bird, C. M., & Zepf, S. E. 1994, *AJ*, 108, 2348
- Bahcall, J. N., Kirhakos, S., Saxe, D. H., & Schneider, D. P. 1997a, *ApJ*, 479, 642
- Bahcall, N. A., Fan, X., & Cen, R. 1997b, *Astrophys. J. Letters*, 485, L53
- Balogh, M. L., Morris, S. L., Yee, H. K. C., Carlberg, R. G., & Ellingson, E. 1999, *ApJ*, 527, 54
- Baraffe, I., Chabrier, G., Allard, F., & Hauschildt, P. H. 1998, *Astron. Astrophys.*, 337, 403
- Barger, A. J., Aragon-Salamanca, A., Ellis, R. S., Couch, W. J., Smail, I., & Sharples, R. M. 1996, *Mon. Not. R. Astron. Soc.*, 279, 1
- Barrow, J. D., Sonoda, D. H., & Bhavsar, S. P. 1985, *Mon. Not. R. Astron. Soc.*, 216, 17
- Baum, W. A. 1962, in *IAU Symposium 15: Problems of Extra-Galactic Research*, ed. G. C. McVittie, Vol. 15 (Macmillan Press, New York), 390

- Bekki, K. 1999, preprint (astro-ph/9904044)
- Bertin, E. 1996, SExtractor 1.0a User's guide
- Bertin, E. & Arnouts, S. 1996, *Astron. Astrophys. Suppl. Ser.*, 117, 393
- Blanton, M., Cen, R., Ostriker, J. P., & Strauss, M. A. 1999, *ApJ*, 522, 590
- Blanton, M., Cen, R., Ostriker, J. P., Strauss, M. A., & Tegmark, M. 2000, *ApJ*, 531, 1
- Bolzonella, M., Miralles, J.-M., & Pelló, R. 2000, *Astron. Astrophys.*, 363, 476
- Bower, R. G., Lucey, J. R., & Ellis, R. S. 1992, *Mon. Not. R. Astron. Soc.*, 254, 601
- Boyle, B. J., Shanks, T., Croom, S. M., Smith, R. J., Miller, L., Loaring, N., & Heymans, C. 2000, *Mon. Not. R. Astron. Soc.*, 317, 1014
- Broadhurst, T. J., Ellis, R. S., Koo, D. C., & Szalay, A. S. 1990, *Nature*, 343, 726
- Brown, M. J. I., Webster, R. L., & Boyle, B. J. 2000, *Mon. Not. R. Astron. Soc.*, 317, 782
- Bruzual, A. G. 2000, in to appear in *Proceedings of the XI Canary Islands Winter School of Astrophysics on Galaxies at High Redshift*, ed. I. Perez-Fournon, M. Balcells, & F. Sanchez
- Bruzual, A. G. & Charlot, S. 1993, *ApJ*, 405, 538
- . 2000, in preparation
- Burns, J. O., Roettiger, K., Ledlow, M., & Klypin, A. 1994, *Astrophys. J. Letters*, 427, L87
- Butcher, H. & Oemler, A. 1978, *ApJ*, 226, 559
- . 1984, *ApJ*, 285, 426
- Caldwell, N., Rose, J. A., Sharples, R. M., Ellis, R. S., & Bower, R. G. 1993, *AJ*, 106, 473

- Calzetti, D., Armus, L., Bohlin, R. C., Kinney, A. L., Koornneef, J., & Storchi-Bergmann, T. 2000, *ApJ*, 533, 682
- Canalizo, G. & Stockton, A. 1997, *Astrophys. J. Letters*, 480, L5
- Carlberg, R. G. 1990, *ApJ*, 350, 505
- Carlberg, R. G., Yee, H. K. C., Ellingson, E., Abraham, R., Gravel, P., Morris, S., & Pritchett, C. J. 1996, *ApJ*, 462, 32
- Carlberg, R. G., Yee, H. K. C., Morris, S. L., Lin, H., Hall, P. B., Patton, D., Sawicki, M., & Shepherd, C. W. 2000, *ApJ*, 542, 57
- Carroll, S. M., Press, W. H., & Turner, E. L. 1992, *Ann. Rev. of Astron. and Astrophys.*, 30, 499
- Casertano, S., de Mello, D. ., Dickinson, M., Ferguson, H. C., Fruchter, A. S., Gonzalez-Lopezlira, R. A., Heyer, I., Hook, R. N., Levay, Z., Lucas, R. A., Mack, J., Makidon, R. B., Mutchler, M., Smith, T. E., Stiavelli, M., Wiggs, M. S., & Williams, R. E. 2000, *AJ*, 120, 2747
- Cavaliere, A. & Padovani, P. 1988, *Astrophys. J. Letters*, 333, L33
- Chabrier, G., Baraffe, I., Allard, F., & Hauschildt, P. 2000, *ApJ*, 542, 464
- Clowes, R. G. & Campusano, L. E. 1991, *Mon. Not. R. Astron. Soc.*, 249, 218
- . 1994, *Mon. Not. R. Astron. Soc.*, 266, 317
- Clowes, R. G., Campusano, L. E., & Graham, M. J. 1999a, *Mon. Not. R. Astron. Soc.*, 309, 48
- Clowes, R. G., Cooke, J. A., & Beard, S. M. 1984, *Mon. Not. R. Astron. Soc.*, 207, 99
- Clowes, R. G., Haines, C. P., Machura, I. K., & Campusano, L. E. 1999b, in *American Astronomical Society Meeting*, Vol. 195, 1706
- Coleman, G. D., Wu, C. ., & Weedman, D. W. 1980, *Astrophys. J. Suppl. Ser.*, 43, 393

- Cowie, L. L., Gardner, J. P., Hu, E. M., Songaila, A., Hodapp, K. ., & Wainscoat, R. J. 1994, *ApJ*, 434, 114
- Crampton, D., Cowley, A. P., & Hartwick, F. D. A. 1987, *ApJ*, 314, 129
- . 1989, *ApJ*, 345, 59
- Crampton, D., Schade, D., & Cowley, A. P. 1985, *AJ*, 90, 987
- Cristiani, S., Barbieri, C., La Franca, F., Iovino, A., & Nota, A. 1989, *Astron. Astrophys. Suppl. Ser.*, 77, 161
- Croom, S. M. & Shanks, T. 1999, *Mon. Not. R. Astron. Soc.*, 303, 411
- Croom, S. M., Shanks, T., Boyle, B. J., Smith, R. J., Miller, L., Loaring, N. S., & Hoyle, F. 2000, Preprint (astro-ph/0012375) Submitted to *Mon. Not. R. Astron. Soc.*
- da Costa, L., Nonino, M., Rengelink, R., Zaggia, S., Benoist, C., Erben, T., Wicenec, A., Scodreggio, M., Olsen, L. F., Guarnieri, M. D., Deul, E., D'Odorico, S., Hook, R., Moorwood, A., & Slijkhuis, R. 1998, Preprint (astro-ph/9812105) Submitted to *Astron. Astrophys.*
- Daddi, E., Cimatti, A., Pozzetti, L., Hoekstra, H., Röttgering, H. J. A., Renzini, A., Zamorani, G., & Mannucci, F. 2000, *Astron. Astrophys.*, 361, 535
- Davis, M. & Peebles, P. J. E. 1983, *ApJ*, 267, 465
- de Bernardis, P., Ade, P. A. R., Bock, J. J., Bond, J. R., Borrill, J., Boscaleri, A., Coble, K., Crill, B. P., De Gasperis, G., Farese, P. C., Ferreira, P. G., Ganga, K., Giacometti, M., Hivon, E., Hristov, V. V., Iacoangeli, A., Jaffe, A. H., Lange, A. E., Martinis, L., Masi, S., Mason, P. V., Mauskopf, P. D., Melchiorri, A., Miglio, L., Montroy, T., Netterfield, C. B., Pascale, E., Piacentini, F., Pogosyan, D., Prunet, S., Rao, S., Romeo, G., Ruhl, J. E., Scaramuzzi, F., Sforna, D., & Vittorio, N. 2000, *Nature*, 404, 955
- de Lapparent, V., Geller, M. J., & Huchra, J. P. 1986, *Astrophys. J. Letters*, 302, L1

- de Robertis, M. 1985, *AJ*, 90, 998
- Dell'Antonio, I. & Bernstein, G. 1997, *BTC Distortion Corrections*
- Dey, A., Graham, J. R., Ivison, R. J., Smail, I., Wright, G. S., & Liu, M. C. 1999, *ApJ*, 519, 610
- Dickinson, M. 1995, in *ASP Conf. Ser. 86: Fresh Views of Elliptical Galaxies*, ed. A. Buzzoni, A. Renzini, & A. Serrano (San Francisco: Astronomical Society of the Pacific), 286–295
- Dickinson, M. 1997, in *HST and the High Redshift Universe*, ed. N. V. Tanvir, A. Aragón-Salamanca, & W. J. V. (World Scientific), 207–215
- Disney, M. J., Boyce, P. J., Blades, J. C., Boksenberg, A., Cane, P., Deharveng, J. M., Macchetto, F., Mackay, C. D., Sparks, W. B., & Phillipps, S. 1995, *Nature*, 376, 150
- Doroshkevich, A. G., Tucker, D. L., Oemler, A. J., Kirshner, R. P., Lin, H., Shectman, S. A., Landy, S. D., & Fong, R. 1996, *Mon. Not. R. Astron. Soc.*, 283, 1281
- Dressler, A. 1980, *ApJ*, 236, 351
- . 1988, *ApJ*, 329, 519
- . 1991, *Astrophys. J. Suppl. Ser.*, 75, 241
- Dressler, A., Oemler, A. J., Butcher, H. R., & Gunn, J. E. 1994, *ApJ*, 430, 107
- Dunlop, J. S. 2001, Preprint (astro-ph/0103238). To appear in the proceedings of "QSO Hosts and their Environments"
- Efstathiou, G., Bernstein, G., Tyson, J. A., Katz, N., & Guhathakurta, P. 1991, *Astrophys. J. Letters*, 380, L47
- Efstathiou, G. & Rees, M. J. 1988, *Mon. Not. R. Astron. Soc.*, 230, 5P
- Eggen, O. J., Lynden-Bell, D., & Sandage, A. R. 1962, *ApJ*, 136, 748

- Einasto, M., Einasto, J., Tago, E., Dalton, G. B., & Andernach, H. 1994, *Mon. Not. R. Astron. Soc.*, 269, 301
- Eke, V. R., Cole, S., & Frenk, C. S. 1996, *Mon. Not. R. Astron. Soc.*, 282, 263
- Ellingson, E., Green, R. F., & Yee, H. K. C. 1991a, *ApJ*, 378, 476
- Ellingson, E., Lin, H., Yee, H. K. C., & Carlberg, R. G. 2001, *ApJ*, 547, 609
- Ellingson, E., Yee, H. K. C., & Green, R. F. 1991b, *ApJ*, 371, 49
- Ellis, R. S., Smail, I., Dressler, A., Couch, W. J., Oemler, A. J., Butcher, H., & Sharples, R. M. 1997, *ApJ*, 483, 582
- Evrard, A. E. 1991, *Mon. Not. R. Astron. Soc.*, 248, 8P
- Fairall, A. P., Palumbo, G. G. C., Vettolani, G., Kauffmann, G., Jones, A., & Baiesi-Pillastrini, G. 1990, *Mon. Not. R. Astron. Soc.*, 247, 21P
- Fan, X., Bahcall, N. A., & Cen, R. 1997, *Astrophys. J. Letters*, 490, L123
- Fisher, K. B., Davis, M., Strauss, M. A., Yahil, A., & Huchra, J. 1994, *Mon. Not. R. Astron. Soc.*, 266, 50
- Freedman, W. L., Madore, B. F., Gibson, B. K., Ferrarese, L., Kelson, D. D., Sakai, S., Mould, J. R., Kennicutt, Jr., R. C., Ford, H. C., Graham, J. A., Huchra, J. P., Hughes, S. M. G., Illingworth, G. D., Macri, L. M., & Stetson, P. B. 2000, Preprint (astro-ph/0012376) Accepted to *ApJ*
- Fujita, Y. & Nagashima, M. 1999, *ApJ*, 516, 619
- Fukugita, M., Shimasaku, K., & Ichikawa, T. 1995, *Publ. Astron. Soc. Pacific*, 107, 945
- Fukunaga, K. 1972, *Introduction to Statistical Pattern Recognition*. (Academic Press, New York)
- Geller, M. J. & Huchra, J. P. 1989, *Science*, 246, 897
- Gladders, M. D., Lopez-Cruz, O., Yee, H. K. C., & Kodama, T. 1998, *ApJ*, 501, 571

- Gladders, M. D. & Yee, H. K. C. 2000, *AJ*, 120, 2148
- Graham, J. R. & Dey, A. 1996, *ApJ*, 471, 720
- Graham, M. J. 1997, PhD thesis, University of Central Lancashire (United Kingdom).
- Graham, M. J., Clowes, R. G., & Campusano, L. E. 1995, *Mon. Not. R. Astron. Soc.*, 275, 790
- Groth, E. J. & Peebles, P. J. E. 1977, *ApJ*, 217, 385
- Haehnelt, M. G. & Rees, M. J. 1993, *Mon. Not. R. Astron. Soc.*, 263, 168
- Haines, C. P., Clowes, R. G., & Campusano, L. E. 2000a, in *IAU Symposium 201: New Cosmological Data and the Values of the Fundamental Parameters*, Vol. 201, E62
- Haines, C. P., Clowes, R. G., & Campusano, L. E. 2000b, in *ESO/ECF/STScI Workshop on Deep Fields*
- Haines, C. P., Clowes, R. G., & Campusano, L. E. 2000c, in Preprint (astro-ph/0012236): To appear in the proceedings of "The New Era of Wide-Field Astronomy", ed. R. G. Clowes, A. J. Adamson, & G. E. Bromage (San Francisco: Astronomical Society of the Pacific)
- Haines, C. P., Clowes, R. G., Campusano, L. E., & Adamson, A. J. 2001, *Mon. Not. R. Astron. Soc.*, 323, 688
- Hall, P. B. & Green, R. F. 1998, *ApJ*, 507, 558
- Hall, P. B., Green, R. F., & Cohen, M. 1998, *Astrophys. J. Suppl. Ser.*, 119, 1
- Hanany, S., Ade, P., Balbi, A., Bock, J., Borrill, J., Boscaleri, A., de Bernardis, P., Ferreira, P. G., Hristov, V. V., Jaffe, A. H., Lange, A. E., Lee, A. T., Mauskopf, P. D., Netterfield, C. B., Oh, S., Pascale, E., Rabbii, B., Richards, P. L., Smoot, G. F., Stompor, R., Winant, C. D., & Wu, J. H. P. 2000, *Astrophys. J. Letters*, 545, L5

- Hartwick, F. D. A. & Schade, D. 1990, *Ann. Rev. of Astron. and Astrophys.*, 28, 437
- Hawarden, T. G., Leggett, S. K., Letawsky, M. B., Ballantyne, D. R., & Casali, M. M. 2001, Preprint (astro-ph/0102287)
- Hawkins, M. R. S. & Veron, P. 1993, *Mon. Not. R. Astron. Soc.*, 260, 202
- . 1996, *Mon. Not. R. Astron. Soc.*, 281, 348
- Hazard, C., Mackay, M. B., & Shimmins, A. J. 1963, *Nature*, 197, 1037
- Henry, J. P. & Arnaud, K. A. 1991, *ApJ*, 372, 410
- Hook, I. M., McMahon, R. G., & Shaver, P. A. 1999, in *Looking Deep in the Southern Sky*, 211–218
- Hoyle, F., Baugh, C. M., Shanks, T., & Ratcliffe, A. 1999, *Mon. Not. R. Astron. Soc.*, 309, 659
- Hoyle, F., Outram, P. J., Shanks, T., Croom, S. M., Boyle, B. J., Loaring, N. S., Miller, L., & Smith, R. J. 2001, Preprint (astro-ph/0102163) Submitted to *Mon. Not. R. Astron. Soc.*
- Hu, E. M. & Ridgway, S. E. 1994, *AJ*, 107, 1303
- Hutchings, J. B., Crampton, D., & Johnson, A. 1995, *AJ*, 109, 73
- Hutchings, J. B., Crampton, D., & Persram, D. 1993, *AJ*, 106, 1324
- Hutchings, J. B. & Neff, S. G. 1992, *AJ*, 104, 1
- Infante, L. 1987, *Astron. Astrophys.*, 183, 177
- Jaffe, A., Ade, P. A., Balbi, R. A., Bock, J. J., Bond, J. R., Borrill, J., Boscaleri, A., Coble, K., Crill, B. P., de Bernardis, P., Farese, P., Ferreira, P. G., Ganga, K., Giacometti, M., Hanany, S., Hivon, E., Hristov, V. V., Iacoangeli, A., Lange, A. E., Lee, A. T., Martinis, L., Masi, S., Mauskopf, P. D., Melchiorri, A., Montroy, T., Netterfield, C. B., Oh, S., Pascale, E., Piacentini, F., Pogosyan, D., Prunet, S., Rabbii, B., Rao, S., Richards, P. L., Romeo, G., Ruhl, J. E., Scaramuzzi, F.,

- Sforna, D., Smoot, G. F., Stompor, R., Winant, C. D., & Wu, J. H. P. 2001, *Phys. Rev. Letters*, 86, 3475
- Kaiser, N. 1984, *Astrophys. J. Letters*, 284, L9
- Kajisawa, M. & Yamada, T. 1999, *Publ. Astron. Soc. Japan*, 51, 719
- Kajisawa, M., Yamada, T., Tanaka, I., Maihara, T., Iwamuro, F., Terada, H., Goto, M., Motohara, K., Tanabe, H., Taguchi, T., Hata, R., Iye, M., Imanishi, M., Chikada, Y., Yoshida, M., Simpson, C., Sasaki, T., Kosugi, G., Usuda, T., & Sekiguchi, K. 2000, *Publ. Astron. Soc. Japan*, 52, 61
- Kauffmann, G., Colberg, J. . M., Diaferio, A., & White, S. D. M. 1999, *Mon. Not. R. Astron. Soc.*, 307, 529
- Keable, C. J. 1987, PhD thesis, University of Edinburgh (United Kingdom).
- Kepner, J., Fan, X., Bahcall, N., Gunn, J., Lupton, R., & Xu, G. 1999, *ApJ*, 517, 78
- Kirshner, R. P., Oemler, A., Schechter, P. L., & Sheckman, S. A. 1981, *Astrophys. J. Letters*, 248, L57
- Kodama, T. & Arimoto, N. 1997, *Astron. Astrophys.*, 320, 41
- Kodama, T., Arimoto, N., Barger, A. J., & Arag'on-Salamanca, A. 1998, *Astron. Astrophys.*, 334, 99
- Kodama, T. & Bower, R. G. 2001, *Mon. Not. R. Astron. Soc.*, 321, 18
- Komberg, B. V., Kravtsov, A. V., & Lukash, V. N. 1996, *Mon. Not. R. Astron. Soc.*, 282, 713
- Komberg, B. V. & Lukash, V. N. 1994, *Mon. Not. R. Astron. Soc.*, 269, 277
- Kormendy, J. & Richstone, D. 1995, *Ann. Rev. of Astron. and Astrophys.*, 33, 581
- Kriessler, J. R. & Beers, T. C. 1997, *AJ*, 113, 80
- Kron, R. G. 1980, *Astrophys. J. Suppl. Ser.*, 43, 305

- Landolt, A. U. 1992, *AJ*, 104, 340
- Landy, S. D. & Szalay, A. S. 1993, *ApJ*, 412, 64
- Lavery, R. J. & Henry, J. P. 1988, *ApJ*, 330, 596
- Leggett, S. K., Ruiz, M. T., & Bergeron, P. 1998, *ApJ*, 497, 294
- Lidman, C. E. & Peterson, B. A. 1996, *Mon. Not. R. Astron. Soc.*, 279, 1357
- Lilly, S., Schade, D., Ellis, R., Le Fevre, O., Brinchmann, J., Tresse, L., Abraham, R., Hammer, F., Crampton, D., Colless, M., Glazebrook, K., Mallen-Ornelas, G., & Broadhurst, T. 1998, *ApJ*, 500, 75
- Lilly, S. J., Cowie, L. L., & Gardner, J. P. 1991, *ApJ*, 369, 79
- Lilly, S. J., Tresse, L., Hammer, F., Crampton, D., & Le Fevre, O. 1995, *ApJ*, 455, 108
- Lin, H., Kirshner, R. P., Sheckman, S. A., Landy, S. D., Oemler, A., Tucker, D. L., & Schechter, P. L. 1996, *ApJ*, 471, 617
- Longo, M. J. 1991, *Astrophys. J. Letters*, 372, L59
- López-Cruz, O. & Yee, H. K. C. 2000, submitted to *ApJ*
- Lubin, L. M., Postman, M., Oke, J. B., Ratnatunga, K. U., Gunn, J. E., Hoessel, J. G., & Schneider, D. P. 1998, *AJ*, 116, 584
- Maddox, S. J., Efstathiou, G., & Sutherland, W. J. 1990, *Mon. Not. R. Astron. Soc.*, 246, 433
- . 1996, *Mon. Not. R. Astron. Soc.*, 283, 1227
- Magorrian, J., Tremaine, S., Richstone, D., Bender, R., Bower, G., Dressler, A., Faber, S. M., Gebhardt, K., Green, R., Grillmair, C., Kormendy, J., & Lauer, T. 1998, *AJ*, 115, 2285
- Matthews, T. A. & Sandage, A. R. 1963, *ApJ*, 138, 30
- Mattig, W. 1958, *Astronomische Nachrichten*, 284, 109

- McCracken, H. J., Shanks, T., Metcalfe, N., Fong, R., & Campos, A. 2000, *Mon. Not. R. Astron. Soc.*, 318, 913
- McLure, R. J. & Dunlop, J. S. 2001, *Mon. Not. R. Astron. Soc.*, 321, 515
- McLure, R. J., Kukulka, M. J., Dunlop, J. S., Baum, S. A., O'Dea, C. P., & Hughes, D. H. 1999, *Mon. Not. R. Astron. Soc.*, 308, 377
- Merritt, D. & Ferrarese, L. 2001, *Mon. Not. R. Astron. Soc.*, 320, L30
- Metcalfe, N., Shanks, T., Campos, A., McCracken, H. J., & Fong, R. 2000, Preprint (astro-ph/0010153) Submitted to *Mon. Not. R. Astron. Soc.*
- Metevier, A. J., Romer, A. K., & Ulmer, M. P. 2000, *AJ*, 119, 1090
- Miller, G. E. & Scalo, J. M. 1979, *Astrophys. J. Suppl. Ser.*, 41, 513
- Moore, B., Katz, N., Lake, G., Dressler, A., & Oemler, A. 1996, *Nature*, 379, 613
- Moustakas, L. A., Davis, M., Graham, J. R., Silk, J., Peterson, B. A., & Yoshii, Y. 1997, *ApJ*, 475, 445
- Mullis, C. R., Henry, J. P., Gioia, I. M., Boehringer, H., Briel, U. G., Voges, W., & Huchra, J. P. 2001, Preprint (astro-ph/0103202) Accepted for publication by *AJ*
- Newman, P. R. 1999, PhD thesis, University of Central Lancashire (United Kingdom).
- Oemler, A. J., Dressler, A., & Butcher, H. R. 1997, *ApJ*, 474, 561
- Osmer, P. S. & Hewett, P. C. 1991, *Astrophys. J. Suppl. Ser.*, 75, 273
- Osmer, P. S. & Smith, M. G. 1980, *Astrophys. J. Suppl. Ser.*, 42, 333
- Parzen, E. 1962, *Stochastic processes (Holden Day Series in Probability and Statistics, San Francisco: Holden-Day, 1962)*
- Percival, W. & Miller, L. 1999, *Mon. Not. R. Astron. Soc.*, 309, 823

- Perlmutter, S., Aldering, G., Goldhaber, G., Knop, R. A., Nugent, P., Castro, P. G., Deustua, S., Fabbro, S., Goobar, A., Groom, D. E., Hook, I. M., Kim, A. G., Kim, M. Y., Lee, J. C., Nunes, N. J., Pain, R., Pennypacker, C. R., Quimby, R., Lidman, C., Ellis, R. S., Irwin, M., McMahon, R. G., Ruiz-Lapuente, P., Walton, N., Schaefer, B., Boyle, B. J., Filippenko, A. V., Matheson, T., Fruchter, A. S., Panagia, N., Newberg, H. J. M., Couch, W. J., & The Supernova Cosmology Project. 1999, *ApJ*, 517, 565
- Phillipps, S., Driver, S. P., Couch, W. J., & Smith, R. M. 1998, *Astrophys. J. Letters*, 498, L119
- Pisani, A. 1993, *Mon. Not. R. Astron. Soc.*, 265, 706
- . 1996, *Mon. Not. R. Astron. Soc.*, 278, 697
- Postman, M., Lauer, T. R., Szapudi, I. ., & Oegerle, W. 1998, *ApJ*, 506, 33
- Postman, M., Lubin, L. M., Gunn, J. E., Oke, J. B., Hoessel, J. G., Schneider, D. P., & Christensen, J. A. 1996, *AJ*, 111, 615
- Press, W. H. & Schechter, P. 1974, *ApJ*, 187, 425
- Rees, M. J. 1984, *Ann. Rev. of Astron. and Astrophys.*, 22, 471
- Renzini, A. & da Costa, L. N. 1997, *The Messenger*, 87, 23
- Roche, N., Eales, S. A., Hippelein, H., & Willott, C. J. 1999, *Mon. Not. R. Astron. Soc.*, 306, 538
- Roettiger, K., Burns, J. O., & Loken, C. 1996, *ApJ*, 473, 651
- Roos, N. 1981, *Astron. Astrophys.*, 104, 218
- . 1985a, *ApJ*, 294, 486
- . 1985b, *ApJ*, 294, 479
- Rosati, P., della Ceca, R., Norman, C., & Giacconi, R. 1998, *Astrophys. J. Letters*, 492, L21

- Rosati, P., Stanford, S. A., Eisenhardt, P. R., Elston, R., Spinrad, H., Stern, D., & Dey, A. 1999, *AJ*, 118, 76
- Sánchez, S. F. & González-Serrano, J. I. 1999, *Astron. Astrophys.*, 352, 383
- Sandage, A. 1972, *ApJ*, 176, 21
- Scaramella, R., Baiesi-Pillastrini, G., Chincarini, G., Vettolani, G., & Zamorani, G. 1989, *Nature*, 338, 562
- Schmidt, M. 1963, *Nature*, 197, 1040
- . 1968, *ApJ*, 151, 393
- Schmidt, M., Schneider, D. P., & Gunn, J. E. 1995, *AJ*, 110, 68
- Shaver, P. A., Wall, J. V., Kellermann, K. I., Jackson, C. A., & Hawkins, M. R. S. 1996, *Nature*, 384, 439
- Shectman, S. A., Landy, S. D., Oemler, A., Tucker, D. L., Lin, H., Kirshner, R. P., & Schechter, P. L. 1996, *ApJ*, 470, 172
- Silk, J. & Weinberg, D. 1991, *Nature*, 350, 272
- Silverman, B. W. 1986, *Density Estimation for Statistics and Data Analysis* (Chapman & Hall, London)
- Smail, I., Hogg, D. W., Yan, L., & Cohen, J. G. 1995, *Astrophys. J. Letters*, 449, L105
- Smith, E. P., Heckman, T. M., Bothun, G. D., Romanishin, W., & Balick, B. 1986, *ApJ*, 306, 64
- Smith, R. J., Boyle, B. J., & Maddox, S. J. 1995, *Mon. Not. R. Astron. Soc.*, 277, 270
- . 2000, *Mon. Not. R. Astron. Soc.*, 313, 252
- Songaila, A., Cowie, L. L., Hu, E. M., & Gardner, J. P. 1994, *Astrophys. J. Suppl. Ser.*, 94, 461

- Stanford, S. A., Eisenhardt, P. R., & Dickinson, M. 1998, *ApJ*, 492, 461
- Stanford, S. A., Elston, R., Eisenhardt, P. R., Spinrad, H., Stern, D., & Dey, A. 1997, *AJ*, 114, 2232
- Stanford, S. A., Holden, B., Rosati, P., Tozzi, P., Borgani, S., Eisenhardt, P. R., & Spinrad, H. 2000, Preprint (astro-ph/0012250). Accepted by *ApJ*
- Steidel, C. C. & Sargent, W. L. W. 1992, *Astrophys. J. Suppl. Ser.*, 80, 1
- Stockton, A. 1982, *ApJ*, 257, 33
- Tanaka, I., Yamada, T., Aragón-Salamanca, A., Kodama, T., Miyaji, T., Ohta, K., & Arimoto, N. 2000, *ApJ*, 528, 123
- Tanaka, I., Yamada, T., Turner, E. L., & Suto, Y. 2001, *ApJ*, 547, 521
- Tucker, D. L., Oemler, A., Kirshner, R. P., Lin, H., Shectman, S. A., Landy, S. D., Schechter, P. L., Muller, V., Gottlober, S., & Einasto, J. 1997, *Mon. Not. R. Astron. Soc.*, 285, L5
- Tully, R. B. 1987, *ApJ*, 323, 1
- Tully, R. B., Scaramella, R., Vettolani, G., & Zamorani, G. 1992, *ApJ*, 388, 9
- Veron-Cetty, M. . & Veron, P. 1987, A Catalogue of quasars and active nuclei (ESO Scientific Report, Garching: European Southern Observatory (ESO), 1987, 3rd ed.)
- . 1991, A Catalogue of quasars and active nuclei (ESO Scientific Report, Garching: European Southern Observatory (ESO), 1991, 5th ed.)
- Viana, P. T. P. & Liddle, A. R. 1996, *Mon. Not. R. Astron. Soc.*, 281, 323
- Warren, S. J., Hewett, P. C., & Osmer, P. S. 1994, *ApJ*, 421, 412
- Webster, A. 1982, *Mon. Not. R. Astron. Soc.*, 199, 683
- White, S. D. M., Efstathiou, G., & Frenk, C. S. 1993, *Mon. Not. R. Astron. Soc.*, 262, 1023

- Williams, R. E., Blacker, B., Dickinson, M., Dixon, W. V. D., Ferguson, H. C., Fruchter, A. S., Giavalisco, M., Gilliland, R. L., Heyer, I., Katsanis, R., Levay, Z., Lucas, R. A., McElroy, D. B., Petro, L., Postman, M., Adorf, H., & Hook, R. 1996, *AJ*, 112, 1335
- Williger, G. M., Campusano, L. E., & Clowes, R. G. 2000, in *American Astronomical Society Meeting*, Vol. 197, 0303
- Wittman, D. M., Dell'Antonio, I., Tyson, J. A., Bernstein, G., Fischer, P., & Smith, D. 2000a, Preprint (astro-ph/0009362) - to appear in *Constructing the Universe with Clusters of Galaxies*, edited by F. Durret & D. Gerbal
- Wittman, D. M., Tyson, J. A., Bernstein, G. M., Lee, R. W., dell'Antonio, I. P., Fischer, P., Smith, D. R., & Blouke, M. M. 1998, *Proc.SPIE*, 3355, 626
- Wittman, D. M., Tyson, J. A., Kirkman, D., Dell'Antonio, I., & Bernstein, G. 2000b, *Nature*, 405, 143
- Wold, M., Lacy, M., Lilje, P. B., & Serjeant, S. 2000, *Mon. Not. R. Astron. Soc.*, 316, 267
- . 2001, *Mon. Not. R. Astron. Soc.*, 323, 231
- Wolf, C., Meisenheimer, K., Röser, H. ., Beckwith, S. V. W., Fockenbrock, R., Hippelein, H., von Kuhlmann, B., Phleps, S., & Thommes, E. 1999, *Astron. Astrophys.*, 343, 399
- Woods, D. & Fahlman, G. G. 1997, *ApJ*, 490, 11
- Yamada, T., Tanaka, I., Aragon-Salamanca, A., Kodama, T., Ohta, K., & Arimoto, N. 1997, *Astrophys. J. Letters*, 487, L125
- Yee, H. K. C. 1998, Preprint (astro-ph/9809347) A review article to appear in the proceedings of the Xth Recontres de Blois: Birth of Galaxies; Blois, France, July 1998
- Yee, H. K. C. & Green, R. F. 1984, *ApJ*, 280, 79
- . 1987, *ApJ*, 319, 28

The galaxy environment of a quasar at $z = 1.226$: a possible cluster merger

C. P. Haines,^{1,2*} † R. G. Clowes,^{1*} L. E. Campusano² and A. J. Adamson³

¹Centre for Astrophysics, University of Central Lancashire, Preston PR1 2HE

²Observatorio Astronómico Cerro Calán, Departamento de Astronomía, Universidad de Chile, Casilla 36-D, Santiago, Chile

³UKIRT, Joint Astronomy Centre, 660 North A'ohōkū Place, University Park, Hilo, HI 96720, USA

Accepted 2000 November 29. Received 2000 November 29; in original form 1999 October 7

ABSTRACT

We have conducted ultra-deep optical and deep near-infrared observations of a field around the $z = 1.226$ radio-quiet quasar 104420.8 + 055739 from the Clowes–Campusano LQG of 18 quasars at $z \sim 1.3$, in search of associated galaxy clustering. Galaxies at these redshifts are distinguished by their extremely red colours, with $I - K > 3.75$, and we find a factor ~ 11 overdensity of such galaxies in a 2.25×2.25 arcmin² field centred on the quasar. In particular, we find 15–18 galaxies that have colours consistent with being a population of passively evolving massive ellipticals at the quasar redshift. They form ‘fingers’ in the $V - K/K$, $I - K/K$ colour–magnitude plots at $V - K \approx 6.9$, $I - K \approx 4.3$ comparable to the red sequences observed in other $z \approx 1.2$ clusters. We find suggestive evidence for substructure among the red sequence galaxies in the K image, in the form of two compact groups, 40 arcsec to the north, and 60 arcsec to the south-east of the quasar. An examination of the wider optical images indicates that this substructure is significant, and that the clustering extends to form a large-scale structure $2\text{--}3 h^{-1}$ Mpc across. We find evidence for a high (≈ 50 per cent) fraction of blue galaxies in this system, in the form of 15–20 ‘red outlier’ galaxies with $I - K > 3.75$ and $V - I < 2.00$, which we suggest are dusty, star-forming galaxies at the quasar redshift. Within 30 arcsec of the quasar we find a concentration of blue ($V - I < 1$) galaxies in a band that bisects the two groups of red sequence galaxies. This band of blue galaxies is presumed to correspond to a region of enhanced star formation. We explain this distribution of galaxies as the early stages of a cluster merger which has triggered both the star formation and the quasar.

Key words: galaxies: clusters: general – galaxies: evolution – quasars: general – large-scale structure of Universe.

1 INTRODUCTION

Quasars are sparsely distributed across the Universe, with the majority appearing to be unrelated to one another. However quasar clustering has been observed on large scales in the form of large quasar groups (LQGs) (e.g. Webster 1982; Crampton, Cowley & Hartwick 1987, 1989; Clowes & Campusano 1991, 1994; Graham, Clowes & Campusano 1995), where 4–25 quasars form structures $100\text{--}200 h^{-1}$ Mpc across. They are thus comparable in size to the largest structures seen at the present epoch, such as the ‘Great Wall’ of galaxies, but are seen at an earlier epoch with $0.4 \lesssim z \lesssim 2$. It has been suggested (Komberg & Lukash 1994) that LQGs represent the progenitors of these local large-scale structures, not only because of their comparable sizes, but also because of a claim that

the comoving number densities of LQGs and local superclusters are comparable (Komberg, Kravtsov & Lukash 1996).

Observations of the galaxy environments of individual quasars lends credence to the hypothesis that LQGs trace superclusters. Quasars at $z \sim 0.5$ are known to favour young, low-to-moderately rich clusters, with richness increasing with both redshift and radio-loudness (Ellingson, Yee & Green 1991). At higher redshifts, a survey of 31 $1 \lesssim z \lesssim 2$ radio-loud quasars (Hall & Green 1998) indicates that they are on average found in moderately rich ($R_{\text{Abell}} \approx 1.5$) clusters. Optical and narrow-band (O II) observations of fields centred on 11 $z \sim 1.1$ quasars from the Crampton et al. (1989) LQG show an excess of galaxies around all but one of the quasars (Hutchings, Crampton & Johnson 1995, hereafter HCJ; Hutchings, Crampton & Persram 1993, hereafter HCP). In particular they find excesses of blue and emission-line galaxies around several of the quasars, indicating regions of significant star formation, a phenomenon probably related to the fact that both quasars and star formation require the disruption of the galaxy,

* Visiting astronomers, Cerro Tololo Inter-American Observatory, National Optical Astronomy Observatories.

† E-mail: cphaines@uclan.ac.uk

causing a collapse of significant amounts of gas. They find no evidence for a coherent structure connecting the quasars, but star formation is likely to be localized, rather than occurring simultaneously across large scales as a cluster mass halo collapses or during a cluster merger.

To determine whether or not LQGs trace superclusters requires observations capable of identifying the quiescent galaxies that mark out any associated supercluster, in particular the massive ellipticals which dominate cluster cores. These are both the most luminous and the reddest galaxies in nearby clusters, and form a homogeneous population with very tight linear colour–magnitude (C–M) relations known as *red sequences* (Bower, Lucey & Ellis 1992), indicative of old (12–13 Gyr) stellar populations. This red sequence has been followed in the optical for clusters out to $z \sim 0.9$ (Aragón-Salamanca et al. 1993; Stanford, Eisenhardt & Dickinson 1998) and is consistent with the passive evolution of galaxies that formed in a monolithic collapse at $z \geq 3$ (Eggen, Lynden-Bell & Sandage 1962). At $z \geq 1$ these galaxies should be characterized by extremely red optical–near-infrared (NIR) colours ($I - K \approx 4$) as the 4000-Å break is redshifted into the *I*-band. Good contrasts of $z \geq 1$ clusters over the background are possible as field $I - K \approx 4$ galaxies appear rare: the Hawaii *K*-band survey finds no galaxies with $I - K > 4$ for $K < 18$ over an area of 86.7 arcmin² (Cowie et al. 1994; Songaila et al. 1994).

Several $z \approx 1.2$ clusters have been found by searching for galaxies with $I - K \approx 4$ in fields around both targeted high-redshift AGN (Dickinson 1995, hereafter D95; Yamada et al. 1997; Tanaka et al. 2000, hereafter T00) and regions of extended X-ray emission (Stanford et al. 1997, hereafter S97; Rosati et al. 1999, hereafter R99). These galaxies are found to have the optical–NIR colours ($I - K \approx 4, R - K \approx 6$) expected for passively evolving galaxies which are 2–3 Gyr old, in good agreement with the monolithic collapse model predictions. D95

also finds a red sequence for the $z = 1.2$ cluster around the radio galaxy 3C 324 with $R - K \approx 5.9$ and a rms scatter of only 0.07 mag, suggesting that these galaxies formed within 300 Myr of one another.

In this study we aim to establish the galaxy environment of LQGs in a manner that is unbiased with respect to galaxy type. We have targeted a 30×30 arcmin² field containing three quasars from the $z \approx 1.3$ Clowes & Campusano LQG (Fig. 1) for ultra-deep optical observations complemented with deep-NIR observations of selected subfields, capable of detecting the passively evolving galaxies that should mark out any coherent large-scale structures. We present here the first results from this study, using ultra-deep *V* and *I* images and a *K* image centred on the $z = 1.226$ radio-quiet (not detected at the 1-mJy level by the FIRST VLA 20-cm survey) quasar 104420.8 + 055739. We have detected clustering of galaxies with the extremely red colours expected of quiescent ellipticals at the quasar redshift. Throughout the paper we adopt $q_0 = 0.5$ and $H_0 = 100 \text{ h km s}^{-1} \text{ Mpc}^{-1}$.

2 OBSERVATIONS

The 30×30 arcmin² field was observed through *V* and *I* filters using the Big Throughput Camera (BTC) on the 4-m Blanco telescope at the Cerro Tololo Inter-American Observatory on 1998 April 21/22 and 22/23. The BTC is made up of four 2048 × 2048 CCDs that have pixels of size 0.43 arcsec, giving a field of view for each CCD of 14.7×14.7 arcmin². The CCDs are arranged in a two-by-two grid and are separated by gaps of 5.6 arcmin. To obtain a contiguous image it was necessary to shift the telescope between exposures. 16 exposures arranged in a four-by-four grid, with each pointing offset by the width of the gap between adjacent pointings, were found to give a contiguous and almost uniform

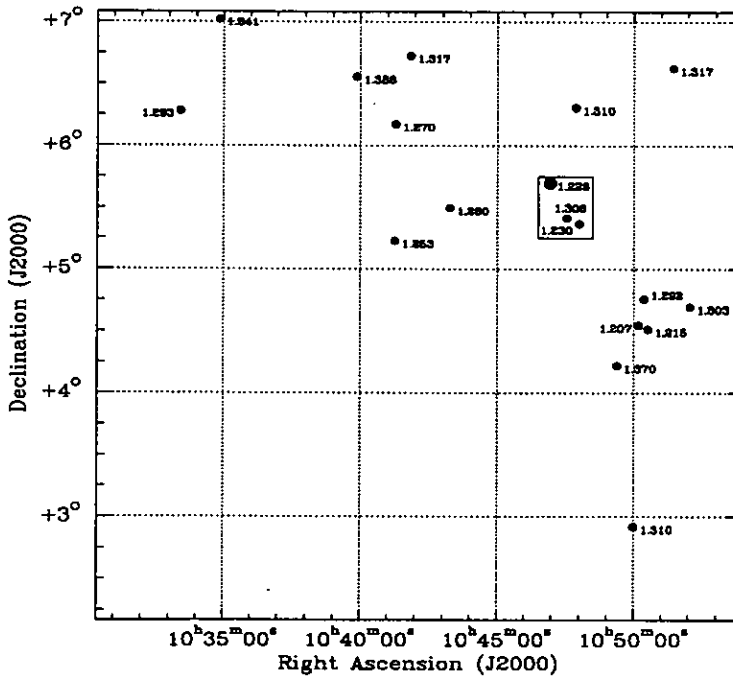


Figure 1. The Clowes–Campusano LQG with each quasar labelled by its redshift. The 30×30 arcmin² region targeted for BTC imaging is indicated by the box, and the quasar for which we have *K* imaging is circled. The boundaries of the plot match the boundaries of the AQD survey of ESO/SERC field 927 (Clowes & Campusano 1991, 1994; Clowes, Campusano & Graham 1999). Note that this plot and Figs 5, 6 and 7 have east to the right.

coverage over a 30×30 arcmin² field, with ~ 90 per cent of the field covered by exactly nine of the 16 exposures. The images had large relative offsets, and so that they could be registered, the effects of the distortions (produced by the camera optics) were removed using models based on observations of astrometric fields. These distortions are significant because of the wide field of the camera, and were of the order of 60 pixels at the corners of the CCD array. After the removal of distortions, the rms errors of registration between images were typically ~ 0.05 arcsec. Details of the observing and reduction procedures for the whole BTC image will be described elsewhere. Most of the reduction processes were performed in the usual way using IRAF tools.

K-imaging was obtained for a 2.25×2.25 arcmin² field centred on the radio-quiet quasar at $10^{\text{h}}46^{\text{m}}56^{\text{s}}.70$, $+05^{\circ}41'50''.5$ (J2000) using the UKIRT Fast-Track Imager (UFTI) camera on the 3.8-m United Kingdom Infrared Telescope (UKIRT) in 1999 March. This has a field of 1.5×1.5 arcmin² with a pixel size of 0.09 arcsec. The field around this quasar was observed in preference to the other two because of its more populous immediate environment (within 5 arcsec), suggesting that it was the most likely to be in an interacting system. No cluster-scale environmental factors were considered, and so, for the overall clustering statistics, the selection can reasonably be regarded as random.

A standard nine-point jitter pattern was used, with each 1-min exposure offset by 20 arcsec relative to adjacent exposures. A dark frame was obtained between each set of jitters, and subtracted before self-flattening the set. Although the 20-arcsec wide strips at the edges of the image have only one third of the exposure time, they have been retained with each source checked visually, and separate magnitude limits determined.

The combined *K* image was convolved to the same seeing as the *I* image, so that galaxy colours could be determined using a single fixed aperture, and then registered with the optical images. Photometric calibration of the *V* and *I* images on to the Landolt system was obtained using Landolt standard stars at varying airmasses, and a UKIRT faint standard was used for the *K* image. Object detection was carried out using SEXTRACTOR (Bertin & Arnouts 1996) for objects with $\approx (\text{FWHM})^2$ contiguous pixels over the 1σ detection threshold. Completeness levels for each filter (for the region covered by the *K* image rather than the whole BTC field) are given in Table 1. They were determined by dimming a bright galaxy to a specified magnitude and adding 100 copies to the image at random positions, and then processing through SEXTRACTOR in the usual way. The 50 and 90 per cent completeness levels are estimated as the magnitude for which 50 and 90 galaxies out of the 100 are recovered. The total magnitudes were taken to be the MAG_BEST output from SEXTRACTOR, and colours were determined using fixed apertures of diameter 2.5 arcsec.

Table 1. Photometric properties of the images, including exposure times and completeness levels. The *V*, *I* figures are for the area covered by the *K* image, rather than for the whole BTC field.

Filter Band (subfield)	Exposure time (sec)	Seeing FWHM (arcsec)	Completeness limits (mag)	
			90 per cent	50 per cent
<i>K</i> (centre)	3780	0.60	19.25	19.95
<i>K</i> (edge)	1260	0.60	18.82	19.53
<i>I</i>	16200	1.15	24.68	25.39
<i>V</i>	8100	1.30	25.40	25.95

Star-galaxy separation of each source was performed using a combination of morphology (using the stellarity classifier in SEXTRACTOR) and a comparison of *V* - *I* and *I* - *K* colours with model star and galaxy tracks. The stellarity classifier uses a neural net trained with a set of artificial stars and galaxies to produce a 'probability' that a source is stellar. Stellarities of sources in both *V* and *I* images were obtained and the weighted mean used for classification. Most of the sources that were morphologically classified as stars also had colours that lay near the model star tracks, but a number of sources had the colours of blue galaxies and were reclassified as such.

3 RESULTS

3.1 Galaxy counts

In total, 100 visually verified sources were detected in the *K* image, of which 95 had counterparts in the *I* image within 1 arcsec, and 79 had counterparts in both *V* and *I* images. 14 of the 79 sources were classed as stars, leaving 86 galaxies in the 2.25×2.25 arcmin² field. Of the five sources detected only in the *K* image, two are the close companion galaxies of the quasar which could not be separated from the quasar point-spread function by SEXTRACTOR in the *V* and *I* images, and the other three must have $I - K > 3.75$ to be undetected in *I*.

Table 2 shows the comparison of galaxy counts seen in the *K* image with those expected from a field region (Songaila et al. 1994). Excesses of galaxies are seen in all magnitude bins, even in the last bin where incompleteness should reduce any excess. If we limit ourselves to $K < 19$ (an L^* galaxy at $z = 1.226$ has $K \approx 19.05$) where we can be reasonably confident of both completeness and photometry, then a 3.5σ excess is observed [accounting for the effect on galaxy statistics of the two-point angular correlation function, $\omega(\theta) = 1.13\theta(\text{arcsec})^{-0.8}$ (Roche et al. 1999), for $K < 19$ galaxies], with 40 galaxies observed, whereas only 19 would be expected. By considering only those galaxies with $I - K > 3.75$, the excess is much more significant, with 23 galaxies observed instead of the expected two. Even though the clustering amplitude of extremely red galaxies is a factor of 10 greater than that of *K*-selected field galaxies (Daddi et al. 2000), we still observe a 9σ excess. It is clear that the total excess is due entirely to these extremely red galaxies, indicating a likely cluster at $z \gtrsim 0.8$, and we consider all $I - K > 3.75$ galaxies to be cluster members.

Table 2. A comparison of total and extremely red ($I - K > 3.75$) galaxy counts in the *K* image, binned by magnitude, and those expected for the same-sized region in the field (Songaila et al. 1994). The numbers include those observed only in the *K* image, with the two companions to the quasar assumed to have $I - K < 3.75$, and the other three sources to have $I - K > 3.75$.

Magnitude	Observed		Expected	
	Total	$I - K > 3.75$	Total	$I - K > 3.75$
$15 < K \leq 16$	1	1	0.533	0
$16 < K \leq 17$	3	1	2.186	0
$17 < K \leq 18$	13	5	4.204	0.050
$18 < K \leq 19$	23	16	11.36	1.939
$19 < K \leq 20$	39	23	21.81	1.896
Total	79	46	41	4

3.2 Galaxy colours and photometric redshift estimates

In Fig. 2 we show the $I - K$ versus $V - I$ colour-colour diagram for galaxies in the K image. To estimate the photometric redshifts of each galaxy from its VIK colours, and to produce the model colour tracks of Fig. 2, we have used the HYPERZ code of Bolzonella, Miralles & Pelló (2000), which uses the Bruzual & Charlot evolutionary code (GISSEL98, Bruzual & Charlot 1993) to build synthetic template galaxies. It has stellar populations that have eight star formation histories, roughly matching the observed properties of local galaxies from E to Im type: an instantaneous burst; six exponentially decaying star formation rates (SFRs) with time-scales τ from 1 to 30 Gyr; and a constant star-forming rate. The models assume solar metallicity and a Miller & Scalo (1979) initial mass function (IMF), with internal reddening considered through the Calzetti et al. (2000) model with A_V allowed to vary between 0 and 1 mag. The HYPERZ software then produces a photometric redshift probability distribution through a chi-squared minimization process, allowing for all possible galaxy ages, star formation histories and A_V s. This approach of determining a range of compatible redshifts, rather than a single best-fitting redshift for a galaxy, is more appropriate in this case given the limited colour information available.

The model curves of Fig. 2 correspond to stellar populations that were formed in an instantaneous burst at $z=4.5$ (solid line), and stellar populations with exponentially decaying SFRs with time-scales (τ) of 1 Gyr (dashed line) and 5 Gyr (dot-dashed line), and are thought to approximate the colour evolution of massive elliptical and disc-dominated galaxies. The galaxy ages for each model are calculated for an $h = 0.5$, $q_0 = 0.5$ universe. The $I - K$

colours of the model tracks increase monotonically with redshift to $z \approx 1.3$, and it is clear that $I - K \approx 4$ is a good indicator of galaxies at $z \geq 1$ with predominantly old stellar populations. The divergence of the disc and burst model tracks at high redshifts is a clear indication of the effect of recent star formation on the $V - I$ colour in particular.

In Figs 3(a)–(d) we show the redshift probability distributions, $P(z)$, for four galaxies which are compatible with being at the quasar redshift, incompatible with being at $z \lesssim 0.8$, and which represent the differing classes of galaxies discussed in the text below.

3.2.1 Red sequence galaxies

There are 15–18 galaxies (hereafter labelled ‘red’) whose extremely red colours ($I - K > 3.75$, $V - I > 2.00$) are consistent with being passively evolving galaxies at $z \approx 1.2$ (indicated by squares in Fig. 2). These red galaxies can be seen (as squares again) in the $V - K$ and $I - K$ against $K C-M$ diagrams of Fig. 4 to form ‘fingers’ at $V - K \approx 6.9$ and $I - K \approx 4.3$, comparable in form to the red sequences observed in lower redshift clusters, and in colour to other clusters at the same redshift. The $z \approx 1.2$ clusters of R99, S97 and D95 are all observed to have red sequences at $R - K \approx 5.9$, each with ≥ 4 members spectroscopically confirmed as being at the cluster redshift. The red sequence galaxy colours can be compared directly for the R99 cluster where $I - K$ colour data exist, and the four spectroscopically confirmed red sequence members all have $4 < I - K < 4.4$, in good agreement with ours. The colours of these red sequence galaxies are well-fitted by the passively evolving

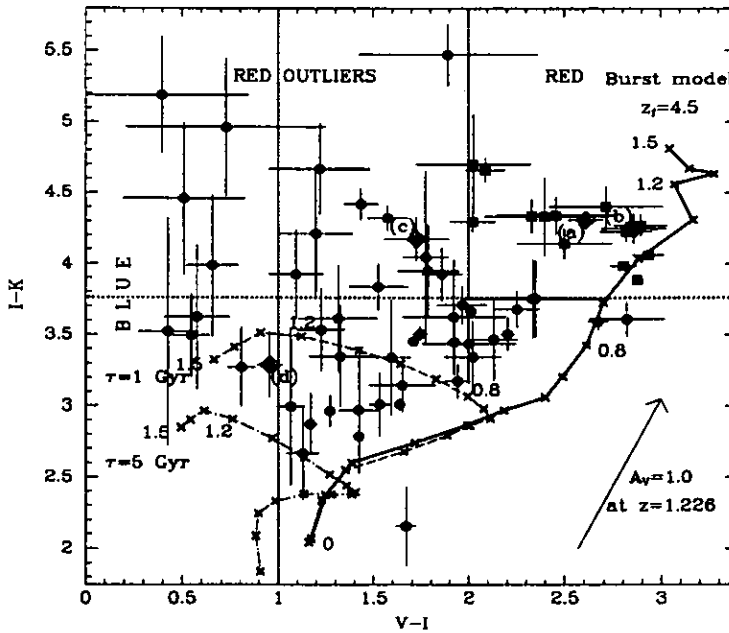


Figure 2. $I - K$ against $V - I$ colour-colour diagram of all galaxies in the K image. Those galaxies whose colours are well described by the burst model at $z = 1.2$ are shown as filled squares. The four galaxies whose redshift probability distributions are shown in Fig. 3 are indicated by superimposed, labelled diamonds. For comparison, model tracks are shown for an instantaneous burst at $z_{\text{formation}} = 4.5$ (solid line), and exponentially decaying star formation rate models with time scales of 1 Gyr (dashed line) and 5 Gyr (dot-dashed line). Each track shows the colour evolution from $z = 1.5$ to $z = 0$ with crosses at 0.1 redshift intervals. The effect of internal extinction at $z = 1.226$ is shown as an arrow in the bottom-right corner. The dotted lines indicate the selection criteria used within this paper: the cluster candidates are selected to have $I - K > 3.75$; with further separations into red ($V - I > 2.00$) and red outlier ($V - I < 2.00$) galaxies; blue galaxies are identified by $V - I < 1.00$.

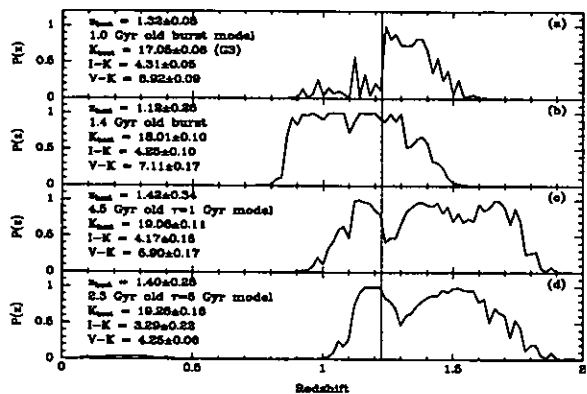


Figure 3. Redshift probability distributions for four galaxies in the K image based on their V/K colours. The best fitting model is described by its redshift z_{best} and star formation history, which is either an instantaneous burst or an exponentially decaying star formation rate with time-scale τ . The vertical dashed line indicates the redshift of the quasar. Distributions (a) and (b) correspond to two galaxies which help make up the observed red sequence in both $V - K/K$ and $I - K/K$ plots. Galaxy (c) is a ‘red outlier’ with a similarly red $I - K$ colour to (a) and (b), but a much bluer $V - I$ colour, indicating more recent star formation. Galaxy (d) is one of the galaxies from the blue ‘band’ and, due to its red $I - K$ colour, is best fitted by a $z \approx 1$ disc galaxy. Note that the central dips in the probability distributions (c) and (d) are only artefacts due to the limited number of star formation regimes available.

monolithic collapse models of elliptical galaxies, and both their spectra and morphologies are similar to present-day ellipticals (Dickinson 1997). Red sequence galaxies are usually the most luminous cluster members, the massive ellipticals, and this also appears to be the case here, with the 10 brightest galaxies with $I - K > 3.75$ also having $V - K \approx 6.9$. Given that these are both the reddest and most luminous galaxies, these should provide the tightest redshift estimates, and Fig. 3(a) shows that the third brightest of these galaxies (G3) has $1.2 \lesssim z \lesssim 1.4$.

The mean $I - K$ colour of the red galaxies is 4.25, with an intrinsic dispersion of 0.15 mag, and is best fitted by a 2-Gyr-old burst with a corresponding age dispersion of 400 Myr. The colour distribution seen in the red sequence is comparable to that seen in the cluster of T00 (0.22 mag in $R - K$), but is larger than that seen in the $z \approx 1.2$ 3C 324 cluster (D95) which has an rms scatter of 0.07 mag in $R - K$, suggesting that our cluster is less dynamically evolved than that of 3C 324.

3.2.2 Red outlier galaxies

Only half of the excess of $I - K > 3.75$ galaxies is accounted for by the red sequence members, and we find comparable numbers (15–20) of $K \approx 19$ galaxies (hereafter labelled ‘red outliers’) with both $I - K > 3.75$ and $V - I < 2.00$, which appear to fit neither the passively evolving nor exponentially decaying star formation galaxy models (Fig. 2).

Galaxies with similar colours and magnitudes have been observed in other $z \approx 1.2$ clusters (e.g. Kajisawa & Yamada 1999; T00; Kajisawa et al. 2000). They have also been observed at $20 \lesssim K \lesssim 22$ in deep optical–NIR surveys (e.g. Moustakas et al. 1997), and appear common (several per square arcminute) at these fainter magnitudes. Much of the discussion (see e.g. Moustakas et al. 1997) of these objects has been limited to speculation because of the lack of spectroscopic observations, but a widely held view is

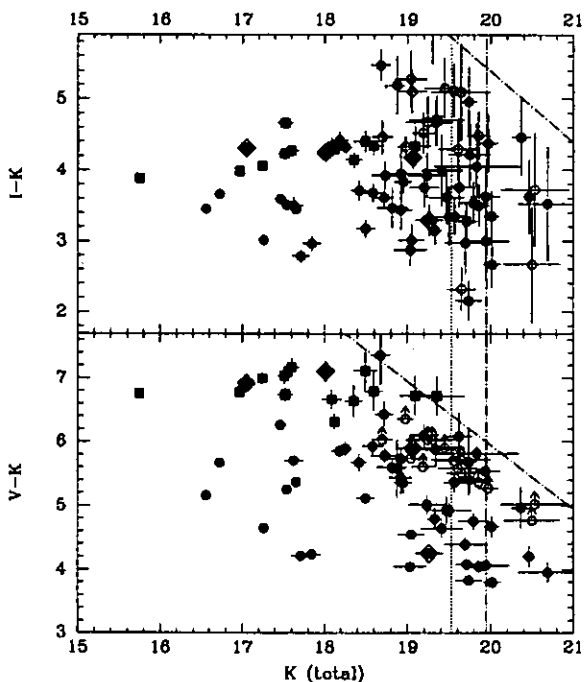


Figure 4. Colour–magnitude diagrams of galaxies in the K image. The solid symbols represent those galaxies detected in all three bands. The empty symbols represent those galaxies detected in I and K only. Galaxies whose colours are well described by the burst model at $z \approx 1.2$ have square symbols. The four galaxies whose redshift probability distributions are shown in Fig. 3 are indicated by diamonds. The dash-dotted lines indicate the 50 per cent completeness levels for each filter in the centre of the image, with the dotted line indicating the completeness level in K for the edge of the image.

that they are probably high-redshift objects ($1 \lesssim z \lesssim 2$) which are undergoing significant star formation and whose extremely red $I - K$ colours are caused by a combination of dust and dominant old stellar populations. There is also some spectroscopic evidence that some $z \approx 1.2$ cluster ellipticals are undergoing star formation, such as O II emission lines seen in object No. 4 of R99 and object No. 237 of S97, both of which appear bluer in optical colours than the other red sequence galaxies in the clusters. Some extreme members of this population have been observed with $I - K > 6$ (e.g. Hu & Ridgway 1994), and one has since been spectroscopically confirmed as an ultraluminous infrared galaxy at $z = 1.44$ with significant ongoing star formation that is heavily obscured by dust (Graham & Dey 1996; Dey et al. 1999). Given that both star formation and dust are likely to have affected the colours of these ‘red outliers’ significantly, it is not possible to constrain the galaxy redshifts beyond $z \approx 1$ (Fig. 3c), but their prevalence in the vicinity of other high-redshift clusters, and the relative rarity of field $I - K > 3.75$ galaxies, suggests that many are associated with the cluster.

3.3 Spatial distribution of galaxies

The spatial distribution of galaxies detected in the K image is shown in Fig. 5, with solid symbols used to differentiate the red galaxies from the remainder.

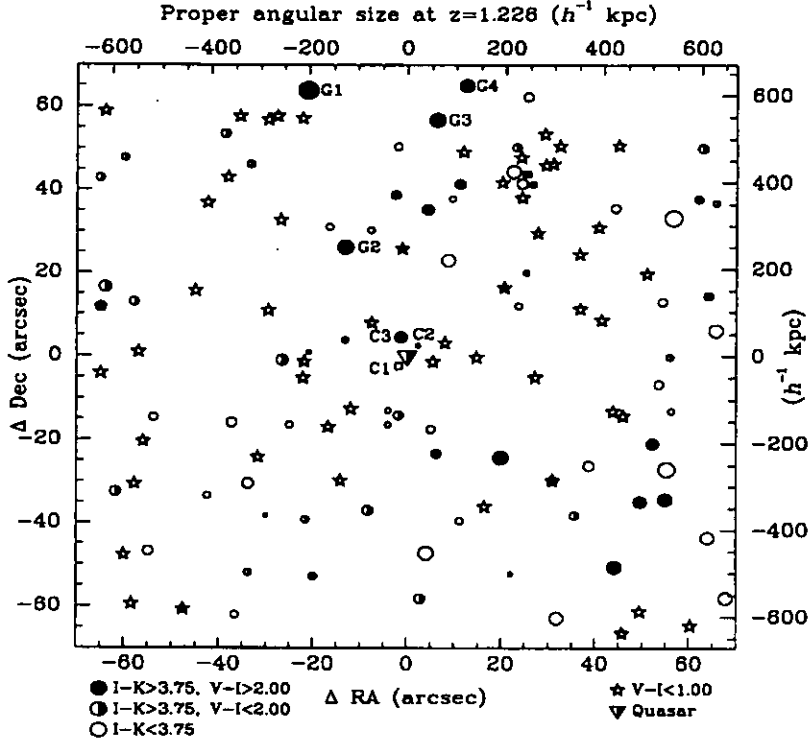


Figure 5. Spatial distribution of galaxies in the field of quasar 104420.8+055739. The different symbols indicate the galaxies' colour, with circles (squares) indicating those galaxies detected (not detected) in I . Solid symbols indicate the red ($I - K > 3.75$, $V - I > 2.00$) galaxies which could be early-type galaxies at the quasar redshift. Half-filled symbols indicate the red outlier ($I - K > 3.75$, $V - I < 2.00$) galaxies which are likely to be high-redshift galaxies with some recent star formation. The star symbols indicate the blue ($V - I < 1.00$) galaxies which are probably undergoing significant star formation. The sizes of the symbols (except stars) indicate the K_{total} magnitude.

3.3.1 Red sequence galaxies

The red galaxies appear to be distributed across the K image $1.29 h^{-1} \text{Mpc}$ at $z = 1.226$ with no concentration towards the quasar. However, the 10 most luminous red galaxies (which we indicated earlier are probably massive ellipticals at the quasar redshift) are concentrated in two compact groups, one towards the top-centre of the image (along with a number of fainter members), and the other in the south-eastern corner. This suggests that the galaxy excesses and red sequences could be due to two clusters at similar redshifts. Assuming that the brightest of the red galaxies, G1, is a quiescent galaxy at the quasar redshift, then it has $L \approx 14L_{\star}^{\dagger}$, and is more luminous in K , by almost a magnitude, than any of the galaxies from other $z \sim 1.2$ clusters (D95; S97; R99). It is also a radio emitter, being the only source in the K image detected by the VLA FIRST 20-cm survey, having an integrated flux of $2.63 \pm 0.15 \text{ mJy}$, which suggests that it has an active nucleus. It is common for the brightest cluster galaxy (which is what we assume this is) also to be a radio source, although it is not as spectacular an example as 3C 324, which is at a similar redshift, but is 1000 times more luminous in the radio. If this galaxy is comparable to 3C 324 then it may also display narrow-line emission, in particular O II and Mg II, and this may explain why it appears bluer than the other red sequence galaxies, as the emission lines boost the optical flux. The brightest cluster galaxy is usually located near the cluster centre, and it appears to be the case here too if Figs 5 and 7 (later) are compared.

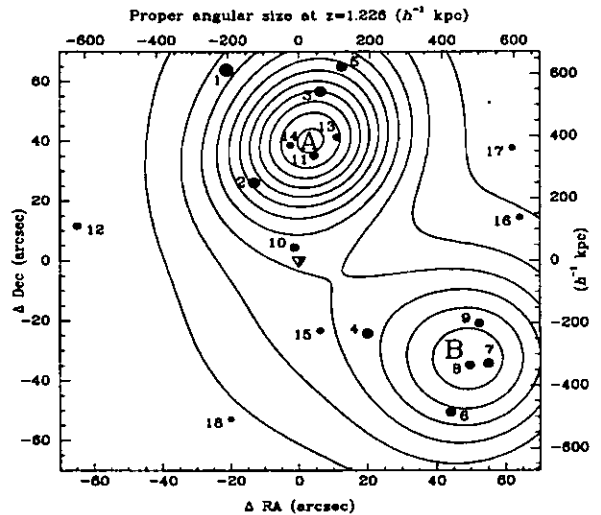


Figure 6. Estimated density distribution of the red galaxies in the field of quasar 104420.8+055739. The first contour corresponds to a density of one galaxy per square arcminute, and the separation of successive contours is also one galaxy per square arcminute. The quasar and red galaxies are marked as in Fig. 5, and the labels correspond to the galaxy IDs of Table 3, which are numbered in order of increasing K -magnitude.

Table 3. Results from the cluster membership analysis of the red galaxies. Column A/B indicates whether a galaxy was assigned to cluster A or B, and the last three columns show the probabilities that a galaxy is isolated or a member of cluster A or B.

ID	K_{tot}	A/B	$P(i \in 0)$	$P(i \in A)$	$P(i \in B)$
1	15.75	A	0.0827	0.9075	0.0098
2	16.97	A	0.0324	0.9259	0.0417
3	17.05	A	0.0259	0.9626	0.0115
4	17.24	B	0.0562	0.1172	0.8266
5	17.52	A	0.0391	0.9468	0.0142
6	17.52	B	0.0438	0.0128	0.9434
7	17.60	B	0.0319	0.0159	0.9522
8	18.01	B	0.0306	0.0164	0.9529
9	18.09	B	0.0357	0.0298	0.9345
10	18.12	A	0.0583	0.6754	0.2663
11	18.35	A	0.0188	0.9582	0.0230
12	18.50	A	0.6440	0.2716	0.0844
13	18.59	A	0.0200	0.9595	0.0205
14	18.95	A	0.0191	0.9641	0.0167
15	18.97	B	0.0732	0.2129	0.7139
16	19.09	B	0.1860	0.2110	0.6030
17	19.24	A	0.2852	0.3465	0.3683
18	19.35	B	0.2512	0.1011	0.6477

To examine the significance of any substructure for the red galaxies, the non-parametric cluster analysis method described by Pisani (1993, 1996) is applied. This is based upon estimating the underlying probability density, $F(x)$, of a data sample $D_N = \{x_1, x_2, \dots, x_N\}$ using an iterative and adaptive kernel method. Each data point, x_i , is initially smoothed by a Gaussian kernel of width σ to produce a pilot fixed-kernel estimate of the local density, $f_p(x_i)$, at each point. The optimal value for the smoothing parameter σ is determined by minimizing the integrated square error (ISE), (f_p) , of the estimation of $F(\bar{x})$. It is possible to show (see Silverman 1986) that minimizing the cross-validation, $M(f_p)$, a function related to ISE(f_p), and that can be written as a sum of functions dependent only on the x_i , is equivalent to minimizing ISE(f_p). The pilot local density estimate is then used to adapt the amount of smoothing applied to each point through $\sigma_i = \sigma[f_p(x_i)/\bar{f}_p]^{-1/2}$, where \bar{f}_p is the geometric mean of the $f_p(x_i)$. The adaptive kernel estimate of the local density $f_a(x)$ is then

$$f_a(x) = \frac{1}{N} \sum_{i=1}^N \frac{1}{2\pi\sigma_i^2} \exp\left(-\frac{1}{2} \frac{|x - x_i|^2}{\sigma_i^2}\right). \quad (1)$$

The adaptive kernels produce both a higher resolution in the clustered regions where it is needed, and increased smoothing in the low-density regions (see Silverman 1986; Pisani 1993; 1996 for detailed discussion), and the non-parametric nature of the method means that the amount of smoothing is dependent solely upon the data points, rather than any prior estimate of what the cluster width should be. The probability density estimate of red galaxies is shown in Fig. 6 with the two density peaks, marked A and B, which are assumed to mark the two cluster centres.

Having produced the probability density estimate, each galaxy is assigned membership to one of the clusters by following a path from the original position x_i along the maximum gradient of $f_a(x)$ until it reaches the local maximum A or B. The contribution to the local density from each cluster, $f_A(x)$, $f_B(x)$, is then taken to be the sum of the kernels for galaxies assigned to that cluster.

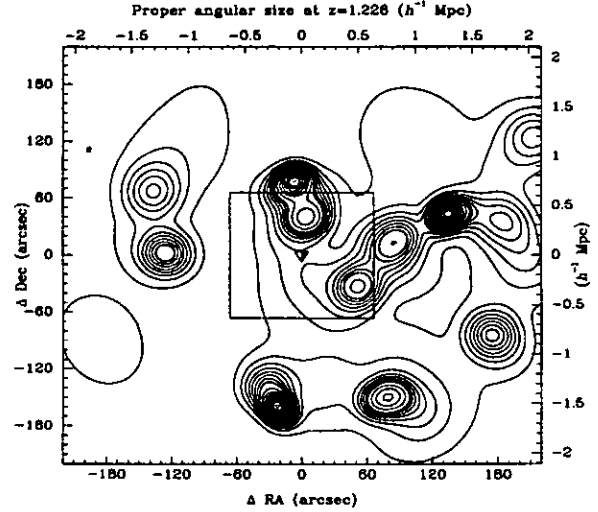


Figure 7. Contour plot of the estimated density distribution of optically red ($V - I \geq 2.25$, $I < 23$) galaxies (including all C-M relation members) in a 7×7 arcmin² (corresponding to $4.06 \times 4.06 h^{-2}$ Mpc² at $z = 1.226$) field centred on the quasar. The first contour corresponds to a density of one galaxy per square arcminute, and the separation of successive contours is also one galaxy per square arcminute. The quasar is marked as previously, and the central box corresponds to the field of the K image.

The expected background contamination from red field galaxies, $f_0(x)$, is unknown, and so we have estimated it to be half that of the $I - K > 3.75$ field galaxies, or 0.5 galaxies per square arcminute, as about half our $I - K > 3.75$ galaxies are also classified as red ($I - K > 3.75$, $V - I > 2.00$). The probability that each galaxy is isolated, and hence is a result of the background component, is just the fractional contribution of the background density to the local density $P(i \in 0) = f_0/f_a(x_i)$. The probability that galaxy i is a member of cluster A is then the fractional contribution of cluster A to the local density, after considering the background contribution $P(i \in A) = [1 - P(i \in 0)] f_A(x_i)/f_a(x_i)$, and for each of the red galaxies these probabilities are shown in Table 3. Looking at this table and Fig. 6, it appears that the two clusters are well defined; 11 out of the brightest 14 galaxies have probabilities greater than 0.90 of having been assigned correctly to cluster A or B. Only galaxies No. 4 and No. 10 have significant doubt over cluster assignment, and No. 12 appears to be isolated, whilst the four faintest red galaxies show no clear membership of either cluster, and may only be part of the combined structure.

As a second estimate of the significance of the substructure, we examine the null hypothesis that the galaxies are all members of a single cluster. One method for examining the null hypothesis is the likelihood ratio test statistic (LRTS) (Ashman, Bird & Zeff 1994; Kreissler & Beers 1997) which evaluates the improvement in fitting the data of a two-component model over a single elliptical Gaussian probability density function. The best fitting single elliptical Gaussian $f_{(1)}(x)$ to the data is found using the mean, \bar{x} , and covariance matrix, \mathbf{A} , of the data, and this unimodal probability density function is used to create 10 000 bootstrap catalogues of 18 galaxies each. The adaptive kernel estimator is applied to each bootstrap catalogue in the same way as the original data, and for those catalogues where bimodality is observed, the cluster membership probabilities $P(i \in \mu)$, for $i = 1, \dots, N$; $\mu = 1, 2$ are calculated. The probable number of galaxies in cluster μ

is then given by $n_\mu = \sum_{i=1}^N P(i \in \mu)$. The best fitting double Gaussians, $f_{(g;\mu)}(x)$, can then be found using the means, \bar{x}_μ , and covariance matrices, \mathbf{A}_μ , of the data set weighted by $P(i \in \mu)$ for $\mu = 1, 2$, before normalizing to $\int_{\mathcal{R}} f_{(g;\mu)}(x) dx = n_\mu$. The measure of the fit by the g -component model is evaluated through the likelihood value

$$L_C(g) = \prod_{i=1}^N \left[\sum_{\mu=1}^R f_{(g;\mu)}(x_i) \right]^{1-P(i \in 0)} \quad (2)$$

The evaluation of the improvement in going from a single- to a double-Gaussian fit is then given by the LRTS $\lambda = -2 \ln \{L_C(2)/L_C(1)\}$. The significance of the substructure observed is estimated by the probability that a null hypothesis bootstrap catalogue produces a value of λ greater than the observed value. For the observed distribution, using 10 000 bootstrap catalogues, we find that the substructure is marginally inconsistent with the null hypothesis at the 8.88 per cent significance level. The low level of significance is due to the small number of galaxies involved, as many of the more significant substructures among the bootstrap catalogues were due to just three or four points that were within a few arcsec of one another.

3.3.2 Clustering across large scales

As both groups are located near the edges of the K image, and so may suffer from truncation, the full extent of clustering associated with the quasar is estimated by considering a 7×7 arcmin² field centred on the quasar from the BTC V and I images. Fig. 2 indicates that any $z \gtrsim 1$ quiescent galaxies should be amongst the reddest galaxies in $V - I$, and so by selecting those galaxies with $V - I > 2.25$ the density contrast arising from any clustering at $z \approx 1.2$ should be maximized. Note that this selection criterion is slightly redder than the $V - I > 2.00$ selection used previously, in order to reduce the contamination of intermediate-redshift quiescent galaxies. In the region covered by the K image, only the red galaxies are selected, including the three with $2.00 < V - I < 2.25$. The estimated density distribution of $V - I > 2.25$, $I < 23$ galaxies is shown in Fig. 7, and it is clear that the clustering extends well beyond the K image. Cluster A now appears to be centred on the northern edge of the K image, and cluster B appears to be part of an elongated structure which extends 2–3 arcmin to the north-east. Two further groups, each of 6–10 optically red galaxies, are apparent 3 arcmin south of the quasar and 1.5 arcmin apart. The significance of the substructure formed by clusters A and B appears to be much higher now, as the density peaks are moved further apart. A re-examination of the null hypothesis, after including the $V - I > 2.25$ galaxies outside the K image, finds the substructure to be inconsistent with the null hypothesis at the 1.86 per cent significance level. The increase in significance suggests that the clusters were truncated by the boundaries of the K image, but the increase is also due partly to the larger galaxy sample.

3.3.3 Companion galaxies to the quasar host

There are two galaxies (labelled C1 and C2 in Fig. 5) that are only 3 arcsec ($12.9 h^{-1}$ kpc) from the quasar, and could well be companion galaxies to the quasar galaxy host. Compact companions are found for a significant fraction of quasars (e.g. Bahcall et al. 1997) and spectroscopic observations confirm that many have stellar populations and redshifts within 500 km s^{-1} of

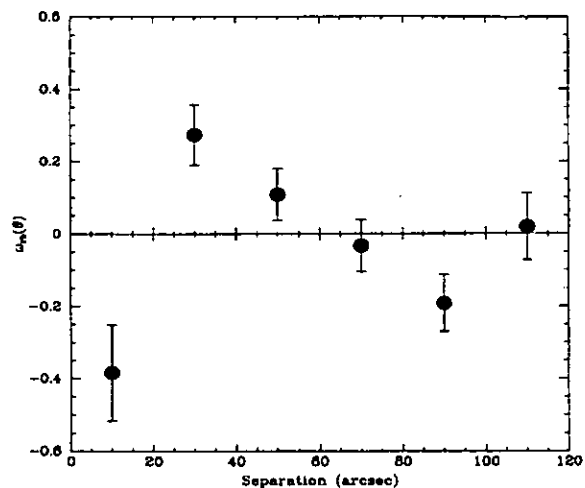


Figure 8. The angular cross-correlation, $w_{rb}(\theta)$, between red ($V - I > 2.00$, $I - K > 3.75$) and blue ($V - I < 1.00$) galaxies in the field covered by the K image. The errors are assumed to be Poissonian with variance $N_{rb}(\theta)$.

the quasar (e.g. Stockton 1982; Canalizo & Stockton 1997). It has been suggested (e.g. Stockton 1982; Bekki 1999) that these companion objects are tidally stripped cores from galaxies that have recently interacted with the quasar host galaxies, and that this interaction provides an efficient fuelling mechanism for quasar activities. Spectroscopic analysis of the companion to quasar PG 1700+518 (Canalizo & Stockton 1997) finds evidence for both a starburst event that occurred roughly 100 Myr ago (and so could be coincident with the quasar activation), and a relatively old stellar population likely to be from the merger progenitor disc. The galaxies C1 and C2 are bluer than the red sequence galaxies (cf. C3), and so, if associated with the quasar, they have undergone a recent episode of star formation, presumably caused by the merger process.

3.3.4 Blue galaxies

To compare this quasar field with the results of HCJ we have also examined the distribution of blue ($V - I < 1$) galaxies for $I < 25$ (indicated by star symbols in Fig. 5). We find a concentration of blue galaxies within 30 arcsec ($290 h^{-1}$ kpc) of the quasar, which appears to be extended towards the north-east, forming a ‘band’ that bisects the two groups of red galaxies. The band presumably corresponds to a region of enhanced star formation. Few, however, are found near the centres of either group of red galaxies. In comparison with adjacent fields (over a 7×7 arcmin² region) in the optical images we do not find an excess of blue galaxies.

To examine the relative spatial distribution of red and blue galaxies, the angular cross-correlation function, $w_{rb}(\theta) = N_{rb}(\theta)/N_{rR} - 1$, is determined (see Fig. 8), where $N_{rb}(\theta)$ is the number of red–blue galaxy pairs with separation θ , and $N_{rR}(\theta)$ is the expected number of pairs with one member from the red catalogue and the other from one of 10 000 randomly distributed catalogues.

At small separations ($\theta < 20$ arcsec), the red and blue galaxies are strongly anti-correlated at the 3σ level, confirming the apparent avoidance of the red groups by the blue galaxies in Fig. 5. In contrast, for $20 < \theta < 60$ arcsec, there is a correlation at the 3σ

level between red and blue galaxies, which is due to the 'band' of blue galaxies that bisects the two groups of red galaxies.

The blue galaxies do not contribute to the excess of galaxies observed at $K < 19$, as only nine of 51 are detected in K , the brightest having $K = 18.87$. These nine all have the red $I - K$ colours indicative of $z \geq 1$ galaxies (e.g. Fig. 3d), and six of the nine help make up the concentration ≈ 30 arcsec from the quasar, which suggests that this at least is real. However, given that the $V - I$ colour is affected much more by recent star formation than redshift, we cannot say anything about the likely redshift of the remaining blue galaxies.

4 DISCUSSION AND CONCLUSIONS

We have found a 3.5σ excess of $K < 19$ galaxies in the 2.25×2.25 arcmin² field around the $z = 1.226$ radio-quiet quasar 104420.8+055739 from the Clowes–Campusano LQG. The excess is due entirely to a factor of ~ 11 overdensity of red ($I - K > 3.75$) galaxies, which must have $z \geq 0.8$ to explain their colour. In particular, we find cluster red sequences of 15–18 galaxies, in the $I - K$ and $V - K$ against K C–M diagrams at $I - K \approx 4.3$, $V - K \approx 6.9$, comparable in both colour and magnitudes to red sequences observed for other $z \approx 1.2$ clusters. These red sequences suggest a population of massive ellipticals at the quasar redshift. In the area of the K image we find tentative evidence of substructure amongst these galaxies, with two apparent groups 40 arcsec to the north and 60 arcsec to the south-east of the quasar. An examination of the optical images over a 7×7 arcmin² area indicates that this substructure is significant at the 2 per cent level, and that the clustering extends well beyond the K image, forming a large-scale structure $2\text{--}3 h^{-1}$ Mpc across. The overall structure is suggestive of being the early stages of formation of a cluster from the progressive coalescence of subclusters.

Only half of the excess of $I - K > 3.75$ galaxies is accounted for by the red sequence members, and we find comparable numbers (15–20) of 'red outlier' galaxies with both $I - K > 3.75$ and $V - I < 2.00$, which appear to fit neither the passively evolving nor exponentially decaying SFR galaxy models (Fig. 2). All we can say is that they are likely to be dusty star-forming galaxies at $1 \lesssim z \lesssim 2$; given that such galaxies are found around other $z \approx 1.2$ clusters (e.g. T00; Kajisawa et al. 1999; 2000), and given their comparative rarity in field regions, it seems reasonable to assume that they are associated with the cluster. This would suggest that the Butcher–Oemler effect (Butcher & Oemler 1978, 1984) observed in intermediate-redshift clusters increases in strength to higher redshifts, with ≈ 50 per cent of likely cluster members exhibiting the blue colours of recent star formation.

We also find a concentration of blue ($V - I < 1$) galaxies within 30 arcsec ($130 h^{-1}$ kpc) of the quasar, with many having the red $I - K$ colours of $z \geq 1$ galaxies, which suggests that the quasar lies in a region of enhanced star formation, in agreement with the results of HCJ. This concentration appears extended in such a way as to separate the two groups of red galaxies, and it is also notable how the blue galaxies appear to avoid the centres of red galaxy clustering. Some foreground contamination is likely, but given that such concentrations appear common around LQG quasars at this redshift, and the highly significant spatial interrelation between the blue and red galaxies, then we can be reasonably confident that this concentration is real, and is associated with the quasar. However, spectroscopic observations

of these and the other cluster candidates will be required to confirm cluster membership and to provide more quantitative information about their star formation histories, such as their approximate ages and current star formation rates.

4.1 A possible cluster merging event

The relative distribution of red and blue galaxies can be explained if we are witnessing the early stages of the merging of the two clusters of red galaxies, which has triggered both the band of enhanced star formation and the quasar itself. A comparable distribution has been observed for the Coma cluster (Caldwell et al. 1993) with a band of post-starburst or 'E + A' galaxies located between the Coma cluster centre and a secondary X-ray peak. Dynamical studies (Burns et al. 1994) indicated that these galaxies had passed through the centre of the Coma cluster about 2 Gyr ago, coincident with the epoch of starbursting predicted from the spectra of the post-starburst galaxies. Unusually high blue galaxy fractions have been observed for a number of low-redshift clusters with bimodal X-ray surface brightness profiles (Metevier, Romer & Ulmer 2000), implying that cluster mergers can induce starbursts simultaneously in a large fraction of cluster galaxies, and they could be a major contributor to the Butcher–Oemler effect. Several mechanisms have been suggested that could cause at first the triggering, and then the termination of a secondary burst of star formation in a galaxy, as a subcluster passes through a cluster. These include ram pressure from the intra-cluster medium (ICM) (Evrard 1991), shocks due to collisions between the two ICMs (Roettiger, Burns & Loken 1996), and the effect of close galaxy encounters (Moore et al. 1996). As the 'band' of blue galaxies is likely to be undergoing, or has recently undergone, star formation, and because the two groups are relatively close together, we suggest that this system is being observed at an earlier epoch of the cluster merger process than Caldwell et al. (1993), either just before or just after core passage, and that the star formation has been triggered by the interaction of galaxies with the shock fronts produced by the collision of the two ICMs (see Roettiger et al. 1996).

Cluster merging events are predicted to be relatively common at high redshifts ($z \geq 1$) in hierarchical clustering models (e.g. Press & Schechter 1974; Bahcall, Fan & Cen 1997; Percival & Miller 1999). Examples of possible merging clusters at high redshifts are the CL0023+00423 groups at $z = 0.8274$ and 0.8452 which, according to a dynamical study, have a 20 per cent chance of merging (Lubin, Postman & Oke 2000), and the R99 and S97 clusters which are separated by only $2.5 h^{-1}$ Mpc.

4.2 Comparison with other work

In a study of seven radio-loud quasars at $1.0 < z < 1.6$, Sánchez & González-Serrano (1999) find excesses of faint ($B > 22.5$ and $R > 22.0$) galaxies on scales of $r < 170$ and $r < 35$ arcsec around the quasars, whose numbers, magnitudes and angular extensions are compatible with being clusters of galaxies at the quasar redshifts. In particular, however, they find that the quasars are in general not located at the peaks of the density distribution, but are some 40–100 arcsec from them, located on the cluster peripheries. This result, and our own, is understandable in the framework of quasar activity being triggered by the infall of gas on to a seed black hole. First, galaxies in the centres of clusters have previously lost most or all of their gas, by having had it stripped off by ram-pressure from the ICM or by tidal forces from close

encounters with other galaxies, or by consuming the gas in a starburst during its first infall into the cluster. Secondly, the encounter velocities for galaxies in the cluster cores greatly exceed the internal velocity distribution of the galaxies, making galaxy mergers much less effective at triggering nuclear activity (Aarseth & Fall 1980).

In a comparable study of the galaxy environment of the radio-loud quasar 1335.8+2834 from the $z \sim 1.1$ Crampton et al. (1989) LQG, Tanaka et al. (2000) obtain results which have several similarities to our own. This quasar had been part of the HCJ study, and was known to lie in a band of blue and emission-line galaxies. Using deep R , I and K observations, a number of extremely red objects with the colours of passively evolving galaxies at the quasar redshift were found, forming a cluster which lies to one side of both the quasar and the band of blue and emission-line galaxies. They also find a similar population of 'red outliers' and estimate the blue galaxy fraction as 60–80 per cent. They also find an indication that this cluster is part of a larger structure with groupings of optically red ($R - I > 1.3$) galaxies, similar to the clustering near the quasar, found across the 8×8 arcmin² ($4.7 \times 4.7 h^{-2}$ Mpc² at $z = 1.086$) R , I optical images.

In a wide-field (48×9 arcmin²) optical imaging survey of the 1338+27 field containing five quasars from the Crampton et al. (1989) LQG, Tanaka et al. (2001) detect significant clustering of faint red galaxies with $I > 21$ and $R - I > 1.2$. These galaxies are concentrated in 4–5 clusters forming a linear structure of extent $\sim 10 h^{-1}$ Mpc that is traced by the group of quasars, although only the one radio-loud quasar of T00 appears to be directly associated with any of the rich clusters. The immediate environments of the other four LQG quasars, all radio-quiet, appear relatively poor in terms of red galaxies, although three have excesses of blue and emission-line galaxies (HCJ) indicating that they are located within regions of enhanced star formation. This is the clearest evidence yet that LQGs trace large-scale structure, even if the majority of the member quasars are only directly associated with regions of enhanced star formation, rather than rich clusters.

4.3 Interpretation – mechanisms for quasar formation

As several of the HCJ quasars were found in regions of enhanced star formation, and as both the quasar of T00 and this paper are located in 'bands' of enhanced star formation, in between, or on the peripheries of, clusters, we propose a causal link between the quasar and star formation whereby both are triggered by the same mechanism: the interaction between the galaxy and the intra-cluster medium. If a galaxy can be disrupted sufficiently by its passage through the ICM to cause it to undergo starbursting, then if it also contains a supermassive black hole, enough gas may be channelled on to the nucleus to trigger a phase of quasar activity. Such a mechanism explains the finding of quasars in regions of enhanced star formation more naturally than the galaxy merger model, as it allows many galaxies to be affected simultaneously, although there is good evidence that a large fraction of quasars have been triggered by galaxy mergers. If there is a connection between the quasar and star formation activation, then it is likely that these quasars are found preferentially in clusters with high blue galaxy fractions, and that these are not representative of $z \approx 1.2$ clusters as a whole.

This work and previous studies show that searching for sources with the $I - K > 3.75$ colours characteristic of quiescent galaxies at $z \approx 1$ is an efficient means of locating $z \approx 1$ clusters. By adding a second optical band it is then possible to obtain qualitative

information on the star formation history of these galaxies. Using this information along with the relative spatial distribution of quiescent and star-forming galaxies, a more complex picture arises in which the evolutions of galaxies, quasars and clusters are all interrelated.

ACKNOWLEDGMENTS

The optical data were obtained with the CTIO 4-m Blanco telescope, and the data reduced with IRAF and the UK Starlink facilities. Advice regarding the removal of distortions from the BTC images was given by Gary Bernstein and Tony Tyson. Roser Pelló provided the photometric redshift estimation software HYPERZ, and gave advice regarding its use and models. CPH acknowledges a PPARC studentship, and the Universidad de Chile and CTIO for their hospitality during his stay in Chile. LEC was partially supported by FONDECYT grant 1970735. We thank the referee for helpful comments regarding the statistics. IRAF is distributed by the National Optical Astronomy Observatories which is operated by the Association of Universities for Research in Astronomy, Inc. (AURA) under cooperative agreement with the National Science Foundation.

REFERENCES

- Aarseth S. J., Fall S. M., 1980, *ApJ*, 236, 43
 Aragón-Salamanca A., Ellis R. S., Couch W. J., Carter D., 1993, *MNRAS*, 262, 764
 Ashman K. M., Bird C. M., Zeff S. E., 1994, *AJ*, 108, 2348
 Bahcall J. A., Kirshner S., Saxe D. H., Schneider D. P., 1997, *ApJ*, 479, 642
 Bahcall N. A., Fan X., Cen R., 1997, *ApJ*, 485, L53
 Bekki K., 1999, preprint (astro-ph/9904044)
 Bertin E., Arnouts S., 1996, *A&AS*, 117, 393
 Bolzonella M., Miralles J.-M., Pelló R., 2000, *A&A*, 363, 476
 Bower R. G., Lucey J. R., Ellis R. S., 1992, *MNRAS*, 254, 601
 Bruzual G., Charlot S., 1993, *ApJ*, 405, 538
 Burns J. O., Roettiger K., Ledlow M., Klypin A., 1994, *ApJ*, 427, 87
 Butcher H., Oemler A., Jr, 1978, *ApJ*, 226, 559
 Butcher H., Oemler A., Jr, 1984, *ApJ*, 285, 426
 Caldwell N., Rose J. A., Sharples R. M., Ellis R. S., Bower R. G., 1993, *AJ*, 106, 473
 Calzetti D., Armus L., Bohlin R. C., Kinney A. L., Koornneef J., Storchi-Bergmann T., 2000, *ApJ*, 533, 682
 Canalizo G., Stockton A., 1997, *ApJ*, 480, 5
 Clowes R. G., Campusano L. E., 1991, *MNRAS*, 249, 218
 Clowes R. G., Campusano L. E., 1994, *MNRAS*, 266, 317
 Clowes R. G., Campusano L. E., Graham M. J., 1999, *MNRAS*, 309, 48
 Cowie L. L., Gardner J. P., Hu E. M., Songaila A., Hodapp K. W., Wainscoat R. J., 1994, *ApJ*, 434, 114
 Crampton D., Cowley A. P., Hartwick F. D. A., 1987, *ApJ*, 314, 129
 Crampton D., Cowley A. P., Hartwick F. D. A., 1989, *ApJ*, 345, 59
 Daddi E., Cimatti A., Pozzetti L., Hoekstra H., Röttgering H. J. A., Renzini A., Zamorani G., Mannucci F., 2000, *A&A*, 361, 535
 Dey A., Graham J. R., Ivison R. J., Smail I., Wright G. S., Liu M. C., 1999, *ApJ*, 519, 610
 Dickinson M., 1995, in Buzzoni A., Renzini A., Serrano A., eds, *ASP Conf. Ser. Vol. 86, Fresh View of Elliptical Galaxies*. Astron. Soc. Pac., San Francisco, p. 286 (D95)
 Dickinson M., 1997, in Tanvir N. R., Aragón-Salamanca A., Wall J. V., eds, *HST and the High Redshift Universe*. World Scientific, Singapore, p. 207
 Eggen O. J., Lynden-Bell D., Sandage A. R., 1962, *ApJ*, 136, 748
 Ellingson E., Yee H. K. C., Green R. F., 1991, *ApJ*, 371, 49
 Evrard A. E., 1991, *MNRAS*, 248, 8
 Graham J. R., Dey A., 1996, *ApJ*, 471, 720

- Graham M. J., Clowes R. G., Campusano L. E., 1995, *MNRAS*, 275, 790
Hall P. B., Green R. F., 1998, *ApJ*, 507, 558
Hu E. M., Ridgway S. E., 1994, *AJ*, 107, 1303
Hutchings J. B., Crampton D., Johnson A., 1995, *AJ*, 109, 73 (HCl)
Hutchings J. B., Crampton D., Persram D., 1993, *AJ*, 106, 1324 (HCP)
Kajisawa M., Yamada T., 1999, *PASJ*, 51, 719
Kajisawa M. et al., 2000, *PASJ*, 52, 61
Komberg B. V., Kravtsov A. V., Lukash V. N., 1996, *MNRAS*, 282, 713
Komberg B. V., Lukash V. N., 1994, *MNRAS*, 269, 277
Kriessler J. R., Beers T. C., 1997, *AJ*, 113, 80
Lubin L. M., Postman M., Oke J. B., 2000, *AJ*, 116, 643
Metevier A. J., Romer A. K., Ulmer M. P., 2000, *AJ*, 119, 1090
Miller G. E., Scalo J. M., 1979, *ApJS*, 41, 513
Moore B., Katz N., Lake G., Dressler A., Oemler A., 1996, *Nat*, 379, 613
Moustakas L. A., Davis M., Graham J. R., Silk J., Peterson B. A., Yoshii Y., 1997, *ApJ*, 475, 445
Percival W., Miller L., 1999, *MNRAS*, 309, 823
Pisani A., 1993, *MNRAS*, 265, 706
Pisani A., 1996, *MNRAS*, 278, 697
Press W., Schechter P., 1974, *ApJ*, 454, 69
Roche N., Eales S. A., Hippelein H., Willott C. J., 1999, *MNRAS*, 306, 538
Roettiger K., Burns J. O., Loken C., 1996, *ApJ*, 473, 651
Rosati P., Stanford S. A., Eisenhardt P. R., Elston R., Spinrad H., Stern D., Dey A., 1999, *AJ*, 118, 76 (R99)
Sánchez S. F., González-Serrano J. I., 1999, *A&A*, 352, 383
Silverman B. W., 1986, *Density Estimation for Statistics and Data Analysis*. Chapman & Hall, London
Songaila A., Cowie L. L., Hu E. M., Gardner J. P., 1994, *ApJS*, 94, 416
Stanford S. A., Eisenhardt P. R., Dickinson M., 1998, *ApJ*, 492, 461
Stanford S. A., Elston R., Eisenhardt P. R., Spinrad H., Stern D., Dey A., 1997, *AJ*, 114, 2232 (S97)
Stockton A., 1982, *ApJ*, 257, 33
Tanaka I., Yamada T., Aragón-Salamanca A., Kodama T., Miyaji T., Ohta K., Arimoto N., 2000, *ApJ*, 528, 123 (T00)
Tanaka I., Yamada T., Turner E. L., Suto Y., 2001, *ApJ*, 547, 521
Webster A., 1982, *MNRAS*, 199, 683
Yamada T., Tanaka I., Aragón-Salamanca A., Kodama T., Ohta K., Arimoto N., 1997, *ApJ*, 487, L125

This paper has been typeset from a \TeX/L\AA\TeX file prepared by the author.